Biological and Medical Physics, Biomedical Engineering

Karol Miller *Editor*

Biomechanics of the Brain

Second Edition

Springer

BIOLOGICAL AND MEDICAL PHYSICS, BIOMEDICAL ENGINEERING

BIOLOGICAL AND MEDICAL PHYSICS, BIOMEDICAL ENGINEERING

The fields of biological and medical physics and biomedical engineering are broad, multidisciplinary and dynamic. They lie at the crossroads of frontier research in physics, biology, chemistry, and medicine. The Biological and Medical Physics, Biomedical Engineering Series is intended to be comprehensive, covering a broad range of topics important to the study of the physical, chemical and biological sciences. Its goal is to provide scientists and engineers with textbooks, monographs, and reference works to address the growing need for information.

Books in the series emphasise established and emergent areas of science including molecular, membrane, and mathematical biophysics; photosynthetic energy harvesting and conversion; information processing; physical principles of genetics; sensory communications; automata networks, neural networks, and cellular automata. Equally important will be coverage of applied aspects of biological and medical physics and biomedical engineering such as molecular electronic components and devices, biosensors, medicine, imaging, physical principles of renewable energy production, advanced prostheses, and environmental control and engineering.

More information about this series at http://www.springer.com/series/3740

Karol Miller
Editor

Biomechanics of the Brain

Second Edition

Springer

Editor
Karol Miller
Intelligent Systems for Medicine Laboratory
The University of Western Australia
Perth, WA, Australia

ISSN 1618-7210 ISSN 2197-5647 (electronic)
Biological and Medical Physics, Biomedical Engineering
ISBN 978-3-030-04995-9 ISBN 978-3-030-04996-6 (eBook)
https://doi.org/10.1007/978-3-030-04996-6

Foreword

Tempora mutantur, nos et mutamur in illis ('Times are changed, we also are changed with them'). While this Latin adage is often used in a political context, it is also true in science, where we are witnessing progress occurring at a rapid, accelerating pace.

The field of neuroscience has seen great advances during the last decade, driven by the progress in many enabling technological capabilities in topics including biomechanical modelling, neuroimaging, sensors, and biology. These advances are happening on a variety of scales, from the molecular, all the way up to macroscopic levels. Similarly, we have seen big changes in the field of biomechanics, with novel algorithmic approaches and greatly expanded simulation capabilities leading to new insights.

The second edition of *Biomechanics of the Brain* addresses this by providing an update on the current state of the art in the field. This update covers the progress made since the first edition of this book published in 2011. All chapters have been updated, and several chapters have been significantly expanded. Karol Miller, the editor, has added several new contributors to the team that brought us the first edition. New chapters have been added on topics which emerged during the last decade.

The second edition of *Biomechanics of the Brain* was written by an international team of experts and is intended for anybody interested in the topic. The book offers a comprehensive update for people in the field and a good introduction and reference for scientists new to the topic.

Surgical Planning Laboratory
Brigham and Women's Hospital and Harvard Medical School
Boston, Massachusetts, USA
University of Bremen, Germany
Fraunhofer MEVIS, Bremen, Germany

Ron Kikinis, M.D.

Contents

1 Introduction 1
Karol Miller

2 Human Brain Anatomy in 3D 5
Wieslaw L. Nowinski

3 Introduction to Brain Imaging 47
Einat Liebenthal and Tarun Singhal

4 Brain Tissue Mechanical Properties 71
Lynne E. Bilston

5 Modelling of the Brain for Injury Simulation and Prevention 97
King H. Yang and Haojie Mao

6 Biomechanical Modelling of the Brain for Neurosurgical Simulation and Neuroimage Registration 135
Karol Miller, Adam Wittek, Angus C. R. Tavner, and Grand Roman Joldes

7 Biomechanical Modelling of the Brain for Neuronavigation in Epilepsy Surgery 165
Karol Miller, Angus C. R. Tavner, Louis P. M. Menagé, Nicholas Psanoudakis, Grand Roman Joldes, Simon K. Warfield, Damon Hyde, and Adam Wittek

8 Dynamics of Cerebrospinal Fluid: From Theoretical Models to Clinical Applications 181
Laurent Geregele, Olivier Baledent, Romain Manet, Afroditi Lalou, Slawomir Barszcz, Magdalena Kasprowicz, Piotr Smielewski, John D. Pickard, Marek Czosnyka, and Zofia Czosnyka

9 Modelling of Cerebrospinal Fluid Flow by Computational Fluid Dynamics 215
Vartan Kurtcuoglu, Kartik Jain, and Bryn A. Martin

10 Finite Element Algorithms for Computational Biomechanics of the Brain 243
Adam Wittek, Grand Roman Joldes, and Karol Miller

11 Meshless Algorithms for Computational Biomechanics of the Brain 273
Adam Wittek, Grand Roman Joldes, and Karol Miller

12 Intra-operative Measurement of Brain Deformation 303
Sarah Frisken, Prashin Unadkat, Xiaochen Yang, Michael I. Miga, and Alexandra J. Golby

13 Computational Biomechanics of the Brain in the Operating Theatre 321
Hadrien Courtecuisse, Fanny Morin, Ingerid Reinertsen, Yohan Payan, and Matthieu Chabanas

Index 345

Chapter 1
Introduction

Karol Miller

The mechanical behaviour of living tissues continues to be the major topic of biomechanical investigations. Over the years a vast amount of knowledge about load-bearing tissues, such as bones, ligaments, muscles, and other components of the musculoskeletal system, blood vessels (and blood), lungs, skin, and hair, has been published in journals and books. The very soft tissues of organs whose role has little or nothing to do with transmitting mechanical loads had been, until recently, outside the scope of the mainstream biomechanical research. Extremely important organs such as the liver, kidneys, prostate and other abdominal organs, and especially the brain have been largely neglected by biomechanics.

Investigation of the mechanical properties of the brain began in the late 1960s. Ommaya described mammalian brain as a 'soft, yielding structure, not as stiff as a gel, nor as plastic as a paste' [1]. These first studies were motivated by the increasing number of traumatic brain injuries resulting from automotive accidents. The first finite element models of the brain appeared in the early 1980s. Since then, the biomechanics of the brain for injury analysis and prevention has been a very active area of research.

There is wide international concern about the cost of meeting rising expectations for health care, particularly if large numbers of people require currently expensive procedures such as brain surgery. Costs can be reduced by using improved machinery to help surgeons perform these procedures quickly and accurately, with minimal side effects. A novel partnership between surgeons and machines, made possible by advances in computing and engineering technology, could overcome many of the limitations of traditional surgery. By extending surgeons' ability to plan and carry out surgical interventions more accurately and with less trauma,

K. Miller (✉)
Intelligent Systems for Medicine Laboratory, The University of Western Australia, Perth, WA, Australia
e-mail: karol.miller@uwa.edu.au

K. Miller (ed.), *Biomechanics of the Brain*, Biological and Medical Physics, Biomedical Engineering, https://doi.org/10.1007/978-3-030-04996-6_1

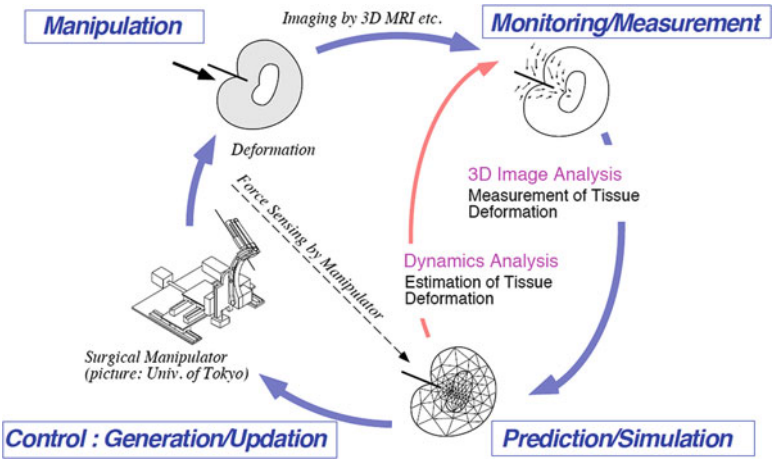

Fig. 1.1 A concept of the image-guided neurosurgical robot with the feed-forward loop based on the biomechanical model in the control system [2, 3]. The concept has not been realised in its entirety; however, it provided a strong stimulus for brain biomechanics research. (Image courtesy of Dr. Kiyoyuki Chinzei, AIST, Tsukuba, Japan)

computer-integrated surgery (CIS) systems could help to improve clinical outcomes and the efficiency of health-care delivery. CIS systems could have a similar impact on surgery to that long since realised in computer-integrated manufacturing (CIM). Recent developments in robotics technology, especially the emergence of automatic surgical tools and robots and advances in virtual reality techniques, have motivated the latest interest in the biomechanics of the brain. An understanding of the brain biomechanics can be used for surgical simulation, computer-integrated and image-guided neurosurgery, and as a supporting tool for diagnosis and prognosis of brain disease.

The initial stimulus for this line of research was provided by the visionary project aiming at designing an image-guided neurosurgical robot. This project was conducted in 1995–1996 at Biomechanics Division of Mechanical Engineering Laboratory, AIST, in Tsukuba, Japan. Figure 1.1 above provides the overview of that project.

Significantly increased interest in the biomechanics of soft tissues, and in particular the brain, as evidenced by the increased number of publications in this area, warrants an attempt to summarise recent developments in the form of a book. This second edition of *Biomechanics of the Brain* brings the current state of the art in the biomechanics of the brain to the reader. I have attempted to include all relevant aspects of biomechanical modelling that have progressed beyond initial investigations and attained a certain level of maturity, as well as the fields of their application. I have insisted that chapter contributors present the current state of the art in their specific fields in an authoritative way. Therefore, some of the newest and still tentative developments (e.g. the biomechanics of cortical folding) have been intentionally omitted.

Biomechanics researchers new to the field often come with an engineering or physics background. I hope these readers will benefit from the introductory chapters on brain anatomy (Chap. 2) and brain imaging (Chap. 3). The information contained in these primers should be easily digestible by readers with no medical background and save them a considerable amount of time spent studying the specialised literature in these fields.

Chapter 4 discusses mechanical properties of brain tissues. The knowledge of these properties is a prerequisite for the development of biomechanical models of the brain.

Chapter 5 describes mathematical modelling and computer simulation of the brain for injury prevention, and Chap. 6 considers brain modelling issues for applications in image-guided surgery for brain tumours and surgical simulation. Chapter 7 extends the methods described in Chaps. 5 and 6 to challenging problem of epileptic seizure onset zone localisation.

Mathematical modelling and computer simulation have proven tremendously successful in engineering. Computational mechanics has enabled technological developments in virtually every area of our lives. One of the greatest challenges for mechanists is to extend the success of computational mechanics to fields outside traditional engineering, in particular to biology, biomedical sciences, and medicine [4]. Chapters 5, 6, and 7 demonstrate that in computational sciences, the most critical step in the solution of the problem is the selection of the physical and mathematical model of the phenomenon to be investigated. Model selection is a heuristic process, based on the analyst's judgment and experience. Often, model selection is a subjective endeavour; different modelers may choose different models to describe the same reality. Nevertheless, the selection of the model is the single most important step in obtaining valid computer simulations of any investigated reality [4].

Chapter 8 discusses the biomechanics of blood and cerebrospinal fluid flow through the brain and the dynamics of intracranial pressure. Unlike the results presented in Chaps. 5, 6, and 7, the findings described in Chap. 8 have already found their way into the clinical practice and care of brain injury and disease sufferers.

Chapter 9 describes the most recent developments in computational fluid dynamics of cerebrospinal fluid and blood flow. This field will very soon strengthen the more heuristic, clinically applicable methods described in Chap. 8.

Often very large and complicated computations are required to extract reliable information from comprehensive, highly nonlinear biomechanical models of the brain. Chapters 10 and 11 describe the current best practice in selection of computational methods for solving models described in Chaps. 5, 6, and 7. This is probably the most technical part of the book. The reader will require a sound understanding of numerical methods for partial differential equations, both finite element and meshless, to fully appreciate these chapters.

This book would not have been possible without the contributions, goodwill, and help of many people. I thank the authors of the chapters for donating their unique

expertise and time to create the content of this book. Each chapter has been reviewed by at least two reviewers. Their most valuable input has contributed enormously to this project. I would also like to acknowledge the Springer editorial staff, without whom this book would not have been possible.

References

1. Ommaya, A.K.: Mechanical properties of tissues of the nervous system. J. Biomech. **1**, 127–138 (1968)
2. Miller, K., Chinzei, K.: Modeling of soft tissues deformation. J. Computer. Aided. Surg. **1**(Supl., Proceedings of Second International Symposium on Computer Aided Surgery, Tokyo Women's Medical College, Shinjuku, Tokyo)), 62–63 (1995)
3. Miller, K., Chinzei, K.: Modeling of soft tissues. Mech. Eng. Lab. News. **11**, 5–7 (1995)
4. Oden, J.T., Belytschko, T., Babuska, I., Hughes, T.J.R.: Research directions in computational mechanics. Comput. Methods Appl. Mech. Eng. **192**, 913–922 (2003)

Chapter 2
Human Brain Anatomy in 3D

Wieslaw L. Nowinski

2.1 Introduction

The animal central nervous system (CNS) has been evolved over the last 600 million years, and the human CNS is the most complex living organ in the known universe. The CNS has been extensively investigated, particularly over a few last centuries, and a vast body of materials, resources, and data have been gathered in the print form and more recently also in electronic format. Neuroanatomy is presented in numerous textbooks [1–22], print brain atlases [23–51], and electronic brain atlases [52–74]. Several textbooks combine text with atlases [14, 15, 43, 44], and some provide neuroanatomy for various specialties including neurosurgery [1, 19, 22], neuroradiology [8, 17, 20], neurology [2], and neuroscience [18].

The comprehension of neuroanatomy is crucial in any neurosurgical, neuroradiological, neuro-oncological, or neurological procedure. Therefore, CNS anatomy has been intensively studied by generations of neuroanatomists, neuroscientists, neurosurgeons, neurologists, neuroradiologists, neurobiologists, psychologists, and psychologists, among others, including Renaissance artists. These efforts resulted, however, in neuroanatomy discrepancies, inconsistencies, and even controversies among various communities in terms of parcellation (subdivision), demarcation, grouping, terminology, and presentation.

This work differs from the existing neuroanatomy primers. Our overall objective is to make the presentation and understanding of human brain anatomy quick and easy. In order to achieve this objective:

W. L. Nowinski (✉)
John Paul II Center for Virtual Anatomy and Surgical Simulation, University of Cardinal Stefan Wyszynski, Warsaw, Poland

Department of Radiology, University of Washington, Seattle, WA, USA
e-mail: w.nowinski@uksw.edu.pl

K. Miller (ed.), *Biomechanics of the Brain*, Biological and Medical Physics, Biomedical Engineering, https://doi.org/10.1007/978-3-030-04996-6_2

- The presentation of neuroanatomy is in three dimensions (3D) with additional supportive planar images in the orthogonal (axial, coronal, and sagittal) planes.
- The brain is subdivided into structure, vasculature, and connections (white matter tracts); consequently, we consider structural, vascular, and connectional neuroanatomies.
- 3D cerebral models of structure, vasculature, and tracts are mutually consistent spatially, because they were derived from the same brain living specimen.
- 3D cerebral models and the planar images are fully parcellated; each parcellated object is uniquely colored.
- 3D cerebral models and the planar images are completely labelled (named); as a terminology we use the *Terminologia Anatomica* [75].
- 3D cerebral models are electronically dissectible into modules, groups, and individual components allowing the atlas user for a fast scene composing (structure assembly and/or disassembly).

In this work I use my digital brain atlases that have been developed for more than two decades [63–69] (see the recent editorial [117]). The 3D cerebral models have been created from multiple 3 and 7 Tesla magnetic resonance scans of my brain [69]. The development of the atlases is addressed in [78–82], tools for their creation in [77], techniques for modelling of cerebral structures in [76, 78, 92], and atlas-based applications in [79–91].

The recent (i.e. from the first edition of this book) developments in our brain atlasing are covered in [93–116], including the extension of the virtual brain to the head and neck. They also contain an overview of computational and mathematical methods for brain atlasing [115] and future directions [116].

2.2 Structural (Gross) Neuroanatomy

We present parcellation (subdivision) of the brain in 3D followed by sectional neuroanatomy. The stereotactic target structures and functional cortical areas also are outlined.

2.2.1 Brain Parcellation

The central nervous system consists of the *brain* and the *spinal cord*. The brain encases the fluid-filled *ventricular system* and is parcellated into three main components[1] (Fig. 2.1a):

[1] We follow here the brain parcellation as in, e.g. [16]. Some other sources (e.g. [18]) subdivide the brain into the cerebrum, diencephalon, cerebellum, and brainstem.

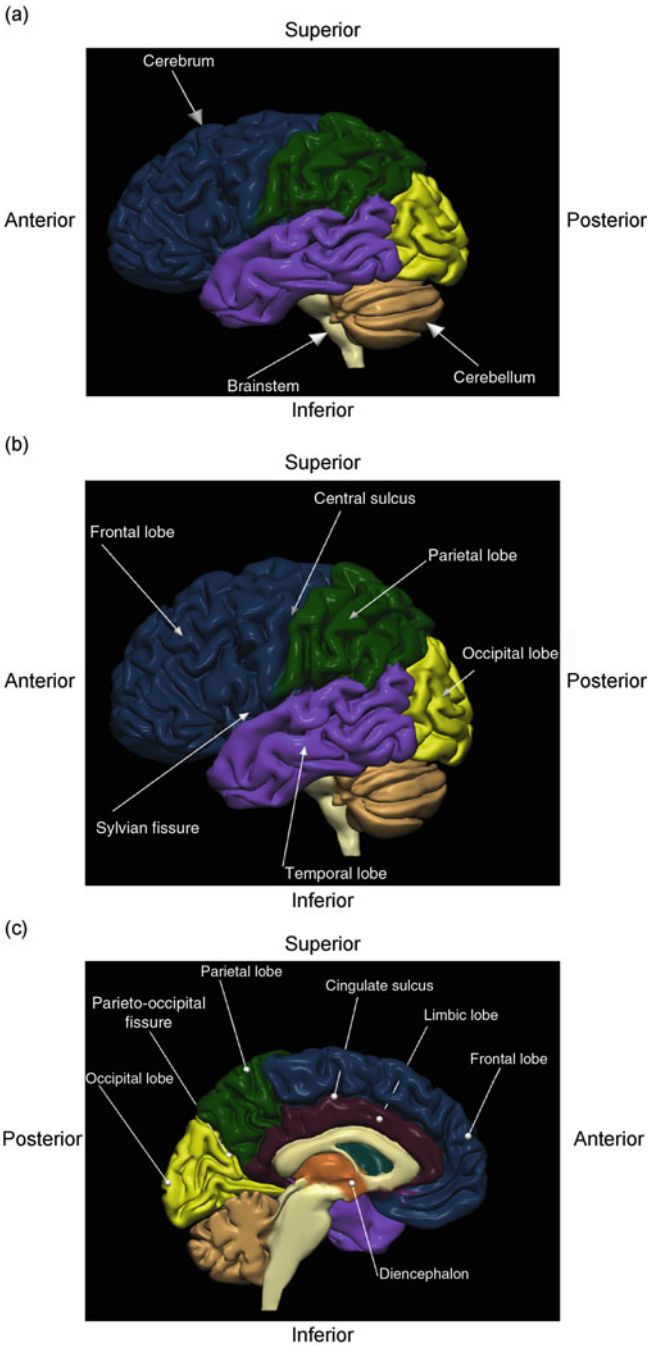

Fig. 2.1 Gross anatomy of the left cerebral hemisphere: (**a**) brain parcellation; (**b**) lobes, lateral view; (**c**) lobes, medial view

- *Cerebrum*
- *Cerebellum* (the little brain)
- *Brainstem*

The cerebrum comprises:

- Left and right *cerebral hemispheres*
- Interbrain between the cerebrum and the brainstem termed the *diencephalon*
- *Deep grey nuclei* (other than diencephalic)

The cerebral hemispheres are the largest compartment of the brain, and they are interconnected by white matter fibres (see Sect. 2.4.2). The hemispheres are composed of:

- Outer *grey matter* termed the *cerebral cortex*
- Inner *white matter* encompassing the diencephalon and deep grey nuclei

The grey matter contains mainly nerve cell bodies, while the white matter is made up predominantly of nerve fibres (axons). The cerebral cortex is highly convoluted. These folds form so-called *gyri* that are separated by grooves termed *sulci* or *fissures* (deep sulci). The cerebral hemispheres are parcellated into five *lobes* (Fig. 2.1b, c):

- *Frontal lobe*
- *Temporal lobe*
- *Parietal lobe*
- *Occipital lobe*
- *Limbic lobe*

The *insula* is sometimes classified as the (sixth) *central* or *insular lobe*. The lobes are partly demarcated by the sulci/fissures (Fig. 2.1). The *central sulcus* separates the frontal lobe anterior from the parietal lobe posterior (Fig. 2.1b). The *Sylvian* (*lateral*) *fissure* demarcates the temporal lobe below from the frontal and parietal lobes above (Fig. 2.1b). The *parieto-occipital fissure* separates the parietal lobe anterior from the occipital lobe posterior (Fig. 2.1c). The *cingulate sulcus* separates the frontal lobe above from the limbic lobe below (Fig. 2.1c).

The diencephalon contains numerous nuclei grouped into four parts (Fig. 2.1c):

- *Thalamus* (see also Fig. 2.6)
- *Subthalamus* including the *subthalamic nucleus* (see Sect. 2.2.6)
- *Hypothalamus* (see also Fig. 2.10a)
- *Epithalamus* (comprising the pineal gland)

The cerebellum is composed of (Fig. 2.2a):

- Left and right *cerebellar hemispheres*
- Midline *vermis* which unites them

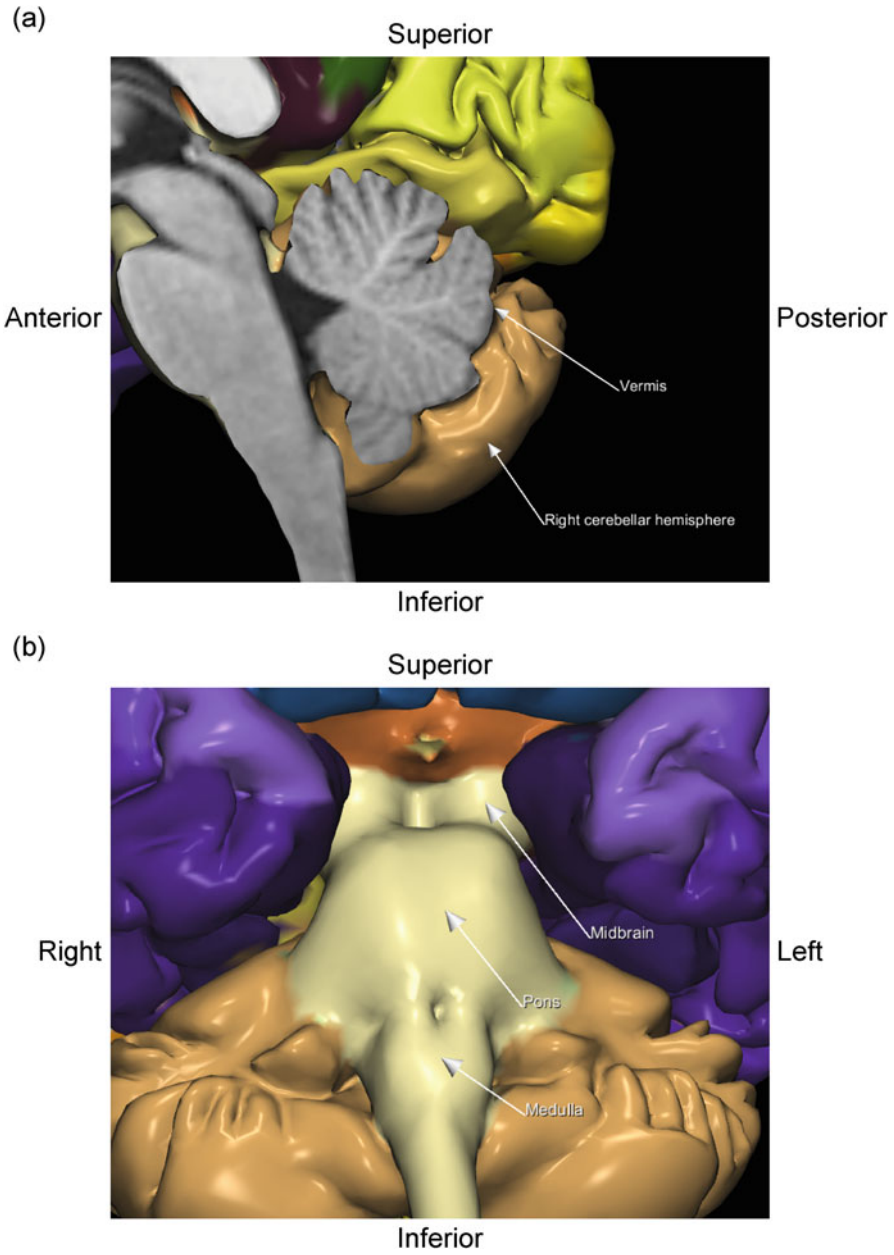

Fig. 2.2 Cerebellum and brainstem: (**a**) right cerebellum (medial view); (**b**) midbrain, pons, and medulla of the brainstem (infero-anterior view)

The brainstem is subdivided into (Fig. 2.2b):

- *Midbrain*
- *Pons*
- *Medulla (oblongata)*

2.2.2 Cortical Areas

The cortex has three surfaces: lateral, medial, and inferior (also called basal or ventral). Moreover, the transitional areas form the frontal, temporal, and occipital poles (see, e.g. Figs. 2.5 and 2.27).

2.2.2.1 Lateral Cortical Surface

Four lobes are present on the lateral cortical surface: frontal, temporal, parietal, and occipital (Fig. 2.1b). The lateral surface of the frontal lobe is subdivided by three sulci (the *superior frontal sulcus*, *inferior frontal sulcus*, and *precentral sulcus*) into four gyri (Fig. 2.3):

- *Superior frontal gyrus*
- *Middle frontal gyrus*
- *Inferior frontal gyrus*
- *Precentral gyrus*

The lateral surface of the temporal lobe is subdivided by two sulci (the *superior temporal sulcus* and *inferior temporal sulcus*) into three gyri (Fig. 2.3):

- *Superior temporal gyrus*
- *Middle temporal gyrus*
- *Inferior temporal gyrus*

The lateral surface of the parietal lobe is subdivided by two sulci (the *postcentral sulcus* and *intraparietal sulcus*) into three gyri (Fig. 2.3):

- *Postcentral gyrus*
- *Superior parietal gyrus* (*lobule*)
- *Inferior parietal gyrus* (*lobule*)
  - *Supramarginal gyrus*
  - *Angular gyrus*

The lateral surface of the occipital lobe is subdivided by two sulci (the *superior occipital sulcus* and *inferior occipital sulcus*) into three gyri (Fig. 2.3):

- *Superior occipital gyrus*
- *Middle occipital gyrus*
- *Inferior occipital gyrus*

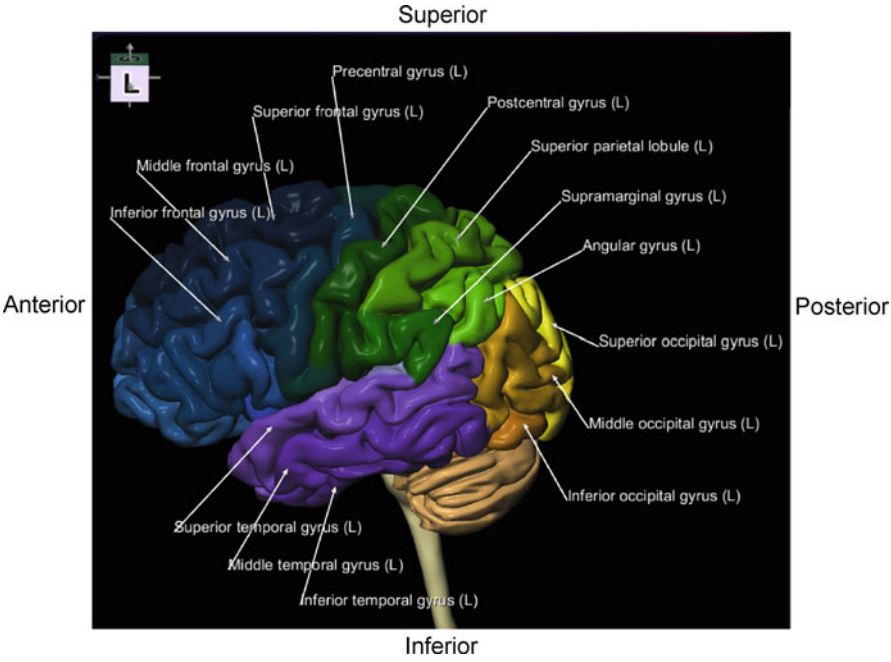

Fig. 2.3 Cortical areas of the left (L) hemisphere: lateral view. The orientation box located in the top-left corner indicates the viewing direction (L, left; R, right; S, superior (dorsal); I, inferior (ventral); A, anterior; and P, posterior). Each gyrus is assigned a unique color

2.2.2.2 Medial Cortical Surface

The frontal, parietal, occipital, and limbic lobes are present on the medial surface of the cortex (Fig. 2.1c). The limbic lobe contains the gyri located at the inner edge (or *limbus*) of the hemisphere including (Fig. 2.4):

- *Subcallosal gyrus* (*areas*)
- *Cingulate gyrus*
- *Isthmus* (*of cingulate gyrus*)
- *Parahippocampal gyrus*

The *medial frontal gyrus* and the *paracentral lobule* separated from the limbic lobe by the *cingulate sulcus* (Fig. 2.1c) occupy most of the medial surface of the frontal lobe (Fig. 2.4). The parietal lobe includes the *precuneus* (Fig. 2.4) separated from the occipital lobe by the *parieto-occipital fissure* (Fig. 2.1c). The occipital lobe comprises the *cuneus* and the *lingual gyrus* separated by the *calcarine sulcus* (*fissure*) (Fig. 2.4).

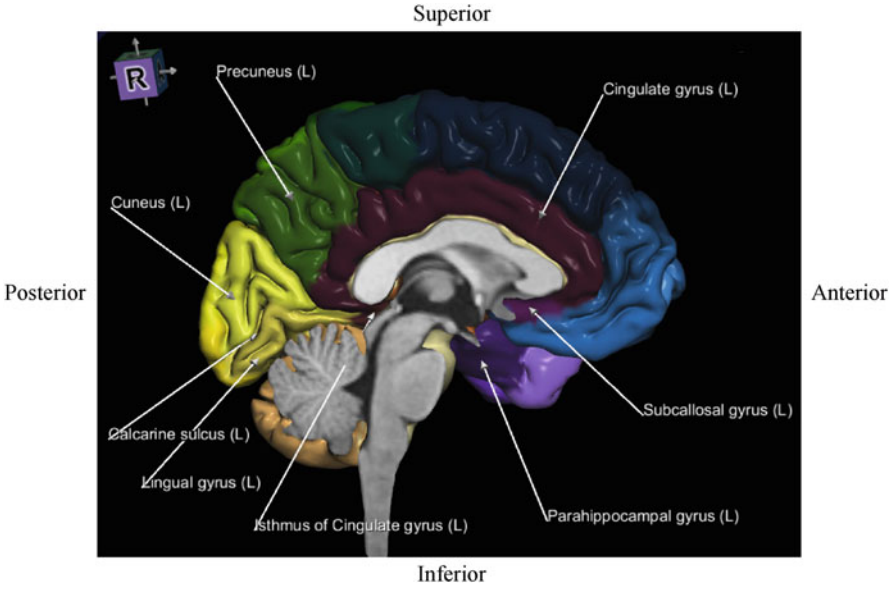

Fig. 2.4 Cortical areas of the left hemisphere: medial view

2.2.2.3 Inferior Cortical Surface

The inferior surface of the cortex includes the frontal, temporal, and occipital lobes. The frontal lobe comprises (Fig. 2.5):

- *Straight gyrus*
- *Orbital gyri* parcellated by the approximately *H-shaped sulcus* into the *anterior, medial, lateral, and posterior orbital gyri*

The temporal and occipital lobes are subdivided by two sulci (the *lateral occipitotemporal sulcus* and *medial occipitotemporal* (*collateral*) *sulcus*) into three gyri (Fig. 2.5):

- *Medial occipitotemporal gyrus* whose temporal part constitutes the *parahippocampal gyrus* and the occipital part the *lingual gyrus*
- *Lateral occipitotemporal gyrus* (called also the *fusiform gyrus*)
- *Inferior temporal gyrus*

2.2.3 Deep Grey Nuclei

The deep grey nuclei are paired grey matter structures. The main deep grey nuclei (other than the diencephalic nuclei discussed in Sect. 2.2.1) are (Fig. 2.6):

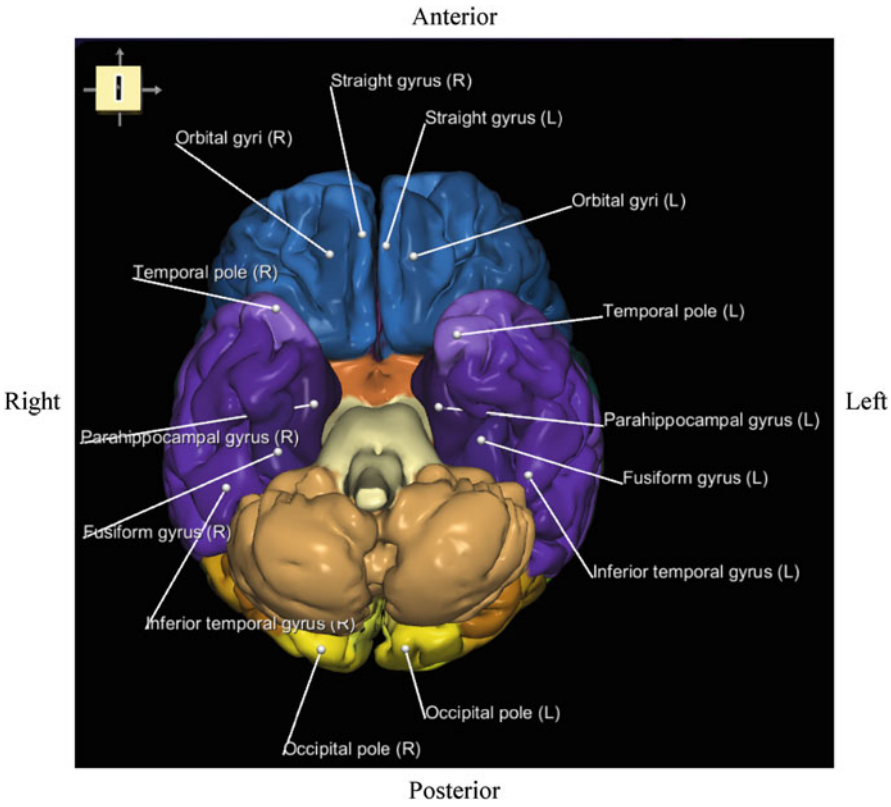

Fig. 2.5 Cortical areas: inferior view

- *Basal ganglia* (*nuclei*)
  - *Caudate nucleus*
  - *Lentiform nucleus*
    - *Putamen*
    - *Globus pallidus*
      - *Lateral* (*or outer*) *segment*
      - *Medial* (*or inner*) *segment* (see also Sect. 2.2.6)
- *Hippocampus*
- *Amygdala* (*amygdaloid body*)

The putamen and the caudate nucleus form the *striatum*.

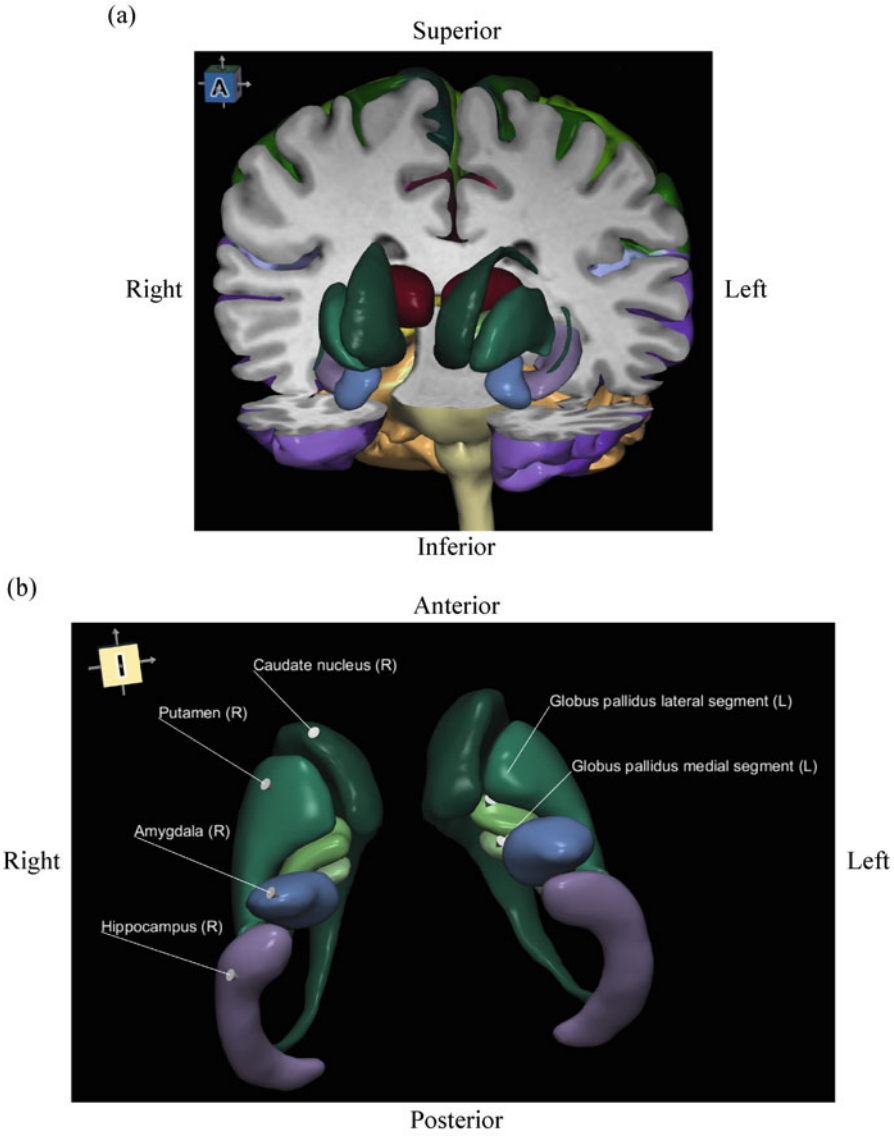

Fig. 2.6 Deep grey nuclei: (**a**) embedded into the brain (anterior view); (**b**) shown in isolation (inferior view); note: the arrowheads indicate the pointed structures

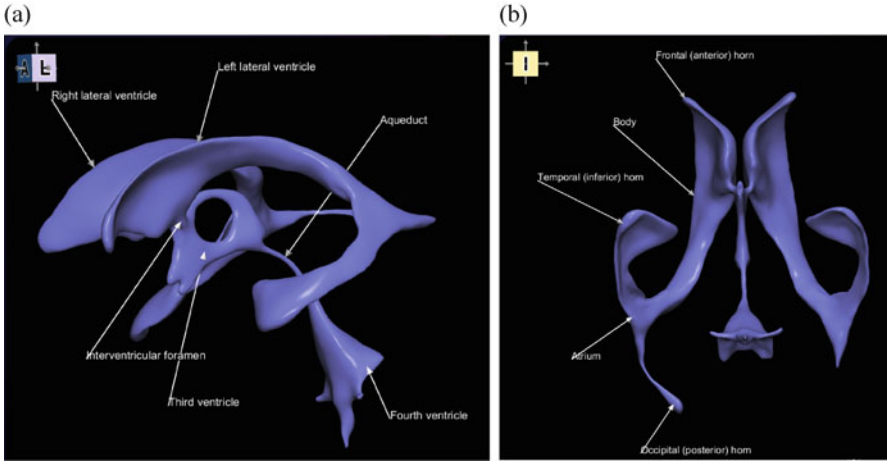

Fig. 2.7 Ventricular system: (**a**) interconnected ventricles; (**b**) components of the lateral ventricle (inferior view)

2.2.4 Ventricular System

The ventricular system contains four interconnected cerebral ventricles (cavities) filled with *cerebrospinal fluid* (CSF) (Fig. 2.7a):

- Left and right *lateral ventricles*
- *Third ventricle*
- *Fourth ventricle*

CSF is secreted mainly in the *choroid plexus* (a network of vessels) and circulates from the lateral ventricles through the paired *interventricular foramina* (of Monro) to the third ventricle and then via the *aqueduct* to the fourth ventricle (Fig. 2.7a). The lateral ventricles are the largest and each contains (Fig. 2.7b):

- *Body* (or *central portion*)
- *Atrium* (or *trigon*)
- *Horns*
  - *Frontal* (*anterior*)
  - *Occipital* (*posterior*)
  - *Temporal* (*inferior*)

2.2.5 Sectional Neuroanatomy

Sectional (planar) neuroanatomy is typically presented on orthogonal (axial, coronal, and sagittal) images. In order to spatially locate the orthogonal images, we place them in the Talairach coordinate system [48], which is a stereotactic reference system based on the anterior and posterior commissures (see also Fig. 2.28a) with the origin at the centre of the anterior commissure (see also Figs. 2.8, 2.9, and 2.10).

Four axial images located at −12 mm, +1 mm, +12 mm, and +24 mm (where '−' denotes the level below and '+' above the anterior commissure) with the cortical areas and deep grey nuclei segmented and labelled are shown in Fig. 2.8.

Two coronal images passing through the anterior and posterior commissures are presented in Fig. 2.9.

Two sagittal images located at 3 mm and 21 mm from the midline are shown in Fig. 2.10.

2.2.6 Main Stereotactic Target Structures

Several subcortical structures (and more recently also some cortical areas) are therapeutic stimulation targets in stereotactic and functional neurosurgery [83] to treat movement disorders (mainly Parkinson's disease), epilepsy, pain, and mental disorders (psychosurgery). The main stereotactic target structures are:

- *Subthalamic nucleus* (a part of the basal ganglia) (Fig. 2.11)
- *Ventrointermediate nucleus of the thalamus* (Fig. 2.12)
- *Globus pallidus interna* (medial segment) (Fig. 2.13)

The subthalamic nucleus presented on the triplanar (the axial, coronal, and sagittal planes) is shown in Fig. 2.11.

The ventrointermediate nucleus of the thalamus on the triplanar is presented in Fig. 2.12.

The globus pallidus interna on the triplanar is illustrated in Fig. 2.13.

All three target structures in 3D placed in the Talairach stereotactic coordinate system are shown in Fig. 2.14.

2.2.7 Functional Areas

Several parcellations are introduced to subdivide the cortical regions into functional areas [16]. Brodmann's parcellation that is based on histology (cytoarchitecture) is the most widely used, and it is illustrated in axial orientation in Fig. 2.15. *Brodmann's areas* are useful in neuroscience and functional studies because many

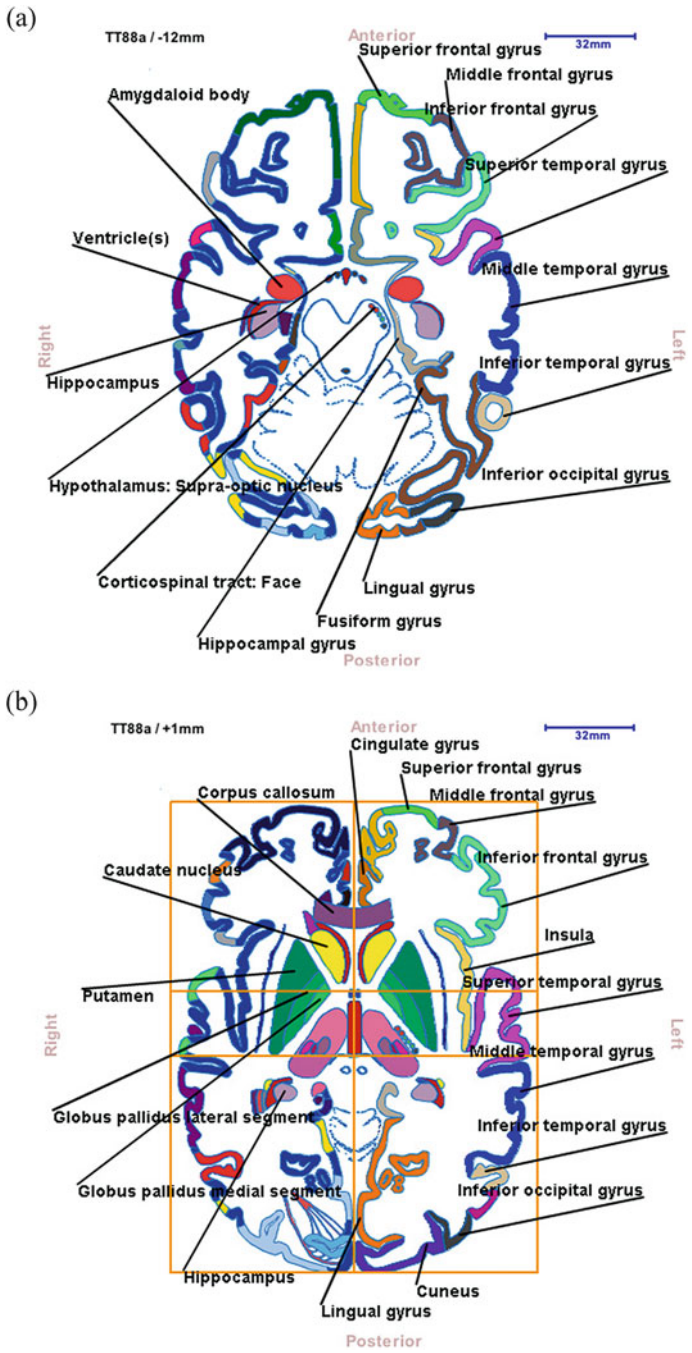

Fig. 2.8 Planar neuroanatomy in axial orientation at (**a**) −12 mm, (**b**) +1 mm (along with the Talairach grid), (**c**) +12 mm, and (**d**) +24 mm ('-' denotes the level below and '+' the level above the anterior commissure)

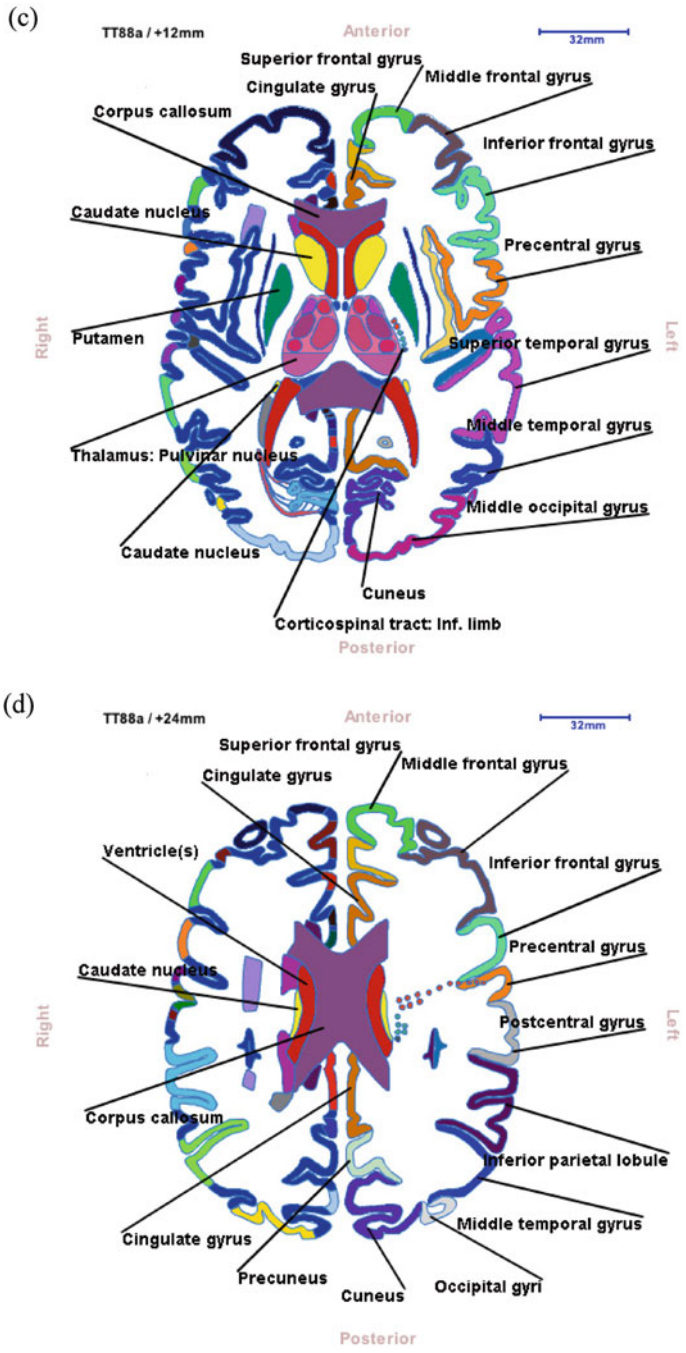

Fig. 2.8 (continued)

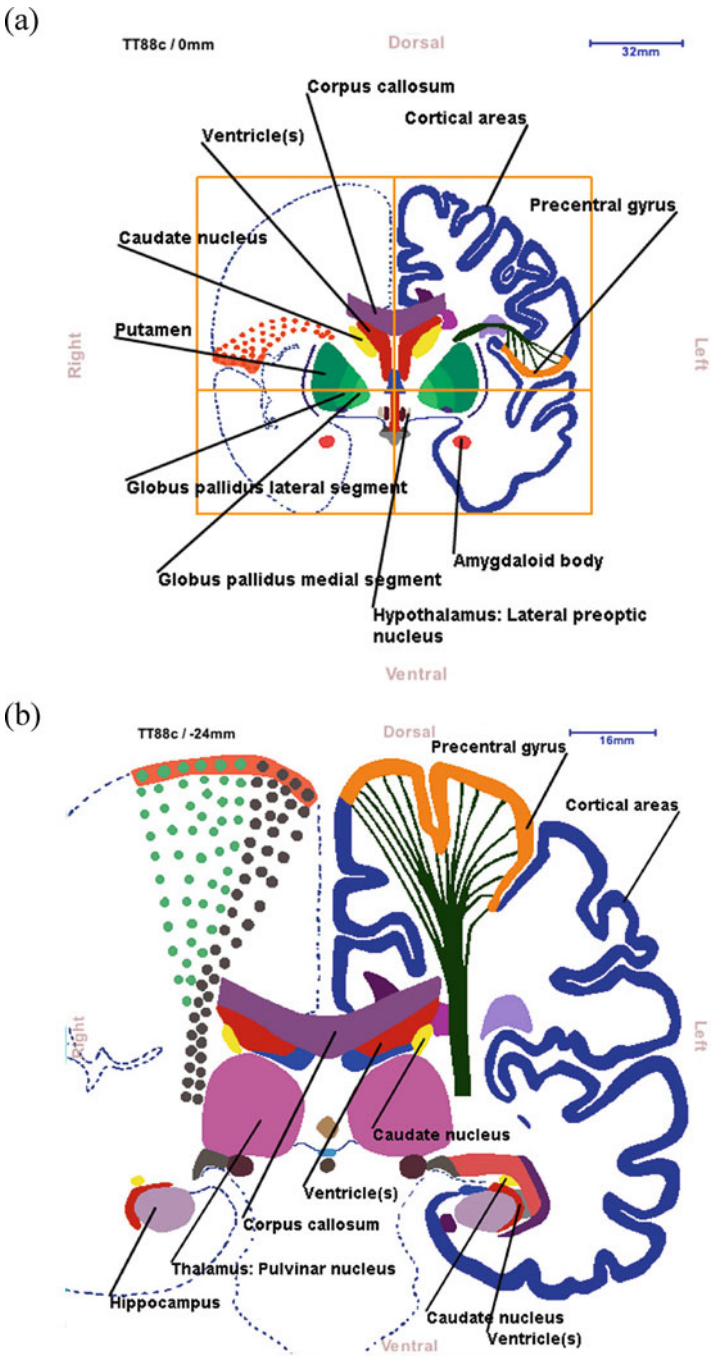

Fig. 2.9 Planar neuroanatomy in coronal orientation at (**a**) 0 mm passing through the anterior commissure (point), i.e. the location on the coronal plane where the horizontal and vertical planes of the Talairach coordinate system intersect, and (**b**) −24 mm passing through the posterior commissure (point)

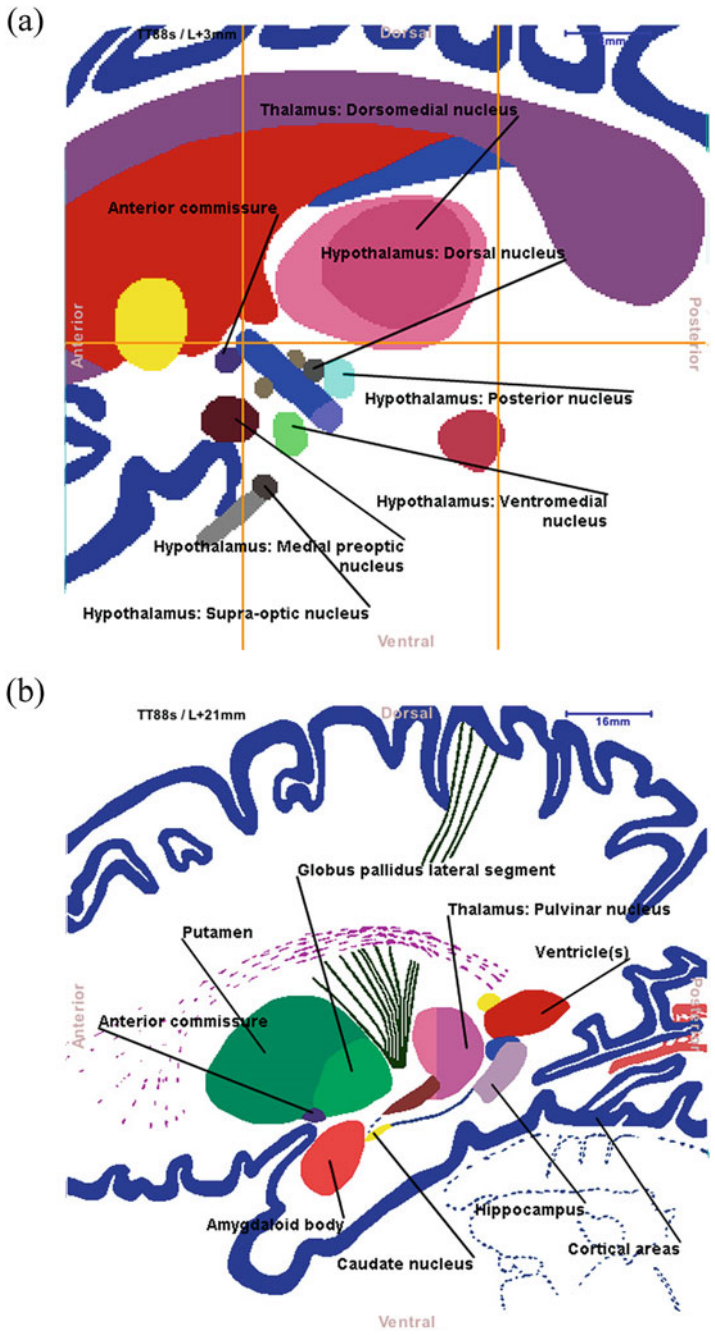

Fig. 2.10 Planar neuroanatomy in sagittal orientation at (**a**) 3 mm (along with the Talairach grid) and (**b**) 21 mm from the midline

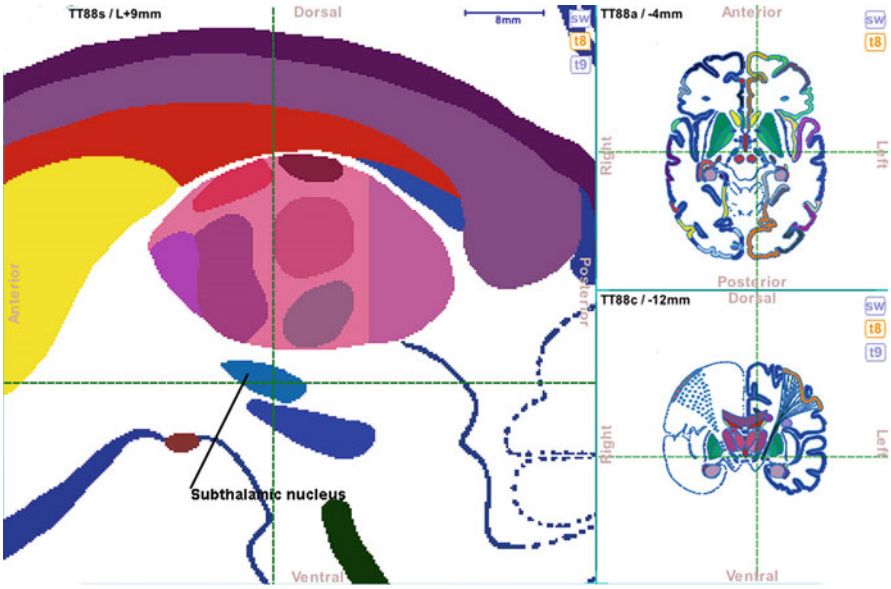

Fig. 2.11 Subthalamic nucleus on sagittal, axial, and coronal planes (the location of the triplanar is marked by the green dashed lines)

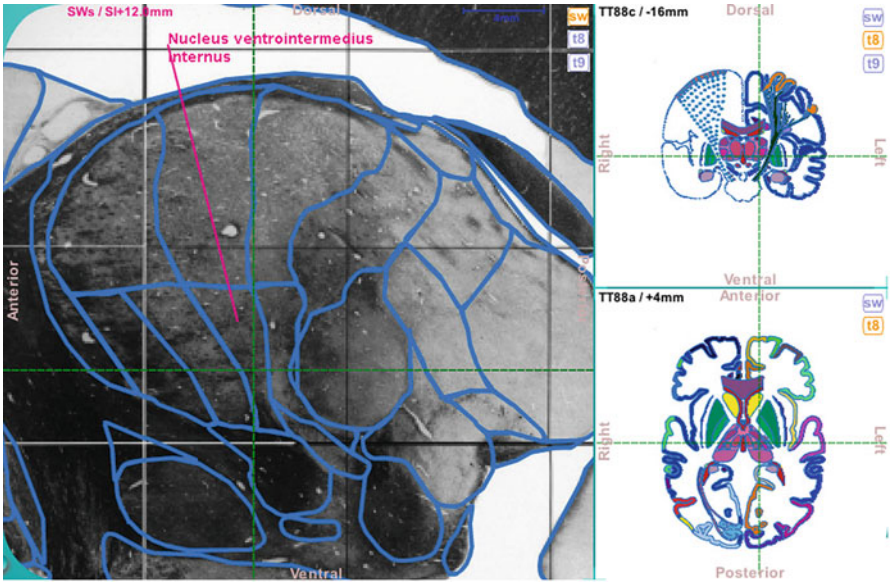

Fig. 2.12 Ventrointermediate nucleus of the thalamus on sagittal, coronal, and axial planes

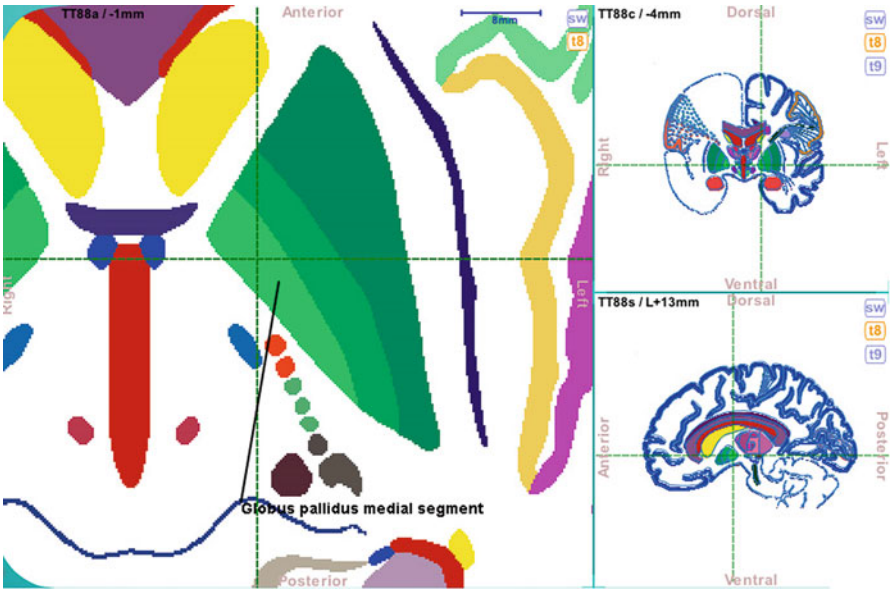

Fig. 2.13 Globus pallidus interna (medial segment) on axial, coronal, and sagittal planes

of Brodmann's areas, defined based on their neuronal organisation, have since been correlated closely to diverse cortical functions.

2.3 Vascular Neuroanatomy

The knowledge of cerebrovasculature is crucial in stroke, vascular, and tumour surgery as well as interventional neuroradiology. The complete cerebrovasculature is highly complex and variable (Fig. 2.16). It is subdivided into:

- *Arterial system*
- *Venous system* with the *cerebral veins* and *dural sinuses*

2.3.1 Arterial System

2.3.1.1 Parcellation of Arterial System

The brain is supplied by two pairs of arteries, left and right *internal carotid arteries* anteriorly and left and right *vertebral arteries* posteriorly forming the *basilar artery* (Fig. 2.17a), that are interconnected by the *circle of Willis* (Fig. 2.21).

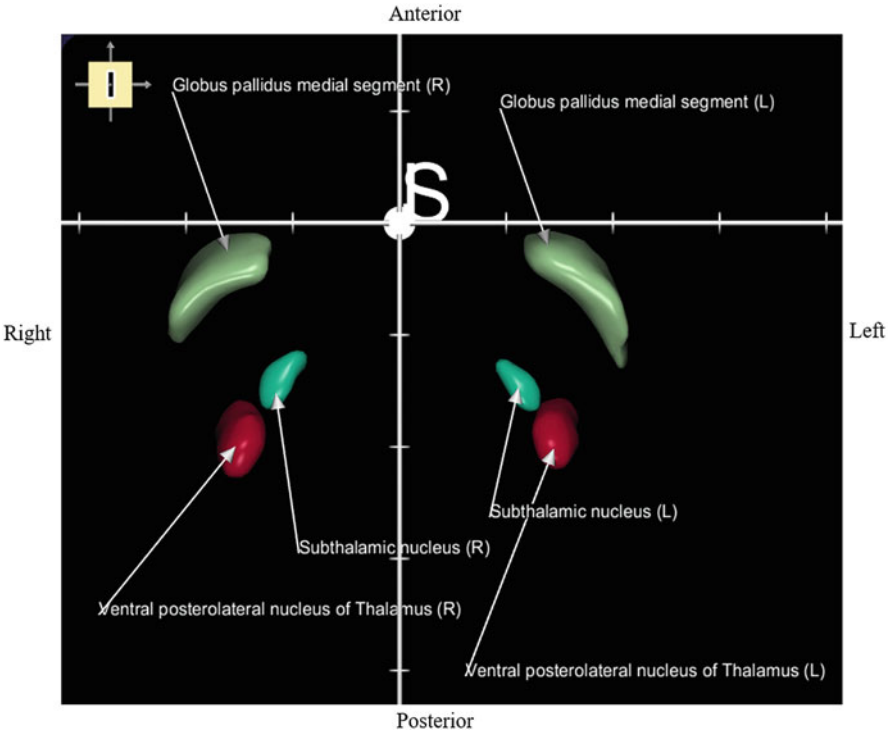

Fig. 2.14 Stereotactic target structures in 3D. The marks on the axes are placed at 10 mm intervals

The internal carotid artery branches into the *anterior cerebral artery* (Fig. 2.17c) and the *middle cerebral artery* (Fig. 2.17d). The left and right *posterior cerebral arteries* originate from the basilar artery (Fig. 2.17e).

2.3.1.2 Anterior Cerebral Artery

The anterior cerebral artery (ACA) has the following main branches (Fig. 2.18):

- *A1 segment* (*precommunicating part*)
- *A2 segment* (*postcommunicating part*)
  - *Pericallosal artery*
  - *Callosomarginal artery*

2.3.1.3 Middle Cerebral Artery

The middle cerebral artery (MCA) is subdivided into four segments (Fig. 2.19a):

- *M1 segment* (*sphenoid part*)
- *M2 segment* (*insular part*)
- *M3 segment* (*opercular part*)
- *M4 segment* (*terminal part*)

The main MCA branches of the left hemisphere are shown in Fig. 2.19b.

2.3.1.4 Posterior Cerebral Artery

The posterior cerebral artery is parcellated into four segments (Fig. 2.20):

- *P1 segment* (*precommunicating part*)
- *P2 segment* (*postcommunicating part*)
- *P3 segment* (*lateral occipital artery*)
- *P4 segment* (*medial occipital artery*)

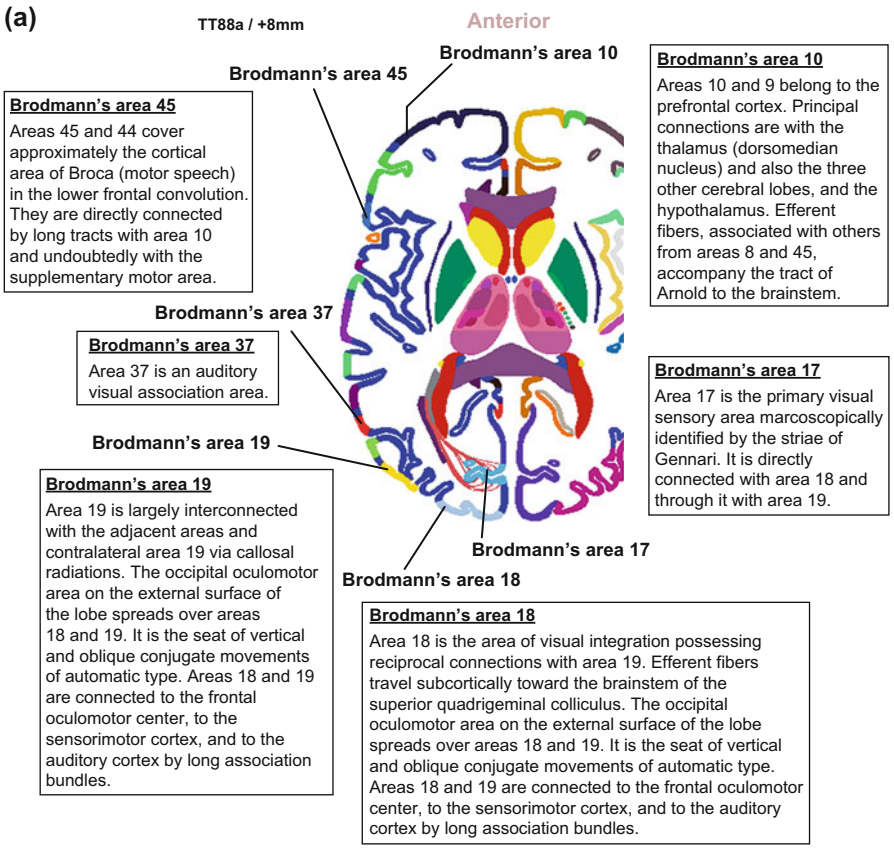

Fig. 2.15 Brodmann's areas in axial orientation: (**a**) vision and speech areas (+8 mm); (**b**) motor and sensory areas (+40 mm). The areas are uniquely color-coded

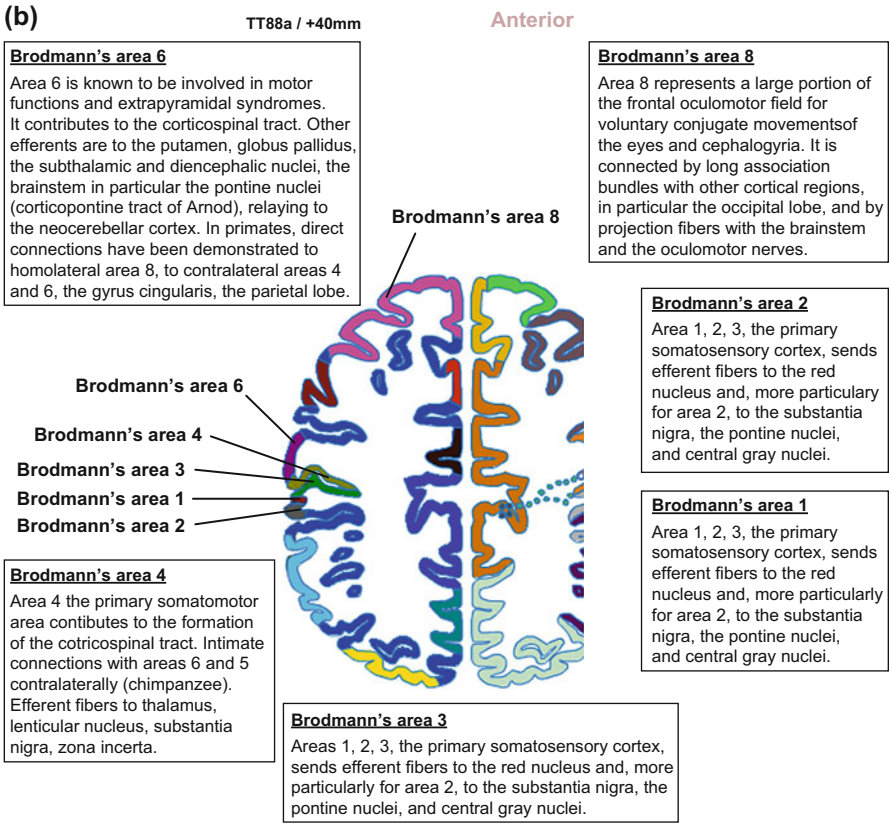

Fig. 2.15 (continued)

2.3.1.5 Circle of Willis

The circle of Willis connects the anterior and posterior circulations. It includes the following vessels (Fig. 2.21):

- *Anterior communicating artery*
- Left and right *posterior communicating arteries*
- Part of the left and right *internal carotid arteries*
- Left and right *A1 segments* of the anterior cerebral arteries
- Left and right *P1 segments* of the posterior cerebral arteries

2.3.2 Venous System

2.3.2.1 Parcellation of Venous System

The main components of the venous system are (Fig. 2.22):

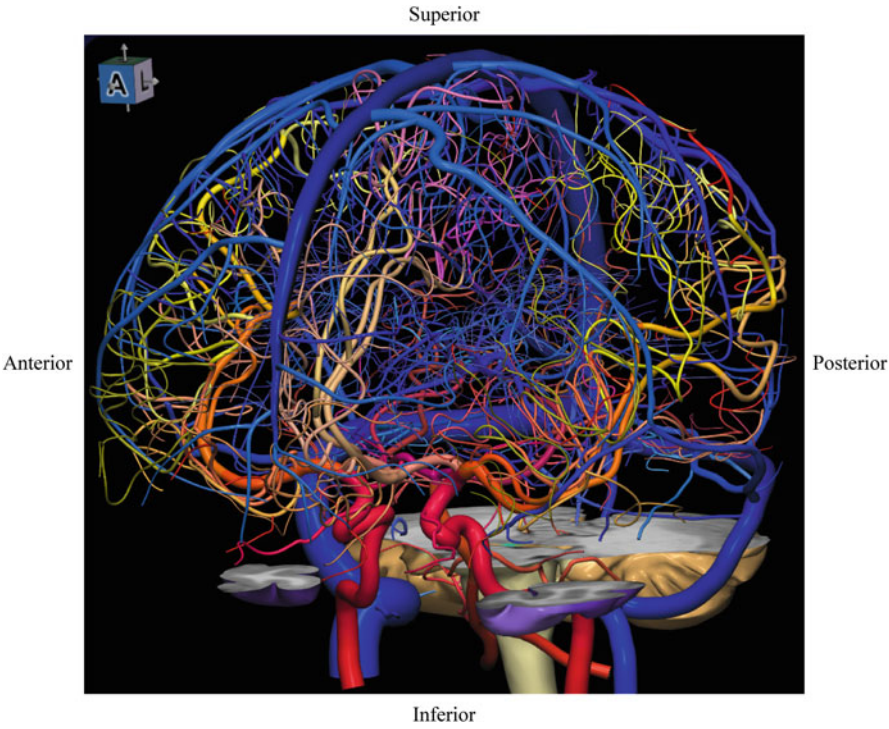

Fig. 2.16 The cerebral vasculature with arteries, veins, and dural sinuses. The vessels are uniquely color-coded such that all the vessels with the same name have the same color

- *Dural sinuses*
- *Cerebral veins*
  - *Superficial veins*
  - *Deep veins*

  The cerebral veins empty into the dural sinuses.

2.3.2.2 Dural Sinuses

The main dural sinuses are (Fig. 2.23):

- *Superior sagittal sinus*
- *Inferior sagittal sinus*
- *Straight sinus*
- Left and right *transverse sinuses*
- Left and right *sigmoid sinuses*

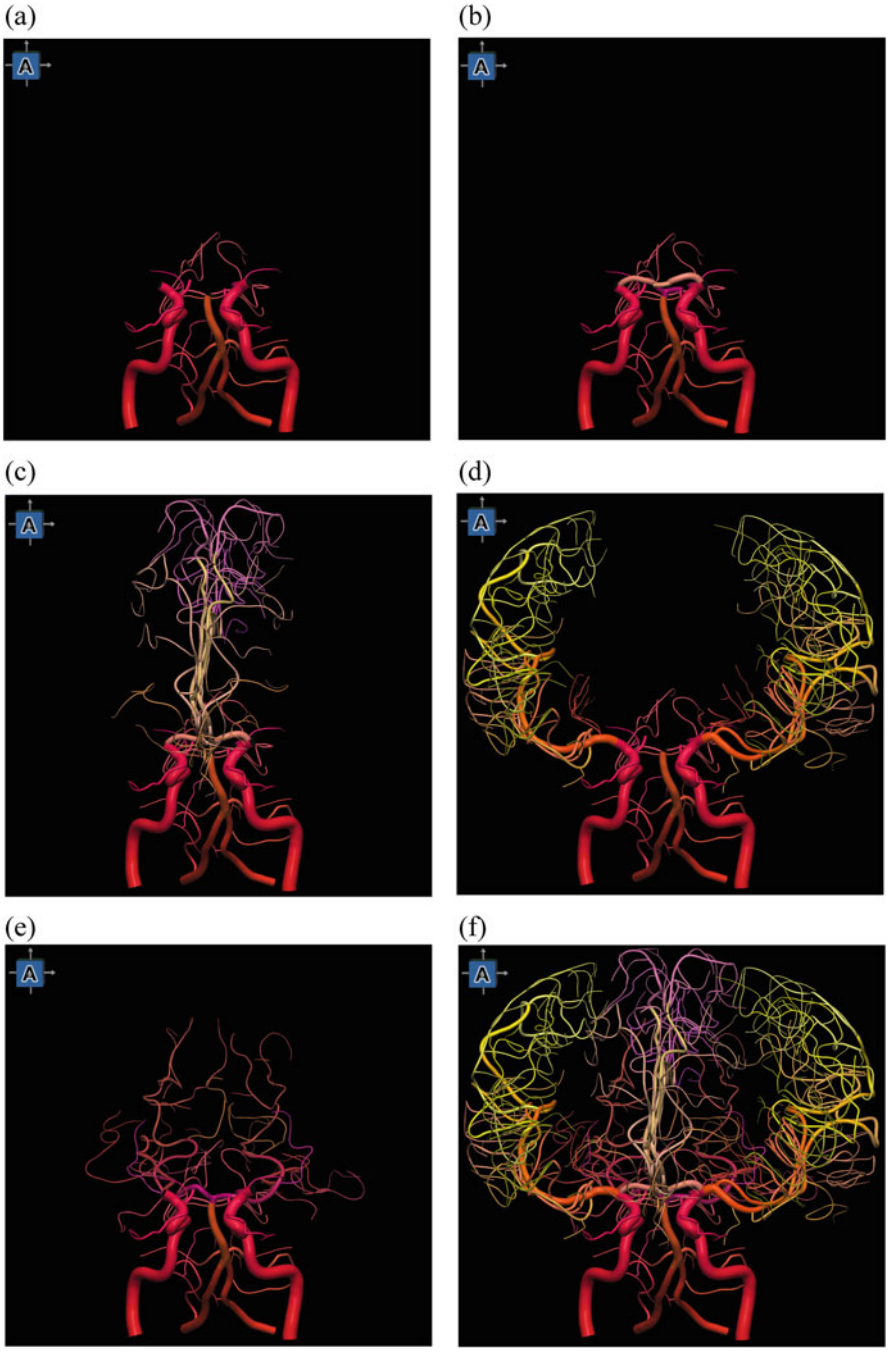

Fig. 2.17 The cerebral arteries: (**a**) blood supply to the brain by the internal carotid artery (ICA) anteriorly and the vertebral artery (VA) and the basilar artery (BA) posteriorly; (b) ICA and VA connected by the circle of Willis; (**c**) anterior cerebral artery along with the ICA, VA, and BA; (**d**) middle cerebral artery along with the ICA, VA, and BA; (**e**) posterior cerebral artery along with the ICA, VA, and BA; (**f**) complete arterial system

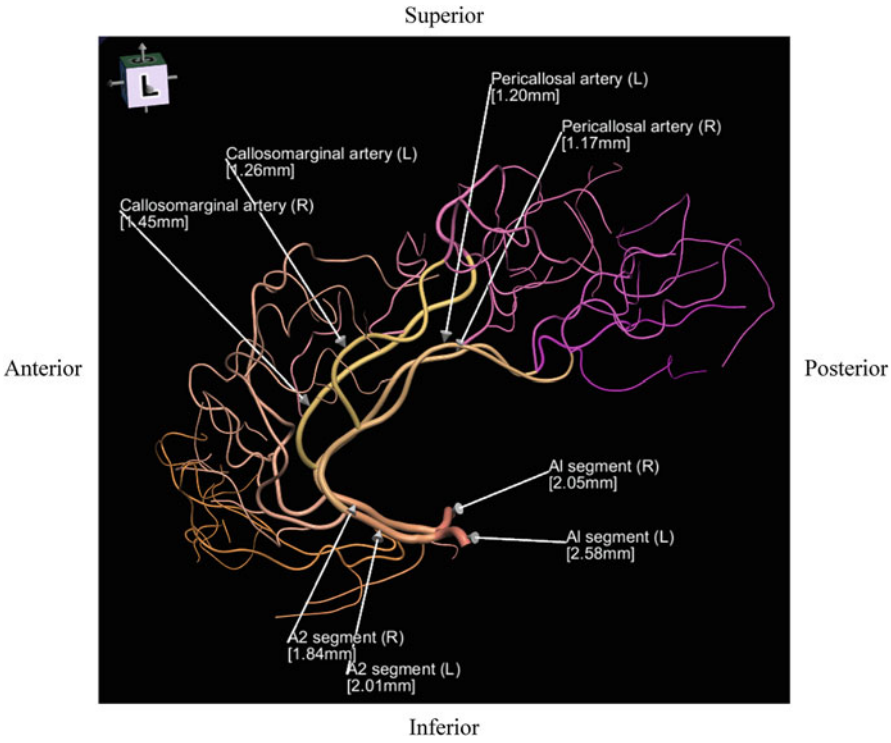

Fig. 2.18 Anterior cerebral artery. The vessel diameter at the arrowhead is given in the brackets

2.3.2.3 Cerebral Veins

The main superficial cerebral veins are (Fig. 2.24):

- *Frontopolar veins*
- *Prefrontal veins*
- *Frontal veins*
- *Parietal veins*
- *Occipital veins*

Other important superficial veins include the *superior* and *inferior anastomotic veins* and the *superficial middle cerebral vein*.

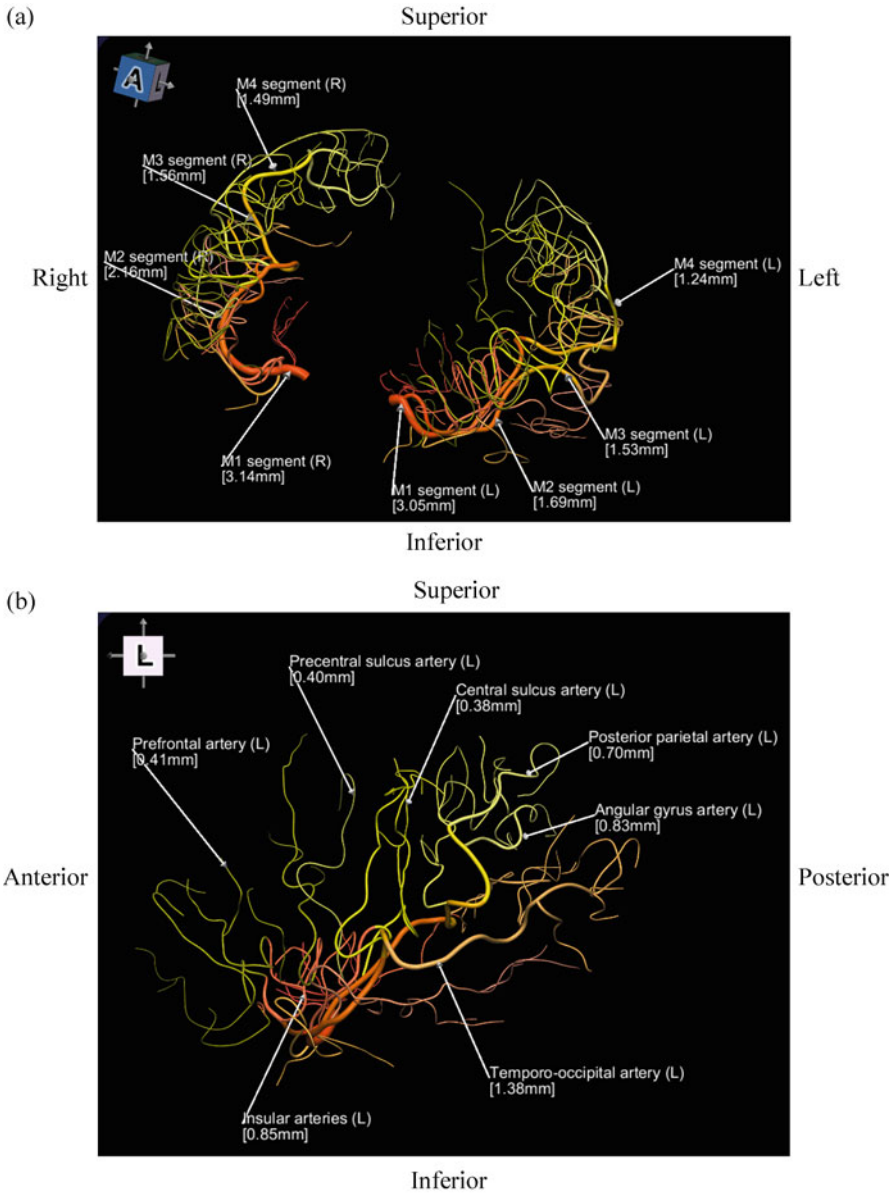

Fig. 2.19 Middle cerebral artery: (**a**) M1, M2, M3, and M4 segments; (**b**) main branches of the left hemisphere

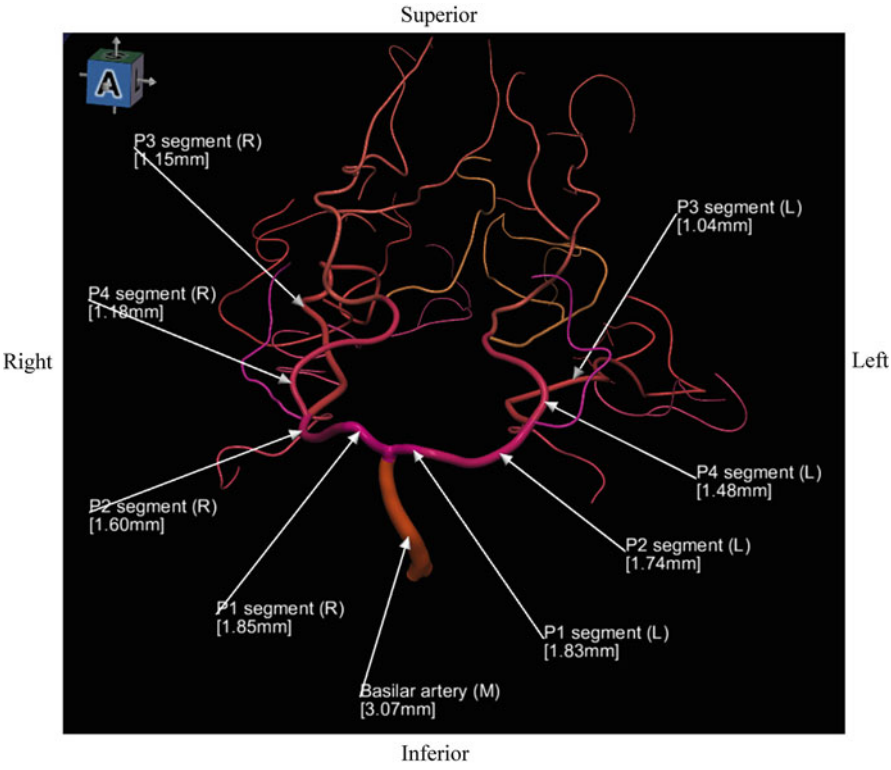

Fig. 2.20 Posterior cerebral artery

The main deep cerebral veins are (Fig. 2.25):

- *Great vein* (of Galen)
- Left and right *basal vein* (of Rosenthal)
- Left and right *internal cerebral veins*

2.3.3 Vascular Variants

The human cerebrovasculature is highly variable and vascular variants have been extensively studied (see, e.g. [6, 10, 13, 22]). Variations exist in terms of origin, location, shape, size, course, branching patterns, as well as surrounding vessels and structures. The knowledge of cerebrovascular variants is central in diagnosis, treatment, and medical education.

Some main variants of the circle of Willis synthesised in 3D are shown in Fig. 2.26 (more 3D vascular variants are presented in [70]).

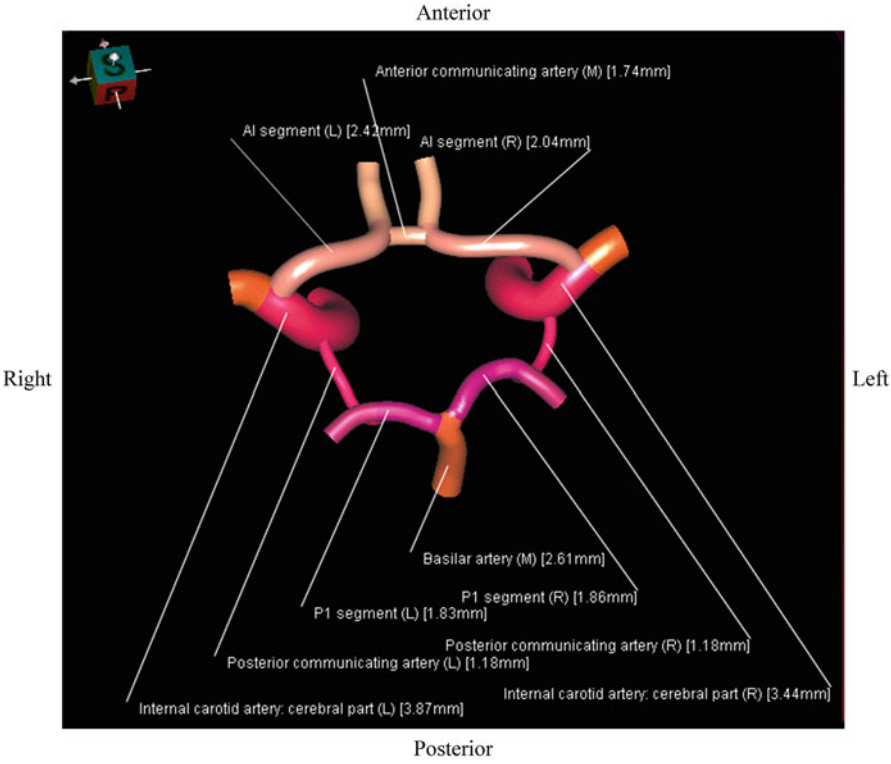

Fig. 2.21 The circle of Willis

2.4 Connectional Neuroanatomy

Three types of white matter connections (or tracts, fibres, bundles, fibre pathways, fascicles) are distinguished in the cerebral hemispheres (Fig. 2.27):

- *Commissural tracts*
- *Association tracts*
- *Projection tracts*

In addition, three cerebellar paired peduncles, *superior peduncle, middle peduncle*, and *inferior peduncle*, connect the cerebellum to the brainstem: midbrain, pons, and medulla, respectively.

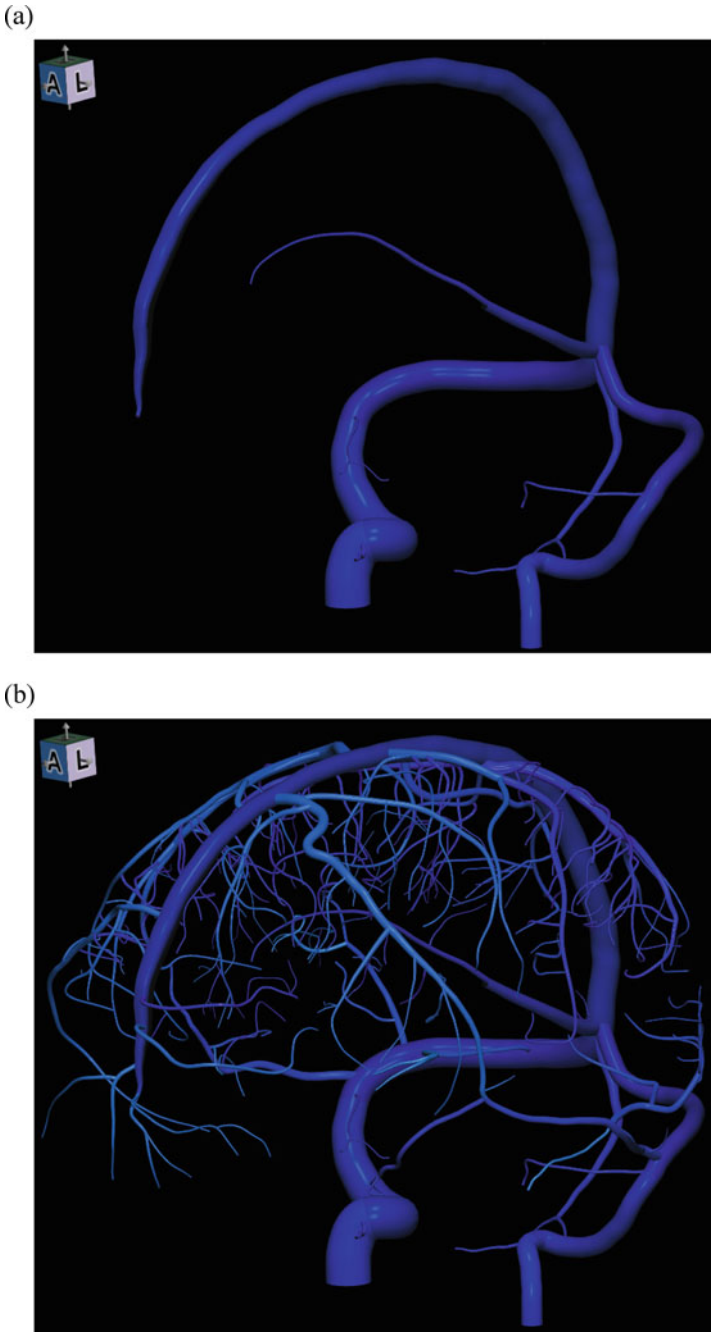

Fig. 2.22 Parcellation of the venous system: (**a**) dural sinuses (DS); (**b**) superficial veins with the DS; (**c**) deep veins with the DS; (**d**) complete venous system

(c)

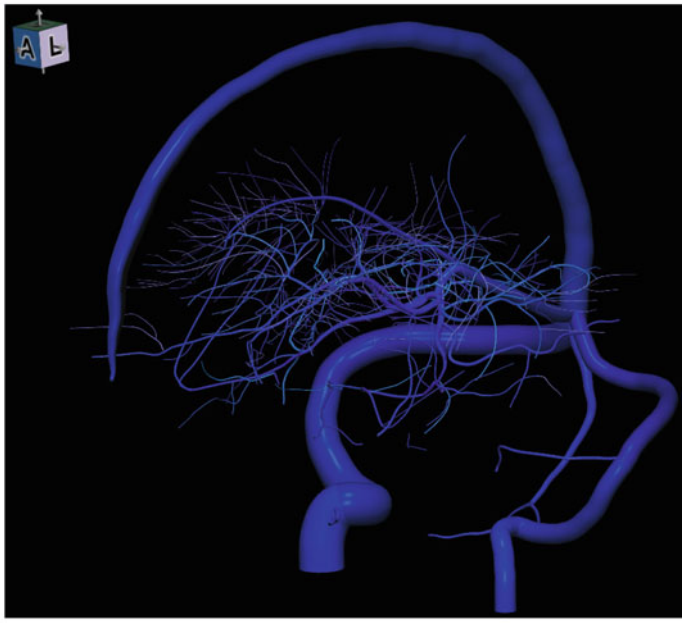

(d)

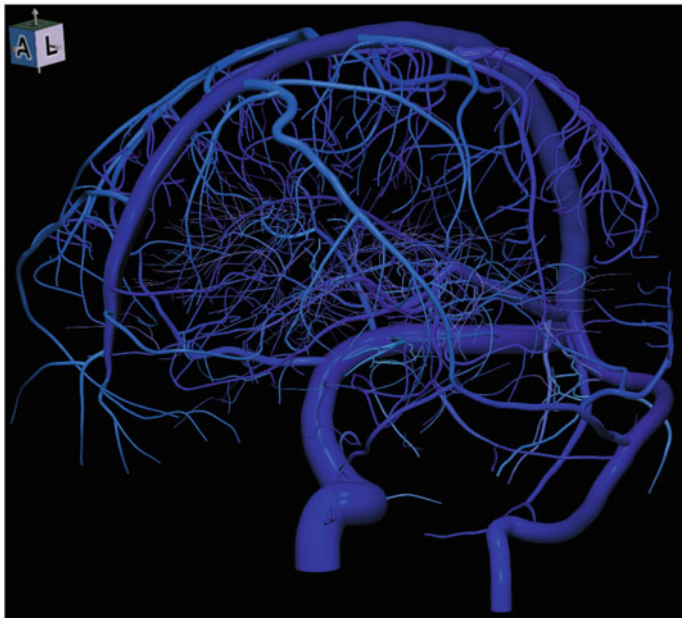

Fig. 2.22 (continued)

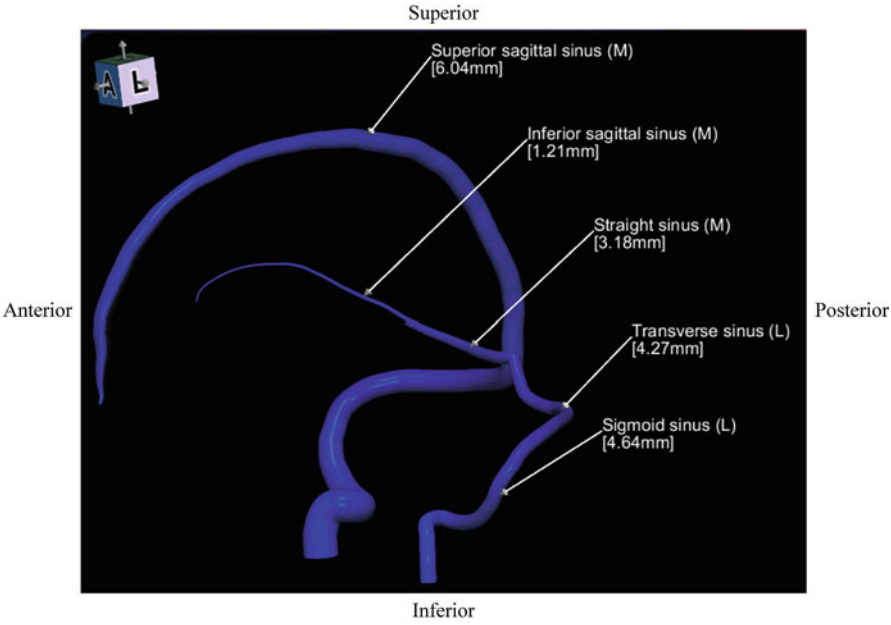

Fig. 2.23 Dural sinuses (the midline and left hemisphere sinuses are labelled)

2.4.1 Commissural Tracts

The commissural tracts interconnect both hemispheres across the median plane. The main commissural tracts are (Fig. 2.28):

- *Corpus callosum*
- *Anterior commissure*
- *Posterior commissure*

The corpus callosum (the great commissure) is the largest commissure. Its three main parts: *genu* (knee), *body*, and *splenium*, connect the frontal lobes, wide areas of hemispheres, and the occipital lobes, respectively.

The anterior commissure connects the temporal lobes, while the posterior commissure links the midbrain, thalamus, and hypothalamus on both sides.

2.4.2 Association Tracts

The association tracts interconnect different cortical regions of the same cerebral hemisphere. There are two types of the association tracts:

- *Short arcuate* fibres that connect adjacent gyri (so-called U fibres)
- *Long arcuate* fibres interconnecting widely separated gyri

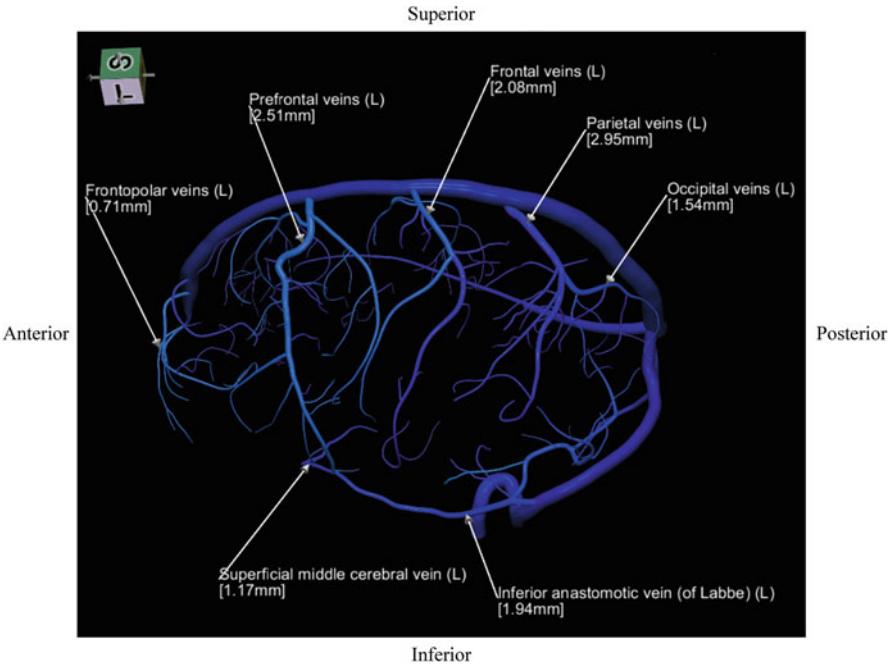

Fig. 2.24 Superficial cerebral veins of the left hemisphere

The main association tracts are (Fig. 2.29):

- *Superior longitudinal fasciculus*
- *Middle longitudinal fasciculus*
- *Inferior longitudinal fasciculus*
- *Superior occipito-frontal fasciculus*
- *Inferior occipito-frontal fasciculus*
- *Cingulum*
- *Uncinate fasciculus*

The superior longitudinal fasciculus connects the frontal lobe with the temporal, parietal, and occipital lobes. The inferior longitudinal fasciculus links the temporal lobe with the occipital lobe. The cingulum deep to the cingulated gyrus interconnects parts of the temporal, parietal, and occipital lobes. The uncinate fasciculus connects the frontal lobe (the orbital gyri and motor speech area) with the temporal lobe.

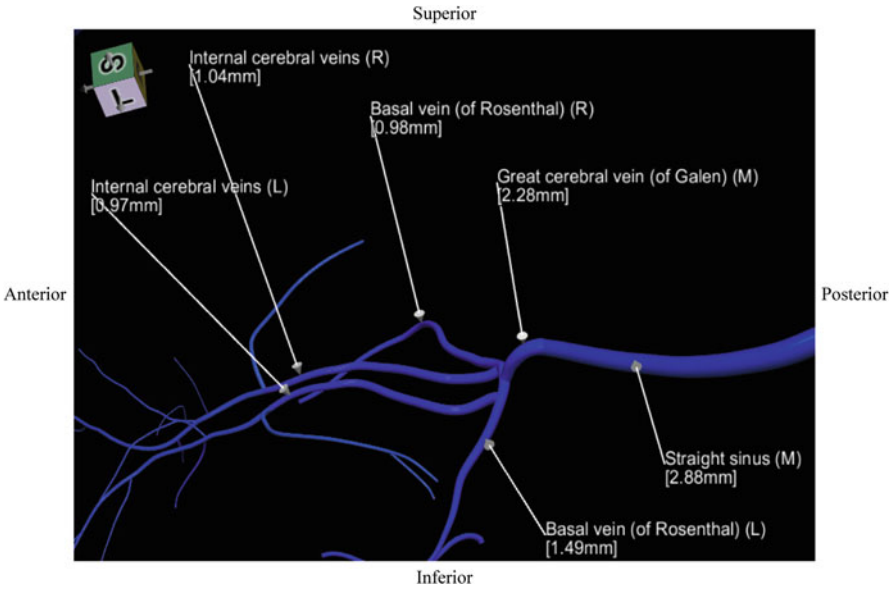

Fig. 2.25 Deep cerebral veins

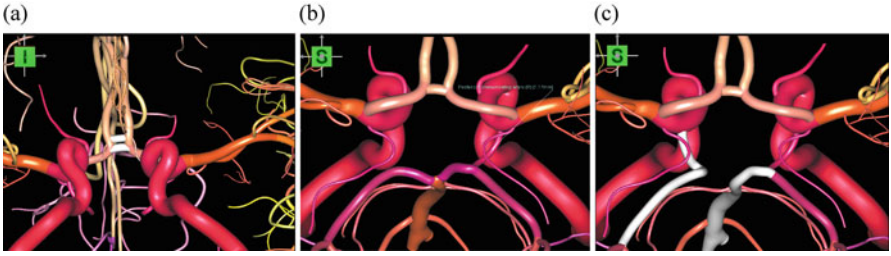

Fig. 2.26 Vascular variants of the circle of Willis: (**a**) double anterior communicating artery; (**b**) absent left posterior communicating artery; (**c**) absent left P1 segment (the variants are in white)

2.4.3 Projection Tracts

The projection tracts connect the cortex with the subcortical structures in the diencephalon, brainstem, and spinal cord. The main projection tracts are (Fig. 2.30):

- *Corticospinal* (*pyramidal*) *tract*
- *Corticothalamic tract* including the *anterior*, *posterior* (*optic*), and *superior thalamic radiations*
- *Corticobulbar tract* (connecting to the brainstem)
- *Corticopontine tract* (projecting to the pons)
- *Auditory radiations*

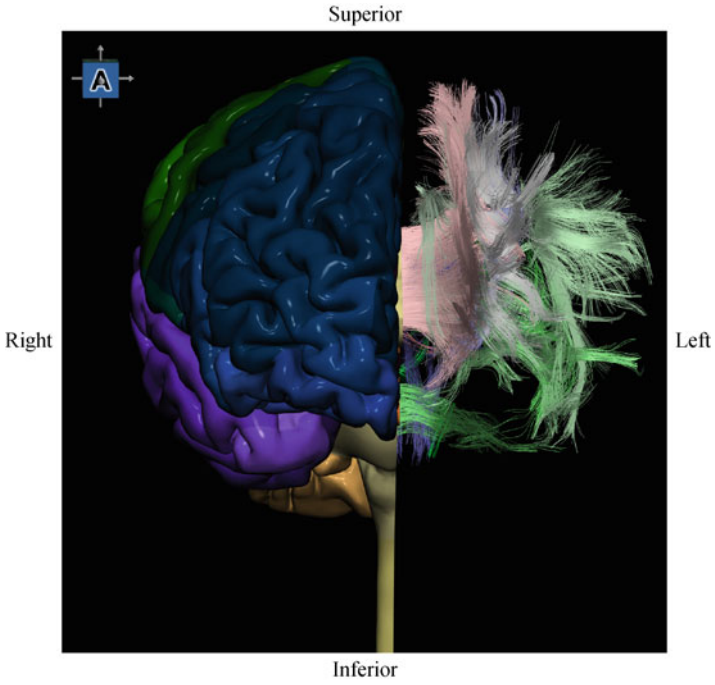

Fig. 2.27 White matter tracts of the left cerebral hemisphere; for comparison, the right hemisphere is shown. The tracts have been mapped by means of diffusion tensor imaging

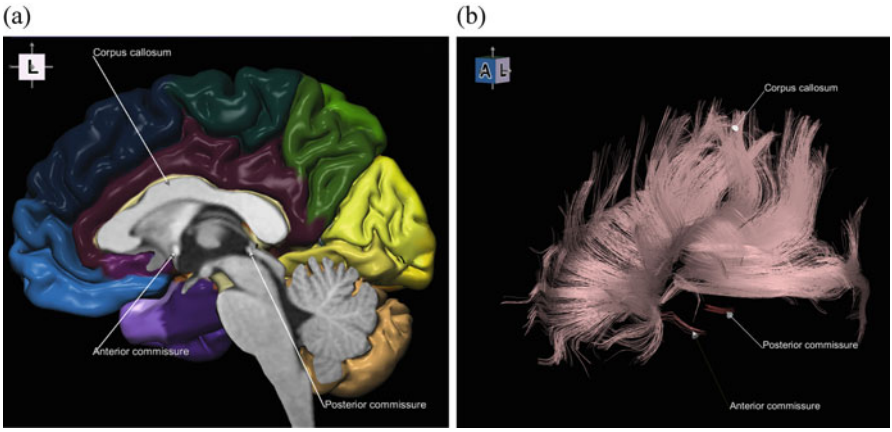

Fig. 2.28 Commissural tracts with the corpus callosum, anterior commissure, and posterior commissure: (**a**) on the midsagittal plane; (**b**) in 3D

The projection fibres located between the striatum and thalamus form the *internal capsule* consisting of the *anterior limb* (containing the corticothalamic tract), *genu*

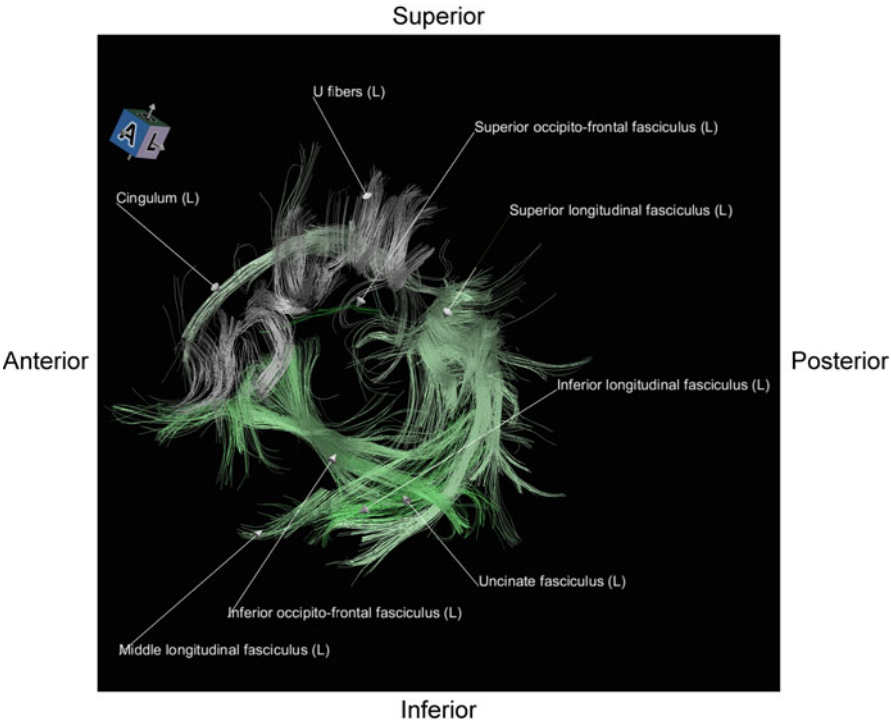

Fig. 2.29 Association tracts of the left cerebral hemisphere

(comprising the corticobulbar tract), and *posterior limb* (containing the corticospinal tract). The fibres radiating from the internal capsule to various parts of the cerebral cortex form the *corona radiata*.

2.5 Recent Extensions and Future Brain Atlas Developments

From the first edition of this book, our brain atlas work has substantially been advanced in terms of atlas creation and development of atlas-based applications. The taxonomy of our brain atlases, grouped into three families, has been presented in [109]. New atlas-based solutions have been proposed for stroke (the probabilistic stroke atlas for outcome prediction [110]), neuroradiology (an atlas assistance in image interpretation in multiple situations and in communication [108]), and neurology (the 3D atlas of neurologic disorders discussed below) [113].

We have created several new editions of the 3D anatomic and reference brain atlas and extended the virtual brain to the head and neck [93–96]. The existing tissue modules (such as the cortex [101] and white matter tracts [102]) have been

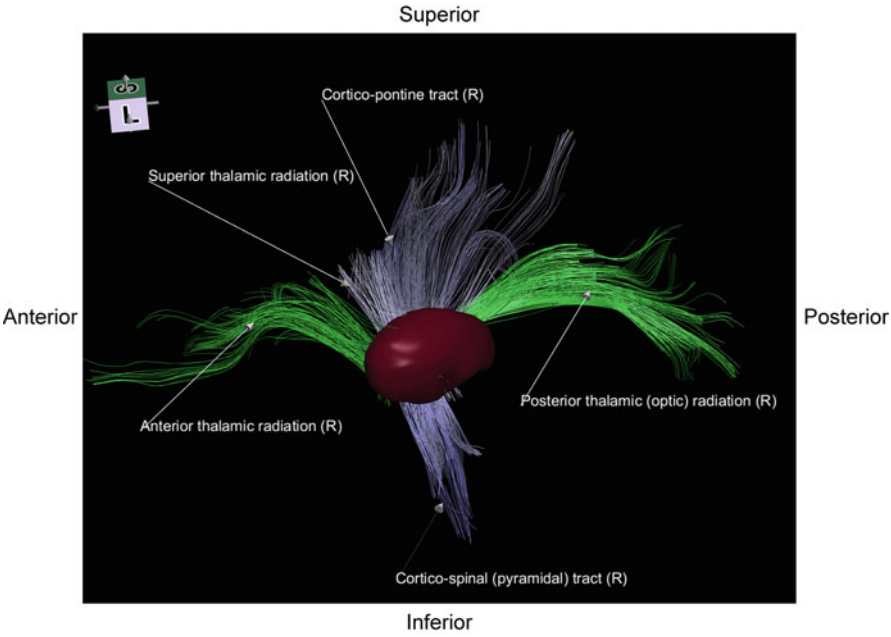

Fig. 2.30 Projection tracts of the right cerebral hemisphere along with the thalamus

further validated and new tissue modules created, including the cranial nerves with brainstem nuclei [103], extracranial arteries and veins [104], head muscles and glands [105], and skull [106]. The latest, most advanced neuroanatomic atlas is entitled *The Human Brain, Head and Neck in 2953 Pieces* [96]. A description of its content, functionality, and usefulness is addressed in [107]. Moreover, the publisher made this atlas publically available from www.thieme.com/nowinski (and also at http://www.wieslawnowinski.com/FreeBrainAtlas). The atlas is an ideal tool to study, explore, and teach brain anatomy extended to the head and neck. The virtual model is parcellated into about 3000 3D pieces. The atlas is interactive, 3D, fully parcellated, completely labelled, advanced, detailed, accurate, reference, realistic, of high resolution, spatially consistent, user-friendly, extendable (scalable), composable (enable to compose any scene), dissectible, explorable, stereotactic, and modular. It provides a user-friendly navigator enabling real-time structure and scan manipulation, 3D labelling of surface and sectional anatomy, structure assembling and disassembling, brain virtual dissection, interaction combined with animation, quantification (distances, vessel diameters, and stereotactic coordinates), and saving the composed and labelled scenes facilitating creation of teaching materials. The reader is encouraged to download this atlas and explore the beauty of virtual brain anatomy by him-/herself.

The neuroanatomic atlas has subsequently been extended towards neurology by creating a 3D interactive atlas of neurologic disorders providing a correspondence

between a brain lesion (damage) and the resulting disorder(s) [97]. We have simulated brain damage at various locations and developed a brain pathology database with focal and distributed vascular [111], cranial nerve-related [112], and regional anatomy-related [113] synthesised lesions. Each lesion has been labelled with the resulting disorder and associated signs, symptoms, and/or syndromes (and additionally linked with relevant neurology textbook materials).

Mobile versions of the anatomic and neurologic disorders atlases also have been developed [98–100].

Finally, celebrating my 25th anniversary of brain atlasing work and 20th anniversary of the release of my first brain atlas product [117], I published two review papers [115, 116]. In [115], I gave an overview of mathematical methods as well as computational methods and tools in brain atlasing, sharing our contribution and experience about the methods devised and tools developed to create brain atlases and develop atlas-based applications. In [116], I presented the state of the art in brain atlasing and summarised my past and present efforts; shared my experience in atlas creation, validation, and commercialisation; compared our work with the state of the art; and proposed future directions, namely, to develop a disruptive, multilevel brain atlas platform with three directions: content spanning from molecules to behaviour; variability covering structure, function, and disorders; and time across the lifespan.

2.6 Summary

The brain contains the cerebrum, cerebellum, and brainstem, and it encases the ventricular system. The cerebrum comprises the paired cerebral hemispheres, diencephalon (with thalamus and hypothalamus), and deep grey matter nuclei, the main of them including the caudate nucleus, putamen, lateral and medial globus pallidus, hippocampus, and amygdala. The cerebral hemispheres are parcellated into the frontal, temporal, parietal, occipital, and limbic lobes. The cerebellum contains the paired cerebellar hemispheres united by the midline vermis. The brainstem is subdivided into the midbrain, pons, and medulla. The ventricular system contains the paired lateral and midline third and fourth ventricles.

The cerebral vasculature comprises the arterial and venous systems. The brain is supplied by two pairs of arteries: internal carotid arteries anteriorly and vertebral arteries posteriorly. The anterior and posterior circulations are connected by the circle of Willis, from which originate three paired branches: anterior cerebral, middle cerebral, and posterior cerebral arteries. The venous system contains the dural sinuses and cerebral superficial and deep veins.

The brain is connected by the commissural, association, and projection tracts. The main commissural tracts (interconnecting both hemispheres) are the corpus callosum and anterior and posterior commissures. The major association tracts (interconnecting different regions of the same hemisphere) are superior longitudinal, middle longitudinal, inferior longitudinal, superior occipito-frontal, inferior occipito-frontal, and uncinate fascicles. The main projection tracts (connecting

the cortex with the subcortical structures) contain corticospinal, corticothalamic (including optic radiation), corticobulbar, and corticopontine tracts as well as auditory radiation.

Acknowledgement The brain atlas development work was funded by A*STAR, Singapore.

References

Neuroanatomy Textbooks

1. Apuzzo, M.L.J., Todd, E.M., Trent Jr., H.W.: Surgery of the Human Cerebrum. Lippincott Williams & Wilkins, Philadelphia (2009)
2. Arslan, O.: Neuroanatomical Basis of Clinical Neurology. Parthenon Publishing Group, Lancaster (2001)
3. Blumenfeld, H.: Neuroanatomy though Clinical Cases. Sinauer Associates, Inc, Sunderland (2002)
4. Borden, N.M.: 3D Angiographic Atlas of Neurovascular Anatomy and Pathology. Cambridge University Press, Cambridge (2007)
5. Carpenter, M.B., Sutin, J.: Human Neuroanatomy. Williams and Wilkins, Baltimore (1983)
6. Grand, W., Hopkins, L.N.: Vasculature of the Brain and Cranial Base: Variations in Clinical Anatomy. Thieme, Stuttgart/New York (1999)
7. Gray, H., Bannister, L.H., Berry, M.M., Williams, P.L.: Gray's Anatomy: The Anatomical Basis of Medicine and Surgery, 38th edn. Churchill Livingstone, Oxford (1995)
8. Harnsberger, H.R., Osborn, A.G., Ross, J., Macdonald, A.: Diagnostic and Surgical imaging anatomy: Brain, head and neck, spine. Amirsys, Salt Lake City (2006)
9. Hendelman, W.J.: Atlas of Functional Neuroanatomy. CRC Press LLC, Boca Raton (2000)
10. Huber, P.: Cerebral Angiography, 2nd edn. Thieme, Stuttgart/New York (1982)
11. Kretschmann, H.J., Weinrich, W.: Neurofunctional Systems. 3D Reconstructions with Correlated Neuroimaging. Thieme, Stuttgart/New York (1998)
12. Kretschmann, H.J., Weinrich, W.: Cranial Neuroimaging and Clinical Neuroanatomy, 3rd edn. Thieme, Stuttgart/New York (2004)
13. Lasjaunias, P., Berenstein, A., ter Brugge, K.G.: Surgical Neuroangiography: Clinical Vascular Anatomy and Variations, 2nd edn. Springer, Berlin (2001)
14. Martin, J.: Neuroanatomy Text and Atlas. Appleton & Lange, Norwalk (1989)
15. Netter, F.H.: The Ciba Collection of Medical Illustrations, Volume 1: Nervous System, Part 1: Anatomy and Physiology. CIBA-GEIGY, Summit (1991)
16. Nieuwennhuys, R., Voogd, J., van Huijzen, C.: The Human Central Nervous System. A Synopsis and Atlas, 4th edn. Springer, Berlin (2008)
17. Osborn, A.G., Ross, J., Crim, J., Salzman, K.L., Blaser, S.I.: Expert Differential Diagnoses: Brain and Spine. Amirsys, Salt Lake City (2008)
18. Purves, D., Augustine, G.J., Fitzpatrick, D., Hall, W.C., LaMantia, A.S., McNamara, J.O., White, L.E.: Neuroscience, 4th edn. Sinauer Associates, Inc, Sunderland (2007)
19. Rhoton, A.L.: Cranial Anatomy and Surgical Approaches. The Congress of Neurological Surgeons, Schaumburg (2003)
20. Salamon, G., Huang, Y.P.: Radiological Anatomy of the Brain. Springer, Berlin (1976)
21. Stephens, R.B., Stilwell, D.L.: Arteries and Veins of the Human Brain. CC Thomas, Springfield (1969)
22. Yasargil, M.G.: Microneurosurgery, vol. 1. Thieme, Stuttgart (1984)

Print Brain Atlases

23. Afshar, E., Watkins, E.S., Yap, J.C.: Stereotactic Atlas of the Human Brainstem and Cerebellar Nuclei. Raven Press, New York (1978)
24. Andrew, J., Watkins, E.S.: A Stereotaxic Atlas of the Human Thalamus and Adjacent Structures. A Variability Study. Williams and Wilkins, Baltimore (1969)
25. Cho, Z.H.: 7.0 Tesla MRI Brain Atlas: In Vivo Atlas with Cryomacrotome Correlation. Springer, Heidelberg (2009)
26. DeArmond, S.J., Fusco, M.M., Dewey, M.M.: Structure of the Human Brain. A Photographics Atlas, 3rd edn. Oxford University Press, New York (1989)
27. Duvernoy, H.M.: The Human Brain. Surface, Three-Dimensional Sectional Anatomy with MRI, and Blood Supply. Springer, New York (1999)
28. Duvernoy, H.M.: The Human Hippocampus: An Atlas of Applied Anatomy. Bergman, Munch (1988)
29. England, M., Wakeley, J.: Color Atlas of the Brain and Spinal Cord, 2nd edn. Mosby, St Louis (2005)
30. Fix, J.D.: Atlas of the Human Brain and Spinal Cord. Aspen, Rockville (1987)
31. Haines, D.E.: Neuroanatomy: An Atlas of Structures, Sections, and Systems, 7th edn. Lippincott Williams & Wilkins, Baltimore (2008)
32. Kraus, G.E., Bailey, G.J.: Microsurgical Anatomy of the Brain. A Stereo Atlas. Williams & Wilkins, Baltimore (1994)
33. Mai, J.K., Assheur, J., Paxinos, G.: Atlas of the Human Brain, 2nd edn. Academic Press, San Diego (2003)
34. Mai, J.K., Paxinos, G., Voss, T.: Atlas of the Human Brain, 3rd edn. Academic Press, Oxford (2008)
35. McMinn, R.M.H., Hutchings, R.T., Pegington, J., Abrahams, P.: Color Atlas of Human Anatomy, 3rd edn. Mosby Year Book, St. Louis (1993)
36. Morel, A., Magnin, M., Jeanmonod, D.: Multiarchitectonic and stereotactic atlas of the human thalamus. J. Comp. Neurol. **387**, 588–630 (1997)
37. Naidich, T.P., Duvernoy, H.M., Delman, B.N., Sorensen, A.G., Kollias, S.S., Haacke, E.M.: Duvernoy's Atlas of the Human Brain Stem and Cerebellum: High-Field MRI, Surface Anatomy, Internal Structure, Vascularization and 3D Sectional Anatomy. Springer, New York (2009)
38. Ono, M., Kubik, S., Abernathey, C.D.: Atlas of the Cerebral Sulci. Thieme, Stuttgart (1990)
39. Orrison Jr., W.W.: Atlas of Brain Function, 2nd edn. Thieme, New-York/Stuttgart (2008)
40. Putz, R.: Sobotta Atlas of Human Anatomy: Head, Neck, Upper Limb, Thorax, Abdomen, Pelvis, Lower Limb, 14th edn. Churchill Livingstone, Oxford (2008)
41. Schaltenbrand, G., Bailey, W.: Introduction to Stereotaxis with an Atlas of the Human Brain. Thieme, Stuttgart (1959)
42. Schaltenbrand, G., Wahren, W.: Atlas for Stereotaxy of the Human Brain. Thieme, Stuttgart (1977)
43. Schitzlein, H.N., Murtagh, F.R.: Imaging Anatomy of the Head and Spine. A Photographic Color Atlas of MRI, CT, Gross, and Microscopic Anatomy in Axial, Coronal, and Sagittal Planes, 2nd edn. Urban & Schwarzenberg, Baltimore (1990)
44. Schuenke, M., Schulte, E., Schumacher, U., Ross, L., Lamperti, E.: Head and Neuroanatomy. Thieme Atlas of Anatomy. Thieme, New York (2007)
45. Speigel, E.A., Wycis, H.T.: Stereoencephalotomy: Part I. Methods and Stereotactic Atlas of the Human Brain. Grune and Stratton, New York (1952)
46. Szikla, G., Bouvier, G., Hori, T.: Angiography of the Human Brain Cortex: Atlas of Vascular Patterns and Stereotactic Localization. Springer, Berlin (1977)
47. Talairach, J., David, M., Tournoux, P.: Atlas d'Anatomie Stereotaxique des Noyaux Gris Centraux. Masson, Paris (1957)

48. Talairach, J., Tournoux, P.: Co-Planar Stereotactic Atlas of the Human Brain. Thieme, Stuttgart/New York (1988)
49. Talairach, J., Tournoux, P.: Referentially Oriented Cerebral MRI Anatomy: Atlas of Stereotaxic Anatomical Correlations for Gray and White Matter. Thieme, Stuttgart (1993)
50. Van Buren, J.M., Borke, R.C.: Variations and Connections of the Human Thalamus. Springer, Berlin (1972)
51. Woolsey, T.A., Hanaway, J., Mokhtar, H.G.: The Brain Atlas: A Visual Guide to the Human Central Nervous System, 2nd edn. Wiley, Hoboken (2003)

Electronic Brain Atlases

52. A.D.A.M: A.D.A.M Animated Dissection of Anatomy for Medicine. User's Guide, A.D.A.M. Atlanta, USA (1996)
53. Bayer. Microvascular Atlas of the Head and Neck. CD-ROM for Macintosh and Windows. Atlanta, USA (1996)
54. Berkovitz, B., Kirsch, C., Moxham, B., Alusi, G., Cheeseman, T.: Interactive Head & Neck. CD-ROM PC and Mac compatible. Primal, London (2003)
55. Bertrand, G., Olivier, A., Thompson, C.J.: Computer display of stereotaxic brain maps and probe tracts. Acta Neurochir. Suppl. **21**, 235–243 (1974)
56. Dev, P., Coppa, G.P., Tancred, E.: BrainStorm: designing in interactive neuroanatomy atlas. Radiology. **185**(P), 413 (1992)
57. Evans, A.C., Collins, L., Milner, B.: An MRI-based stereotactic atlas from 250 young normal subjects. Soc. Neurosci. Abstr. **18**, 408 (1992)
58. Ganser, K.A., Dickhaus, H., Metzner, R., Wirtz, C.R.: A deformable digital brain atlas system according to Talairach and Tournoux. Med. Image Anal. **8**(1), 3–22 (2004)
59. Greitz, T., Bohm, C., Holte, S., Eriksson, L.: A computerized brain atlas: construction, anatomical content, and some applications. J. Comput. Assist. Tomogr. **15**(1), 26–38 (1991)
60. Hoehne, K.H.: VOXEL-MAN, Part 1: Brain and Skull, Version 2.0. Springer, Heidelberg (2001)
61. Kazarnovskaya, M.I., Borodkin, S.M., Shabalov, V.A.: 3-D computer model of subcortical structures of human brain. Comput. Biol. Med. **21**, 451–457 (1991)
62. Netter's Anatomy. http://evolve.elsevier.com/staticPages/s_netter_iphone.html (2008)
63. Nowinski, W.L., Bryan, R.N., Raghavan, R.: The Electronic Clinical Brain Atlas. Multiplanar Navigation of the Human Brain. Thieme, New York (1997)
64. Nowinski, W.L., Thirunavuukarasuu, A., Kennedy, D.N.: Brain Atlas for Functional Imaging. Clinical and Research Applications. Thieme, New York (2000)
65. Nowinski, W.L., Thirunavuukarasuu, A., Bryan, R.N.: The Cerefy Atlas of Brain Anatomy. An Introduction to Reading Radiological Scans for Students, Teachers, and Researchers. Thieme, New York (2002)
66. Nowinski, W.L., Thirunavuukarasuu, A.: The Cerefy Clinical Brain Atlas on CD-ROM. Thieme, New York (2004)
67. Nowinski, W.L., Thirunavuukarasuu, A., Benabid, A.L.: The Cerefy Clinical Brain Atlas: Enhanced Edition with Surgical Planning and Intraoperative Support. Thieme, New York (2005)
68. Nowinski, W.L., Thirunavuukarasuu, A., Volkau, I., Marchenko, Y., Runge, V.M.: The Cerefy Atlas of Cerebral Vasculature. Thieme, New York (2009)
69. Nowinski, W.L., Chua, B.C., Qian, G.Y., Marchenko, Y., Puspitasari, F., Nowinska, N.G., Knopp, M.V.: The Human Brain in 1492 Pieces. Structure, Vasculature, and Tracts. Thieme, New York (2011)
70. Nowinski, W.L., Thirunnavuukarasuu, A., Volkau, I., Marchenko, Y., Aminah, B., Puspitasaari, F., Runge, V.M.: A three-dimensional interactive atlas of cerebral arterial variants. Neuroinformatics. **7**(4), 255–264 (2009)

71. Sramka, M., Ruzicky, E., Novotny, M.: Computerized brain atlas in functional neurosurgery. Stereotact. Funct. Neurosurg. **69**, 93–98 (1997)
72. Sundsten, J.W., Brinkley, J.F., Eno, K., Prothero, J.: The Digital Anatomist. Interactive Brain Atlas. CD ROM for the Macintosh. University of Washington, Seattle (1994)
73. Yelnik, J., Bardinet, E., Dormont, D., Malandain, G., Ourselin, S., Tandé, D., Karachi, C., Ayache, N., Cornu, P., Agid, Y.: A three-dimensional, histological and deformable atlas of the human basal ganglia. I. Atlas construction based on immunohistochemical and MRI data. NeuroImage. **34**(2), 618–638 (2007)
74. Yoshida, M.: Three-dimensional maps by interpolation from the Schaltenbrand and Bailey atlas. In: Kelly, P.J., Kall, B.A. (eds.) Computers in Stereotactic Neurosurgery, pp. 143–152. Blackwell, Boston (1992)

Other Materials

75. Federative Committee on Anatomical Terminology (FCAT): Terminologia Anatomica. Thieme, Stuttgart/New York (1999)
76. Gelas, A., Valette, S., Prost, R., Nowinski, W.L.: Variational implicit surface meshing. Comput. Graph. **33**, 312–320 (2009)
77. Marchenko, Y., Volkau, I., Nowinski, W.L.: Vascular editor: from images to 3D vascular models. J. Digit. Imaging. **23**(4), 386–398 (2010)
78. Nowinski, W.L., Volkau, I., Marchenko, Y., Thirunavuukarasuu, A., Ng, T.T., Runge, V.M.: A 3D model of the human cerebrovasculature derived from 3 tesla 3 dimensional time-of-flight magnetic resonance angiography. Neuroinformatics. **7**(1), 23–36 (2009)
79. Nowinski, W.L., Thirunavuukarasuu, A., Volkau, I., Marchenko, Y., Aminah, B., Gelas, A., Huang, S., Lee, L.C., Liu, J., Ng, T.T., Nowinska, N., Puspitasari, F., Qian, G., Runge, V.M.: A new presentation and exploration of human cerebral vasculature correlated with surface and sectional neuroanatomy. Anat. Sci. Educ. **2**(1), 24–33 (2009)
80. Nowinski, W.L.: The cerefy brain atlases: continuous enhancement of the electronic talairach-tournoux brain atlas. Neuroinformatics. **3**(4), 293–300 (2005)
81. Nowinski, W.L.: Electronic brain atlases: features and applications. In: Caramella, D., Bartolozzi, C. (eds.) 3D Image Processing: Techniques and Clinical Applications Medical Radiology series, pp. 79–93. Springer, Berlin (2002)
82. Nowinski, W.L., Fang, A., Nguyen, B.T., Raphel, J.K., Jagannathan, L., Raghavan, R., Bryan, R.N., Miller, G.: Multiple brain atlas database and atlas-based neuroimaging system. Comput. Aided Surg. **2**(1), 42–66 (1997)
83. Nowinski, W.L.: Anatomical and probabilistic functional atlases in stereotactic and functional neurosurgery. In: Lozano, A., Gildenberg, P., Tasker, R. (eds.) Textbook of Stereotactic and Functional Neurosurgery, 2nd edn, pp. 395–441. Springer, Berlin (2009)
84. Nowinski, W.L., Qian, G., Bhanu Prakash, K.N., Volkau, I., Thirunavuukarasuu, A., Hu, Q., Ananthasubramaniam, A., Liu, J., Gupta, V., Ng, T.T., Leong, W.K., Beauchamp, N.J.: A CAD system for acute ischemic stroke image processing. Int. J. Comput. Assisted Radiol. Surg. **2**(Suppl. 1), 220–222 (2007)
85. Nowinski, W.L., Qian, G., Bhanu Prakash, K.N., Thirunavuukarasuu, A., Hu, Q.M., Ivanov, N., Parimal, A.S., Runge, V.L., Beauchamp, N.J.: Analysis of ischemic stroke MR images by means of brain atlases of anatomy and blood supply territories. Acad. Radiol. **13**(8), 1025–1034 (2006)
86. Nowinski, W.L., Belov, D.: The Cerefy Neuroradiology Atlas: a Talairach-Tournoux atlas-based tool for analysis of neuroimages available over the internet. NeuroImage. **20**(1), 50–57 (2003)
87. Nowinski, W.L., Thirunavuukarasuu, A.: A locus-driven mechanism for rapid and automated atlas-assisted analysis of functional images by using the Brain Atlas for Functional Imaging. Neurosurg. Focus. **15**(1), Article 3 (2003)

88. Nowinski, W.L., Benabid, A.L.: New directions in atlas-assisted stereotactic functional neurosurgery. In: Germano, I.M. (ed.) Advanced Techniques in Image-Guided Brain and Spine Surgery, pp. 162–174. Thieme, New York (2002)
89. Nowinski, W.L.: Computerized brain atlases for surgery of movement disorders. Semin. Neurosurg. **12**(2), 183–194 (2001)
90. Nowinski, W.L., Yang, G.L., Yeo, T.T.: Computer-aided stereotactic functional neurosurgery enhanced by the use of the multiple brain atlas database. IEEE Trans. Med. Imaging. **19**(1), 62–69 (2000)
91. Nowinski, W.L., Chua, B.C., Volkau, I., Puspitasari, F., Marchenko, Y., Runge, V.M., Knopp, M.V.: Simulation and assessment of cerebrovascular damage in deep brain stimulation using a stereotactic atlas of vasculature and structure derived from multiple 3T and 7T scans. J. Neurosurg. **113**(6), 1234–1241 (2010)
92. Volkau, I., Zheng, W., Aziz, A., Baimouratov, R., Nowinski, W.L.: Geometric modeling of the human normal cerebral arterial system. IEEE Trans. Med. Imaging. **24**, 529–539 (2005)

Recent Brain Atlases Created (Products)

93. Nowinski, W.L., Chua, B.C., Qian, G.Y., Marchenko, Y., Puspitasari, F., Nowinska, N.G., Knopp, M.V.: The Human Brain in 1492 Pieces: Structure, Vasculature, and Tracts (version 1.1 for MAC). Thieme, New York (2011)
94. Nowinski, W.L., Chua, B.C., Qian, G.Y., Nowinska, N.G.: The Human Brain in 1969 Pieces: Structure, Vasculature, Tracts, Cranial Nerves, and Systems. Thieme, New York (2013)
95. Nowinski, W.L., Chua, B.C.: The Human Brain in 1969 Pieces: Structure, Vasculature, Tracts, Cranial Nerves, Systems, Head Muscles, and Glands (version 2.0). Thieme, New York (2014)
96. Nowinski, W.L., Chua, B.C., Thaung, T.S.L., Wut Yi, S.H.: The Human Brain, Head and Neck in 2953 Pieces. Thieme, New York (2015). http://www.thieme.com/nowinski/
97. Nowinski, W.L., Chua, B.C., Wut Yi, S.H.: 3D Atlas of Neurologic Disorders (version 1.0). Thieme, New York (2014)
98. Nowinski, W.L., Chua, B.C.: The Complete Human Brain (version 1.0 for iPad). Thieme, New York (2013). /AppStore
99. Nowinski, W.L., Chua, B.C., Ngai, V.: The 3D Brain Atlas (version 1.0 for Android). Thieme, New York (2014)
100. Nowinski, W.L., Chua, B.C., Ngai, V.: 3D Atlas of Neurologic Disorders (version 1.0 for iPad). Thieme, New York (2013). /AppStore

Recent Extensions and Future Directions in Brain Atlasing

101. Nowinski, W.L., Chua, B.C., Qian, G.Y., Nowinska, N.G.: The human brain in 1700 pieces: design and development of a three-dimensional, interactive and reference atlas. J. Neurosci. Methods. **204**(1), 44–60 (2012)
102. Nowinski, W.L., Chua, B.C., Yang, G.L., Qian, G.Y.: Three-dimensional interactive human brain atlas of white matter tracts. Neuroinformatics. **10**(1), 33–55 (2012)
103. Nowinski, W.L., Johnson, A., Chua, B.C., Nowinska, N.G.: Three-dimensional interactive and stereotactic atlas of cranial nerves and nuclei correlated with surface neuroanatomy, vasculature and magnetic resonance imaging. J. Neurosci. Methods. **206**(2), 205–216 (2012)
104. Nowinski, W.L., Thaung, T.S.L., Chua, B.C., Wut Yi, S.H., Yang, Y., Urbanik, A.: Three-dimensional stereotactic atlas of the extracranial vasculature correlated with the intracranial vasculature, cranial nerves, skull and muscles. Neuroradiol. J. **28**(2), 190–197 (2015)

105. Nowinski, W.L., Chua, B.C., Johnson, A., Qian, G., Poh, L.E., Wut Yi, S.H., Aminah, B., Nowinska, N.G.: Three-dimensional interactive and stereotactic atlas of head muscles and glands correlated with cranial nerves and surface and sectional neuroanatomy. J. Neurosci. Methods. **215**(1), 12–18 (2013)
106. Nowinski, W.L., Thaung, T.S.L., Chua, B.C., Wut Yi, S.H., Ngai, V., Yang, Y., Chrzan, R., Urbanik, A.: Three-dimensional stereotactic atlas of the adult human skull correlated with the brain, cranial nerves and intracranial vasculature. J. Neurosci. Methods. **246**, 65–74 (2015)
107. Nowinski, W.L.: 3D Atlas of the brain, head and neck in 2953 pieces. Neuroinformatics. **15**(4), 395–400 (2017)
108. Nowinski, W.L.: Usefulness of brain atlases in neuroradiology: current status and future potential. Neuroradiol. J. **29**(4), 260–268 (2016)
109. Nowinski, W.L.: Towards the holistic, reference and extendable atlas of the human brain, head and neck. Brain Inform. **2**(2), 65–76 (2015)
110. Nowinski, W.L., Gupta, V., Qian, G.Y., Ambrosius, W., Kazmierski, R.: Population-based stroke atlas for outcome prediction: method and preliminary results for ischemic stroke from CT. PLoS One. **9**(8), e102048 (2014). eCollection 2014; http://www.plosone.org/article/info%3Adoi%2F10.1371%2Fjournal.pone.0102048
111. Nowinski, W.L., Chua, B.C.: Stroke Atlas: a 3D interactive tool correlating cerebrovascular pathology with underlying neuroanatomy and resulting neurological deficits. Neuroradiol. J. **26**(1), 56–65 (2013)
112. Nowinski, W.L., Chua, B.C.: Three-dimensional interactive atlas of cranial nerve-related disorders. Neuroradiol. J. **26**(3), 263–275 (2013)
113. Nowinski, W.L., Chua, B.C.: Bridging neuroanatomy, neuroradiology and neurology: three-dimensional interactive atlas of neurological disorders. Neuroradiol. J. **26**(3), 252–262 (2013)
114. Nowinski, W.L., Thaung, T.S.L.: A 3D stereotactic atlas of the adult human skull base. Brain Inform. **5**(2), 1 (2018). https://rdcu.be/UOLj
115. Nowinski, W.L.: Computational and mathematical methods in brain atlasing. Neuroradiol. J. **30**(6), 520–534 (2017)
116. Nowinski, W.L.: Human brain atlasing: past, present and future. Neuroradiol. J. **30**(6), 504–519 (2017)
117. Krejza, J.: Professor Wieslaw Nowinski: 25 years of contribution to the development of digital brain atlases. Neuroradiol. J. **30**(6), 501–503 (2017). (editorial)

Chapter 3
Introduction to Brain Imaging

Einat Liebenthal and Tarun Singhal

3.1 Structural and Functional Brain Imaging: A Comparative Overview of Techniques

There is tremendous individual variability in both the structure and the functional organisation of the human brain. Like fingerprints, each brain has a unique configuration of gyri and sulci (crests and troughs, respectively, in the surface of the brain) [75, 122]. The brain's functional organisation can be approximated based on the gross neuroanatomy. For example, the primary sensorimotor cortices are in the pre- and postcentral gyri, the primary auditory cortex is in Heschl's gyrus, and the primary visual cortex is in the calcarine sulcus [84]. However, gross neuroanatomical structures are generally not valid markers of the microstructural and functional organisation of the cortex [136]. In patients with a brain pathology, oedema or mass effects may obliterate the structure of gyri and sulci and can induce plasticity in the functional organisation, further limiting the validity of gross neuroanatomical landmarks for deriving function. Thus, personalised structural and functional neuroimaging is necessary for mapping brain function. In this chapter, the main structural and functional neuroimaging methods relevant to diagnosis and management of patients with a brain tumour or epilepsy are reviewed.

E. Liebenthal (✉) · T. Singhal
Brigham & Women's Hospital, Harvard Medical School, Boston, MA, USA
e-mail: ELIEBENTHAL@BWH.HARVARD.EDU

K. Miller (ed.), *Biomechanics of the Brain*, Biological and Medical Physics, Biomedical Engineering, https://doi.org/10.1007/978-3-030-04996-6_3

3.1.1 Magnetic Resonance Imaging (MRI)-Based Brain Imaging Techniques

3.1.1.1 Magnetic Resonance Imaging (MRI)

Magnetic resonance imaging (MRI) provides good contrast resolution between different soft tissues, making it particularly useful in the brain. The discoveries that led to the development of modern MRI were first reported in the 1970s [62, 74], and since its introduction as a diagnostic tool in the 1980s, MRI has become the main modality for structural neuroimaging. The advent of higher-field magnets (3 Tesla) has resulted in standard imaging at an exquisite spatial resolution of approximately 1 mm^3, permitting visualisation of fine anatomic details at clinically acceptable short acquisition times. MRI is vastly superior to other structural imaging methods such as X-ray, computed tomography (CT), and ultrasound, in terms of spatial resolution and the delineation of tumours [4]. In addition, different from X-ray and CT which involve ionising radiation, MRI is based on noninvasive radio-frequency excitation of biological molecules with magnetic properties.

3.1.1.2 Functional Magnetic Resonance Imaging (fMRI)

Functional magnetic resonance imaging (fMRI) is used to map function in the entire brain noninvasively. fMRI is an indirect measure that is based on the premise of a relationship between local changes in neural activity and cerebral blood dynamics [70, 71]. fMRI using the blood oxygenation level-dependent (BOLD) contrast is a method to measure local changes in the concentration of paramagnetic deoxyhaemoglobin that are associated with an increase in blood flow to active regions in the brain [58, 89]. First reports of fMRI in humans demonstrated that visual stimulation produces a detectable transient increase in the intensity of water proton magnetic resonance signal in the primary visual cortex [12, 90]. Similar increases in fMRI signal were found in the motor cortex during finger movement [9]. The spatial resolution of fMRI is high, typically ranging 3–5 mm for most common applications. But the temporal resolution is low, with a mean rise time for signal change of 4–6 seconds, approximately two orders of magnitude slower than the underlying neural activity.

fMRI has transformed research in cognitive neuroscience, as well as clinical applications such as presurgical mapping of eloquent cortex, because of the low invasiveness, imaging of function in the entire brain with exquisite spatial resolution, and relatively wide availability [33]. Two decades of fMRI research in cognitive neuroscience have highlighted the distributed and individual (related to learning and memory or caused by pathological changes) nature of brain function, largely contradicting the classic view emerging form earlier lesion studies of a fixed and focal relationship between brain anatomy and function [78]. The modern understanding of the organisation of cognitive brain functions emphasises the value of fMRI mapping for identifying neural network systems in individual patients and

the limitation of this technique for predicting the necessity of a specific brain region for carrying out certain functions.

3.1.1.3 Diffusion Tensor Imaging (DTI)

Diffusion tensor imaging (DTI) is a relatively newer method to detect the orientation and integrity of white matter fibres in vivo [11, 97]. DTI has generated much interest because it currently is the only approach available to noninvasively study the three-dimensional architecture of white matter tracts [79]. DTI is sensitive to the diffusion of water molecules in the direction of the field gradient. Diffusion is anisotropic in white matter tracts because the axonal membranes and myelin sheaths limit the motion of water molecules to the orientation parallel to the fibre. Thus, the direction of maximum diffusivity has been shown to coincide with the white matter fibre tract orientation [80]. A minimum of six diffusion-encoded measurements are required to accurately describe the diffusion tensor (mathematical 3D model of diffusion), but using more directions will improve the accuracy of the tensor measurement [91]. Fibre tractography is a post-processing derivation of the diffusion data whereby three-dimensional trajectories of white matter tracts are reconstructed based on the estimates of fibre orientation in each voxel. The visualisation in three dimensions can assist in identifying specific fibre tracts.

3.1.1.4 Ultrahigh Magnetic Fields

At ultrahigh magnetic fields (7 Tesla and above), the intrinsic signal-to-noise ratio (SNR) of MRI and the BOLD signal change of fMRI are increased, enabling even higher-resolution anatomic and functional imaging compared to traditional field strengths (1.5 and 3 Tesla). The enhanced imaging can afford finer detail of the brain's functional organisation and improved detection of subtle anatomic and functional abnormalities associated with neurologic disorders. However, at ultrahigh magnetic fields, increased vulnerability to image artifacts and restrictions on image acquisition time pose limitations on the spatial coverage of the brain and require the development of customised acquisition sequences and specialised hardware (recently reviewed in [8, 55, 129]).

3.1.2 Electrophysiological Brain Imaging Techniques

3.1.2.1 Electroencephalography (EEG) and Magnetoencephalography (MEG)

Electrophysiological techniques to probe the electrical activity of the brain directly (i.e. not via the haemodynamic reactivity) and noninvasively were introduced in

the last century. The discovery that small fluctuations in electrical potentials can be measured from the human scalp, a method termed scalp electroencephalography (EEG), was first reported by the German psychiatrist Berger in 1929. Magnetoencephalography (MEG), or the recording of magnetic fields produced by the electrical currents in the brain, was first achieved in the late 1960s [21, 22]. Both EEG and MEG have since evolved to include more recording channels and improved amplification technology. From a practical standpoint, EEG devices are widely available, have relatively low cost, and can also be portable and used for long-term recordings. On the other hand, multichannel MEG is more practical than multichannel EEG because EEG (but not MEG) requires manually establishing contact between each channel sensor and the scalp. Nevertheless, MEG scanners are still scant, generally limiting the use of this technology.

EEG and MEG both measure currents arising primarily from excitatory and inhibitory postsynaptic potentials along the dendritic tree of pyramidal neurons in the cerebral cortex [88]. Neurons in large areas of cortex, on the order of a few square centimetres, must be synchronously active to generate a detectable electrical or magnetic field on the scalp. Both EEG and MEG have exquisite temporal resolution on the order of 1 millisecond, highly superior to the temporal resolution of fMRI. Despite the correspondence in the neural origin of the EEG and MEG signals, there are important differences that result in different sensitivity of the techniques in certain brain areas. Scalp EEG is sensitive to neural sources generating electrical fields both tangential and radial to the scalp, whereas MEG is sensitive primarily to sources generating electrical fields tangential to the scalp. Thus, MEG selectively measures activity in the grey matter of the sulci of the brain, whereas scalp EEG measures activity both in the grey matter of the sulci and gyri. Magnetic fields are also less distorted by the resistive properties of the skull and scalp, and they decay faster as a function of distance from the source, than electrical fields. Thus, MEG has increased sensitivity and superior spatial resolution for superficial cortical activity, compared to EEG [2, 43].

Modelling of EEG and MEG scalp activity to localise the neural source(s) is fundamentally ill posed because no unique solution exists to this inverse problem [117]. However, modelling of MEG activity is somewhat simplified by the fact that fewer sources are identified with this technique and at higher spatial resolution. Generally good agreement has been reported between EEG and MEG source localisations, although differences exist and can be attributed to the differences in sensitivity to source orientation discussed above. Thus, the techniques are best considered complementary [7, 69].

EEG and MEG responses associated with specific external or internal events, termed event-related potentials (ERPs), can be obtained by simple averaging of many epochs, aligned by the time of occurrence of the event of interest [31, 132]. ERP waveforms consist of a sequence of peaks characterised by their polarity, absolute and inter-peak latency, type of stimuli and experimental conditions that elicit them, and scalp topography. Latency measures are by far the most useful aspect of ERPs for clinical applications. Deviations in peak latency measures can indicate abnormal neural conduction, for example, as a result of demyelination in

a neurodegenerative disease such as multiple sclerosis [40]. ERPs are particularly useful in cases when MRI indices of multiple sclerosis are inconclusive [5]. Routine clinical evaluations can include the measurement of short- and middle-latency visual, somatosensory, and auditory evoked potentials for the differential diagnosis of sensory (peripheral) and central nervous system disorders. The measurement of ERPs is objective in that most clinically useful responses are obligatory and independent of the patient's compliance. ERPs can be used to assess the neurological status in patients who are anaesthetised or comatose.

3.1.2.2 Simultaneous fMRI and EEG

Simultaneous recording of brain activity with two neuroimaging modalities can provide information beyond that attainable with each modality alone. The development of simultaneous MRI/EEG was motivated by clinical interest in mapping sources of epileptic discharges onto MR images [47]. Simultaneous fMRI/EEG is particularly attractive because it holds the promise of capitalising on the fine spatial resolution of fMRI and the fine temporal resolution of EEG. The combination of fMRI and EEG may allow improved localisation of neural generators identified with EEG, as well as enhanced temporal resolution of focal activity measured with BOLD fMRI [60, 66, 67]. Simultaneous recordings are preferable to sequential recordings in that they allow perfect correspondence of the experimental conditions (acoustic and visual environment) and cognitive factors (task performance, attention) between the recordings. This is critical for studying cognitive functions involving learning, memory, or attention. However, simultaneous recordings are technically challenging as they essentially involve running two experiments at the same time. The analysis of simultaneous fMRI/EEG data entails extracting small EEG signals from measurements made in the electromagnetically noisier MRI environment [17, 28, 107], as well as integrating EEG and fMRI signals with inherently different spatiotemporal scales [73]. The primary clinical application of simultaneous fMRI/EEG is for the localisation of epileptic zones [35, 59].

3.1.2.3 Intracranial EEG (iEEG)

EEG can also be obtained intracranially, using strips or grids of electrodes implanted in the subdural space (electrocorticography – ECog), or using wires of electrodes inserted into deeper brain structures such as the hippocampus (stereotactic EEG – sEEG) [93]. Intracranial EEG provides high spatial and high temporal resolution of neural activity, however only in the brain areas covered by the electrodes. Because it is an invasive procedure, in humans, iEEG is performed strictly when clinically indicated. iEEG is performed for presurgical localisation of seizure foci in patients with medically intractable epilepsy and provides a unique opportunity to study cognitive functions in vivo and at high spatiotemporal resolution, with the caveats

that the subjects have a brain disease and the electrode location may not be optimal for the research [29, 81].

3.1.3 Molecular Brain Imaging Techniques

3.1.3.1 Positron Emission Tomography (PET)

Molecular brain imaging techniques such as positron emission tomography (PET) provide functional, neurochemical, and neuropathological information at a molecular level, thereby playing a complementary role to anatomical and electrophysiological methods of brain mapping. PET utilises radiolabelled biomolecules to study in vivo biological systems [96]. The PET radioisotopes undergo reactive decay by emission of a 'positron', which is a positively charged subatomic particle that has the same mass but opposite charge as compared to an electron. The most common positron-emitting radioisotopes used in PET imaging include carbon-11 (C-11), oxygen-15 (O-15), nitrogen-13 (N-13), fluorine-18 (F-18), and others. A unique advantage of these positron-emitting isotopes is that they are chemically indistinguishable from the elemental building blocks of biomolecules, that is, carbon-12, oxygen-16, and nitrogen-14. Fluorine-18 often substitutes for a negatively charged hydroxyl group in a given biomolecule. The radiolabelled molecules behave exactly as the parent compound chemically, and this enables in vivo tracing of biomolecular pathways. In addition, these radiopharmaceuticals are injected in extremely small, often picomolar, 'tracer' quantities and, hence, do not interfere with the mass kinetics of the biomolecular process of interest. The positron-emitting radioisotopes have a short physical half-life, ranging from approximately 2 minutes for O-15, 10 minutes for N-13, 20 minutes for C-11, and up to 110 minutes for F-18. Given their nuclear instability, these radioisotopes do not naturally exist in nature and must typically be produced in a medical cyclotron or a generator. A medical cyclotron is a carefully shielded device, which accelerates charged particles to extremely high velocities (close to the speed of light). The particles are then organised into a focused beam to bombard an atomic target and generate the desired PET radioisotope. For example, the production of C-11 involves the bombardment of a N-14 target with an accelerated helium nuclear particle [48]. The underlying nuclear reaction can be represented as follows:

$$^{14}\mathrm{N} + ^{1}\mathrm{H} \rightarrow ^{11}\mathrm{C} + ^{4}\mathrm{He}$$

The next step is to label a 'precursor' molecule with the PET isotope through a series of chemical reactions to generate the desired PET radiopharmaceutical (PRP). The chemical reactions take place in well-shielded semiautomated modules that may require some manual modification using robotic arms to minimise radiation exposure to the involved staff. After its production, the PET radiopharmaceutical undergoes a series of quality control steps to ensure its chemical integrity, the

absence of impurities, and its safety for injection in humans. These steps involve a range of processes, including high-performance liquid chromatography and thin-layer and gas chromatography. Following preparation and passing the quality control steps, the PRP is aliquoted into separate doses for individual patients. The most common PRPs used for human imaging include F-18-labelled fluorodeoxyglucose (FDG), O-15-labelled H2O, N-13-labelled ammonia, and C-11-labelled Pittsburgh compound B, and these PRPs are used for imaging glucose metabolism, tissue perfusion, blood flow, and cerebral amyloid deposition, respectively [50].

The PET scanner detects 511 keV gamma photons produced as a result of the annihilation of positrons emitted by the PRP, when the positron interacts with negatively charged electrons in the tissue environment. Positrons and electrons are antimatter and matter, respectively, and their interaction results in their annihilation and conversion of their mass into energy, according to the $E = mc^2$ rule, thereby leading to the release of two 511 keV gamma photons in opposite directions from the site of annihilation. The law of conservation of momentum governs the release of two gamma photons in two opposite directions because as the positron and electron interact and annihilate, they tend to come to rest. There is, however, some residual momentum (in other words, the positron and electron do not completely come to rest), so the two gamma photons are released at a slight angle to one another. This phenomenon has implications for the resolution of the PET scanner. Scanners with smaller axial diameters have a better spatial resolution than their larger bore counterparts because increasing distance from the site of radioactive decay leads to greater errors in its assessment. Further, the speed of emitted positrons varies with individual PET radioisotopes and determines the distance travelled before interaction with an electron, their subsequent annihilation, and release of photons. This phenomenon also affects the PET resolution. For example, positrons emitted by O-15 decay have higher momentum, travel longer distances before annihilation, and hence lead to poorer spatial resolution, as compared to positrons emitted by F-18 decay. The typical spatial resolution of clinically used PET scanners is approximately 4–4.5 mm. Higher-resolution PET scanners dedicated for human brain imaging are available with a resolution of 2.5 mm. Micro-PET scanners used for animal imaging have a much better resolution (up to 1.2 mm) given their small axial diameters [48, 50]. This is superior to the resolution of single-photon emission computed tomography (SPECT) cameras that typically have a resolution of 6–10 mm.

Image reconstruction algorithms generate a two- and three-dimensional map of the distribution of PRP concentration, which is subsequently utilised for visual interpretation as a PET image and/or for further quantitative analyses.

PET imaging procedure involves positioning of the human or animal subject in a PET scanner. PRP is injected prior to or after subject positioning, depending on individual scanning protocols. Subjects may be scanned at variable intervals after PRP injection, for example, approximately 45 minutes after [F-18] FDG injection to assess glucose metabolism in a ‘static’ image; or the scanning may begin simultaneously with the PRP injection, when ‘kinetic’ data is needed, for

example, in brain receptor studies that require an assessment of changes in tracer concentration over time to derive pharmacokinetic parameters.

From a surgical standpoint, the most common uses of brain PET imaging include identification of a seizure focus and diagnostic and therapeutic planning in brain tumour cases [113].

3.2 Clinical Applications of Brain Imaging for Image-Guided Neurosurgery in Epilepsy and Brain Tumour Patients

The objective of presurgical and intrasurgical brain mapping is to obtain patient-specific structural and functional information that could facilitate maximal tumour or epileptic tissue surgical resection while minimising damage to surrounding grey and white matter structures supporting vital sensorimotor and cognitive functions. Presurgical mapping of functional brain regions and their spatial relationship to a brain lesion can help predict deficits in sensory, motor, or cognitive functions due to surgery or due to continued lesion growth. Presurgical mapping can help guide the decision for course of intervention (extent of resection, alternative treatment) and the decision to conduct intrasurgical functional mapping. Presurgical mapping is also valuable for planning of the surgical approach. Noninvasive neuroimaging imposes less discomfort to the patient than invasive methods such as intra-arterial amobarbital (Wada) testing, which requires a surgical procedure.

A limitation of presurgical mapping is that significant and difficult to predict brain shifts, up to 20 mm in size, can occur during the surgery, primarily in relation to craniotomy and tumour removal [41]. A variety of factors affect the brain shift, including the tissue characteristics, intrasurgical patient positioning, size of craniotomy, and the resected volume [85]. Presurgical information must therefore be compensated for such brain shift throughout the surgery for accurate registration to the intrasurgical space [83]. Estimation of intrasurgical brain shifts can be achieved with intrasurgical ultrasound [53] or MRI [85, 110]. However, accurate nonrigid registration of presurgical images to the intrasurgical space is computationally expensive and time-consuming and therefore challenging for real-time implementation [6, 133]. Recent advances achieved in this field [32] are discussed in detail in other chapters of this book.

A more recent application of MRI is for intrasurgical imaging, to detect residual tumour or lesion tissue *during* surgery and minimise the need for corrective surgery [18]. Intrasurgical MRI requires a dedicated intrasurgical MR scanner or the adaptation of existing MRI scanner technology to the operating theatre [3, 77]. Structural MRI is acquired in the operating room, usually after the planned resection is completed, and sometimes also immediately after craniotomy to estimate intrasurgical brain shifts. Intrasurgical MRI was shown to improve the estimate of residual tumour burden compared to a subjective evaluation by the operating neurosurgeon [15, 86, 106]. Presurgical structural and functional images

such as contrast-enhanced MRI, fMRI, and DTI maps can also be registered to the intrasurgical images, to make this information more readily available during the surgery [87].

3.2.1 Structural MRI

MRI is used to detect cerebral tumours or lesions that may cause seizures. In brain tumour patients, resection of primary tumours can improve survival, functional capability, and the effect of adjuvant therapies, provided that postsurgical neurological deficits can be avoided [4, 52, 128]. In epilepsy patients, resection of an MR-visible lesion near the site of seizure onset, such as mesial temporal sclerosis (scarring of the hippocampus) or cortical dysplasia (cellular maturation abnormality), dramatically increases the chances of freedom from seizures [116]. The use of higher-field MR scanners and thinner image slices and the implementation of advanced sequences such as fluid-attenuated inversion recovery (FLAIR) improve the odds of detecting subtle focal cortical dysplasia [27]. However, in approximately 25% of epilepsy surgery candidates, structural MRI produces inconclusive evidence of brain lesions or evidence that is inconsistent with scalp EEG results. In some of those cases, positron emission tomography (PET) can be used to characterise cerebral metabolism and indicate the location of subtle abnormalities that can cause seizures. This information can further be used to guide the positioning of intracranial electrodes to confirm the seizure locus [63, 103].

3.2.2 Presurgical fMRI Mapping

The main application of fMRI for neurosurgical planning is for the mapping of sensorimotor, language, and memory functions, because these functions are considered most vulnerable to neurosurgical procedures and most important for postsurgical quality of life (Fig. 3.1). Reports suggest that presurgical planning using fMRI may reduce surgical time, affect decisions regarding the targeted extent of resection [95, 127], and improve surgery outcome [124]. Compared to the gold standard cortical stimulation mapping [26, 39], fMRI is noninvasive and performed presurgically, without the time constraints and possible side effects on cognitive function associated with the surgical environment. The fast T2*-weighted imaging capabilities required for fMRI are a standard feature on MRI clinical systems, and the implementation of audiovisual stimulation and response equipment needed for most fMRI activation paradigms is relatively low cost.

Nevertheless, major obstacles to clinical deployment of fMRI presurgical mapping remain, including the following: (1) a lack of standardised acquisition paradigms and analysis procedures for sensitive and specific functional mapping in individual patients [102, 119], (2) spatial imprecision in presurgical maps due

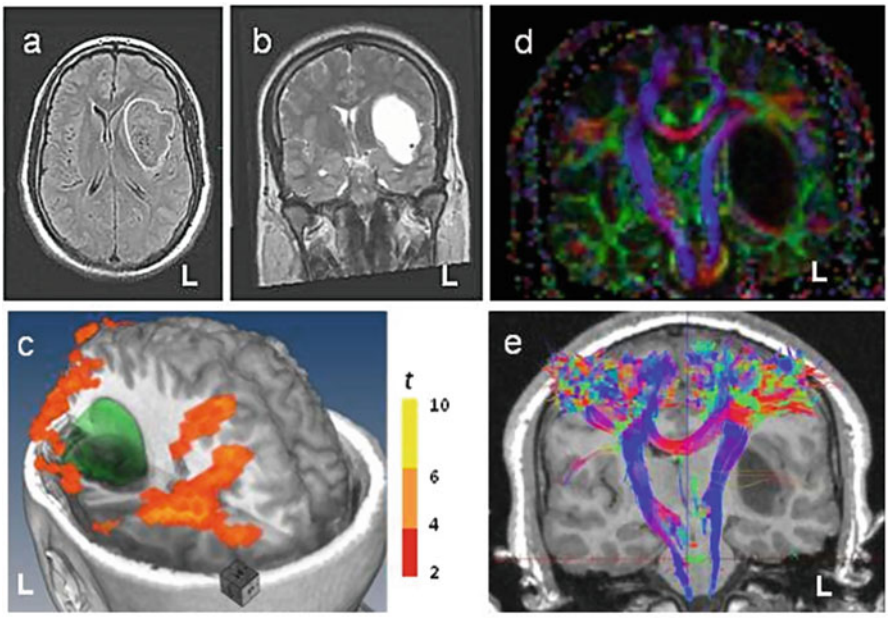

Fig. 3.1 Presurgical fMRI and DTI in 29-year-old male with left frontotemporal low-grade glioma showing symptoms of seizures, mild word finding difficulty, and right arm and leg weakness. (**a**) FLAIR and (**b**) T2-weighted structural MRI showing tumour outline. (**c**) Language map in a semantic task overlaid on 3D head model with segmented tumour (in green). (**d**) Fractional anisotropy and (**e**) DTI tractography of corticospinal tracts. fMRI suggests anterior displacement of language areas in the left frontal cortex. DTI shows inward displacement of the left corticospinal tract. L, left

to surgically induced nonlinear brain shifts [126], (3) a reduction of the fMRI response near tumours (particularly malignant glial tumours) despite the presence of viable neuronal tissue (neurovascular uncoupling) [45, 123], and (4) a lack of systematic evaluation of the accuracy and predictive value of fMRI mapping for patient outcome [119].

The problem of lack of standardised acquisition paradigms and analysis procedures is that different paradigms and procedures can produce different patterns of brain activation. Thus, an area that is active in one scheme may not be active in another. In addition, whole brain fMRI may reveal entire networks associated with a function including regions that are perhaps expendable [25]. Thus, fMRI presurgical mapping carries two types of risks: (1) resecting critical functional areas that were not active in the selected scheme, resulting in postsurgical neurological deficit, and (2) surgically sparing fMRI active regions that are not essential for function, leading to suboptimal surgical resection [13, 72]. Given the serious implications of presurgical mapping, it is critical that paradigms and analysis procedures reliably and robustly detect clinically relevant brain regions.

Perhaps even more problematic is the sparse knowledge of the predictive value of various fMRI paradigms and analysis procedures for patient postsurgical outcome. Given the complex representation of function in the brain, the large intraindividual variability in brain anatomy and function, and the potential for functional reorganisation and plasticity in healthy brains and due to disease, there is not a simple relationship between focal brain lesions and functional deficits. Therefore, the predictive value of fMRI presurgical mapping for patient outcome must be estimated based on experimental data and in the context of specific activation paradigms and analysis procedures. Systematic large-scale studies to determine the value of fMRI presurgical mapping of different activation paradigms in various patient populations are still rare. Nevertheless, recent efforts have yielded white papers with recommended paradigms for universal presurgical fMRI mapping and systematic assessment of the diagnostic accuracy and prognostic value (D. F. [16]), for determining hemispheric lateralisation and predicting postsurgical deficits of cognitive functions such as language and memory [121].

Nevertheless, it is important to remember that alternative mapping methods such as the gold standard cortical stimulation method suffer from similar limitations. Cortical stimulation is considered to identify regions that are functionally essential, and their damage during surgery would therefore result in neurological deficit. However, this technique cannot account for possible postsurgical functional reorganisation that could prevent permanent loss of function [56, 102]. Cortical stimulation can also in some cases indirectly interfere with brain areas connected with, but removed from, the stimulated site. Thus, there is a risk of false-positive results with cortical stimulation, and like fMRI, the predictive power for patient outcome needs to be estimated based on systematic analysis of experimental data.

3.2.2.1 Language and Memory Hemispheric Lateralisation

An important application of fMRI mapping is for assessing hemispheric dominance for language and memory (Fig. 3.2). The rationale for the test is the assumption that surgery on the dominant hemisphere carries a higher risk for postsurgical cognitive decline. The clinical gold standard to assess hemispheric dominance is the Wada test [131], which involves intracarotid injection of a barbiturate to sedate one hemisphere at a time and carries risk and discomfort for the patient. Several factors may confound the interpretation of the Wada results, including agitation or somnolence of the patient related to the anaesthetisation, inadequate disabling of certain brain regions in the anaesthetised hemisphere, or uncontrolled crossover of the anaesthetic to the examined hemisphere [76, 112]. In comparison, fMRI is noninvasive and performed under conditions of close-to-normal language processing. fMRI also provides sub-hemispheric spatial resolution. For these reasons, language fMRI has the potential of being more sensitive and accurate than the Wada test. Concordance between fMRI and Wada language lateralisation has generally been reported as very high, in the range of 80–90% [14, 64, 68], although this evaluation depended on an assignment to dominance categories (left, right, bilateral)

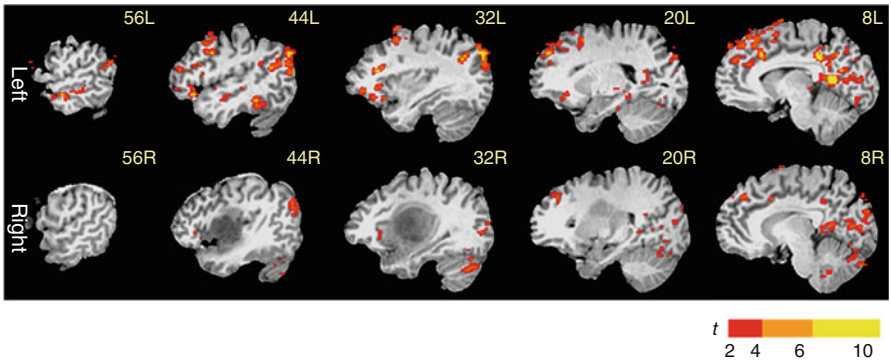

Fig. 3.2 Presurgical language fMRI in 35-year-old male with high-grade glioma in the right medial temporal lobe. The patient is left-handed and therefore at higher chance of atypical (right or bilateral) language dominance. The fMRI language map during semantic processing, overlaid on a series of sagittal slices in the left (top) and right (bottom) hemispheres, shows typical left hemispheric dominance in the middle temporal, inferior and middle frontal, angular, and fusiform gyri. Independent Wada testing results in this patient were also consistent with left hemisphere dominance for language

with arbitrarily defined boundaries [120]. A recent review of studies to assess the diagnostic accuracy and prognostic value of fMRI in determining lateralisation and predicting postsurgical language and memory outcomes concluded that fMRI was a valid alternative to Wada testing in patients with many types of epilepsy, but the evidence was insufficient for temporal neocortical epilepsy and temporal tumours [121].

3.2.2.2 Functional Mapping in Patients with Malignant Brain Tumours

In patients with glial tumours, a significant difficulty with fMRI mapping is that the BOLD response can be reduced in the area surrounding the tumour despite the presence of viable neuronal tissue, a phenomenon known as neurovascular uncoupling [30, 109]. Loss or reduction in cerebrovascular reactivity and tumour-induced changes in microvasculature have been suggested to contribute to the reduced BOLD response in the area adjacent to malignant tumours [45, 46]. Reduction in signal intensity in the tumour hemisphere relative to the healthy hemisphere was found to be significantly more pronounced in high-grade (IV) relative to lower-grade (II–III) gliomas, consistent with the notion that neurovascular uncoupling disproportionately affects malignant tumours [20]. Neurovascular uncoupling is an inherent limitation of fMRI for presurgical mapping in tumour patients, because it can lead to erroneous interpretation of fMRI activation maps and lateralisation patterns [123, 124]. In tumour patients (and particularly high-grade gliomas), it is therefore imperative to couple fMRI mapping with an assessment of cerebrovascular

reactivity. Furthermore, maps of cerebrovascular reactivity can potentially provide useful information regarding the nature of the tumour and its boundaries [99].

Cerebrovascular reactivity can be studied with BOLD fMRI, by examining changes induced by a hypercapnia challenge such as Co2 inhalation or breath-hold [51, 101]. Hypercapnia induces vasodilation and causes an increase in cerebral blood flow and oxygen concentration in normal blood vessels, resulting in an increase in the BOLD signal [65]. In tumours, increased cellularity or necrosis and low vascular density may cause reduced perfusion and hypoxia [100]. In tumours with neovasculature, in which there is abnormal microanatomy and cerebrovascular regulation, blood from a region of the tumour in which the vessels do not dilate can be redistributed to a responsive tumour region or to surrounding normal tissue, causing a focal worsening of tumour perfusion. Thus, in tumours with abnormal cerebrovascular microstructure or abnormal cerebrovascular regulation, low BOLD reactivity during hypercapnia is expected.

3.2.3 Presurgical DTI Mapping

DTI is a unique method for describing noninvasively the spatial relationship between brain tumours or lesions and white matter tracts. Combined fMRI and DTI mapping can reveal both functional regions and their white matter connectivity and thus provide a more accurate estimate of the proximity of tumour borders to vital brain networks [42, 92, 108, 125].

DTI can be useful in distinguishing between different effects of space-occupying lesions such as displacement, disruption, or infiltration of the white matter tracts by the tumour [23, 49, 108, 134, 135]. White matter fibres may remain intact but be displaced by a tumour, in which case their anisotropy would be maintained and their new location and orientation would be detectable on directional DTI maps. This pattern could confirm the existence of a peritumoural tract that could potentially be preserved during resection. Alternatively, oedema or infiltration by the tumour may reduce the anisotropy of tracts, either still leaving enough directional organisation to remain detectable on DTI maps or completely disrupting the directional organisation.

DTI-based fibre tractography can be more challenging in cases of brain pathologies with space-occupying lesions, because displaced fibres may not readily be traced with common methods for seed selection based on anatomical landmarks. In addition, tumour infiltration and oedema may cause tissue deformation, resulting in reduced reliability of fibre tracking [38]. Fibre tracking in regions with oedema can potentially be improved by using sophisticated post-processing algorithms for separating diffusion properties of neural tissue from surrounding free water [94].

3.2.4 Presurgical Electrophysiological Mapping

EEG is central to the diagnosis and management of patients with seizure disorders. EEG is available in all clinical centres and incurs relatively low costs. EEG is particularly useful if epileptic discharges are captured during the EEG recording session, as this form of abnormal EEG activity is highly correlated with seizure disorders and is of clinical use. EEG can help determine the seizure type (focal or generalised) and epilepsy syndrome and thereby guide the choice of antiepileptic medication and the prognosis. In patients with medically refractory epilepsy who are candidates for epilepsy surgery, long-term EEG monitoring may be recommended to characterise and quantify the frequency and type of seizures and to localise the sources of the epileptogenic activity.

Like EEG, the primary clinical application of MEG is for presurgical localisation and characterisation of epileptic sources, particularly in cases when MRI is inconclusive with regard to the seizure focus. The location, orientation, and spatial extent of epileptic discharges with respect to other spontaneous brain activities all contribute to the sensitivity of MEG and EEG, making it difficult to predict which method is best suited for each patient. Most electrical discharges can be detected by both EEG and MEG, but, MEG is more effective for the detection of epileptic activity arising from the superficial cortical convexity, such as in lateral neocortical epilepsy and cortical dysplasia [10, 24, 54, 118].

Scalp EEG can be recorded simultaneously with fMRI to map changes in the BOLD signal that are associated with epileptic discharges [34, 37, 104]. The advantage of this multimodal method is that it informs the source modelling of the epileptic activity, particularly in complicated cases when multiple epileptic sources are suspected, or when no underlying structural pathology has been identified [36, 130]. Intracranial EEG is recommended when deep spike sources such as in the hippocampus are suspected [1, 111].

3.2.5 Presurgical PET

In epilepsy, asymmetric hypometabolism in the medial temporal lobe, as assessed by FDG-PET scans, may indicate the seizure focus in refractory epilepsy that occurs due to mesial temporal sclerosis. Unilateral temporal hypometabolism is a marker of more favourable surgical outcomes in such cases. Hypometabolic foci noted on FDG-PET may serve as regions for intra-operative electrode placement to further identify clinically relevant seizure foci using electrophysiological methods. On the other hand, multifocal hypometabolism may predict poor surgical outcomes in refractory epilepsy [19, 61, 113]. Metabolic information provided by FDG-PET can be complimentary to brain perfusion changes noted on ictal and interictal SPECT. A combination of these techniques can enhance localisation of seizure focus in refractory epilepsy patients [113].

In addition to FDG-PET, other radiopharmaceuticals have been used in assessment of refractory epilepsy. C-11 flumazenil PET and F-18 flumazenil PET are markers for GABA-A receptor concentration in the brain. Flumazenil is a benzodiazepine receptor ligand, which is otherwise used therapeutically to treat benzodiazepine toxicity. When labelled with the PET radioisotope, it can be used for imaging benzodiazepine receptor concentration in the brain. Benzodiazepine receptors are ubiquitous and surrogate markers for neuronal integrity. Reduced flumazenil binding on PET scans, reflecting neuronal injury, is seen in epileptogenic foci. Asymmetrically reduced flumazenil PET signal in the medial temporal lobe has been recently shown to more precisely delineate the seizure focus in refractory epilepsy cases, as compared to FDG-PET scans. The degree of abnormality on flumazenil PET has been shown to correlate with seizure frequency in refractory epilepsy [44, 61, 113]. C-11-labelled alpha-methyl tryptophan (AMT)-PET enables assessment of cellular incorporation of amino acids in brain tissue. AMT-PET has been studied in tuberous sclerosis and cortical developmental malformations. Increased uptake of AMT is seen in epileptogenic tissue and can be used to guide surgical planning in these conditions [57, 105, 113].

In brain tumour patients, FDG-PET can be used for grading of gliomas and for identifying hypermetabolic lymphomas. High-grade gliomas, particularly glioblastoma multiforme, demonstrate a high degree of FDG uptake. Hypermetabolic foci within lesions can be used to guide biopsy and can contribute to decision-making when distinguishing tumour recurrence and radiation necrosis. However, low-grade gliomas may demonstrate reduced tracer uptake as compared to the surrounding brain parenchyma because there is high background FDG uptake in the normal brain tissue. Therefore, accurate delineation of tumour margins for surgical therapy planning purposes is suboptimal with FDG-PET in brain tumours. However, other radiopharmaceuticals have been used to circumvent this problem. C-11 methionine and F-18 fluoroethyl tyrosine are radiolabelled amino acid analogues that have low uptake in the normal brain tissue but demonstrate significantly greater accumulation in both low- and high-grade gliomas [113–115]. Increased concentration of L-type amino acid transporter in the neoplastic tissue has been shown to correlate with tracer uptake [114]. The sharper contrast between abnormal neoplastic tissue and the surrounding normal brain enables more accurate assessment of tumour margins for surgical and radiotherapy planning. In multiple studies, abnormal C-11 methionine uptake areas were found to extend beyond contrast-enhanced MRI lesions in the majority of brain tumour patients [114] (Fig. 3.3). Similarly, use of FET-PET increases the specificity of biopsy planning in brain tumour patients as compared to MRI alone [82, 98].

3.3 Summary and Conclusions

MR imaging at high spatial resolution is used for noninvasive localisation of brain tumours and seizure-causing lesions and for the mapping of functional brain areas and white matter fibre tracks with respect to structural abnormalities. The goal of

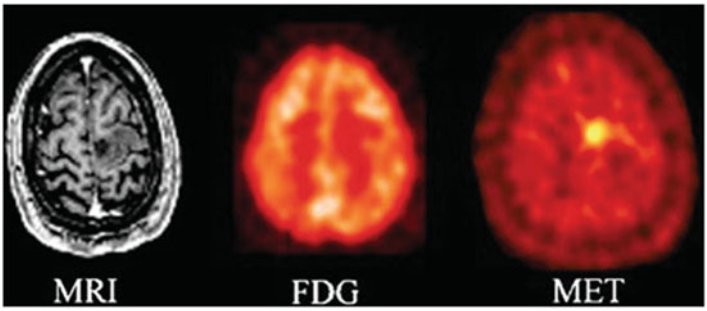

Fig. 3.3 Contrast-enhanced T1-weighted magnetic resonance imaging (MRI; left), coregistered images of [F-18] fluorodeoxyglucose (FDG; centre) and [C-11] methionine (MET; right) PET in a case of low-grade (grade II) glioma. No contrast enhancement on MRI and no FDG uptake are seen, but significant increased methionine uptake is present in the same area. Amino acid PET (e.g. MET-PET, FET-PET) imaging can aid in tumour identification and tumour margin delineation in such cases. (Reprinted with permission from Singhal et al. [114])

presurgical MR imaging is to provide structural and functional information that can facilitate maximal tumour or epileptic tissue surgical resection, with minimal damage to surrounding grey and white matter brain structures supporting vital sensorimotor and cognitive functions. MR imaging can assist in assessing the risks of a brain surgery, the benefit of conducting alternative brain mapping, and the planning of the surgical approach.

Wider clinical implementation of functional MRI is impeded by the lack of standardised acquisition paradigms and analysis procedures that are demonstrated to produce highly reliable and robust activity in clinically relevant brain region. Systematic evaluation in large-scale studies specifically designed to establish the diagnostic accuracy and prognostic value for patient outcome of specific fMRI paradigms and analysis procedures is warranted.

Electrophysiological functional brain mapping techniques such as EEG and MEG are complementary to fMRI in that they probe the neural activity directly and at high temporal resolution. The primary clinical application of these techniques is for presurgical localisation and characterisation of epileptic sources, particularly in cases when MRI is inconclusive with regard to the seizure focus. Similarly, PET imaging identifies functional and molecular changes corresponding to structural and electrophysiological changes and serves to improve the sensitivity and specificity of overall brain mapping.

Acknowledgements The image data shown in Figs. 3.1 and 3.2 was collected at the National Research Council Institute for Biodiagnostics (NRC-IBD) from patients treated in the Neurosurgery Department of the Health Science Centre (HSC) in Winnipeg. The author would like to thank Dr. Michael West, Head of the Neurosurgery Department at HSC, and Dr. Owen Williams from the same Department, for their involvement in referring patients and interpreting the image data shown in the figures in this chapter, and Dr. Uta Sboto-Frankenstein and Dr. Jordan Hovdebo from NRC-IBD for their assistance in collecting and analysing the images. The authors would also like to thank Dr. Emily Stern, Director of Functional and Molecular Imaging at Brigham and Women's Hospital, for constructive comments on a previous version of this chapter.

References

1. Agirre-Arrizubieta, Z., Huiskamp, G.J., Ferrier, C.H., van Huffelen, A.C., Leijten, F.S.: Interictal magnetoencephalography and the irritative zone in the electrocorticogram. Brain. **132**(Pt 11), 3060–3071 (2009)
2. Ahlfors, S.P., Han, J., Belliveau, J.W., Hamalainen, M.S.: Sensitivity of MEG and EEG to source orientation. Brain Topogr. **23**(3), 227–232 (2010)
3. Albayrak, B., Samdani, A.F., Black, P.M.: Intraoperative magnetic resonance imaging in neurosurgery. Acta Neurochir. (Wien.). **146**(6), 543–556 (2004)
4. Albert, F.K., Forsting, M., Sartor, K., Adams, H.P., Kunze, S.: Early postoperative magnetic resonance imaging after resection of malignant glioma: objective evaluation of residual tumor and its influence on regrowth and prognosis. Neurosurgery. **34**(1), 45–60 (1994)
5. Aminoff, M.J., Eisen, A.A.: AAEM minimonograph 19: somatosensory evoked potentials. Muscle Nerve. **21**(3), 277–290 (1998)
6. Archip, N., Clatz, O., Whalen, S., Kacher, D., Fedorov, A., Kot, A., Chrisochoides, N., Jolesz, F., Golby, A., Black, P.M., Warfield, S.K.: Non-rigid alignment of preoperative MRI, fMRI, and DT-MRI with intraoperative MRI for enhanced visualization and navigation in image-guided neurosurgery. NeuroImage. **35**(2), 609–624 (2007)
7. Baillet, S., Garnero, L., Marin, G., Hugonin, J.P.: Combined MEG and EEG source imaging by minimization of mutual information. I.E.E.E. Trans. Biomed. Eng. **46**(5), (1999). http://www.ncbi.nlm.nih.gov/entrez/query.fcgi?cmd=Retrieve&db=PubMed&dopt=Citation&list_uids=10230131
8. Balchandani, P., Naidich, T.P.: Ultra-high-field MR neuroimaging. AJNR Am. J. Neuroradiol. **36**(7), 1204–1215 (2015)
9. Bandettini, P.A., Wong, E.C., Hinks, R.S., Tikofsky, R.S., Hyde, J.S.: Time course EPI of human brain function during task activation. Magn. Reson. Med. **25**(2), 390–397 (1992)
10. Barkley, G.L., Baumgartner, C.: MEG and EEG in epilepsy. J. Clin. Neurophysiol. **20**(3), 163–178 (2003)
11. Basser, P.J., Pajevic, S., Pierpaoli, C., Duda, J., Aldroubi, A.: In vivo fiber tractography using DT-MRI data. Magn. Reson. Med. **44**(4), 625–632 (2000)
12. Belliveau, J.W., Kwong, K.K., Kennedy, D.N., Baker, J.R., Stern, C.E., Benson, R., Chesler, D.A., Weisskoff, R.M., Cohen, M.S., Tootell, R.B.: Magnetic resonance imaging mapping of brain function. Human visual cortex. Investig. Radiol. **27**(Suppl 2), S59–S65 (1992)
13. Binder, J.R.: Functional MRI is a valid noninvasive alternative to Wada testing. Epilepsy Behav. **20**(2), 214–222 (2011)
14. Binder, J.R., Swanson, S.J., Hammeke, T.A., Morris, G.L., Mueller, W.M., Fischer, M., Benbadis, S., Frost, J.A., Rao, S.M., Haughton, V.M.: Determination of language dominance using functional MRI: a comparison with the Wada test. Neurology. **46**(4), 978–984 (1996)
15. Black, P.M., Alexander III, E., Martin, C., Moriarty, T., Nabavi, A., Wong, T.Z., Schwartz, R.B., Jolesz, F.: Craniotomy for tumor treatment in an intraoperative magnetic resonance imaging unit. Neurosurgery. **45**(3), 423–431 (1999)
16. Black, D.F., Vachha, B., Mian, A., Faro, S.H., Maheshwari, M., Sair, H.I., Petrella, J.R., Pillai, J.J., Welker, K.: American Society of Functional Neuroradiology-Recommended fMRI paradigm algorithms for Presurgical language assessment. AJNR Am. J. Neuroradiol. **38**(10), E65–E73 (2017)
17. Bonmassar, G., Purdon, P., Jaaskelainen, I., Chiappa, K., Solo, V., Brown, E., Belliveau, J.W.: Motion and Ballistocardiogram artifact removal for interleaved recording of EEG and EPs during MRI. NeuroImage. **16**(4), 1127 (2002)
18. Bradley, W.G.: Achieving gross total resection of brain tumors: intraoperative MR imaging can make a big difference. AJNR Am. J. Neuroradiol. **23**(3), 348–349 (2002)
19. Casse, R., Rowe, C.C., Newton, M., Berlangieri, S.U., Scott, A.M.: Positron emission tomography and epilepsy. Mol. Imaging Biol. **4**(5), 338–351 (2002)

20. Chen, C.M., Hou, B.L., Holodny, A.I.: Effect of age and tumor grade on BOLD functional MR imaging in preoperative assessment of patients with glioma. Radiology. **248**(3), 971–978 (2008). PM:18647847
21. Cohen, D.: Magnetoencephalography: evidence of magnetic fields produced by alpha-rhythm currents. Science. **161**(843), 784–786 (1968)
22. Cohen, D.: Magnetoencephalography: detection of the brain's electrical activity with a superconducting magnetometer. Science. **175**(22), 664–666 (1972)
23. Cruz Jr., L.C., Sorensen, A.G.: Diffusion tensor magnetic resonance imaging of brain tumors. Magn. Reson. Imaging Clin. N. Am. **14**(2), 183–202 (2006)
24. de Jongh, A., de Munck, J.C., Goncalves, S.I., Ossenblok, P.: Differences in MEG/EEG epileptic spike yields explained by regional differences in signal-to-noise ratios. J. Clin. Neurophysiol. **22**(2), 153–158 (2005)
25. Desmond, J.E., Annabel Chen, S.H.: Ethical issues in the clinical application of fMRI: factors affecting the validity and interpretation of activations. Brain Cogn. **50**(3), 482–497 (2002)
26. Duffau, H., Lopes, M., Arthuis, F., Bitar, A., Sichez, J.P., Van, E.R., Capelle, L.: Contribution of intraoperative electrical stimulations in surgery of low grade gliomas: a comparative study between two series without (1985-96) and with (1996-2003) functional mapping in the same institution. J. Neurol. Neurosurg. Psychiatry. **76**(6), 845–851 (2005)
27. Duncan, J.S.: Imaging in the surgical treatment of epilepsy. Nat. Rev. Neurol. **6**(10), 537–550 (2010)
28. Ellingson, M.L., Liebenthal, E., Spanaki, M.V., Prieto, T.E., Binder, J.R., Ropella, K.M.: Ballistocardiogram artifact reduction in the simultaneous acquisition of auditory ERPS and fMRI. NeuroImage. **22**(4), 1534–1542 (2004)
29. Engel, A.K., Moll, C.K., Fried, I., Ojemann, G.A.: Invasive recordings from the human brain: clinical insights and beyond. Nat. Rev. Neurosci. **6**(1), 35–47 (2005)
30. Fujiwara, N., Sakatani, K., Katayama, Y., Murata, Y., Hoshino, T., Fukaya, C., Yamamoto, T.: Evoked-cerebral blood oxygenation changes in false-negative activations in BOLD contrast functional MRI of patients with brain tumors. NeuroImage. **21**(4), (2004). PM:15050571
31. Galambos, R., Sheatz, G.C.: An electroencephalograph study of classical conditioning. Am. J. Phys. **203**, 173–184 (1962)
32. Garlapati, R.R., Mostayed, A., Joldes, G.R., Wittek, A., Doyle, B., Miller, K.: Towards measuring neuroimage misalignment. Comput. Biol. Med. **64**, 12–23 (2015)
33. Glover, G.H.: Overview of functional magnetic resonance imaging. Neurosurg. Clin. N. Am. **22**(2), 133–139. , vii. (2011)
34. Gotman, J., Benar, C.G., Dubeau, F.: Combining EEG and fMRI in epilepsy: methodological challenges and clinical results. J. Clin. Neurophysiol. **21**(4), 229–240 (2004)
35. Gotman, J., Kobayashi, E., Bagshaw, A.P., Benar, C.G., Dubeau, F.: Combining EEG and fMRI: a multimodal tool for epilepsy research. J. Magn. Reson. Imaging. **23**(6), 906–920 (2006)
36. Groening, K., Brodbeck, V., Moeller, F., Wolff, S., van Baalen, A., Michel, C.M., Jansen, O., Boor, R., Wiegand, G., Stephani, U., Siniatchkin, M.: Combination of EEG-fMRI and EEG source analysis improves interpretation of spike-associated activation networks in paediatric pharmacoresistant focal epilepsies. NeuroImage. **46**(3), 827–833 (2009)
37. Grova, C., Daunizeau, J., Kobayashi, E., Bagshaw, A.P., Lina, J.M., Dubeau, F., Gotman, J.: Concordance between distributed EEG source localization and simultaneous EEG-fMRI studies of epileptic spikes. NeuroImage. **39**(2), 755–774 (2008)
38. Guye, M., Parker, G.J., Symms, M., Boulby, P., Wheeler-Kingshott, C.A., Salek-Haddadi, A., Barker, G.J., Duncan, J.S.: Combined functional MRI and tractography to demonstrate the connectivity of the human primary motor cortex in vivo. NeuroImage. **19**(4), 1349–1360 (2003)
39. Haglund, M.M., Berger, M.S., Shamseldin, M., Lettich, E., Ojemann, G.A.: Cortical localization of temporal lobe language sites in patients with gliomas. Neurosurgery. **34**(4), 567–576 (1994)
40. Halliday, A.M.: Evoked Potentials in Clinical Testing, 2nd edn. Churchill Livingstone, Edinburgh (1993)

41. Hartkens, T., Hill, D.L., Castellano-Smith, A.D., Hawkes, D.J., Maurer Jr., C.R., Martin, A.J., Hall, W.A., Liu, H., Truwit, C.L.: Measurement and analysis of brain deformation during neurosurgery. IEEE Trans. Med. Imaging. **22**(1), 82–92 (2003)
42. Hendler, T., Pianka, P., Sigal, M., Kafri, M., Ben Bashat, D., Constantini, S., Graif, M., Fried, I., Assaf, Y.: Delineating gray and white matter involvement in brain lesions: three-dimensional alignment of functional magnetic resonance and diffusion-tensor imaging. J.Neurosurg. **99**(6), 1018–1027 (2003)
43. Hillebrand, A., Barnes, G.R.: A quantitative assessment of the sensitivity of whole-head MEG to activity in the adult human cortex. NeuroImage. **16**(3 Pt 1), 638–650 (2002)
44. Hodolic, M., Topakian, R., Pichler, R.: (18)F-fluorodeoxyglucose and (18)F-flumazenil positron emission tomography in patients with refractory epilepsy. Radiol. Oncol. **50**(3), 247–253 (2016)
45. Holodny, A.I., Schulder, M., Liu, W.C., Wolko, J., Maldjian, J.A., Kalnin, A.J.: The effect of brain tumors on BOLD functional MR imaging activation in the adjacent motor cortex: implications for image-guided neurosurgery. AJNR Am. J. Neuroradiol. **21**(8), (2000). PM:11003273
46. Hou, B.L., Bradbury, M., Peck, K.K., Petrovich, N.M., Gutin, P.H., Holodny, A.I.: Effect of brain tumor neovasculature defined by rCBV on BOLD fMRI activation volume in the primary motor cortex. NeuroImage. **32**(2), (2006). PM:16806983
47. Ives, J.R., Warach, S., Schmitt, F., Edelman, R.R., Schomer, D.L.: Monitoring the patient's EEG during echo planar MRI. Electroencephalogr. Clin. Neurophysiol. **87**(6), 417–420 (1993)
48. James, M.L., Gambhir, S.S.: A molecular imaging primer: modalities, imaging agents, and applications. Physiol. Rev. **92**(2), 897–965 (2012)
49. Jellison, B.J., Field, A.S., Medow, J., Lazar, M., Salamat, M.S., Alexander, A.L.: Diffusion tensor imaging of cerebral white matter: a pictorial review of physics, fiber tract anatomy, and tumor imaging patterns. AJNR Am. J. Neuroradiol. **25**(3), 356–369 (2004)
50. Jones, T., Rabiner, E.A., Company, P. E. T. R. A: The development, past achievements, and future directions of brain PET. J. Cereb. Blood Flow Metab. **32**(7), 1426–1454 (2012)
51. Kastrup, A., Li, T.Q., Takahashi, A., Glover, G.H., Moseley, M.E.: Functional magnetic resonance imaging of regional cerebral blood oxygenation changes during breath holding. Stroke. **29**(12), (1998). PM:9836778
52. Keles, G.E., Lamborn, K.R., Berger, M.S.: Low-grade hemispheric gliomas in adults: a critical review of extent of resection as a factor influencing outcome. J. Neurosurg. **95**(5), 735–745 (2001)
53. Keles, G.E., Lamborn, K.R., Berger, M.S.: Coregistration accuracy and detection of brain shift using intraoperative sononavigation during resection of hemispheric tumors. Neurosurgery. **53**(3), 556–562 (2003)
54. Knake, S., Halgren, E., Shiraishi, H., Hara, K., Hamer, H.M., Grant, P.E., Carr, V.A., Foxe, D., Camposano, S., Busa, E., Witzel, T., Hamalainen, M.S., Ahlfors, S.P., Bromfield, E.B., Black, P.M., Bourgeois, B.F., Cole, A.J., Cosgrove, G.R., Dworetzky, B.A., Madsen, J.R., Larsson, P.G., Schomer, D.L., Thiele, E.A., Dale, A.M., Rosen, B.R., Stufflebeam, S.M.: The value of multichannel MEG and EEG in the presurgical evaluation of 70 epilepsy patients. Epilepsy Res. **69**(1), 80–86 (2006)
55. Kraff, O., Quick, H.H.: 7T: physics, safety, and potential clinical applications. J. Magn. Reson. Imaging. **46**(6), 1573–1589 (2017)
56. Krainik, A., Duffau, H., Capelle, L., Cornu, P., Boch, A.L., Mangin, J.F., Le, B.D., Marsault, C., Chiras, J., Lehericy, S.: Role of the healthy hemisphere in recovery after resection of the supplementary motor area. Neurology. **62**(8), 1323–1332 (2004)
57. Kumar, A., Asano, E., Chugani, H.T.: alpha-[(1)(1)C]-methyl-L-tryptophan PET for tracer localization of epileptogenic brain regions: clinical studies. Biomark. Med. **5**(5), 577–584 (2011)
58. Kwong, K.K., Belliveau, J.W., Chesler, D.A., Goldberg, I.E., Weisskoff, R.M., Poncelet, B.P., Kennedy, D.N., Hoppel, B.E., Cohen, M.S., Turner, R.: Dynamic magnetic resonance imaging

of human brain activity during primary sensory stimulation. Proc.Natl.Acad.Sci.U.S.A. **89**(12), 5675–5679 (1992)
59. Laufs, H., Duncan, J.S.: Electroencephalography/functional MRI in human epilepsy: what it currently can and cannot do. Curr. Opin. Neurol. **20**(4), 417–423 (2007)
60. Laufs, H., Daunizeau, J., Carmichael, D.W., Kleinschmidt, A.: Recent advances in recording electrophysiological data simultaneously with magnetic resonance imaging. NeuroImage. **40**(2), (2008). http://www.ncbi.nlm.nih.gov/entrez/query.fcgi?cmd=Retrieve&db=PubMed&dopt=Citation&list_uids=18201910
61. Laufs, H., Richardson, M.P., Salek-Haddadi, A., Vollmar, C., Duncan, J.S., Gale, K., Lemieux, L., Loscher, W., Koepp, M.J.: Converging PET and fMRI evidence for a common area involved in human focal epilepsies. Neurology. **77**(9), 904–910 (2011)
62. Lauterbur, P.C.: Image formation by induced local interactions. Examples employing nuclear magnetic resonance. Nature. **242**, 190–191 (1973)
63. Lee, K.K., Salamon, N.: [18F] fluorodeoxyglucose-positron-emission tomography and MR imaging coregistration for presurgical evaluation of medically refractory epilepsy. AJNR Am. J. Neuroradiol. **30**(10), 1811–1816 (2009)
64. Lehericy, S., Cohen, L., Bazin, B., Samson, S., Giacomini, E., Rougetet, R., Hertz-Pannier, L., Le Bihan, D., Marsault, C., Baulac, M.: Functional MR evaluation of temporal and frontal language dominance compared with the Wada test. Neurology. **54**(8), 1625–1633 (2000)
65. Li, T.Q., Moseley, M.E., Glover, G.: A FAIR study of motor cortex activation under normo- and hypercapnia induced by breath challenge. NeuroImage. **10**(5), 562–569 (1999). PM:10547333
66. Liebenthal, E., Ellingson, M.L., Spanaki, M.V., Prieto, T.E., Ropella, K.M., Binder, J.R.: Simultaneous ERP and fMRI of the auditory cortex in a passive oddball paradigm. NeuroImage. **19**(4), 1395–1404 (2003)
67. Liebenthal, E., Sabri, M., Beardsley, S.A., Mangalathu-Arumana, J., Desai, A.: Neural dynamics of phonological processing in the dorsal auditory stream. J. Neurosci. **33**, 15414 (2013)
68. Liegeois, F., Connelly, A., Salmond, C.H., Gadian, D.G., Vargha-Khadem, F., Baldeweg, T.: A direct test for lateralization of language activation using fMRI: comparison with invasive assessments in children with epilepsy. NeuroImage. **17**(4), 1861–1867 (2002)
69. Liu, H., Tanaka, N., Stufflebeam, S., Ahlfors, S., Hamalainen, M.: Functional mapping with simultaneous MEG and EEG. J. Vis. Exp. **40**, (2010). https://doi.org/10.3791/1668
70. Logothetis, N.K.: What we can do and what we cannot do with fMRI. Nature. **453**(7197), (2008). http://www.ncbi.nlm.nih.gov/pubmed/18548064
71. Logothetis, N.K., Pauls, J., Augath, M., Trinath, T., Oeltermann, A.: Neurophysiological investigation of the basis of the fMRI signal. Nature. **412**(6843), 150–157 (2001)
72. Loring, D.W., Meador, K.J., Allison, J.D., Pillai, J.J., Lavin, T., Lee, G.P., Balan, A., Dave, V.: Now you see it, now you don't: statistical and methodological considerations in fMRI. Epilepsy Behav. **3**(6), 539–547 (2002)
73. Mangalathu-Arumana, J., Liebenthal, E., Beardsley, S.A.: Optimizing within-subject experimental designs for jICA of Multi-Channel ERP and fMRI. Front. Neurosci. **12**, 13 (2018)
74. Mansfield, P., Maudsley, A.A.: Medical imaging by NMR. Br. J. Radiol. **50**(591), 188–194 (1977)
75. Mazziotta, J.C., Toga, A.W., Evans, A., Fox, P., Lancaster, J.: A probabilistic atlas of the human brain: theory and rationale for its development. The International Consortium for Brain Mapping (ICBM). NeuroImage. **2**(2), 89–101 (1995)
76. Meador, K.J., Loring, D.W.: The Wada test: controversies, concerns, and insights. Neurology. **52**(8), 1535–1536 (1999)
77. Merkle, E.M., Lewin, J.S., Liebenthal, R., Lorenz, C.H.: The interventional MR imaging suite: magnet designs and equipment requirements. Magn. Reson. Imaging Clin. N. Am. **13**(3), 401–413 (2005)
78. Mesulam, M.M.: From sensation to cognition. Brain. **121**(Pt 6), 1013–1052 (1998)

79. Mori, S., van Zijl, P.C.: Fiber tracking: principles and strategies - a technical review. NMR Biomed. **15**(7–8), 468–480 (2002)
80. Moseley, M.E., Cohen, Y., Kucharczyk, J., Mintorovitch, J., Asgari, H.S., Wendland, M.F., Tsuruda, J., Norman, D.: Diffusion-weighted MR imaging of anisotropic water diffusion in cat central nervous system. Radiology. **176**(2), 439–445 (1990)
81. Mukamel, R., Fried, I.: Human intracranial recordings and cognitive neuroscience. Annu. Rev. Psychol. **63**, 511–537 (2012)
82. Muoio, B., Giovanella, L., Treglia, G.: Recent developments of 18F-FET PET in neuro-oncology. Curr. Med. Chem. **25**, 3061 (2017)
83. Nabavi, A., Black, P.M., Gering, D.T., Westin, C.F., Mehta, V., Pergolizzi Jr., R.S., Ferrant, M., Warfield, S.K., Hata, N., Schwartz, R.B., Wells III, W.M., Kikinis, R., Jolesz, F., Jolesz, F.A.: Serial intraoperative magnetic resonance imaging of brain shift. Neurosurgery. **48**(4), 787–797 (2001)
84. Naidich, T.P., Valavanis, A.G., Kubik, S.: Anatomic relationships along the low-middle convexity: Part I–Normal specimens and magnetic resonance imaging. Neurosurgery. **36**(3), 517–532 (1995)
85. Nimsky, C., Ganslandt, O., Cerny, S., Hastreiter, P., Greiner, G., Fahlbusch, R.: Quantification of, visualization of, and compensation for brain shift using intraoperative magnetic resonance imaging. Neurosurgery. **47**(5), 1070–1079 (2000)
86. Nimsky, C., Ganslandt, O., Buchfelder, M., Fahlbusch, R.: Glioma surgery evaluated by intraoperative low-field magnetic resonance imaging. Acta Neurochir. Suppl. **85**, 55–63 (2003)
87. Nimsky, C., Ganslandt, O., Buchfelder, M., Fahlbusch, R.: Intraoperative visualization for resection of gliomas: the role of functional neuronavigation and intraoperative 1.5 T MRI. Neurol. Res. **28**(5), 482–487 (2006)
88. Nunez, P.L., Srinivasan, R.: Electric fields of the brain : the neurophysics of EEG. In: Oxford. Oxford University Press, New York (2006)
89. Ogawa, S., Lee, T.M., Kay, A.R., Tank, D.W.: Brain magnetic resonance imaging with contrast dependent on blood oxygenation. Proc. Natl. Acad. Sci. U.S.A. **87**(24), 9868–9872 (1990)
90. Ogawa, S., Tank, D.W., Menon, R., Ellermann, J.M., Kim, S.G., Merkle, H., Ugurbil, K.: Intrinsic signal changes accompanying sensory stimulation: functional brain mapping with magnetic resonance imaging. Proc. Natl. Acad. Sci. U.S.A. **89**(13), 5951–5955 (1992)
91. Papadakis, N.G., Murrills, C.D., Hall, L.D., Huang, C.L., Adrian, C.T.: Minimal gradient encoding for robust estimation of diffusion anisotropy. Magn Reson. Imaging. **18**(6), 671–679 (2000)
92. Parmar, H., Sitoh, Y.Y., Yeo, T.T.: Combined magnetic resonance tractography and functional magnetic resonance imaging in evaluation of brain tumors involving the motor system. J. Comput. Assist. Tomogr. **28**(4), 551–556 (2004)
93. Parvizi, J., Kastner, S.: Promises and limitations of human intracranial electroencephalography. Nat. Neurosci. **21**(4), 474–483 (2018)
94. Pasternak, O., Sochen, N., Gur, Y., Intrator, N., Assaf, Y.: Free water elimination and mapping from diffusion MRI. Magn Reson. Med. **62**(3), 717–730 (2009)
95. Petrella, J.R., Shah, L.M., Harris, K.M., Friedman, A.H., George, T.M., Sampson, J.H., Pekala, J.S., Voyvodic, J.T.: Preoperative functional MR imaging localization of language and motor areas: effect on therapeutic decision making in patients with potentially resectable brain tumors. Radiology. **240**(3), 793–802 (2006)
96. Phelps, M.E.: PET: a biological imaging technique. Neurochem. Res. **16**(9), 929–940 (1991)
97. Pierpaoli, C., Jezzard, P., Basser, P.J., Barnett, A., Di Chiro, G.: Diffusion tensor MR imaging of the human brain. Radiology. **201**(3), 637–648 (1996)
98. Rachinger, W., Goetz, C., Popperl, G., Gildehaus, F.J., Kreth, F.W., Holtmannspotter, M., Herms, J., Koch, W., Tatsch, K., Tonn, J.C.: Positron emission tomography with O-(2-[18F]fluoroethyl)-l-tyrosine versus magnetic resonance imaging in the diagnosis of recurrent gliomas. Neurosurgery. **57**(3), 505–511 (2005).; discussion 505–511

99. Rauscher, A., Sedlacik, J., Fitzek, C., Walter, B., Hochstetter, A., Kalff, R., Kaiser, W.A., Reichenbach, J.R.: High resolution susceptibility weighted MR-imaging of brain tumors during the application of a gaseous agent. Rofo. **177**(8), (2005). PM:16021537
100. Robinson, S.P., Rijken, P.F., Howe, F.A., McSheehy, P.M., van der Sanden, B.P., Heerschap, A., Stubbs, M., van der Kogel, A.J., Griffiths, J.R.: Tumor vascular architecture and function evaluated by non-invasive susceptibility MRI methods and immunohistochemistry. J. Magn Reson. Imaging. **17**(4), 445–454 (2003). PM:12655584
101. Rostrup, E., Larsson, H.B., Toft, P.B., Garde, K., Thomsen, C., Ring, P., Sondergaard, L., Henriksen, O.: Functional MRI of CO2 induced increase in cerebral perfusion. NMR Biomed. **7**(1-2), 29–34 (1994). PM:8068522
102. Rutten, G.J., Ramsey, N.F.: The role of functional magnetic resonance imaging in brain surgery. Neurosurg. Focus. **28**(2), E4 (2010)
103. Salamon, N., Kung, J., Shaw, S.J., Koo, J., Koh, S., Wu, J.Y., Lerner, J.T., Sankar, R., Shields, W.D., Engel Jr., J., Fried, I., Miyata, H., Yong, W.H., Vinters, H.V., Mathern, G.W.: FDG-PET/MRI coregistration improves detection of cortical dysplasia in patients with epilepsy. Neurology. **71**(20), 1594–1601 (2008)
104. Salek-Haddadi, A., Diehl, B., Hamandi, K., Merschhemke, M., Liston, A., Friston, K., Duncan, J.S., Fish, D.R., Lemieux, L.: Hemodynamic correlates of epileptiform discharges: an EEG-fMRI study of 63 patients with focal epilepsy. Brain Res. **1088**(1), 148–166 (2006)
105. Sarikaya, I.: PET studies in epilepsy. Am. J. Nucl. Med. Mol. Imaging. **5**(5), 416–430 (2015)
106. Schneider, J.P., Schulz, T., Schmidt, F., Dietrich, J., Lieberenz, S., Trantakis, C., Seifert, V., Kellermann, S., Schober, R., Schaffranietz, L., Laufer, M., Kahn, T.: Gross-total surgery of supratentorial low-grade gliomas under intraoperative MR guidance. AJNR Am. J. Neuroradiol. **22**(1), 89–98 (2001)
107. Schomer, D.L., Bonmassar, G., Lazeyras, F., Seeck, M., Blum, A., Anami, K., Schwartz, D., Belliveau, J.W., Ives, J.: EEG-linked functional magnetic resonance imaging in epilepsy and cognitive neurophysiology. J. Clin. Neurophysiol. **17**(1), 43–58 (2000)
108. Schonberg, T., Pianka, P., Hendler, T., Pasternak, O., Assaf, Y.: Characterization of displaced white matter by brain tumors using combined DTI and fMRI. NeuroImage. **30**(4), 1100–1111 (2006)
109. Schreiber, A., Hubbe, U., Ziyeh, S., Hennig, J.: The influence of gliomas and nonglial space-occupying lesions on blood-oxygen-level-dependent contrast enhancement. AJNR Am. J. Neuroradiol. **21**(6), 1055–1063 (2000). PM:10871013
110. Schwartz, R.B., Hsu, L., Wong, T.Z., Kacher, D.F., Zamani, A.A., Black, P.M., Alexander III, E., Stieg, P.E., Moriarty, T.M., Martin, C.A., Kikinis, R., Jolesz, F.A.: Intraoperative MR imaging guidance for intracranial neurosurgery: experience with the first 200 cases. Radiology. **211**(2), 477–488 (1999)
111. Shigeto, H., Morioka, T., Hisada, K., Nishio, S., Ishibashi, H., Kira, D., Tobimatsu, S., Kato, M.: Feasibility and limitations of magnetoencephalographic detection of epileptic discharges: simultaneous recording of magnetic fields and electrocorticography. Neurol. Res. **24**(6), 531–536 (2002)
112. Simkins-Bullock, J.: Beyond speech lateralization: a review of the variability, reliability, and validity of the intracarotid amobarbital procedure and its nonlanguage uses in epilepsy surgery candidates. Neuropsychol. Rev. **10**(1), 41–74 (2000)
113. Singhal, T.: Positron emission tomography applications in clinical neurology. Semin. Neurol. **32**(4), 421–431 (2012)
114. Singhal, T., Narayanan, T.K., Jain, V., Mukherjee, J., Mantil, J.: 11C-L-methionine positron emission tomography in the clinical management of cerebral gliomas. Mol. Imaging Biol. **10**(1), 1–18 (2008)
115. Singhal, T., Narayanan, T.K., Jacobs, M.P., Bal, C., Mantil, J.C.: 11C-methionine PET for grading and prognostication in gliomas: a comparison study with 18F-FDG PET and contrast enhancement on MRI. J. Nucl. Med. **53**(11), 1709–1715 (2012)
116. Spencer, S., Huh, L.: Outcomes of epilepsy surgery in adults and children. Lancet Neurol. **7**(6), 525–537 (2008)

117. Stok, C.J., Meijs, J.W., Peters, M.J.: Inverse solutions based on MEG and EEG applied to volume conductor analysis. Phys. Med. Biol. **32**(1), 99–104 (1987)
118. Stufflebeam, S.M., Tanaka, N., Ahlfors, S.P.: Clinical applications of magnetoencephalography. Hum. Brain Mapp. **30**(6), 1813–1823 (2009)
119. Sunaert, S.: Presurgical planning for tumor resectioning. J. Magn Reson. Imaging. **23**(6), 887–905 (2006)
120. Swanson, S.J., Sabsevitz, D.S., Hammeke, T.A., Binder, J.R.: Functional magnetic resonance imaging of language in epilepsy. Neuropsychol. Rev. **17**(4), 491–504 (2007)
121. Szaflarski, J.P., Gloss, D., Binder, J.R., Gaillard, W.D., Golby, A.J., Holland, S.K., Ojemann, J., Spencer, D.C., Swanson, S.J., French, J.A., Theodore, W.H.: Practice guideline summary: use of fMRI in the presurgical evaluation of patients with epilepsy: report of the guideline development, dissemination, and implementation Subcommittee of the American Academy of neurology. Neurology. **88**(4), 395–402 (2017)
122. Toga, A.W., Thompson, P.M., Mori, S., Amunts, K., Zilles, K.: Towards multimodal atlases of the human brain. Nat. Rev. Neurosci. **7**(12), 952–966 (2006)
123. Ulmer, J.L., Krouwer, H.G., Mueller, W.M., Ugurel, M.S., Kocak, M., Mark, L.P.: Pseudo-reorganization of language cortical function at fMR imaging: a consequence of tumor-induced neurovascular uncoupling. AJNR Am. J. Neuroradiol. **24**(2), 213–217 (2003). PM:12591636
124. Ulmer, J.L., Hacein-Bey, L., Mathews, V.P., Mueller, W.M., DeYoe, E.A., Prost, R.W., Meyer, G.A., Krouwer, H.G., Schmainda, K.M.: Lesion-induced pseudo-dominance at functional magnetic resonance imaging: implications for preoperative assessments. Neurosurgery. **55**(3), 569–579 (2004a). PM:15335424
125. Ulmer, J.L., Salvan, C.V., Mueller, W.M., Krouwer, H.G., Stroe, G.O., Aralasmak, A., Prost, R.W.: The role of diffusion tensor imaging in establishing the proximity of tumor borders to functional brain systems: implications for preoperative risk assessments and postoperative outcomes. Technol. Cancer Res. Treat. **3**(6), 567–576 (2004b). PM:15560714
126. Upadhyay, U.M., Golby, A.J.: Role of pre- and intraoperative imaging and neuronavigation in neurosurgery. Expert. Rev. Med. Devices. **5**(1), 65–73 (2008)
127. Van Westen, D., Skagerberg, G., Olsrud, J., Fransson, P., Larsson, E.M.: Functional magnetic resonance imaging at 3T as a clinical tool in patients with intracranial tumors. Acta Radiol. **46**(6), 599–609 (2005)
128. Vlieger, E.J., Majoie, C.B., Leenstra, S., den Heeten, G.J.: Functional magnetic resonance imaging for neurosurgical planning in neurooncology. Eur. Radiol. **14**(7), 1143–1153 (2004)
129. Vu, A.T., Jamison, K., Glasser, M.F., Smith, S.M., Coalson, T., Moeller, S., Auerbach, E.J., Ugurbil, K., Yacoub, E.: Tradeoffs in pushing the spatial resolution of fMRI for the 7T human connectome project. NeuroImage. **154**, 23–32 (2017)
130. Vulliemoz, S., Thornton, R., Rodionov, R., Carmichael, D.W., Guye, M., Lhatoo, S., McEvoy, A.W., Spinelli, L., Michel, C.M., Duncan, J.S., Lemieux, L.: The spatio-temporal mapping of epileptic networks: combination of EEG-fMRI and EEG source imaging. NeuroImage. **46**(3), 834–843 (2009)
131. Wada, J., Rasmussen, T.: Intracarotid injection of sodium amytal for the lateralization of cerebral speech dominance. J. Neurosurg. **17**(6), 262–282 (1960)
132. Walter, W.G., Cooper, R., Aldridge, V.J., McCallum, W.C., Winter, A.L.: Contingent negative variation: an electric sign of sensorimotor association and expectancy in the human brain. Nature. **203**, 380–384 (1964)
133. Warfield, S.K., Haker, S.J., Talos, I.F., Kemper, C.A., Weisenfeld, N., Mewes, A.U., Goldberg-Zimring, D., Zou, K.H., Westin, C.F., Wells, W.M., Tempany, C.M., Golby, A., Black, P.M., Jolesz, F.A., Kikinis, R.: Capturing intraoperative deformations: research experience at Brigham and Women's Hospital. Med. Image Anal. **9**(2), 145–162 (2005)
134. Wieshmann, U.C., Symms, M.R., Parker, G.J., Clark, C.A., Lemieux, L., Barker, G.J., Shorvon, S.D.: Diffusion tensor imaging demonstrates deviation of fibres in normal appearing white matter adjacent to a brain tumour. J. Neurol. Neurosurg. Psychiatry. **68**(4), 501–503 (2000)

135. Witwer, B.P., Moftakhar, R., Hasan, K.M., Deshmukh, P., Haughton, V., Field, A., Arfanakis, K., Noyes, J., Moritz, C.H., Meyerand, M.E., Rowley, H.A., Alexander, A.L., Badie, B.: Diffusion-tensor imaging of white matter tracts in patients with cerebral neoplasm. J. Neurosurg. **97**(3), 568–575 (2002)
136. Zilles, K., Schleicher, A., Langemann, C., Amunts, K., Morosan, P., Palomero-Gallagher, N., Schormann, T., Mohlberg, H., Burgel, U., Steinmetz, H., Schlaug, G., Roland, P.E.: Quantitative analysis of sulci in the human cerebral cortex: development, regional heterogeneity, gender difference, asymmetry, intersubject variability and cortical architecture. Hum. Brain Mapp. **5**(4), 218–221 (1997)

Chapter 4
Brain Tissue Mechanical Properties

Lynne E. Bilston

4.1 Introduction

The human brain is a soft highly metabolically active tissue, floating in cerebrospinal fluid (CSF) within the rigid cranium. This environment acts to isolate the brain from the majority of external mechanical loads experienced by the head during normal daily life. The brain does experience a range of mechanical loads directly, as a result of blood and CSF flow and to some extent, body posture. The dynamic balance of pulsatile hydrodynamic forces in the skull is maintained by blood and CSF flow into and out of the skull throughout the cardiac cycle (the Monro-Kellie hypothesis), since the internal volume of the skull is constant. Reflex responses maintain blood flow during changes in posture and activity, so as to stabilise the mechanical and biochemical environment of the brain.

Brain tissue consists of white and grey matter, and different regions of the brain are made up of different proportions of white and grey matter. White matter is largely composed of myelinated axons of nerve fibres, while the grey matter is dominated by unmyelinated axons and cell bodies.

Since the brain is so well insulated from mechanical perturbations under normal circumstances, one might ask why it is important to understand the mechanical properties of brain tissue. While mechanical factors are thought to play a role in a range of conditions, including brain development [1], brain mechanics have been most commonly studied in an attempt to understand conditions where loads are applied either directly or indirectly to the brain. Much of the early work on brain mechanics was focused on understanding the biomechanics of traumatic brain injury, where high loading rate motion of, or impacts to, the skull results

L. E. Bilston (✉)
Neuroscience Research Australia and University of New South Wales, Sydney, NSW, Australia
e-mail: L.Bilston@neura.edu.au

K. Miller (ed.), *Biomechanics of the Brain*, Biological and Medical Physics, Biomedical Engineering, https://doi.org/10.1007/978-3-030-04996-6_4

in internal damage to the brain. At the other end of the loading rate spectrum lie neurostructural conditions such as hydrocephalus, where very slow dilatation of the ventricles deep within the brain, often due to obstruction of a CSF outflow pathway, compresses the surrounding brain tissue. Either slow or fast loading can lead to neural injury and neurological and/or cognitive dysfunction. Brain tissue mechanical behaviour has also been suggested to vary in some disease conditions [2–5], and noninvasive methods of measuring tissue properties in vivo could potentially be useful for discriminating between conditions that have similar symptoms and imaging appearance, but different treatment outcomes. An example of this is discriminating between normal pressure hydrocephalus, which responds well to surgical shunt placement, and cerebral atrophy due to other neurological disorders which does not [6, 7].

Another key driver for research aimed at understanding the fundamental biomechanical response of brain tissue is to provide high-quality experimental data to allow for development of mathematical and computational models of brain behaviour. This includes development of accurate constitutive models of brain tissue behaviour, relevant to the problem being studied, and also to allow finite element and other computational models to accurately simulate the brain response to complex loading conditions. Such simulations might include analysis of traumatic brain injury mechanisms and tissue injury thresholds, simulation of brain diseases that have a mechanical component (e.g. hydrocephalus), and simulation of surgical procedures for surgical planning or surgical training systems.

Brain tissue mechanics have become an increasing focus of research in the last couple of decades, in part due to emerging methods for measuring in vivo brain properties and associations between changes in brain mechanics and a variety of neurological disorders.

In this chapter, the fundamental viscoelastic properties of brain tissue will be critically reviewed, and limitations of the current state of knowledge and directions for future research will be identified.

4.2 Shear Properties of Brain Tissue

Interest in the shear response of brain tissue arose from early studies by Holbourn [8] who hypothesised that diffuse axonal damage seen in the brain parenchyma after traumatic brain injury occurred as a result of rotational shear within the brain. This was further substantiated in the 1980s by Thibault and Gennarelli's experimental work with non-human primates [9].

Methodological issues have played a major role in the apparently disparate shear properties reported for brain tissue in the literature, and only in the late 1990s did the rigour of rheology begin to be applied to measurement of shear properties of brain tissue. Much of the large disparity between the previously reported data can be explained in the light of more rigorous approaches to control of sample preparation, test conditions, and the use of standard rheological test

procedures. However, there is also considerable intra-study variability in reported brain mechanical properties data, to which biological variation is likely to be at least a substantial contributor. A key flaw of many early studies of shear properties in the literature was the (sometimes unstated) assumption of linear viscoelastic behaviour and therefore flawed interpretation of large amplitude oscillatory data. The appropriate approach is to first identify the linear viscoelastic limit for a tissue, conduct tests to characterise the linear viscoelastic response, and then conduct appropriate large-amplitude (nonlinear) tests with appropriate analysis methods.

Shear response of a viscoelastic material is characterised in terms of the shear modulus, usually denoted by the symbol G. This quantity represents the unit stress response to a unit shear strain and is constant for a given frequency in linear viscoelastic materials. The relaxation shear modulus represents the temporal stress response to a unit shear strain and is typically denoted $G(t)$. The storage and loss moduli represent the elastic (G') and viscous (G'') components of the linear viscoelastic shear modulus, respectively, and are a function of loading rate, often reported as frequency.

4.2.1 Linear Viscoelastic Properties

The traditional rheological approach to measuring viscoelastic properties of complex materials is to first establish the linear viscoelastic limit and characterise the material behaviour at or below this limit. In the linear viscoelastic region, the stress generated is proportional to the strain applied, so that the shear modulus is constant.

4.2.1.1 Oscillatory Loading

Oscillatory testing of tissues is most often carried out using parallel plate geometries, where one plate is fixed, while the other is moved sinusoidally parallel to the fixed plate, while torque is recorded. Parallel plates are used because of the difficulty of cutting brain tissue samples to fit the cone-and-plate setup that is often used for viscoelastic fluids. The moving plate is typically either rotated about an axis perpendicular to the plates, as in traditional rotational rheometers, or moved linearly parallel to the fixed plate. Other methods have been used, including an eccentrically loaded sample in a rotational rheometry setup [10], and shear wave propagation methods such as magnetic resonance elastography [11].

Oscillatory loading results are typically reported as the storage (G') and loss (G'') moduli, which represent the elastic and viscous components of the dynamic shear modulus ($G^* = G' + iG''$). This complex notation is used for the shear modulus to indicate that the stress associated with the viscous response is temporally out of phase with the elastic response and the input sinusoidal displacement (by $\pi/2$).

Figure 4.1 summarises the data reported in the literature within the linear viscoelastic region [10, 12–15]. From this, it can be seen that brain tissue is a very

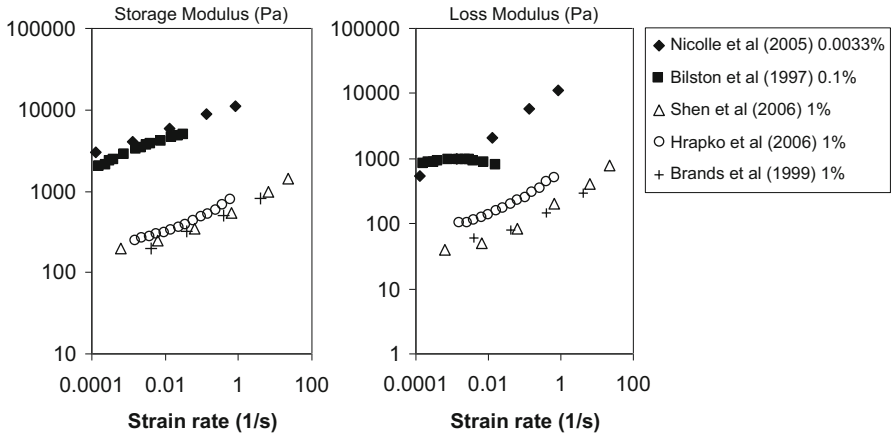

Fig. 4.1 Linear viscoelastic shear moduli for brain tissue from ex vivo brain samples

soft solid, with a shear modulus of the order of a few kilopascals at physiological loading rates. The shear modulus increases in a power-law fashion with loading rate. This figure also shows reasonable consistency for both G' and G" measurements made at similar strains, but the studies who reported the linear viscoelastic regime to be at higher strains (e.g. 1%) report the brain to be softer than those who made measurements at lower strains. Since the brain exhibits shear thinning once the linear viscoelastic limit is exceeded, resulting in lower apparent shear moduli, it seems likely that the measurements made at larger strains are not, in fact, made within the linear viscoelastic regime, and this explains the discrepancy. The strain sweep data presented by Bilston et al. [12] indicates that between 0.1% and 1% strain, the apparent storage modulus drops by approximately 40%, supporting this contention, and thus the data collected at 1% strain is likely not to be truly within the linear viscoelastic limit. The values reported by Bilston et al. [12] are also consistent with more recent in vivo elastography methods discussed below. The data of Shen et al. [15] was collected at long post-mortem times and is thus less likely to be reliable (see discussion below on methodological issues).

Interestingly, the trend in strain-rate sensitivity is very similar for all test data, with a power-law increase of storage moduli with strain rate, where stress increases by an order of magnitude over approximately five decades of loading rate.

4.2.1.2 Relaxation

The linear viscoelastic relaxation modulus for brain tissue has been measured less frequently than the oscillatory properties, at least partly because of the technical challenges in measuring these properties at very low strains. It is, however, quite important, since the most commonly used nonlinear models used to describe brain

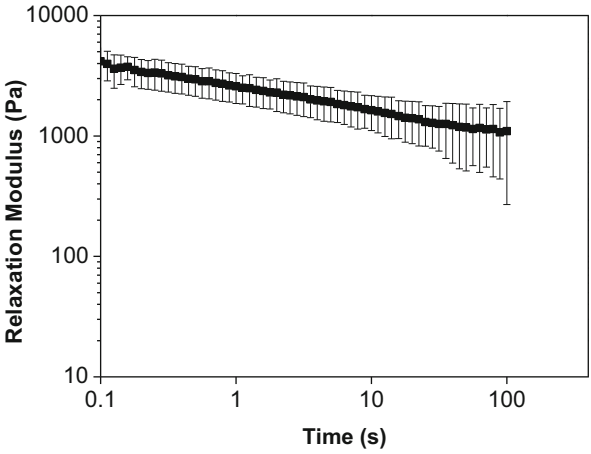

Fig. 4.2 Linear viscoelastic relaxation modulus for brain tissue measured ex vivo. (Adapted from Bilston et al., 1997)

tissue rely on quasilinear viscoelastic theory (QLV, [16]), which has as a key requirement that the shape of the relaxation modulus be independent of strain. The only data set that is convincingly within the linear viscoelastic region is that of Bilston et al. [12], and the relaxation modulus is shown in Fig. 4.2. Indeed, this data has been shown to be consistent with the small amplitude oscillatory data, since using it to predict the linear viscoelastic response gives results similar to the oscillatory data at 0.1% shown in Fig. 4.1 (see [12] for further details).

4.2.1.3 Other Measurements

In recent years, researchers have attempted to use novel techniques to measure brain tissue properties, with a particular focus on those testing situations that are difficult to measure using traditional rheometry, such as very high loading rates and in vivo measurements.

4.2.1.4 Elastography Measurements

One technique that has received significant recent attention is magnetic resonance elastography (MRE), which relies on the relationship between the amplitude, wavelength, and velocity of propagating mechanical waves to extract linear viscoelastic properties of soft tissues. The MR scanner is used to image small amplitude vibration within the brain parenchyma, which is usually created by transmitting mechanical vibration (of frequency typically 30–100 Hz) to the skull and into the brain parenchyma. Mathematical analysis, involving localised inversion of the wave equation at each pixel in the image plane, allows estimation of the local shear

modulus. In the simplest implementation, the local wavelength is used to estimate the 'elastic' shear modulus of the tissue, according to Muthupillai et al. [17]:

$$G = \nu^2 \lambda^2 \rho,$$

where ν = frequency, λ = the local wavelength, and ρ = density.

More advanced implementations solve the full wave equation over the three-dimensional image domain. Some of these techniques use a correspondence principle approach, whereby the shear modulus is considered to be a complex quantity in the wave equation, allowing both the elastic and viscous components (*G'* and *G"*, respectively) of the shear modulus to be extracted, if a sufficiently high signal to noise ratio is present in the image data. This relies on the attenuation of the propagating wave as it penetrates the brain parenchyma to estimate the viscous damping.

The estimated shear moduli for healthy brain tissue that has been gathered using MRE, while not as widely varying as some of the early ex vivo brain data, are nevertheless somewhat variable, due in large part to the different analytical approaches taken to estimating the elastic and/or viscoelastic properties and data quality. Although there is still considerable debate about the best methods of both wave induction in brain elastography and data analysis, numerous studies have used MRE to examine both healthy populations and also several clinical populations. Selected data from a selection of brain MRE studies in healthy adults is shown in Fig. 4.3.

Many of the early brain MRE studies used small sample sizes, but more recently, larger studies have been performed, giving greater confidence in their findings. Such studies have suggested that brain shear modulus may decline slightly with age and that females may have very slightly stiffer brains than males [21, 23]. The practical significance of these small differences is not yet clear. Some research groups have

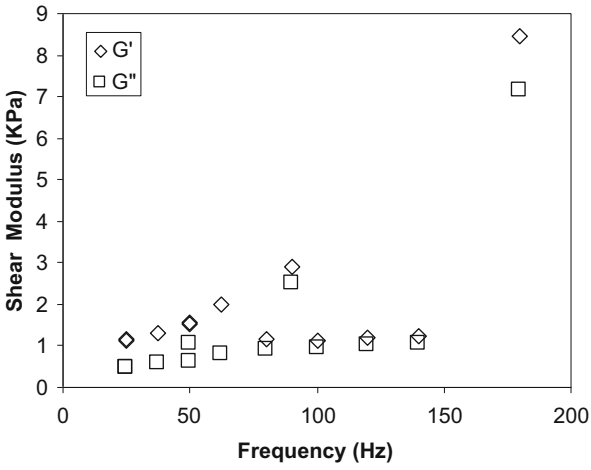

Fig. 4.3 Brain shear modulus measurements made using MR elastography. (Data from [11, 18–22])

attempted to create 'maps' of regional brain properties in healthy adults using MRE [24, 25], although the regional differences are not large and regions and values reported vary between groups. The most consistent finding is that the cerebellum is considerably less stiff than the cerebral hemispheres [25, 26], possibly due to its finer structure [26]. There has also been progress towards estimating differences in white and grey matter and also in methods to estimate anisotropy of white matter tracts. Although consensus remains to be reached on the precise quantitative differences, it is reasonably clear that the differences in white and grey matter shear moduli are likely fairly small and that the degree of mechanical anisotropy is also modest in most brain regions.

Vappou et al. [27] have published a direct comparison of rheometry data on ex vivo brain tissue with MRE measurements, but it is difficult to draw direct conclusions about the validity of MRE on the basis of their work, since their testing frequencies did not overlap for the two methods, their MRE shear moduli were estimated from a simple wavelength-based formula rather than full inversion of the wave equation, and their rheometry testing was conducted at a shear strain of 0.5%, which the above discussion suggests may have been beyond the linear viscoelastic limit, and thus have slightly underestimated the shear modulus. Further rigorous validation of MRE is required before the absolute values estimated from this technique can be considered quantitatively reliable or results from different analytical techniques can be compared. Studies performed using different MRE techniques still tend to report differing shear modulus values at similar frequencies [28], although general trends towards higher moduli at higher frequencies are consistent with rheometry studies.

Brain MRE has recently begun to be used in research studies in clinical populations, including demyelination [29, 30], dementia [31, 32], cerebrospinal fluid flow disorders such as hydrocephalus [33–35], and brain cancers [36–38]. These studies, while intriguing, remain to be repeated in independent cohorts, and typically show substantial overlap between patient and control groups, and occasionally have contradictory results, which may indicate that they are limited in their diagnostic power using current methods.

Despite these issues, MRE has great promise as a relatively noninvasive method of measuring in vivo human tissue properties, which is impossible using other more traditional techniques.

Ultrasound has also been used to estimate brain tissue properties, in the linear viscoelastic (small amplitude) range ex vivo. Lippert et al. (2004) used the 'wave in a tube' technique, where a sample is placed in a tube and an ultrasonic (100 kHz–10 MHz) waves passed through the sample. By measuring this wave propagation, the wave speed in the tube is estimated and the linear viscoelastic shear modulus (G*) extracted. Lippert et al. [39] estimated the shear modulus for juvenile ovine brain tissue samples to be in the range of 140–400 MPa, where the larger values are associated with the higher frequencies. These values are orders of magnitude larger than values from lower frequencies, and somewhat higher than simple extrapolation of the power-law behaviour measured at lower frequencies (e.g. the data shown in Fig. 4.1) would predict. Atay et al. [40] measured mouse brain shear modulus

using MR elastography at an intermediate frequency of 1 kHz, obtaining values of approximately 10–15 kPa, still well below the values obtained by high-frequency ultrasound. Ultrasound shear wave elastography has also recently been applied to brain tissue in vivo in human subjects [41] and ex vivo porcine samples [42], yielding tissue shear modulus estimates more in keeping with MRE measures.

In summary, the linear viscoelastic properties of brain tissue, while a fundamental stepping stone for understanding the more complex nonlinear properties, have been measured using reliable techniques in only a small number of studies, and methodologically flawed data sets are common. There is still room for more robust characterisation of these properties under a wider range of loading conditions, including further cross-validation of data from one testing mode against another (e.g. oscillation vs relaxation or tension vs compression). The former has rarely been done (e.g. see Bilston et al. [12]) and would create greater confidence in the quality and reliability of the data.

4.2.2 Nonlinear Viscoelastic Properties

Most soft biological tissues are thought to be nonlinearly viscoelastic at moderate to large amplitudes of loading [16]. Nonlinear viscoelastic materials require more complex mechanical testing protocols in order to characterise the behaviour of the material, in order to ascertain how the properties change with loading type, loading amplitude, and loading rate. Brain tissue has a very low linear viscoelastic limit, rendering it nonlinearly viscoelastic at most strains of practical interest.

4.2.2.1 Oscillatory Response

While there are several reports of oscillatory response of brain tissue in the literature [13, 43–45], most of these have interpreted data without proper analysis of the nonlinear viscoelastic effects and are thus of questionable validity. The key problem is that in the nonlinear viscoelastic regime, the shear modulus is a function of strain and not independent of strain as it is within the linear viscoelastic regime. In the case of brain tissue, there is substantial shear thinning at strains beyond the linear viscoelastic regime, and the shear modulus estimated from larger amplitude test data can be significantly underestimated (as discussed above). In this context, shear thinning is observed as a decreasing shear modulus with increasing applied shear strain. Oscillatory tests at large amplitude require analysis of the full loading and unloading cycle, which is non-sinusoidal at large amplitudes, and thus the simple calculation of G' and G'' from the phase difference between the peak torque and the peak shear strain is no longer valid. In addition, the decomposition of the complex modulus into the storage and loss modulus is typically based on the phase difference between the peak input shear strain and the peak torque generated. If the torque signal is non-sinusoidal, decomposition of the shear modulus based on this method will give erroneous values. Newer rheometers have the capacity to measure the full

loading cycle, and thus more rheologically rigorous methodologies can, and should, be applied to study oscillatory loading of brain tissue, to better characterise not only the fully nonlinear behaviour but also the transition regime between 0.1% and 1% strain just above the linear viscoelastic limit. Newer methods such as applying large amplitude oscillatory shear and using shear in combination with other loading conditions [46] in which inertial effects are properly considered, may also be useful for brain tissue.

4.2.2.2 Relaxation

Beyond the linear viscoelastic regime, the relaxation modulus for brain tissue decreases with applied shear strain (see data from the literature [12, 13, 15, 43, 47, 48] summarised in Fig. 4.4). This is consistent with the shear thinning seen in the oscillatory data noted above. Relaxation in brain tissue ex vivo appears to continue over the whole time period that has been measured to date, and while there are some minor differences in the shape of the relaxation curve at the early and later parts of the curves, there is moderate consistency of the approximate shape across much of the data. Note that the shape of the early part of the relaxation curve can be affected by the loading rate used for the initial 'step', which can never be instantaneous in practice [49]. At longer times, tests may be affected by post-mortem tissue changes, including degradation and/or dehydration. This is more marked at low strains where the torques are near the resolution of the test instrument and may explain some of the differences in shape in the relaxation curves at long times.

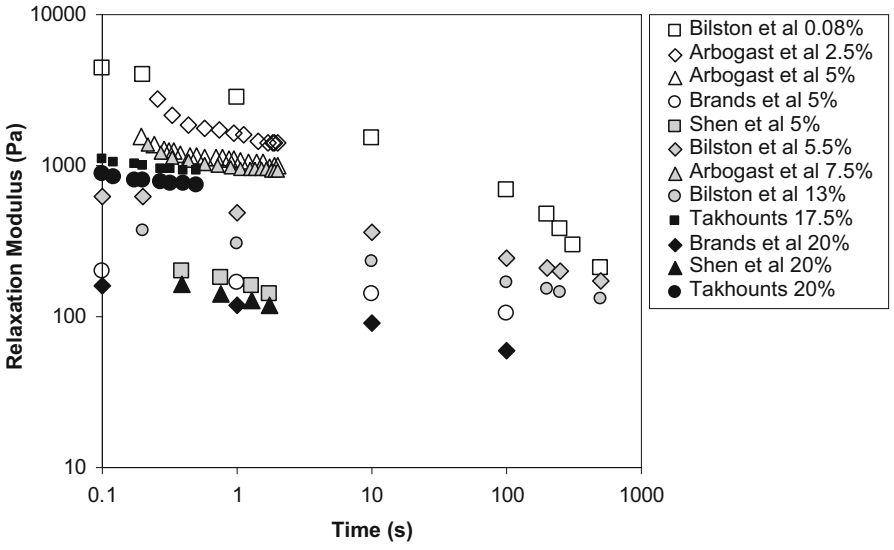

Fig. 4.4 Relaxation modulus for brain tissue in shear

4.2.2.3 Constant Loading Rate

Shear tests, analogous to the traditional engineering tensile tests, aimed at constructing a stress-strain curve have also been conducted by several researchers over a wide range of loading rates. These tests demonstrate the nonlinear response of brain tissue, and almost all test series have shown a clear increase in apparent stiffness with increasing loading rate. Failure or tissue yield in shear appears to begin at approximately 100–200% strain at low to moderate loading rates, according to Bilston et al. [47]. This is significantly a higher strain than the brain can withstand in tension and compression. Few constant shear rate tests in the literature have had inertia corrections applied to the data, and at high loading rates, the sample inertia may contribute to the recorded load. Data from the literature [10, 47, 50] are summarised in Fig. 4.5.

4.2.2.4 Other Test Types

In rheological studies of polymers, it is standard practice to further characterise complex fluids and soft solids using combination and multistep loading histories, such as multiple steps, including those in opposite directions. This has rarely been done in the study of brain tissue and would likely provide significant

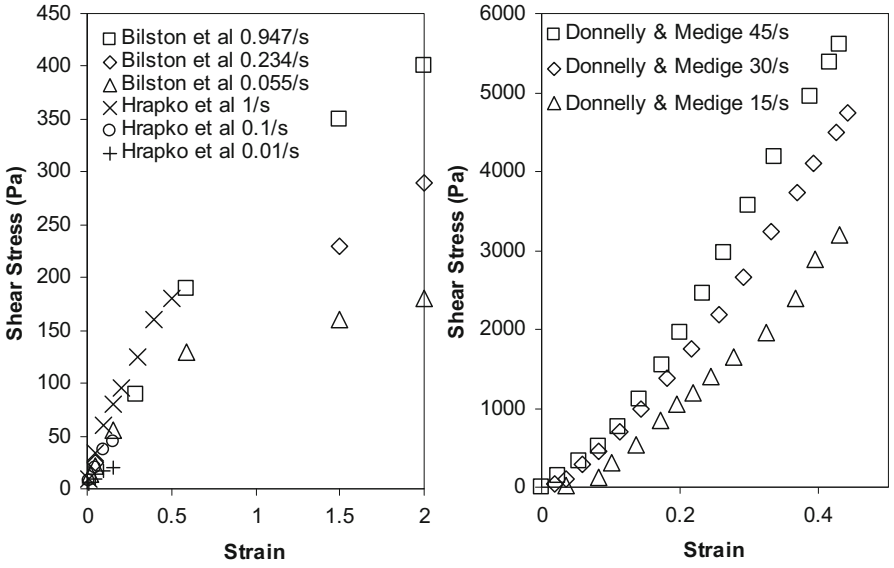

Fig. 4.5 Constant shear rate test data for brain tissue at low to moderate loading rates (left) and high (right) loading rates

new information that would help in developing and establishing the validity of constitutive models for brain tissue.

4.3 Compressive Properties of Brain Tissue

The earliest data for compressive properties of brain tissue are those of Estes and McElhaney [51], who compressed rhesus and human brain tissue to large strains over a broad range of loading rates. They found that brain tissue was notably strain-rate sensitive, with increasing stiffness at higher loading rates, and increasing stiffness with applied strain, resulting in a concave upward nonlinear stress-strain curve (see Fig. 4.6). Miller and Chinzei [52] conducted compressive tests at lower strain rates and obtained similar qualitative results, although their data showed lower stresses for similar strains and strain rates. Cheng and Bilston [53] recently conducted compression tests of brain at very low strain rates, with similar stress-strain responses to those of Chinzei and Miller. Data from these tests are shown in Fig. 4.6. Tamura et al. [54] conducted moderate to high rate compression tests, and their data lies somewhat below that of Estes and McElhaney, suggesting the long post-mortem time used for Estes and McElhaney's work may have affected their results. Most recently, Pervin and Chen [55] conducted both quasistatic and high loading rate tests of brain tissue in compression, using a modified Hopkinson split bar technique, again confirming the brain's strong strain-rate sensitivity. Their data, collected at 1000–3000/s from very fresh samples, lies well above that of Estes and

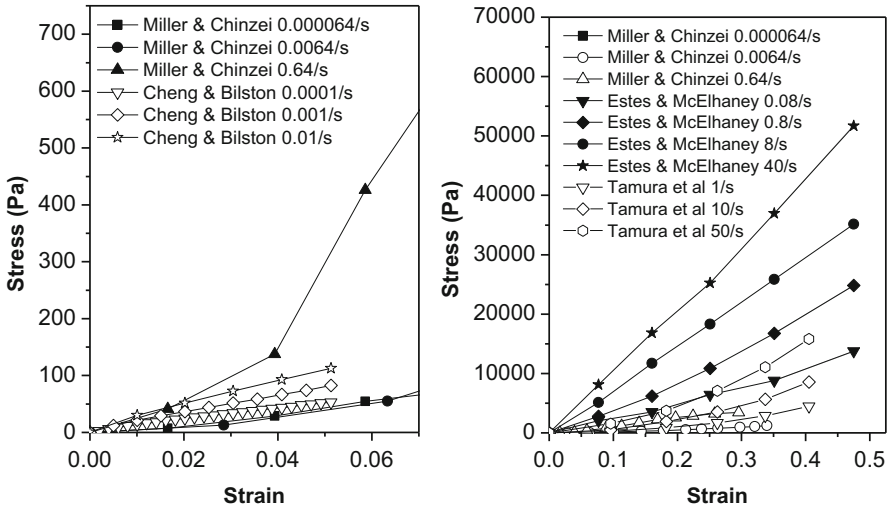

Fig. 4.6 Selected compressive properties of brain tissue at low to moderate loading rates (left) and moderate to high loading rates (right)

McElhaney (an order of magnitude higher at 1000/s, not shown), which suggests that the strain-rate sensitivity does not disappear, even at very high loading rates. Data is reported for peak strains up to 30–50% in compression, suggesting this is the onset of failure. Rashid et al. [56] observed strain-rate effects at compressive strain rates of 30–90/s also. None of these studies explicitly considered inertial effects, which can be expected to be significant.

Traditional rheological test protocols have rarely been applied to compression testing, and thus the linear viscoelastic properties of brain in compression have not been ascertained. Fallenstein et al. used sinusoidal indentation tests in the live macaque brain and showed that for very small indentations (25 μm) the force response was sinusoidal, suggesting linear response, but for larger indentations (300 μm) the responses were non-sinusoidal. The linear limit may lie between these two, but the local strain field is difficult to estimate, especially since the pia mater was intact underneath the probe, and thus these data do not give a clear value for the compressive linear viscoelastic strain limit, although it is likely to be quite low. Miller et al. [57] indented porcine brain in vivo, using a finite element model to extract parameters for a hyper-viscoelastic constitutive model.

Relaxation moduli in compression at large strains have been reported in a small number of studies [53, 54]. Cheng and Bilston [53] found that the relaxation response was relatively independent of loading rate, after the short period after the initial ramp (see Fig. 4.7). Tamura et al. [54] found a consistent reduced relaxation modulus over a range of large strains (20–70%). Rashid et al. [56] reported relaxation force after high strain tests (10–50% unconfined compression), observing rapid relaxation in the first few milliseconds of relaxation, slowing thereafter but continuing until measurement ceased after half a second.

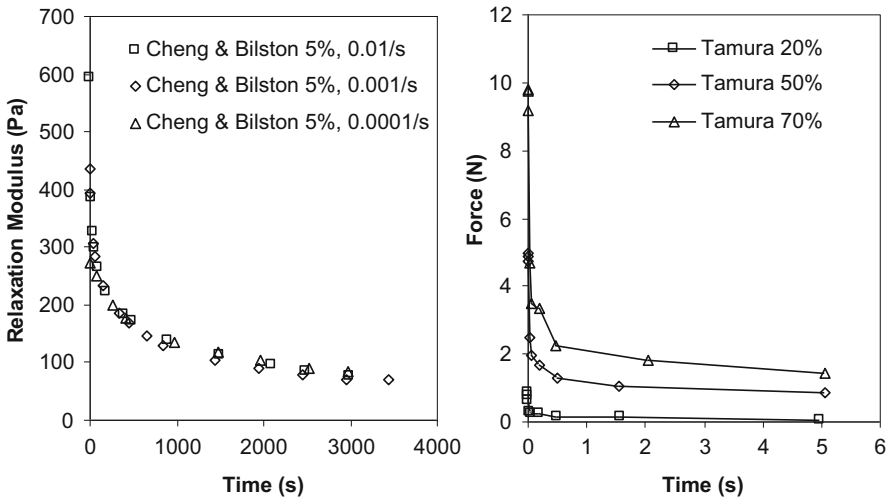

Fig. 4.7 Compressive relaxation data for brain tissue

Compressive properties have also been considered in the context of brain tissue being a fluid-saturated two-phase material. The main application of this type of modelling has been in the study of hydrocephalus. The simpler biphasic or poroelastic models, similar to those developed for modelling soils, assume a linear elastic tissue matrix saturated with an inviscid (or alternatively a Newtonian) fluid. This gives rise to flow through the interstitial spaces of the tissue according to Darcy's Law, coupled to linear elastic deformation.

Conducting the traditional soil consolidation tests on brain tissue samples has been said to be technically challenging [53], and thus unconfined compression data is often used to estimate the properties. Chinzei and Miller [58, 59] showed that a simple poroelastic model is not able to simulate the strain-rate sensitivity observed in brain tissue. That group have also published information on methodological issues with such multiphase models and for specific applications such as hydrocephalus [58, 60]. Cheng and Bilston [53] used a poroviscoelastic model for brain tissue to model their compressive data at low loading rates. There is a wide range of values (approximately 3–4 orders of magnitude reported for the hydraulic conductivity of brain tissue in the literature (2×10^{-10}–4×10^{-7} m/s) [53, 61, 62], of which very few are based on definitive experimental work (e.g. [53]. who reported 4.0×10^{-7} m/s), and further research is needed to accurately characterise these parameters. Chapter 6 contains additional discussion of the application of multiphase models in surgical simulation.

4.4 Tensile Properties of Brain Tissue

Brain tissue properties in tension are less well characterised than in other loading modes, with only a few studies reporting tensile properties. This is at least in part due to the difficulties of conducting these tests, particularly in gripping samples effectively. General observations of the behaviour of brain tissue in tension are that it appears to soften with increasing strain and exhibits a strain-rate sensitivity that is consistent with the response in other loading modes, that is, increasing apparent stiffness with increasing loading rate. Figure 4.8 shows some of the data from the literature [63, 64]. At higher loading rates, Rashid et al. [65] also observed strong rate dependence in ex vivo porcine brain specimens, with stresses approximately doubling for a given strain between 30/s and 90/s strain rates. Failure limits in tension are not well characterised, but appear to be in the range of 20–60% strain.

More recently, Schiavone et al. [66] have used an aspiration method to measure in vivo brain deformation with tensile loading at the surface intra-operatively on a human patient. They used a simplified finite element model to estimate hyperelastic parameters for that patient.

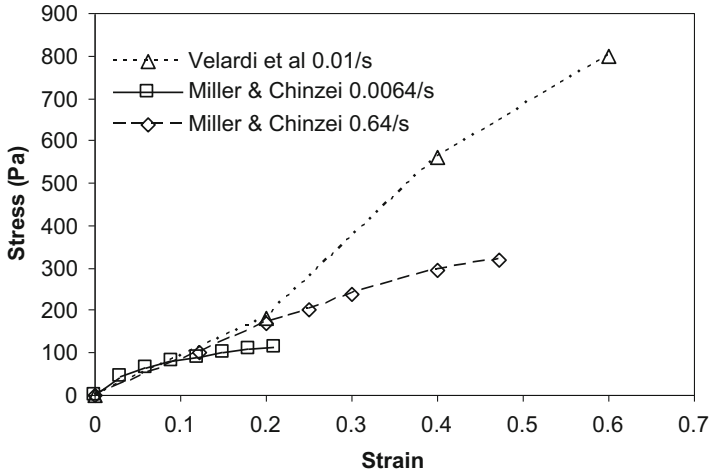

Fig. 4.8 Tensile properties of brain tissue

4.5 Constitutive Models for Brain Tissue

As can be seen from the previous sections on brain tissue mechanical response, capturing the mechanical response of brain tissue in three dimensions over a broad range of loading types and loading rates is a very challenging task. The ideal constitutive equation would be able to model the shear, compressive, and tensile response of brain tissue, within the loading rate regime of interest for a particular study. There have been many studies that have developed constitutive equations for specific aspects of brain mechanical response, but few that have been widely used beyond the original description of test data. To date, there is no widely accepted constitutive model for brain tissue that is able to match the full spectrum of the strongly strain-rate sensitive, nonlinearly viscoelastic behaviour of brain tissue. Recently, researchers have focused attention on modelling multiple loading types (compression, tension, shear, etc.) with a single constitutive law. The nonlinear elastic behaviour of ex vivo human brain tissue in multiple loading modes was able to be reconciled with a single-term Ogden model [67], and a more complex viscoelastic model had some success in capturing viscoelastic behaviour [68]. However, a good fit was only obtained by using all the test data, and while this is a major step forward, the predictive capacity of the model needs testing. Moreover, the test data modelled was from samples tested a long time post mortem, and attempts to model fresh tissue, in vivo data, or viscoelastic behaviour in multiple loading conditions remain an area of active research.

The most commonly used constitutive models used for computational calculations are based on quasilinear viscoelastic (QLV) theory (see [16] for full discussion of this theory). These typically use a hyperelastic model to describe the nonlinear elasticity, combined with a linear viscoelastic relaxation modulus to describe the time-dependent behaviour.

Hyperelastic models were originally developed to describe the nonlinear elastic behaviour of rubbers. They use the concept of a strain energy potential function, from which the relationship between stress and strain tensors is derived. The strain energy function, W, is usually defined in terms of the invariants (I_1, I_2, I_3) of the strain tensor, $\boldsymbol{S}$, which is itself defined by the deformation gradient tensor, $\boldsymbol{F}$. If a material is incompressible, then the third strain invariant is unity, and the strain energy function is only a function of the first two invariants. The stress-strain relationship is then obtained from a partial derivative of the strain energy potential with respect to $\boldsymbol{F}$. Depending on the choice of the strain energy potential, the particular stress and strain tensors used, and the invariants that the definition uses, this derivation can become algebraically complex, and the reader is referred to solid mechanics texts for further details. Common hyperelastic models include those that use strain energy functions that are polynomial functions of the invariants, such as the Mooney-Rivlin model, and the Ogden model, which uses a strain energy function defined in terms of the principal stretch ratios occurring in a material. The Mooney-Rivlin model [69, 70] for an incompressible material defines the strain energy potential in terms of the material parameters, μ_i, as

$$W = \frac{\mu_1}{2}(I_1 - 3) + \frac{\mu_2}{2}(I_2 - 3) \tag{4.1}$$

The Ogden model [71] defines the strain energy potential in terms of the material parameters, μ_i and α_i, and the principal stretch ratios, λ_i, as

$$W = \sum_N \frac{2\mu_i}{{\alpha_i}^2}\left({\lambda_1}^{\alpha_i} + {\lambda_2}^{\alpha_i} + {\lambda_3}^{\alpha_i} - 3\right) \tag{4.2}$$

The viscous or time-dependent behaviour is often modelled as the sum of a series of Maxwell elements, so that the relaxation modulus is given by

$$G(t) = \sum_N G_i e^{-t/\tau_i} \tag{4.3}$$

One example of a model in this class is that of Miller and Chinzei [63], which is often used for neurosurgical modelling. This is based on the combination of an Ogden-like hyperelastic model and a Prony series relaxation modulus, defined by Eqs. 4.4 and 4.5:

$$W = \frac{2}{\alpha^2}\int_0^t \left[\mu(t-\tau)\frac{d}{d\tau}\left(\lambda_1^\alpha + \lambda_2^\alpha + \lambda_3^\alpha - 3\right)\right] d\tau \tag{4.4}$$

$$\mu = \mu_0\left[1 - \sum_{k=1}^{n} g_k\left(1 - e^{-\frac{t}{\tau_k}}\right)\right] \tag{4.5}$$

Values for the material constants, α, and the Prony series coefficients suitable for modelling of surgical procedures are given in [63]. The model has been based on tension and compression data from animals, and it has not yet been validated for human brain or for shear loading.

Other models use rate-dependent viscosity, such as the Carreau model (e.g. [47]) or Ellis model [10]. The stress is then given by

$$\mathbf{S}(t) = \int_{-\infty}^{t} G\,(t-s)\,\frac{\partial \mathbf{T}}{\partial s} ds, \tag{4.6}$$

where $\mathbf{T}$ is the elastic stress-strain function derived from the strain energy potential.

The use of this class of model assumes that the time-dependent behaviour can be separated from the nonlinear elastic behaviour, an assumption that is not universally supported by experimental data (e.g. [47]). Nevertheless, the errors introduced by deviation from such assumptions are probably less than the variation seen in the reported experimental data, as noted above.

Other researchers have developed, and implemented into finite element simulation software, more complex rheological models, including fully nonlinear models in which strain-time separability is not assumed, and that capture some of the yield behaviour at large strains [15, 47].

The most appropriate constitutive model used to describe brain tissue will depend heavily on the application of interest. Neurosurgical simulation not including cutting procedures has been shown to require a suitable large deformation framework, but is not sensitive to the specific constitutive model used [72]. Modelling of hydrocephalus may be done with a single-phase model if the fluid distribution in the brain is not of particular interest (e.g. [73]) but also with suitable poroviscoelastic models with appropriate large deformation formulation [53, 74]. Injury simulations are often done with simpler constitutive models due to the high computational demands of large 3D explicit simulations, despite their limitations. These include linear viscoelastic models (e.g. [75, 76]) as well as hyperelastic models, with or without the viscous component (e.g. [77, 78]). A more detailed comparison of brain tissue constitutive models has recently been published [79].

4.6 Discussion

4.6.1 Mechanical Characteristics of Brain Tissue

Decades of research on brain tissue mechanics has established that brain tissue is a very soft, nonlinearly viscoelastic solid material, with a very low linear viscoelastic strain limit, of the order of 0.1–0.3%. Brain tissue is strain-rate sensitive, with increasing stiffness with increasing strain rate. Failure occurs at moderate strains, of the order of 25–100%, depending on the loading type.

However, there is still much that is either not yet known about brain tissue mechanics or the subject of debate, due to inconsistent or contradictory data in the literature. Some of the reasons for these inconsistencies are discussed below.

Despite the well-defined structural anisotropy of white matter arising from the axonal fibre bundles, mechanical anisotropy has not been comprehensively established. Some studies suggest that there is moderate mechanical anisotropy in white matter under shear, with the axonal fibre direction up to twice as stiff as the perpendicular direction [43, 80] and in tension [64], while others have not found significant mechanical anisotropy in compression [55]. The strains used to estimate properties are likely to have an influence, as increasing stretch of axons may stiffen the tissue, as occurs in other fibrous soft tissues.

Regional variations in tissue properties across the brain have been suggested by some studies [43, 80, 81], although the differences are not large, and some of these studies suffer from methodological problems. A recent post-mortem human brain study indicated some indication of small variations across different regions [82]. This modest, at best, regional variation is consistent with more recent MRE studies, with the exception of the softer cerebellum [26].

Like most very soft hydrated tissues, brain tissue is usually assumed to be incompressible, or nearly incompressible, due to its very high water content (e.g. [52, 83]). There have been only a few studies that have directly examined this assumption, and its validity almost certainly depends on the mechanical process of interest. In very slow processes involving displacement of interstitial fluid within the brain parenchyma, such as hydrocephalus or mass lesions in the brain involving brain oedema, this assumption may not be valid, as there is time for fluid to move within the brain tissue, and regions could locally appear compressible due to fluid transfer. For processes at shorter time scales, there is no evidence that brain tissue is significantly compressible, at least at macroscopic length scales. Indeed, Franceschini et al. [61] report that the undrained (i.e. whole tissue) Poisson's ratio for brain tissue is 0.5, while the 'drained' compressibility is 0.496, lending credence to the incompressibility assumption. A recent study used image correlation methods to confirm that incompressibility holds, at least at slow loading rates [84].

Age dependence of brain tissue properties has also been described in a small number of studies. Prange and Margulies [80] suggested neonatal brain tissue is stiffer than in adults, as did Gefen and Margulies [85]. On the other hand, Thibault and Margulies [86] found that shear modulus of the brain was significantly greater for adult brain tissue than neonatal tissue. It is fair to say that this issue is not yet settled and methodologically robust studies are required. As noted on p. 76 of this Chapter, Sack et al. [21] found that brain tissue shear modulus decreases with age from early adulthood to old age, using MR elastography in vivo, which has been confirmed by other studies, which suggest such changes vary by brain region, e.g. [23]. These studies also observed a small difference between females and males, with female brain tissue being marginally stiffer [86].

Differences between measured properties of brain tissue in vivo and ex vivo have been debated for decades. Some studies show significant drops in situ immediately after death [45, 87, 88]. Weaver et al. attributed this change to drops in interstitial

and cerebral perfusion pressure. A recent study comparing in vivo and ex vivo brain properties using MRE indicates that brain stiffness declines after death, but also that frequency dependence is different in vivo compared to ex vivo [89], further emphasising the difficulties of extrapolating from ex vivo data to in vivo brain properties. Others show an increase in shear modulus beyond 6 hours for samples tested ex vivo [90], while indentation tests have shown no effect on overall stiffness when comparing in vivo to in situ but decreases in shear modulus ex vivo (within 6 hours of death) compared to in vivo and in situ [91]. It seems likely on the basis of this data that there are drops in apparent tissue stiffness immediately after death, and possibly increases at longer times post mortem. Since the ex vivo studies in the literature have used a range of times after death up to days, this may be a significant factor in differences in reported data, and such data should be viewed with caution. A recent MRE study suggested that venous pressure, as manipulated by constriction of jugular outflow from the head, can also influence brain mechanical properties [92].

Few studies have directly compared different species under the same testing protocols. The studies that have been done show that properties are similar, at least between human and porcine brains and human [86] and human and rhesus monkey [51].

4.6.2 Methodological Considerations

As mentioned throughout the above sections, characterisation of brain tissue properties has been plagued by differences in results arising from differences in test methods. These differences fall into three main categories – sample preparation, post-mortem time, and testing conditions.

The issue of post-mortem time is discussed in the previous sections above, but it is likely that much of the data in the literature conducted at long times after death is of limited value due to significant changes in tissue properties post mortem.

Sample preparation has received less attention, but it is also of importance. Delicate brain tissue is easily dehydrated and is also subject to osmotic swelling if bathed in fluids with inappropriate osmotic content [47]. Despite this, a range of bathing fluids have been used, including PBS [90], simple saline [50], and silicon oil [15] in addition to artificial CSF [47], which has a similar osmotic content to CSF. Ensuring that the sample has suitable dimensions to minimise the influence of edge effects, slip at gripping surfaces or test platens, and sample inertial effects at high loading rates is also essential. These issues are often not fully considered in published studies. Liu [93] showed that sample thickness affects measured shear moduli in a parallel plate configuration, and similar results were observed by Garo et al. [90]. Recently, storage temperature has also been suggested to affect the measured properties [94].

Sample preconditioning processes have not been studied in detail in brain tissue, although several studies have noted the effects of previous strain loading cycles

on subsequent measured data. Gefen and Margulies discuss this in some detail [91]. A recent study in spinal cord tissue suggests that the amplitude of the preconditioning has a strong effect on the subsequently measured properties [95], and more recent data from our laboratory also suggests preconditioning strain rate can alter subsequently measured properties.

It must be remembered here that the properties of prime interest are the in vivo properties of human brain tissue. It is only very recently that it has been possible to measure human brain properties in vivo, using MR elastography, and then only at very small deformations, corresponding to the linear viscoelastic regime. Response of brain tissue in vivo at larger deformations must be inferred from a combination of ex vivo tests and animal in vivo tests. This brings with it much uncertainty about how to extrapolate the available ex vivo data and animal in vivo results to the in vivo human brain.

4.7 Future Directions

It is clear from the discussion above that while we have made great strides in characterising the mechanical properties of brain tissue, there is still much to be done. Consistent data sets for different loading regimes, such as shear, compression, and tension, are still not readily available. Data for complex loading histories, such as multiple step loading and step reversals, which have been found to be useful in developing and testing accurate constitutive models for other complex nonlinearly viscoelastic materials are highly desirable. It is essential that such data be collected with full consideration of the methodological issues noted above.

The use of more rigorous rheological testing protocols in compression and testing may allow for more definitive determination of the true linear viscoelastic limit for brain tissue. The collection of data through the full loading and unloading cycle in oscillatory testing may also assist in all test modes.

The other key gap in the body of knowledge regarding brain tissue is integration of data from different loading types – particularly reconciling shear, compression, and tensile loading data. To date, this is not possible because data that has been collected in different testing modes comes from different species and has been subject to different loading regimes (strains, strain rates), been subject to different preparation methods, and been tested at different post-mortem times. There is a clear need for multimodal data (shear, compression, tension, and combination loading) to be collected using robust rheological techniques so that reliable constitutive models can be developed and validated across all loading types. One recent ex vivo human brain rheological study has begun this endeavour by testing tension, compression, and shear loading in a single study [82].

Definitive conclusions about the effect of tissue perfusion pressure on the properties of brain tissue would be valuable in determining what corrections (if any) are required to adapt ex vivo data to predict in vivo brain response. Further in vivo measurements, of both linear viscoelastic (e.g. using MR elastography or similar

methods) and large deformation measurements (e.g. by indentation, aspiration, or other methods), are needed.

Brain mechanics at high loading rates still requires more study, including separating out tissue inertial effects from inherent tissue viscoelasticity. At low loading rates, high-quality quantitative data on interstitial fluid flow in the brain, as is thought to be relevant for diseases such as hydrocephalus, is still lacking.

The use of easily interpretable constitutive models may also assist the field of brain tissue mechanics. While some mechanical properties have intrinsic definitions that are interpretable without reference to a constitutive model, such as the linear viscoelastic moduli, other parameters that are widely reported, often incorrectly, to describe tissue properties beyond this linear range are parameters within constitutive models, with their own inherent assumptions. Given the complexity and strong nonlinearity of brain tissue mechanical response, it is unrealistic to expect that one constitutive model will fit all circumstances, and those who wish to describe brain tissue properties in a given context will need to select and use a model that can capture the features of brain tissue mechanics within the relevant loading regime. A model that works for quasistatic brain deformation during surgery will likely not be suitable for high-velocity impact loading, for example.

4.8 Conclusions

While interest in brain tissue mechanics is enjoying a resurgence of late, and much data has been collected to characterise the response of brain tissue to mechanical loading, there is still much to be done to rigorously characterise this complex material. New developments in measuring techniques, including MRE, however, have great potential for noninvasively measuring tissue properties in vivo, which may allow these properties to be used for diagnostic purposes, as well as shedding light on how this complex organ responds to loads, be they due to dynamic processes that lead to traumatic brain injury or slow processes involved in neurological diseases such as brain tumours or hydrocephalus.

Acknowledgements Lynne Bilston is supported by an NHMRC Senior Research Fellowship.

References

1. Geng, G., Johnston, L.A., Yan, E., Britto, J.M., Smith, D.W., Walker, D.W., Egan, G.F.: Biomechanisms for modelling cerebral cortical folding. Med. Image Anal. **13**, 920–930 (2009)
2. McHedlishvili, G., Itkis, M., Sikharulidze, N.: Mechanical properties of brain tissue related to oedema development in rabbits. Acta Neurochir. **96**, 137–140 (1989)
3. Pang, D., Altschuler, E.: Low-pressure hydrocephalic state and viscoelastic alterations in the brain. Neurosurgery. **35**, 643–655; discussion 655–656 (1994)

4. Kuroiwa, T., Yamada, I., Katsumata, N., Endo, S., Ohno, K.: Ex vivo measurement of brain tissue viscoelasticity in postischemic brain edema. Acta Neurochir. Suppl. **96**, 254–257 (2006)
5. Xu, L., Lin, Y., Han, J.C., Xi, Z.N., Shen, H., Gao, P.Y.: Magnetic resonance elastography of brain tumors: preliminary results. Acta Radiol. **48**, 327–330 (2007)
6. Mase, M., Miyati, T., Kasai, H., Demura, K., Osawa, T., Hara, M., Shibamoto, Y., Yamada, K.: Noninvasive estimation of intracranial compliance in idiopathic NPH using MRI. Acta Neurochir. Suppl. **102**, 115–118 (2008)
7. Tarnaris, A., Kitchen, N.D., Watkins, L.D.: Noninvasive biomarkers in normal pressure hydrocephalus: evidence for the role of neuroimaging. J. Neurosurg. **110**, 837–851 (2009)
8. Holbourn, A.: The mechanics of brain injury. Br. Med. Bull. **3**, 147–149 (1945)
9. Gennarelli, T.A., Thibault, L.E., Adams, J.H., Graham, D.I., Thompson, C.J., Marcincin, R.P.: Diffuse axonal injury and traumatic coma in the primate. Ann. Neurol. **12**, 564–574 (1982)
10. Hrapko, M., van Dommelen, J.A.W., Peters, G.W.M., Wismans, J.S.H.M.: The mechanical behaviour of brain tissue: large strain response and constitutive modelling. Biorheology. **43**, 623–636 (2006)
11. Green, M.A., Bilston, L.E., Sinkus, R.: In vivo brain viscoelastic properties measured by magnetic resonance elastography. NMR Biomed. **21**, 755–764 (2008)
12. Bilston, L.E., Liu, Z., Phan-Thien, N.: Linear viscoelastic properties of bovine brain tissue in shear. Biorheology. **34**, 377–385 (1997)
13. Brands, D.W.A., Bovendeerd, P. H. M., Peters, G. W. M., and Wismans, J: The large shear strain dynamic behaviour of in vitro porcine brain tissue and a silicone gel model material, paper presented at Stapp Car Crash Conference, SAE (2000)
14. Nicolle, S., Lounis, M., Willinger, R., Palierne, J.F.: Shear linear behavior of brain tissue over a large frequency range. Biorheology. **42**, 209–223 (2005)
15. Shen, F., Tay, T.E., Li, J.Z., Nigen, S., Lee, P.V.S., Chan, H.K.: Modified Bilston nonlinear viscoelastic model for finite element head injury studies. J. Biomech. Eng. **128**, 797–801 (2006)
16. Fung, Y.C.: Biomechanics: mechanical properties of living tissues, vol. 568, 2nd edn. Springer, New York (1993)
17. Muthupillai, R., Lomas, D.J., Rossman, P.J., Greenleaf, J.F., Manduca, A., Ehman, R.L.: Magnetic resonance elastography by direct visualization of propagating acoustic strain waves. Science. **269**, 1854–1857 (1995)
18. Hamhaber, U., Sack, I., Papazoglou, S., Rump, J., Klatt, D., Braun, J.: Three-dimensional analysis of shear wave propagation observed by in vivo magnetic resonance elastography of the brain. Acta Biomater. **3**, 127–137 (2007)
19. Kruse, S.A., Rose, G.H., Glaser, K.J., Manduca, A., Felmlee, J.P., Jack Jr., C.R., Ehman, R.L.: Magnetic resonance elastography of the brain. NeuroImage. **39**, 231–237 (2008)
20. Sack, I., Beierbach, B., Hamhaber, U., Klatt, D., Braun, J.: Non-invasive measurement of brain viscoelasticity using magnetic resonance elastography. NMR Biomed. **21**, 265–271 (2008)
21. Sack, I., Beierbach, B., Wuerfel, J., Klatt, D., Hamhaber, U., Papazoglou, S., Martus, P., Braun, J., Sack, I., Beierbach, B., Wuerfel, J., Klatt, D., Hamhaber, U., Papazoglou, S., Martus, P., Braun, J.: The impact of aging and gender on brain viscoelasticity. NeuroImage. **46**, 652–657 (2009)
22. Vappou, J., Breton, E., Choquet, P., Willinger, R., Constantinesco, A.: Assessment of in vivo and post-mortem mechanical behavior of brain tissue using magnetic resonance elastography. J. Biomech. **41**, 2954–2959 (2008)
23. Arani, A., Murphy, M.C., Glaser, K.J., Manduca, A., Lake, D.S., Kruse, S.A., Jack Jr., C.R., Ehman, R.L., Huston 3rd, J.: Measuring the effects of aging and sex on regional brain stiffness with MR elastography in healthy older adults. NeuroImage. **111**, 59–64 (2015)
24. Guo, J., Hirsch, S., Fehlner, A., Papazoglou, S., Scheel, M., Braun, J., Sack, I.: Towards an elastographic atlas of brain anatomy. PLoS One. **8**, e71807 (2013)
25. Murphy, M.C., Huston 3rd, J., Jack Jr., C.R., Glaser, K.J., Senjem, M.L., Chen, J., Manduca, A., Felmlee, J.P., Ehman, R.L.: Measuring the characteristic topography of brain stiffness with magnetic resonance elastography. PLoS One. **8**, e81668 (2013)

26. Zhang, J., Green, M.A., Sinkus, R., Bilston, L.E.: Viscoelastic properties of human cerebellum using magnetic resonance elastography. J. Biomech. **44**, 1909–1913 (2011)
27. Vappou, J., Breton, E., Choquet, P., Goetz, C., Willinger, R., Constantinesco, A.: Magnetic resonance elastography compared with rotational rheometry for in vitro brain tissue viscoelasticity measurement. MAGMA. **20**, 273–278 (2007)
28. Hiscox, L.V., Johnson, C.L., Barnhill, E., McGarry, M.D., Huston, J., van Beek, E.J., Starr, J.M., Roberts, N.: Magnetic resonance elastography (MRE) of the human brain: technique, findings and clinical applications. Phys. Med. Biol. **61**, R401–R437 (2016)
29. Schregel, K., Wuerfel née Tysiak, E., Garteiser, P., Gemeinhardt, I., Prozorovski, T., Aktas, O., Merz, H., Petersen, D., Wuerfel, J., Sinkus, R.: Demyelination reduces brain parenchymal stiffness quantified in vivo by magnetic resonance elastography. PNAS. **109**, 6650–6655 (2012)
30. Wuerfel, J., Paul, F., Beierbach, B., Hamhaber, U., Klatt, D., Papazoglou, S., Zipp, F., Martus, P., Braun, J., Sack, I.: MR-elastography reveals degradation of tissue integrity in multiple sclerosis. NeuroImage. **49**, 2520–2525 (2010)
31. Huston 3rd, J., Murphy, M.C., Boeve, B.F., Fattahi, N., Arani, A., Glaser, K.J., Manduca, A., Jones, D.T., Ehman, R.L.: Magnetic resonance elastography of frontotemporal dementia. J. Magn. Reson. Imaging. **43**, 474–478 (2016)
32. Murphy, M.C., Huston 3rd, J., Jack Jr., C.R., Glaser, K.J., Manduca, A., Felmlee, J.P., Ehman, R.L.: Decreased brain stiffness in Alzheimer's disease determined by magnetic resonance elastography. J. Magn. Reson. Imaging. **34**, 494–498 (2011)
33. Fattahi, N., Arani, A., Perry, A., Meyer, F., Manduca, A., Glaser, K., Senjem, M., Ehman, R., Huston, J.: MR elastography demonstrates increased brain stiffness in normal pressure hydrocephalus. Am. J. Neuroradiol. **37**, 462–467 (2016)
34. Freimann, F.B., Streitberger, K.J., Klatt, D., Lin, K., McLaughlin, J., Braun, J., Sprung, C., Sack, I.: Alteration of brain viscoelasticity after shunt treatment in normal pressure hydrocephalus. Neuroradiology. **54**, 189–196 (2012)
35. Streitberger, K.-J., Wiener, E., Hoffmann, J., Freimann, F.B., Klatt, D., Braun, J., Lin, K., McLaughlin, J., Sprung, C., Klingebiel, R., Sack, I.: In vivo viscoelastic properties of the brain in normal pressure hydrocephalus. NMR Biomed. **24**, 385–392 (2011)
36. Jamin, Y., Boult, J.K., Li, J., Popov, S., Garteiser, P., Ulloa, J.L., Cummings, C., Box, G., Eccles, S.A., Jones, C., Waterton, J.C., Bamber, J.C., Sinkus, R., Robinson, S.P.: Exploring the biomechanical properties of brain malignancies and their pathological determinants in vivo with magnetic resonance elastography. Cancer Res. **75**, 1216–1212 (2015)
37. Murphy, M.C., Huston 3rd, J., Glaser, K.J., Manduca, A., Meyer, F.B., Lanzino, G., Morris, J.M., Felmlee, J.P., Ehman, R.L.: Preoperative assessment of meningioma stiffness using magnetic resonance elastography. J. Neurosurg. **118**, 643–648 (2013)
38. Streitberger, K.J., Reiss-Zimmermann, M., Freimann, F.B., Bayerl, S., Guo, J., Arlt, F., Wuerfel, J., Braun, J., Hoffmann, K.T., Sack, I.: High-resolution mechanical imaging of glioblastoma by multifrequency magnetic resonance elastography. PLoS One. **9**, e110588 (2014)
39. Lippert, S.A., Rang, E.M., Grimm, M.J.: The high frequency properties of brain tissue. Biorheology. **41**, 681–691 (2004)
40. Atay, S.M., Kroenke, C.D., Sabet, A., Bayly, P.V., Atay, S.M., Kroenke, C.D., Sabet, A., Bayly, P.V.: Measurement of the dynamic shear modulus of mouse brain tissue in vivo by magnetic resonance elastography. J. Biomech. Eng. **130**, 021013 (2008)
41. Ertl, M., Raasch, N., Hammel, G., Harter, K., Lang, C.: Transtemporal investigation of brain parenchyma elasticity using 2-D shear wave elastography: definition of age-matched normal values. Ultrasound Med. Biol. **44**, 78–84 (2018)
42. Jiang, Y., Li, G., Qian, L.X., Liang, S., Destrade, M., Cao, Y.: Measuring the linear and nonlinear elastic properties of brain tissue with shear waves and inverse analysis. Biomech. Model. Mechanobiol. **14**, 1119–1128 (2015)

43. Arbogast, K.B., Meaney, D. F., and Thibault, L. E: Biomechanical characterization of the constitutive relationship for the brainstem. Paper presented at Proceedings of the 39th Stapp Car Crash Conference, SAE, Coronado, CA (1995)
44. Darvish, K.K., Crandall, J.R.: Nonlinear viscoelastic effects in oscillatory shear deformation of brain tissue. Med. Eng. Phys. **23**, 633–645 (2001)
45. Fallenstein, G.T., Hulce, V.D., Melvin, J.W.: Dynamic mechanical properties of human brain tissue. J. Biomech. **2**, 217–226 (1969)
46. Tan, K., Cheng, S., Jugé, L., Bilston, L.E.: Characterising soft tissues under large amplitude oscillatory shear and combined loading. J. Biomech. **46**, 1060–1066 (2013)
47. Bilston, L.E., Liu, Z., Phan-Thien, N.: Large strain behaviour of brain tissue in shear: some experimental data and differential constitutive model. Biorheology. **38**, 335–345 (2001)
48. Takhounts, E., Crandall, J.R., Darvish, K.: On the importance of nonlinearity of brain tissue under large deformations. Stapp Car Crash J. **47**, 79–92 (2003)
49. Ferry, J.: Viscoelastic properties of polymers, 641 pp. Wiley, New York (1980)
50. Donnelly, B.R., Medige, J.: Shear properties of human brain tissue. J. Biomech. Eng. **119**, 423–432 (1997)
51. Estes, M.S., McElhaney, J.H.: Response of brain tissue to compressive loading, ASME Paper 70-BHF-13 (1970)
52. Miller, K., Chinzei, K.: Constitutive modelling of brain tissue: experiment and theory. J. Biomech. **30**, 1115–1121 (1997)
53. Cheng, S., Bilston, L.E.: Unconfined compression of white matter. J. Biomech. **40**, 117–124 (2007)
54. Tamura, A., Hayashi, S., Watanabe, I., Nagayama, K., Matsumoto, T.: Mechanical characterization of brain tissue in high-rate compression. J. Biomech. Sci. Eng. **2**, 115–126 (2007)
55. Pervin, F., Chen, W.W.: Dynamic mechanical response of bovine gray matter and white matter brain tissues under compression. J. Biomech. **42**, 731–735 (2009)
56. Rashid, B., Destrade, M., Gilchrist, M.D.: Mechanical characterization of brain tissue in compression at dynamic strain rates. J. Mech. Behav. Biomed. Mater. **10**, 23–38 (2012)
57. Miller, K., Chinzei, K., Orssengo, G., Bednarz, P.: Mechanical properties of brain tissue in-vivo: experiment and computer simulation. J. Biomech. **33**, 1369–1376 (2000)
58. Miller, K.: Modelling soft tissue using biphasic theory — a word of caution. Comput. Methods Biomech. Biomed. Eng. **1**, 261–263 (1998)
59. Chinzei, K., Miller, K.: Compression of swine brain tissue: experiment in vitro. J. Mech. Eng. Lab. **50**, 106–115 (1996)
60. Taylor, Z., Miller, K.: Reassessment of brain elasticity for analysis of biomechanisms of hydrocephalus. J. Biomech. **37**, 1263–1269 (2004)
61. Franceschini, G., Bigoni, D., Regitnig, P., Holzapfel, G.A.: Brain tissue deforms similarly to filled elastomers and follows consolidation theory. J. Mech. Phys. Solids. **54**, 2592–2620 (2006)
62. Kaczmarek, M., Subramaniam, R., Neff, S.: The hydromechanics of hydrocephalus: steady-state solutions for cylindrical geometry. Bull. Math. Biol. **59**, 295–323 (1997)
63. Miller, K., Chinzei, K.: Mechanical properties of brain tissue in tension. J. Biomech. **35**, 483–490 (2002)
64. Velardi, F., Fraternali, F., Angelillo, M.: Anisotropic constitutive equations and experimental tensile behavior of brain tissue. Biomech. Model. Mechanobiol. **5**, 53–61 (2006)
65. Rashid, B., Destrade, M., Gilchrist, M.D.: Mechanical characterization of brain tissue in tension at dynamic strain rates. J. Mech. Behav. Biomed. Mater. **33**, 43–54 (2014)
66. Schiavone, P., Chassat, F., Boudou, T., Promayon, E., Valdivia, F., Payan, Y.: In vivo measurement of human brain elasticity using a light aspiration device. Med. Image Anal. **13**, 673–678 (2009)
67. Budday, S., Sommer, G., Birkl, C., Langkammer, C., Haybaeck, J., Kohnert, J., Bauer, M., Paulsen, F., Steinmann, P., Kuhl, E., Holzapfel, G.A.: Mechanical characterization of human brain tissue. Acta Biomater. **48**, 319–340 (2017)

68. Budday, S., Sommer, G., Holzapfel, G.A., Steinmann, P., Kuhl, E.: Viscoelastic parameter identification of human brain tissue. J. Mech. Behav. Biomed. Mater. **74**, 463–476 (2017)
69. Mooney, M.: A theory of large elastic deformation. J. Appl. Phys. **11**, 582–592 (1940)
70. Rivlin, R.: Large elastic deformations of isotropic materials IV. Further developments of the general theory. Phil. Trans. R. Soc. Lond. A. **241**, 379–397 (1948)
71. Ogden, R.W.: Large deformation isotropic elasticity - on the correlation of theory and experiment for incompressible rubberlike solids. Proc. R. Soc. Lond. A Math. Phys. Sci. **326**, 565–584 (1972)
72. Wittek, A., Hawkins, T., Miller, K.: On the unimportance of constitutive models in computing brain deformation for image-guided surgery. Biomech. Model. Mechanobiol. **8**, 77–84 (2009)
73. Dutta-Roy, T., Wittek, A., Miller, K.: Biomechanical modelling of normal pressure hydrocephalus. J. Biomech. **41**, 2263–2271 (2008)
74. Cheng, S., Bilston, L.E.: Computational model of the cerebral ventricles in hydrocephalus. J. Biomech. Eng. **132**, 054501–054504 (2010)
75. Ruan, J.S., Khalil, T., King, A.I.: Dynamic response of the human head to impact by three-dimensional finite element analysis. J. Biomech. Eng. **116**, 44–50 (1994)
76. Zhang, L., Yang, K.H., King, A.I.: Comparison of brain responses between frontal and lateral impacts by finite element modeling. J. Neurotrauma. **18**, 21–30 (2001)
77. Ho, J., Kleiven, S.: Can sulci protect the brain from traumatic injury? J. Biomech. **42**, 2074–2080 (2009)
78. Kleiven, S.: Influence of impact direction on the human head in prediction of subdural hematoma. J. Neurotrauma. **20**, 365–379 (2003)
79. de Rooij, R., Kuhl, E.: Constitutive modeling of brain tissue: current perspectives. Appl. Mech. Rev. **68**, 010801 (2016)
80. Prange, M.T., Margulies, S.S.: Regional, directional, and age-dependent properties of the brain undergoing large deformation. J. Biomech. Eng. **124**, 244–252 (2002)
81. Coats, B., Margulies, S.S.: Material properties of porcine parietal cortex. J. Biomech. **39**, 2521–2525 (2006)
82. Jin, X., Zhu, F., Mao, H., Shen, M., Yang, K.H.: A comprehensive experimental study on material properties of human brain tissue. J. Biomech. **46**, 2795–2801 (2013)
83. Brands, D.W.A., Peters, G.W.M., Bovendeerd, P.H.M.: Design and numerical implementation of a 3-D non-linear viscoelastic constitutive model for brain tissue during impact. J. Biomech. **37**, 127–134 (2004)
84. Libertiaux, V., Pascon, F., Cescotto, S.: Experimental verification of brain tissue incompressibility using digital image correlation. J. Mech. Behav. Biomed. Mater. **4**, 1177–1185 (2011)
85. Gefen, A., Gefen, N., Zhu, Q., Raghupathi, R., Margulies, S.S.: Age-dependent changes in material properties of the brain and braincase of the rat. J. Neurotrauma. **20**, 1163–1177 (2003)
86. Thibault, K.L., Margulies, S.S.: Age-dependent material properties of the porcine cerebrum: effect on pediatric inertial head injury criteria. J. Biomech. **31**, 1119–1126 (1998)
87. Weaver, J.B., Perrinez, P.R., Bergeron, J.A., Kennedy, F.E., Wang, H., Lollis, S.S., Doyley, M.M., Hoopes, P.J., Paulsen, K.D.: The effects of interstitial tissue pressure on the measured shear modulus in vivo. In: Manduca, A., Hu, X.P. (eds.) Medical imaging: physiology, function, and structure from medical images, Proc. of SPIE, pp. 1A-1–1A-11, SPIE (2007)
88. Metz, H., McElhaney, J., Ommaya, A.K.: A comparison of the elasticity of live, dead, and fixed brain tissue. J. Biomech. **3**, 453–458 (1970)
89. Guertler, C.A., Okamoto, R.J., Schmidt, J.L., Badachhape, A.A., Johnson, C.L., Bayly, P.V.: Mechanical properties of porcine brain tissue in vivo and ex vivo estimated by MR elastography. J. Biomech. **69**, 10–18 (2018)
90. Garo, A., Hrapko, M., van Dommelen, J.A.W., Peters, G.W.M.: Towards a reliable characterisation of the mechanical behaviour of brain tissue: the effects of post-mortem time and sample preparation. Biorheology. **44**, 51–59 (2007)
91. Gefen, A., Margulies, S.S.: Are in vivo and in situ brain tissues mechanically similar? J. Biomech. **37**, 1339–1352 (2004)

92. Hatt, A., Cheng, S., Tan, K., Sinkus, R., Bilston, L.E.: MR elastography can be used to measure brain stiffness changes as a result of altered cranial venous drainage during jugular compression. AJNR Am. J. Neuroradiol. **36**, 1971–1977 (2015)
93. Liu, Z.: Rheological properties of biological soft tissues. University of Sydney, Sydney (2001)
94. Rashid, B., Destrade, M., Gilchrist, M.D.: Influence of preservation temperature on the measured mechanical properties of brain tissue. J. Biomech. **46**, 1276–1281 (2013)
95. Cheng, S., Clarke, E.C., Bilston, L.E.: The effects of preconditioning strain on measured tissue properties. J. Biomech. **42**, 1360–1362 (2009)

Chapter 5
Modelling of the Brain for Injury Simulation and Prevention

King H. Yang and Haojie Mao

5.1 Introduction

5.1.1 The Incidence and Prevalence of Traumatic Brain Injury

According to the Centres for Disease Control and Prevention (CDC), traumatic brain injuries (TBIs) accounted for more than 1.4 million emergency department visits, 275,000 hospitalisations, and 52,000 deaths each year [15] in the USA. Additionally, Langlois et al. [53] at CDC estimated that 1.6 to 3.8 million concussion cases occur in sports and recreational activities annually. They speculated that available injury surveillance data systems might have underestimated the magnitude of TBI cases, because these systems typically did not include those treated in hospital outpatient settings or physicians' offices, those treated in military facilities both in the USA and abroad, and those receiving medical care, but the TBIs were not properly diagnosed. At least 5.3 million Americans, approximately 2% of the US population, are living with long-term or lifelong disability associated with a TBI that resulted in hospitalisation. In European countries, Tagliaferri et al. [91] estimated that the incidence rate for hospitalised and fatal TBI patients was 235 per 100,000 population per year, which is more than double the number (103 per 100,000) reported for the USA.

The most common cause of TBI in the USA is falls (35.2%) with large percentages of these cases happening in children and elderly [15]. For children aged 0 to 14 years and adults aged 65 and older, fall-induced TBIs accounted for 50.2%

K. H. Yang (✉)
Biomedical Engineering, Wayne State University, Detroit, MI, USA
e-mail: aa0007@wayne.edu

H. Mao
Western University, London, ON, Canada

K. Miller (ed.), *Biomechanics of the Brain*, Biological and Medical Physics, Biomedical Engineering, https://doi.org/10.1007/978-3-030-04996-6_5

and 60.7% of all TBI cases, respectively, for these two age groups. Other studies suggested that transportation-associated incidents, construction- and sports-related events, and violent assaults are other leading causes of TBIs [52, 91]. In recent Middle East military conflicts, blast exposure became the leading cause of mild TBI (mTBI) for active duty military personnel in war zones [66].

Summarised from these injury causation studies, TBI is most commonly induced by mechanical forces that instigate a direct impact (e.g. head hitting windshield, falling onto sidewalk, struck by an object, a direct blow to the head in a fist fight) or an indirect impact (e.g. sudden motion of a well-restrained occupant in an abruptly stopped car, exposure to blast waves) to the head. Both direct and indirect impacts could cause immediate damage to the brain (primary injury mechanism) or delayed impairment responses (secondary injury mechanism) due to biochemical and pathophysiological reactions after the primary injury. Despite great progresses have been made in a large number of animal studies, preclinical investigations, and phase I clinical trials, it is unfortunate that nearly all phase II and III clinical trials have failed to provide consistent treatment options for TBI patients [88, 102]. In the USA, phase I clinical studies refer to the assessment of a drug/device safety, phase II studies are related to testing the efficacy of a drug/device, and phase III studies involve randomised and blind testing in a large number of patients.

5.1.2 Investigating the Mechanisms of TBI

As little can be done clinically to reverse the initial brain damage caused by trauma at present, preventing TBI from happening and stabilising a TBI victim to prevent further injury are two key areas of research for the biomechanical community. To this end, a better understanding of the causations and mechanisms of TBI, especially mTBI (e.g. concussion), can provide the scientific basis for designing better protective devices (e.g. sports helmet), improving diagnosis and prognosis tools, and devising new therapeutic methods for protecting the healthy ones and stabilising the injured victims.

To study injury mechanisms or to create TBI in animals for drug testing, impact equipment (such as sleds, pendulum, drop tower, fluid percussion devices, or controlled cortical impact devices) are commonly used to generate sufficient force or acceleration for the development of experimental models. During the test, globally quantifiable variables (e.g. impact force, ambient pressure) and local response variables (e.g. head acceleration, intracranial pressure) at a limited number of locations are measured. Based on these measurements, a number of injury mechanisms and associated thresholds (e.g. head injury criterion (HIC) less than 700, Brain Injury Criteria (BrIC) less than 1) have been hypothesised. As these mechanisms do not always correlate with clinical or pathological observations, considerable controversies still exist regarding the validity of these competing hypotheses.

Recently, sports-related concussions have attracted substantial media coverages and become a prominent public health problem, which Harrison [32] characterised it as a 'concussion crisis'. Several decades before concussion became a 'crisis', some consumer protection and regulatory agencies, such as the Snell Foundation, Consumer Product Safety Commission (CPSC), and National Operating Committee on Standards for Athletic Equipment (NOCSAE), have started prescribing minimal helmet performance criteria or thresholds, despite the fact that the exact head/brain injury mechanism has not been totally understood. These performance criteria are, in general, based on a linear acceleration mechanism that was derived at Wayne State University (WSU) from correlating the presence of skull fracture and peak resultant linear acceleration using a stress-coat technique and lab-made accelerometers [25, 27]. Nearly simultaneously, researchers at Oxford University proposed a rotational acceleration mechanism due to the fact that brain tissues are very compliant in shear [35]. Because most helmets are designed to meet the linear acceleration standards prescribed by Snell, CPSC, and NOCSAE, their main function would be to reduce the linear acceleration. Consequently, the inevitable question is why the helmet is somehow effective in reducing head and brain injury [49] even though most researchers believe that rotation is the main culprit for TBI? Was it really true that wearing a football helmet reduced the risk of TBI by 20% only when 10 most popular helmets used in the USA were tested (the American Academy of Neurology [5])?

To partially address these questions, Zhang et al. [110] conducted a series of mini-sled experiments to simulate American football-relevant impacts using the head and neck complex of a Hybrid III dummy that is instrumented for measuring both linear and angular accelerations. Compared to the non-helmeted head, the authors found that the peak linear acceleration was reduced by an average of 29.5% and 22.1%, respectively, when mounting a VSR4 (Riddell Elyria, OH) and a BIKE (Bike Athletic Company, Atlanta, GA, USA) helmets to the dummy head in all conditions tested. However, reduction in the peak angular acceleration was only 5.6%. Additionally, angular acceleration was positively correlated with that of the linear acceleration in both helmeted and non-helmeted tests. These experimental results were not surprising, because physics dictated that the magnitude of angular acceleration induced by linear impact is proportional to that of the magnitude of linear acceleration and the perpendicular distance of the impact vector to the centre of gravity (CG) of the struck object. For impacts delivered directly to the CG, there wouldn't be any angular acceleration. This is the reason why rotational acceleration was only slightly lower when the impact was aimed near the CG of the helmeted dummy head, despite that linear acceleration was knowingly reduced.

Because global head kinematic data (e.g. linear and angular accelerations) can be measured and measurements collected can provide valuable data to estimate the extent of player exposure, these kinematic data have been used to estimate the risk of sustaining a TBI. As human cannot be instrumented like a crash dummy, concussion observed in NFL football games provided a unique 'human laboratory' for studying mechanisms of concussion and human tolerances [72, 73, 77, 97]. In this series of NFL studies that initially involved 28 players (22 concussed and 6 with no injury),

high-speed game video recordings were first analysed to determine the relative speed, direction, and impact sites on player's heads. Data obtained were then used to reconstruct the collisions with instrumented crash dummies to measure the three linear and three angular accelerations. Finally, the kinematic responses were used to drive a finite element (FE) model of the human brain to predict intracranial distortion patterns. Viano et al. [97] reported that the strongest correlation of concussion was with HIC and severity index (SI) measured directly from the Hybrid III dummy and strain rate in the midbrain and fornix in FE simulations. Although this series of experimental and computational studies represented the best efforts possible at that time, many limitations did exist, for example, the validity and accuracy of the 3D reconstructions from the NFL game videos, the rightfulness of using helmeted Hybrid III dummies to simulate the actual players' head, and the fact that only one FE model was used to represent all involved players. Kleiven [50] later extended the 28 cases reported in the Viano study to include 58 players (25 concussed and 33 uninjured) and one motorcycle accident using the head model developed at his institution. Despite this effort, the same limitations seen in the Viano study continued to exist.

Recently, the kinematic data reconstructed at Biokinetics (e.g. [73]) were found to include some inconsistencies, including the uncertainty of accelerometer sensitivity due to a faulty accelerometer or amplifier (personal communication with Professor Jeff Crandall at University of Virginia). Sanchez et al. [87] corrected these inconsistencies using analytical techniques and found that the median peak angular velocity for the previously reconstructed concussion cases were 16.6% lower than that corrected in their study. The authors suggested that any conclusions drawn previously using the kinematic data reported in the original reconstructions should be re-examined.

To partially correct the indirect method (i.e. through video analyses and dummy tests) used to acquire kinematic data described above, a variety of devices have been invented to quantify the linear and angular accelerations during head impact [101]. In collegiate football, Rowson et al. [82] reported a positive correlation between the magnitude of linear and angular accelerations using specially arranged accelerometer array imbedded in helmets albeit that the correlation was not statistically significant. Their data were in contradiction to the statistically significant positive correlation found in the study by Zhang et al. [110]. The reason for the differences was that the same impact location was imposed throughout all experiments in the Zhang's study, in contrast to the varying locations of impact found in Rowson's real-world study.

Despite these efforts, real-world kinematic data collected from American football players thus far have yet to provide sufficient specificity and sensitivity needed to predict concussion with high degree of confidence [75]. While the low predictability could be partially attributed to gender, age, position of the player, etc., inaccuracies associated with using the helmet-mounted devices [39] could contribute even more errors to the idea of using FE models driven by kinematic data, which are obtained from head-/helmet-mounted sensors, to predict the risk of concussion.

5.1.3 Finite Element Modelling of the Head and Brain

Many researchers agree that injury mechanisms and associated thresholds based on externally measured linear and/or angular acceleration do not address the underlying biomechanical basis for injury. A number of studies have pointed out that brain deformation or strain is a principal cause of injury. Unfortunately, measuring strain, particularly in vivo, is almost impossible during an impact. At present, the best method for predicting intracranial biomechanical responses is through numerical modelling. In particular, the FE method is exclusively suitable to model structures of irregular geometries, multiple material compositions, and complex loading and boundary conditions. The FE method has been the preferred method to study head injury since the last decade. Numerical models developed using the FE method can provide tissue-level responses for correlation with the location and severity of injury outcomes. Considering the fact that globally, kinematic-based injury criteria have yet to bring about a further reduction in the incidence rate of TBI, it is perhaps necessary to seek criteria that are based on brain response, using FE computational models. In this chapter, emphases will be placed on developing and using FE models to better understand the injury mechanism.

A number of human and animal FE brain models have been reported since the 1980s when computers became powerful enough to run these models. The general belief of these studies is that a fully validated human FE head model is needed to identify the injury mechanism, which in turn can be used as a surrogate to design countermeasures to mitigate head injury severity or eliminate head injury altogether. Because traffic-induced TBI accounted for a majority of the TBI cases, many of these numerical models were published in the Stapp Car Crash Conference Proceedings or Journals. Yang et al. [103] conducted a comprehensive review of these models on the occasion of the 50th anniversary of the Conference. It was concluded that even though significant insight into head injury biomechanics was attained through exercising these models, there was a glaring lack of human brain material properties under loading rates relevant to impact-induced TBI. Until now, most experiments conducted to depict brain properties were conducted at quasi-static conditions, while a limited number of studies were tested at high strain rates (over 100 s^{-1}) on nonhuman brain tissues. For example, Prabhu et al. [80] tested porcine brain tissues at a strain rate between 50 and 750 s^{-1}, while Pervin and Chen [78] tested bovine brains at 1000, 2000, and 3000 s^{-1}. High-rate material properties acquired from human brain tissues are rare. For medium-rate testing, Jin et al. [44] reported tensile, compressive, and shear properties obtained from human cadavers at rates of up to 30 s^{-1}.

Additionally, experimental and real-world data needed to properly validate these numerical models were in short supply. To date, the only cadaveric data available consist of three sets of intracranial pressure data reported by Nahum et al. [71], Trosseille et al. [95], and Hardy et al. [30] and a few sets of relative motion data between the brain and skull reported by Hardy et al. [30, 31]. There are also live human data available for various extents of model validations. They consisted of

some 58 cases reconstructed from National Football League games with 22–25 among them being concussion cases [77, 97], a total of 300,977 sub-concussive and 57 concussive head impacts head acceleration data [83], 13 cases of reconstructed motorcycle data [50, 64], and four sets of graded AIS scale head injury data derived from real-world car crashes [16].

With ever-increasing computational power, more and more human head models are being reported. Several institutions have devoted their resources in creating better head models. Mao et al. [62] at *WSU* partially validated their head model against experimental data obtained from 35 different loading cases. The developed and validated model was then used to determine the maximum principal strain (MPS) and other parameters for studying the injury mechanism and tolerance for brain contusion. This model is currently available through the Global Human Body Modelling Consortium (GHBMC). Takhounts et al. [92] at the *National Highway Traffic Safety Administration* (NHTSA) developed a simulated injury monitor (SIMon) head model and associated injury criteria known MPS, cumulative strain damage measure (CSDM), brain injury criteria (BrIC), etc.

Kleiven [50] at the *Royal Institute of Technology* (Kungliga Tekniska Högskolan, KTH) in Sweden found it necessary to introduce different constants needed by the Ogden material law in order to properly reflect the tension-compression asymmetry reported by Franceschini et al. [14] and Miller and Chinzei [67, 68]. The KTH group also reported a head model in which fractional anisotropy (FA) calculated from diffusion tensor imaging (DTI) was averaged to obtain the 'axonal orientation' for each element and to implement element-specific anisotropic properties [21]. Additionally, Giordano and Kleiven [22] evaluated the 'axonal strain' and found that this response variable had a much higher area under the receiver operating characteristic (ROC) curve than other response variables. While these results sounded promising, the inherited deficiencies of using a coarse-mesh FE model (about 7000 elements for the whole brain in this KTH model) to address the directional dependency of white matter are further discussed in Sect. 5.3.1 of this chapter. It is worthy mentioned that Ho and Kleiven [34] developed two fine-mesh FE models with an average element size of 1 mm that was quite different from other coarse-mesh models reported from KTH. The authors recommended that future FE head models should include sulci as it altered the strain distribution in an FE model. Perhaps this fine-mesh model was computationally too expensive, this suggestion was not followed in other papers came from the same group.

Sahoo et al. [85] at the *University of Strasbourg* discussed the use of their relatively coarse-mesh model (about 13,000 elements or 4–10 mm typical element size for the whole head) to study the direction-dependent axonal strain so that the risk of sustaining diffuse axonal injury (DAI) could be predicted. Ji et al. [40] at *Dartmouth College* developed a Dartmouth Head Injury Model (DHIM) from a concussed athlete that included consideration of axonal directions. The same group then used it to pre-compute a number of potential impact scenarios to determine the model-predicted responses rapidly [41]. As a side note, Dr. Ji has since moved to Worcester Polytechnic Institute (WPI) to continue his brain modelling efforts.

Clark et al. [9] at the *University College Dublin* used a combined experimental and numerical approach by inputting the experimentally obtained linear and angular kinematic data to run the University College Dublin Brain Trauma Model (UCDBTM) for assessing the injury risk on ice hockey goaltender. As part of the Total Human Model for Safety (THUMS) continuing advancements at the *Toyota Central R&D Labs*, Atsumi et al. [6] reported a head model consisted of detailed descriptions of the deep brain (e.g. the basal ganglia and fornix) and incorporated strain rate-dependent, anisotropic properties for the brain parenchyma. Additionally, Miller et al. [69] at *Wake Forest University* developed a voxel-based human head model from a brain atlas available at the International Consortium for Brain Mapping (ICBM) and included gyral folds in this model, just like that recommended by Ho and Kleiven [34]. Many of the recently developed head models were quantitatively evaluated in accordance to the CORrelation and Analysis (CORA) method, which combined the evaluation of extent of cross correlation and phase shift and the degree of convergence between the simulation and experimental results [17].

As more head/brain FE models are reported from around the world, it is noticed that many models are repetitive of previous versions with limited incremental advancements [104]. The same limited experimental datasets were treated as 'gold standard' and repetitively used for model validation without ever questioning the size differences among the experimental subjects and the head models developed. As long as site-specific injury-based model validations are not achieved, any new models will continue to provide limited insights into the solution of the head injury problem. The purpose of this chapter is to outline what have learned in the past several decades regarding the development of human and animal brain models and how the knowledge gained in studying head injury biomechanics has helped us approaching the goals of mitigating brain injury.

5.2 Challenges of Investigating TBI Using FE Head Models

Mechanical properties of multiphasic biological tissues, by nature, are nonlinear, viscoelastic, and anisotropic. Additionally, properties of these tissues are likely to be age-, gender-, species-, and site-specific. Until a large-scale experimental study is conducted to clarify the rate-, direction-, gender-, and age-dependent constitutive laws and associated properties, cautions are needed before trusting any models developed thus far which can actually be used to accurately predict the extent and location of TBI. Discussion for the various structures and materials within the brain will not be covered in this chapter as more information are provided in Chaps. 2 and 4. Aside from this big issue related to proper identifications of mechanical properties, many other challenges exist, and these issues are briefly discussed in this section.

5.2.1 *Lack of Sufficient Biomechanical and Injury Data for Model Validations*

One major advantage of using an FE head model lies in its capability of predicting the site-specific head and brain responses. Experimental studies using human cadavers have provided valuable insights into fractures of the cranial [81, 106, 107] and facial bones [2, 74], regional intracranial pressures [30, 71, 95], and how the brain moved within the skull upon closed-head impacts at some target locations [30, 31]. Results from these studies have been widely cited for validating the head models described in the previous section. However, these experiments were not explicitly designed to secure data for model validations. For example, none of these studies acquired detailed head geometries, both external (such as width and breath of the head) and internal (such as the size of ventricles) dimensions, to create subject-specific models.

Also, only a limited number of subjects were tested and results were scattered widely. Even though extraordinary efforts have been invested to perfuse the cadaver head and to resolve issues like intracranial air bubbles, which could greatly affect brain motion, there were still significant inconsistent results seen in tests subjected to the same impact severities. As such, several datasets were discarded in the Hardy experiments. Also, it is difficult to determine whether the variations seen in the remaining datasets were due to experimental errors, subject-specific geometric effects, age differences, or other potential reasons. With all the deficiencies that could potentially occurred in experiments, Giordano and Kleiven [23] developed a weighted averaging method to screen out datasets that might have significant biases. On one hand, this proposed rigorous approach may help in improving the repeatability of experimental data, thus increasing the model correlation scores. On the other hand, removals of any datasets in order to better correlate the computational model predictions with experimental data have hardly ever been the standard procedures. More research is needed on this topic.

For TBI (especially the mild form of TBI or mTBI) cases in which no structural damages were presented soon after the initial impact, cadaveric studies are of limited benefits. To resolve this issue, kinematic data and corresponding injury outcomes collected from live subjects, such as animals and volunteers, are commonly accepted for studying TBI. In animal studies using simple experimental protocol, kinematic data can be easily deduced. In American football games and motor sports in which 'volunteers' are involved, kinematic data can be derived indirectly from high-speed videos or directly from athletes wearing various types of acceleration and velocity sensors. For injury outcomes, behavioural studies are conducted to determine the overall state of brain injury, while histologic methods are used to identify the location and extent of histopathological changes in animals at various post-impact time points. Due to the lengthy processes of conducting histologic evaluations, only a handful regions of interest (ROIs) are investigated in most animal studies. In human, evaluations that are based on combined neuropsychological assessment, structural and functional magnetic resonance imaging (MRI), electroencephalography (EEG),

and newly developed sensors for deep brain functional detection are commonly used. Unfortunately, these investigating modalities for human are not as specific as histologic methods in animal studies. At present, how the brain mechanically responds to impact during trauma and how these mechanical brain responses lead to damage that showed up hours/days/weeks later remain largely unknown. To summarise, the paucity of biomechanical responses and corresponding site-specific injuries hinders the model advancements in two major aspects:

(i) The biofidelity of any existing models cannot be confirmed with high degree of confidence.
(ii) Except some cortical contusion cases (e.g. [13, 79]), correlations between the model-predicted biomechanical responses and diffuse types of injury can only be conducted at the whole brain level (such as concussion or no concussion) instead of region-specific correlations.

5.2.2 Lack of Proven Injury Mechanism

Intracranial strains, which are induced mostly by head rotation, seem to be a plausible injury mechanism for correlations with TBI. By direct stretching of the right optic nerve of an adult male guinea pig, Bain and Meaney [8] were able to determine the strain-based threshold for morphological impairment of axon. Several hypothesised injury mechanisms, such as CSDM, MPS, and BrIC, are derived from the peak magnitudes of intracranial strains calculated from FE models. Nevertheless, other experimental data appeared to suggest that strain is not the sole culprit responsible for TBI. For example, Morrison et al. [70] reported an in vitro model of TBI in which organotypic hippocampal slice cultures adhere to silicone membranes and then stretched in an equi-biaxial manner at different loading rates. Although the authors found positive correlations between cell damages and strains, results also showed that not all brain regions were injured at the same rate and injuries were not evenly distributed within the same region. Understanding that the entire brain slice was subjected to the same mechanical stretches everywhere but the damages were not evenly distributed, one must question what was the cause for those tissues to be uninjured under the same mechanical stimuli? Additionally, these results suggested that different substructure of the brain must possess different injury thresholds. Such region-specific injury thresholds have been largely neglected in literatures.

In recent Middle East conflicts, blast-induced TBI (bTBI) victims returned from military theatres revealed that the primary blast overpressures did not produce large head rotation. As such, intracranial strains were extremely small. In this case, intracranial pressures and its gradients induced by blast waves, rather than the magnitude of strain, are being investigated as the injury mechanism (e.g. [48]). Other studies suggested that other parameters should be considered when determining the risk of bTBI. For example, Zhu et al. [113] considered the effect

of skull thickness, brain radius, and snout length in addition to the peak incident pressure when analysing bTBI using a decision tree data mining method based on a highly simplified FE pig model.

In addition, the rate at which strain increases or decreases was found to be correlated to mTBI observed in NFL games [111]. In this study, the product of the strain rate and strain was found to be a better predictor of injury risk than the strain alone. All aforementioned studies suggested that TBI mechanisms may be more complex than those reported in literatures. As computational head models, especially FE head models, are expected to thoroughly reveal regional brain responses during impact that are correlated with brain injuries, proper injury mechanisms should be identified prior to using such models to design protection equipment.

5.3 Challenges of Developing a Biofidelic FE Head Model

The four key constituents of any FE model are the model geometry, material properties, boundary conditions, and loading conditions. Medical images are typically segmented to acquire various anatomical features within the brain. The segmented data can then be used to develop model geometry, or mesh. Detailed descriptions of brain imaging and segmentation can be found in Chap. 3 and will not be discussed here. In this chapter, emphasis will be placed on selecting the anatomical features of the brain for inclusion in an FE head model, boundary conditions, and loading conditions. Nevertheless, readers are advised of the fact that accurate material properties are key to model the brain accurately.

5.3.1 Selection of Anatomical Features

In terms of selecting the anatomical features, the skin and scalp layers need to be included in an FE head model even though these structures are not needed when simulating a closed-head injury in which skull deformation is of no concern. In these cases, it is a common practice to apply all three components of linear and angular accelerations to the centre of gravity of the head model to determine intracranial tissue responses (e.g. [97, 111]). If simulation time is of concern, these layers can be assigned as rigid materials to reduce the computational cost. On the other hand, a model with skin and scalp representation can be used directly if a real-world direct impact scenario is to be considered. This same approach is also recommended for facial bones.

The bony skull plays a vital role in the protection of the brain from external loading. Mechanically, the rigidity of the skull (in terms of its modulus and thickness) determines the magnitude of the intracranial pressure due to direct impact or inertial loading. The adult human skull is made up of eight bones that are rigidly

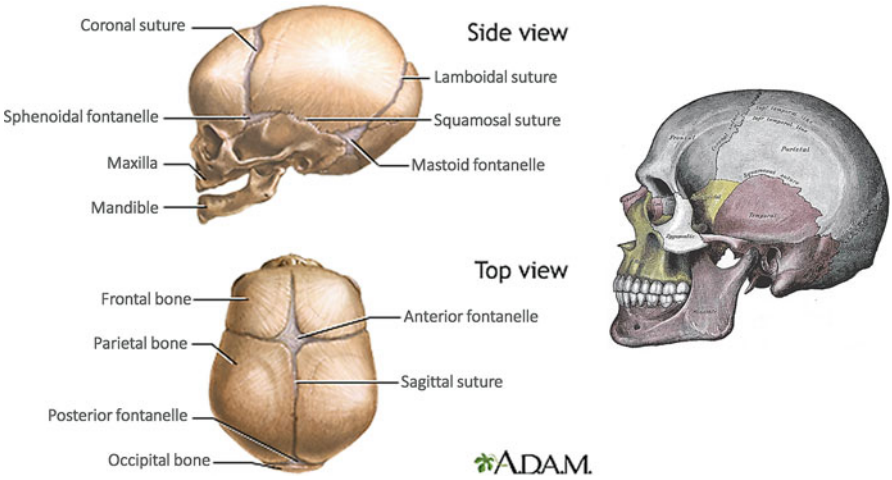

Fig. 5.1 Fontanelles and sutures of the infant skull from http://www.nlm.nih.gov/medlineplus/ency/imagepages/1127.htm (left), while the skull is fully fused for adult (right)

connected by sutures. For this reason, there is no need to model them as separate bones. The skull is made up of three distinct layers, the outer table, diploe, and inner table. It has been reported that the skull thickness can vary from 4 to 9 mm [84]. However, there is no report on the thickness for each individual layer, extent of variation in the thickness for different bones, and age/gender dependency of the thickness. Models such as the GHBMC head model were developed with various cortical and trabecular bone thickness based on clinical images of a single subject. Again, the skull bone may be treated as rigid material if closed-head injury without any skull deformation is the only concern.

Cranial sutures in the adult allow only minimal movement between skull bones. In the infant, the skull bones can move relative to each other as they are separated by gaps called fontanelles (or soft spots) which are covered by a reasonably strong membrane with a smaller elastic modulus compared to skull bones (Fig. 5.1). Continued ossification and closure of the fontanelles occur at different times, while complete closure of the sutures does not occur till the third decade of life [47]. For this reason, the infant skull cannot be modelled as a single bone as in the adult head model. Several FE models of infant heads that represented the fontanelles have been reported (e.g. [51, 56, 57]).

Cranial meninges consist of the dura mater, arachnoid mater, and pia mater. Dural partitions include the falx cerebri, a sagittal partition which divides the brain into the left and right hemispheres, and the tentorium, which separates the cerebellum from the occipital lobes. It has been noted that a model without the falx cerebri and tentorium could not accurately predict brain motion within each compartment [33, 55, 99]. For this reason, the falx and tentorium should be included in any head model. Additionally, Haines et al. [29] reported multilayer structures between the skull and brain (Fig. 5.2). Because there is normally no space for fluid

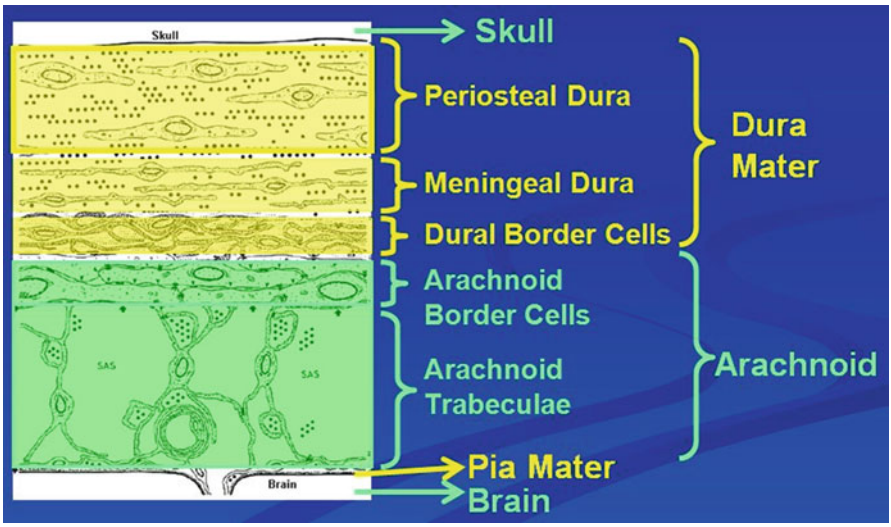

Fig. 5.2 Anatomical layers between the skull and brain reported by Haines et al. [29]

between the arachnoid and dura, the dural and arachnoid border cells and dura mater are considered as a single entity in most models. The arachnoid trabeculae and cerebrospinal fluid (CSF) resemble a biphasic structure with CSF surrounding the solid arachnoid trabeculae. Due in part to the irregular distribution of trabeculae and a lack of computational power, most modellers define the subarachnoid space as a boundary condition between the skull and brain which will be discussed later. Using a 2D FE model, Cloots et al. [10] reported that gyri and sulci had no effect on the mean von Mises stress but had a significant effect on its maximum value. The head model developed by Miller et al. [69] included gyral folds, and the authors claimed that this feature is needed for correlations with chronic traumatic encephalopathy (CTE). Ho and Kleiven [34] demonstrated that the head model with explicit representation of the sulci could predict high strains that better matched with DAI compared to the head model without it.

The cerebral ventricular system consists of four interconnected ventricles: the left and right lateral ventricles, third ventricle, and fourth ventricle. CSF occupies the ventricles and the subarachnoid space surrounding the brain and the spinal cord. Most models reported so far include the lateral ventricles, while a small number of finely meshed models also simulate the third and fourth ventricles. Since the ventricles are filled with CSF, fluid elements are generally used to represent this structure.

The MRI is one of the most powerful imaging modalities for detection, diagnosis, and treatment monitoring of TBIs. Under a strong magnetic force, protons within the water inside the human body would be aligned with the direction of the magnetic field. Upon stimulations through radiofrequency (RF) current, these protons would spin away from that direction. By exciting and detecting the changes in the rotational

axis of protons due to different stimulations, MRI signals offer a three-dimensional (3D), noninvasive, and radiation-free technique for the distinction between the grey and white matter for TBI detections and can also be used for diagnosing brain tumours.

The diffusion tensor imaging (DTI) is a diffusion-weighted MRI technique aimed at providing the measurements of the 3D magnitude, orientation, and extent of anisotropy of water (e.g. [1] and Hulkower et al. [37]). More specifically, a method called the DTI tractography is now a popular method for 3D visualisation of white matter connectivity patterns. When an axon is injured, it is hypothesised that the diffusion along its axis will decrease, while the diffusion perpendicular to the same axis will increase [3]. Because white matter is largely parallel to each other in several brain regions, DTI is considered to be a powerful technique for the detection of DAI, despite that large, longitudinal studies utilising standardised protocols have not been conducted to determine the efficacy of DTI as a tool for TBI patient care [37].

Because white matter represents axons, some researchers have contemplated the use of orthotropic properties to highlight its directional dependency (e.g. [6, 21, 40, 85]) and to better predict the location and severity of DAI. In our opinion, many practical issues need to be resolved before this approach is used. First, neuronal tissue is anatomically divided into grey matter and white matter. Grey matter is made up mostly by cell bodies or neurons, while white matter is made up mostly by myelinated axons. Due to this morphological variation, mechanical properties of grey and white matter are expected to be different. Unfortunately, data reported in literature are not consistent in terms of which brain matter is stiffer than the other (see Chap. 4).

Second, there is a lack of mechanical property data on directional dependency of axons to justify the use of such a computationally expensive representation. Third, the accuracy of DTI tractography for predicting the true patterns of white matter course is still being debated. For example, Thomas et al. [94] reported an inherent limitation in using tractography for 'determining long-range anatomical projections based on voxel-averaged estimates of local fibre orientation'. Similarly, Mandelli et al. [60] found that DTI has poor sensitivity in defining the motor pathways in lateral region.

Fourth, some of the FE models utilised a coarse mesh with typical element size of 5 mm or larger. Fig. 5.3 shows axonal tracts of a whole brain overlaid by a 5 mm FE grid. Because a typical axon has a diameter of 1 micrometre (μm), numerous axonal fibres are needed to form an axonal tract, and numerous axonal tracts are needed to form an 'element' in an FE model. A typical high-resolution DTI tractography has a voxel size of around 3 mm^3. Projecting these voxels to a coarse-mesh model with an element size of 5 mm (125 mm^3 in volume) would need a lot of averaging to define the 'axonal direction' in an element. As such, the computed 'axonal direction' could vary greatly from one element to the other in the same neighborhood. We believe that comprehensive and accurate representation of axonal structures is necessary for ensuring accurate prediction of axonal injuries. However, including the representation of axonal tracts is not recommended in coarse-mesh model. When accurate representation of axonal structures cannot be guaranteed,

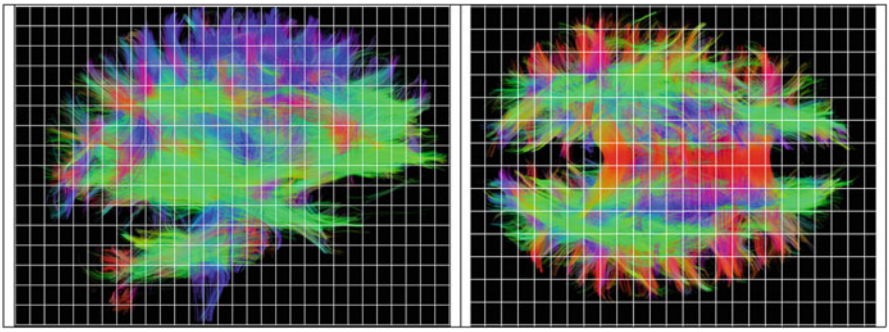

Fig. 5.3 Sagittal and coronal tractographic images of a whole brain overlaid by a grid that represents a typical element size of 5 mm. Tractographic images were derived from MR images with a resolution of 1.3 × 1.3 × 2 mm (courtesy of Drs. Zhifeng Kou and Ramtilak Gattu, Wayne State University)

including such representation would become a confounding factor, not a beneficial one. In addition, because the FE method is based on continuum assumptions, neighboring elements should not have large variations in terms of geometrical discontinuities. The violation of the continuum assumption would be even more overwhelming for FE models using under-integrated scheme on bilinear or trilinear interpolated elements. For these reasons, inclusion of directional properties should be treated with great care unless a very fine mesh is employed and direction-dependent properties are known.

Some models simulate the thalamus and hippocampus explicitly as separate organs mainly because of their important physiological functions. However, material properties used for these structures were based mainly on data taken from animal testing acquired at low speed [11, 96]. We recommend that grey matter structures should include (but not limited to) the cortex, thalamus, and basal ganglia. The white matter in an FE head model should include the corpus callosum, corticospinal tract, and brainstem, including detailed geometry of the midbrain around the tentorium opening.

Parasagittal bridging veins have been included in many FE head models. Numerous articles have reported that acute subdural hematoma (ASDH) is due to rupture of these veins as a result of large relative motion between the brain and skull (e.g. [18]). The reader is cautioned that the number of ASDH of arterial origin equals, if not exceeds, that of ASDH of venous origin [65]. Thus, calculating bridging vein stretch alone cannot fully predict the occurrence of ASDH. In any event, the direction, location, and length of the bridging vein all contribute to its strain, and these data are not readily available. Additionally, readers should be aware that rate sensitivity of the bridging vein is still a controversial issue [54, 58].

Besides the bridging vein, brain arteries and veins both surround and go deep into the brain. The inlets of the brain vasculature network start from the circle of Willis, which connects to the two internal carotid arteries (left and right) and the

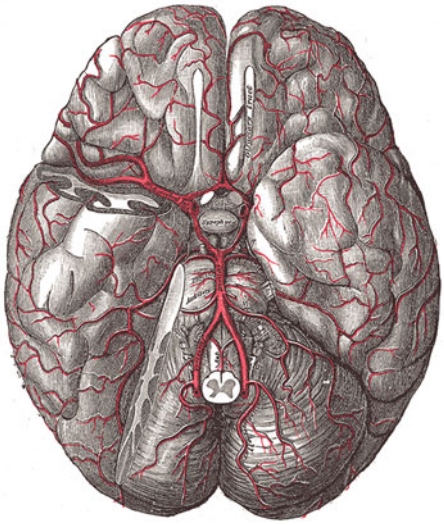

Fig. 5.4 The brain vasculature from the bottom view (Grey H., Wikimedia Commons)

one basilar artery. The outlets are veins that draw blood out of the brain. Hence, the vasculature system introduces two levels of challenges in terms of modelling. First, the vessels have much more complex geometry (Fig. 5.4) than the brain does in terms of developing meshes. Second, the blood inside the vessels is non-Newtonian fluid, which may generate irritable flows during trauma loading. Due to the complexity, simulating the entire 3D, brain vasculature network in a head model remains challenging. So far, most 3D head models do not represent the vasculature. However, these vessels are hundreds of orders stiffer than the brain tissue (more details in Chap. 4) and are expected to act as reinforcement fibres or networks that could induce heterogeneous brain deformations.

These vessels may (or may not) have a profound effect on overall in vivo material properties of the brain in contrast to brain properties measured in vitro where this tethering effect is not considered. Ho and Kleiven [33] developed a 3D head model in which major arteries and veins were represented by 'beam' elements to study the effect of cerebral vasculature on brain response. The authors found minimal discrepancy between the models with and without explicit cerebral vasculature representations. Their result is different from that reported by Zhang et al. [109] using 2D FE models with and without major branches of cerebral arteries. Such differences can be attributed to the number of vessels included in the head model, difference in mechanical properties between the brain parenchyma and cerebral vessels, and method used to represent the blood vessels – 'beam' elements or solid elements. Considering the fact that the diameter of the largest cerebral arteries is no more than 3 mm [89] while other vessels are 0.5 mm and less in diameter, inclusion of cerebral vasculature remains a major challenge for FE head model developers.

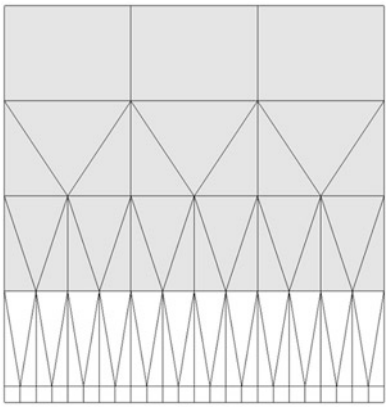

Fig. 5.5 Application of triangular elements to increase the mesh density of 4-node bilinear elements

5.3.2 Issues Related to Quality of Mesh

Before the turn of the century, when computational power was relatively limited, a problem-specific FE model was formulated to solve a specific problem. For example, if an FE model was created to find the displacement of a clamped plate with a concentrated load at its centre, the mesh near the centre was greatly refined, while regions away from the centre were modelled using larger elements. Two problems are associated with this approach. First, transitional elements are needed to gradually refine the mesh size towards the point of loading. In general, transitional elements are of lesser quality than regular elements, and hence the solutions can be less accurate. As an example, triangular elements are commonly used as 2D transitional elements to refine bilinear quadrilateral elements (Fig. 5.5). Since the strain magnitude in a triangular element is constant, a lot of triangular elements are needed to study large strain variations near the loading position and hence not computationally efficient. Second, this type of problem-specific model cannot be used when different loading conditions are applied. Thus, a new model is needed for every new loading condition. As computing power became more widely available, most FE model developers made their models more versatile to handle all kinds of loading conditions, using a fine mesh for the entire model.

An FE model that employs a low-quality mesh cannot yield the best results. This is particularly true for explicit finite element modelling in which the one-point reduced integration scheme is the default integration method. The explicit scheme decreases computational cost while at the same time improves solution accuracy by avoiding mesh locking. Factors that can affect the quality of a mesh include Jacobian, warpage, aspect ratio, skew angle, and internal (edge) angle. Practically, all finite element methods involve the shape functions *[N]*, from which the strain-displacement matrix *[B]* and element stiffness matrix *[k]* are derived [105]. These three matrices form the foundation for determining structural response under load. The standard or 'parent' elements commonly adopted for 2D plane and 3D solid element formulations are the square and the cube, respectively. Obviously, it is

not practical to use only square- or cube-shaped elements to represent a complex structure. Thus, isoparametric formulation, based on natural coordinate systems, is needed to allow for elements with more general shapes. Intuitively, one is led to believe that a mesh with all elements shaped very closely to their corresponding parent elements will yield the best solution, and indeed this is the case.

The Jacobian matrix is a function which maps one Euclidean space to another. The determinant of the Jacobian matrix (often simply called the Jacobian) reports the maximum variation of an element from the idealised element based on the same shape functions. Definition for the aspect ratio, warpage, and skew angle varies slightly depending on the type of elements used [105]. For example, aspect ratio is defined as the length to width ratio in a triangular or quadrilateral element, as the ratio of height to square root of opposing face area in a tetrahedral element, or the ratio of the maximum to minimum distance between opposing faces for a hexahedral element. Warpage tests the extent of deviation out of the plane formed by the other three nodes one of same face of a quadrilateral, wedge, or hexahedral element. The skew angle is generally calculated using an edge bisector method. Although there are no specific guidelines available, our in-house practice is to have an ideal minimum Jacobian of 0.7 with a hard limit of 0.4, all internal angles between 45 and 135 degrees, a maximum aspect ratio of 3, and a maximum skew angle of 30 degrees. Additionally, the mesh quality goal for warpage angle, taper, and element length to thickness ratio shall be less than 20 degrees, 0.5, and 3, respectively, for 2D elements, and the warpage angle and tetra collapse shall be less than 5 degrees and 0.5, respectively, for 3D elements. The same recommendations for the mesh quality check have been proposed at the onset of the GHBMC project and have been adapted as its standard practice since the formation of this group. Figure 5.6 shows some 2D and 3D elements with qualities right at these recommended limits. Readers are also referred to a set of test problems reported by MacNeal and Harder [59] to learn more about large errors induced by ill-shaped elements compared to elements with standard shapes.

As the structure of interest becomes more complex, meshing it with isoparametric 2D quadrilateral elements or 3D brick elements can be quite challenging. On the other hand, the use of 2D triangular elements and 3D tetrahedral elements is an easy task because there are numerous software packages available to automatically generate meshes based on triangular and tetrahedral elements. In general, formulations of triangular and tetrahedral elements are based on degenerations of 4-node plane or 8-node brick elements, respectively. For example, a 4-node

Fig. 5.6 Quadrilateral elements with mesh quality exceed the minimal in-house recommended values of a Jacobian of 0.7 (left); internal angle of 55 degrees, 10 degrees exceeding the recommended 45 degrees (centre); and a warpage of 1.65 (right)

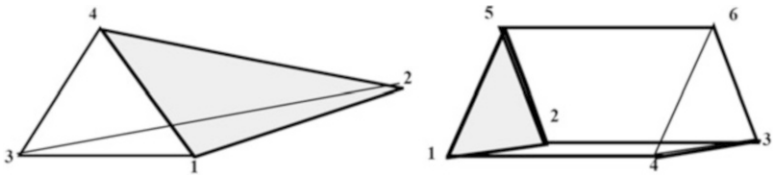

Fig. 5.7 When mixed with 8-node hexahedral elements, 4-node tetrahedral elements and 6-node pentahedral elements in LS-DYNA are treated as degeneration of 8-node hexahedral elements

tetrahedral element (N1-N2-N3-N4), when mixed with other hexahedral elements, is treated as a degenerate 8-node solid element with node number N1-N2-N3-N4-N4-N4-N4-N4 in LS-DYNA code (LS-DYNA user manual). One problem associated with degenerated elements is related to an uneven mass distribution. For example, node 4 of a degenerate tetrahedron has five times the mass of nodes 1, 2, and 3. Similarly, a 6-node pentahedral element is degenerated from 8-node brick with node number N1-N2-N3-N4-N5-N5-N6-N6 (Fig. 5.7). Different software packages employ different degeneration schemes. For example, some may assign node 4 of a triangular element, with nodes 1, 2, and 3, to be located at the same coordinates as node 3, while others may assign node 3 to be located between nodes 2 and 4 on one side of a triangle formed by nodes 1, 2, and 4. These degenerated elements are very different in shape compared to standard elements and have been shown to require a lot of elements to achieve the same accuracy as what a small number of standard elements can do. If the element density does not increase when degenerated elements are used, the solution may not be as accurate. For our in-house FE models, we recommend that less than 10% of all elements be in the form of triangular or tetrahedral elements.

Taking two widely used high-quality human head models, the SIMon and GHBMC, as an example, these two models were mostly constructed with high-quality hexahedral elements. The GHBMC model has a relatively uniform mesh distribution, but the SIMon model shows a mesh density mismatch at the posterior portion of the brain (Fig. 5.8). This mesh density mismatch contributes to the artificially high strains seen at a later time of impact simulation [12]. Other 'artificial' strains from SIMon were due to the use of large-internal-angle elements (Fig. 5.8), which have been recognised as being problematic in the field. Hence, we strongly emphasise that new model developers should be very careful with the 'convenient' way of relying on mesh generation software to automatically grow meshes that may mimic the shape of the brain but could sacrifice the prediction accuracy due to severe mesh density mismatch.

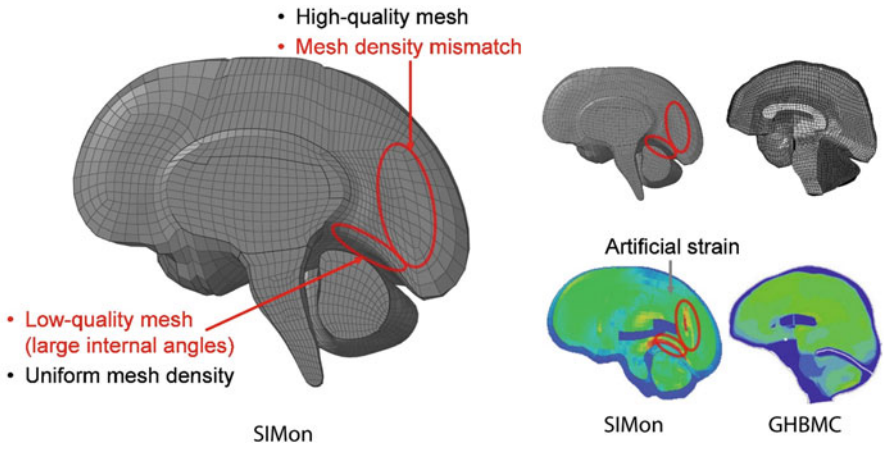

Fig. 5.8 Mesh patterns in the SIMon and GHBMC models. Left: A mesh density mismatch is highlighted in the SIMon model, together with large-internal-angle elements. Right: Artificially high-strain areas seen in the SIMon model are associated with the mesh density mismatch area, as well as poor element quality area [12]

5.3.3 Numerical Convergence and Hourglass Energy

Mesh convergence refers to how small the element size should be in an FE model to ensure that simulation results are unaffected by changing the size of the mesh. The convergence issue is frequently overlooked for three reasons. First, an FE model with high mesh density may not be solvable when computing resources are limited. This issue is no longer a critical one as newer computers are capable of handling a large quantity of random access memory. Second, developing FE models with a different mesh density requires significant effort. Unless each refinement represents a division of one 3D element into eight elements (i.e. dividing each edge of an element into two), substantial work is involved when refining a mesh. While this issue persists to the present, it is less critical now because there are software packages which allow users to parameterise the mesh so that little effort is needed to adjust the mesh density. Still, refinement of the mesh using such automatic meshing software usually has limitations if the parameterised surface is poorly formulated and there is no guarantee that the refined mesh will be of high quality. Third, many research groups have in their databases numerous models available and hence have a tendency to take an old model that was previously published for use in a new loading condition without testing for convergence to ensure that the mesh density is sufficient to solve the new problem.

To check for convergence, strains or stresses in several regions of interest are computed and plotted as a function of mesh density. If simulation results from two FE models with different mesh densities are within a few percentage points of each other, then mesh convergence has been achieved. Otherwise, continued refinement

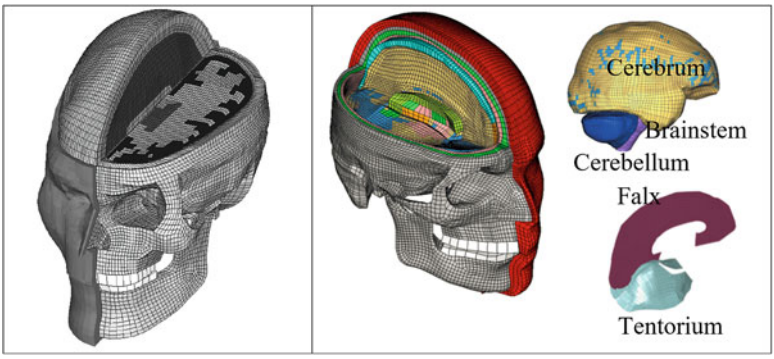

Fig. 5.9 Similar mesh densities were used in the development of the WSU [108] and GHBMC [62] head injury models

of the mesh should be carried out and the FE simulation repeated. Typically, differences in strains or stresses in two consecutive refinements will decrease as the mesh is refined. Eventually, the difference will be sufficiently small so that convergence is deemed achieved. In some cases, such as impact of soft tissue by a very small diameter pendulum, convergence is very difficult to achieve due to the large deformation confined to a small region. In this case, a report must be generated to indicate how far away the mesh is from full convergence. Although some advanced FE solution methods are, in theory, not affected by mesh size, testing for convergence is a recommended practice in our laboratory in the event that the software does not live up to its expectation.

Figure 5.9 shows the Wayne State University head injury model, consisting of more than 314,000 uniformly meshed high-quality elements. The solution was found to be convergent when the model was used to simulate direct and indirect impacts with combined accelerations of up to 200 g and 12,000 rad/s^2. The similar mesh size was utilised when developing the GHBMC head model, which demonstrated a very good numerical stability and desired accuracy and has been widely used by academic, governmental, and industrial users. We recommend mesh sizes 0.5–2 mm based on our experience with a small portion of elements above 2 mm being deemed as acceptable to represent complex brain surfaces and components.

In explicit finite element analysis of soft tissue subjected to dynamic loading, large hourglass energy is frequently needed to prevent the mesh from going into various hourglass modes. This is of great concern. Formation of hourglass modes is primarily due to rank deficiency. Consider a 4-node bilinear 2D element, the element stiffness matrix *[k]* has a size of 8 x 8 but only a rank of 5, which can be calculated by taking away 3 rigid body motions (2 translations and 1 rotation) from the 8 degrees of freedom available for a 2D bilinear element. A 1-point reduced integration scheme would decrease the rank from 5 to 3, which means 2 hourglass modes could occur. Explanations of hourglass modes and the energy needed to

control these modes are tedious, and the reader is referred to relevant papers on the subject, such as Hughes [36] and Yang [105]. Many software packages allow changing the hourglass energy coefficient to adjust the extent hourglass energy. It has been recommended that the hourglass energy should not exceed 10% of the total energy in order to assure accuracy of simulation results [62].

5.3.4 Boundary Conditions

Representing the pia-arachnoid complex (PAC), within which the CSF flows, remains an unresolved issue in brain modelling. Techniques used in the past include a direct connection with no slip, direct coupling at the junction, sliding interface with different coefficients of friction, or tie-break with a preset threshold. A major reason for these selections is probably due to the fact that some researchers were either unaware of or decided to ignore the existence of trabeculae within the subarachnoid space. Also, the complex and random nature of the distribution of trabeculae in the PAC makes it impossible to model them explicitly. While the exact method to model the PAC and the CSF within it has not been agreed upon, it has been noted that representing this layer by a gap cannot be used to generate tension in the contrecoup site, thus making it unsuitable to model the contrecoup phenomenon reported by clinicians. To accurately predict brain-skull relative motion, it's necessary to represent the meninges and the CSF that's between the arachnoid and the pia [98]. A recent study also suggested using fluid elements to represent the CSF [112].

Experimental data reported by Jin et al. [42, 43] on bovine PAC showed that the trabeculae in the CSF layer offer finite shear resistance; thus it would be a mistake to model this layer as an incompressible fluid. A set of constitutive equations has been developed for bovine PAC [45]. Effort should be devoted to determine in-plane, traction, and shear loading responses in human pia-arachnoid samples using methods similar to those reported by Jin et al. [42, 43]. Once a set of constitutive equations is developed to represent the PAC and CSF, this combined structure can be properly modelled. There is no evidence to suggest the need to model the CSF surrounding the spinal cord. Unless there is new information to suggest otherwise, the sliding of the cord relative to the surrounding dura can be represented by a sliding interface.

The large oval opening in the occipital bone of the skull, or foramen magnum, is frequently represented by a membrane in most head models. The material properties selected for this membrane regulate the magnitude of intracranial pressure as a flexible membrane would allow some deformation at the foramen and this increase in brain volume will decrease the pressure within the skull. In other models, a set of boundary conditions were assigned when modelling the foramen magnum. More research is needed to determine the best way to model this anatomic opening.

5.3.5 *Types of Injury to Be Simulated*

Because an FE head model can only be used to calculate the corresponding responses at the instant of impact, secondary head injury (defined as the pathological, physiological, and biochemical changes to the brain tissue after the primary injury) is beyond the capability of current FE head models and will not be discussed in this chapter. A good understanding of the injury mechanism is one of the most important components when studying injury prevention. Without knowing the proper injury mechanism and the associated injury threshold, it is not possible to use an FE head model to predict the type, location, and severity of TBI. As previously discussed in Sect. 5.2 of this chapter, it is unfortunately that proper injury mechanisms have not been appropriately established yet.

The mechanism of open- and closed-head injury is quite different. Because skull and facial bone fractures do not always correlate with brain injury, such fractures are not simulated in most FE head models. Nevertheless, readers should be aware that a fractured skull could affect subsequent intracranial response and a skull fracture is more complicated than a long bone fracture. Gurdjian and Webster [26] in their stress-coating and strain gauge study showed that there was a momentary in-bending at the site of impact and out-bending at the adjacent regions with linear fractures occurring in the out-bended area. Additionally, an instantaneous increase in intracranial pressure upon impact may contribute to the incident rate of skull fracture or to the fracture length. Four types of brain injury (cerebral contusion, DAI, acute subdural hematoma, and subarachnoid hematoma) are discussed in this chapter.

Figures 5.10 shows two MR images of a cerebral contusion case. Cerebral contusion is a bruising of the brain surface where haemorrhagic necrosis and acute brain swelling occur. Contusions usually involve the surface of the brain, especially the crowns of gyri, and are more frequent in the orbital surfaces of the frontal lobes and the tips of the temporal lobes irrespective of the site of impact [27, 76]. Most researchers believe that this focal injury is associated with intracranial pressure generated as a result of high linear acceleration. Positive pressure, typically associated with the so-called coup injury mechanism, is assumed to be the result of the moving skull towards the stationary brain, producing a compressive wave in the brain at the time of impact or direct compression of the brain due to in-bending of the skull. Negative pressure, which has been associated with the so-called contrecoup injury mechanism, is hypothesised to be the result of tension generated by the skull moving away from the brain that is lagging behind the skull. If pressure is the underlining mechanism of this coup-contrecoup phenomenon, FE model-predicted pressure levels can be used to estimate the risk of contusion injury. Alternately, the negative pressure could be due to a tensile wave that was formed by the reflection of the original compression wave off the skull. Cavitation (collapse of a vapor bubble) occurs if negative pressure is lower than the vapor pressure of water. In this case, negative pressures below atmospheric pressure may be a good indicator for contusion injury. This cavitation-induced injury mechanism has not

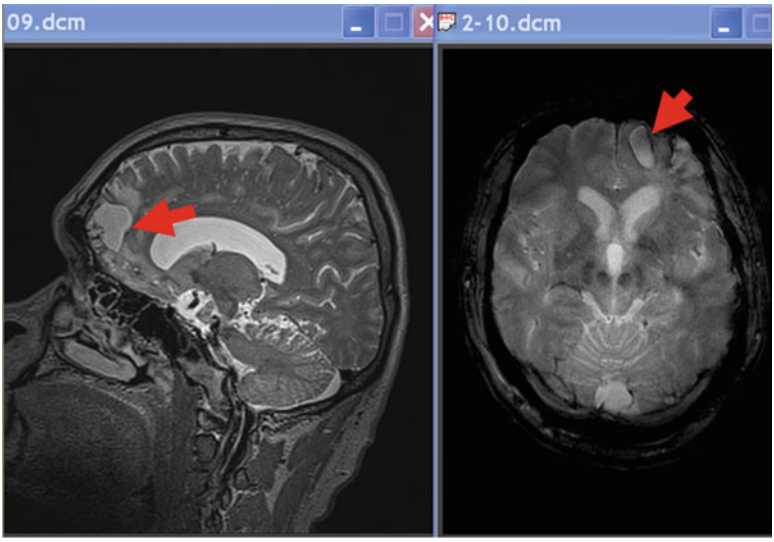

Fig. 5.10 T2 images of a patient suffering focal contusion (left image, sagittal view; right image, axial view). As shown in the above images indicated by arrows, a focal contusion happened on the surface area of the right frontal lobe. In radiology, right side of an image represents left side of the brain and vice versa (courtesy of Professor Zhifeng Kou, Wayne State University)

been proven experimentally, and readers should bear in mind that this may not be the only mechanism. For example, Mao et al. [61] showed in an open-skull animal neurotrauma experimental model that contusions were caused by high tissue strain of around 30%.

Diffuse axonal injury (DAI) is a well-known consequence of blunt head injury and is characterised by immediate onset of coma at the time of injury or cognitive dysfunction. Pathologically, DAI comprises diffuse changes in the white matter tracts, including focal perturbation of axolemma, cytoskeletal misalignment, disruption of axoplasmic transport (manifested as axonal swelling), formation of retraction balls, and axonal disconnection. A typical case of DAI is shown in Fig. 5.11. As most FE head models are too coarse to include explicit representation of these anatomical features, overall model-predicted response at the tissue level is used to correlate with the risk of DAI. Although extremely high angular acceleration was needed, Gennarelli et al. [19, 20] were able to induce DAI in an experimental animal model. Since brain material has a very low shear modulus and a very high in bulk modulus, high shear strains or stresses can be easily generated during rotational loading. Consequently, the magnitude of shear strain or MPS predicted by an FE head model is commonly used to indicate the risk of DAI. The CSDM, proposed by Bandak and Eppinger [7] and Takhounts et al. [93], hypothesised that DAI is associated with the cumulative volume of all brain tissue elements which experienced a strain higher than a prescribed threshold. From a biomechanical point

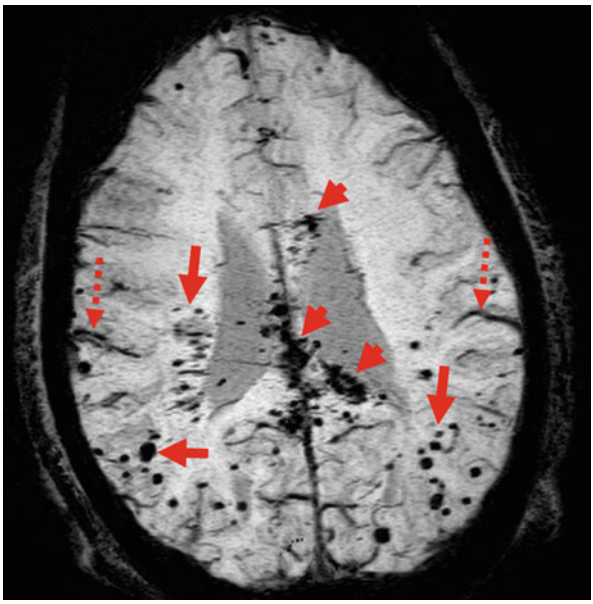

Fig. 5.11 Susceptibility-weighted imaging (SWI) of a severe brain injury case. The patient is a classical DAI case with numerous haemorrhagic lesions at the genu, body, and splenium of corpus callosum (see arrow heads) and grey and white matter junction area (see arrows). The patient also suffers subarachnoid haemorrhage (SAH), which travels into the brain sulcus area on both sides of the brain (see dashed arrows) (courtesy of Professor Zhifeng Kou, Wayne State University)

of view, this measure seems to be very reasonable, but experiments specifically designed to verify this hypothesis are needed to ensure its validity.

Concussion, a mild form of DAI, is becoming a major health concern in recent years as mentioned in Sect. 5.1. Understanding the mechanisms of concussion and proposing effective injury thresholds remain a challenging issue for the researchers in the field of sports-induced injury. A concussed patient usually does not show any contusion or bleeding as shown in Figs. 5.10 and 5.11. Although axonal damage may be revealed as interrupted axons for some concussed patients in tractography (as demonstrated in Fig. 5.3), others might not show any evidences using current imaging modalities. Additionally, neurometabolic cascades, which include abrupt neuronal depolarisation, release of excitatory neurotransmitters, ionic shifts, changes in glucose metabolism, altered cerebral blood flow, and impaired axonal function [24], may not be straightforwardly correlated to mechanical responses within the brain. Nevertheless, these neurobiological effects are triggered, and only triggered, by mechanical events. Hence, understanding biomechanical changes inside concussed subjects is one of many utter important challenges to overcome.

As previously discussed in Sect. 5.1.3 of this chapter, several studies have incorporated axonal directions in their head models. We do not recommend this approach if the mesh density of the brain model is not sufficiently fine, such as 5 mm, as shown in Fig. 5.3. Even with very fine mesh FE models, experimental data will be needed to check the biomechanical validity and predicting accuracy of these models. Nevertheless, any means that will enable researchers of looking into the complex structural networks of the brain would be needed for continuing development of human brain model.

Acute subdural hematoma (ASDH) describes an abnormal blood collection between the dura and arachnoid maters. ASDHs are one of the most frequently seen forms of high severity acute head injuries. There is evidence that ASDH is usually formed within the first several minutes and certainly by the end of the first hour after a severe impact. Many researchers believe that the cause of ASDH is the rupture of parasagittal bridging veins. Hence, relative motions between the brain and skull are a good predictor to estimate the risk of ASDH. While this hypothesis may have clinical correlation in a number of cases, Maxeiner and Wolff [65] showed that there was an equal probability of ASDH caused by bridging vein rupture and by cortical artery rupture. Moreover, Shenkin [90] reviewed 39 consecutive cases of ASDH and found that there was a high incidence rate of cortical artery rupture (61.5%). Additionally, relative motions between the brain and skull measured by Hardy et al. [30] indicated that relative motions in the peripheral region of the cortex were less than those measured in the central region of the brain. For these reasons, we cannot confirm the precise injury mechanisms of ASDH until new experiments are carried out.

Subarachnoid hematoma (SAH) or haemorrhage is the result of ruptured cortico-meningeal vessels or bridging veins upon blunt impact. As the haemorrhage occurs in the CSF space, intracranial pressure is not likely to rise significantly, and this injury type does not present a significant challenge in clinical practice. Additionally, it is computationally too expensive to explicitly model these cortico-meningeal vessels. Hence, this type of brain injury has been mostly ignored by most FE models. Similarly, epidural hematoma (EPH) is seen in less than 5% of TBI cases and has a low mortality rate. Although there is no space between the skull and dura, there is a natural epidural space around the spinal cord for the haemorrhage to move into. Consequently, simulating the risk of EPH is not a great concern to many researchers.

5.3.6 Acquisition of Experimental Data Specifically Conducted for Model Validation

As mentioned in Sect. 5.2, only limited datasets are available to validate FE models. These datasets can be grouped into two categories: laboratory experiments and reconstructed real-world data. Practically, any FE head model that has been validated include the use of intracranial pressure data from the oft-cited Test 37 reported by Nahum et al. [71] probably due to the fact that this was the only time history data presented in the paper. Note that the same publication [71] also included peak data in tabular form, reporting on a number of experiments in which intracranial pressures were measured. For example, there were padded and rigid impacts, using three different impactor masses (2.7, 5.23, 5.59 kg) and six different velocities (4.36, 6.3, 8.69, 8.75, 9.94, 12.95 m/s). Some of the intracranial pressure data did not make sense from a mechanical point of view and were

apparently outliers. Obviously, there were inherent problems associated with these experiments.

Gurdjian et al. (1953) once wrote: 'Due to the error introduced resulting from deformation of the scalp, muscles, skull, and striker itself, it appeared more accurate to measure the acceleration of the skull.' As a result, the most commonly used head injury criteria are all based on acceleration without considering the intracranial responses. Explanations for the unreasonable measurements reported by Nahum et al. [71] may include data acquisition system errors, variations in the cadaveric anthropometry, and the unspecified locations of pressure transducer placements. Similar problems can also be found in newer laboratory-generated experimental data reported by other authors. For example, Hardy et al. [30] reported large standard deviations observed in the motions of the brain with respect to the skull using the same cadaveric head under very similar loading conditions. Lastly, using real-world accident reconstruction data for model validation presents even more problems because the only known variable is the injury outcome.

To correct this deficiency, experiments specifically designed to generate data for model validation are needed. One such dataset has been generated to validate human neck models subjected to rear-end impact [100]. In this series of experiments, high-resolution CT scans were conducted on each cadaver to document the cervical spine geometry and to generate subject-specific neck models, while cervical spine kinematics were obtained by a high-speed biplanar x-ray system for model validation. Obviously, experiments of this kind will be very expensive and require pooling of financial resources from all stakeholders to achieve the goal. In the recent Warrior Injury Assessment Manikin (WIAMan) project [4], every cadaver tested were CT scanned to provide geometric information needed for potential modelling efforts. If FE models are to be used as a tool for mitigating the societal problems associated with TBI, we sincerely hope that government and industrial leaders will step up their efforts by organising systematic studies to identify material properties and to conduct experiments specifically designed for model validations, just like that has been done for the WIAMan project.

5.4 Revamp FE Modelling of Human Head: A Look into the Future

We hypothesise that successful development of human head models for preventing blunt impact-induced TBI depends to a great extent on animal experiments. There are several reasons for this. First, freshly dead human heads (and brains) are very hard to obtain, and studying the TBI mechanism and threshold requires a large number of cadavers because of the inherent variability of cadaveric data. Second, for those cadavers available for impact testing, it is very difficult to prepare them to imitate in vivo conditions. Third, cadaver experiments will not reveal critical brain injury besides contusion or tearing. Animal studies, on the other hand, enable the

measurement of biomechanical parameters, investigation of behavioural changes, and evaluation of histological changes to identify the type and severity of brain injury due to impact. More importantly, laboratory-raised animals are genetically the same and can be well controlled for testing, once the experimental protocol passes the stringent protocol review process.

Although experiments involving 'volunteers' (such as a collegiate football player) provide valuable data for predicting the risk of brain injury, methods of observing injuries within a live human brain are limited. To this extent, conducting animal brain injury experiments and creating models based on these experiments become critical. For studies on animal brains, we can compare brain regions with high MPS, as predicted by a computational animal head model, to brain regions with damage, as examined thoroughly using various histological methods. If the model predictions and histology observations match, then we can conclude that the MPS is a valid injury predictor, and if they do not match, new injury predictors, such as pressure, strain rate, or others, could be evaluated. For example, a high-definition 3D rat head model with a detailed hippocampus, including the CA1, CA2, CA3, and dentate gyrus (DG), has been used to demonstrate that high MPS is correlated to region-specific hippocampal cell death [63] when subjected to equi-biaxial strain fields. Similarly, Fig. 5.12 shows a simulated 3D rat brain responses under controlled cortical impact. It can be seen that high-strain areas were concentrated not only under the impactor but also away from the impactor near the occipital bone when there were additional craniotomies performed (indicated as red-shaded circles in Fig. 5.12) on the occipital bone. In this simple, straightforward experimental model, the injury mechanism and associated injury threshold can be developed with higher confidence than that from a concussed football player. Studies of this type will help in developing more accurate region-specific injury assessment functions that will help to better predict human head injury through human head models. Even though animals are not human, if one cannot model the animal brain with high degree of confidence, he/she is certainly not able to model the human brain where experimental data are very hard to secure.

It has been nearly 20 years since animals larger than rodents were used to determine TBI mechanisms and thresholds due to blunt impact. While valuable data were gathered from animals in the old days, biomechanical parameters measured were limited to mostly external impact parameters (such as the pendulum mass and speed) and global responses (such as linear and angular accelerations). Unfortunately, computer modelling technologies were not sophisticated enough to model these experiments at that time, and hence anthropometry and other data needed for validation of numerical models were not obtained. Nevertheless, full utilisation of these data should be attempted so that no additional animals need to be sacrificed unless it is absolutely necessary. It is our understanding that the US Department of Transportation (DOT) is organising an effort to revive some primate data from its archives across the globe. Successful retrieval of these primate data in conjunction with numerical modelling of these animal impacts will promote a better understanding of the relationship between injury outcome and model-predicted intracranial responses.

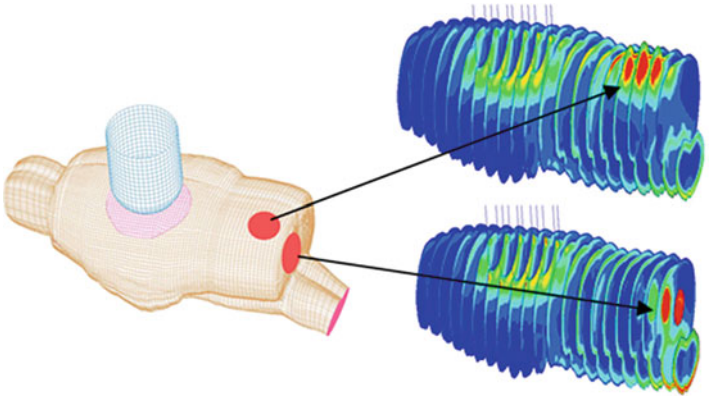

Fig. 5.12 3D contours of the maximum principal strain in a simulated controlled cortical impact of a rat brain

As previously described, earlier experiments were not conducted for the purpose of obtaining data for model validation. Thus, it is fully expected that new animal experimental data are necessary. The following list outlines some key information needed if financial resources are put in place for doing such experiments:

1. Clear identification of animal head anthropometry and experimental conditions. For example, stiffness of the foam used to soften a blow in pendulum testing or used as a cushion in weight drop Marmarou type of testing should be measured.
2. Sufficient biomechanical parameters should be measured during impact and used for model validation. When possible, intracranial tissue kinematics should be measured using biplanar x-ray techniques such as those reported by Hardy et al. [31]. Efforts should be devoted to accurate modelling of the pia-arachnoid junction because the complex anatomy at this region greatly affects the model-predicted responses.
3. Thorough histological investigations of TBI are needed. Because the counting of brain lesions under the microscope can be an extremely labour-intensive process, even with the aid of a computer, researchers typically only study a handful of sections at a couple of selected regions of interest. Studies have shown that brain injury can occur in regions remote from the impact site (e.g. [38]), but these data are not routinely acquired and reported upon. An entire 3D injury map is needed for correlation with FE model-predicted tissue-level responses.
4. Careful correlation between injury outcome and FE model-predicted biomechanical responses is needed to identify region-specific injury thresholds. Intuitively, one can imagine that a 10% stretch in grey matter may not be injurious, while the same magnitude of stretch in white matter may be devastating. Hence, it is fully expected that injury threshold should be different for different regions of the brain.
5. A suitable scaling methodology should be developed so that injury threshold derived from animals can be scaled to protect the human. A minimum of two

animal experimental models (a small and a large one) need to be conducted to develop a scaling method based on parameters such as age, gender, size, material properties, etc. Preferably, a third animal model should be tested to validate the accuracy of the scaling law and to develop a scaling method to estimate the tissue level injury threshold in humans. Note that this method does not account for species differences in tolerance and may not provide a direct correlation between size and tolerance.

Once these animal experiments are completed, there are still numerous hurdles to overcome in developing fully validated animal brain models. For example, while material properties available on animal brain tissues are more abundant compared to human tissues, more studies are still needed to develop proper constitutive laws and more accurate material properties at strain rates relevant to the impact condition. Even in a systematic series of investigations, the data are expected to have a fairly large standard deviation due to biological variations. Presently, FE brain models are based on a deterministic approach by inserting a set of material properties into the model which is then subjected to a set of loading conditions to calculate intracranial responses. Because variations exist in material properties and loading conditions, a probabilistic approach should be applied to determine the spectrum of response variables. In other words, there will be a range of model-predicted intracranial responses reflecting the dissimilarities among the population and the relative risk of injury.

It can be expected that accurate FE human head models can only be developed with success after completing the modelling of animal brains through which one can identify material laws and associated constants, define with accuracy the loading conditions, and ascertain regional tissue level injury thresholds through 3D injury mapping. The human head models developed based on this principle can then be used as the surrogate to design better countermeasures to prevent or mitigate brain injury. As the human brain is better protected against blunt impact, the incident rate of TBI should decrease. Nevertheless, complete elimination of TBI may not be immediately achievable. Thus, newer and higher-quality real-world data need to be gathered continuously to improve the simulation models so that their capability in accurately predicting the risk of brain injury under a variety of blunt impact conditions is augmented.

To improve the prediction power of a model, we will need to represent more comprehensive anatomical details of the human head. For example, the complex space between the skull and brain, which includes dura, arachnoid, cerebrospinal fluid, pia, as well as various border cells between these meninges, is demonstrated to have a nonlinear, viscoelastic property under tension and shear loading modes [42, 43, 46]. However, limited by existing computational power and preferred by users for improving model stability, several of the most advanced human head models have been developed by adopting a contact algorithm to connect the skull to the brain. Even though such simplification might not affect the prediction of deep brain responses, it limits the models' ability to predict injuries specifically in the brain-skull interface, such as vessel-damage-induced subdural hematoma. Besides

the skull-brain interface, the complex 3D human brain vasculature, which includes arteries, arterioles, capillaries, venules, and veins, has not been fully represented in a human head model. In addition, there are efforts being made to represent axonal fibres inside the brain. However, the application and validity in predicting axon-related brain damage need to be further investigated, and better representation of axonal fibres inside the brain is needed. As such, future improvements to human head models will likely take the form of continued additions of more details. However, with these added details, and the same requirements of computational stability, efficiency, and comprehensive validation, the costs of developing a future head model with these improvements could be huge. Hence, collaboration among researchers to develop and share a high-quality head model is much preferred for generating high-quality brain-biomechanics data for the entire research community.

With the computational human head model being available to predict head responses, the following need is about injury assessment functions that can be used to interpret model predictions and predict risks of real-world head injury. With the understanding that cadaver heads do not have biological consequences and do not represent most brain injuries, studies from live human beings are needed. One valid method is to use a computational human head model to reconstruct impacts of live human subjects and then test and evaluate several injury assessment functions to investigate whether these functions can be used to predict risks that the human subjects experience after trauma. While many studies have demonstrated that strain-based injury assessment functions can predict brain injury, one recent work demonstrated that the maximum principal strain-based injury evaluation functions predicted about 80 concussions and 14 cases of diffuse axonal injury out of 335 noninjury cases [86]. Such results highlight the great needs for improving the specificity of any injury prediction functions in the future.

The human brain is a biological organ that reacts to impacts at various levels (macro, micro, cellular, and molecular levels). A traditional human head model can provide stresses and strains of neural tissues, but it lacks in detail in terms of how neural structures respond. Hence, finer scale models to predict neural responses, such as Ranvier node strains during axonal stretch [114], would be beneficial. In addition to the various levels, the human brain is a biological organ that has bioelectrical and biochemical activations due to impact. The mechanisms of these activations can be better studied with a multi-physics model that couples strains/stresses to bioelectrical and biochemical equations. In addition, the brain is filled with fluids, such as blood flow in the vessels, CSF in the ventricles, and fluids in the extracellular spaces. The fluids' movements due to trauma and disease, plus movement-induced shearing loads to nearby vascular and neuronal cells, may cause damage. Overall, multi-scale, multi-physics computational head models, with the FE method being an integral part, will be largely needed in the future. Collaborations across disciplines will be more important in the future for brain injury-related studies.

5.5 Conclusions

A large number of FE human and animal brain models for blunt impact simulations have been published. We do not know what motivated the development of so many brain injury models but one of the reasons must be related to the desire of model developers to show that their model is better than existing ones. This reason alone should not be the primary basis for more model development. To varying extents, these models have been validated against a very limited number experimental datasets in which insufficient details were available to accurately define the model geometry, loading conditions, and impact responses. For this reason, continued development of new human brain models is not likely to improve the quality of these models or provide additional insights. However, the possibility of having another 'run-of-the-mill' human brain model published in the literature is highly likely because the resources needed to develop a computer model is nothing more than a high-end computer and a commercially available software package. The 'convenient' way of automatically generating meshes in a brain shape probably added more incentives of developing a new head model. It is sad to see that some journal reviewers are not requiring all models to demonstrate proper convergence, validation, and accuracy. More importantly, we will continue to see FE model-derived injury thresholds without the acknowledgement that these thresholds are *model dependent* and not necessarily universally valid or even reliable. On the other hand, sharing of high-quality human head models is becoming popular in recent years through GHBMC, THUMS, and NHTSA at near-zero costs for academic research institutions. At WSU, we provide a 10-year-old and a 70-year-old female whole-body human models free of charge for academic research institutions to investigate injury-related issues (https://automotivesafety.wayne.edu/). The recent European PIPER project aimed at developing and providing open-source tools to position and personalise existing adult human body models, as well as a new open-source human body model of a child scalable to represent ages between 1.5 and 10 years old (http://piper-project.org), may also speed up model development. As the user base increases, it is hoped that continued improvements of these models can be made.

To stream the model development effort into the focus of high-quality, accurate models, we need high-quality experimental data, especially animal experiments, designed to acquire biomechanical and injury data for model validation. With a majority of government (such as NIH) funding being directed towards translational research and treatment, very little resources are still available to prevent TBI from happening even though prevention is the best treatment for TBI. Automotive and sports equipment manufacturers have a keen interest in preventing TBI. However, these companies are not willing to support animal research because bad press can hurt their business. Until this culture is changed, one may continue to see more TBI victims in the years to come. It is hoped that this chapter can change some minds to redirect more effort and funding to developing better FE human head models to reduce the number of future TBI victims. Meanwhile, modellers in the field are

strongly encouraged to develop, share, and use high-quality models while generating fundamental knowledges, such as more accurate material properties, kinematic data for model validations, and 3D injury maps towards better understanding the mechanisms of TBI. A low-mesh-quality FE head model could easily jeopardise the effort in collecting accurate head kinematics and brain damage data and would provide misleading interpretations based on the wrongful brain stresses and strains.

Acknowledgement Dr. Haojie Mao acknowledges the financial support provided by the Canada Research Chairs program.

References

1. Alexander, A.L., Lee, J.E., Lazar, M., Field, A.S.: Diffusion tensor imaging of the brain. Neurotherapeutics. **4**(3), 316–329 (2007)
2. Allsop, D.L., Warner, C.Y., Wille, M.G., Scheider, D.C., Nahum, A.M.: Year Facial impact response – A comparison of the Hybrid III dummy and human cadaver. In: Proc. 32nd Stapp Car Crash Conference, SAE Paper No. 881719 (1988)
3. Arfanakis, K., Haughton, V.M., Carew, J.D., Rogers, B.P., Dempsey, R.J., Meyerand, M.E.: Diffusion tensor MR imaging in diffuse axonal injury. AJNR Am. J. Neuroradiol. **23**(5), 794–802 (2002)
4. Army Research Laboratory, https://www.arl.army.mil/www/default.cfm?article=2965 2018
5. American Academy of Neurology, https://www.aan.com/PressRoom/Home/PressRelease/1241 (2014)
6. Atsumi, N., Nakahira, Y., Tanaka, E., Iwamoto, M.: Human brain modeling with its anatomical structure and realistic material properties for brain injury prediction. Ann. Biomed. Eng. **46**, 736–748 (2018)
7. Bandak, F.A., Eppinger, R.H.: A three-dimensional fi nite element analysis of the human brain under combined rotational and translational accelerations. Proceedings of the 38th Stapp Car Crash Conference, Ft. Lauderdale, FL. SAE, Warrendale (1994)
8. Bain, A.C., Meaney, D.F.: Tissue-level thresholds for axonal damage in an experimental model of central nervous system white matter injury. J. Biomech. Eng. **122**, 615–622 (2000)
9. Clark, J.M., Hoshizaki, B., Gilchrist, M.D.: Protective capacity of an ice hockey goaltender helmet for three events associated with concussion. Comput. Methods Biomech. Biomed. Engin. **20**(12), 1299–1311 (2017)
10. Cloots, R.J., Gervaise, H.M., van Dommelen, J.A., Geers, M.G.: Biomechanics of traumatic brain injury: influences of the morphologic heterogeneities of the cerebral cortex. Ann. Biomed. Eng. **36**(7), 1203–1215 (2008)
11. Elkin, B.S., Azeloglu, E.U., Costa, K.D., Morrison 3rd, B.: Mechanical heterogeneity of the rat hippocampus measured by atomic force microscope indentation. J. Neurotrauma. **24**(5), 812–822 (2007)
12. Elkin, B.S., Gabler, L.F., Panzer, M.B., Siegmund, G.P.: Brain tissue strains vary with head impact location: a possible explanation for increased concussion risk in struck versus striking football players. Clin. Biomech. (2018)
13. Fahlstedt, M., Halldin, P., Kleiven, S.: The protective effect of a helmet in three bicycle accidents – a finite element study. Accid. Anal. Prev. **91**, 133–143 (2016)
14. Franceschini, G., Bigoni, D., Regitnig, P., Holzapfel, G.A.: Brain tissue deforms similarly to filled elastomers and follows consolidation theory. J. Mech. Phys. Solids. **54**(12), 2592–2620 (2006)

15. Faul, M., Xu, L., Wald, M.M., Coronado, V.G.: Traumatic brain injury in the United States: Emergency department visits, hospitalizations and deaths 2002–2006. https://www.cdc.gov/traumaticbraininjury/ (2010)
16. Franklyn, M., Fildes, B., Zhang, L., Yang, K., Sparke, L.: Analysis of finite element models for head injury investigation: reconstruction of four real-world impacts. 49th Stapp Car Crash Conference. Washington, DC, STAPP (2005)
17. Gehre, C., Gades, H., Wernicke, P.: Objective rating of signals using test and simulation responses. Paper presented at: 21st ESV Conference, June 15–18, 2009, Stuttgart (2009)
18. Gennarelli, T.A., Thibault, L.E.: Biomechanics of acute subdural hematoma. J. Trauma. **22**(8), 680–686 (1982)
19. Gennarelli, T.A., Adams, J.H., Graham, D.I.: Acceleration induced head injury in the monkey. I. The model, its mechanical and physiological correlates. Acta Neuropathol. Suppl. **7**, 23–25 (1981)
20. Gennarelli, T.A., Thibault, L.E., Adams, J.H., Graham, D.I., Thompson, C.J., Marcincin, R.P.: Diffuse axonal injury and traumatic coma in the primate. Ann. Neurol. **12**(6), 564–574 (1982)
21. Giordano, C., Cloots, R.J.H., van Dommelen, J.A.W., Kleiven, S.: The influence of anisotropy on brain injury prediction. J. Biomech. **47**, 1052–1059 (2014)
22. Giordano, C., Kleiven, S.: Evaluation of axonal strain as a predictor for mild traumatic brain injuries using finite element modeling. Stapp Car Crash J. **58**, 14S–16S (2014)
23. Giordano, C., Kleiven, S.: Development of an unbiased validation protocol to assess the biofidelity of finite element head models used in prediction of traumatic brain injury. Stapp Car Crash J. **60**, 363–471 (2016)
24. Giza, C.C., Hovda, D.A.: The neurometabolic cascade of concussion. J. Athl. Train. **36**(3), 228–235 (2001)
25. Gurdjian, E.S., Lissner, H.R.: Deformations of the skull in head injury studied by the stresscoat technique, quantitative determinations. Surg. Gynecol. Obstet. **83**, 219–233 (1946)
26. Gurdjian, E.S., Webster, J.E.: Head Injuries, pp. 62–76. Little Brown, Boston (1958)
27. Gurdjian, E.S., Lissner, H.R., Hodgson, V.R., Patrick, L.M.: Mechanism of head injury. Clin. Neurosurg. **12**, 112–128 (1964)
28. Gurdjian, E.S., Lissner, H.R., Latimer, F.R., Haddad, B.F., Webster, J.E.: Quantitative determination of acceleration and intracranial pressure in experimental head injury; preliminary report. Neurology. **3**(6), 417–423 (1953)
29. Haines, D.E., Harkey, H.L., Al-Mefty, O.: The "subdural" space: a new look at an outdated concept. Neurosurgery. **32**(1), 111–120 (1993)
30. Hardy, W.N., Foster, C.D., Mason, M.J., Yang, K.H., King, A.I., Tashman, S.: Investigation of head injury mechanisms using neutral density technology and high-speed biplanar X-ray. Stapp Car Crash J. **45**, 337–368 (2001)
31. Hardy, W.N., Mason, M.J., Foster, C.D., Shah, C.S., Kopacz, J.M., Yang, K.H., King, A.I., Bishop, J., Bey, M., Anderst, W., Tashman, S.: A study of the response of the human cadaver head to impact. Stapp Car Crash J. **51**, 17–80 (2007)
32. Harrison, E.A.: The first concussion crisis: head injury and evidence in early American football. Am. J. Public Health. **104**(5), 822–833 (2014)
33. Ho, J., Kleiven, S.: Dynamic response of the brain with vasculature: a three-dimensional computational study. J. Biomech. **40**(13), 3006–3012 (2007)
34. Ho, J., Kleiven, S.: Can sulci protect the brain from traumatic injury? J. Biomech. **42**, 2074–2080 (2009)
35. Holbourn, A.H.S.: Mechanics of head injury. Lancet. **2**, 438–441 (1943)
36. Hughes, T.J.R.: The Finite Element Method – Linear Static and Dynamic Finite Element Analysis, Chapter 4. Prentice-Hall, Englewood Cliffs (1987). ISBN 0-13-317025-X
37. Hulkower, M.B., Poliak, D.B., Rosenbaum, S.B., Zimmerman, M.E., Lipton, M.L.: A decade of DTI in traumatic brain injury: 10 years and 100 articles later. AJNR Am. J. Neuroradiol. **34**(11), 2064–2074 (2013)
38. Igarashi, T., Potts, M.B., Noble-Haeusslein, L.J.: Injury severity determines Purkinje cell loss and microglial activation in the cerebellum after cortical contusion injury. Exp. Neurol. **203**(1), 258–268 (2007)

39. Jadischke, R., Viano, D.C., Dau, N., King, A.I., McCarthy, J.: On the accuracy of the Head Impact Telemetry (HIT) system used in football helmets. J. Biomech. **46**(13), 2310–2315 (2013)
40. Ji, S., Zhao, W., Li, Z., McAllister, T.W.: Head impact accelerations for brain strain-related responses in contact sports: a model-based investigation. Biomech. Model. Mechanobiol. **13**(5), 1121–1136 (2014)
41. Ji, S., Zhao, W.: A pre-computed brain response atlas for instantaneous strain estimation in contact sports. Ann. Biomed. Eng. **43**, 1877–1895 (2015)
42. Jin, X., Lee, J.B., Leung, L.Y., Zhang, L., Yang, K.H., King, A.I.: Biomechanical response of the bovine pia-arachnoid complex to tensile loading at varying strain-rates. Stapp Car Crash J. **50**, 637–649 (2006)
43. Jin, X., Ma, C., Zhang, L., Yang, K.H., King, A.I., Dong, G., Zhang, J.: Biomechanical response of the bovine pia-arachnoid complex to normal traction loading at varying strain rates. Stapp Car Crash J. **51**, 115–126 (2007)
44. Jin, X., Zhu, F., Mao, H., Shen, M., Yang, K.H.: A comprehensive experimental study on material properties of human brain tissue. J. Biomech. **46**, 2795–2801 (2013)
45. Jin, X.: Biomechanical response and constitutive modeling of bovine pia-arachnoid complex. Ph.D. thesis, Wayne State University (2009)
46. Jin, X., Yang, K.H., King, A.I.: Mechanical properties of bovine pia-arachnoid complex in shear. J. Biomech. **44**(3), 467–474 (2011)
47. Kabbani, H., Raghuveer, T.S.: Craniosynostosis. Am. Fam. Physician. **69**(12), 2863–2870 (2004)
48. Kalra, A., Feng, K., Saif, T., Jin, X., Kallakuri, S., Yang, K.H., King, A.I.: Development and validation of a numerical model of the swine head subjecteto open field blasts. Shock Waves. **27**(6), 947–964 (2017)
49. King, A.I., Yang, K.H., Zhang, L., Hardy, W.N.: Is head injury caused by linear or angular acceleration? IRCOBI. Lisbon, Portugal 2003
50. Kleiven, S.: Predictors for traumatic brain injuries evaluated through accident reconstructions. Stapp Car Crash J. **51**, 81–114 (2007)
51. Klinich, K.D., Hulbert, G.M., Schneider, L.W.: Estimating infant head injury criteria and impact response using crash reconstruction and finite element modeling. Stapp Car Crash J. **46**, 165–194 (2002)
52. Kushner, D.: Mild traumatic brain injury: toward understanding manifestations and treatment. Arch. Intern. Med. **158**(15), 1617–1624 (1998)
53. Langlois, J.A., Rutland-Brown, W., Wald, M.M.: The epidemiology and impact of traumatic brain injury: a brief overview. J. Head Trauma Rehabil. **21**, 375–378 (2006)
54. Lee, M.C., Haut, R.C.: Insensitivity of tensile failure properties of human bridging veins to strain rate: implications in biomechanics of subdural hematoma. J. Biomech. **22**(6–7), 537–542 (1989)
55. Li, J., Zhang, J., Yoganandan, N., Pintar, F., Gennarelli, T.: Regional brain strains and role of falx in lateral impact induced head rotational acceleration. Biomed. Sci. Instrum. **43**, 24–29 (2007)
56. Li, Z., Hu, J., Reed, M.P., Rupp, J.D., Hoff, C.N., Zhang, J., Cheng, B.: Erratum to:development, validation, and application of a parametric pediatric head finite element model for impact simulations. Ann. Biomed. Eng. **41**, 215–220 (2013)
57. Li, X., Sandler, H., Kleiven, S.: The importance of nonlinear tissue modelling in finite element simulations of infant head impacts. Biomech. Model. Mechanobiol. **16**, 823–840 (2017)
58. Löwenhielm, P.: Dynamic properties of the parasagittal bridging veins. Z. Rechtsmed. **74**, 55–62 (1974)
59. MacNeal, R.H., Harder, R.L.: A proposed standard set of problems to test finite element accuracy. Finite Elem. Anal. Des. **1**, 3–20 (1985)
60. Mandelli, M.L., Berger, M.S., Bucci, M., Berman, J.I., Amirbekian, B., Henry, R.G.: Quantifying accuracy and precision of diffusion MR tractography of the corticospinal tract in brain tumors. J. Neurosurg. **121**(2), 349–358 (2014)

61. Mao, H., Zhang, L., Yang, K.H., King, A.I.: Application of a finite element model of the brain to study traumatic brain injury mechanisms in the rat. Stapp Car Crash J. **50**, 583–600 (2006)
62. Mao, H., Zhang, L., Jiang, B., Genthikatti, V.V., Jin, X., Zhu, F., Makwana, R., Gill, A., Jandir, G., Singh, A., Yang, K.H.: Development of a finite element human head model partially validated with thirty five experimental cases. J. Biomech. Engg. **135**(11), 111002 (2013)
63. Mao, H., Elkin, B.S., Genthikatti, V.V., Morrison 3rd, B., Yang, K.H.: Why is CA3 more vulnerable than CA1 in experimental models of controlled cortical impact-induced brain injury? J. Neurotrauma. **30**(17), 1521–1530 (2013b)
64. Marjoux, D., Baumgartner, D., Deck, C., Willinger, R.: Head injury prediction capability of the HIC, HIP, SIMon and ULP criteria. Accid. Anal. Prev. **40**(3), 1135–1148 (2008)
65. Maxeiner, H., Wolff, M.: Pure subdural hematomas: a postmortem analysis of their form and bleeding points. Neurosurgery. **50**, 503–509 (2002)
66. McKee, A.C., Robinson, M.E.: Military-related traumatic brain injury and neurodegeneration. Alzheimers Dement. **10**(3 Suppl), S242–S253 (2014)
67. Miller, K., Chinzei, K.: Constitutive modelling of brain tissue; experiment and theory. J. Biomech. **30**(11/12), 1115–1121 (1997)
68. Miller, K., Chinzei, K.: Mechanical properties of brain tissue in tension. J. Biomech. **35**, 483–490 (2002)
69. Miller, L.E., Urban, J.E., Stitzel, J.D.: Development and validation of an atlas-based finite element brain model. Biomech. Model. Mechanobiol. **15**(5), 1201–1214 (2016)
70. Morrison 3rd, B., Cater, H.L., Benham, C.D., Sundstrom, L.E.: An in vitro model of traumatic brain injury utilising two-dimensional stretch of organotypic hippocampal slice cultures. J. Neurosci. Methods. **150**(2), 192–201 (2006). Epub 2005 Aug 10
71. Nahum, A.M., Smith, R., Ward, C.C.: Intracranial pressure dynamics during head impact. Proceedings of the 21st Stapp Car Crash Conference, SAE Paper No. 770922 (1977)
72. Newman, J., Beusenberg, M., Fournier, E., Shewchenko, N., Withnall, C., King, A., Yang, K., Zhang, L., McElhaney, J., Thibault, L., McGinnis, G.: A new biomechanical assessment of mild traumatic brain injury: Part I—Methodology. From the Proceedings of the IRCOBI Conference, pp 17–36 (1999)
73. Newman, J., Barr, C., Beusenberg, M., Fournier, E., Shewchenko, N., Welbourne, E., Withnall, C. A new biomechanical assessment of mild traumatic brain injury Part 2 – Results and Conclusions, From the Proceedings of the IRCOBI, pp. 223–233 (2000)
74. Nyquist, G.W., Cavanaugh, J.M., Goldberg, S.J., King, A.I.: Year Facial impact tolerance and response. In Proc. 30th Stapp Car Crash Conference, SAE Paper No. 861896 (1986)
75. O'Connor, K.L., Rowson, S., Duma, S.M., Broglio, S.P.: Head-impact-measurement devices: a systematic review. J. Athl. Train. **52**(3), 206–227 (2017)
76. Ommaya, A.K., Grubb, R.L., Naumann, R.A.: Coup and contrecoup injury: observations on the mechanics of visible brain injuries in the rhesus monkey. J. Neurosurg. **35**, 503–516 (1971)
77. Pellman, E.J., Viano, D.C., Tucker, A.M., Casson, I.R., Waeckerle, J.F.: Concussion in professional football: location and direction of helmet impacts: part II. Neurosurgery. **53**, 1328–1341 (2003)
78. Pervin, F., Chen, W.W.: Dynamic mechanical response of bovine gray matter and white matter brain tissues under compression. J. Biomech. **42**, 731–735 (2009)
79. Pleasant, J.M., Carlson, S.W., Mao, H., Yang, K.H., Saatman, K.E.: Rate of neurodegeneration in the mouse controlled cortical impact model is influenced by impactor tip shape: implications for mechanistic and therapeutic studies. J. Neurotrauma. **28**, 2245–2262 (2011)
80. Prabhu, R., Horstemeyer, M.F., Tucker, M.T., Marin, E.B., Bouvard, J.L., Sherburn, J.A., Liao, J., Williams, L.N.: Coupled experiment/finite element analysis on the mechanical response of porcine brain under high strain rates. J. Mech. Behav. Biomed. Mater. **4**(7), 1067–1080 (2011)
81. Raymond, D., Van Ee, C., Crawford, G., Bir, C.: Tolerance of the skull to blunt ballistic temporo-parietal impact. J. Biomech. **42**, 2479–2485 (2009)

82. Rowson, S., Brolinson, G., Goforth, M., Dietter, D., Duma, S.: Linear and angular head acceleration measurements in collegiate football. J. Biomech. Eng. **131**(6), 061016 (2009)
83. Rowson, S., Duma, S.M., Beckwith, J.G., Chu, J.J., Greenwald, R.M., Crisco, J.J., Brolinson, P.G., Duhaime, A.C., McAllister, T.W., Maerlender, A.C.: Rotational head kinematics in football impacts: an injury risk function for concussion. Ann. Biomed. Eng. **40**(1), 1–13 (2012). Epub 2011 Oct 20
84. Ruan, J., Prasad, P.: The effects of skull thickness variations on human head dynamic impact responses. Stapp Car Crash J. **45**, 395–414 (2001)
85. Sahoo, D., Deck, C., Willinger, R.: Brain injury tolerance limit based on computation of axonal strain. Accid. Anal. Prev. **92**, 53–70 (2016)
86. Sanchez, E.J., Gabler, L.F., McGhee, J.S., Olszko, A.V., Chancey, V.C., Crandall, J.R., Panzer, M.B.: Evaluation of head and brain injury risk functions using sub-injurious human volunteer data. J. Neurotrauma. **34**(16), 2410–2424 (2017). Epub 2017 Jun 9
87. Sanchez, E.J., Gablera, L.F., Good, A.B., Funk, J.R., Crandall, J.R., Panzer, M.B.: A reanalysis of football impact reconstructions for head kinematics and finite element modeling. Clin. Biomech. (2018). https://doi.org/10.1016/j.clinbiomech.2018.02.019
88. Schouten, J.W.: Neuroprotection in traumatic brain injury: a complex struggle against the biology of nature. Curr. Opin. Crit. Care. **13**, 134–142 (2007)
89. Serrador, J.M., Picot, P.A., Rutt, B.K., Shoemaker, J.K., Bondar, R.L.: MRI measures of middle cerebral artery diameter in conscious humans during simulated orthostasis. Stroke. **31**(7), 1672–1678 (2000)
90. Shenkin, H.A.: Acute subdural hematoma. Review of 39 consecutive cases with high incidence of cortical artery rupture. J. Neurosurg. **57**, 254–257 (1982)
91. Tagliaferri, F., Compagnone, C., Korsic, M., Servadei, F., Kraus, J.: A systematic review of brain injury epidemiology in Europe. Acta Neurochir. **148**, 255–268 (2006)
92. Takhounts, E.G., Craig, M.J., Moorhouse, K., McFadden, J., Hasija, V.: Development of brain injury criteria (BrIC). Stapp Car Crash J. **57**, 243–266 (2013)
93. Takhounts, E.G., Eppinger, R.H., Campbell, J.Q., Tannous, R.E., Power, E.D., Shook, L.S.: On the development of the SIMon finite element head model. Stapp Car Crash J. **47**, 107–133 (2003)
94. Thomas, C., Ye, F.Q., Irfanoglu, M.O., Modi, P., Saleem, K.S., Leopold, D.A., Pierpaoli, C.: Anatomical accuracy of brain connections derived from diffusion MRI tractography is inherently limited. Proc. Natl. Acad. Sci. U. S. A. **111**(46), 16574–16579 (2014)
95. Trosseille, X., Tarriere, C., Lavaste, F., Guilon, F., Domont, A. Development of a F.E.M. of the human head according to a specific test protocol. Proc. 36th Stapp Car Crash Conference, SAE Paper No. 922527, Society of Automotive Engineers, Warrendale, PA. (1992)
96. van Dommelen, J.A., van der Sande, T.P., Hrapko, M., Peters, G.W.: Mechanical properties of brain tissue by indentation: interregional variation. J. Mech. Behav. Biomed. Mater. **3**(2), 158–166 (2010)
97. Viano, D.C., Casson, I.R., Pellman, E.J., Zhang, L., King, A.I., Yang, K.H.: Concussion in professional football: brain responses by finite element analysis: part 9. Neurosurgery. **57**(5), 891–916; discussion 916 (2005)
98. Wang, F., Han, Y., Wang, B., Peng, Q., Huang, X., Miller, K., Wittek, A.: Prediction of brain deformations and risk of traumatic brain injury due to closed-head impact: quantitative analysis of the effects of boundary conditions and brain tissue constitutive model. Biomech. Model. Mechanobiol. **17**(4), 1165–1185 (2018)
99. Ward, C. C., Thompson, R. B.: The Development of a detailed finite element brain model. Proc. 19th Stapp Gar Crash Conf., SAE Paper No. 751163 (1975)

100. White, N.A., Begeman, P.C., Hardy, W.N., Yang, K.H., Ono, K., Sato, F., Kamiji, K., Yasuki, T., Bey, M.J.: Investigation of upper body and cervical spine kinematics of postmortem human subjects (PMHS) during low-speed, rear-end impacts. SAE 2009 World Congress and Expo 2009-01-0387 (2009)
101. Williams, R.M., Dowling, M., O'Connor, K.L.: Head impact measurement devices. Sports Health. **8**(3), 270–273 (2016)
102. Xiong, Y., Mahmood, A., Chopp, M.: Emerging treatments for traumatic brain injury. Expert Opin. Emerg. Drugs. **14**(1), 67–84 (2009)
103. Yang, K.H., Hu, J., White, N.A., King, A.I., Chou, C.C., Prasad, P.: Development of numerical models for injury biomechanics research: a review of 50 years of publications in the Stapp Car Crash Conference. Stapp Car Crash J. **50**, 429–490 (2006)
104. Yang, K.H., Mao, H., Wagner, C., Zhu, F., Chou, C.C., King, A.I.: Modeling of the brain for injury prevention. In: Bilston, L.E. (ed.) Neural Tissue Biomechanics. Springer, Berlin/Heidelberg (2011)
105. Yang, K.H.: Basic Finite Element Method and Analysis as Applied to Injury Biomechanics, 1st edn., Paperback ISBN: 9780128098318. Elsevier, London (2017)
106. Yoganandan, N., Pintar, F.A., Sances Jr., A., Walsh, P.R., Ewing, C.L., Thomas, D.J., Snyder, R.G.: Biomechanics of skull fracture. J. Neurotrauma. **12**, 659–668 (1995)
107. Yoganandan, N., Zhang, J., Pintar, F.A.: Force and acceleration corridors from lateral head impact. Traffic Inj. Prev. **5**, 368–373 (2004)
108. Zhang, L., Yang, K.H., Dwarampudi, R., Omori, K., Li, T., Chang, K., Hardy, W.N., Khalil, T.B., King, A.I.: Recent advances in brain Injury research: a new human head model development and validation. Stapp Car Crash J. **45**, 369–393 (2001)
109. Zhang, L., Bae, J., Hardy, W.N., Monson, K.L., Manley, G.T., Goldsmith, W., Yang, K.H., King, A.I.: Computational study of the contribution of the vasculature on the dynamic response of the brain. Stapp Car Crash J. **46**, 145–163 (2002)
110. Zhang, L., Ramesh, S., Yang, K.H., King, A.I.: Effectiveness of the football helmet assessed by finite element modeling and impact testing. Proceedings of the IRCOBI Conference, 2003, Lisbon, Portugal (2003)
111. Zhang, L., Yang, K.H., King, A.I.: A proposed injury threshold for mild traumatic brain injury. J. Biomech. Eng. **126**, 226–236 (2004)
112. Zhou, Z., Li, X., Kleiven, S.: Fluid–structure interaction simulation of the brain–skull interface for acute subdural haematoma prediction. Biomec. Model Mechanobiol. 1–19 (2018). https://doi.org/10.1007/s10237-018-1074-z, ISSN: 1617–7959
113. Zhu, F., Karla, A., Saif, T., Yang, Z., Yang, K.H., King, A.I.: Parametric analysis of the biomechanical response of head subjected to the primary blast loading – a data mining approach. Comput. Methods Biomech. Biomed. Engin. **19**(10), 1053–1059 (2016a)
114. Zhu, F., Gatti, D., Yang, K.H.: Nodal versus total axonal strain and the role of cholesterol in traumatic brain injury. J. Neurotrauma. **33**(9), 859–870 (2016b). Epub 2015 Sep 22

Chapter 6
Biomechanical Modelling of the Brain for Neurosurgical Simulation and Neuroimage Registration

Karol Miller, Adam Wittek, Angus C. R. Tavner, and Grand Roman Joldes

6.1 Introduction

During neurosurgery, the brain can deform significantly. Despite the enormous complexity of the brain (see Chap. 2), many aspects of its response can be reasonably described in purely mechanical terms, such as displacements, strains and stresses. Therefore the mechanical behaviour of the brain can be analysed using the established methods of continuum mechanics. In this chapter we discuss approaches to biomechanical modelling of the brain from the perspective of two distinct applications: neurosurgical simulation and neuroimage registration in image-guided surgery. These two challenging applications are described below.[1]

6.1.1 Neurosurgical Simulation for Operation Planning, Surgeon Training and Skills Assessment

The goal of surgical simulation research is to model and simulate deformable materials for applications requiring real-time interaction. Medical applications for this include simulation-based training, skills assessment and operation planning.

[1]Parts of this chapter were previously published in *International Journal for Numerical Methods in Biomedical Engineering*.

K. Miller (✉) · A. Wittek · A. C. R. Tavner · G. R. Joldes
Intelligent Systems for Medicine Laboratory, School of Mechanical Engineering, The University of Western Australia, Perth, WA, Australia
e-mail: karol.miller@uwa.edu.au

K. Miller (ed.), *Biomechanics of the Brain*, Biological and Medical Physics, Biomedical Engineering, https://doi.org/10.1007/978-3-030-04996-6_6

Surgical simulation systems are used to provide visual and haptic feedback to a surgeon or trainee. Various haptic interfaces for medical simulation are especially useful for training surgeons for minimally invasive procedures (laparoscopy/interventional radiology) and remote surgery using tele-operators. These systems must compute the deformation field within a soft organ and the interaction force between a surgical tool and the tissue to present visual and haptic feedback to the surgeon. Haptic feedback must be provided at frequencies of at least 500 Hz. From a solid-mechanics perspective, the problem involves large deformations, non-linear material properties and non-linear boundary conditions. Moreover, it requires extremely efficient solution algorithms to satisfy the stringent requirements of the frequency of haptic feedback. Thus, surgical simulation is a very challenging problem in solid mechanics.

When a simulator is intended to be used for surgeon training, a generic model developed from average organ geometry and material properties can be used in computations. However, when the intended application is for operation planning, the computational model must be patient-specific. This requirement adds to the difficulty of the problem – the question of how to rapidly generate patient-specific computational models still awaits a satisfactory answer [1].

6.1.2 Image Registration in Image-Guided Neurosurgery

One common element of most new therapeutic technologies, such as gene therapy, stimulators, focused radiation, lesion generation, nanotechnological devices, drug polymers, robotic surgery and robotic prosthetics, is that they have extremely localised areas of therapeutic effect. As a result, they have to be applied precisely in relation to the patient's current (i.e. intra-operative) anatomy, directly at the specific location of anatomic or functional abnormality [2]. Nakaji and Speltzer [3] list the 'accurate localisation of the target' as the first principle in modern neurosurgical approaches.

As only pre-operative anatomy of the patient is known precisely from medical images, usually magnetic resonance images (MRIs), it is now recognised that the ability to predict soft organ deformation (and therefore intra-operative anatomy) during the operation is the main problem in performing reliable surgery on soft organs. In the context of brain surgery, it is very important to be able to predict the effect of procedures on the position of pathologies and critical healthy areas in the brain. If displacements within the brain can be computed during the operation, then they can be used to warp pre-operative high-quality MR images so that they represent the current, intra-operative configuration of the brain; see Fig. 6.1.

The neuroimage registration problem involves large deformations, non-linear material properties and non-linear boundary conditions, as well as the difficult issue of generating patient-specific computational models. However, it is easier than the surgical simulation problem discussed above in two important ways. Firstly, we are interested in accurate computations of the displacement field only. Accuracy of

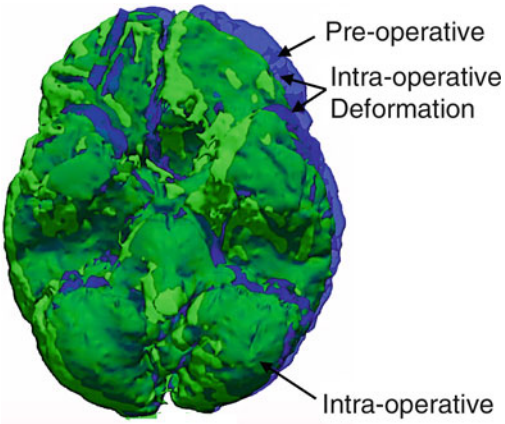

Fig. 6.1 Comparison of a brain surface determined from images acquired pre-operatively with the one determined intra-operatively from images acquired after craniotomy. Inferior (i.e. 'bottom') view. Pre-operative surface is semi-transparent. Deformation of the brain surface due to craniotomy is clearly visible. Intra-operative displacements of over 20 mm have been reported in medical literature [4]. Surfaces were determined from the images provided by the Department of Surgery, Brigham and Women's Hospital (Harvard Medical School, Boston, Massachusetts, USA)

stress computations is not required. Secondly, the computations must be conducted intra-operatively, which practically means that the results should be available to an operating surgeon in less than 40 seconds [5–10]. This still requires computational efficiency but is much more easily satisfied than the 500 Hz haptic feedback frequency requirement for neurosurgical simulation.

Following the Introduction (Sect. 6.1), in Sect. 6.2 we describe difficulties in modelling geometry, boundary conditions, loading and material properties of the brain. In Sect. 6.3 we consider example applications in the area of computational radiology. Numerical algorithms devised to efficiently solve brain deformation behaviour models are described in Chaps. 10 and 11. We conclude this chapter with some reflections about the state of the field.

6.2 Biomechanics of the Brain: Modelling Issues

When considering approaches to modelling the brain, one should first determine whether the intended application is *generic* or *patient-specific* [110]. If the biomechanical model is intended for a generic application, for example, a neurosurgical simulator for surgeon training, the typical 'average' geometry and mechanical properties of an organ and tissues can be modelled. However, if a patient-specific model is required, for example, for operation planning, then clearly a 'generic' model is of limited utility, and patient-specific data must be incorporated into the model. The reader is warned here that the problem of how to generate patient-

specific biomechanical models quickly and reliably remains unresolved (see [1] and Chap. 7 for current attempts to address this issue using meshless methods). Another aspect worth considering is that for computational biomechanics to be accepted and beneficial in clinical practice, biomechanical computations must be seamlessly incorporated into the clinical work flow. This can only be achieved if these computations are conducted at least in close to real time (how to achieve this is discussed in Chap. 2; see also [11]).

In the remainder of this section, we will discuss the main modelling issues: geometry, boundary conditions, loading and tissue mechanical properties.

6.2.1 Geometry

Detailed geometric information is needed to define the domain in which the deformation field needs to be computed. Such information is provided by electronic brain atlases described in detail in Chap. 2 and is readily available as some atlases are web-based; see, e.g. Surgical Planning Laboratory Brain Atlas, Fig. 6.2.

In applications that do not require patient-specific data (such as neurosurgical simulators for education and training), the geometric information provided by these atlases is sufficient. However, other applications such as neurosurgical simulators for operation planning and image registration systems do require patient-specific data. Such data can be obtained from radiological images (e.g. see Fig. 6.3 and Chap. 3); however the quality is significantly inferior to the data available from anatomical atlases (see Chap. 2).

The accuracy of neurosurgery is typically not better than 1 mm [2]. Voxel size in high-quality pre-operative MR images is usually of similar magnitude. Therefore, we can conclude that patient-specific models of the brain geometry

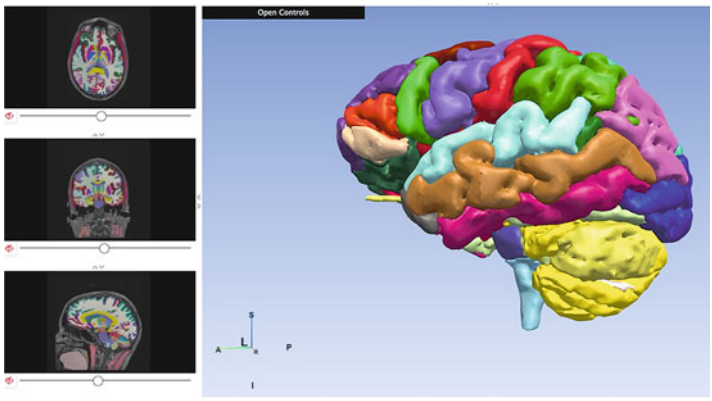

Fig. 6.2 Multimodality MRI-based atlas of the brain [13]

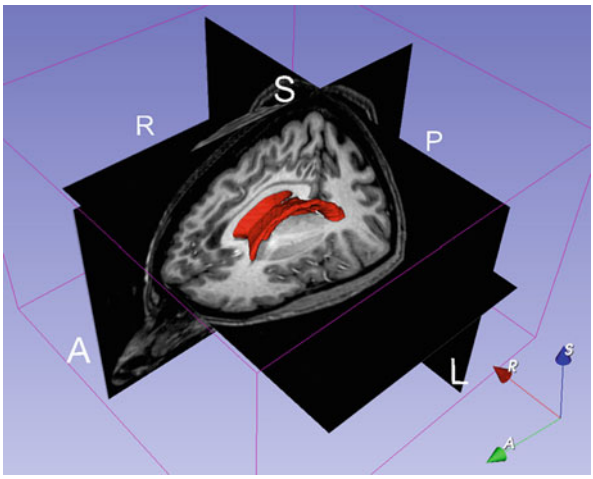

Fig. 6.3 3D magnetic resonance image presented as a triplanar cross-section. 3D rendering of ventricles is shown in red. Public domain software Slicer (www.slicer.org), developed by our collaborators from the Surgical Planning Laboratory, Harvard Medical School, was used to generate the image

can be constructed with approximately 1 mm accuracy and that higher accuracy is probably not required. One must then decide which brain structures should be explicitly included in the model and which omitted. As described in Chap. 2, anatomists recognise well over a thousand structures within the brain. However, very little is known about the relative mechanical properties of these structures. The 'maps' of brain regional mechanical properties from MR elastography are not yet reliable and are only valid for small strain (linear viscoelastic) [14, 15]. Therefore, even the most sophisticated models in current use by the scientific community typically only include brain parenchyma, ventricles, tumour (if present, for attempts to estimate tumour mechanical properties, see, e.g. [16–18].) and skull. I refer the reader to Chap. 4 of this book where mechanical properties of brain tissues are discussed in great detail.

A necessary step in constructing patient-specific models of brain geometry is medical image *segmentation*. Segmentation is a process that identifies different parts of the brain on the image; see Fig. 6.4.

Unfortunately, despite years of effort by the medical image analysis community, a generally accepted automatic segmentation method for brain MR images is not yet available. In practice, very laborious semi-automatic or manual methods are employed [10, 19]. It is clear that if one attempted to include many brain structures in the patient-specific biomechanical model, then one would need to identify them in the medical image and segment them. This would be a daunting task that at the time of writing does not appear to be practical.

On the other hand, when a generic application that does not require patient-specific data is considered, the 3D geometry of essentially all structures that might possibly be of interest can be imported from electronic brain atlases. For example, a hippocampus is often of interest, and its geometry and location can be clearly seen in Fig. 2.6 of Chap. 2.

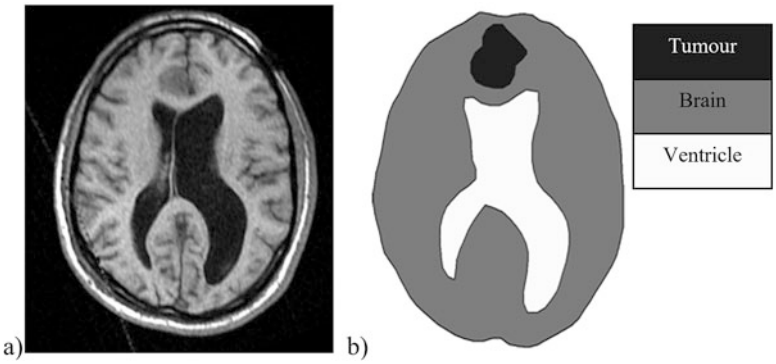

Fig. 6.4 (**a**) 2D slice of 3D brain MR volume; (**b**) segmented image. Such 'hard' segmentation is necessary for finite element mesh development

To develop a numerical model of brain biomechanics, it is necessary to create a computational grid, which in most practical cases is a finite element mesh (or a cloud of points required by a meshless method; see also Chaps. 5, 6, 10, and 11). Because of the stringent computation time requirements, the mesh must be constructed using low-order elements that are computationally inexpensive. The linear under-integrated hexahedron is the preferred choice.

Many algorithms are now available for fast and accurate automatic mesh generation using tetrahedral elements, but not for automatic hexahedral mesh generation [20–22]. Template-based meshing algorithms can be used for discretising different organs using hexahedrons [23–25], but these types of algorithms only work for healthy organs. In the case of severe pathologies (such as a brain tumour or severely enlarged ventricles), such algorithms cannot be used as the shape, size and position of the pathology are unpredictable. This is one reason why many authors proposed the use of tetrahedral meshes for their models [5, 6, 26, 27]. In order to automate the simulation process, mixed meshes having both hexahedral and linear tetrahedral elements are the most convenient. Examples of such meshes are shown in Fig. 6.10 in the next section.

An alternative to using the finite element method is to use one of the available meshless methods. The problem of generating the computational grid disappears as one needs only to drop a cloud of points into the volume defined by a 3D medical image [1, 28–34]; see Fig. 6.5. Details of the meshless total Lagrangian explicit dynamics (MTLED) algorithm for computing soft tissue deformations are given in Chap. 11.

6.2.2 Boundary Conditions

The formulation of appropriate boundary conditions for computation of brain deformation during surgery constitutes a significant problem because of the complexity

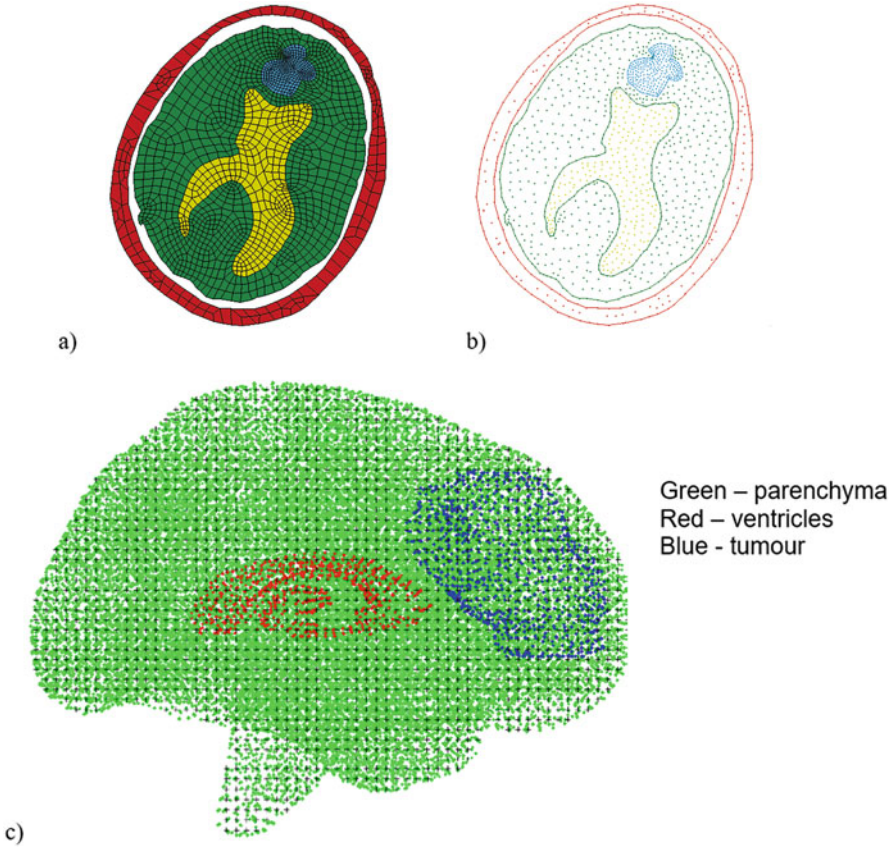

Fig. 6.5 A 2D slice of the brain discretised by (**a**) quadrilateral finite elements and (**b**) nodes of the modified element-free Galerkin method [35]. (**c**) 3D meshless discretisation of the brain [36]. Development of a good-quality finite element mesh is time-consuming; generation of the meshless grid is almost instantaneous

of the brain – skull interface (see Fig. 5.2 in Chap. 5 on modelling the brain for injury prevention where this problem is also highlighted).

A number of researchers 'fix' the brain surface to the skull [37, 38]. We do not recommend this approach as it is clearly inconsistent with the brain's anatomy; see Chap. 2. One alternative is to use a gap between the brain and the skull that allows for motion of the brain within the cranial cavity [8, 39–44]. Another alternative is to use a frictionless sliding (with separation) contact model [45, 46] that can be incorporated into finite element computations very efficiently; see Chap. 10. This approach is partially supported by MR elastography measurements [47]. The reader should be aware that biomechanical knowledge about the properties of the brain-skull interface is very limited [48–51]. The brain-skull interface models used in the literature are 'best guesses' that, while effective in practice, might have little relation to reality.

The skull should be included in the model either explicitly or in the form of an appropriate boundary condition for the brain. As the skull is orders of magnitude stiffer than the brain tissue, it can be assumed to be rigid. The constraining effects of the spinal cord on the brain's rigid body motion can be simulated by constraining the spinal end of the model.

6.2.3 Loading

We advocate loading the models through imposed displacements on the model surface [41, 52]; see Fig. 6.6. In the case of neurosurgical simulation, this loading will be imposed by known motion of a surgical tool. In the case of intra-operative image registration, the current (intra-operative) position of the exposed part of the brain surface can be measured using various techniques; see Chaps. 12 and 13 of this book. This information can then be used to define model loading.

For problems where loading is prescribed as forced motion of boundaries, the unknown deformation field within the domain depends very weakly on the mechanical properties of the continuum [41, 52]. Because this feature is of great importance in biomechanical modelling, where there are always uncertainties in patient-specific properties of tissues, it warrants more detailed discussion.

If we consider an (oversimplified) quasistatic linear elastic case, the following dimensional reasoning applies. The loading is provided by the enforced motion of boundaries measured in metres [m]; the result of computations is displacements measured in [m]; therefore the result cannot depend on the stress parameter measured in [Pa = N/m^2]. We should note here that the result can depend on (dimensionless) Poisson's ratio and on (dimensionless) ratios of stress parameters if the model contains materials with different stiffnesses. The dependence on

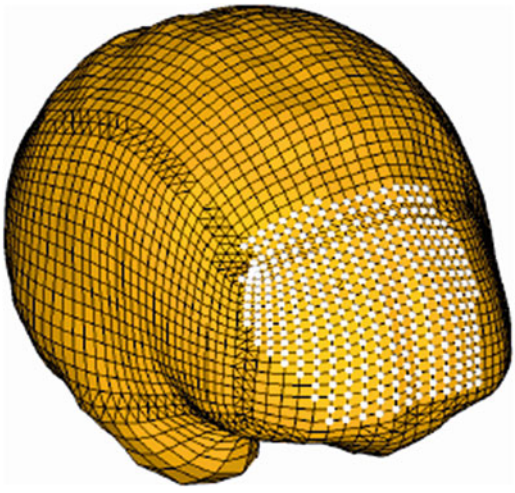

Fig. 6.6 Model loading through prescribed nodal displacements (on white surface nodes) at the exposed brain surface

the volumetric response (e.g. Poisson's ratio) is of minor consequence for soft organ biomechanics because tissues such as the brain, liver, kidney or prostate are considered almost incompressible; see, e.g. Chap. 4 of this book and [53–55].

In the general non-linear case, the displacement results will still remain insensitive to the stress parameter appearing in the non-linear material law but may depend on the particular form of that law (as the functional form of a constitutive law does not have a dimension). However, this dependency will be rather weak, as explicitly demonstrated in [56, 57] where the shapes of compressed and extended cylinders were shown to be essentially independent of the material law used for the cylinder's material; see Fig. 6.7. These results suggest a move away from mechanics towards kinematics where the main quantities of interest in this approach are displacements, strains and their histories.

We now consider nonrigid image registration in image-guided procedures where high-resolution pre-operative scans are warped onto lower-quality intra-operative images [58, 59]. The task of particular clinical interest is registering high-resolution pre-operative MRIs with lower-quality intra-operative imaging modalities, such as intra-operative ultrasound and multiplanar MRIs.

The brain, for which a detailed pre-operative image is available, deforms after craniotomy due to several physical and physiological reasons (i.e. brain shift, the specific mechanisms of the brain shift include decompression, response to anaesthesia and other possible and hotly contested phenomena). We are interested in the intra-operative (i.e. current) position of the brain, for which partial information is provided by low-resolution intra-operative images. In mathematical terms this problem can be described with equations of solid mechanics.

Consider the motion of a deforming body in a stationary coordinate system, Fig. 6.8. In the analysis we follow the motion of all particles from their original position to the final configuration of the body, which means that the Lagrangian (or material) formulation of the problem is adopted. Motion of the system sketched in Fig. 6.8 can be described by equations of motion often written in weak form:

$$\int_V \tau_{ij}\delta\varepsilon_{ij}dV = \int_V f_i^B \delta u_i dV + \int_S f_i^S \delta u_i dS \tag{6.1}$$

where ε is the Almansi strain, $\int_V \tau_{ij}\delta\varepsilon_{ij}dV$ is the internal virtual work, $\int_V f_i^B \delta u_i dV$ is the virtual work of external body forces (this includes inertial effects) and $\int_S f_i^S \delta u_i dS$ is the virtual work of external surface forces. As the brain undergoes finite deformation, the current volume V and surface S over which the integration is conducted are unknown: they are part of the solution rather than input data. Therefore, appropriate solution procedures which allow finite deformation must be used; see Chaps. 10 and 11. The integral Eq. (6.1) must be supplemented by formulae describing the mechanical properties of materials, i.e. appropriate constitutive models. However, an important advantage of the weak formulation is that the essential (displacement) boundary conditions are automatically satisfied [60].

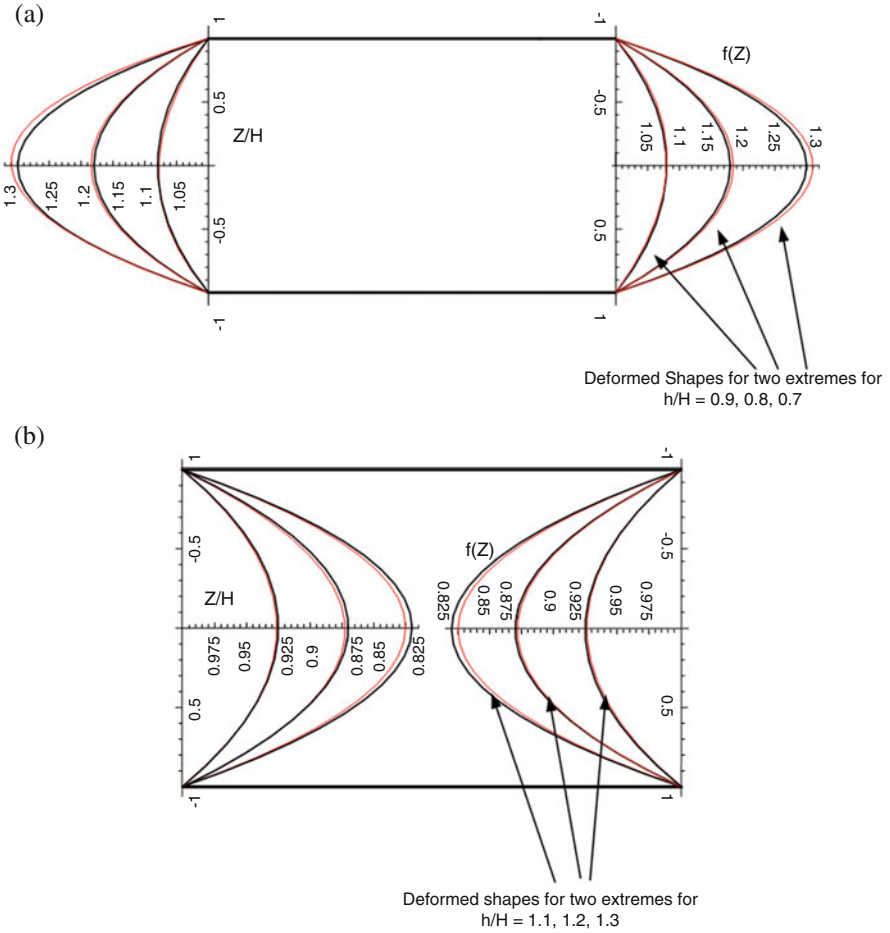

Fig. 6.7 Shapes of cylinders modelled as extreme-Mooney and neo-Hookean materials. (**a**) Compression by 10, 20 and 30%. (**b**) Extension by 10, 20 and 30%. Z/H denotes a dimensionless coordinate along the height of the cylinder. f(Z) stands for the shape of the side of the deformed cylinder. The shape of a cylinder made from a 'real' material is expected to fall between the two extremes

Boundary conditions may prescribe kinematic variables such as displacements and velocities (essential boundary conditions) or tractions (natural boundary conditions, these also include concentrated forces). It should be noted that 'boundary conditions' do not have to be applied at the physical boundary of the deforming object: if convenient, they can be prescribed at, for example, the locations of easily identifiable anatomical landmarks with precisely known locations in both the pre-operative and intra-operative configuration of the brain.

Depending on the amount of information available about the intra-operative position of the brain from intra-operative imaging modalities, neuroimage registration

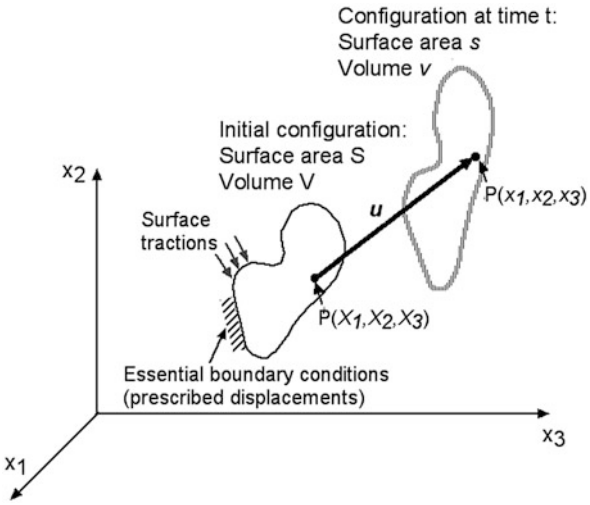

Fig. 6.8 Motion of a body in a stationary coordinate system. Initial configuration, described by uppercase coordinates, can be considered as a high-quality pre-operative image. Current, deformed configuration (described by lowercase coordinates) is unknown; however partial information is available from a lower-resolution intra-operative image

can be described mathematically in two ways. If the entire boundary of the brain can be extracted from the intra-operative image, then we know both the initial position of the domain (i.e. the brain), as determined from pre-operative MRI, and the current position of the entire boundary of the domain. We are looking for the unknown displacement field within the domain (the brain), in particular the current position of, for example, a tumour and healthy tissues (critically important from a surgical perspective). No information about surface tractions is required for the solution of this problem. In theoretical elasticity, problems of this type are called 'pure displacement problems' [61].

If only limited information is available about the boundary (e.g. only the position of the brain surface exposed during craniotomy and perhaps the current positions of clearly identifiable anatomical landmarks, as described in [62]) and no external forces are applied to the boundary, a slightly different mathematical description is needed. We know the initial position of the domain (i.e. the brain), as determined from pre-operative MRI, and the current position of some parts of the boundary of the domain (the brain), and we know that there are no pressure or traction forces everywhere else on the boundary. Consequently, contacts need to be modelled kinematically as in [45, 46]; see also Chap. 10 of this book. We do not know the displacement field within the domain (the brain), which means that we would not know the current positions of, for instance, a tumour and healthy tissues.

Problems of this type are very special cases of 'displacement – traction problems' [61] that have not, to the best of our knowledge, been considered as a separate class, and no special methods of solution for these problems exist. Reference [63] contains the suggestion to call such problems 'displacement – zero traction problems'. More recently we named such problems Dirichlet-type [52].

The solutions in displacements (the variable of interest in the context of image-guided surgery) for both pure displacement and displacement-zero traction

Table 6.1 Comparison of predicted displacements of tumour and ventricle centres of gravity obtained with various constitutive models [41]. It is clear that while using the proper non-linear solution procedure is essential, the choice of constitutive model makes little difference

Center of Gravity Displacements (mm)						
Material Model/ Analysis Type	Ventricles			Tumor		
	ΔX	ΔY	ΔZ	ΔX	ΔY	ΔZ
MRI Determined	3.4	0.2	1.7	5.5	-0.2	1.7
Hyperviscoelastic material/ Geometrically non-linear analysis	2.6	-0.1	2.1	5.2	-0.4	2.7
Hyperelastic material/ Geometrically non-linear analysis	2.6	-0.1	2.1	5.2	-0.4	2.7
Linear elastic material/ Geometrically non-linear analysis	2.6	-0.1	2.1	5.0	-0.5	2.7
Linear elastic material/ Linear analysis	0.7	0.2	1.9	3.7	-0.3	2.6

problems (Dirichlet-type) are only very weakly sensitive to mechanical properties of the deforming continuum and therefore can be obtained without knowledge of patient-specific properties of the brain tissue.

In the case of the full-scale brain deformation computation, our experience confirms the expected insensitivity of computed displacement fields to different tissue constitutive models [41]. Table 6.1 contains observed and computed displacements for centres of gravity of ventricles and tumour for a case of tumour removal described in detail in [41]. In the computations the same general geometrically non-linear formulation was used together with various constitutive models.

When interpreting the results summarised in Table 6.1, note that the accuracy of determining positions of centres of gravity of tumour and ventricles is limited by the voxel size in the intra-operative MRI images used in this study – 0.85 mm $\times$ 0.85 mm $\times$ 2.5 mm. We also need to consider that the accuracy of manual neurosurgery is approximately 1 mm [7]. Therefore, for practical purposes, values differing by less than 0.80 mm can be considered equivalent. The slightly different results seen in the second-last row of Table 6.1 are due to the fact that the linear elastic constitutive model is not compatible with the finite deformation solution procedure [64]. It is apparent that the choice of the constitutive model does not make any practical difference in the solution for displacements, and therefore we recommend the use of neo-Hookean material model. However, if geometrically linear analysis is used – see the last row of Table 6.1 – the results are clearly erroneous.

6.2.4 Models of Mechanical Properties of Brain Tissue

The first question to address is whether a single-phase continuum model for the tissue should be used or if biphasic or even more complicated multiphase models are required. Many researchers conclude that the brain is obviously a hydrated tissue and therefore use biphasic models based on consolidation theory; see, e.g. [65] and references cited therein. We are of the opinion that biphasic, consolidation theory-based models are inconsistent with brain tissue behaviour observed in simple experiments. For example, no leakage of CSF was observed in brain tissue samples loaded by CSF pressure difference [66, 67]. Another argument against using biphasic models is that during numerous unconfined compression experiments [68], we never observed fluid leaking from the side of the samples. Such leakage is predicted by biphasic theory. Therefore, in the remainder of this chapter, we will discuss only single-phase modelling approaches.

Experimental results show that the mechanical response of brain tissue to external loading is very complex. The stress-strain relationship is clearly non-linear with no portion in the plots suitable for estimating a meaningful Young's modulus. It is also obvious that the stiffness of the brain in compression is much higher than in extension [69]. The non-linear relationship between stress and strain rate is also apparent. Detailed exposition of the current knowledge about the mechanical properties of brain tissue is given in Chap. 4. Here we will only discuss issues directly pertinent to modelling neurosurgery.

The great majority of brain models assume brain tissue is *incompressible* and *isotropic* (see also Chaps. 4 and 5). The assumption of incompressibility is not contentious. Whether it is reasonable to assume that brain tissue is isotropic (i.e. mechanical properties the same in all directions) is less clear, especially in view of the obviously directional character of white matter fibres. Brain tissues do not normally bear mechanical loads and do not exhibit directional structure, provided that a large-enough length scale is considered. Therefore, they may be assumed to be initially isotropic; see, e.g. [69–77]. When modelling brain deformations during surgery, we need to keep in mind that the accuracy of displacement computations rarely needs to be better than about 1 mm – the claimed accuracy of neurosurgery. Therefore, 'average isotropic' properties at the length scales relevant to surgical procedures are most probably sufficient. These properties are relatively well accounted for by an Ogden-type hyperviscoelastic model [78] described in Chap. 4, Eqs. 4.4 and 4.5.

Average properties, such as those described above, are not sufficient for patient-specific computations of stresses and reaction forces because of the very large variability inherent in biological materials. This variability is clearly demonstrated in the biomechanics literature [69, 80–81]. Unfortunately, despite recent progress in elastography using ultrasound [82, 83] and magnetic resonance (see Chap. 4) [84–88], reliable methods of measuring patient-specific properties of the brain are not yet available.

Nevertheless, as shown in the previous section on modelling loading, much can be achieved even without a patient-specific model of brain tissue mechanical properties, if the model is loaded by the enforced motion of a boundary and the problem is formulated as Dirichlet-type: a pure displacement or displacement-zero traction problem. As the computed results are then almost insensitive to the assumed mechanical properties of the tissue, we advocate using the simplest model that is compatible with finite deformation solution procedures, a neo-Hookean model:

$$ {}^{t}_{0}S = \mu \cdot J^{-2/3} \left(I_3 - \frac{1}{3} \cdot I \cdot {}^{t}_{0}C^{-1} \right) + k \cdot (J - 1) \cdot J \cdot {}^{t}_{0}C^{-1} \tag{6.2} $$

where ${}^{t}_{o}S$ is the second Piola-Kirchhoff stress, I is the first invariant of the deviatoric right Cauchy-Green deformation tensor C (the first strain invariant), J is the determinant of the deformation gradient (representing the volume change), I_3 is the 3×3 identity matrix, μ is the shear modulus and k is the bulk modulus of the material.

The accuracy of this approach is demonstrated in Sect. 6.3 of this chapter.

6.2.5 Model Validation

For mathematical modelling and computer simulation to be of any practical use – to be *reliable* [89] – the results derived from the models must be known to lie within the prescribed margins of accuracy. As we have seen in Chap. 5, ascertaining that this is the case when modelling high-speed impacts and brain injury is a very difficult task. Modellers of the brain for neurosurgery are however in a better position: they have at their disposal intra-operative imaging modalities (see Chap. 12) providing images that can be used for a relatively straightforward validation of the results of computer simulations of brain deformations.

Biomechanical models of the brain contain a lot of simplifying assumptions to make them mathematically and computationally tractable. To be of practical use, solutions to these models must be obtained in real or close to real time. Therefore nonstandard specially designed solution algorithms and software implementations are often used (see Chaps. 10 and 11). It is very important, and unfortunately overlooked by many researchers, that the biomechanical model and solution method be validated separately. If we were to evaluate a 'software system' consisting of implemented nonstandard solution algorithms to a complicated biomechanical model and found discrepancies when compared with experiments, we would have no indication whether these discrepancies arose from inappropriate modelling assumptions or faulty numerical procedure (or both).

We recommend that new real-time solution algorithms be verified against well-established solution procedures implemented in commercial software. The assumptions of the biomechanical model need to be evaluated against available experimental data. The biomechanical model should then be validated by comparing the solutions computed using established numerical procedures and experimental results. If these hurdles are cleared and it can be also demonstrated that replacing established numerical procedures with the specialised ones developed for real-time applications does not affect the computed results, then one may treat the 'software system' with some degree of confidence.

How accurate should the results of the computational biomechanics model of the brain be? Accuracy of manual neurosurgery is not better than 1 mm. The voxel size of the best available experimental tool for model validation – currently the intra-operative MRI – is of the same order. Therefore, the computed intra-operative displacements do not need to be more accurate than about 1 mm. We may note here that, paradoxically, this accuracy requirement is much less stringent than those used in traditional engineering disciplines. In image-guided surgery applications, we are not interested in stress distributions, only in the displacement field. This is one of the reasons why simple constitutive models of the brain tissue can be used. However, for surgical simulation applications, we need to compute reaction forces on surgical tools that will be fed back to the user through a haptic interface. At present there is no consensus regarding how accurate this haptic feedback should be to facilitate a realistic experience. Given the present state of biomechanical knowledge, the best that can be achieved is qualitative agreement between real and computed interaction forces; see, e.g. [71]. This is despite examples of excellent agreement between computations and phantom experiments [90] as well as controlled in vitro experiments [91].

6.3 Application Example: Computer Simulation of Brain Shift

A particularly exciting application of nonrigid image registration is in intra-operative image-guided procedures, where pre-operative scans are warped onto sparse intra-operative images [7, 58]. We are especially interested in registering high-resolution pre-operative MRIs with lower-quality intra-operative imaging modalities, such as multiplanar MRIs and intra-operative ultrasound. To achieve accurate matching of these modalities, precise and fast algorithms to compute tissue deformations are fundamental.

Here we present selected results of the analysis of 33 cases of craniotomy-induced brain shift representing different situations that may occur during neuro-surgery [92, 93].

6.3.1 *Generation of Computational Grids: From Medical Images to Finite Element Meshes*

Pre-operative and intra-operative medical image datasets of 33 patients with cerebral gliomas were randomly selected from a retrospective database of 859 intracranial tumour cases available at Boston Children's Hospital [94]. Imaging was performed using a 0.5 T open MR system in the neurosurgical suite. The resolution of the images is $0.85 \times 0.85 \times 2.5$ mm^3. Consent was obtained for the use of the anonymised retrospective image database, in accordance with the Institutional Review Board of Boston Children's Hospital.

A three-dimensional (3D) surface model of each patient's brain was created from segmented pre-operative magnetic resonance images (MRIs). Following our previous studies on predicting craniotomy-induced deformations within the brain [11, 95–98], in this investigation, different material properties were assigned to the parenchyma, tumour and ventricles. Accordingly, to obtain the information for building the computational grids (finite element meshes), the parenchyma, tumour and ventricles were segmented using the region growing algorithm implemented in 3D Slicer, followed by manual correction.

The meshes were constructed using low-order elements (linear tetrahedron or hexahedron) to meet the requirement that computations be conducted intra-operatively, i.e. within no more than ca. 1 min. To prevent volumetric locking, tetrahedral elements with average nodal pressure (ANP) formulation were used [99]. The meshes were generated using IA-FEMesh [100] and HyperMesh (commercial FE mesh generator by Altair of Troy, MI, USA). A typical mesh (Case 1) is shown in Fig. 6.9. This mesh consists of 14,447 hexahedral elements, 13,563 tetrahedral elements and 18,806 nodes. Each node in the mesh has three degrees of freedom.

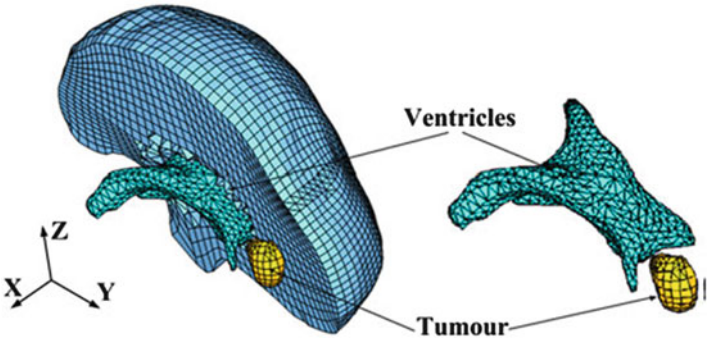

Fig. 6.9 Typical example (Case 1) of a patient-specific mesh built for this study. This mesh consists of 14,447 hexahedral elements, 13,563 tetrahedral elements and 18,806 nodes

6.3.2 Displacement Loading

The models were loaded by prescribing displacements on the exposed part (due to craniotomy) of the brain surface. As this requires only replacing the brain-skull contact boundary condition with prescribed displacements, no mesh modification is required at this stage. At first the pre-operative and intra-operative coordinate systems were aligned by rigid registration. Then the displacements at the mesh nodes located in the craniotomy region were estimated with the interpolation algorithm we described in [101].

As explained above (Sect. 2.3 and 2.4), for problems where loading is prescribed as forced motion of boundaries, the unknown deformation field within the domain depends very weakly on the mechanical properties of the continuum. This feature is of great advantage in biomechanical modelling where there are always uncertainties in patient-specific properties of tissues [102].

6.3.3 Boundary Conditions

The stiffness of the skull is several orders of magnitude higher than that of the brain tissue. Therefore, in order to define the boundary conditions for the unexposed nodes of the brain mesh, a contact interface [103] was defined between the rigid skull model and the deformable brain. The interaction was formulated as a finite sliding, frictionless contact between the brain and the skull. The effects of assumptions regarding the brain boundary conditions on the results of prediction of deformations within the brain have been analysed and discussed in [96, 104] and more recently in [51].

6.3.4 Mechanical Properties of the Intracranial Constituents

For Dirichlet-type problems, the predicted deformation field within the brain is only weakly affected by the constitutive model of the brain tissue [98]. Therefore, for simplicity a hyper-elastic neo-Hookean model was used [105]. The Young's modulus of 3000 Pa was selected for parenchyma [106]. The Young's modulus for tumour was assigned a value two times larger than that for the parenchyma, keeping it consistent with the experimental data of Sinkus et al. [107]. As the brain tissue is almost incompressible, a Poisson's ratio of 0.49 was chosen for the parenchyma and tumour [96]. The ventricles were assigned properties of a very soft compressible elastic solid with a Young's modulus of 10 Pa and Poisson's ratio of 0.1 [96].

6.3.5 Solution Algorithm

A suite of efficient algorithms for integrating the equations of solid mechanics and its implementation on a graphics processing unit for real-time applications are described in detail in Chap. 10 and [11, 108]. The computational efficiency of this algorithm is achieved by using a total Lagrangian (TL) formulation [109] for updating the calculated variables and an explicit integration in the time domain combined with mass proportional damping. In the TL formulation, all the calculated variables (such as displacements and strains) are referred to the original configuration of the analysed continuum [111]. The decisive advantage of this formulation is that all derivatives with respect to spatial coordinates can be precomputed. The total Lagrangian formulation also leads to a simplification of the material law implementation as these material models can be easily described using the deformation gradient [108].

The integration of equilibrium equations in the time domain was performed using an explicit method. When a diagonal (lumped) mass matrix is used, the discretised equations are decoupled. Therefore, no matrix inversions and iterations are required when solving non-linear problems. Application of the explicit time integration scheme reduces the time required to compute the brain deformations by two orders of magnitude in comparison to implicit integration typically used in commercial finite element codes like ABAQUS [112]. This algorithm is also implemented on GPU (NVIDIA Tesla C1060 installed on a PC with Intel Core2 Quad CPU) for real-time computation [11] so that the entire model solution takes less than 4 seconds on commonly available hardware.

The application of the biomechanics-based approach does not require any parameter tuning, and the results presented in the next section demonstrate the predictive (rather than explanatory) power of this method.

6.3.6 Results and Validation

6.3.6.1 Qualitative Evaluation

Deformation field The physical plausibility of the registration results is verified by examining the computed displacement vector at voxels of the pre-operative image domain. The deformations are computed at voxel centres only for a region of interest near the tumour.

Overlap of edges To obtain a qualitative assessment of the degree of alignment after registration, one must examine the overlap of corresponding anatomical features of the intra-operative and registered pre-operative image. For this purpose, tumours and ventricles in both registered pre-operative and intra-operative images can be segmented, and their surfaces can be compared [97]. Image segmentation is time-consuming, subjective, not fully automated and not suitable for comparing

a large number of image pairs [113]. Therefore we chose Canny edges [114] as features for comparison [9]. Edges are regarded as useful and easily recognisable features, and they can be detected using techniques that are automated and fast. Canny edges obtained from the intra-operative and registered pre-operative image slices are labelled in different colours and overlaid.

6.3.6.2 Quantitative Evaluation

For a quantitative evaluation of the accuracy of the displacement calculations, we used the edge-based Hausdorff distance. This methodology, based on pioneering work of [115], is described in detail in [9].

While measuring the misalignments between two medical images, it is desirable to calculate the distance between local features (in the case of brain MRI considered here, the automatically detected Canny edges) in two images that correspond to each other. We define directed distance between two sets of edges as

$$h_e\left(\mathbf{A}^e, \mathbf{B}^e\right) = \underset{a_i^e \in \mathbf{A}^e}{\arg\max} \left[\underset{b_j^e \in \mathbf{B}^e}{\arg\min} \left\| a_i^e - b_j^e \right\| \right] \tag{6.3}$$

where $\mathbf{A}^e = \left\{a_1^e, \cdots, a_m^e\right\}$ and $\mathbf{B}^e = \left\{b_1^e, \cdots, b_n^e\right\}$ are two sets of edges.

The quantity $\left\| a_i^e - b_j^e \right\|$ in Eq. 6.3 is just the point-based Hausdorff distance between two point sets $\mathbf{M} = \{m_1, \cdots, m_p\}$ and $\mathbf{T} = \{t_1, \cdots, t_q\}$ representing edges a_i^e and b_i^e, respectively,

$$\left\| a_i^e - b_j^e \right\| := d\left(a_i^e - b_j^e\right) = \max\left(h\left(\mathbf{T}, \mathbf{M}\right), h\left(\mathbf{M}, \mathbf{T}\right)\right) \tag{6.4}$$

Now the edge-based Hausdorff distance is defined as

$$H_e\left(\mathbf{A}^e, \mathbf{B}^e\right) = \max\left(h_e\left(\mathbf{A}^e, \mathbf{B}^e\right), h_e\left(\mathbf{B}^e, \mathbf{A}^e\right)\right) \tag{6.5}$$

Similar to the percentile point-based Hausdorff distance, one can construct a percentile edge-based Hausdorff distance:

$$h_{\mathrm{P}_e}\left(\mathbf{A}^e, \mathbf{B}^e\right) = \underset{a_i^e \in \mathbf{A}^e}{\mathrm{P}^{\mathrm{th}}} \left[\underset{b_j^e \in \mathbf{B}^e}{\arg\min} \left\| a_i^e - b_j^e \right\| \right] \tag{6.6}$$

This percentile edge-based Hausdorff distance is not only useful for removing outlier edge pairs but can also be interpreted in a different way. The Pth percentile Hausdorff distance, 'D', between two images means that 'P' percent of total edge pairs has a Hausdorff distance below D. Therefore, instead of reporting only one Hausdorff distance value (using Eq. 6.5), Eq. 6.6 can be used to report Hausdorff

distance values for different percentiles. A plot of the Hausdorff distance values at different percentiles immediately reveals the percentage of edges that have misalignments below an acceptable error.

6.3.6.3 Results

Qualitative Evaluation of Registration Results

Deformation Field

The deformation fields predicted by the biomechanical model are compared to these obtained from the BSpline transform (available in 3D Slicer [116]) used to register pre- to intra-operative neuroimages. These deformation fields are three dimensional. However, for clarity, only arrows representing 2D vectors (x and y components of displacement) are shown overlaid on undeformed pre-operative slices. Each of these arrows represents the displacement of a voxel of the pre-operative image domain. In general the displacement fields calculated by the BSpline registration algorithm are similar to the predicted displacements by the biomechanical model at the outer surface of the brain, but in the interior of the brain volume, the displacement vectors differ in both magnitude and direction (Fig. 6.10).

Overlap of Canny Edges

From Fig. 6.11 we can see that misalignment between the edges detected from the intra-operative images and the edges from the pre-operative images updated to the intra-operative brain geometry is much lower for the biomechanics-based warping than for BSpline registration. This is an indication that the biomechanics-based prediction of brain deformations may perform more reliably than the BSpline registration algorithm if large deformations are involved.

Quantitative Evaluation of Registration Results

The plot of percentile edge-based Hausdorff distance (HD) versus the corresponding percentile provides an estimation of the percentage of edges whose displacements have been computed with sufficient accuracy. As the accuracy of edge detection is limited by the image resolution, an alignment error smaller than two times the original in-plane resolution of the intra-operative image (which is 0.86 mm for the 13 cases considered) is difficult to avoid [117]. Hence, for the clinical cases analysed here, we considered any edge pair having an HD value less than 1.7 mm to be successfully registered. This choice is consistent with the fact that it is generally considered that manual neurosurgery has an accuracy of no better than 1 mm [117, 118]. It is obvious from Fig. 6.12 that biomechanical warping was able to successfully register more edges than the BSpline registration.

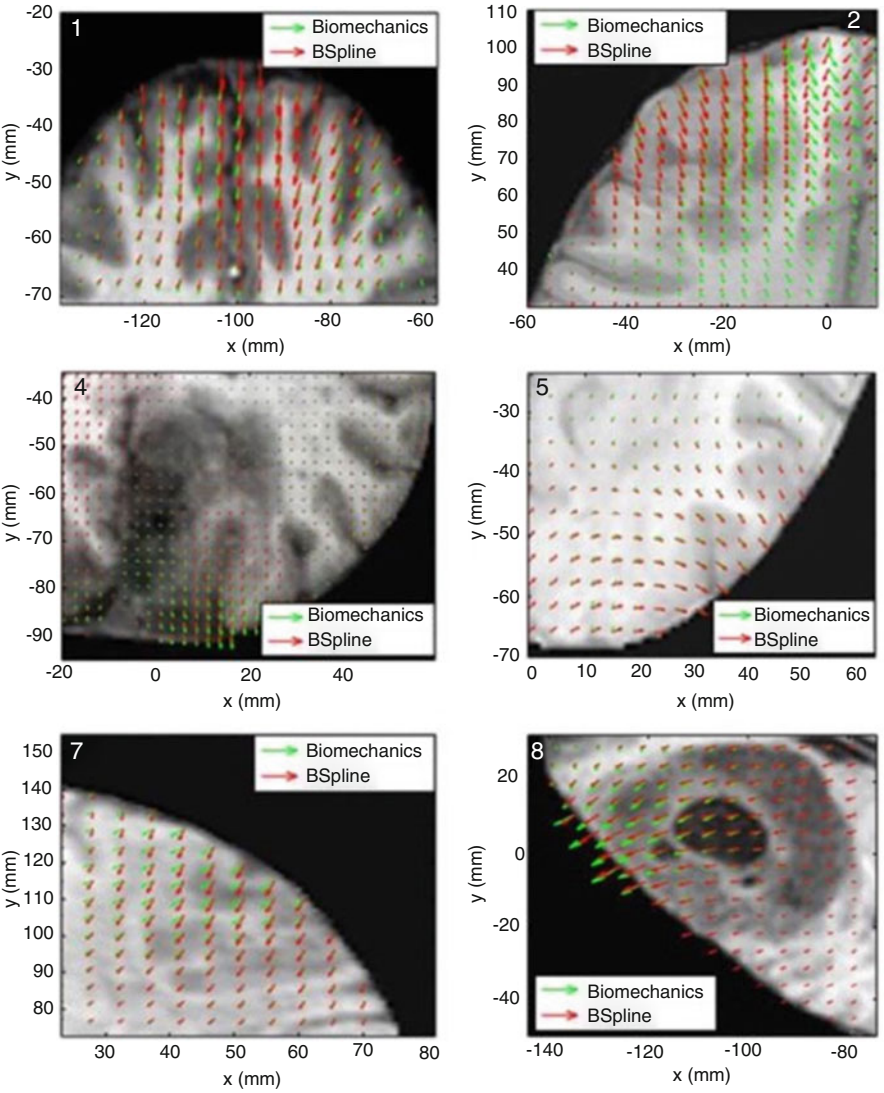

Fig. 6.10 The predicted deformation fields overlaid on an axial slice of pre-operative image (six examples). An arrow represents a 2D vector consisting of the x (R-L) and y (A-P) components of displacement at a voxel centre. Green arrows show the deformation field predicted by the biomechanical model. Red arrows show the deformation field calculated by the BSpline algorithm. The number on each image denotes a particular neurosurgery case. (Modified from [93])

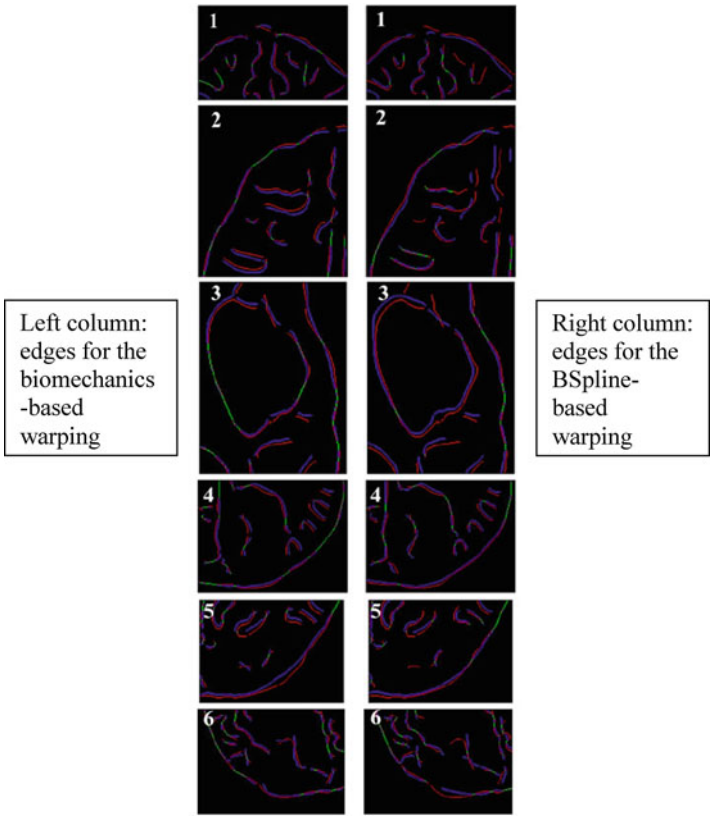

Fig. 6.11 Canny edges extracted from intra-operative and the registered pre-operative image slices overlaid on each other. Red lines represent the nonoverlapping pixels of the intra-operative slice, and blue lines represent the nonoverlapping pixels of the pre-operative slice. Green lines represent the overlapping pixels. The number on each image denotes a particular neurosurgery case. For each case, the left image shows edges for the biomechanics-based warping, and the right image shows edges for the BSpline-based registration. (Image modified from [81])

6.4 Conclusions

Computational mechanics has become a central enabling discipline that has led to greater understanding and advances in modern science, technology and engineering [119]. It is now in a position to make a similar impact in medicine. We have discussed modelling approaches to two applications of clinical relevance: surgical simulation and neuroimage registration. These problems can be reasonably characterised with the use of purely mechanical terms such as displacements, internal forces, etc. Therefore they can be analysed using the methods of continuum mechanics. Moreover similar methods may find applications in modelling the development of structural diseases of the brain [42, 120–122].

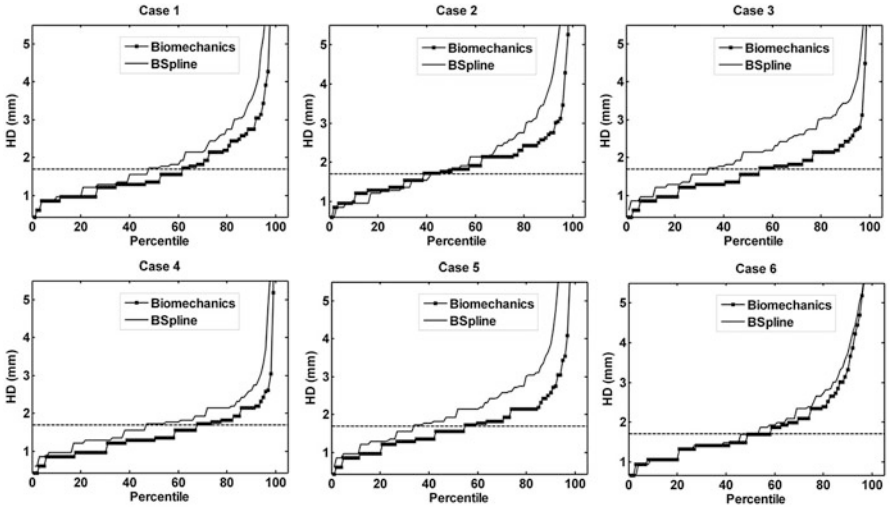

Fig. 6.12 The plot of percentile edge-based Hausdorff distance between intra-operative and registered pre-operative images against the corresponding percentile of edges for axial slices. The horizontal line is the 1.7 mm mark. Six representative examples. Image modified from [93]

As the brain undergoes large displacements (∼10–20 mm in the case of a brain shift) and its mechanical response to external loading is strongly non-linear, we advocate the use of general, non-linear procedures for the numerical solution of the proposed models.

The brain's complicated mechanical behaviour: non-linear stress strain, stress-strain-rate relationships and much lower stiffness in extension than in compression require very careful selection of the constitutive model for a given application. The selection of the constitutive model for surgical simulation problems depends on the characteristic strain rate of the process to be modelled and to a certain extent on computational efficiency considerations. Fortunately, as shown in Sections 6.2.3 and 6.2.4, as well as in [41, 52], the precise knowledge of patient-specific mechanical properties of brain tissue is not required for intra-operative image registration.

A number of challenges must be met before computer-integrated surgery systems based on computational biomechanical models can become as widely used as computer-integrated manufacturing systems are now. As we deal with individual patients, methods to produce patient-specific computational grids quickly and reliably must be improved [1]. Substantial progress in automatic meshing methods is required, or alternatively meshless methods [12] may provide a solution (see Chap. 12 of this book). Computational efficiency is an important issue, as intra-operative applications, requiring reliable results within approximately 40 seconds, are most appealing. Progress can be made in non-linear algorithms by identifying parts that can be precomputed and parts that do not have to be calculated at every time step. One such possibility is to use the total Lagrangian formulation of the finite element method [64, 109, 123], where all field variables are related to the original (known) configuration of the system, and therefore most spatial derivatives

can be calculated before the simulation commences during the preprocessing stage (see Chap. 10 of this book). Implementation of algorithms in parallel on networks of processors and harnessing the computational power of graphics processing units [11] provide a challenge for the coming years.

Acknowledgements The financial support of the Australian Research Council (Grants No. DP0343112, DP0664534, DP1092893, DP120100402, DP160100714 and LX0560460), National Health and Medical Research Council (Australia) (APP1006031, APP1144519, APP1162030) and National Institutes of Health (Grant No. 1-RO3-CA126466-01A1) is gratefully acknowledged. We thank our collaborators Dr. Ron Kikinis and Dr. Simon Warfield from Harvard Medical School and Dr. Kiyoyuki Chinzei and Dr. Toshikatsu Washio from Surgical Assist Technology Group of AIST, Japan, for the help in various aspects of our work.

The medical images used in the present study (provided by Dr. Simon Warfield) were obtained in the investigation supported by a research grant from the Whitaker Foundation and by NIH grants R21 MH67054, R01 LM007861, P41 RR13218 and P01 CA67165.

We thank Toyota Central R&D Labs. (Nagakute, Aichi, Japan) for providing the THUMS brain model.

References

1. Wittek, A., Grosland, N.M., Joldes, G.R., Magnotta, V., Miller, K.: From finite element meshes to clouds of points: a review of methods for generation of computational biomechanics models for patient-specific applications. Ann. Biomed. Eng. **44**(1), 3–15 (2016)
2. Bucholz, R., MacNeil, W., McDurmont, L.: The operating room of the future. Clin. Neurosurg. **51**, 228–237 (2004)
3. Nakaji, P., Speltzer, R.F.: Innovations in surgical approach: the marriage of technique, technology, and judgement. Clin. Neurosurg. **51**, 177–185 (2004)
4. Roberts, D.W., Hartov, A., Kennedy, F.E., Miga, M.I., Paulsen, K.D.: Intraoperative brain shift and deformation: a quantitative analysis of cortical displacement in 28 cases. Neurosurgery. **43**, 749–758 (1998)
5. Ferrant, M., Nabavi, A., Macq, B., Black, P., Jolesz, F.A., Kikinis, R., Warfield, S.K.: Serial registration of interoperative MR images of the brain. Med. Image Anal. **6**(4), 337–359 (2002)
6. Warfield, S.K., Talos, F., Tei, A., Bharatha, A., Nabavi, A., Ferrant, M., Black, P.M., Jolesz, F.A., Kikinis, R.: Real-time registration of volumetric brain MRI by biomechanical simulation of deformation during image guided neurosurgery. Comput. Vis. Sci. **5**, 3–11 (2002)
7. Warfield, S.K., Haker, S.J., Talos, F., Kemper, C.A., Weisenfeld, N., Mewes, A.U.J., Goldberg-Zimring, D., Zou, K.H., Westin, C.F., Wells III, W.M., Tempany, C.M.C., Golby, A., Black, P.M., Jolesz, F.A., Kikinis, R.: Capturing intraoperative deformations: research experience at Brigham and Women's hospital. Med. Image Anal. **9**(2), 145–162 (2005)
8. Wittek, A., Miller, K., Kikinis, R., Warfield, S.K.: Patient-specific model of brain deformation: application to medical image registration. J. Biomech. **40**, 919–929 (2007)
9. Garlapati, R.R., Mostayed, A., Joldes, G.R., Wittek, A., Doyle, B., Miller, K.: Towards measuring neuroimage misalignment. Comput. Biol. Med. **64**, 12–23 (2015)
10. Mostayed, A., Garlapati, R.R., Joldes, G.R., Wittek, A., Roy, A., Kikinis, R., Warfield, S.K., Miller, K.: Biomechanical model as a registration tool for image-guided neurosurgery: evaluation against BSpline registration. Ann. Biomed. Eng. **41**(11), 2409–2425 (2013)
11. Joldes, G.R., Wittek, A., Miller, K.: Real-time nonlinear finite element computations on GPU - application to neurosurgical simulation. Comput. Methods Appl. Mech. Eng. **199**(49–52), 3305–3314 (2010)

12. Joldes, G.R., Bourantas, G., Zwick, B., Chowdhury, H., Wittek, A., Agrawal, S., Mountris, K., Hyde, D., Warfield, S.K., Miller, K.: Suite of meshless algorithms for accurate computation of soft tissue deformation for surgical simulation. Med. Image Anal. **56**, 152–171 (2019)
13. Halle, M., Talos, I-F., Jakab, M., Makris, N., Meier, D., Wald, L., Fischl, B., Kikinis, R.: Multi-modality MRI-based Atlas of the Brain. 2017 [cited 2018; Available from: http://www.spl.harvard.edu/publications/item/view/2037
14. Arani, A., Murphy, M.C., Glaser, K.J., Manduca, A., Lake, D.S., Kruse, S.A., Jack Jr., C.R., Ehman, R.L., Huston 3rd, J.: Measuring the effects of aging and sex on regional brain stiffness with MR elastography in healthy older adults. NeuroImage. **111**, 59–64 (2015)
15. Guo, J., Hirsch, S., Fehlner, A., Papazoglou, S., Scheel, M., Braun, J., Sack, I.: Towards an elastographic atlas of brain anatomy. PLoS One. **8**(8), e71807 (2013)
16. Hughes, J.D., Fattahi, N., Van Gompel, J., Arani, A., Meyer, F., Lanzino, G., Link, M.J., Ehman, R., Huston, J.: Higher-resolution magnetic resonance elastography in meningiomas to determine intratumoral consistency. Neurosurgery. **77**(4), 653–658; discussion 658–9 (2015)
17. Reiss-Zimmermann, M., Streitberger, K.J., Sack, I., Braun, J., Arlt, F., Fritzsch, D., Hoffmann, K.T.: High resolution imaging of viscoelastic properties of intracranial tumours by multi-frequency magnetic resonance elastography. Clin. Neuroradiol. **25**(4), 371–378 (2015)
18. Murphy, M.C., Huston 3rd, J., Glaser, K.J., Manduca, A., Meyer, F.B., Lanzino, G., Morris, J.M., Felmlee, J.P., Ehman, R.L.: Preoperative assessment of meningioma stiffness using magnetic resonance elastography. J. Neurosurg. **118**(3), 643–648 (2013)
19. Garlapati, R.R., Roy, A., Joldes, G.R., Wittek, A., Mostayed, A., Doyle, B., Warfield, S.K., Kikinis, R., Knuckey, N., Bunt, S., Miller, K.: Biomechanical modeling provides more accurate data for neuronavigation than rigid registration. J. Neurosurg. **120**(6), 1477–1483 (2014)
20. Owen, S.J.: A survey of unstructured mesh generation technology. In: 7th International Meshing Roundtable. Dearborn, Michigan, USA, (1998)
21. Viceconti, M., Taddei, F.: Automatic generation of finite element meshes from computed tomography data. Crit. Rev. Biomed. Eng. **31**(1), 27–72 (2003)
22. Owen, S.J.: Hex-dominant mesh generation using 3D constrained triangulation. Comput. Aided Des. **33**, 211–220 (2001)
23. Castellano-Smith, A.D., et al.: Constructing patient specific models for correcting intraoperative brain deformation. In: 4th International Conference on Medical Image Computing and Computer Assisted Intervention MICCAI Lecture Notes in Computer Science 2208. Utrecht, The Netherlands (2001)
24. Couteau, B., Payan, Y., Lavallée, S.: The mesh-matching algorithm: an automatic 3D mesh generator fo finite element structures. J. Biomech. **33**, 1005–1009 (2000)
25. Luboz, V., Chabanas, M., Swider, P., Payan, Y.: Orbital and maxillofacial computer aided surgery: patient-specific finite element models to predict surgical outcomes. Comput. Methods Biomech. Biomed. Eng. **8**(4), 259–265 (2005)
26. Ferrant, M., Macq, B., Nabavi, A., Warfield, S.K.: Deformable modeling for characterizing biomedical shape changes. In: Discrete Geometry for Computer Imagery: 9th International Conference. Springer, Uppsala (2000)
27. Clatz, O., Delingette, H., Bardinet, E., Dormont, D., Ayache, N.: Patient specific biomechanical model of the brain: application to Parkinson's disease procedure. In: International Symposium on Surgery Simulation and Soft Tissue Modeling (IS4TM'03), Springer, Juan-les-Pins (2003)
28. Horton, A., Wittek, A., Miller, K.: Computer simulation of brain shift using an element free Galerkin method. In: 7th International Symposium on Computer Methods in Biomechanics and Biomedical Engineering CMBEE 2006. Antibes, France (2006)
29. Horton, A., Wittek, A., Miller, K.: Towards meshless methods for surgical simulation. In: Computational Biomechanics for Medicine Workshop, Medical Image Computing and Computer-Assisted Intervention MICCAI 2006. Copenhagen, Denmark (2006)
30. Horton, A., Wittek, A., Miller, K.: Subject-specific biomechanical simulation of brain indentation using a meshless method. In: International Conference on Medical Image Computing and Computer-Assisted Intervention MICCAI 2007. Springer, Brisbane (2007)

31. Belytschko, T., Lu, Y.Y., Gu, L.: Element-free Galerkin methods. Int. J. Numer. Methods Eng. **37**, 229–256 (1994)
32. Liu, G.R.: Mesh Free Methods: Moving Beyond the Finite Element Method. CRC Press, Boca Raton (2003)
33. Li, S., Liu, W.K.: Meshfree Particle Methods. Springer-Verlag Berlin Heidelberg (2004)
34. Horton, A., Wittek, A., Joldes, G., Miller, K.: A meshless Total Lagrangian explicit dynamics algorithm for surgical simulation. Int. J. Numer. Methods Biomed. Eng. **26**, 117–138 (2010)
35. Zhang, J.Y., Joldes, G.R., Wittek, A., Horton, A., Warfield, S.K., Miller, K.: Neuroimage as a biomechanical model. Towards new computational biomechanics of the brain. In: Nielsen, P.M.F., Miller, K., Wittek, A. (eds.) Computational Biomechanics for Medicine: Deformation and Flow, pp. 19–28. Springer, New York (2012)
36. Miller, K., Horton, A., Joldes, G., Wittek, A.: Beyond finite elements: a comprehensive, patient-specific neurosurgical simulation utilising a meshless method. J. Biomech. (2012). Accepted for publication on 31 July 2012
37. Hagemann, A., Rohr, K., Stiehl, H.S., Spetzger, U., Gilsbach, J.M.: Biomechanical modeling of the human head for physically based, nonrigid image registration. IEEE Trans. Med. Imaging – Special Issue Model-Based Anal Med Images. **18**(10), 875–884 (1999)
38. Miga, M.I., Paulsen, K.D., Hoopes, P.J., Kennedy, F.E., Hartov, A., Roberts, D.W.: In vivo quantification of a homogenous brain deformation model for updating preoperative images during surgery. IEEE Trans. Biomed. Eng. **47**(2), 266–273 (2000)
39. Wittek, A., Omori, K.: Parametric study of effects of brain-skull boundary conditions and brain material properties on responses of simplified finite element brain model under angular acceleration in sagittal plane. JSME Int. J. **46**(4), 1388–1398 (2003)
40. Wittek, A., Kikinis, R., Warfield, S.K., Miller, K.: Brain shift computation using a fully nonlinear biomechanical model. In: 8th International Conference on Medical Image Computing and Computer Assisted Surgery MICCAI 2005. Palm Springs (2005)
41. Wittek, A., Hawkins, T., Miller, K.: On the unimportance of constitutive models in computing brain deformation for image-guided surgery. Biomech. Model. Mechanobiol. **8**, 77–84 (2009)
42. Dutta-Roy, T., Wittek, A., Miller, K.: Biomechanical modelling of Normal pressure hydrocephalus. J. Biomech. **41**(10), 2263–2271 (2008)
43. Mostayed, A., Garlapati, R.R., Joldes, G.R., Wittek, A., Kikinis, R., Warfield, S.K., Miller, K.: Intraoperative update of neuro-images: comparison of performance of image warping using patient-specific biomechanical model and BSpline image registration. In: Wittek A., Miller K., Nielsen P.M.F. (eds) Computational Biomechanics for Medicine: Models, Algorithms and Implementation, pp. 127–141. Springer, New York (2013)
44. Hu, J., Jin, X., Lee, J.B., Zhang, L., Chaudhary, V., Guthikonda, M., Yang, K.H., King, A.I.: Intraoperative brain shift prediction using a 3D inhomogeneous patient-specific finite element model. J. Neurosurg. **106**, 164–169 (2007)
45. Joldes, G.R., Wittek, A., Miller, K.: Suite of finite element algorithms for accurate computation of soft tissue deformation for surgical simulation. Med. Image Anal. **13**(6), 912–919 (2009)
46. Joldes, G.R., Wittek, A., Miller, K., Morriss, L.: Realistic and efficient brain-skull interaction model for brain shift computation. In: Computational Biomechanics for Medicine III Workshop, MICCAI. New-York (2008)
47. Yin, Z., Hughes, J.D., Glaser, K.J., Manduca, A., Van Gompel, J., Link, M.J., Romano, A., Ehman, R.L., Huston 3rd, J.: Slip interface imaging based on MR-elastography preoperatively predicts meningioma-brain adhesion. J. Magn. Reson. Imaging. **46**(4), 1007–1016 (2017)
48. Jin, X.: Biomechanical Response and Constitutive Modeling of Bovine Pia-Arachnoid Complex. Wayne State University, Detroit, Michigan, USA (2009)
49. Agrawal, S., Wittek, A., Joldes, G.R., Bunt, S., Miller, K.: Mechanical properties of brain-skull interface in compression. In: Doyle, B.J., Miller, K., Wittek, A., Nielsen, P.M.F. (eds.) Computational Biomechanics for Medicine: New Approaches and New Applications, pp. 83–91. Springer, New York (2015)

50. Mazumder, M.M.G., Miller, K., Bunt, S., Mostayed, A., Joldes, G., Day, R., Hart, R., Wittek, A.: Mechanical properties of the brain–skull interface. Acta Bioeng. Biomech. **15**(2), 9 (2013)
51. Wang, F., Han, Y., Wang, B., Peng, Q., Huang, X., Miller, K., Wittek, A.: Prediction of brain deformations and risk of traumatic brain injury due to closed-head impact: Quantitative analysis of the effects of boundary conditions and brain tissue constitutive model. Biomech. Model. Mechanobiol. (2018). https://doi.org/10.1007/s10237-018-1021-z
52. Miller, K., Lu, J.: On the prospect of patient-specific biomechanics without patient-specific properties of tissues. J. Mech. Behav. Biomed. Mater. **27**, 154–166 (2013)
53. McAnearney, S., Fedorov, A., Joldes, G., Hata, N., Tempany, C., Miller, K., Wittek, A.: The effects of Young's Modulus on predicting prostate deformation for MRI-guided interventions. In: Computation Biomechanics for Medicine V. The Workshop affiliated with Medical Image Computing and Computer Assisted Intervention Conference MICCAI 2010. Beijing (2010)
54. Miller, K.: Constitutive modelling of abdominal organs (Technical note). J. Biomech. **33**, 367–373 (2000)
55. Bilston, L.E. (ed.): Neural Tissue Biomechanics. Studies in Mechanobiology, Tissue Engineering and Biomaterials. Springer, Berlin (2011)
56. Miller, K.: Method of testing very soft biological tissues in compression. J. Biomech. **38**, 153–158 (2005)
57. Miller, K.: How to test very soft biological tissues in extension. J. Biomech. **34**(5), 651–657 (2001)
58. Ferrant, M., Nabavi, A., Macq, B., Jolesz, F.A., Kikinis, R., Warfield, S.K.: Registration of 3-D intraoperative MR images of the brain using a finite-element biomechanical model. IEEE Trans. Med. Imaging. **20**, 1384–1397 (2001)
59. Warfield, S.K., Haker, S.J., Talos, F., Kemper, C.A., Weisenfeld, N., Mewes, A.U.J., Goldberg-Zimring, D., Zou, K.H., Westin, C.F., Wells III, W.M., Tempany, C.M.C., Golby, A., Black, P.M., Jolesz, F.A., Kikinis, R.: Capturing intraoperative deformations: research experience at Brigham and Women's Hospital. Med. Image Anal. **9**(2), 145–162 (2005)
60. Fung, Y.C.: A First Course In Continuum Mechanics, p. 301. Prentice-Hall, London (1969)
61. Ciarlet, P.G.: Mathematical Elasticity: Three-Dimensional Elasticity, vol. 1. North Holland, The Netherlands (1988)
62. Nowinski, W.L.: Modified Talairach Landmarks. Acta Neurochir. **143**, 1045–1057 (2001)
63. Miller, K., Wittek, A.: Neuroimage registration as displacement - zero traction problem of solid mechanics (lead lecture). In: Computational Biomechanics for Medicine MICCAI-associated Workshop. MICCAI, Copenhagen (2006)
64. Bathe, K.-J.: Finite Element Procedures. Prentice-Hall, Englewood Cliffs (1996)
65. Dumpuri, P., Thompson, R.C., Dawant, B.M., Cao, A., Miga, M.I.: An atlas-based method to compensate for brain shift: preliminary results. Med. Image Anal. **11**(2), 128–145 (2007)
66. Dutta Roy, T.: Does Normal Pressure Hydrocephalus have Mechanistic Causes? The University of Western Australia, Perth (2010)
67. Tavner, A., Roy, T.D., Hor, K.W.W., Majimbi, M., Joldes, G.R., Wittek, A., Bunt, S., Miller, K.: On the appropriateness of modelling brain parenchyma as a biphasic continuum. J. Mech. Behav. Biomed. Mater. **61**, 511–518 (2016)
68. Miller, K., Chinzei, K.: Constitutive modelling of brain tissue: experiment and Theory. J. Biomech. **30**, 1115–1121 (1997)
69. Miller, K., Chinzei, K.: Mechanical properties of brain tissue in tension. J. Biomech. **35**, 483–490 (2002)
70. Mendis, K.K., Stalnaker, R.L., Advani, S.H.: A constitutive relationship for large deformation finite element modeling of brain tissue. J. Biomech. Eng. **117**, 279–285 (1995)
71. Miller, K.: Constitutive modelling of abdominal organs. J. Biomech. **33**, 367–373 (2000)
72. Miller, K., Chinzei, K., Orssengo, G., Bednarz, P.: Mechanical properties of brain tissue in-vivo: experiment and computer simulation. J. Biomech. **33**, 1369–1376 (2000)
73. Miller, K.: Constitutive model of brain tissue suitable for finite element analysis of surgical procedures. J. Biomech. **32**, 531–537 (1999)

74. Nasseri, S., Bilston, L.E., Phan-Thien, N.: Viscoelastic properties of pig kidney in shear, experimental results and modelling. Rheol. Acta. **41**, 180–192 (2002)
75. Bilston, L., Liu, Z., Phan-Tiem, N.: Large strain behaviour of brain tissue in shear: some experimental data and differential constitutive model. Biorheology. **38**, 335–345 (2001)
76. Farshad, M., Barbezat, M., Flüeler, P., Schmidlin, F., Graber, P., Niederer, P.: Material characterization of the pig kidney in relation with the biomechanical analysis of renal trauma. J. Biomech. **32**(4), 417–425 (1999)
77. Walsh, E.K., Schettini, A.: Calculation of brain elastic parameters in vivo. Am. J. Phys. **247**, R637–R700 (1984)
78. Miller, K., Chinzei, K.: Mechanical properties of brain tissue in tension. J. Biomech. **35**, 483–490 (2002)
79. Bilston, L.E., Liu, Z., Phan-Tien, N.: Linear viscoelastic properties of bovine brain tissue in shear. Biorheology. **34**(6), 377–385 (1997)
80. Miller, K.: Biomechanics of the Brain for Computer Integrated Surgery. Publishing House of Warsaw University of Technology, Warsaw (2002)
81. Prange, M.T., Margulies, S.S.: Regional, directional, and age-dependent properties of the brain undergoing large deformation. ASME J. Biomech. Eng. **124**, 244–252 (2002)
82. Seo, J., Kim, Y.-s.: Ultrasound imaging and beyond: recent advances in medical ultrasound. Biomed. Eng. Lett. **7**(2), 57–58 (2017)
83. Dietrich, C.F., Cantisani, V.: Current status and perspectives of elastography. Eur. J. Radiol. **83**(3), 403–404 (2014)
84. Sinkus, R., Tanter, M., Xydeas, T., Catheline, S., Bercoff, J., Fink, M.: Viscoelastic shear properties of in vivo breast lesions measured by MR elastography. Magn. Reson. Imaging. **23**, 159–165 (2005)
85. McCracken, P.J., Manduca, A., Felmlee, J., Ehman, R.L.: Mechanical transient-based magnetic resonance elastography. Magn. Reson. Med. **53**(3), 628–639 (2005)
86. Green, M.A., Bilston, L.E., Sinkus, R.: In vivo brain viscoelastic properties measured by magnetic resonance elastography. NMR Biomed. **21**(7), 755–764 (2008)
87. Glaser, K.J., Manduca, A., Ehman, R.L.: Review of MR elastography applications and recent developments. J. Magn. Reson. Imaging. **36**(4), (2012)
88. Murphy, M.C., Huston 3rd, J., Ehman, R.L.: MR elastography of the brain and its application in neurological diseases. NeuroImage. **187**, 176–183 (2019, Feb)
89. Bathe, K.J.: Finite Element Procedures. Prentice-Hall, Inc., Upper Saddle River (1996)
90. Ma, J., Wittek, A., Singh, S., Joldes, G., Washio, T., Chinzei, K., Miller, K.: Evaluation of accuracy of non-linear finite element computations for surgical simulation: study using brain phantom. Comput. Methods Biomech. Biomed. Eng. **13**(6), 783–794 (2010)
91. Wittek, A., Dutta-Roy, T., Taylor, Z., Horton, A., Washio, T., Chinzei, K., Miller, K.: Subject-specific non-linear biomechanical model of needle insertion into brain. Comput. Methods Biomech. Biomed. Eng. J. **11**(2), 135–146 (2008)
92. Garlapati, R., Roy, A., Joldes, G., Wittek, A., Mostayed, A., Doyle, B., Warfield, S., Kikinis, R., Knuckey, N., Bunt, S., Miller, K.: More accurate neuronavigation data provided by biomechanical modeling instead of rigid registration. J. Neurosurg. **120**(6), 1477–1483 (2014)
93. Mostayed, A., Garlapati, R.R., Joldes, G.R., Wittek, A., Roy, A., Kikinis, R., Warfield, S.K., Miller, K.: Biomechanical model as a registration tool for image-guided neurosurgery: evaluation against BSpline registration. Ann. Biomed. Eng. **41**(11), 2409–2425 (2013)
94. Warfield, S.K., Haker, S.J., Talos, I.-F., Kemper, C.A., Weisenfeld, N., Mewes, U.J., Goldberg-Zimring, D., Zou, K.H., Westin, C.-F., Wells, W.M., Tempany, C.M.C., Golby, A., Black, P.M., Jolesz, F.A., Kikinis, R.: Capturing intraoperative deformations: research experience at Brigham and Women's hospital. Med. Image Anal. **9**(2), 145–162 (2005)
95. Joldes, G.R., Wittek, A., Miller, K.: An adaptive dynamic relaxation method for solving nonlinear finite element problems. Application to brain shift estimation. Int. J. Numer. Methods Biomed. Eng. **27**(2), 173–185 (2011)
96. Wittek, A., Miller, K., Kikinis, R., Warfield, S.K.: Patient-specific model of brain deformation: application to medical image registration. J. Biomech. **40**(4), 919–929 (2007)

97. Wittek, A., Joldes, G., Couton, M., Warfield, S.K., Miller, K.: Patient-specific non-linear finite element modelling for predicting soft organ deformation in real-time; application to non-rigid neuroimage registration. Prog. Biophys. Mol. Biol. **103**(2–3), 292–303 (2010)
98. Wittek, A., Hawkins, T., Miller, K.: On the unimportance of constitutive models in computing brain deformation for image-guided surgery. Biomech. Model. Mechanobiol. **8**(1), 77–84 (2009)
99. Joldes, G.R., Wittek, A., Miller, K.: Non-locking tetrahedral finite element for surgical simulation. Commun. Numer. Methods Eng. **25**(7), 827–836 (2009)
100. Grosland, N.M., Shivanna, K.H., Magnotta, V.A., Kallemeyn, N.A., DeVries, N.A., Tadepalli, S.C., Lislee, C.: IA-FEMesh: an open-source, interactive, multiblock approach to anatomic finite element model development. Comput. Methods Prog. Biomed. **94**(1), 96–107 (2009)
101. Joldes, G.R., Wittek, A., Miller, K.: Cortical surface motion estimation for brain shift prediction. In: Miller, K., Nielsen, P.M.F. (eds.) Computational Biomechanics for Medicine, pp. 53–62. Springer, New York (2010)
102. Miller, K., Lu, J.: On the prospect of patient-specific biomechanics without patient-specific properties of tissues. J. Mech. Behav. Biomed. Mater. **27**, 154 (2013)
103. Joldes, G.R., Wittek, A., Miller, K., Morriss, L.: Realistic and efficient brain-skull interaction model for brain shift computation. In: Miller, K., Nielsen, P.M.F. (eds.) Computational Biomechanics for Medicine III. Springer, New York (2008)
104. Wittek, A., Omori, K.: Parametric study of effects of brain-skull boundary conditions and brain material properties on responses of simplified finite element brain model under angular acceleration impulse in sagittal plane. JSME Int. J. **46**(4), 1388–1399 (2003)
105. Joldes, G.R., Wittek, A., Couton, M., Warfield, S.K., Miller, K.: Real-time prediction of brain shift using nonlinear finite element algorithms. In: Yang, G.Z., Hawkes, D., Rueckert, D., Nobel, A., Taylor, C. (eds.) Medical Image Computing and Computer-Assisted Intervention - Miccai 2009, Pt II, pp. 300–307. Springer, Berlin/Heidelberg (2009)
106. Miller, K., Chinzei, K.: Mechanical properties of brain tissue in tension. J. Biomech. **35**(4), 483–490 (2002)
107. Sinkus, R., Tanter, M., Xydeas, T., Catheline, S., Bercoff, J., Fink, M.: Viscoelastic shear properties of in vivo breast lesions measured by MR elastography. Magn. Reson. Imaging. **23**(2), 159–165 (2005)
108. Joldes, G.R., Wittek, A., Miller, K.: Suite of finite element algorithms for accurate computation of soft tissue deformation for surgical simulation. Med. Image Anal. **13**(6), 912–919 (2009)
109. Miller, K., Joldes, G., Lance, D., Wittek, A.: Total Lagrangian explicit dynamics finite element algorithm for computing soft tissue deformation. Commun. Numer. Methods Eng. **23**(2), 121–134 (2007)
110. Miller, K., Joldes, G.R., Bourantas, G., Warfield, S.K., Hyde, D.E., Kikinis, R., Wittek, A.: Biomechanical Modeling and Computer Simulation of the Brain during Neurosurgery. arXiv:1904.01192 (2019)
111. Joldes, G.R., Wittek, A., Miller, K.: Computation of intraoperative brain shift using dynamic relaxation. Comput. Methods Appl. Mech. Eng. **198**(41–44), 3313–3320 (2009)
112. ABAQUS: Abaqus 6.14 Documentation. Rhode Island. USA (2018)
113. Fedorov, A., Billet, E., Prastawa, M., Gerig, G., Radmanesh, A., Warfield, S.K., Kikinis, R., Chrisochoides, N.: Evaluation of brain MRI alignment with the Robust Hausdorff Distance Measures. In: Bebis, G. (ed.) Advances in Visual Computing, Pt I, pp. 594–603 (2008)
114. Canny, J.: A computational approach to edge detection. IEEE Trans. Pattern Anal. Mach. Intell. **8**(6), 679–698 (1986)
115. Huttenlocher, D.P., Klanderman, G.A., Rucklidge, W.J.: Comparing images using the Hausdorff distance. IEEE Trans. Pattern Anal. Mach. Intell. **15**(9), 850–863 (1993)
116. Fedorov, A., Beichel, R., Kalpathy-Cramer, J., Finet, J., Fillion-Robin, J.C., Pujol, S., Bauer, C., Jennings, D., Fennessy, F., Sonka, M.: 3D slicer as an image computing platform for the quantitative imaging network. Magn. Reson. Imaging. **30**(9), 1323–1341 (2012)

117. Warfield, S.K., Haker, S.J., Talos, I.F., Kemper, C.A., Weisenfeld, N., Mewes, A.U.J., Goldberg-Zimring, D., Zou, K.H., Westin, C.F., Wells, W.M., Tempany, C.M.C., Golby, A., Black, P.M., Jolesz, F.A., Kikinis, R.: Capturing intraoperative deformations: research experience at Brigham and Women's Hospital. Med. Image Anal. **9**(2), 145–162 (2005)
118. Nakaji, P., Spetzler, R.F.: Innovations in surgical approach: the marriage of technique, technology, and judgment. Clin. Neurosurg. **51**, 177–185 (2004)
119. Oden, J.T., Belytschko, T., Babuska, I., Hughes, T.J.R.: Research directions in computational mechanics. Comput. Methods Appl. Mech. Eng. **192**, 913–922 (2003)
120. Taylor, Z., Miller, K.: Reassessment of brain elasticity for analysis of biomechanisms of hydrocephalus. J. Biomech. **37**, 1263–1269 (2004)
121. Miller, K., Taylor, Z., Nowinski, W.L.: Towards computing brain deformations for diagnosis, prognosis and neurosurgical simulation. J. Mech. Med. Biol. **5**(1), 105–121 (2005)
122. Berger, J., Horton, A., Joldes, G., Wittek, A., Miller, K.: Coupling finite element and mesh-free methods for modelling brain deformations in response to tumour growth. In: Computational Biomechanics for Medicine III MICCAI-Associated Workshop. MICCAI, New York City (2008)
123. Zienkiewicz, O.C., Taylor, R.L.: The Finite Element Method. Mcgraw-Hill Book Company, London (2000)

Chapter 7
Biomechanical Modelling of the Brain for Neuronavigation in Epilepsy Surgery

Karol Miller, Angus C. R. Tavner, Louis P. M. Menagé, Nicholas Psanoudakis, Grand Roman Joldes, Simon K. Warfield, Damon Hyde, and Adam Wittek

7.1 Introduction

It is commonly believed that epilepsy can be treated and managed, but ultimately not cured; a quick internet search for 'epilepsy' will confirm this. However this is not the case, as amongst the more medically informed, it is well known that precisely targeted surgery is a curative treatment [7]. Engel also argues that the surgical treatment of epilepsy is 'arguably the most underutilised of all proven effective therapeutic interventions in the field of medicine' [7]. The explanation for this apparent underuse of surgery to cure epilepsy lies in the phrase 'precisely targeted': clinicians are often unable to characterise or locate epileptic activity within the brain accurately enough to identify which regions to resect and proceed with surgery [19].

In this chapter we describe how computational biomechanics of the brain (see also Chap. 6 in this book) can help to precisely and reliably locate seizure-onset zones (SOZ) and visualise them with respect to pre-operative brain anatomy as part of a system to improve intra-operative visualisation, navigation and monitoring.

K. Miller (✉) · A. C. R. Tavner · L. P. M. Menagé · N. Psanoudakis · G. R. Joldes · A. Wittek
Intelligent Systems for Medicine Laboratory, The University of Western Australia, Perth, WA, Australia

Institute of Mechanics and Advanced Materials, Cardiff School of Engineering, Cardiff University, Cardiff, Wales, UK
e-mail: karol.miller@uwa.edu.au

S. K. Warfield · D. Hyde
Computational Radiology Laboratory, Boston Children's Hospital and Harvard Medical School, Boston, MA, USA

K. Miller (ed.), *Biomechanics of the Brain*, Biological and Medical Physics, Biomedical Engineering, https://doi.org/10.1007/978-3-030-04996-6_7

7.1.1 Background

Epilepsy is a chronic neurological disorder that affects over 70 million people, costs over $50 billion annually and first arises during childhood for 75% of patients [18]. Surgical intervention can be curative but is rarely used because of difficulties with localisation of epileptogenic regions of the brain and subsequent surgical planning. When MRI-visible lesions are not present, surgical planning must rely on functional localisation. Intracranial EEG (iEEG) is the most effective method for functional localisation of the SOZ; invasive electrodes are implanted and monitored for several days and then removed during a second surgery when the resection is performed [4]. Collecting data from directly on or within the cortex significantly increases the spatial data fidelity when compared to scalp EEG measurements and allows more accurate identification and location of the SOZ.

Despite being the most accurate available technology for monitoring seizure activity, iEEG does not guarantee surgical success. Unsuccessful surgeries are performed, in part, due to difficulties in the clinical interpretation of the measured invasive data. In current practice, electrodes are aligned to the cortex using a combination of intra-operative photographs and diagrams to estimate the placements of electrode grids and depth electrodes. While this allows generalised alignment, it is not quantitative and does not provide the degree of accuracy necessary for emerging precision surgical techniques such as radio frequency (RF) and laser ablation [6, 24] and focused ultrasound [17]. To fully utilise the precision of these emerging techniques, accurate alignment algorithms are needed to enable precise identification of the SOZ with respect to both pre-operative and intra-operative imaging.

A significant factor contributing to electrode alignment error is the physical shifting of brain tissue during invasive measurement (see Fig. 7.1 next page). Electrode grids in the intracranial space, and the body's inflammatory response to the craniotomy, displace and deform the brain from the configuration observed in pre-surgical MR imaging [23, 27]. To ensure accurate alignment of electrode placements and correct clinical evaluation of invasive data, brain shift must be accurately modelled and accounted for.

In Chap. 6 we described in detail effective approaches for computing brain deformations during neurosurgery. In this chapter we focus on applying these modelling methods to the particularly challenging and clinically relevant problem of the registration of pre-operative MRI to intra-operative CT (with electrodes implanted) images.

Accurate registration is achieved using reliable computation of the deformations within the brain due to invasive electrode placement. An accurate model of brain shift enables us to accurately map presurgical imaging onto the deformed intra-operative space, accurately aligning these scans with X-ray CT (Fig. 7.1), thereby providing the location of electrodes as well as the SOZ identified by them relative to the anatomical structures of the brain as seen on pre-operative MRI 'warped' onto intra-operative CT images.

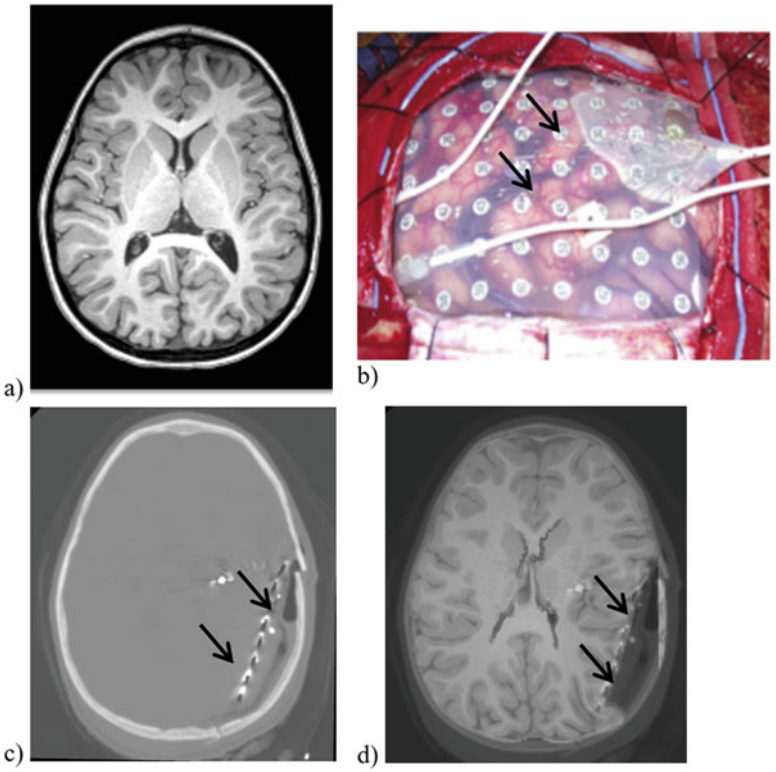

Fig. 7.1 (**a**) Pre-operative MRI, (**b**) intra-operative photograph of implanted intracranial electrodes (pointed by arrows), (**c**) intra-operative CT with electrodes implanted and (**d**) pre-operative MRI registered onto intra-operative CT. In this chapter we explain how to obtain image 1D using computational biomechanics of the brain. These are two-dimensional sections of three-dimensional image volumes. We have successfully registered four cases [12]

7.1.2 Modelling the Intra-operative Deformation

A recent review [8] summarises brain shift causes, measurements and compensation methods. Modelling the behaviour of the brain remains a key issue to provide a priori knowledge for image-guided surgery [16]. The biomechanical property experiments of Miller [14] and others (see, e.g. [5]) significantly contributed to the understanding of the physics of brain tissue. We also quantified the relative importance of various parameters required for accurate modelling of intra-operative deformations of the brain, such as geometry, boundary conditions, loading and constitutive properties (see Chap. 6 of this book and [14]). Moreover, we have developed very computationally efficient algorithms that allow the equations describing brain biomechanical models to be solved intra-operatively (i.e. in less than 10 seconds) on standard computing hardware [10].

A number of groups have investigated the use of intra-operative ultrasound in order to provide data that could be used to update pre-operative models to account for brain shift [20, 21]. Laser range scanners (LRS) [13, 22] and stereo cameras [22] have also been used. However the data obtained using these techniques cannot be directly used for surgical navigation, as images typically have poor contrast and resolution, and surface data alone is not sufficient to guide neuronavigation.

Summary

1. Inaccuracies in the identification of invasive electrode placements and the limited ability to relate the SOZ identified by these electrodes to features of brain anatomy prevent iEEG data from being fully utilised to identify appropriate resection regions.
2. A method to reliably and precisely identify the location of seizure-onset zones could lead to curing millions of patients of epilepsy.
3. The key technology we describe in this chapter is biomechanics-based prediction of brain deformations resulting from the invasive electrode placement and the use of these deformations to register a pre-operative MRI image onto an intra-operative CT image with electrodes in place (Fig. 7.1d).

In Sect. 7.2 we describe how to adapt the methods presented in Chap. 6 to model brain deformations resulting from invasive electrode placement. In Sect. 7.3, to demonstrate the appropriateness and effectiveness of our biomechanics-based methods, we consider results of brain deformation computation for a specific example of a paediatric epilepsy patient from Boston Children's Hospital. The numerical algorithms devised to efficiently solve brain deformation models are described in Chaps. 10 and 11.

7.2 Computing Brain Deformations Due to Insertion of Invasive Electrodes

Biomechanical modelling issues related to *geometry and finite element mesh, boundary conditions, loading and material properties* are briefly summarised below. For a more detailed discussion of these issues, please refer to Chap. 6.

A high-level depiction of the inputs, outputs and software packages used in each step of the analysis is shown in Fig. 7.2, next page.

7.2.1 Geometry

The first step in the construction of model geometry is to develop surface models of the brain parenchyma and ventricles. 3D Slicer (http://www.slicer.org/) is used to segment the regions of interest (ROI) from the patient's MRI with the help of

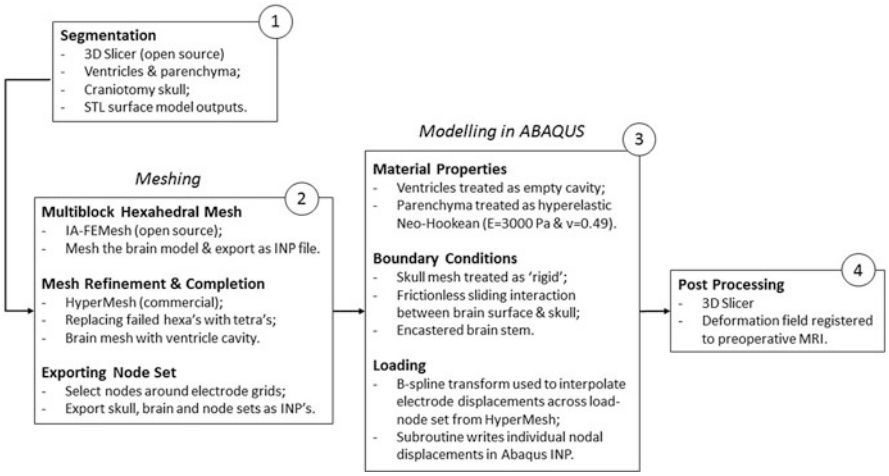

Fig. 7.2 Model formulation diagram

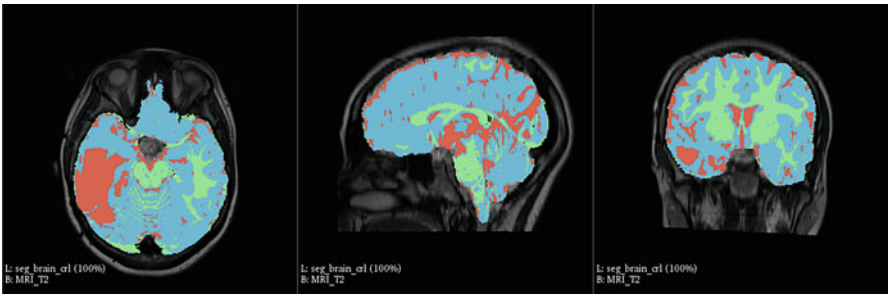

Fig. 7.3 Boston Children's Hospital segmentation maps; Anonymous Case 192

automated thresholding tools. The data is segmented into three separate label maps, including the CSF in red, white matter in green and grey matter in blue (Fig. 7.3).

This map is then manually edited to remove the cerebellum, which simplifies the mesh generation and computational analysis. The cerebellum is not mechanically integral with the left and right hemispheres and can therefore be ignored from the analysis. Label map smoothing is also needed to remove the detail of deep sulci and fissures, which are problematic for mesh generation. If the smoothing process is carefully controlled, there is little impact on the deformation computed within the ROI of the brain. The *LabelStatistics* module is used to check the voxel count before and after smoothing to ensure that the smoothing never results in more than 3% volume change. Visual inspection of the sagittal, axial and coronal views also helps to maintain accuracy in the segmentation. Finally, the smoothed label map is exported as an STL surface model, ready for meshing.

The contrast and resolution of the MRI data in the area surrounding the ventricles makes it difficult to accurately apply thresholding and marching algorithms, so the

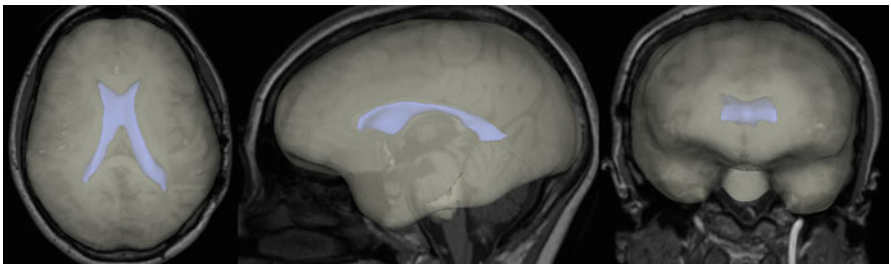

Fig. 7.4 Segmented parenchyma and ventricle surface models

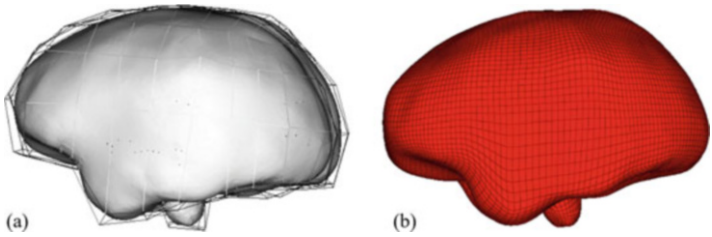

Fig. 7.5 Multiblock meshing in IA-FEMesh. (**a**) Blocks; (**b**) mesh

ventricle segmentation must be performed almost entirely by hand. The label map is again smoothed, to remove surface imperfections, and exported as an STL file. The completed surface models are shown in Fig. 7.4.

7.2.2 Finite Element Meshing

To create the hexa-dominant mesh required for reliable computations (see Chaps. 5 and 10) of a geometry as irregular as the brain, a multiblock method is applied through the open-source package IA-FEMesh from the University of Iowa (https://www.ccad.uiowa.edu/MIMX/projects/IA-FEMesh). The parenchyma surface model is loaded into the programme, and a centralised block is created around it. The block is then split into smaller interconnected grids whose nodes can be dragged to fit closer around the surface of the model (Fig. 7.5a). A completely hexahedral mesh is generated by seeding the edges and projecting through each of the blocks (Fig. 7.5b).

The resulting mesh features good-quality hexahedral elements throughout most of the volume but poor-quality elements close to the surface and around complex changes in geometry. To identify and improve these elements, the model is loaded as an input (INP) file into HyperMesh (https://altairhyperworks.com/product/hypermesh), and quality checks are performed for the warpage, element length and Jacobian characteristics. As discussed in Chaps. 5 and 10, the metrics

to apply in biomechanical models are uncertain and depend on the situation. In this case, it was found that the following targets give a mesh of sufficient quality:

- Warpage: 90°
- Length: 0.5 mm
- Jacobian: 0.5

Elements that fail to meet these criteria are isolated into a separate component and converted into tetrahedral elements before being merged back into the original mesh. Next, the ventricles are imported and a 2D triangular mesh is generated across the surface. To integrate the two components into a single mesh, elements surrounding the ventricles in the parenchyma model are removed to create a void between the two. By selecting the internal faces of this void, tetrahedral elements can be propagated from the brain elements to the 2D surface elements on the ventricles, as shown in Fig. 7.6.

The finl steps in HyperMesh are to create a surface mesh for the skull, which is necessary for modelling the brain/skull interface. The skull is created by copying the outer faces of the brain mesh, offsetting the elements outwards by 0.1 mm to prevent overlap and creating openings at the brainstem and craniotomy. The shape and location of the craniotomy opening in the skull is best obtained by segmenting the skull from the patient's intra-operative CT scan and loading the geometry into HyperMesh as a new component (Fig. 7.7).

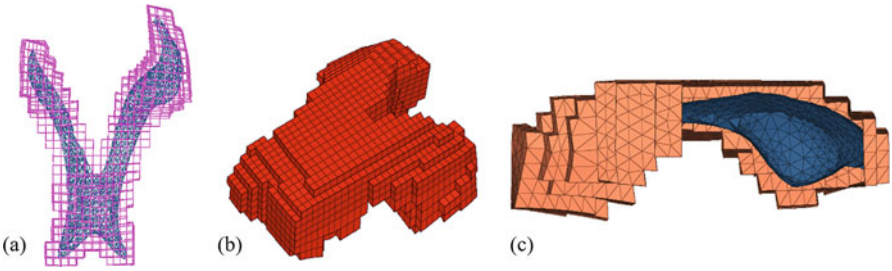

Fig. 7.6 (**a**) Boolean elements; (**b**) faces surrounding void; (**c**) filled tetrahedral elements

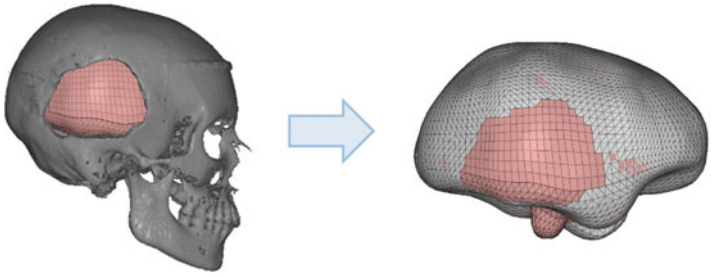

Fig. 7.7 Skull mesh

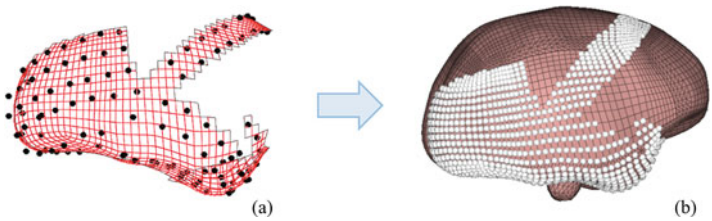

Fig. 7.8 (**a**) Pre-operative electrodes on brain mesh; (**b**) selected node set

Table 7.1 Mesh characteristics

	Brain	Skull
No. of elements (nodes)	48,953 (24,213)	8056 (4073)
Element type(s)	4-noded tetrahedral (66.3% elements) 8-noded hexahedral (33.7% elements)	3-noded triangles
Node set	950 nodes	N/A

N/A Not Applicable

Before exporting the brain and skull meshes, a node set must be created for applying the measured surface displacement loading (see Sect. 7.2.4 of this chapter). To do this, the patient's 3D coordinate data for the electrodes in their pre-operative position are converted to an STL surface model and loaded into HyperMesh. As shown in Fig. 7.8, this allows the elements encompassing the electrodes to be isolated, and then by previewing the nodal equivalence between the selected elements and the original brain mesh, it is possible to save a nodal set corresponding to the displaced surface.

Finally, the meshed parts and node set are exported and combined into a single INP file for importing into Abaqus for analysis. Table 7.1 summarises the mesh attributes.

7.2.3 Boundary Conditions

As explained in Chap. 6, frictionless sliding contact between the brain and the skull is an appropriate choice for the model's boundary condition. We implement this in Abaqus by defining a general surface interaction with a *hard* contact behaviour and a *frictionless* interaction property (equivalent to a penalty condition of 0). Abaqus applies this interaction by calculating the relative overclosure (penetration) of a deforming body into the rigid surface and subsequently modelling the kinematic contact and shear sliding [1]. The remaining boundary conditions in the initial step include assigning a *rigid-body* constraint to the skull, fixing a reference point on the skull mesh in space and fixing a selection of nodes along the base of the brainstem.

7.2.4 Loading

We load the model through imposed displacements on the model surface (see Chap. 6 and [27]). In intra-operative CT (Fig. 7.1c), the implanted electrodes, and the grid which define the deformed surface of the brain, are clearly visible. Rigid alignment of pre-operative MRI with intra-operative CT and projection of the electrode positions onto the deformed brain surface (seen on CT) from the undeformed brain surface (seen on the pre-operative MRI) allow precise definition of surface displacements [23].

Using the intra-operative and pre-operative electrode coordinates, we define a B-spline transform using the *Scattered Transform*[1] module in 3D Slicer. The B-spline transform interpolates the difference between the intra-operative and pre-operative electrode coordinates across all points within the node set defined in HyperMesh. This allows us to calculate an approximation of the intra-operative position of the surface nodes in the brain mesh. To apply the transform, the INP file containing the node set coordinates is first converted into a VTK format so that it can be read into 3D Slicer. Once transformed, the data is converted back to a text-based or csv format so that it can be read into MATLAB for processing. Figure 7.9 is a visual representation of the electrode transform applied to the node set from HyperMesh. The MATLAB script was written to import the two data sets, compute the displacements and subsequently write each displacement as an Abaqus-compatible nodal boundary condition in INP format. In this case, the subroutine

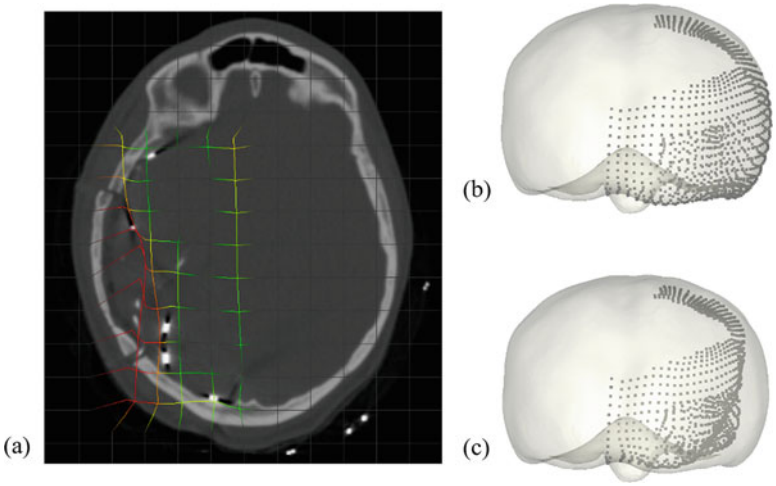

Fig. 7.9 (**a**) Electrode transform in 3D Slicer; (**b**) pre-operative node set; (**c**) node set transformed to the intra-operative position

[1] https://www.slicer.org/wiki/Documentation/Nightly/Extensions/ScatteredTransform

outputs 2850 individual boundary conditions, which are easily transferred to the INP file containing the part and element definitions, before loading into Abaqus CAE for analysis.

The loading is applied gradually over a period of 10 seconds using the *smooth step* amplitude function in Abaqus, which implements a 345 polynomial [1]. This is necessary to prevent excessive distortion in the elements resulting from large displacement increments in each time step.

7.2.5 Material Properties

As explained in Chap. 6 of this book and our papers [15, 26], for problems where loading is prescribed as forced motion of boundaries, the unknown deformation field within the domain depends very weakly on the mechanical properties of the continuum. This feature is of great importance in biomechanical modelling where there are always uncertainties in patient-specific properties of tissues. Therefore we use a simple neo-Hookean [26] constitutive model with Young's modulus of 3000 Pa. To account for approximate incompressibility of brain tissue (see Chap. 4 of this book), we chose a Poisson's ratio of 0.49.

7.2.6 Solution Algorithm and Software

Although the analysis is static, an explicit algorithm is the preferred solver because the nonlinearity of the model makes it difficult and computationally expensive to achieve convergence in every time step (see Chap. 10). The model is run in Abaqus Explicit for 100 simulation seconds to allow sufficient time for a steady-state solution to be achieved. To ensure stability, a minimum time step has been estimated from the characteristic length of the mesh and the dilatational wave speed [1] to be ca. 4×10^{-5} seconds. The default parameters for linear and quadratic bulk viscosity are used, providing a means of damping to control high-frequency oscillations in the solution.

The element formulations available in Abaqus Explicit include linear or quadratic elements. For efficiency, the linear reduced integration hexahedrons (C3D8R) and tetrahedrons (C3D4) are chosen with default hourglass and distortion control (for discussion about appropriate element types for explicit analysis of approximately incompressible materials, see also Chaps. 6 and 10 of this book). The skull is assigned rigid triangular facet elements (R3D3).

7.3 Results

Figure 7.10 shows the computed deformation along the loaded surface of the brain, while Fig. 7.11 shows a comparison of internal sectional views, before and after the simulation.

It should be noted that some areas of the model are being displaced by up to 20 mm. Figure 7.11 also shows a significant amount of compression in the ventricles, which reflects the modelling assumption that enough time passes for the CSF to be displaced. The visualisation of these results illustrates the complexity of the internal brain shift and the severity of the inaccuracies that exist in current localisation practices. It is also important to note that volumetric locking is commonly an issue for first-order tetrahedral elements in an almost incompressible media. Although the tetrahedral elements around the ventricles show quite large deformations on the load side, the results could be an underrepresentation of reality if artificial stiffening is present – particularly on the opposite side of the brain (left hemisphere).

The images above also show a rather blocky and unnatural edge along the indentation where the electrode displacements have been applied. We believe that this unnatural curvature in the deformed model is a result of the mesh quality. The elements within these problematic areas can be up to 11 mm, even though the average element is approximately 4 mm for the rest of the model. This means that the elements are probably too large to capture the smoothness of the deformation in these regions of extreme compression.

In assessing the reliability of the results, we note that a comparison of the energy and displacement outputs over time suggests that a bounded solution has been achieved. Figure 7.12 shows a plot of various energy variables computed over

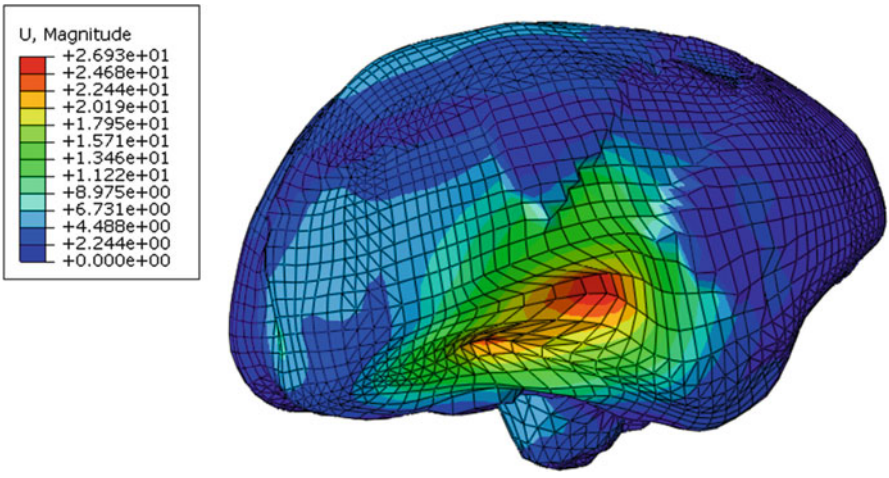

Fig. 7.10 Isometric view of the deformed brain

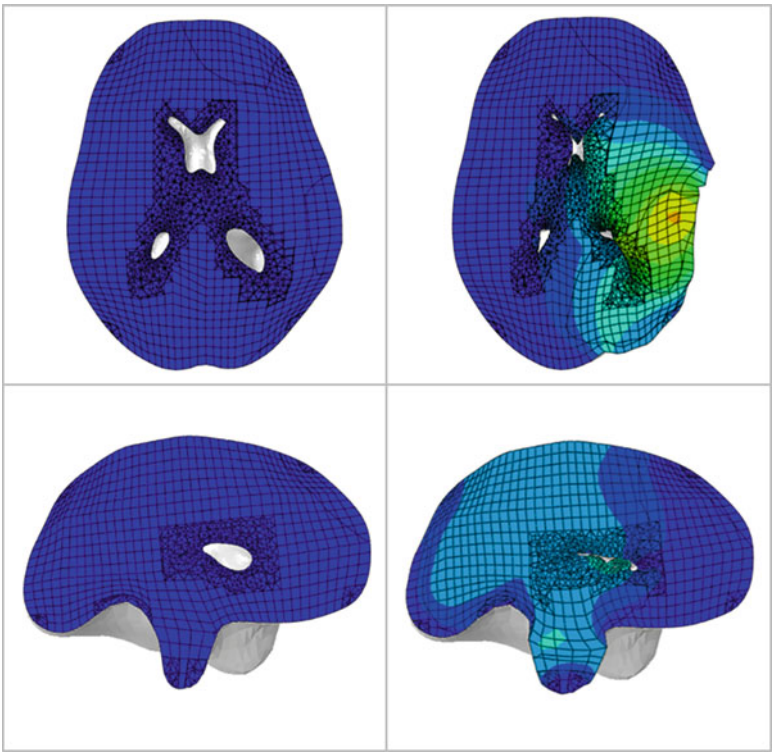

Fig. 7.11 Sectional views of the deformed brain

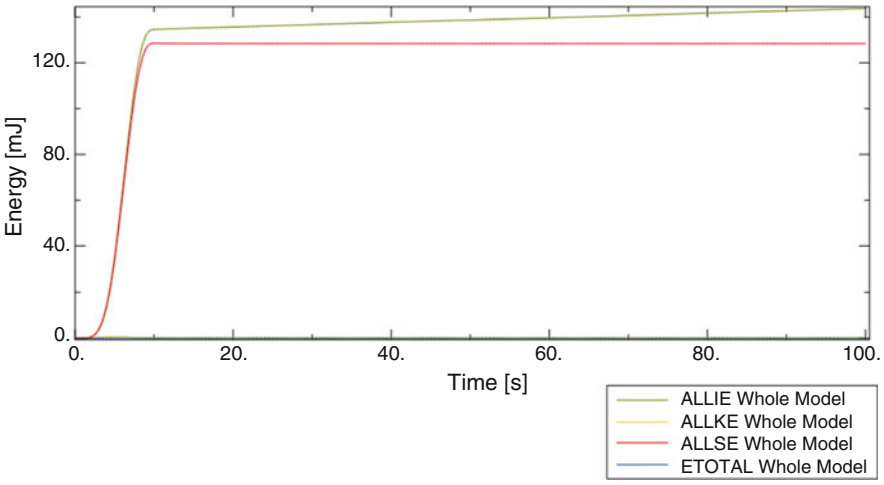

Fig. 7.12 Plot of energy over time

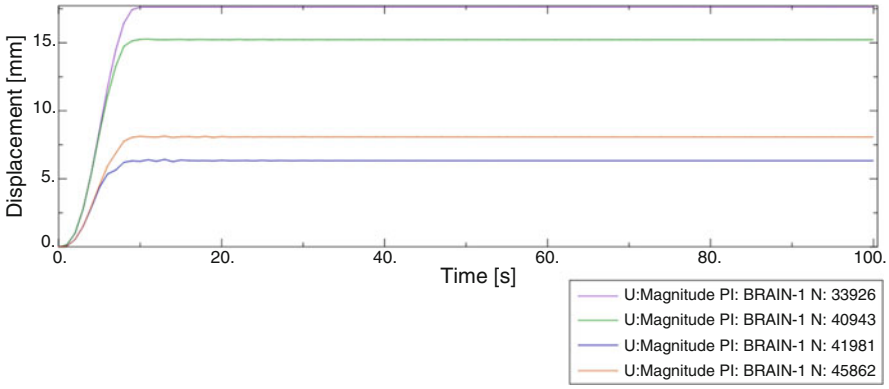

Fig. 7.13 Nodal displacement at ventricle wall over time

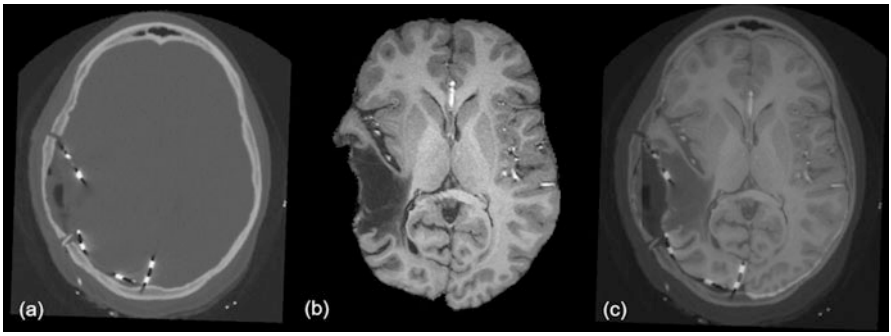

Fig. 7.14 (**a**) Intra-operative CT; (**b**) transformed MRI; (**c**) transformed MRI overlaid on CT

time, including internal energy (ALLIE), kinetic energy (ALLKE), total energy (ETOTAL) and strain energy (ALLSE), which all appear to show stability in the solution output. The displacement of a node along the loaded side of the ventricle cavity is shown in Fig. 7.13, which also shows a steady-state result after about 60 simulation seconds.

The computed nodal displacements are then used to warp pre-operative MRI. Warping the MRI is achieved by exporting the deformed nodal coordinates and using them to create another B-spline transform in the 3D Slicer *Scattered Transform* module [9]. The transform is then applied to interpolate the computed deformation field across all voxels in the MRI and warp the image to the intra-operative position.

The result of the transform applied to the MRI is shown in Fig. 7.14b. The transform closely reflects the deformation field shown in the Abaqus results, and overlaying the transformed MRI with the intra-operative CT (Fig. 7.14c) shows that the electrodes are visibly aligned with the edge of the MRI. This result achieves the overall objective of this chapter, by demonstrating that a biomechanical model *can*

be used to solve for the internal deformation field of a patient-specific epilepsy case and warp the pre-operative MRI to the intra-operative position. Comparing the poor resolution and detail of the CT in Fig. 7.14a, to the overlaid image in Fig. 7.14c, it is clear to see the vast improvement in accuracy that is possible with patient-specific modelling.

7.4 Conclusions

The surgical treatment of epilepsy has the potential to permanently cure seizures, but the process is hindered by the inability to confidently locate the seizure-onset zone (SOZ) in the planning stage. Through the analysis of a real, patient-specific case from the Boston Children's Hospital, we have shown that it is possible to apply biomechanical modelling and finite element methods to compute the deformation field within the brain arising from invasive electrode placement and warp a pre-operative MRI into the intra-operative configuration of the brain. This provides a highly detailed map of the electrodes relative to neurological landmarks, making it easier to confidently identify what tissue to resect and how. The generation of the finite element mesh and model input took an experienced analyst approximately 2 days. This is acceptable in the research environment but too long for compatibility with existing clinical workflows. Further work into more efficient methods of patient-specific model generation is clearly needed [11, 28] (see Chaps. 10 and 11 of this book).

The model was analysed in Abaqus for 100 simulation seconds, which took approximately 2 hours to complete and a further hour to process the results and register the deformation field. As close to real-time processing speeds are not demanded by this application, these simulation and analysis times are compatible with existing clinical workflows, and further improvements, while helpful, are not strictly necessary. These timeframes would fit within the 5–7-day period of data collection, while the electrodes are on the brain.

The accuracy of segmentation is a limitation that affects the accuracy of the model geometry. Segmentation remains a challenging and subjective process that does not guarantee repeatability. Improvements in this area can only really come from research into improved imaging and more robust segmentation algorithms; however it is likely that manual input will always be required in this process. For example, intensity and label fusion algorithms have demonstrated very high reproducibility and accuracy indistinguishable from that of human experts [2, 3, 25].

Because manual surgery cannot achieve accuracy better than 1 mm, even slight deviations by one or two voxels can still produce a better method of localisation than is currently used in practice.

Finally, another area of interest in the surgical treatment of epilepsy is in the modelling of depth electrodes. These are very long and slender needles that pierce deep into the parenchyma and are extremely difficult to control and locate during

their insertion. Surgeons may benefit from the ability to predict how the needle will behave in the tissue or be able to practise using haptic feedback simulations before they conduct the operation on the patient.

Acknowledgements The funding from the Australian government through the Australian Research Council (ARC) (Discovery Project Grants DP160100714, DP1092893 and DP120100402) and National Health and Medical Research Council (NHMRC) (Project Grants APP1006031, APP1144519 and APP1162030) is greatly acknowledged. We thank the Raine Medical Research Foundation, for supporting G. R. Joldes through a Raine Priming Grant, and the Department of Health, Western Australia, for funding G. R. Joldes through a Merit Award. This investigation was also supported in part by NIH grants R01 NS079788, R01 EB019483 and R42 MH086984 and by a research grant from the Boston Children's Hospital Translational Research Program.

References

1. ABAQUS: ABAQUS Theory Manual Version 6.13. Dassault Systèmes Simulia Corp, Providence (2013)
2. Akhondi-Asl, A., Warfield, S.K.: Simultaneous truth and performance level estimation through fusion of probabilistic segmentations. IEEE Trans. Med. Imaging. **32**(10), 1840–1852 (2013)
3. Akhondi-Asl, A., Hoyte, L., Lockhart, M.E., Warfield, S.K.: A logarithmic opinion pool based STAPLE algorithm for the fusion of segmentations with associated reliability weights. IEEE Trans. Med. Imaging. **33**(10), 1997–2009 (2014)
4. Bauman, J.A., Feoli, E., Romanelli, P., Doyle, W.K., Devinsky, O., Weiner, H.L.: Multistage epilepsy surgery: safety, efficacy, and utility of a novel approach in pediatric extratemporal epilepsy. Neurosurgery. **62**(Suppl 2), 489–505 (2008)
5. Bilston, L.E. (ed.): Neural Tissue Biomechanics. Studies in Mechanobiology, Tissue Engineering and Biomaterials. Springer-Verlag, Berlin, Heidelberg (2011)
6. Curry, D.J., Gowda, A., McNichols, R.J., Wilfong, A.A.: MR-guided stereotactic laser ablation of epileptogenic foci in children. Epilepsy Behav. E&B. **24**(4), 408–414 (2012)
7. Engel Jr., J.: A greater role for surgical treatment of epilepsy: why and when? Epilepsy Curr. **3**(2), 37–40 (2003)
8. Gerard, I.J., Kersten-Oertel, M., Petrecca, K., Sirhan, D., Hall, J.A., Collins, D.L.: Brain shift in neuronavigation of brain tumors: a review. Med. Image Anal. **35**, 403–420 (2017)
9. Joldes, G.R.: Scattered Transform – a 3D Slicer Extension, from https://github.com/grandwork2/ScatteredTransform (2017)
10. Joldes, G.R., Wittek, A., Miller, K.: Real-time nonlinear finite element computations on GPU – application to neurosurgical simulation. Comput. Methods Appl. Mech. Eng. **199**, 3305–3314 (2010)
11. Joldes, G.R., Bourantas, G., Zwick, B., Chowdhury, H., Wittek, A., Agrawal, S., Mountris, K., Hyde, D., Warfield, S.K., Miller, K.: Suite of meshless algorithms for accurate computation of soft tissue deformation for surgical simulation. Med. Image Anal. **56**, 152–171 (2019)
12. Menagé, L.P.M.: Computer Simulation of Brain Deformations for the Surgical Treatment of Paediatric Epilepsy. Master of Engineering, The University of Western Australia, Perth, WA (2017)
13. Miga, M.I., Sun, K., Chen, I., Clements, L.W., Pheiffer, T.S., Simpson, A.L., Thompson, R.C.: Clinical evaluation of a model-updated image-guidance approach to brain shift compensation: experience in 16 cases. Int. J. Comput. Assist. Radiol. Surg. **11**(8), 1467–1474 (2016)
14. Miller, K. (ed.): Biomechanics of the Brain. New York, Springer (2011)

15. Miller, K., Lu, J.: On the prospect of patient-specific biomechanics without patient-specific properties of tissues. J. Mech. Behav. Biomed. Mater. **27**, 154–166 (2013)
16. Miller, K., Joldes, G.R., Bourantas, G., Warfield, S.K., Hyde, D.E., Kikinis, R., Wittek, A.: Biomechanical Modeling and Computer Simulation of the Brain during Neurosurgery. arXiv:1904.01192 (2019)
17. Monteith, S., Sheehan, J., Medel, R., Wintermark, M., Eames, M., Snell, J., Kassell, N.F., Elias, W.J.: Potential intracranial applications of magnetic resonance-guided focused ultrasound surgery. J. Neurosurg. **118**(2), 215–221 (2013)
18. NINDS: Curing the Epilepsies: the Promise of Research. NIH Neurological Institute, Bethesda, MD, USA (2007)
19. Noachtar, S., Borggraefe, I.: Epilepsy surgery: a critical review. Epilepsy Behav. E&B. **15**(1), 66–72 (2009)
20. Reinertsen, I., Lindseth, F., Askeland, C., Iversen, D.H., Unsgård, G.: Intraoperative correction of brain-shift. Acta Neurochir. **156**(7), 1301–1310 (2014)
21. Rivaz, H., Collins, D.L.: Deformable registration of preoperative MR, pre-resection ultrasound, and post-resection ultrasound images of neurosurgery. Int. J. Comput. Assist. Radiol. Surg. **10**(7), 1017–1028 (2015)
22. Sun, H., Lunn, K.E., Farid, H., Ziji, W., Roberts, D.W., Hartov, A., Paulsen, K.D.: Stereopsis-guided brain shift compensation. IEEE Trans. Med. Imaging. **24**(8), 1039–1052 (2005)
23. Taimouri, V., Akhondi-Asl, A., Tomas-Fernandez, X., Peters, J.M., Prabhu, S.P., Poduri, A., Takeoka, M., Loddenkemper, T., Bergin, A.M., Harini, C., Madsen, J.R., Warfield, S.K.: Electrode localization for planning surgical resection of the epileptogenic zone in pediatric epilepsy. Int. J. Comput. Assist. Radiol. Surg. **9**(1), 91–105 (2014)
24. Tovar-Spinoza, Z., Carter, D., Ferrone, D., Eksioglu, Y., Huckins, S.: The use of MRI-guided laser-induced thermal ablation for epilepsy. Childs Nerv. Syst. **29**(11), 2089–2094 (2013)
25. Velasco-Annis, C., Akhondi-Asl, A., Stamm, A., Warfield, S.K.: Reproducibility of brain MRI segmentation algorithms: empirical comparison of local MAP PSTAPLE, FreeSurfer, and FSL-FIRST. J. Neuroimaging. **28**(2), 162–172 (2018)
26. Wittek, A., Hawkins, T., Miller, K.: On the unimportance of constitutive models in computing brain deformation for image-guided surgery. Biomech. Model. Mechanobiol. **8**, 77–84 (2009)
27. Wittek, A., Joldes, G.R., Couton, M., Warfield, S.K., Miller, K.: Patient-specific non-linear finite element modelling for predicting soft organ deformation in real-time; application to non-rigid neuroimage registration. Prog. Biophys. Mol. Biol. **103**, 292–303 (2010)
28. Wittek, A., Grosland, N., Joldes, G., Magnotta, V., Miller, K.: From finite element meshes to clouds of points: a review of methods for generation of computational biomechanics models for patient-specific applications. Ann. Biomed. Eng. **44**, 3–15 (2016)

Chapter 8
Dynamics of Cerebrospinal Fluid: From Theoretical Models to Clinical Applications

Laurent Geregele, Olivier Baledent, Romain Manet, Afroditi Lalou, Slawomir Barszcz, Magdalena Kasprowicz, Piotr Smielewski, John D. Pickard, Marek Czosnyka, and Zofia Czosnyka

8.1 Introduction

Modelling of cerebrospinal fluid (CSF) circulation usually differs from models of brain tissue deformation. Hydrodynamics of CSF and its links with cerebral blood flow (CBF) are here of interest, as opposed to displacement of anatomical structures

L. Geregele
Neurosurgical Unit, University of Cambridge, Department of Clinical Neurosciences, Cambridge, UK

Department of Intensive Care, Ramsay Générale de Santé, Hôpital privé de la Loire, Saint Etienne, France

O. Baledent
Department of Imaging and Biophysics, Jules Verne University hospital, Amiens, France

R. Manet
Department of Neurosurgery B, Neurological Hospital Wertheimer, University of Lyon, Lyon, France

A. Lalou · P. Smielewski · J. D. Pickard · Z. Czosnyka
Neurosurgical Unit, University of Cambridge, Department of Clinical Neurosciences, Cambridge, UK

S. Barszcz
Department of Neurosurgery and Traumatology, Public Pediatric Teaching Clinical Hospital, Medical University of Warsaw, Warsaw, Poland

M. Kasprowicz
Institute of Biomedical Engineering and Instrumentation, Wroclaw University of Technology, Wrocław, Poland

M. Czosnyka (✉)
Neurosurgical Unit, University of Cambridge, Department of Clinical Neurosciences, Cambridge, UK

Institute of Electronic Systems, Warsaw Univeristy of Technology, Warsaw, Poland
e-mail: mc141@medschl.cam.ac.uk

K. Miller (ed.), *Biomechanics of the Brain*, Biological and Medical Physics, Biomedical Engineering, https://doi.org/10.1007/978-3-030-04996-6_8

or distribution of stress-strain in the brain tissue in deformation modelling. In clinical practice, dynamics of the pressure may be easily monitored (although invasively, with directly placed pressure transducers), and dynamics of CSF flow and CBF can be imaged with phase-contrast MRI (PC-MRI, noninvasively). These two methods have an established clinical application in diagnosis and management of diseases associated with CSF circulatory dysfunctions, like hydrocephalus of various types, idiopathic intracranial hypertension, syringomyelia, etc.

This chapter describes the methodology of modelling of CSF dynamics and attempts to illustrate some most common clinical applications to give a reader a taste of links between physics and a practice of clinical neurosciences. Before embarking on the particulars, it is worth considering the question: why quantitatively assess CSF dynamics? Quantitative assessment in general provides robust evidence to support clinical intuition as well as imparting a measure of the degree of dysfunction, particularly useful where clinical parameters are subtle and ambiguous [1]. For normal pressure hydrocephalus (NPH), where this is particularly true, theoretical consensus regarding the use of physiological parameters in conjunction with clinical information and imaging has been reached. It has been published in the latest guidelines for the management of NPH [2].

More specifically, the ability to obtain variables that describe CSF dynamics allows us to more categorically address some key questions in the clinical decision-making process: (1) Scope for improvement with CSF shunting: shunts work by providing an alternative (normal resistance) pathway for CSF outflow. If resistance to CSF outflow (R_{CSF}) is in the normal range, a shunt will theoretically not be of benefit [3]. (2) To determine which is the best shunt system to use. (3) In suspected shunt failure, providing a baseline for postshunt comparison. Shunt failure occurs at a rate of approximately 20–30% in the first year and 3–5% per annum subsequently [4]. Deterioration is often gradual and subtle rather than sudden and dramatic, and in such cases, it can be difficult to justify revision without quantitative evidence and comparative analysis [5–7]. Similarly, in patients presenting with persistent symptoms postshunting, CSF dynamics assessment is a useful means of excluding revision, if relative normalisation of CSF dynamics has been demonstrated [8]. The current range of clinical application for CSF dynamics testing includes hydrocephalus, idiopathic intracranial hypertension [9], craniosynostosis, and traumatic brain injury (TBI) – the latter useful in differentiating posttraumatic hydrocephalus from atrophy [10] and assessing CSF pathways following decompressive craniectomy [11].

8.2 Physiology and Pathophysiology

CSF dynamics comprises the interaction between five components: CSF production, flow, absorption, pulsations, and dynamics of CBF. CSF production occurs by active secretion at a relatively constant rate, but is dependent upon brain metabolic rate and reducing with age [12]. The role of free, unobstructed flow of CSF is threefold: (1)

it provides a shock absorptive function for the brain and spinal cord, important in trauma; (2) allows even distribution of pressure throughout the intracranial vault, cancelling out pressure gradients and preventing brain shift or herniation; and (3) allows washing out brain metabolites.

The second point explains why a very high ICP (>40 mmHg) can be tolerated relatively asymptomatically in communicating hydrocephalus, for example, during CSF infusion tests [13]. In contrast, when CSF pathways are obstructed, for example, by diffuse cerebral oedema in TBI, marked clinical deterioration is seen at ICP exceeding only 20 mmHg.

Absorption occurs in a pressure-dependent fashion via the arachnoid granulations at the superior sagittal sinus (except for newborns), first mathematically described by Davson [14]. This equation was recently validated in a population of patients suffering from idiopathic normal pressure hydrocephalus [15]. Alternative outflow of CSF may occur by periventricular leakage into the brain parenchyma, as suggested in NPH patients [16, 17]. CSF circulates not only in a constant way with a rate equivalent to CSF production but also in pulsations. CSF pulsatile flow is observed in the cerebral aqueduct (approximately 40 μL in stroke volume) and in the cervical region of subarachnoid spaces (SAS) (approximately 500 μL stroke volume) [18]. For a half of the cardiac cycle, CSF flows down into the spinal SAS, and for the other half, upward from it. The role of pulsatile CSF flow and pressure pulsations is still unclear, but becomes more often studied in hydrocephalus and other diseases manifesting with abnormal CSF dynamics [19–21]. Recently, Nedergaard et al. [22] described an additional CSF rapid convective flow via the *glymphatic* system, a highly organised brain-wide pathway, associating a paraarterial CSF influx route, an intracellular transastrocytic path, and a paravenous ISF clearance route. Aquaporin 4 (AQP4) water channels, disposed on the vascular end feet of astrocytes, facilitate fast exchanges between CSF and interstitial fluid (ISF), allowing a rapid clearance of waste products related to high metabolic activity of neurons, which is not possible with only the low CSF 'classic' bulkflow and the large tissue distances in most of the brain regions and CSF spaces. This CSF flow through the brain is also discussed in Bulat-Klarica-Orešković hypothesis [23].

A specific pattern of CSF flow impairment should be distinguished from the other situation: external hydrocephalus, which has been extensively described in paediatric cases but very few in brain injured adult patients, refers to an extra-axial CSF flow impairment with an enlargement of the subarachnoid spaces concomitant to raised ICP [24] and CSF dynamics [25] alteration but not with ventriculomegaly. Occurrence of traumatic or non-traumatic subarachnoid haemorrhage is probably a significant cause of such condition. It should not be confused with 'subdural hygroma', which is primarily caused by a vacuum effect on CSF precipitated by atrophic brain sinking, without raised ICP [26]. Recently Nakae et al. describe the same mechanism after a chemical meningitis with a patient improvement by a ventriculo-peritoneal shunting [27]. In these two last references, the authors insist on the difference between external hydrocephalus and hygroma (Fig. 8.1). Despite several other publications [28–30] that describe this distinction, the concept of external hydrocephalus is currently largely underknown and should be more spread

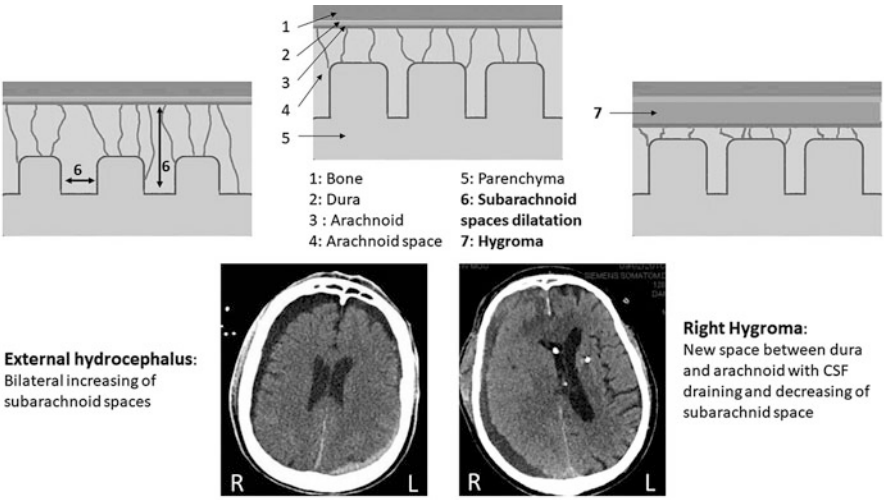

Fig. 8.1 Difference between external hydrocephalus and subdural hygroma. The CSF diffuses in a physiological space in external hydrocephalus (subarachnoid spaces), while the CSF collects in a 'new subdural space' in hygroma. Tears in the arachnoid can probably explain mixt situations that we have not describe on this figure

because the treatment is not the same. Indeed, CSF drainage improves external hydrocephalus (include lumbar drainage) [26] and can be very dangerous in the case of hygroma.

8.3 Model of CSF Circulation

The mathematical model of CSF pressure-volume compensation, introduced by A. Marmarou [31] and modified in later studies [32, 33], provides a theoretical basis for the differential diagnosis in hydrocephalus. Since then, components of this model have been identified in many clinical scenarios [34–40], and it is in use in clinical diagnostic procedures [2, 10, 25].

Under normal conditions, without long-term fluctuations of the cerebral blood volume, production of CSF is balanced by its storage and reabsorption to sagittal sinus:

$$\text{Production of CSF} = \text{Storing of CSF} + \text{Reabsorption of CSF} \tag{8.1}$$

Production of CSF is almost constant. Reabsorption is proportional to the gradient between CSF pressure (P) and pressure in sagittal sinuses (P_{ss}):

$$\text{Reabsorption} = \frac{p - p_{ss}}{R} \tag{8.2}$$

P_{ss} is considered to be a constant parameter, determined by central venous pressure. However, it is not certain that interaction between changes in CSF pressure and P_{ss} does not exist in all circumstances: in patients with idiopathic intracranial hypertension, P_{ss} is frequently elevated due to stenosis of transverse sinuses. Similar situation can be seen in venous sinus thrombosis.

The coefficient R (symbol R_{CSF} is also used) is termed the resistance to CSF reabsorption or outflow (units: [mmHg/(mL/min)]).

Storage of CSF is proportional to the cerebrospinal compliance C (units: [mL/mmHg]):

$$\text{Storage} = C \cdot \frac{dp}{dt} \tag{8.3}$$

The compliance of the cerebrospinal space is inversely proportional to the gradient of CSF pressure p and the reference pressure P_o (8.4) [2]:

$$C = \frac{1}{E \cdot (p - p_o)} \tag{8.4}$$

Some authors suggest that the relationship (8.4) is valid only above a certain pressure level called the 'optimal pressure' [33]; however, this is still a point of some dispute. The coefficient E is termed the cerebral elasticity (or elastance coefficient) (units: [mL^{-1}]). Elevated elasticity (>0.18 mL^{-1}) signifies a poor pressure-volume compensatory reserve [41]. This coefficient has been confirmed to be useful in predicting response to third ventriculostomy [40]. Coefficient E is inversely associated with the resistance to CSF outflow [41].

The reference pressure P_o is a parameter of uncertain significance. Some authors suggest that it is the pressure in the venous compartment and may be equal to P_{ss}. Others assume that this variable can be neglected [25].

The relationship (8.4) expresses a fundamental law of the cerebrospinal dynamic compensation: When the CSF pressure increases, the compliance of the brain decreases.

Combination of (8.1) with (8.2) and (8.4) gives a final Eq. (8.5):

$$\frac{1}{E \cdot (p - p_o)} \cdot \frac{dp}{dt} + \frac{p - p_b}{R} = I(t) \tag{8.5}$$

where $I(t)$ is the rate of external volume addition and P_b is a baseline pressure.

The model described by this equation may be presented in the form of its electric equivalent (Fig. 8.2) [31].

Equation (8.5) can be solved for various types of external volume additions $I(t)$. The most common in clinical practice is:

(a) A constant infusion of CSF ($I(t) = 0$ for $t < 0$ and $I(t) = I_{inf}$ for $t > 0$) (see Fig. 8.3):

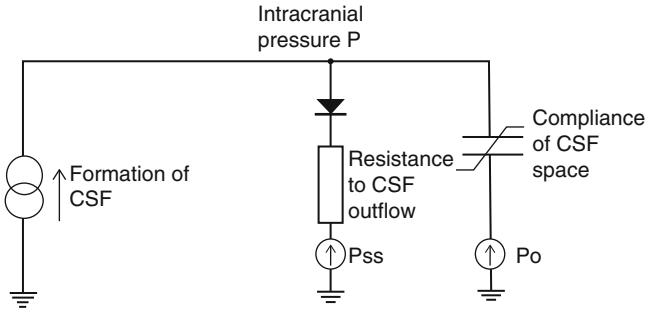

Fig. 8.2 Electrical model of CSF circulation. Current source represents production of CSF, resistor, and diode – unilateral absorption to sagittal sinus (voltage source P_{ss} represents sagittal sinus pressure). Capacitor – nonlinear compliance of CSF space

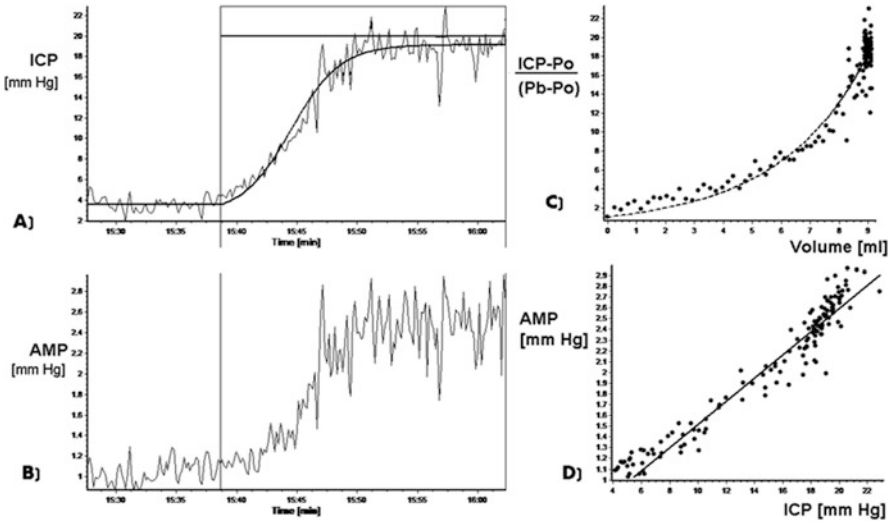

Fig. 8.3 Methods of identification of the model of CSF circulation during constant rate infusion study. (**a**) Recording of real CSF pressure (ICP) vs. time increasing during infusion with interpolated modelling curve (8.7). Infusion of constant rate of 1.5 (mL/min) starts from vertical line. (**b**) Recording of pulse amplitude (AMP) during infusion. It is customary presented as different variable, in addition to mean ICP. Rise in AMP is usually well correlated with rise in ICP. (**c**) Pressure-volume curve. On *x*-axis, effective volume increase is plotted (i.e. infusion and production minus reabsorption of CSF). On *y*-axis – increase in pressure measured as a gradient of current pressure minus reference pressure P_o, relative to baseline pressure p_b. (**d**) Linear relationship between pulse amplitude and mean ICP. Intercept of the line with *x*-axis (ICP) theoretically indicates the reference pressure P_o

$$P(t) = \frac{\left[I_{\text{inf}} + \frac{p_{\text{b}} - p_{\text{o}}}{R}\right] \cdot [p_{\text{b}} - p_{\text{o}}]}{\frac{p_{\text{b}} - p_{\text{o}}}{R} + I_{\text{inf}} \cdot \left[e^{-E\left[\frac{p_{\text{b}} - p_{\text{o}}}{R} + I_{\text{inf}}\right] \cdot t}\right]} + p_{\text{o}} \tag{8.6}$$

The analytical curve (8.6) can be matched to the real recording of the pressure during the test, which results in an estimation of the unknown parameters: R, E, and P_{o} (see Fig. 8.3a).

The pulse amplitude can be followed by a direct measurement of the difference between systolic ICP and diastolic ICP, but with this technic, the value is often contaminated by the respiratory waves. The analysis of the amplitude of the 'ICP pic' value on the Fourier transformation is more robust. For the follow the term of ICP amplitude corresponds at the amplitude of the 'ICP pic' on the Fourier transformation. The value 'real' ICP amplitude can be extrapolated with the multiplication of this value by a factor 2.5.

(b) A bolus injection of CSF (volume ΔV):

$$P(t) = \frac{(p_{\text{b}} - p_{\text{o}}) \cdot e^{E\left[\Delta V + \frac{p_{\text{b}} - p_{\text{o}}}{R} \cdot t\right]}}{1 + e^{E\Delta V} \cdot \left[e^{E \cdot \frac{p_{\text{b}} - p_{\text{o}}}{R} \cdot t} - 1\right]} + p_{\text{o}} \tag{8.7}$$

The bolus injection can be used for calculation of the so-called pressure-volume index (PVI), defined as the volume added externally to produce a tenfold increase in the pressure [20]:

$$\text{PVI} \stackrel{\text{def}}{=} \frac{\Delta V}{\log 10 \left(\frac{p_{\text{p}} - p_{\text{o}}}{p_{\text{b}} - p_{\text{o}}}\right)} \tag{8.8a}$$

$$\text{PVI} \cong \frac{1}{0.434 \cdot E} \tag{8.8b}$$

P_{p} in a formula (8.8a) is a peak pressure recorded just after addition of the volume ΔV. PVI is theoretically proportional to the inverse of the brain elastance coefficient E. The pressure-volume compensatory reserve is insufficient when PVI <13 mL. A value of PVI above 26 mL signifies an 'over-compliant' brain. These norms are valid for the PVI calculated as inverse of E (according to 8.8b) using slow infusion. If the bolus test is used, norms for PVI are higher (the threshold equivalent to 13 mL is around 25 mL [31]).

The formula (8.7) for time $t = 0$ describes the shape of the relationship between the effective volume increase ΔV and the CSF pressure, called the pressure-volume curve – Fig. 8.3c:

$$p = (p_{\text{b}} - p_{\text{o}}) \cdot e^{E\Delta V} + p_{\text{o}} \tag{8.9}$$

It is interesting that pressure-volume curve plotted during increase in ICP has different shape than plotted using the subsequent decrease [42].

Finally, the Eq. (8.7) can be helpful in the theoretical evaluation of the relationship between the pulse wave amplitude of ICP and the mean CSF pressure. If we presume that the rise in the blood volume after a heart contraction is equivalent to a rapid bolus addition of CSF fluid at the baseline pressure P_b, the pulse amplitude (AMP) can be expressed as

$$\mathrm{AMP} = p_p - p_b = (p_b - p_o) \cdot \left(e^{E\Delta V} - 1\right) \tag{8.10}$$

In almost all the cases, when CSF pressure is being increased by an external volume addition, the pulse amplitude rises [2, 40] (see Fig. 8.3b, d). The gradient of the regression line between AMP and p is proportional to the elasticity. The intercept, theoretically, marks the reference pressure P_o.

In all pressure-volume testing techniques, parameters of model (8.5) are estimated using various algorithms and various volume-adding techniques. However, the presented model has a limited scope: it cannot interpret dynamic interactions between the rising CSF pressure, expanding ventricles, and cerebral blood volume. More sophisticated models have been formulated, but none of them has yet become established in clinical practice.

8.4 Infusion Test

The computerised infusion test [43, 44] is a modification of the traditional constant rate infusion as described by Katzman and Hussey [39]. The method requires fluid infusion to be made into any accessible CSF compartment. Lumbar infusion, even if it has understandable limitations, is less invasive than intraventricular.

The alternative is an infusion into a subcutaneously positioned reservoir, connected to an intraventricular catheter or shunt antechamber. In such cases, two hypodermic needles (gauge 25) are used: one for the pressure measurement and the second for the infusion.

During the infusion, the computer calculates and graphically presents mean pressure and pulse amplitude over time (Fig. 8.3a, b). The resistance to CSF outflow can be calculated using simple arithmetic as the difference between the value of the plateau pressure during infusion and the baseline pressure, divided by the infusion rate. However, the precise measurement of the final plateau pressure is not possible when strong vasogenic waves arise or an excessive elevation of the pressure above the safe limit of 40 mmHg is recorded. Computerised analysis produces results even in difficult cases when the infusion is terminated prematurely. The pressure-volume curve is additionally investigated (Fig. 8.3c). It represents relative rise in CSF pressure as a function of effective change of CSF volume (i.e. volume infused and produced minus volume absorbed). The algorithm utilises time series analysis for

volume-pressure curve retrieval, the least-mean-square model fitting, and an examination of the relationship between the pulse amplitude and the mean CSF pressure (Fig. 8.3d).

8.5 Long-Term ICP Monitoring

Monitoring of ICP over a longer period can be performed safely using intraparenchymal probes [45, 46]; less frequently, this is performed by lumbar puncture or a needle inserted in a preimplanted reservoir. Continuous, real-time analysis of the data, using a pressure monitor connected to a computerised system, is very helpful. We have found that the most reliable results require overnight monitoring [46]; however, when this is impossible, a minimum half an hour monitoring is necessary. New devices allowing telemetric intracranial pressure monitoring over long periods could be helpful for ICP-guided valve adjustments in complex situations [47, 48]. In contrast, it is well established that a single manometric lumbar CSF pressure measurement may be misleading [49].

8.6 Compensatory Parameters Derived from the Infusion Test and ICP Monitoring

8.6.1 RCSF and Pb

Infusion study (constant rate [50] or any other variation of controlled but variable rate [36, 38, 51]) allows variables describing the state of CSF compensatory reserve to be estimated. Traditionally, the two most important parameters are resistance to CSF outflow (R_{CSF}) and baseline CSF pressure (p_b). Elevated R_{CSF} (>13 mmHg/(mL/min) [35, 42] or >18 mmHg/(mL/min) [34]) signifies disturbed CSF circulation. Elevated baseline pressure (p_b > 18 mmHg) may signify an uncompensated cerebrospinal volume-expanding process.

8.6.2 Pulsatility and Pulse Amplitude

Analysis of ICP pulse pressure amplitude could be valuable in managing iNPH patients: elevated mean pulse amplitudes during long-term ICP monitoring [52] and potential reduction pulse pressure [53] could be associated with significant clinical response to shunt surgery. Moreover, the presence of a ‘lower breakpoint point’ of the pulse pressure amplitude during infusion tests [54] could be associated with significant clinical response to shunt surgery.

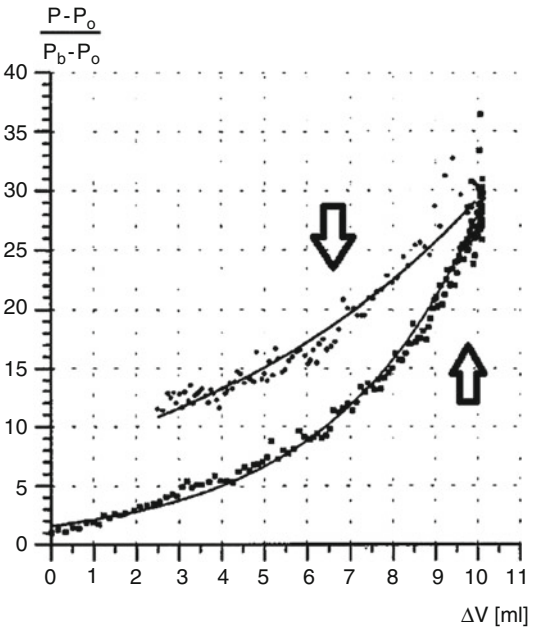

Fig. 8.4 'Hysteresis' of pressure-volume curve. After the test (decreasing ICP – down arrow), branch of the curve is shifted upward in comparison to the curve plotted from the ascending part of the test (upright arrow)

8.6.3 Elastance Coefficient (or Elasticity)

The exact clinical significance and interpretation of the elastance coefficient (E) is not yet fully documented, though theoretically it describes brain stiffness. Tans and Poortvliet [41] showed that E weakly correlated with the resistance to CSF outflow, though no further studies exploring this concept have followed (Fig. 8.4).

Tisell [40] demonstrated that E correlated positively with the result of third ventriculostomy: those with a stiffer brain (higher E) have a better chance to improve after surgery. In addition to absolute values of elastance coefficient, the pressure-volume curve itself can be derived from any given infusion study, as demonstrated by Frieden [37].

8.6.4 Pressure-Volume Curve and Its Hysteresis

The pressure-volume curve described by (8.9) can be empirically retrieved from infusion test (see Fig. 8.3c). However, slope of the curve in most of cases is different during ascending and descending phase of the test (Fig. 8.4). Width of hysteresis was significantly associated with a higher cerebral elastance coefficient and clinical presentation [55].

8.6.5 ICP Waveform Components

Furthermore, ICP recording made overnight [46] or at baseline before the infusion test allows the observation of various cyclical or random dynamic changes in ICP of vasogenic origin (i.e. forced by change in cerebral blood volume). These include pulse, respiratory, or slow vasogenic waves.

With respect to pulse waves (caused by changes in cerebral blood volume related to the heartbeat), the ICP waveform can be processed through a Fourier transform to determine the pulse amplitude of ICP (AMP) as the magnitude of the first harmonic component related to the heart rate (Fig. 8.5) [44]. This method is an alternative to time-domain analysis [56] and, in our experience, both methods are generally equivalent. They produce different numerical values which are perfectly linearly associated. During the infusion study, AMP increases with mean ICP, and the rate of increase of amplitude per rise in ICP is called the AMP/P slope [32, 33]. Lundberg 'B waves' [57] – slow waves of ICP with periods of 20 s to 2 min – are almost universally present in ICP recordings, probably even in healthy volunteers. According to historical standards [16, 35, 58], when they were present for more than 80% of the time of overnight ICP monitoring, shunting was recommended. Using spectral analysis, a variable has been proposed, being an equivalent of the amplitude (i.e. the amplitude of sine wave bearing the same energy) of the slow waves. B waves are associated with fluctuations of CBF and arterial blood pressure [59] as well as brain tissue oxygenation (detected with near-infrared spectroscopy)

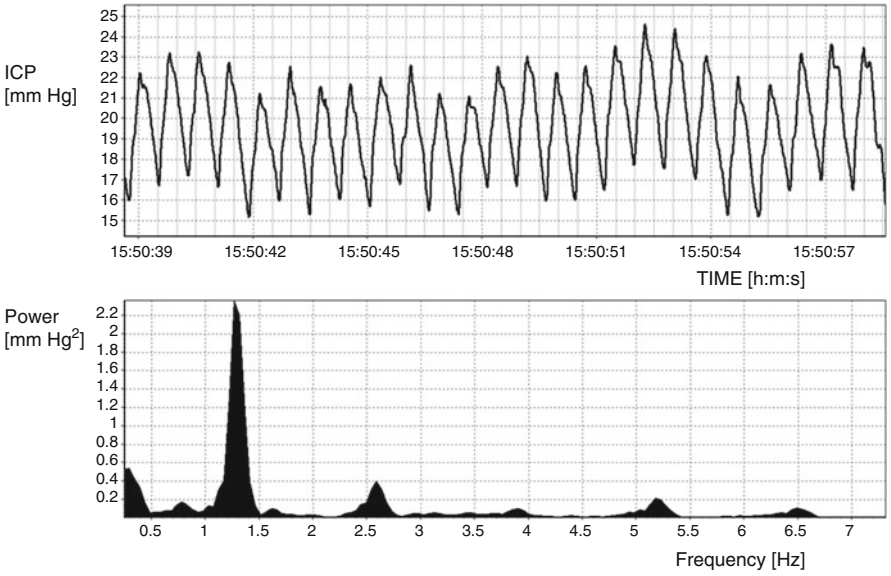

Fig. 8.5 Example of pulse wave of ICP. Time plot and spectral analysis showing fundamental amplitude (frequency equivalent to a heart rate) and higher harmonics

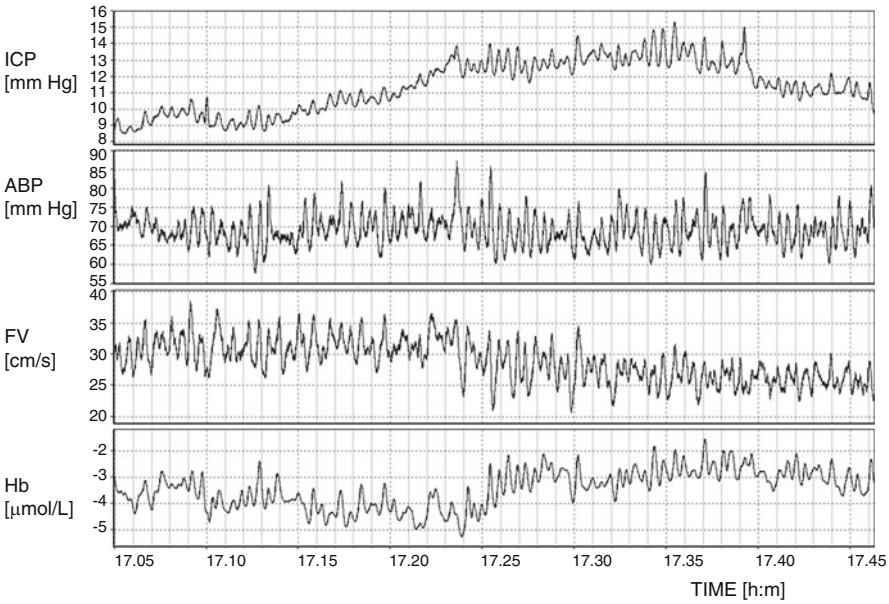

Fig. 8.6 B waves seen in ICP, arterial pressure (ABP), blood flow velocity in MCA (FV, detected noninvasively using transcranial Doppler ultrasonography), and concentration of deoxygenated haemoglobin (detected with near-infrared spectroscopy). Recording was performed during infusion study in patients with initial diagnosis of NPH. Infusion of 1.5 mL/min rate started around 17:12, and overall pressure increased was from 9 to 13 mmHg, revealing low resistance to CSF outflow

(Fig. 8.6). Respiratory waves, associated with changes in venous blood volume and changes in sagittal sinus pressure as a result of ventilation, are probably less useful in assessment of CSF dynamics.

8.6.6 Derived Parameters, RAP Index

Conventionally, pressure-volume compensatory reserve is assessed using intracranial volume addition [25, 31, 60]. Changes in ICP in response to a known volume change allow such parameters as PVI to be derived from bolus volume addition or *E* (which characterises the shape of the pressure-volume curve over its exponential region) to be derived from constant rate infusion. However, under certain assumptions, external volume addition is not necessary as it is possible to assess pressure-volume compensation by taking into account the change in pressure with every heartbeat, where a certain volume of arterial blood is added to the cerebrospinal space in a pulsatile manner. Although the added volume is not known, the pressure response is recorded continuously in the form of the 'pulse waveform' of the ICP recording. The RAP index (correlation coefficient [R]

between the pulse amplitude [A] and the mean intracranial pressure [P]) is derived by linear correlation between 30 consecutive, time-averaged data points of pulse amplitude of ICP (AMP) and mean ICP acquired within a 10-s-wide time window. RAP describes the degree of correlation between AMP and mean ICP over short periods of time (5 min). Theoretically, the RAP coefficient indicates the relationship between ICP and changes in intracerebral volume – the 'pressure-volume' curve. *E* and PVI describe how fast pressure rises per unit of volume addition in an exponential region of the curve. RAP coefficient close to 0 indicates a lack of coupling between the changes in AMP and the mean ICP. This denotes a good pressure-volume compensatory reserve at low ICP, i.e. the 'working point' is still below exponential region of the curve. When the pressure-volume curve starts to increase exponentially, AMP covaries directly with ICP and consequently RAP rises to +1. This indicates a low compensatory reserve [45, 61].

8.7 Pulsatile Flow of CSF: Phase-Contrast MRI Perspective

Previous sections described theory and clinical applications of the methods, which may be implemented using CSF volume-pressure tests or continuous monitoring of ICP. However, CSF flows in pulsatile manner. These pulsations can be detected using phase-contrast MRI [62–66].

8.8 Pulsatile CSF Flow-Basic Models

Pulsatile movement of CSF is a consequence of pulsatile inflow and outflow of cerebral blood. Therefore, the introductory modelling considerations start from the dynamics of CBF.

Value of ICP directly results from the circulation of cerebral blood, CSF, compliance of the cranio-spinal system, and conditions for venous blood outflow [31, 67]. Mean CBF is around 700 mL/min in adult, but arterial inflow is not constant during the cardiac cycle (systolic peak flow is around 1000 mL/min and diastolic around 550 mL/min) [63]. Compared to arterial flow, cerebral venous outflow is delayed with lower peak flow amplitude (around 800 mL/min) and a time profile of flow shape less pulsatile [63]. The difference in time profile between arterial and venous flows results in a net change in intracranial blood volume during a cardiac cycle. The blood volume expansion during one cycle is of order of few millilitres [64].

CSF moves into the spinal canal during systole and returns to the cranial compartment during diastole (Fig. 8.7) [63, 64, 68–70].

The volume ('stroke volume') of intracranial CSF displaced during one cardiac cycle is around 450 mL [63, 66]. Ventricular CSF contributes only in a small part (around 10%) of cerebrospinal volume exchange [63, 66, 71].

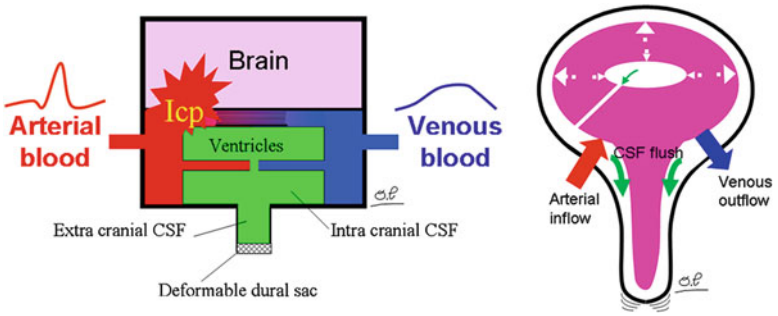

Fig. 8.7 Intracranial fluids relationships. Left: general scheme showing equilibrium between volumes, arterial (red) and venous (blue) blood, brain tissue (pink), and CSF (green). Right: anatomical equivalent. Intracranial arteriovenous blood volume increases during systole and mainly expands the brain outward (white large arrows) flushing extra-ventricular CSF through the spinal canal. White thinner arrows symbolise small brain displacement caused by expansion of the ventricular CSF compartments

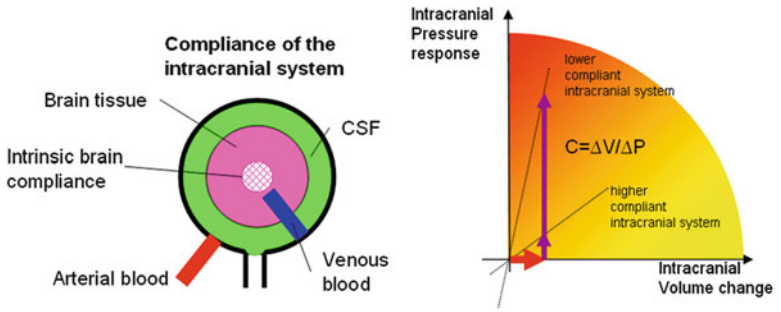

Fig. 8.8 Intracranial compliance compartments *(left)* and compliance definition *(right)*

During systolic phase of blood inflow, the brain mainly expands outward into the intracranial subarachnoid space (SAS). These CSF oscillations during a cardiac cycle are possible because of the compliance of the lumbar space which may expand within spinal channel against venous plexi.

The CSF and cerebral blood volume interaction also depend on the ability of liquids to move from one compartment of the cranio-spinal system to another.

Compliance of the cranio-spinal system is a fundamental mechanism limiting large ICP rise after systolic arterial brain expansion (Fig. 8.8). In the rigid cranial box, without displacement of other volumes, pulsatile blood inflow would be impossible.

The compliance of cranio-spinal system is mainly moderated by a venous blood outflow and the 'intrinsic brain' compliance (spinal displacements), the CSF moving in the spinal canal. Compliance of the cranio-spinal system is therefore a function of the abilities of fluids to move from the cranial compartment to the extracranial

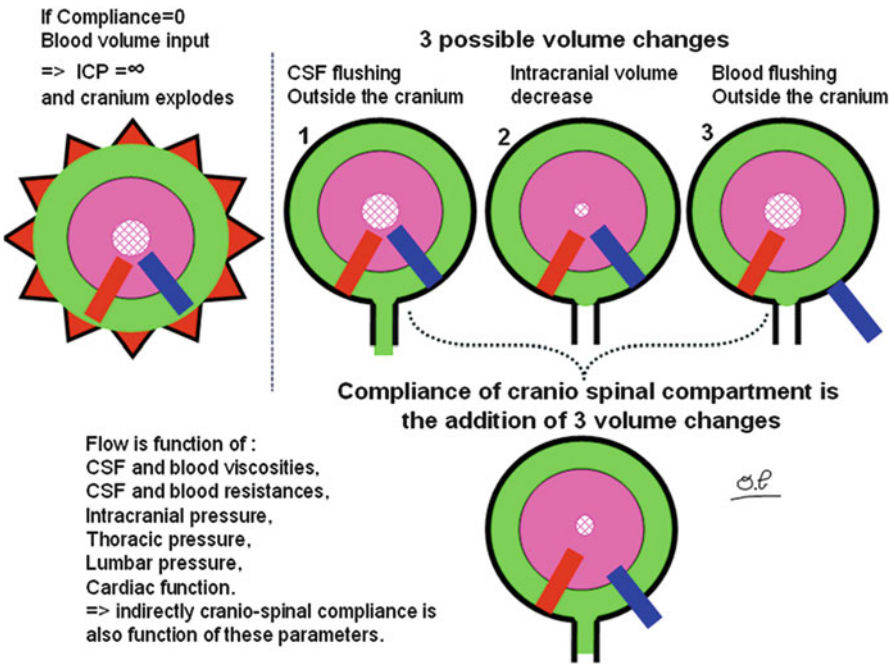

Fig. 8.9 Intracranial compliance response to arterial blood flow input. Intracranial arterial input blood volume during systole implies (1) CSF flushing into the spinal canal, (2) intracranial volume displacement (in the eye and ear cavities, in the spinal canal), and (3) venous blood outflow. These volumes displacements correspond to the net compliance of the intracranial space

part (Fig. 8.9). In this way, the CSF and blood viscosities, flow resistances of blood vessels and CSF SAS, intracranial pressure, thoracic pressure, lumbar pressure, and cardiac aspiration can impact the cranio-spinal compliance.

Part of the knowledge of interactions between intracranial flows during the cardiac cycle has been gathered thanks to the use of phase-contrast magnetic resonance imaging [72].

8.9 Methodology of Phase-Contrast MRI

Phase-contrast MRI, which depicts motions and flows through the cardiac cycle, can be used to evaluate the presence, direction, and temporal flow dynamics, both qualitatively and quantitatively [68, 69, 72–74]. This ability to characterise direction, pulsatility, and distribution of fluid flows in physiological conditions offers a powerful tool to study physiological cerebral dynamic interactions and provides complementary view to understand pathological processes such as hydrocephalus [62, 71, 75–79].

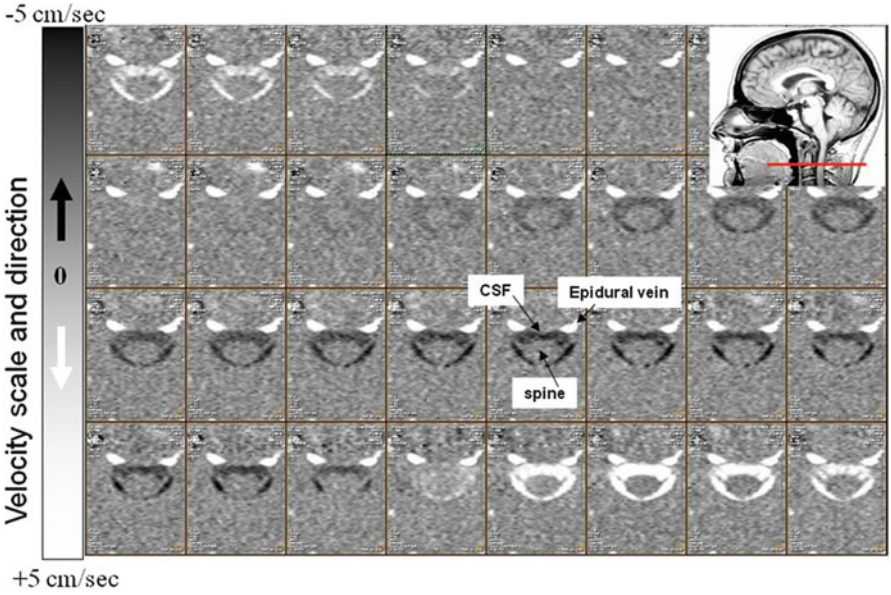

Fig. 8.10 PC-MRI images of the CSF around the spine during one cardiac cycle. It is a visualisation of 32 images of cervical CSF flow around the spine during cardiac cycle. White pixels depict downward CSF flow flushing into the spinal canal, and black pixels correspond to upward motion of CSF filling the cranium

Phase-contrast MRI exploits the fact that spins moving through magnetic field gradients acquire a phase different from static spins. Then, flow sensitive images, where pixel intensities represent the phase parameters allowing velocity calculation [80], can be produced. This technique can be associated with cardiac triggering or gating in order to decompose the cardiac cycle into several time intervals. Series of temporal images are then generated [74].

Because CSF flows' velocities (around 5 cm/s) are largely different from blood flows' velocities (60 cm/s), PC-MRI sensitivity must be adapted using a velocity encoding (V_{enc}) set to a value near the maximum velocity of the studied flow.

In the MR image example depicted in Fig. 8.10, hyperintense regions correspond to voxels where flow velocity, positively directed cranio-caudally perpendicular to the slice plane, approaches the V_{enc} absolute value. Conversely, hypointense areas represent the voxels in which the flow is directed from caudal to cranial. Immobile tissues, corresponding to no flow regions, will be represented with grey pixels. This color convention can be reversed according to the MRI manufacturer.

For quantitative characterisation and to increase the accuracy of velocity measurements [80], the acquisition plane must be selected perpendicular to the flow direction, positioned in the anatomic part corresponding to a supposed laminar flow. Such an acquisition, providing 32 images per cardiac cycle can be accomplished, with an acceptable quality, using 3 Tesla MR, in nearly 2 min.

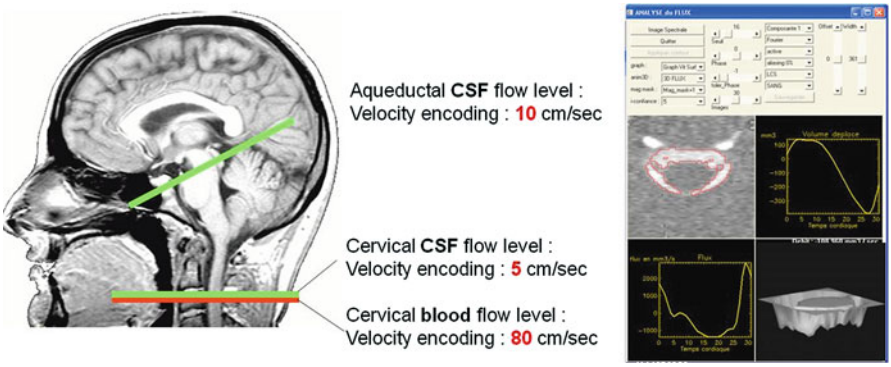

Fig. 8.11 PC-MRI acquisition planes and example of cervical CSF segmentation

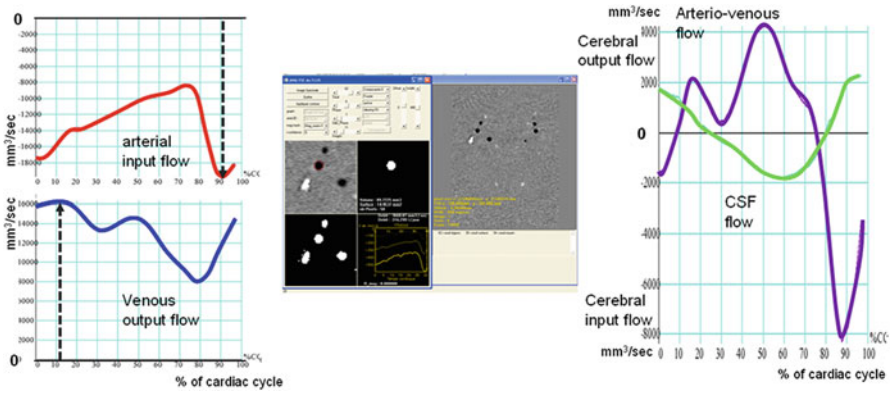

Fig. 8.12 Arterial, venous, and CSF intracranial flows calculated from PC-MRI acquisition

Phase-contrast MRI is able to quantify flows of moving liquids (see Fig. 8.10).

From those PC-MRI data, it is possible to calculate cerebral CSF flows using an image processing software including an optimised CSF and blood flows segmentation algorithm (see Fig. 8.11). The same technique can be applied to carotid/vertebral arteries and jugular vein blood flows.

Knowledge of all individual flow curves permits reconstruction of cerebral blood inflow (sum of arterial flows in left and right internal carotids and vertebral arteries) and cerebral venous flow (sum of venous flows in left and right internal jugular and epidural veins) and then, by summing the 'positive' venous flow with the 'negative' arterial flow, to obtain the arteriovenous flow curves (Fig. 8.12). This curve describes the global instantaneous displacement of cerebral blood during a cardiac cycle [63, 80].

The cerebral vascular flow curve presents a negative systolic peak flow (arterial flow > venous flow) and two diastolic positive bumps (venous flow > arterial flow). This curve is reversed compared to the CSF oscillation curve in the cervical spaces.

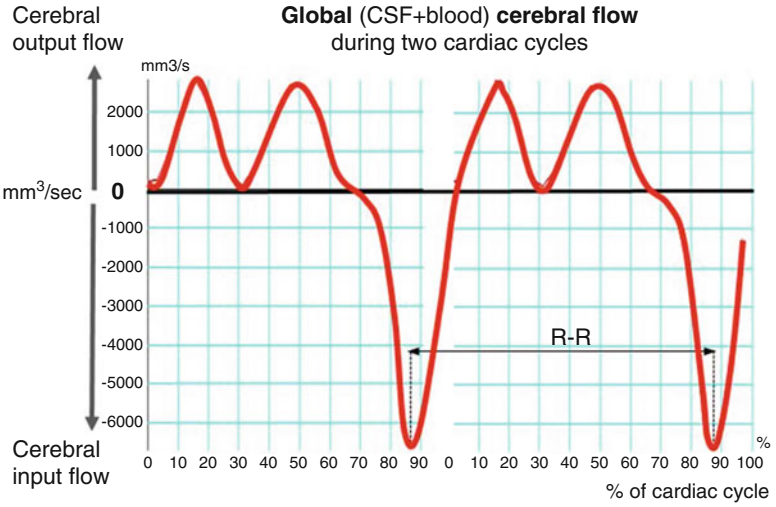

Fig. 8.13 Global cerebral flows during two cardiac cycles calculated from PC-MRI acquisition

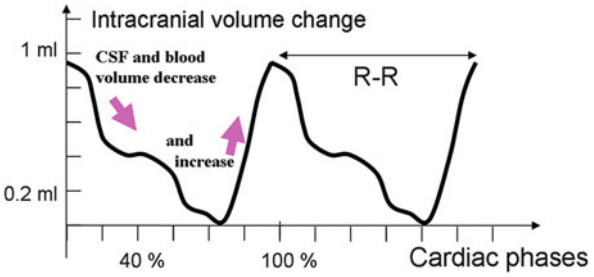

Fig. 8.14 Intracranial volume change during cardiac cycle calculated from PC-MRI data

In the same manner, the net CSF and vascular flow curves can be computed to obtain the total cerebral brain fluid flow oscillation during the cardiac cycle (Fig. 8.13) [63, 80].

After time integration of the global cerebral flow curve, the intracranial volume change (IVC) during a cardiac cycle can be calculated (Fig. 8.14). When intracranial volume increases quickly and largely during systole, the decrease in intracranial volume takes place in two steps corresponding to the two bumps of Fig. 8.13 [81].

As a function of the cranio-lumbar compliance, IVC generates pressure variations. In order to model ICP, IVC can be transformed by Marmarou's equation (see Fig. 8.15; [31]). Figure 8.15 shows the result of the simulation during a cardiac cycle using a resting pressure P_o and brain elastance index k (equivalent to elasticity E), respectively, set to 10 mm Hg and 0.11 mL^{-1}.

Four phases of ICP cycle can be defined to explain the intracranial dynamics (P1–P4; see Fig. 8.15). During the first period (denoted by P1), a sudden pressure rises, induced by the arterial systolic inflow inside the cranial cavity that occurred. Then, during the second period P2, the CSF and the venous flows are set in motion

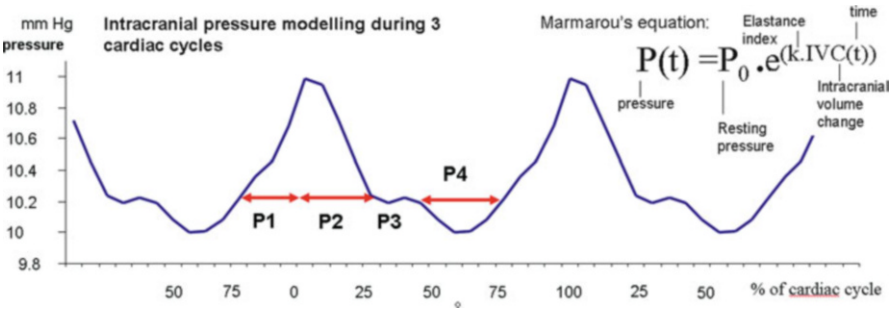

Fig. 8.15 Modelling ICP pulse from PCMRI data

to reduce intracranial pressure until a pressure balance between intracranial and extracranial spaces is reached. This balance defines the brain equilibrium pressure, i.e. P3. During equilibrium pressure phase, arterial flow equals venous flow and cervical CSF flow is null.

At the beginning of P4, ICP decrease continues. We hypothesised that this could be explained by the venous negative pressure caused by opening of the tricuspid valve and filling of the right ventricle. At the end of P4, this low pressure is finally compensated by CSF filling from cervical spaces to intracranial spaces. This would show that the influence of intracranial venous flow on brain pressure regulation is not only inherent to passive mechanisms [82] but is also shaped by heart aspiration.

Assessment of all cerebral flows allows the study of the interactions between arterial, venous, and CSF flows in the brain which control ICP. Alperin had proposed a method to directly measure ICP by PC-MRI and image processing [82], and mathematical models of cerebral hydrodynamics are used to study CSF and blood relationships in the brain [83, 84].

8.10 Clinical Applications

The review of clinical applications is based on 2620 clinical infusion studies and 250 overnight ICP monitoring performed at Addenbrooke's Hospital, Cambridge, UK, in more than 1400 patients suffering from hydrocephalus of various etiologies (idiopathic NPH 47%, postsubarachnoid haemorrhage NPH 12%, other communicating hydrocephalus 19%, noncommunicating hydrocephalus 22%). The mean age of the patients was 65 (range 24–94) and the male to female ratio was around 2:1. All of the patients were referred to the CSF clinic by their treating neurosurgeon, geriatrician, or neurologist, based on the presence of ventricular dilatation on brain scan (CT or MRI) and symptoms within Hakim's triad and other clinical presentations like headaches, etc. This group of patients, in addition to the clinical and imaging assessment, was investigated with a constant rate infusion study (via the lumbar

approach 20%, a preimplanted Ommaya reservoir 38%, shunt prechamber 40%, or open EVD 2%).

PC-MRI material was derived from the database at the Department of Image Processing, Amiens University Hospital, France, containing more than 500 volunteers and patients suffering from hydrocephalus, syringomyelia, and other CSF circulatory defects.

Although illustrative material is derived from two centres, similar results are reported from many other hospitals worldwide, known as a centre of excellence in studies on hydrocephalus and CSF disorders [4, 10, 25, 34–36, 38, 46, 64, 77, 83, 84].

8.10.1 *Differentiation Between Brain Atrophy and Normal Pressure Hydrocephalus*

CSF dynamics in NPH is characterised by a normal baseline pressure (ICP < 18 mmHg). The resistance to CSF outflow is increased (>13 [mmHg/(mL/min)]). B waves recorded during infusion are regular. Pulse amplitude is well correlated with mean ICP. Compensatory reserve at baseline is usually good (RAP index below 0.6), and usually elastance coefficient slightly increased ($E > 0.2$ mL^{-1}) (see Fig. 8.16).

Patients suffering predominantly from brain atrophy have normal CSF circulation. Typically, opening pressure, resistance to CSF outflow, and pulse amplitude are low (ICP < 12 mmHg, R_{CSF} < 12 mmHg/(mL/min), amplitude <2 mmHg). The compensatory reserve at baseline is good (RAP < 0.5), reflecting low elasticity of the atrophic brain ($E < 0.2$ mL^{-1}). Vasogenic waves are rather limited during recording. The mean ICP increases smoothly during the infusion and decreases in a similar fashion following infusion, comparable to the inflation and deflation of a balloon – Fig. 8.17.

8.10.2 *Noncommunicating and Acute Communicating Hydrocephalus*

Lumbar infusion is not recommended in noncommunicating hydrocephalus because of the risk of brain herniation in the event of uncontrolled CSF leak. However, this type of hydrocephalus may not always be easy to detect by the brain scan. In those few instances of noncommunicating hydrocephalus where lumbar infusion is performed, the resistance to CSF outflow is normal because the lumbar infusion is not able to detect the proximal narrowing in CSF circulatory pathways. Paradoxically elasticity is relatively low ($E < 0.20$ mL^{-1}). In acute hydrocephalus,

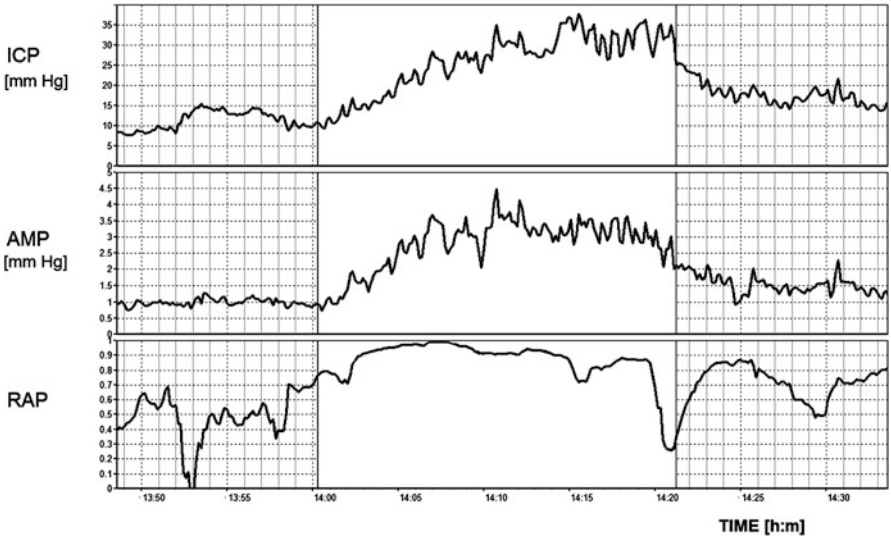

Fig. 8.16 Example of infusion study in patient suffering from NPH: normal baseline pressure (9 mmHg), normal baseline pulse amplitude, and good compensatory reserve (RAP index at baseline below 0.6). During infusion with a rate of 1.5 mL/min (unchecked area), pressure increased to 35 mmHg (resistance to CSF outflow was 17.8 [mmHg/(mL/min)]), pulse amplitude increased proportionally to mean ICP, RAP coefficient increased to +1 (indicating decrease in compensatory reserve during infusion), and slow vasogenic waves appeared in ICP and AMP recordings

R_{CSF} is elevated, the resting pressure and pulse amplitude are also elevated (ICP >15 mmHg, pulse amplitude > 4 mmHg), and compensatory reserve is poor (RAP >0.6 at baseline).

Obstructive hydrocephalus can be safely assessed using ventricular infusion (via a reservoir). This demonstrates high intracranial resting pressure and high resistance to CSF outflow (ICP > 15 mmHg, R_{CSF} > 13 mmHg/(mL/min)). The elasticity is high (>0.20 mL^{-1}), RAP is elevated above 0.6, and the pulse amplitude is high (>4 mmHg), indicating poor compensatory reserve (see Fig. 8.18). Acute communicating hydrocephalus (as in post-SAH) presents with a similar pattern of parameters, with frequent deep vasogenic waves (including plateau waves [57]) (Fig. 8.19).

8.10.3 Testing of CSF Dynamics in Shunted Patients

The methods for evaluation of CSF dynamics in shunted patients can be supportive for assessment of shunt function [4, 85, 86]. When a shunt drains properly, the resting pressure remains at or below the shunt's operating pressure.

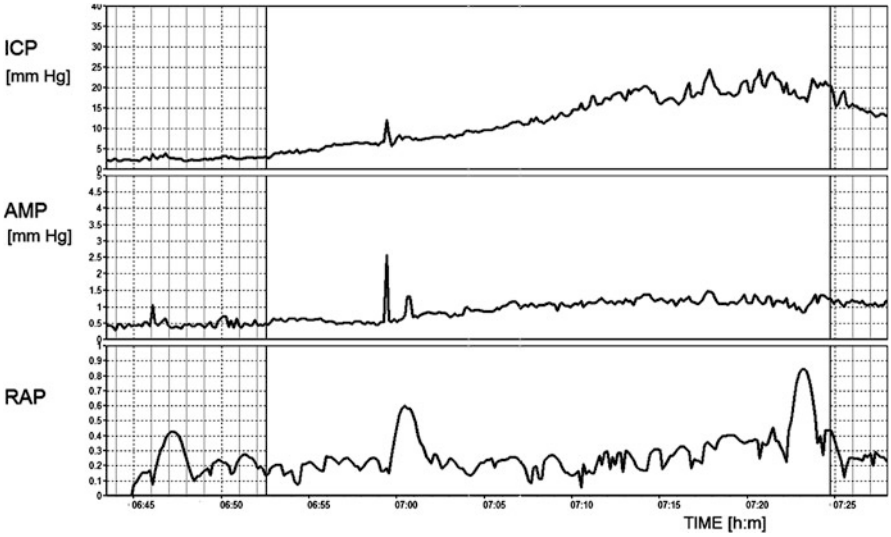

Fig. 8.17 Example of infusion study in patient with predominant atrophy. Baseline pressure was low (3 mmHg) and increased only slightly to 18 mmHg during infusion of a rate of 1.5 mL/min, giving normal value of resistance to CSF outflow (10 mmHg/(mL/min)). Compensatory reserve was good, even during infusion (RAP did not increase), pulse amplitude increased very modestly in response to rising ICP, and there was very little slow waves in recording

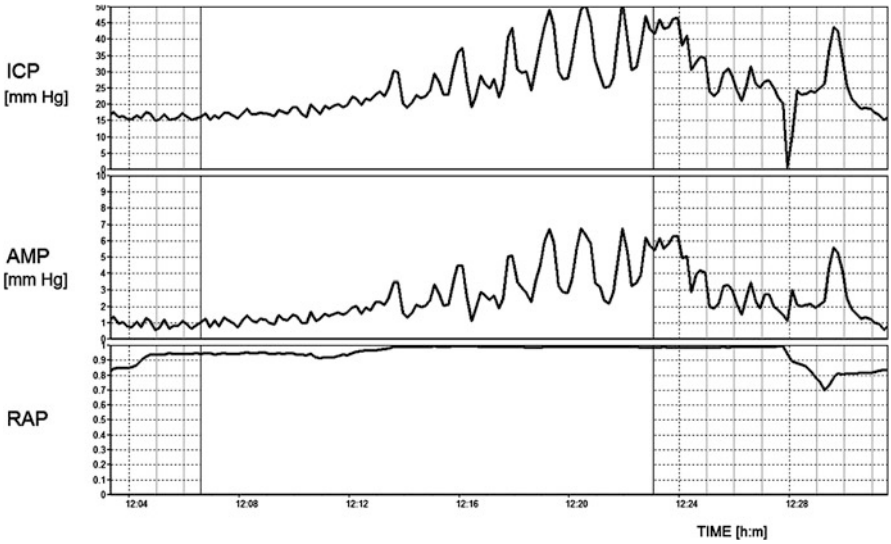

Fig. 8.18 Acute hydrocephalus. Opening pressure was slightly elevated (17 mmHg), resistance to CSF outflow was 26 mmHg/(mL/min), and RAP close to +1 all the time indicated permanently depleted compensatory reserve. Very strong vasogenic waves were recorded during the test (of maximum magnitude around 25 mmHg)

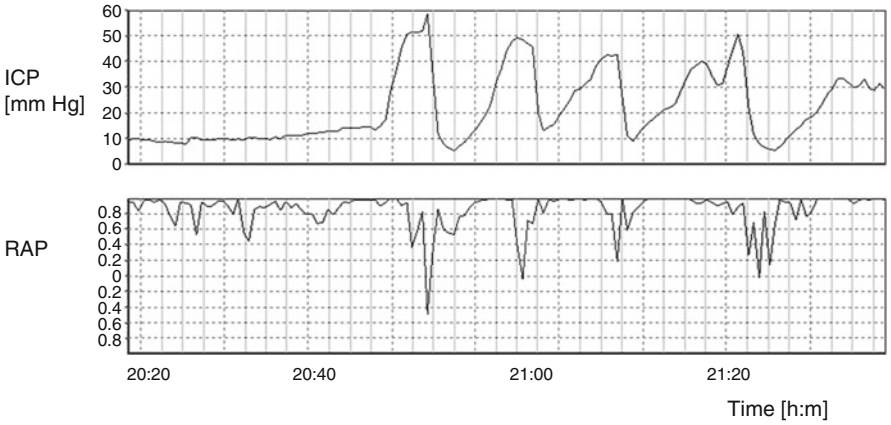

Fig. 8.19 Example of recording of ICP in patient after SAH, with moderate ventricular dilatation, in whom baseline pressure was normal (10 mmHg). Computer recording revealed a regular pattern of plateau waves up to 60 mmHg. This patient previously had a series of manometric lumbar CSF measurements yielding mixed results: some measurements indicating normal pressure, while others showed elevated ICP

Infusion testing or overnight ICP monitoring repeated after shunting should always be considered for comparison with the tests performed before surgery. Abnormal cerebrospinal compensatory parameters, such as high resting pressure, increased resistance to CSF outflow, low compensatory reserve, increased activity of slow waves, or high amplitude of pulse waveform, should return to normal after successful shunting [7, 8]. In valves with a low hydrodynamic resistance and a well-defined opening pressure, a sharp plateau of the pressure trend is seen at about 1–5 mmHg above the level of the shunt's operating pressure [87]. The magnitude of this plateau should not exceed a value as defined by the equation:

$$\text{Critical pressure} = \text{Shunt operating pressure} + (R_{\text{shunt}} \times \text{Infusion rate}) + 5\text{mmHg},$$

where R_{shunt} is the hydrodynamic resistance of the opened shunt and 5 mmHg is a 'safety margin' and a credit for possible nonzero abdominal pressure (in patients with possible increased abdominal pressure, this value should be increased to 10–15 mmHg). Both shunt operating pressures and R_{shunt} can be measured in the laboratory, but once evaluated, these parameters provide an unvaluable guidelines for shunt testing in vivo (Fig. 8.20) [86].

These methods of assessing CSF dynamics in shunted patients can be based on different techniques. The simplest and least invasive way is an infusion study through a previously implanted subcutaneous CSF reservoir. Lumbar puncture in communicating hydrocephalus or measurement of the pressure inside the chamber

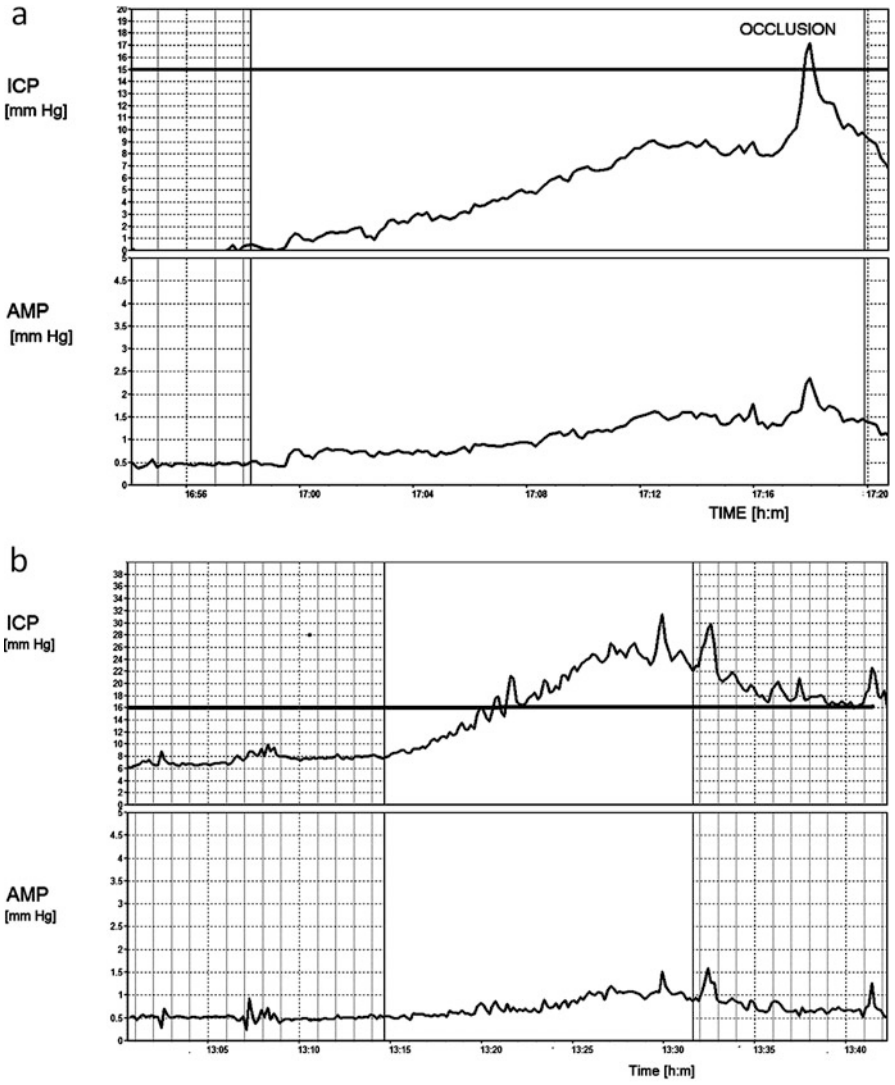

Fig. 8.20 Examples of infusion studies performed in shunted patients through shunt prechamber with working (**a**) and blocked (**b**) shunt. (**a**) Patient with a Strata Valve set for 1.5 in situ. Pulse amplitude was low but clearly recordable, confirming patency of ventricular drain. Opening pressure was low, and during infusion pressure increased to the value below 'critical threshold' for this valve (thick vertical line). During infusion, transcutaneous occlusion (external compression of siphon-control device) was performed. Such a compression stops the drainage through the valve. Pressure started to rise immediately, confirming that shunt system was patent. (**b**) Patient with Hakim Programmable Valve set at 100 mm H2O. Pressure increased well above 'critical threshold' (horizontal line). Spontaneous vasogenic waves were recorded during the test. Pulse waveform was present in recording. There was distal obstruction of shunt system confirmed during the revision of the shunt

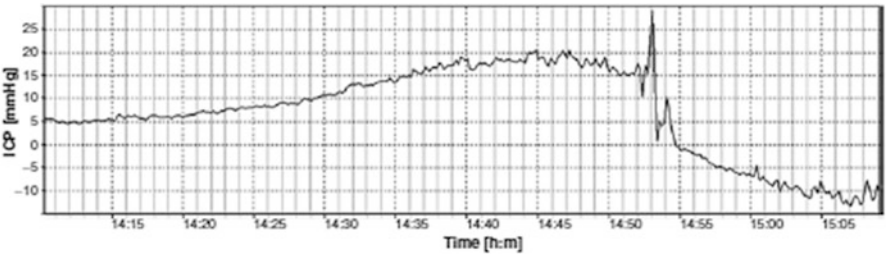

Fig. 8.21 Overdrainage test. Showing excessive decrease in ICP(below −14 mm Hg) during sitting up at the time point indicated after 14:53. During the test pulse amplitude often decrease, but it may not change or even increase in some cases

of the shunt is also possible. Pressure measurement and infusion into shunt chamber are only possible with shunts having a CSF sampling reservoir proximal to the valve; therefore, the method is not useful for the testing of majority of burr hole valves. With pressure measurement via the shunt chamber, the presence of a CSF pressure pulse wave and a pressure increase in response to coughing should indicate pressure transmission between the needle and the CSF space, confirming the patency of the ventricular catheter.

When a shunted patient presents with low-pressure headache, small or slit ventricles, subdural collections, or chronic subdural hematomas, CSF overdrainage can be suspected. Overdrainage related to body posture may be assessed using a tilting test. When the baseline pressure measured in the horizontal body position is low (usually negative), overdrainage is possible. A change of posture to sitting usually produces a further decrease in pressure. If the pressure decreases to a value lower than −10 mmHg (95% confidence limit for ICP in upright position in nonshunted patients is approximately −8 mmHg), overdrainage is likely (Fig. 8.21).

The majority of contemporary valves usually have a low hydrodynamic resistance [85], a feature which may cause overdrainage resulting from the periodic oscillations of cerebrovascular volume. The expanding vascular bed would act like the membrane of a water pump with a distal low-resistance valve [88]. Early morning headache should not be always assumed to be a ‘high pressure’: they may instead be a consequence of low pressure caused by nocturnal overdrainage. In shunted patients with slit ventricles, baseline pressure recorded from the shunt prechamber would not comprise a pulse waveform as the ventricle walls would be collapsed around the catheter, and therefore no pressure transmission would take place. Often, however, the pulse wave appears after infusion starts, as the pressure builds up and opens up the ventricles (Fig. 8.22).

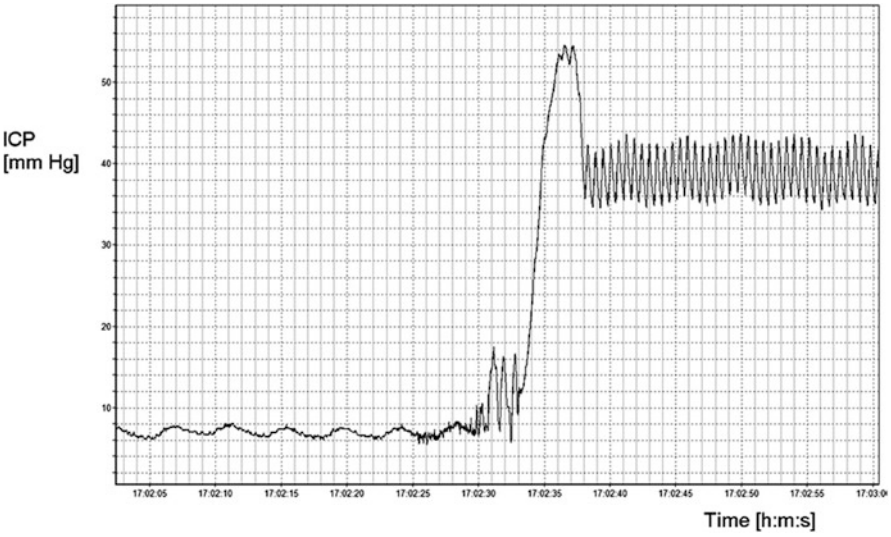

Fig. 8.22 In patients with slit ventricles, the pulse wave of ICP is rarely visible in recording. During infusion into shunt prechamber, all fluid is drained; distally recorded pressure is equivalent to shunt operating pressure plus pressure gradient along distal tube plus abdominal pressure. Respiratory wave can be visible – it is commonly transmitted from abdominal space. In patients with membrane siphon, preventing device occlusion can be performed during infusion (17:02). Pressure increases quickly to very high values (in this case above 50 mmHg), collapsed ventricles open within relatively short time, and pressure stabilises at lower level with a pulse wave clearly visible. The 'stabilisation pressure' is elevated, as in slit ventricles syndrome, and intraparenchymal ICP is usually high. Ventricles may stay open over longer time, but more frequently they collapse again after the end of infusion

8.10.4 Phase-Contrast MRI in Clinical Practice

PC-MRI is used in clinical practice to study hydrocephalus and other CSF circulatory disorders. In the case of obstructive hydrocephalus, PC-MRI is a rapid and accurate tool to confirm aqueduct stenosis, detecting no flow in the aqueduct [65]. In the case of noncommunicating hydrocephalus depicted in Fig. 8.23**,** treatment by endoscopic third ventriculostomy (ETV) was an alternative to ventricular shunting for the treatment of hydrocephalus. The PC-MRI technique is now largely widespread to measure CSF flow in the third ventricle aperture to check the viability of ETV.

For many authors, in the case of communicating hydrocephalus, increased ventricular CSF oscillations are predictive of a favourable outcome of shunting [71, 75, 77–79]. A recent study found a relationship between poor clinical outcome and low ventricular CSF pulsation [89]. It has been suggested [75] that increase in aqueductal CSF pulsatile flow was not associated with increased CSF flow at

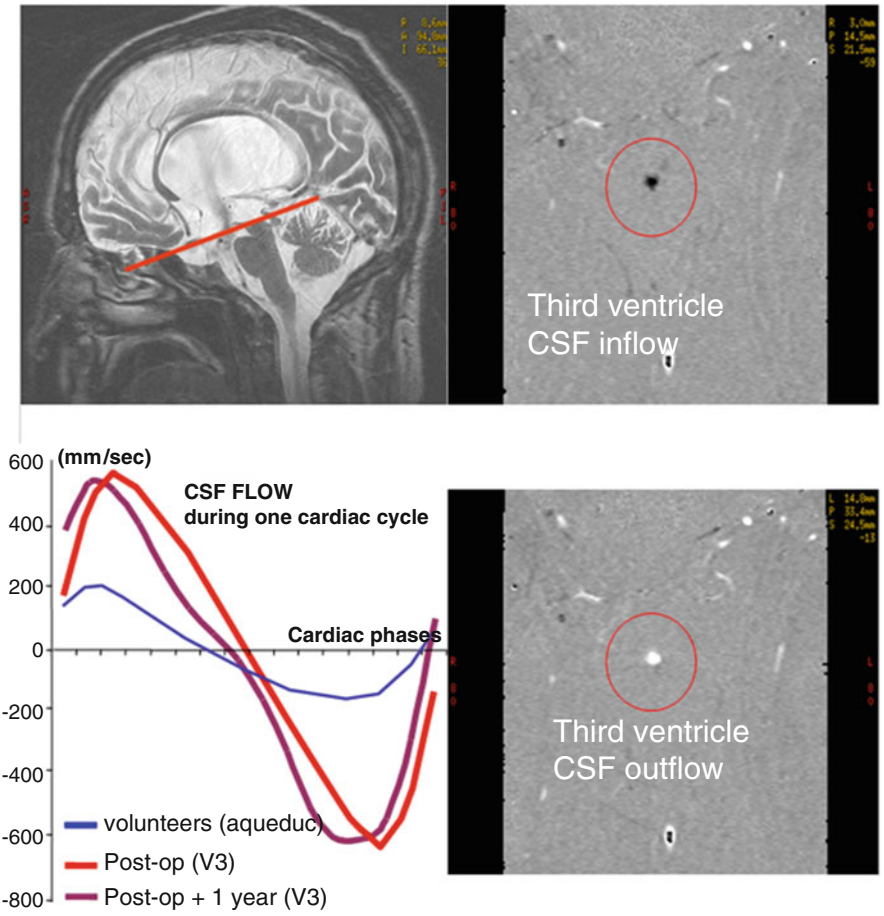

Fig. 8.23 Example of noncommunicating hydrocephalus studied using PC-MRI examination. The patient had aqueductal stenosis, detected by PC-MRI and treated by ETV. PC-MRI was performed 3 months after surgery to confirm the aperture of the third ventricle. In comparison with volunteer curve flow (in blue), we can see that CSF flow in the third ventricle aperture has the same temporal evolution, whereas its amplitude is increased. This difference can be due to the third ventricle aperture flow resistance which is smaller than in normal aqueduct. One year later, PC-MRI in the same patient showed a similar CSF flow curve at the third ventricle aperture

the cervical level (Fig. 8.24). Therefore, if communicating hydrocephalus cervical flow was stable while ventricular flow was dramatically increased, then intracranial subarachnoid space (SAS) flow must have been dramatically decreased. These results confirm that, in healthy volunteers, the intracranial mobile compliance predominantly depends on the intracranial subarachnoid pulsation. Communicating hydrocephalus seems to be an adaptation process of the vascular brain expansion when intracranial subarachnoid space CSF pulsation is altered.

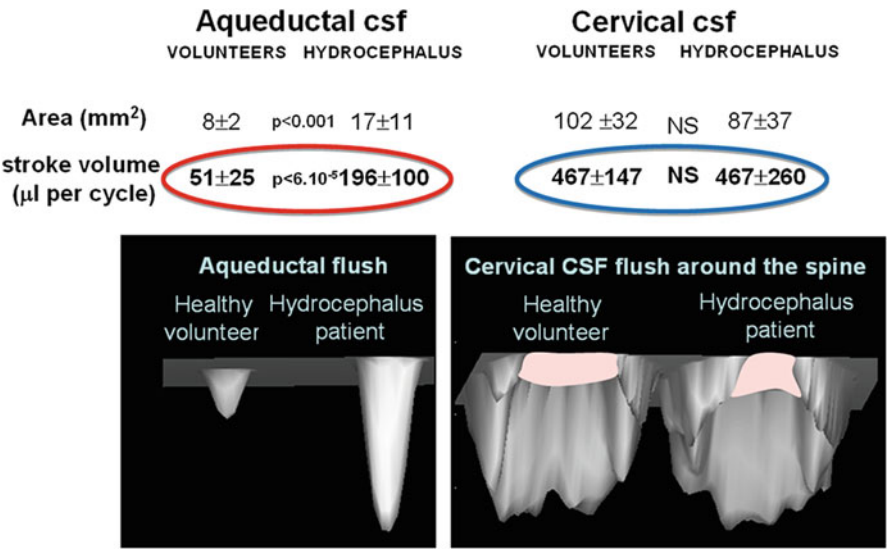

Fig. 8.24 CSF flows in communicating hydrocephalus population studied using PC-MRI

PC-MRI, now available to neurosurgeons, is complementary to morphological MR and provides quantitative information on cerebral hydrodynamics (Fig. 8.25). This information is mainly used to confirm alteration of CSF flow in the cerebral and spinal compartments. PC-MRI is also a functional tool to better understand the pathophysiology of hydrocephalus, and it should lead in the medium term to an assessment of intracranial pressure.

8.11 Conclusion

Understanding of dual aspects of CS dynamics emerging of time profiles of pressures (studied using ICP monitoring, infusion tests, etc.) and flows (visualised and analysed using PC-MRI) is paramount in contemporary diagnostic of hydrocephalus and other CSF disorders. Fluid circulation and pressure-volume compensation can be studied using invasive pressure measurement or noninvasive PC-MRI techniques, allowing description of patients' status using modelling parameters: resistance to CSF outflow, elasticity, or CSF stroke volume in various craniocerebral compartments (Table 8.1). Future clinical works should be focused on integration of pressure measurement techniques and PC-MRI.

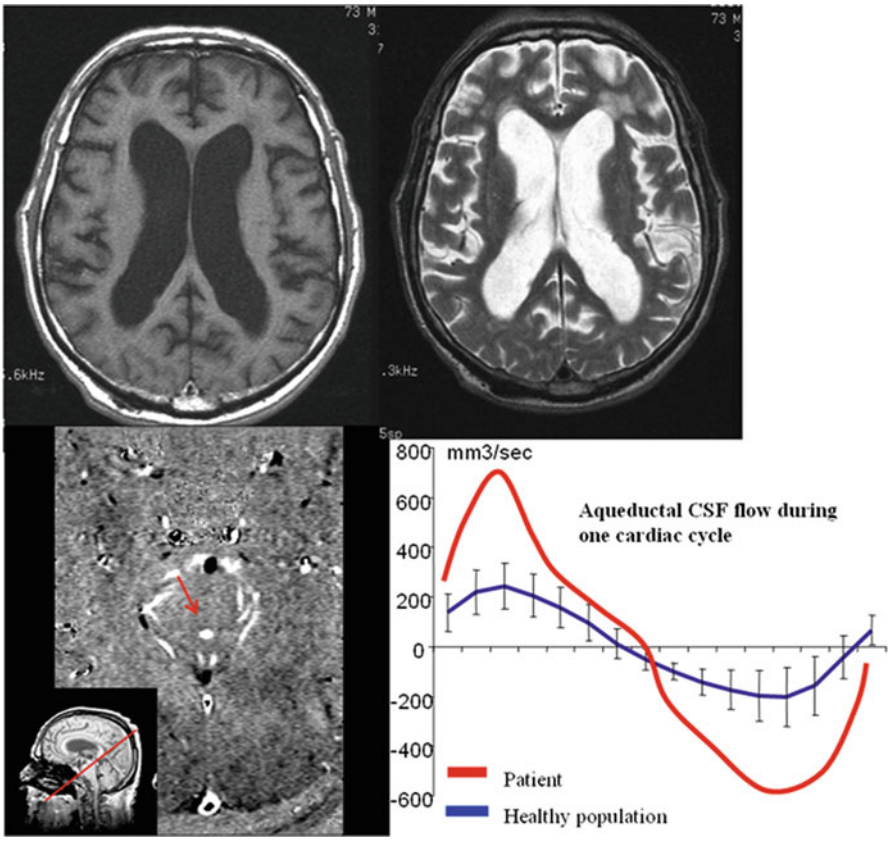

Fig. 8.25 CSF flows in communicating hydrocephalus patient studied by PC-MRI. This 73-year-old man, with a history of hypertension, was referred for assessment of disorders of higher functions associated with gait disorders (ataxia) and sphincter disorders. Morphological MR demonstrated a dilation of the ventricular system, some deep cortical sulci, and nonspecific abnormalities of the periventricular white matter. The clinical and morphological assessment was unable to formally demonstrate the active nature of the ventricular dilation and the indication for ventricular shunting. The oscillatory flow volume measured in the cerebral aqueduct was very high, but normal CSF fluctuations were observed in the cervical subarachnoid spaces. The blood flow was small (334 mL/min), and the peak jugular vein outflow velocity was observed early after the arterial systolic peak. Ventriculoperitoneal shunting induced a marked clinical improvement with resolution of the gait disorders and sphincter disorders. Radiological follow-up demonstrated a reduction of ventricular volume. In this clinical case, demonstration of a markedly hyperdynamic ventricular system supported the indication for ventricular shunting in this patient; as for many authors, increased ventricular activity is predictive of a favourable outcome of shunting

Table 8.1 Typical values for parameters of CSF dynamics in nonshunted patients

	Atrophy	NPH	Acute hydrocephalus
p_b [mmHg]	<10	<15	>15
R_{CSF} [mmHg/(mL/min)]	<10	>13	>18
AMP [mmHg]	<2	>2	>4
E [mL^{-1}]	<0.1	<0.2	>0.2
Vasogenic waves	No vasogenic waves	B waves present and increased during infusion	Increased B waves and plateau waves
RAP	<0.6 all time	<0.6 at baseline	>0.6 all time
		>0.6 during test	

p_b baseline value of intracranial pressure, R_{CSF} resistance to CSF outflow, *AMP* pulse amplitude of intracranial pressure, *E* elasticity or elastance coefficient, *RAP* index of brain compliance

References

1. Stein, S.C., Burnett, M.G., Sonnad, S.S.: Shunts in normal pressure hydrocephalus: do we place too many or too few? J. Neurosurg. **105**, 815–822 (2006)
2. Marmarou, A., Black, P., Bergsneider, M., P. Klinge & N. Relkin, International NPH Consultant Group: Guidelines for management of idiopathic normal pressure hydrocephalus: progress to date. Acta Neurochir. Suppl. **95**, 237–240 (2005)
3. Pickard, J.D., Spiegelhalter, D., Czosnyka, M.: Health economics and the search for shunt-responsive symptomatic hydrocephalus in the elderly. J. Neurosurg. **105**, 811–814 (2006)
4. Drake, J.M., Saint-Rose, C.H. (eds.): Shunt complications. In: The Shunt Book, pp. 23–92. Blackwell Science, Oxford (1995)
5. Czosnyka, M., Maksymowicz, W., Batorski, L., Koszewski, W., Czosnyka, Z.: Comparison between classic differential and automatic shunt functioning on the basis of infusion tests. Acta Neurochir. **106**, 1–8 (1990)
6. Maksymowicz, W., Czosnyka, M., Koszewski, W., Szymanska, O., Zabolotny, W.: Post shunting improvement in hydro-cephalic patients described by cerebrospinal compensatory parameters. In: Avezaat, C.J.J., van Eijndhoven, J.H.M., Maas, A.I.R., Tans, J.T.J. (eds.) Intracranial Pressure VIII, pp. 829–832. Springer, Berlin (1994)
7. Maksymowicz, W., Czosnyka, M., Koszewski, W., Szymanska, A., Traczewski, W.: The role of cerebrospinal system compensatory parameters in estimation of functioning of implanted shunt system in patients with communicating hydrocephalus. Acta Neurochir. **101**, 112–116 (1989)
8. Petrella, G., Czosnyka, M., Keong, N., Pickard, J.D., Czosnyka, Z.: How does CSF dynamics change after shunting? Acta Neurol. Scand. **118**(3), 182–188 (2008)
9. Sorenson, P.S., Gjerris, F., Schmidt, J.: Resistance to CSF outflow in benign intracranial hypertension (pseudotumor cerebri). In: Gjerris, F., Borgesen, S.E., Sorensen, P.S. (eds.) Outflow of Cerebrospinal Fluid, pp. 343–355. Munskgaard, Copenhagen (1989)
10. Tans, J.T., Boon, A.J., Study Group: How to select patients with normal pressure hydrocephalus for shunting. Acta Neurochir. Suppl. **81**, 3–5 (2002)
11. Czosnyka, M., Copeman, J., Czosnyka, Z., McConnell, R., Dickinson, C., Pickard, J.D.: Post-traumatic hydrocephalus: influence of craniectomy on the CSF circulation. J. Neurol. Neurosurg. Psychiatry. **68**, 246–247 (2000)
12. May, C., Kaye, J.A., Atack, J.R., Schapiro, M.B., Friedland, R.P., Rapoport, S.I.: Cerebrospinal fluid production is reduced in healthy aging. Neurology. **40**, 500–503 (1990)

13. Manet, R., Fabre, N., Moyse, E., Laurent, B., Schmidt, E.A.: Intracranial hypertension is painless! Acta Neurochir. Suppl. **122**, 275–277 (2016)
14. Davson, H., Welch, K., Segal, M.B.: The Physiology and Pathophysiology of Cerebrospinal Fluid. Churchill Livingstone, New York (1987)
15. Lalou, A.D., Levrini, V., Garnett, M., Nabbanja, E., Kim, D.J., Gergele, L., Bjornson, A., Czosnyka, Z., Czosnyka, M.: Validation of Davson's equation in patients suffering from idiopathic normal pressure hydrocephalus. Acta Neurochir. (Wien). **160**(5), 1097–1103 (2018)
16. Gjerris, F., Borgesen, S.E.: Pathophysiology of CSF circulation. In: Crockard, A., Hayward, A., Hoff, J.T. (eds.) Neurosurgery. The Scientific Basis of Clinical Practice, pp. 146–174. Blackwell Scientific, Oxford (1992)
17. Momjian, S., Owler, B.K., Czosnyka, Z., Czosnyka, M., Pena, A., Pickard, J.D.: Pattern of white matter regional cerebral blood flow and autoregulation in normal pressure hydrocephalus. Brain. **127**(pt 5), 965–972 (2004)
18. Stoquart-ElSankari, S., Lehmann, P., Villette, A., Czosnyka, M., Meyer, M.E., Deramond, H., Baledent, O.: A phase-contrast MRI study of physio-logical cerebral venous flow. J. Cereb. Blood Flow Metab. **29**, 1208–1215 (2009)
19. Bradley Jr., W.G., Whittemore, A.R., Kortman, K.E., Watanabe, A.S., Homyak, M., Teresi, L.M., Davis, S.J.: Marked cerebrospinal fluid void: indicator of successful shunt in patients with suspected normal-pressure hydrocephalus. Radiology. **178**(2), 459–466 (1991)
20. Egnor, M., Zheng, L., Rosiello, A., Gutman, F., Davis, R.: A model of pulsations in communicating hydro-cephalus. Pediatr. Neurosurg. **36**(6), 281–303 (2002)
21. Eide, P.K.: Intracranial pressure parameters in idiopathic normal pressure hydrocephalus patients treated with ventriculo-peritoneal shunts. Acta Neurochir. **148**(1), 21–29 (2006)
22. Nedergaard, M.: Neuroscience. Garbage truck of the brain. Science. **340**(6140), 1529–1530 (2013)
23. Orešković, D., Radoš, M., Klarica, M.: New concepts of cerebrospinal fluid physiology and development of hydrocephalus. Pediatr. Neurosurg. **52**(6), 417–425 (2017)
24. Manet, R., Payen, J.F., Gergelé, L.: Using external lumbar CSF drainage to treat communicating external hydrocephalus in adult patients after acute traumatic or non-traumatic brain injury. Acta Neurochir. **159**(10), 2003–2009 (2017)
25. Marmarou, A., Foda, M.A., Bandoh, K.: Posttraumatic ventriculomegaly: hydrocephalus or atrophy? A new approach for diagnosis using CSF dynamics. J. Neurosurg. **85**(6), 1026–1035 (1996)
26. Huh, P.W., Yoo, D.S., Cho, K.S., Park, C.K., Kang, S.G., Park, Y.S., Kim, D.S., Kim, M.C.: Diagnostic method for differentiating external hydrocephalus from simple subdural hygroma. J. Neurosurg. **105**(1), 65–70 (2006)
27. Nakae, S., Murayama, K., Adachi, K., Kumai, T., Abe, M., Hirose, Y.: Novel application of time-spatial labeling inversion pulse magnetic resonance imaging for diagnosis of external hydrocephalus. World Neurosurg. **109**, 197–201 (2018)
28. Zanini, M.A., de Lima Resende, L.A., de Souza Faleiros, A.T., Gabarra, R.C.: Traumatic subdural hygromas: proposed pathogenesis-based classification. J. Trauma. **64**(3), 705–713 (2008)
29. Yoshimoto, Y., Wakai, S., Hamano, M.: External hydrocephalus after aneurysm surgery: paradoxical response to ventricular shunting. J. Neurosurg. **88**(3), 485–489 (1998)
30. Tzerakis, N., Orphanides, G., Antoniou, E., Sioutos, P.J., Lafazanos, S., Seretis, A.: Subdural effusions with hydrocephalus after severe head injury: successful treatment with ventriculoperitoneal shunt placement: report of 3 adult cases. Case Rep. Med. **2010**, 743784 (2010)
31. Marmarou, A., Shulman, K., Rosende, R.M.: A non-linear analysis of CSF system and intracranial pressure dynamics. J. Neurosurg. **48**, 332–344 (1978)
32. Avezaat, C.J.J., Eijndhoven, J.H.M.: Cerebrospinal fluid pulse pressure and craniospinal dynamics. A theoretical, clinical and experimental study (thesis). Jongbloedrr A, The Hague (1984)
33. Sliwka, S.: A clinical system for the evaluation of selected dynamic properties of the intracranial system. PhD Thesis, Polish Academy of Sciences, Warsaw (in Polish) (1980)

34. Boon, A.J., Tans, J.T., Delwel, E.J., Egeler-Peerdeman, S.M., Hanlo, P.W., Wurzer, H.A., Avezaat, C.J., de Jong, D.A., Gooskens, R.H., Hermans, J.: Dutch normal-pressure hydrocephalus study: prediction of outcome after shunting by resistance to outflow of cerebrospinal fluid. J. Neurosurg. **87**(5), 687–693 (1997)
35. Borgesen, S.E., Gjerris, F.: The predictive value of conductance to outflow of CSF in normal pressure hydrocephalus. Brain. **105**, 65–86 (1982)
36. Ekstedt, J.: CSF hydrodynamic studies in man. Method of constant pressure CSF infusion. J. Neurol. Neurosurg. Psychiatry. **40**, 105–119 (1977)
37. Frieden, H., Ekstedt, J.: Instrumentation for cerebrospinal fluid hydrodynamic studies in man. Med. Biol. Eng. Comput. **20**, 167–180 (1982)
38. Jurkiewicz, J., Czernicki, Z., Berdyga, J., Uchman, G.: Three-phase infusion test. Neurol. Neurochir. Pol. **28**, 363–369 (1994)
39. Katzman, R., Hussey, F.: A simple constant infusion manometric test for measurement of CSF absorption. Neurology. **20**, 534–544 (1970)
40. Tisell, M., Edsbagge, M., Stephensen, H., Czosnyka, M., Wikkelso, C.: Elastance correlates with outcome after endo-scopic third ventriculostomy in adults with hydrocephalus caused by primary aqueductal stenosis. Neurosurgery. **50**, 70–76 (2002)
41. Tans, J.T., Poortvliet, D.C.: Relationship between compliance and resistance to outflow of CSF in adult hydrocephalus. J. Neurosurg. **71**(1), 59–62 (1989)
42. Borgesen, S.E., Gjerris, F., Sorensen, S.C.: The resistance to cerebrospinal fluid absorption in humans: a method of evaluation by lumbo-ventricular perfusion, with particular reference to normal pressure hydrocephalus. Acta Neurol. Scand. **57**, 88–96 (1978)
43. Borgesen, S.E., Albeck, M.J., Gjerris, F., Czosnyka, M., Laniewski, P.: Computerized infusion test compared to steady pressure constant infusion test in measurement of resistance to CSF outflow. Acta Neurochir. **119**, 12–16 (1992)
44. Czosnyka, M., Batorski, L., Laniewski, P., Maksymowicz, W., Koszewski, W., Zaworski, W.: A computer system for the identification of the cerebrospinal compensatory model. Acta Neurochir. **105**, 112–116 (1990)
45. Czosnyka, M., Czosnyka, Z., Momjian, S., Pickard, J.D.: Cerebrospinal fluid dynamics. Physiol. Meas. **25**, R51–R76 (2004)
46. Schuhmann, M.U., Sood, S., McAllister, J.P., Jaeger, M., Ham, S.D., Czosnyka, Z., Czosnyka, M.: Value of overnight monitoring of intracranial pressure in hydrocephalic children. Pediatr. Neurosurg. **44**(4), 269–279 (2008)
47. Antes, S., Stadie, A., Müller, S., Linsler, S., Breuskin, D., Oertel, J.: Intracranial pressure-guided shunt valve adjustments with the Miethke sensor reservoir. World Neurosurg. **109**, e642 (2018)
48. Welschehold, S., Schmalhausen, E., Dodier, P., Vulcu, S., Oertel, J., Wagner, W., Tschan, C.A.: First clinical results with a new telemetric intracranial pressure-monitoring system. Neurosurgery. **70**(1 Suppl Operative), 44–49 (2012).; discussion 49
49. Owler, B.K., Fong, K.C., Czosnyka, Z.: Importance of ICP monitoring in the investigation of CSF circulation disorders. Br. J. Neurosurg. **15**(5), 439–440 (2001)
50. Czosnyka, M., Whitehouse, H., Smielewski, P., Simac, S., Pickard, J.D.: Testing of cerebrospinal compensatory reserve in shunted and non-shunted patients: a guide to interpretation based on an observational study. J. Neurol. Neurosurg. Psychiatry. **60**, 549–558 (1996)
51. Sklar, F.H., Beyer, C.W., Ramanathan, M., Elashvili, I., Cooper, P.R., Clark, W.K.: Servo-controlled lumbar infusions: a clinical tool for determination of CSF dynamics as a function of pressure. Neurosurgery. **3**, 170–178 (1978)
52. Eide, P.K., Brean, A.: Intracranial pulse pressure amplitude levels determined during pre-operative assessment of subjects with possible idiopathic normal pressure hydrocephalus. Acta Neurochir. **148**(11), 1151–1156 (2006).; discussion 1156
53. Qvarlander, S., Lundkvist, B., Koskinen, L.-O.D., Malm, J., Eklund, A.: Pulsatility in CSF dynamics: pathophysiology of idiopathic normal pressure hydrocephalus. J. Neurol. Neurosurg. Psychiatry. **84**(7), 735–741 (2013)

54. Czosnyka, Z.H., Lalou, A.D., Nabanja, E., Pickard, J.D., Garnett, M., Keong, N.C., Schmidt, E.A., Kim, D.J., Czosnyka, M.: Lower breakpoint of intracranial amplitude-pressure relationship in NPH. Fluids Barriers CNS. **15**(Suppl 1), A31 (2018)
55. Kasprowicz, M., Czosnyka, M., Czosnyka, Z., Momjian, S., Smielewski, P., Juniewicz, H., Pickard, J.D.: Hysteresis of the cerebrospinal pressure-volume curve in hydrocephalus. Acta Neurochir. Suppl. **86**, 529–532 (2003)
56. Eide, P.K.: A new method for processing of continuous intracranial pressure signals. Med. Eng. Phys. **28**(6), 579–587 (2006)
57. Lundberg, N.: Continuous recording and control of ventricular fluid pressure in neurosurgical practice. Acta Psychiatr. Scand. Suppl. **36**(149), 1–193 (1960)
58. Pickard, J.D., Teasdale, G., Matheson, M., Lindsay, K., Galbraith, S., Wyper, D., Macpherson, P.: Intraventricular pressure waves – the best predictive test for shunting in normal pressure hydrocephalus. In: Shulman, K., Marmarou, A., Miller, J.D., Becker, D.P., Hochwald, D.M., Brock, M. (eds.) Intracranial Pressure IV, pp. 498–500. Springer, Berlin (1980)
59. Droste, D.W., Krauss, J.K.: Intracranial pressure B-waves precede corresponding arterial blood pressure oscillations in patients with suspected normal pressure hydrocephalus. Neurol. Res. **21**(7), 627–630 (1999)
60. Piper, I.R., Miller, J.D., Whittle, I.R., Lawson, A.: Automated time-averaged analysis of craniospinal compliance (short pulse response). Acta Neurochir. Suppl. **51**, 387–390 (1990)
61. Kim, D.J., Czosnyka, Z., Keong, N., Radolovich, D.K., Smielewski, P., Sutcliffe, M.P., Pickard, J.D., Czosnyka, M.: Index of cerebrospinal compensatory reserve in hydrocephalus. Neurosurgery. **64**(3), 494–501 (2009)
62. Baledent, O., Gondry-Jouet, C., Stoquart-Elsankari, S., Bouzerar, R., Le Gars, D., Meyer, M.E.: Value of phase contrast magnetic resonance imaging for investigation of cerebral hydrodynamics. J. Neuroradiol. **33**(5), 292–303 (2006)
63. Baledent, O., Henry-Feugeas, M.C., Idy-Peretti, I.: Cerebrospinal fluid dynamics and relation with blood flow: a magnetic resonance study with semiautomated cerebrospinal fluid segmentation. Investig. Radiol. **36**(7), 368–377 (2001)
64. Bhadelia, R.A., Bogdan, A.R., Kaplan, R.F., Wolpert, S.M.: Cerebrospinal fluid pulsation amplitude and its quantitative relationship to cerebral blood flow pulsations: a phase-contrast MR flow imaging study. Neuroradiology. **39**(4), 258–264 (1997)
65. Stoquart-El Sankari, S., Lehmann, P., Gondry-Jouet, C., Fichten, A., Godefroy, O., Meyer, M.E., Baledent, O.: Phase-contrast MR imaging support for the diagnosis of aqueductal stenosis. AJNR Am. J. Neuroradiol. **30**(1), 209–214 (2009)
66. Stoquart-ElSankari, S., Baledent, O., Gondry-Jouet, C., Makki, M., Godefroy, O., Meyer, M.E.: Aging effects on cerebral blood and cerebrospinal fluid flows. J. Cereb. Blood Flow Metab. **27**(9), 1563–1572 (2007)
67. Marmarou, A., Schulman, K., LaMorgese, J.: Compartmental analysis of compliance and outflow resistance of cerebrospinal fluid system. J. Neurosurg. **43**, 523–534 (1975)
68. Enzmann, D.R., Pelc, N.J.: Cerebrospinal fluid flow measured by phase-contrast cine MR. AJNR Am. J. Neuroradiol. **14**(6), 1301–1307; discussion 1309–1310 (1993)
69. Greitz, D., Wirestam, R., Franck, A., Nordell, B., Thomsen, C., Stahlberg, F.: Pulsatile brain movement and associated hydrodynamics studied by magnetic resonance phase imaging. The Monro-Kellie doctrine revisited. Neuroradiology. **34**(5), 370–380 (1992)
70. Henry-Feugeas, M.C., Idy-Peretti, I., Baledent, O., Poncelet-Didon, A., Zannoli, G., Bittoun, J., Schouman-Claeys, E.: Origin of subarachnoid cerebrospinal fluid pulsations: a phase-contrast MR analysis. Magn. Reson. Imaging. **18**(4), 387–395 (2000)
71. Wagshul, M.E., Chen, J.J., Egnor, M.R., McCormack, E.J., Roche, P.E.: Amplitude and phase of cerebrospinal fluid pulsations: experimental studies and review of the literature. J. Neurosurg. **104**(5), 810–819 (2006)
72. Feinberg, D.A., Crooks, L.E., Sheldon, P., Hoenninger 3rd, J., Watts, J., Arakawa, M.: Magnetic resonance imaging the velocity vector components of fluid flow. Magn. Reson. Med. **2**(6), 555–566 (1985)

73. Henry-Feugeas, M.C., Idy-Peretti, I., Blanchet, B., Hassine, D., Zannoli, G., Schouman-Claeys, E.: Temporal and spatial assessment of normal cerebrospinal fluid dynamics with MR imaging. Magn. Reson. Imaging. **11**(8), 1107–1118 (1993)
74. Nayler, G.L., Firmin, D.N., Longmore, D.B.: Blood flow imaging by cine magnetic resonance. J. Comput. Assist. Tomogr. **10**(5), 715–722 (1986)
75. Baledent, O., Gondry-Jouet, C., Meyer, M.E., De Marco, G., Le Gars, D., Henry-Feugeas, M.C., Idy-Peretti, I.: Relationship between cerebrospinal fluid and blood dynamics in healthy volunteers and patients with communicating hydrocephalus. Investig. Radiol. **39**(1), 45–55 (2004)
76. Bateman, G.A.: Vascular compliance in normal pressure hydrocephalus. AJNR Am. J. Neuroradiol. **21**(9), 1574–1585 (2000)
77. Bradley, W., Scalzo, D., Queralt, J., Nitz, W.N., Atkinson, D.J., Wong, P.: Normal-pressure hydrocephalus: evaluation with cerebrospinal fluid flow measurements at MR imaging. Radiology. **198**(2), 523–529 (1996)
78. Luetmer, P.H., Huston, J., Friedman, J.A., Dixon, G.R., Petersen, R.C., Jack, C.R., McClelland, R.L., Ebersold, M.J.: Measurement of cerebrospinal fluid flow at the cerebral aqueduct by use of phase-contrast magnetic resonance imaging: technique validation and utility in diagnosing idiopathic normal pressure hydrocephalus. Neurosurgery. **50**(3), 534–543; discussion 543–534 (2002)
79. Mase, M., Yamada, K., Banno, T., Miyachi, T., Ohara, S., Matsumoto, T.: Quantitative analysis of CSF flow dynamics using MRI in normal pressure hydrocephalus. Acta Neurochir. Suppl. **71**, 350–353 (1998)
80. Buonocore, M.H., Bogren, H.: Factors influencing the accuracy and precision of velocity-encoded phase imaging. Magn. Reson. Med. **26**(1), 141–154 (1992)
81. Baledent, O., Fin, L., Khuoy, L., Ambarki, K., Gauvin, A.C., Gondry-Jouet, C., Meyer, M.E.: Brain hydrodynamics study by phase-contrast magnetic resonance imaging and transcranial color doppler. J. Magn. Reson. Imaging. **24**(5), 995–1004 (2006)
82. Enzmann, D.R., Ross, M.R., Marks, M.P., Pelc, N.J.: Blood flow in major cerebral arteries measured by phase-contrast cine MR. AJNR Am. J. Neuroradiol. **15**(1), 123–129 (1994)
83. Egnor, M., Rosiello, A., Zheng, L.: A model of intracranial pulsations. Pediatr. Neurosurg. **35**(6), 284–298 (2001)
84. Penn, R.D., Linninger, A.: The physics of hydrocephalus. Pediatr. Neurosurg. **45**(3), 161–174 (2009)
85. Aschoff, A., Kremer, P., Benesch, C., Fruh, K., Klank, A., Kunze, S.: Overdrainage and shunt technology. Childs Nerv. Syst. **11**, 193–202 (1995)
86. Czosnyka, Z.H., Czosnyka, M., Pickard, J.D.: Shunt testing in-vivo: a method based on the data from the UK shunt evaluation laboratory. Acta Neurochir. Suppl. **81**, 27–30 (2002)
87. Taylor, R., Czosnyka, Z., Czosnyka, M., Pickard, J.D.: A laboratory model of testing shunt performance after implantation. Br. J. Neurosurg. **16**, 30–35 (2002)
88. Czosnyka, Z., Czosnyka, M., Richards, H.K., Pickard, J.D.: Posture-related overdrainage: comparison of the performance of 10 hydrocephalus shunts in vitro. Neurosurgery. **42**(2), 327–333 (1998)
89. Scollato, A., Gallina, P., Gautam, B., Pellicano, G., Cavallini, C., Tenenbaum, R., Di Lorenzo, N.: Changes in aqueductal CSF stroke volume in shunted patients with idiopathic normal-pressure hydrocephalus. AJNR Am. J. Neuroradiol. **30**(8), 1580–1586 (2009)

Chapter 9
Modelling of Cerebrospinal Fluid Flow by Computational Fluid Dynamics

Vartan Kurtcuoglu, Kartik Jain, and Bryn A. Martin

9.1 Introduction

The movement of cerebrospinal fluid (CSF) is linked to the cardiovascular and respiratory systems. The heart not only drives blood flow but is also at the origin of CSF pulsation through the expansion and contraction of cerebral blood vessels. Respiration modulates this cardiovascular action while also directly influencing spinal subarachnoid space (SAS) volume. CSF dynamics may be altered by pathologies such as hydrocephalus, Chiari malformation, syringomyelia and glioblastoma, and, in turn, dynamics of the CSF can be analysed to aid in disease diagnosis and prognosis. Several reviews delineate the current understanding of CSF motion [1–3]. This chapter describes the basic approach of and trends in computational fluid dynamics (CFD) modelling of CSF flow.

There are multiple types of computational models of fluid flow within and around the central nervous system (CNS). These can be roughly categorized into bulk models aimed at providing information on macroscale CSF dynamics and CFD models that yield spatially resolved data. The principal advantage of bulk models is their low computational demand, enabling calculations on personal computers rather than necessitating high-performance computing (HPC) resources. This is especially important in view of potential clinical applications, where access to HPC is scarce and results must be provided with minimal time delay. However, bulk models do not take into account the complex anatomy of the CSF spaces and cannot fully resolve the intricate dynamics of CSF flow. In contrast, three-dimensional (3D) CFD

V. Kurtcuoglu (✉) · K. Jain
University of Zurich, Institute of Physiology, Zurich, Switzerland
e-mail: vartan.kurtcuoglu@uzh.ch

B. A. Martin
University of Idaho, Department of Biological Engineering, Moscow, ID, USA

K. Miller (ed.), *Biomechanics of the Brain*, Biological and Medical Physics, Biomedical Engineering, https://doi.org/10.1007/978-3-030-04996-6_9

models can provide spatially and temporally resolved information on flow, pressure and mass transport, making them suitable for subject-specific calculations of CSF dynamics based on medical image data.

The laws of mass, momentum and energy conservation constitute the basis of CFD modelling. While the continuity equation is used to describe mass conservation, the Navier-Stokes equations are employed to characterize momentum conservation in Newtonian fluids. Energy conservation is often not imposed in CSF modelling, unless relevant temperature gradients are expected, such as in thermal ablation or CNS cooling applications.

CSF can be considered an incompressible Newtonian fluid with dynamic viscosity of approximately 0.8 mPa·s [4, 5]. For incompressible flow of a Newtonian fluid without external body forces, Eqs. 9.1 and 9.2 show Navier-Stokes and continuity equation, respectively:

$$\rho\left(\frac{\partial \boldsymbol{u}}{\partial t}+\boldsymbol{u}\cdot\nabla\boldsymbol{u}\right)=-\nabla p+\mu\nabla^2\boldsymbol{u} \tag{9.1}$$

$$\nabla\cdot\boldsymbol{u}=0 \tag{9.2}$$

Here, ρ is density, $\boldsymbol{u}$ is the velocity vector, t is time, p is pressure and μ is dynamic viscosity.

The calculation of solute transport with CSF is an important application of CFD. Depending on the solute molecular size, its solubility and biochemical and physical interactions with tissues and CNS fluids, more or less complex mathematic descriptions are required. In the simplest case, the solute can be considered a passive scalar that diffuses within CSF and is transported with its flow. This can be described by the advection-diffusion equation

$$\frac{\partial c}{\partial t}=D\,\nabla^2 c-(\boldsymbol{u}\cdot\nabla)\,c, \tag{9.3}$$

where c is the solute concentration and D is the diffusion coefficient of the solute in CSF.

CFD modelling of CSF dynamics started in 1996 with the work of Jacobson et al. [6]. This is much later than the first application of CFD in hemodynamics in the early 1970s, which may be due to better recognition of the cardiovascular system by engineers, mathematicians, computer scientists and physicists who are the primary developers and users of CFD tools. Furthermore, advances in the understanding of CSF space anatomy and cerebrospinal fluid dynamics physiology – prerequisites for meaningful CFD modelling – are linked to the emergence of commercial magnetic resonance imaging (MRI) systems in the 1980s. With MRI, it became possible to obtain anatomically accurate descriptions of the CSF spaces and noninvasive measurements of fluid velocities. These are needed to specify realistic CFD model domains and set model boundary conditions, respectively.

The procedural steps in CFD modelling of cerebrospinal fluid dynamics are similar to those encountered in generic problems of incompressible, isothermal internal flows. In a first step, the model domain must be defined, which consists of at least one fluid domain and, if the deformation of surrounding tissue is to be modelled, one or more solid domains. In the second step, these domains must be discretized, which includes choosing a spatial discretization scheme and generating a computational grid. Depending on the manageable grid size, which is primarily determined by the available computer resources, and expected flow conditions, a turbulence modelling scheme may be necessary as well. Next, the behaviour of the fluids and solids at their respective domain boundaries must be prescribed, i.e. corresponding pressures, velocities or their derivatives in those areas must be determined a priori and set accordingly. In the fourth step, the physical properties of the fluids and solids (rheology, material properties) have to be set. Finally, the Navier-Stokes, continuity and, if considered, transport equations must be solved based on appropriate initial conditions. If the problem is transient, a suitable temporal discretization scheme is required. The following section discusses these steps for the case of subject-specific CSF flow simulations based on MRI data.

9.2 Procedural Steps in CFD Modelling of CSF Dynamics

9.2.1 Obtaining the Model Domain

The cerebrospinal fluid spaces consist of a number of connected compartments (Fig. 9.1). For modelling purposes, MRI is the most widely used method for determining their shapes and the anatomies of associated blood vessels. Due to limits in resolution, the largest part of the cerebral vasculature cannot be acquired in sufficient detail for CFD. If the interaction between blood and CSF flow is to be taken into account explicitly by calculating the transient displacements of the arterial walls and transmission to the CSF space, smaller vessels have to be simulated via lower-order models. These models can be coupled to the CFD representations of larger vessels. However, this coupling poses numerical and computational challenges [7]. MRI partial volume effects also limit CSF space representation of small features such as the foramina of Monro, Luschka and Magendie, posterior horns of the lateral ventricles, aqueduct of Sylvius and recesses of the third and fourth ventricle [8]. Nevertheless, the overall size of these entities is large enough that lower-order modelling is not required. In contrast, the SAS features minute structures such as nerve roots, denticulate ligaments and arachnoid trabeculae that cannot be imaged adequately or captured at all by current clinical MRI systems. Despite their small sizes, these entities may increase the pressure drop along the SAS substantially [9, 10]. Nerve roots and similar structures can be integrated into the computational domain artificially by computer-aided design based on generic high-resolution anatomy data [11, 12]. The contribution of arachnoid trabeculae to flow

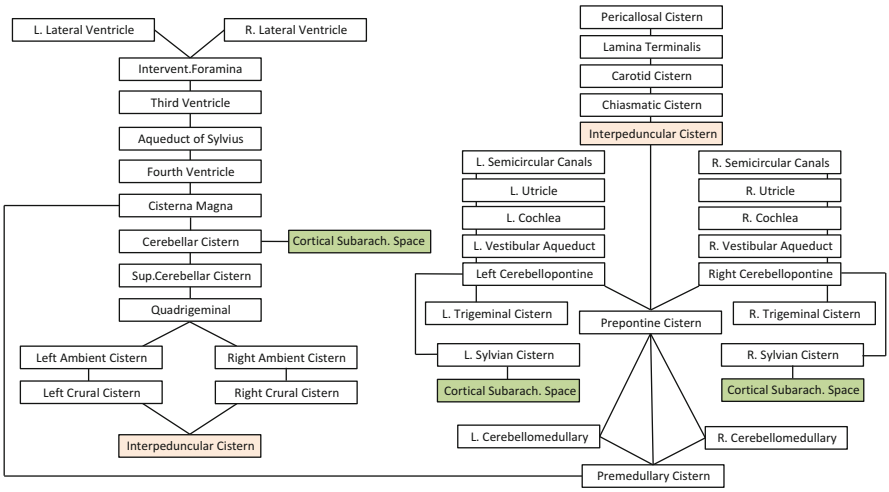

Fig. 9.1 Flow chart depicting CSF space fluid connections between the SAS, cisterns and ventricles. Boxes with similar colours represent connected regions (without line shown). Note: the L and R cochlea, utricle and semicircular canals are not commonly included as part of the CSF system, although they do feature fluid connections with CSF. (Abbreviations: L left, R right, Intervent. interventricular, Sup. superior)

resistance can be taken into account by approximating the model domain as a porous medium with a defined CSF space permeability [9].

An important challenge associated with the porous medium approach is the lack of experimental data on SAS permeability. Consequently, permeability must be estimated based on microscale structure and distribution. Such anatomic data can be obtained, for example, by electron microscopy [13–15] or optical coherence tomography [16]. A review of arachnoid trabeculae morphology is provided by Mortazavi et al. [17]. Once a quantitative description is determined, permeability can be estimated through CFD or analytical exploration in an idealized SAS microstructure representation, most likely the simplest of which is an array of straight circular cylinders connecting two parallel plates that represent the pia and arachnoid layers [18]. For this case, the relationship between porosity and permeability can be approximated by

$$\frac{k_\mathrm{l}}{r^2} = \frac{\varepsilon^2\left(\pi + 2.157\,(1-\varepsilon)\right)}{48(1-\varepsilon)^2} \quad \text{and} \quad \frac{k_\mathrm{t}}{r^2} = \frac{\pi\varepsilon\left(1-\sqrt{1-\varepsilon}\right)^2}{24(1-\varepsilon)^{3/2}}, \tag{9.4}$$

where k_l is longitudinal permeability (i.e. permeability in direction parallel to the cylinders representing the trabeculae), k_t is transverse permeability, r is the radius of the cylinders and ε is SAS porosity. Flow resistance caused by the SAS microstructure can then be accounted for by the addition of a pressure gradient to

the right-hand side of the Navier-Stokes equation. For a coordinate system aligned with the direction of the trabeculae, this results in

$$\rho\left(\frac{\partial \boldsymbol{u}}{\partial t}+\boldsymbol{u}\cdot\nabla\boldsymbol{u}\right)=-\nabla p+\mu\nabla^2\boldsymbol{u}-\mu\begin{pmatrix}u_1/k_l\\ u_2/k_t\\ u_3/k_t\end{pmatrix}. \tag{9.5}$$

Equation 9.5 is valid if inertial losses due to the porous microstructure are small compared to viscous drag [19]. While this is likely the case in parts of the SAS [9], more accurate information on trabecular geometry and configuration is needed for validation. Inertial losses in the SAS become relevant when larger obstacles such as blood vessels are considered. However, these vessels cannot be treated as part of the homogeneous trabecular microstructure, but could be introduced within the framework of a multiscale porous model [20], following the approach applied in other areas of flow modelling [21].

Once MR images of the CNS have been acquired, the anatomic structures to be included in the CFD model must be extracted by image segmentation. While a large number of approaches exist for the automatic segmentation of blood vessels [22], multipurpose image segmentation tools such as ITK-SNAP [23] and VMTK [24] are generally used for the CSF spaces. An example of CSF space segmentation is shown in Fig. 9.2. Segmentation of the CSF spaces is a time-consuming process in which considerable manual intervention is needed to obtain satisfactory results. While this presently imposes limits on the applicability of CFD for clinical CSF flow simulations, recent developments in the area of machine learning suggest that fast segmentation with minimal user intervention is on the horizon [26, 27], provided that a sufficient number of high-quality training data sets are produced by the community or major progress is made in unsupervised learning [28].

The output of the segmentation step is a volumetric representation of the anatomic structures of interest. For CFD modelling, a distinction needs to be made between the internal fluid region and its boundaries. This is generally achieved by surface triangulation [29]. The triangulation step is straightforward and can be carried out by various open-source and commercial programs. As an alternative to segmentation and triangulation, splines [30] can be used to delineate the contour of the structure of interest in each MR image, followed by a surface reconstruction step that smoothly joins the splines to an approximation of the respective boundary. Surface reconstruction can also be performed after triangulation, which combines the benefits of voxel-based segmentation (preservation of original shape details) with those of spline description (scalability, small file size, best template for computational grid generation). The disadvantage is that surface reconstruction of complex triangulated surfaces requires substantial manual work.

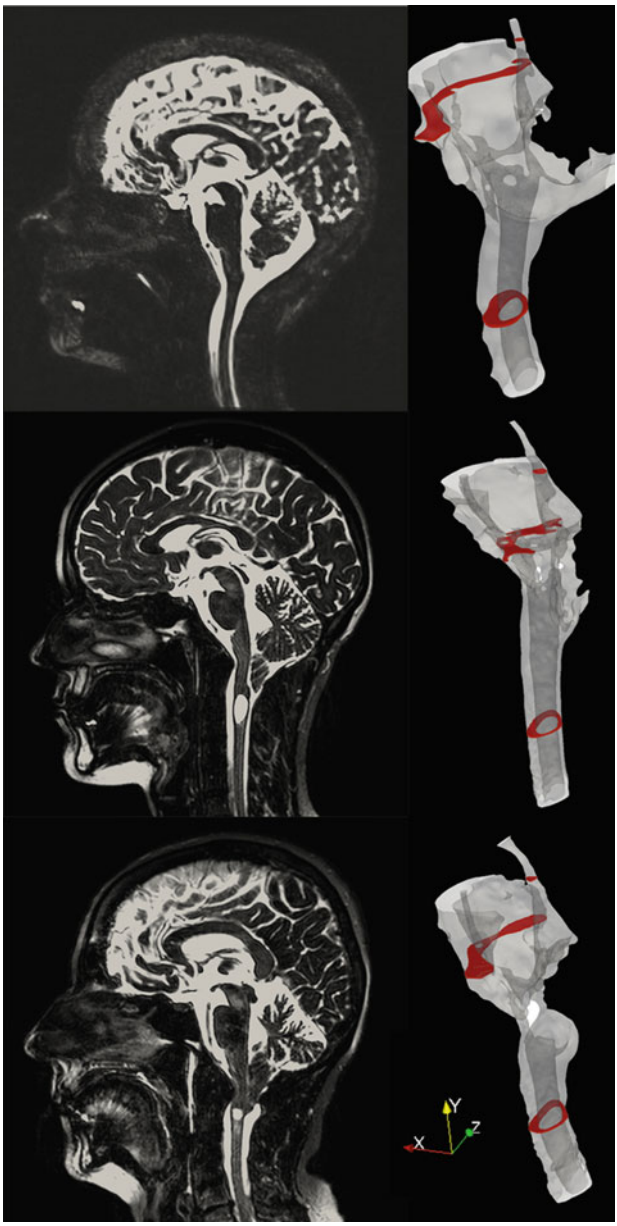

Fig. 9.2 Segmentation of spinal SAS from MR images using VMTK. Left: Heavily fluid-weighted MRI (3D constructive interference in steady state, CISS) of one control subject and two Chiari I patients, females of 40, 26 and 63 years of age, respectively. Right: 3D reconstructed surface models. (Reproduced with permission from [25])

9.2.2 Spatial Discretization

CFD requires the discretization of the governing equations in space and, if transient flows are to be studied, also in time. The discretized set of equations is solved in the CFD software of choice, aspects of which are discussed in Sect. 9.2.4. For spatial discretization, the domain under investigation must be divided into small sub-volumes, i.e. a computational grid has to be generated. For the study of CSF dynamics, the finite volume discretization [9, 31, 32] scheme is most often used, followed by the finite element method [33, 34]. The lattice Boltzmann method is an alternative technique that represents the fluid at mesoscale and recovers the Navier-Stokes equations within limits of low Mach and Knudsen numbers. It has gained traction in CSF flow modelling due to its good scalability on parallel computing architectures [35, 36]. While this approach is not based on macroscopic continuum equations, it still requires discretization of the model domain.

For anatomically accurate modelling of CSF flow, either unstructured grids or an immersed boundary method [37] needs to be used, as structured grids that follow the domain contours are very difficult to generate due to the geometric complexity of the CSF spaces. State-of-the-art grid generation software allows for mostly automatic unstructured meshing. Higher grid densities are implemented in areas with expected large velocity gradients, such as at domain walls. This is important, because the accuracy of the obtained solution depends, among other factors, on the quality of the computational grid. Since the solution of the original, not discretized set of governing equations is generally not known and, thus, the error of the discretized solution cannot be specified, solutions obtained with different grid densities have to be compared in a procedure termed grid independence or mesh convergence study. Such grid independence studies will give an estimate of the relative error introduced by the spatial discretization. If the flow is in transition to turbulence, the quality of spatial discretization can be assessed using Kolmogorov's theory [31, 35]. Ultimately, a balance between the accuracy of the results and cost in terms of grid generation and computational time must be struck.

9.2.3 Boundary and Initial Conditions

Boundary conditions (BC) need to be specified at the domain margins for closure of the governing equations. CFD models of CSF flow are typically based on MRI-derived BC. Unfortunately, it is not possible to obtain absolute pressures via MRI. This leads to the unsatisfactory situation that only velocity, flow rate or similar BC can be prescribed in a subject-specific manner, while pressure or impedance BC that are required to ensure mass conservation in non-compliant domains are generic or based on generalized lower-order models. The ideal locations for acquisition of CSF flow BC are typically the aqueduct of Sylvius and the cervical spinal canal. The geometry of these areas is well defined and flow therein is primarily

in axial direction, allowing for the placement of a single transverse measurement plane for velocity-encoded MRI. Furthermore, there are closed-form solutions of flow in idealized representations of the aqueduct (e.g. straight elliptic pipe) [38] and the spinal canal (straight elliptic annulus) [39], allowing for the filtering of higher frequency noise components in the acquired flow data. This can be done by first integrating the flow profile in space for each measured point in time, which yields a volumetric or mass flow curve that contains less noise. In order to recuperate the spatial velocity field, this flow rate is applied to the respective idealized geometry with available closed-form solution of the governing equations [32]. Finally, conformal mapping is performed to map the solution back to the actual domain [40].

The pulsatile components in CSF flow are caused primarily by the expansion and contraction of blood vessels in and around the CNS, and by respiration, which changes central venous pressure and affects pressure conditions in the spinal compartment. This suggests that the CSF boundaries have to be flexible entities that can transfer momentum by deformation. Nevertheless, most CFD models assume rigid CSF domain boundaries, as this simplifies model setup and calculations tremendously. There are two general approaches by which boundary motion can be taken into account: either the entire chain of displacements from blood vessels or the diaphragm to tissue and CSF is modelled, or the displacement of the boundaries is measured directly. The former approach poses great challenges, the most serious of which is the lack of material data to model the interaction between CSF and the surrounding deformable structures. In addition, the complexity of the vascular network in the brain and limits in the effective resolution of MRI require simplifications of the vascular model (see Sect. 9.2.1), introducing errors that are difficult to quantify.

Direct measurement of the motion of CSF space boundaries is not trivial, but feasible. As early as 1992, Enzmann and Pelc used phase-contrast MRI to measure brain motion [41]. With displacement-encoded MR imaging, brain displacement down to 0.01 mm can be measured [42, 43]. This is sufficient for deriving ventricle wall motion, though it has to be noted that averaging over several cardiac cycles is necessary. Such averaging may lead to underestimation of the actual displacement if respiration is not accounted for by, e.g. additional respiratory gating. In contrast to ventricular wall movement, the motion of the pia mater is likely too small for direct measurement. The MRI acquisitions result in a discrete displacement map within which the CSF boundaries do not necessarily coincide with the measured locations. Hence, spatial interpolation must be performed first to cover the boundaries. Since the temporal frequency spectrum of blood flow into the brain through the carotid and vertebral arteries does not extend beyond 10 Hz under normal resting conditions, a brain motion acquisition interval of 0.05 s within a cardiac cycle is sufficient to meet the Nyquist-Shannon sampling criterion [44, 45]. However, the temporal discretization of the governing equations requires much smaller time steps, necessitating a temporal interpolation of the acquired brain motion data. This can be performed by Fourier decomposition of the acquired discrete signal and resampling of the reconstructed continuous signal [32].

The relative contributions of pia mater and ventricular wall motion to CSF dynamics are unclear, in particular because there are no reliable quantitative data on pia movement. While ventricular wall displacement is larger (as qualitatively discernible in phase-based amplified MRI [46]), the pia mater surface area is much bigger. Therefore, pia motion cannot necessarily be neglected. To account for the effect of pia movement in an approximate fashion, simplified BC can be introduced. One option is to prescribe uniform perpendicular flow across the pia, such that the corresponding flow rate is equal to the difference between in- and outflow at the aqueduct of Sylvius and the spinal canal [10]. This simplified BC is relatively easy to implement but will lead to errors in the reported flow velocities close to the pia surface.

The pulsatile motion of CSF is superimposed onto its steady flow caused by production in the choroid plexus and removal through the arachnoid granulations, extracranial lymphatic pathways and possibly through cerebral capillaries [3, 47]. The choroid plexus has a filamentous structure that cannot be acquired by MRI in its full detail. For CFD modelling, its simplified macroscopic shape can be segmented from MR images, and CSF flow rates corresponding to the production value can be imposed on the idealized boundaries. Alternatively, the choroid plexus geometry can be neglected altogether and inflow imposed at a part of the respective ventricle wall. Combined CSF production rates in the choroid plexus of the third and lateral ventricles can, principally, be obtained by integrating the MRI-acquired CSF flow profile in the aqueduct of Sylvius over a cardiac cycle. While this method is used throughout the literature, there is no conclusive data on the accuracy of this approach. Obtaining CSF production rates in the fourth ventricle via MRI is more difficult and would require measurement of flow through the small foramina of Luschka and Magendie. This is not possible with a sufficient level of accuracy on current clinical MRI scanners. In order to still take CSF production in the fourth ventricle into account, a ratio between the production rates in this and the remaining cerebral ventricles can be assumed.

Under physiologic conditions, the average rate of CSF removal is equal to the production rate. While it is accepted that there are multiple locations of absorption or drainage throughout the cranial and spinal cavity, there is no consensus on the relative contributions of the individual exit routes. The classically purported but increasingly questioned main locations of CSF reabsorption are the arachnoid granulations that drain into the superior sagittal, transverse and sigmoid sinuses. It is possible to locate large granulations through MRI, but most of the smaller ones cannot be detected. Cadaver data on their distribution is available [48], and areas of the arachnoid mater boundary can be assigned absorption functionality in CFD simulations. Concretely, the arachnoid granulations can be assumed to act as one-way differential pressure valves with associated permeability of approximately 92.5 $\mu l \cdot min^{-1} \cdot mmHg^{-1} \cdot cm^{-2}$ [49]. Recent studies in rodents have highlighted the importance of lymphatic CSF drainage [47, 50, 51]. While it is unclear how these findings translate to humans, it is reasonable that lymphatic drainage should be considered in models of CSF dynamics. Further experimental work is needed to obtain quantitative data on the connection between the two fluid spaces.

Once the boundary conditions are in place, initial conditions in the form of velocity and pressure have to be defined throughout the computational domain. If results from previous calculations, usually on a coarse computational grid, are available, they can be extra- or interpolated to the new grid as initial conditions. Otherwise, zero initial velocity and constant pressure are usually applied. Since the corresponding fluid dynamic state will not match to the actual flow field, transient calculations are performed over a few cardiac and, if considered, respiratory cycles, until no significant difference in the state between two subsequent cycles can be observed. Depending on the CFD solver and the numerical method employed, a constant initial condition may render the calculations unstable. In that case, the magnitudes or amplitudes of the applied boundary conditions can be scaled down initially and increased to their actual values over several cycles.

9.2.4 Calculating the Flow

A wide range of CFD tools suitable for CSF dynamics modelling exist, from user-friendly commercial software [9, 10, 12, 52–54] to free open-source codes [33–35, 53], each with their unique strengths and weaknesses. CFD tool choice depends primarily on the complexity of the envisioned model, licensing cost and familiarity with the tool. High complexity in terms of model size calls for software that can utilize HPC resources. While most relevant CFD tools offer parallel processing, the comparably low parallel efficiency of traditional finite volume and element codes is an important limiting factor. This issue is exacerbated by the continuing trend towards larger numbers of cores per CPU but only slow increase in clock speed and available memory per core. As a result, approaches that offer better parallel scaling, such as lattice Boltzmann methods, have seen rising interest in the recent years. The speed increase with such methods is particularly relevant for transient calculations.

In the vascular area, steady-state calculations of blood flow are employed when details of the flow field do not need to be captured, for example, to estimate average wall shear stress distribution or other similar parameters linked to long-term processes such as atherosclerosis [55]. In contrast to haemodynamics, CSF flow has a much stronger oscillatory component compared to its net flow, which makes steady-state simulations typically not applicable. For transient CFD simulations, the proper temporal discretization step size has to be chosen, which will depend on the expected flow frequencies (see Sect. 9.2.3), the discretization scheme, the spatial resolution of the computational grid and the CFD solver. Commonly used time step sizes in the CSF space are on the order of 1 ms [32]. As with the grid independence study (Sect. 9.2.2), time step independence of the acquired solution must be ensured.

CSF flow is generally considered laminar. Recent studies employing direct numerical simulation (DNS) have challenged this assumption [31, 35], raising the question if currently used time step sizes and grid resolutions are adequate and

whether turbulence modelling should be considered. In contrast to DNS, in which also the smallest flow features are captured by employing very high spatial and temporal resolution, turbulence models approximate the effect of these features, thereby reducing computational cost [56].

9.3 Existing CFD Models

This section gives an overview of CFD models of CSF dynamics, starting with the early studies that established the field. These initial models in particular covered small subdomains of the expansive CSF space, beginning with parts of the ventricular system, wherefrom the focus shifted over time to the subarachnoid and perivascular spaces. The current trend goes towards both modelling multiple CSF compartments at once and increasing the fidelity of smaller-scale models.

9.3.1 Ventricular Space

The first CFD study on flow in the CSF space was carried out by Jacobson and co-workers in 1996, investigating fluid dynamics through a representation of the aqueduct of Sylvius with stiff walls [6]. The same authors followed up with an investigation of aqueduct stenosis in 1999, in which they approximated the geometry of the aqueduct of Sylvius based on published anatomic data [57]. Several years later, Fin and Grebe modelled the aqueduct wall as a deformable membrane and compared these results to data attained with rigid walls [58]. The domain geometry was obtained by MRI and CSF flow was calculated using finite element and immersed boundaries methods. Under steady flow conditions, they obtained a 37% lower pressure drop in the case with deformable walls compared to rigid walls. This remarkable difference raises the question whether such a large influence of boundary conditions on the results does not diminish the value of CFD, as the actual aqueduct wall stiffness is not known. One may ask why the substantial additional time and effort needed for CFD modelling should be invested compared to simple bulk models. Bulk models will be sufficient if bulk values such as the pressure drop across a simple structure are sought. If, however, one is interested in the effect of local geometric features on flow, CFD models will provide added value. To be clear, this still requires that the boundary conditions, which largely determine the accuracy of the model, are well chosen.

After the CFD studies of the aqueduct of Sylvius, other researchers directed their efforts at the remainder of the ventricular space, using varying levels of detail both in the representation of the anatomy and in the acquisition of the boundary conditions. In 2005, Kurtcuoglu et al. published results of simulations on a simplified representation of the entire ventricular space, within which CSF flow was driven by the expansion and contraction of the third ventricle walls [59], as

originally suggested by Du Boulay [60]. While it is not entirely clear how vascular deformation is translated to CSF motion, the third ventricle is no longer considered the primary source [32, 61]. In 2010, Cheng et al. investigated with an MRI-derived CFD model of the third ventricle and aqueduct of Sylvius how the position of the interthalamic adhesion affects CSF flow [62]. They imposed flow at the foramina of Monro based on published values, set constant pressure at the distal end of the aqueduct and assumed rigid ventricle walls.

In 2008, Howden and co-workers presented the first anatomically accurate 3D CFD model of the entire ventricular space [63]. Instead of using constant pressure boundary conditions at the domain outlets (the foramina of Luschka and Magendie), the authors applied transient pressure. Pressures were estimated using a geometrically simplified 3D model of the combined cranial and spinal CSF spaces that featured a pulsatile velocity inlet at the choroid plexus and constant pressure at the arachnoid granulations. While such a staggered approach is, in principle, preferable to using constant pressure, it is difficult to carry out in practice. This is because choroid plexus pulsation is not the sole origin of CSF oscillation, and the relative importance of the choroid plexus, ventricles and subarachnoid space as potential contributors to pulsatile flow is unknown. The origin of CSF motion in the ventricular space was addressed by Siyahhan et al. in 2014 [53], focusing on the effect of ependymal cilia, which are believed to play a major role in CSF propulsion in mice. Ciliary action was taken into account by momentum sources. The computations showed that near the ventricular surface, ependymal cilia contribute substantially to the local flow conditions.

Changes in cerebral ventricle size are characteristic of several pathologic conditions, most notably hydrocephalus, which is usually treated by ventriculo-peritoneal CSF shunting [64]. Gholampour et al. investigated CSF dynamics using a fluid-structure interaction model in the ventricular space of hydrocephalus patients with aqueduct stenosis before and after shunting, focusing on changes in flow and pressure [65]. Another approach for treating hydrocephalus is endoscopic third ventriculostomy (ETV) [66], which Gholampour addressed with the same modelling framework [67]. Farnoush et al. investigated how CSF dynamics are affected by ETV in the presence and absence of aqueduct stenosis [68]. CFD was performed in the third ventricle, with the ventriculostomy modelled as a 5 mm diameter hole. The results showed a threefold higher reduction in ventricular pressure in the case with stenosis and a temporal shift in pressure conditions in the stenosis-free setup.

The continuous increase in computing power and advances in magnetic resonance technology have allowed for a gradual expansion of the investigated CSF domain sizes. By considering multiple CSF compartments at once, the number of required boundary conditions can be decreased. For example, if the ventricular space and the cranial subarachnoid space are modelled together, no boundary conditions are needed at the foramina of Luschka and Magendie. Such descriptions including both ventricular and other CSF spaces are included in the following sections.

9.3.2 *Subarachnoid Space*

A number of CFD models have been applied to elucidate CSF dynamics in the SAS. These models can be roughly divided into studies investigating (a) CSF flow under normal physiologic conditions, (b) syringomyelia, (c) Chiari malformation and (d) intrathecal drug delivery and solute transport. A review of spinal SAS CFD studies was provided by Khani et al. in 2018 [69], a review of syringomyelia biomechanics was provided by Elliott et al. in 2013 [70], and a review of Chiari malformation biomechanics was provided by Shaffer et al. in 2011 [71]. An example of spinal SAS CFD model derivation is shown in Fig. 9.3.

9.3.2.1 Normal Physiologic Conditions

The first CFD model of the spinal canal was formulated by Loth et al. in 2001 [72]. The authors constructed an idealized 2D SAS geometry without spinal cord

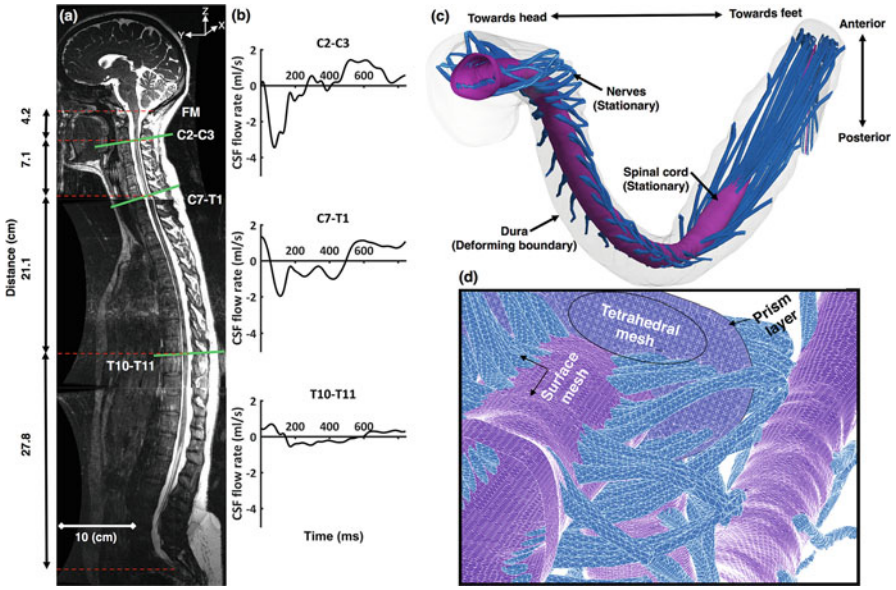

Fig. 9.3 Diagram of subject-specific computational modelling of spinal CSF dynamics in a healthy subject: (**a**) High-resolution anatomic MRI with slice locations shown where CSF flow rate waveforms were measured and their relative axial distance below the foramen magnum (FM). (**b**) CSF flow rate waveforms measured by phase-contrast MRI at C2–C3, C7–T1 and T10–T11. (**c**) Geometric domain used for the spinal CFD model based on a freely downloadable spinal SAS 3D geometry [12]. (**d**) Depiction of the surface and volumetric mesh applied in the CFD model including a close-up view of a location in the cervical spine. (Reproduced with permission from [69])

nerve roots based on the Visual Human Project's Visible Man [73] and assessed the effects of spinal cord eccentricity and cross-sectional geometry on CSF flow. They found that spinal SAS CSF flow is inertia dominated and predicted that patient-specific CFD models could become a noninvasive tool to explain abnormal CSF dynamics and distribution of intrathecal drugs. In 2006, Stockman presented a 3D lattice Boltzmann model of a subsection of the spinal canal with idealized spinal cord nerve roots and arachnoid trabeculae [74]. Model findings indicated that inclusion of trabecular microstructure had relatively little impact on the CSF velocity profiles but did influence local flow mixing to a great degree and could, therefore, impact tracer dispersion. In 2009 and 2010, Gupta et al. investigated flow in an anatomically accurate representation of a healthy cranial subarachnoid space and fourth ventricle [9, 10]. They imposed CSF flow velocities obtained through MRI at the pontine and cerebellomedullary cisterns and at the foramen magnum in the spinal canal. The subarachnoid space was modelled as an anisotropic homogeneous porous medium. Their main finding was that the SAS microstructure clearly contributes to the pressure drop along the domain. In contrast, Sweetman et al. focused on the integration of spinal and cranial SAS as well as ventricular system into one CFD model without accounting for microstructures [75], expanding their previous 2D and 3D work on the cranial compartments [76, 77]. CSF pulsation was produced by an imposed volume change in brain tissue transmitted to the fluid domain through deformable superior wall sections of the lateral ventricles.

A series of studies was conducted by various researchers to understand more deeply the impact of anatomy on CSF dynamics. Yiallourou et al. used the finite volume method for several subject-specific 3D models of the cervical spine and found peak CSF velocities to compare poorly with 4D phase-contrast MRI [78], suggesting that differences could be due to lack of spinal cord nerve roots in the model. Similarly, Lindstrøm et al. also found relatively poor agreement of MRI-measured CSF velocities and CFD without spinal cord nerve roots [79]. In contrast, research by Clarke et al. showed relatively good agreement of CFD and MRI-measured CSF velocities [80]. Pahlavian et al. investigated the impact of anatomically realistic spinal cord nerve roots and denticulate ligaments on CSF flow within the cervical spine [11]. Results showed that these anatomic structures increased peak CSF velocities, mixing and bidirectional flow. Pahlavian and colleagues then investigated the reliability of CFD-predicted CSF velocities using MRI data collected from an in vitro model with spinal cord nerve roots [81–83]. Results indicated that in vitro MRI compared well to CFD results, but lacked agreement with in vivo measurements. Thus, Martin et al. studied inter-operator reliability of MRI-based CFD prediction of CSF motion, finding fluid dynamic and geometric results to have a high degree of reliability for healthy subject geometries [84].

For all of the above simulations, either the SAS was modelled as a rigid structure or CSF flow was imposed assuming a monotonically decreasing flow waveform magnitude along the spinal axis. However, in vivo measurements indicate that the CSF flow waveform changes in both magnitude and shape along the spine [78, 85, 86]. Thus, in 2017, Khani et al. carried out a CFD study of a cynomolgus monkey

with a non-uniformly moving boundary method to more accurately reproduce the axial distribution of CSF flow measured by MRI [87]. This study was followed up in 2018 with a similar model of the human spinal SAS but with 31 pairs of anatomically realistic spinal cord nerve roots [12, 69]. Results showed that the complex geometry resulted in considerable steady streaming of CSF, which was greatly impacted by the presence of spinal cord nerve roots.

In combination, the CFD studies representing normal physiologic conditions indicate that small anatomic structures such as nerve roots and trabeculae must be accounted for to reproduce in vivo CSF velocity profiles accurately. However, they also show that it is difficult to directly validate CFD results with MRI measurements due to a lack of spatial resolution and noise in the experiments [82, 83].

9.3.2.2 Syringomyelia

Syringomyelia is a spinal cord disorder characterized by formation of a fluid-filled cyst within the cord tissue that can progressively expand over time and cause neurological damage [88, 89]. The exact mechanism underlying cyst formation and progression remains unclear. Thus, numerical modelling has been applied to identify mechanical factors that could help explain cyst pathogenesis and/or investigate the plausibility of various hypotheses brought forth by clinicians [70].

The first study to apply numerical modelling to investigate syringomyelia, and perhaps the first model to investigate spinal SAS CSF dynamics, was conducted by Lockey et al. in 1975 [90]. This study used 1D analytic models of wave propagation to predict the impact of a spinal stenosis on cough-related pressure pulse propagation along the spinal SAS. Since that time, many numerical models of syringomyelia have been formulated with varying degrees of anatomic and physiologic complexity. From 1999 to 2003, Carpenter, Berkouk and colleagues published a series of fluid-filled elastic coaxial tube models and proposed an "elastic jump" hypothesis for syringomyelia pathogenesis based on a wave steepening effect that could potentially greatly increase pressure pulse along the spinal SAS [91–93]. However, Bertram et al. [64, 94] and subsequently Elliott et al. found the elastic jump hypothesis to be quantitatively implausible [95]. Chang and Nakagawa constructed an electric circuit analogue for syringomyelia with the cystic cavity connected to the fourth ventricle by the obex [96].

These models opened many questions on the relevance of mechanical properties of the tissue, such as viscoelasticity and porosity, as well as tissue geometry. To answer these, a number of 1D and 2D numerical models of spinal SAS wave propagation were formulated, including those brought forth by Bertram and colleagues [97–99], Elliott et al. [100–102], Cirovic et al. [103–105] and Bilston, Cheng and colleagues [106–108]. Bertram used the finite element method to investigate wave phenomena and anatomic conditions such as spinal arachnoiditis that could lead to a pressure environment favourable for cystic growth. Elliott et al. built on these models by investigating the importance of tissue permeability and how permeability, in combination with wave propagation, could lead to cyst formation. Cirovic et al.

made the first animal-specific numerical model of wave propagation for a Cavalier King Charles Spaniel [103] – a dog species that often develops syringomyelia – and found that repetitive stressing of the spinal cord could initiate cyst development. Cheng et al. conducted the first 3D fluid-structure-interaction (FSI) simulation of the upper spinal SAS with spinal stenosis [106]. Further models were developed to elucidate the influence of the relative timing of arterial and CSF pressure waves on perivascular transport of fluid into syrinxes (see Sect. 9.3.3).

9.3.2.3 Chiari Malformation

Chiari malformation is a craniospinal disorder characterized by protrusion of the cerebellar tonsils out of the cranial cavity into the spinal SAS. This protrusion results in partial blockage of fluid movement between cranial and spinal CSF spaces. The exact mechanism of pathogenesis remains unclear. Thus, as a potential indicator of disease state or surgical effectiveness, researchers have applied CFD to predict the pressure and fluid velocities within the region of CSF restriction.

In 2009, Roldan et al. [109] completed the first subject-specific CFD simulation of Chiari malformation and predicted anterolateral flow jets located around the spinal cord near the point of tonsillar obstruction to CSF flow. Linge et al. conducted parametric investigations with varying degrees of tonsillar obstruction at the foramen magnum [10, 110]. Rutkowska et al. [34], Yiallourou et al. [78], Clarke et al. [80] and Martin et al. [111] compared CFD-predicted parameters of CSF dynamics in Chiari patients versus controls and found CSF velocities to be elevated in patients. These velocities tended to decrease following surgical treatment.

Martin et al. proposed the use of longitudinal impedance [111] as a new parameter to quantify unsteady resistance to CSF flow at the craniocervical junction. Longitudinal impedance was found by Shaffer et al. to be elevated in Chiari patients compared to controls and to decrease following surgical treatment [112], indicating a potentially clinical relevant use of CFD for modelling CSF dynamics in Chiari. Longitudinal impedance tended to increase with tonsillar descent into the spine. In 2017, Jain et al. completed a DNS study of CSF flow using the lattice Boltzmann method [35], observing high velocities in the spinal SAS of Chiari I patients and predicting the presence of transitional flow near the region of stenosis (Figs. 9.4 and 9.5). Pahlavian et al. conducted the first CFD study of Chiari malformation that included patient-specific pulsatile motion of the cerebellar tonsils [113]. Results from that study indicated that pulsatile motion of the tonsils can greatly affect CSF velocities. Subsequently, Pahlavian et al. applied displacement-encoded MR imaging to quantify regional displacement and strain within the brain [43]. In combination, these studies support the application of CFD in the quantification of Chiari malformation disease states. However, the most appropriate model boundary conditions for Chiari malformation have yet to be established.

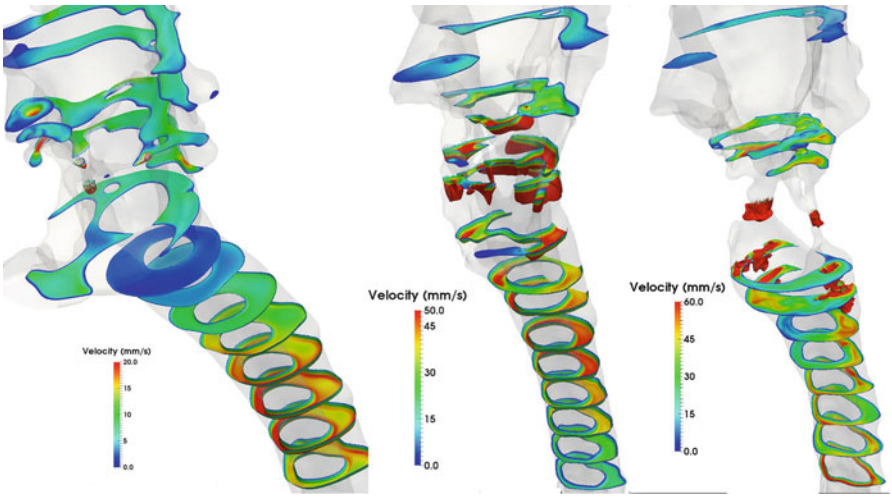

Fig. 9.4 Peak systolic velocity field across several axial planes in the spinal SAS of the control subject and two Chiari I patients shown in Fig. 9.2. The planar velocity field is warped in space according to the direction and magnitude of underlying velocity vectors to depict the spatial variation of the flow. (Reproduced with permission from [25])

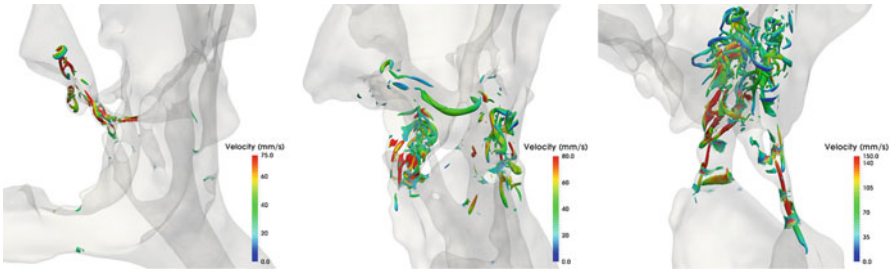

Fig. 9.5 Velocity-coloured instantaneous Q-isosurfaces ($Q = 0.4$) during peak diastole of the 8th cardiac cycle in the control subject and 50th cardiac cycle in the two Chiari patients shown in Fig. 9.2. (Reproduced with permission from [25])

9.3.2.4 Intrathecal Drug Delivery and Solute Transport

Delivery of drugs or biologics to the CNS via CSF shows promise for the treatment of many devastating diseases [2]. A soluble substance injected into the CSF mixes rapidly [114], spreads throughout the CSF system and may then be taken up by the brain parenchyma, e.g. via perivascular spaces [54, 115]. This process bypasses the blood-brain barrier, allowing delivery of many agents that cannot be delivered through the blood [116, 117], including cell-based and gene therapies [118, 119].

Meyers developed the first 3D computational model of intrathecal drug delivery in 1996 [120]. It was not until 2010 that Kuttler et al. conducted the second numerical model of intrathecal solute transport for a subject-specific 3D geometry

without fine anatomic structures [121]. Their approach involved calculation of the steady streaming velocity field over one CSF flow cycle and using it to predict drug concentration in the entire spinal domain over several hours. The authors predicted that there would be no clear difference in drug distribution range for a bolus injection versus slow infusion. By using different models for phenomena occurring at different time scales, they were able to progress towards a potentially clinically relevant CFD application in the CSF space.

Since then, a number of studies have been carried out to help understand factors that could impact intrathecal drug spread, including CSF waveform [122], drug injection rate and volume [123, 124], catheter position within the SAS [123], impact of trabecular microstructure [125], drug diffusivity [123] and absorption into CNS tissue [126–128]. Tangen et al. conducted the first CFD study to investigate clearance of blood from the CSF following subarachnoid haemorrhage by a lumbar drain [129, 130]. The authors conducted rigorous in vitro verification of results, adding confidence to the study findings. In combination, these studies found that drug properties, bolus size, injection rate, injection location, CSF flow pulsation amplitude, macroscale anatomy and microscale anatomy can play a role in CSF solute transport and that these factors require further detailed investigation.

Computational modelling has also been applied to help understand how radionuclide studies of molecules injected into the CSF indicate a net CSF flow direction [131], while MRI studies appear to show zero net CSF flow. Combined CFD and bulk models were also used to assess the relation between changes in CSF net flow and increase in CSF protein concentration [132]. Sanchez et al. used an anatomically idealized spinal SAS model without spinal cord nerve roots or curvature, showing that CSF steady streaming can be produced by convective acceleration depending on the degree of spinal cord eccentricity [133]. This finding was also observed by Khani et al. within an anatomically detailed model of the SAS with spinal cord nerve roots and non-uniform subject-specific CSF flow waveform along the spine [69]. Asgari et al. formulated a one-dimensional model of protein dispersion in the spinal SAS, determining dispersion coefficients using a 3D advection-diffusion model [132]. They investigated two hypothesized causes of increased CSF albumin levels, finding blood-brain barrier dysfunction to be a more likely cause than a reduction in the rate of CSF outflow. This finding may help in the clinical interpretation of Reiber diagrams.

9.3.3 Perivascular Space

Starting in 2003 with the work of Bilston et al. [134], CFD modelling of perivascular CSF flow was initially driven by the desire to understand the pathophysiology of syringomyelia. Bilston idealized the perivascular space with a 2D rectangular domain with no-slip boundary conditions at the walls and prescribed pressure boundary conditions at the inlet and outlet. Transient deformation was prescribed on the wall representing the boundary closer to the artery lumen, whereas the outer

wall was considered rigid. The authors reported that fluid transport occurs in the direction of arterial wave propagation up to a specific pressure gradient determined by pulse wave velocity and amplitude. Since the wavelengths investigated in this model were smaller than physiologically expected, the authors followed up with a corrected model where the arterial wall was approximated to be uniform [135]. Wang and Olbricht [136] performed a theoretical analysis and reported a lower maximal adverse pressure gradient for the same conditions. In 2010, Bilston and co-workers expanded their original CFD model to take into account a time-varying pressure gradient along the perivascular domain, reflecting the pulsation of CSF in the subarachnoid space and showing that the relative timing of the arterial pulse wave and subarachnoid pressure wave could influence perivascular fluid flow [137]. Elliott et al. continued the investigations of wave propagation in an axisymmetric fluid-structure interaction model [102], while Lloyd et al. used CFD modelling to predict that Chiari I malformation can change the magnitude and timing of the subarachnoid pressure-time profiles and lead to greater influx of CSF into the spinal cord [135].

While the spinal perivascular spaces have been studied primarily within the context of syrinx formation, their cerebral counterparts have drawn interest because of their contribution to CNS solute transport. In 2006, Schley et al. formulated a numerical model to evaluate solute transport in the periarterial space [138]. Almost a decade later, Asgari et al. assessed potential net flow between periarterial and perivenous fluid spaces [139], and Sharp et al. investigated the possibility of periartieral amyloid-β clearance by peristalsis [140]. These studies were followed by a number of computational investigations of flow through perivascular and interstitial fluid spaces and associated solute transport [141–146]. Because of the importance of metabolite clearance in the development of neurodegenerative diseases and limitations of experimental tools to study such cerebral solute transport, numerical models have drawn attention beyond the computational community. It can be expected that computational studies of perivascular fluid flow, in particular in conjunction with CSF dynamics in the subarachnoid space, will continue to gain traction and that CFD will take on an increasingly important role therein.

9.4 Conclusion

While most of the early CFD models of CSF dynamics focused on method development, now that the methodology has matured, an increasing number of studies address specific questions of physiology and pathophysiology and test hypotheses that cannot be addressed by experimental techniques alone. New insights provided by these studies include the characterization of the CSF flow regime (predominantly laminar with transient, local occurrences of turbulence, particularly in certain disease states), assessment of the contribution of ependymal cilia on CSF flow (dominates near ventricular wall dynamics) and identification of dispersion and steady streaming as important mechanisms for solute transport in the perivascular

and spinal subarachnoid spaces. We can state with confidence that CFD has become an important tool for CSF dynamics research.

At the same time, further efforts are needed to characterize CSF space geometry and boundary deformation, to optimize inclusion of microstructures and coupling of CSF with interstitial fluid and to model the connection to the lymphatic system. Overarching developments in CFD, namely, more efficient use of HPC resources, must be adopted to enable large-scale calculations of CSF dynamics.

CFD complements and extends MRI. For example, while subject-specific CFD is dependent to a large extent on anatomic and physiologic data derived from magnetic resonance imaging, information on CSF pressure gradients cannot be derived from MRI without flow computations. What we will likely see in the future is the integration of CFD in MRI sequences and scanner software, ensuring mass and momentum conservation while making use of measured velocities in the entire domain rather than only at selected boundaries. Stand-alone CFD will continue to play a major role when it comes to, for example, investigating the effects of virtually imposed changes in physiology and anatomy, calculating transport processes, optimizing medical devices and surgical interventions and interpreting in vivo tracer studies.

References

1. Hladky, S.B., Barrand, M.A.: Mechanisms of fluid movement into, through and out of the brain: evaluation of the evidence. Fluids Barriers CNS. **11**(1), 26 (2014)
2. Linninger, A.A., Tangen, K., Hsu, C.-Y., Frim, D.: Cerebrospinal fluid mechanics and its coupling to cerebrovascular dynamics. Annu. Rev. Fluid Mech. **48**(1), 219–257 (2016)
3. Brinker, T., Stopa, E., Morrison, J., Klinge, P.: A new look at cerebrospinal fluid circulation. Fluids Barriers CNS. **11**, 10 (2014)
4. Bloomfield, I.G., Johnston, I.H., Bilston, L.E.: Effects of proteins, blood cells and glucose on the viscosity of cerebrospinal fluid. Pediatr. Neurosurg. **28**(5), 246–251 (1998)
5. Brydon, H.L., Hayward, R., Harkness, W., Bayston, R.: Physical properties of cerebrospinal fluid of relevance to shunt function. 1: the effect of protein upon CSF viscosity. Br. J. Neurosurg. **9**(5), 639–644 (1995)
6. Jacobson, E.E., Fletcher, D.F., Morgan, M.K., Johnston, I.H.: Fluid dynamics of the cerebral aqueduct. Pediatr. Neurosurg. **24**(5), 229–236 (1996)
7. Caiazzo, A., Vignon-Clementel, I.E.: Mathematical modeling of blood flow in the cardiovascular system. In: Sack, I., Schaeffter, T. (eds.) Quantification of Biophysical Parameters in Medical Imaging, pp. 45–70. Springer, Cham (2018)
8. Ballester, M.A.G., Zisserman, A., Brady, M.: Segmentation and measurement of brain structures in MRI including confidence bounds. Med. Image Anal. **4**(3), 189–200 (2000)
9. Gupta, S., Soellinger, M., Boesiger, P., Poulikakos, D., Kurtcuoglu, V.: Three-dimensional computational modeling of subject-specific cerebrospinal fluid flow in the subarachnoid space. J. Biomech. Eng. **131**(2), 021010 (2009)
10. Gupta, S., Soellinger, M., Grzybowski, D.M., Boesiger, P., Biddiscombe, J., Poulikakos, D., Kurtcuoglu, V.: Cerebrospinal fluid dynamics in the human cranial subarachnoid space: an overlooked mediator of cerebral disease. I. Computational model. J. R. Soc. Interface. **7**(49), 1195–1204 (2010)

11. Heidari Pahlavian, S., Yiallourou, T., Tubbs, R.S., Bunck, A.C., Loth, F., Goodin, M., Raisee, M., Martin, B.A.: The impact of spinal cord nerve roots and denticulate ligaments on cerebrospinal fluid dynamics in the cervical spine. PLoS One. **9**(4), e91888 (2014)
12. Sass, L.R., Khani, M., Natividad, G.C., Tubbs, R.S., Baledent, O., Martin, B.A.: A 3D subject-specific model of the spinal subarachnoid space with anatomically realistic ventral and dorsal spinal cord nerve rootlets. Fluids Barriers CNS. **14**(1), 36 (2017)
13. Cloyd, M.W., Low, F.N.: Scanning electron microscopy of the subarachnoid space in the dog. I. Spinal cord levels. J. Comp. Neurol. **153**(4), 325–368 (1974)
14. Allen, D.J., Low, F.N.: Scanning electron microscopy of the subarachnoid space in the dog. III. Cranial levels. J. Comp. Neurol. **161**(4), 515–539 (1975)
15. Killer, H.E., Laeng, H.R., Flammer, J., Groscurth, P.: Architecture of arachnoid trabeculae, pillars, and septa in the subarachnoid space of the human optic nerve: anatomy and clinical considerations. Br. J. Ophthalmol. **87**(6), 777–781 (2003)
16. Scott, G.G., Coats, B.: Microstructural characterization of the pia-arachnoid complex using optical coherence tomography. IEEE Trans. Med. Imaging. **34**(7), 1452–1459 (2015)
17. Mortazavi, M.M., Quadri, S.A., Khan, M.A., Gustin, A., Suriya, S.S., Hassanzadeh, T., Fahimdanesh, K.M., Adl, F.H., Fard, S.A., Taqi, M.A., Armstrong, I., Martin, B.A., Tubbs, R.S.: Subarachnoid trabeculae: a comprehensive review of their embryology, histology, morphology, and surgical significance. World Neurosurg. **111**, 279–290 (2018)
18. Vandenwesthuizen, J., Duplessis, J.P.: Quantification of unidirectional fiber bed permeability. J. Compos. Mater. **28**(7), 619–637 (1994)
19. Chai, Z.H., Shi, B.C., Lu, J.H., Guo, Z.L.: Non-Darcy flow in disordered porous media: a lattice Boltzmann study. Comput. Fluids. **39**(10), 2069–2077 (2010)
20. Tully, B., Ventikos, Y.: Cerebral water transport using multiple-network poroelastic theory: application to normal pressure hydrocephalus. J. Fluid Mech. **667**, 188–215 (2011)
21. Kang, Q.J., Zhang, D.X., Chen, S.Y.: Unified lattice Boltzmann method for flow in multiscale porous media. Phys. Rev. E. **66**(5), 056307 (2002)
22. Lesage, D., Angelini, E.D., Bloch, I., Funka-Lea, G.: A review of 3D vessel lumen segmentation techniques: models, features and extraction schemes. Med. Image Anal. **13**(6), 819–845 (2009)
23. Yushkevich, P.A., Piven, J., Hazlett, H.C., Smith, R.G., Ho, S., Gee, J.C., Gerig, G.: User-guided 3D active contour segmentation of anatomical structures: significantly improved efficiency and reliability. NeuroImage. **31**(3), 1116–1128 (2006)
24. The Vascular Modeling Toolkit. Available from: www.vmtk.org
25. Jain, K.: Transition to turbulence in physiological flows: Direct numerical simulation of hemodynamics in intracranial aneurysms and cerebrospinal fluid hydrodynamics in the spinal canal. 2016, Universität Siegen
26. Almotiri, J., Elleithy, K., Elleithy, A.: Retinal vessels segmentation techniques and algorithms: a survey. Appl. Sci. **8**(2), 155 (2018)
27. Simonovsky, M., et al.: A deep metric for multimodal registration. In: 19th International Conference on Medical Image Computing and Computer-Assisted Intervention. Springer, Athens, Greece (2016)
28. Akkus, Z., Galimzianova, A., Hoogi, A., Rubin, D.L., Erickson, B.J.: Deep learning for brain MRI segmentation: state of the art and future directions. J. Digit. Imaging. **30**(4), 449–459 (2017)
29. Hjelle, Ø., Dæhlen, M.: Triangulations and applications. In: Mathematics and Visualization, p. 234. Springer-Verlag, Berlin/New York (2006)
30. De Boor, C.: A practical guide to splines. In: Applied Mathematical Sciences, Rev edn, p. 346. Springer. xviii, New York (2001)
31. Helgeland, A., Mardal, K.A., Haughton, V., Reif, B.A.: Numerical simulations of the pulsating flow of cerebrospinal fluid flow in the cervical spinal canal of a Chiari patient. J. Biomech. **47**(5), 1082–1090 (2014)
32. Kurtcuoglu, V., Soellinger, M., Summers, P., Boomsma, K., Poulikakos, D., Boesiger, P., Ventikos, Y.: Computational investigation of subject-specific cerebrospinal fluid flow in the third ventricle and aqueduct of Sylvius. J. Biomech. **40**(6), 1235–1245 (2007)

33. Stoverud, K.H., Langtangen, H.P., Ringstad, G.A., Eide, P.K., Mardal, K.A.: Computational investigation of cerebrospinal fluid dynamics in the posterior cranial fossa and cervical subarachnoid space in patients with Chiari I malformation. PLoS One. **11**(10), e0162938 (2016)
34. Rutkowska, G., Haughton, V., Linge, S., Mardal, K.A.: Patient-specific 3D simulation of cyclic CSF flow at the craniocervical region. Am. J. Neuroradiol. **33**(9), 1756–1762 (2012)
35. Jain, K., Ringstad, G., Eide, P.K., Mardal, K.A.: Direct numerical simulation of transitional hydrodynamics of the cerebrospinal fluid in Chiari I malformation: the role of cranio-vertebral junction. Int. J. Numer. Method Biomed. Eng. **33**(9), (2017)
36. Stockman, H.W.: Effect of anatomical fine structure on the flow of cerebrospinal fluid in the spinal subarachnoid space. J. Biomech. Eng. **128**(1), 106 (2005)
37. Mittal, R., Iaccarino, G.: Immersed boundary methods. Annu. Rev. Fluid Mech. **37**, 239–261 (2005)
38. Haslam, M., Zamir, M.: Pulsatile flow in tubes of elliptic gross sections. Ann. Biomed. Eng. **26**(5), 780–787 (1998)
39. Gupta, S., Poulikakos, D., Kurtcuoglu, V.: Analytical solution for pulsatile viscous flow in a straight elliptic annulus and application to the motion of the cerebrospinal fluid. Phys. Fluids. **20**(9), (2008)
40. Boutsianis, E., Gupta, S., Boomsma, K., Poulikakos, D.: Boundary conditions by Schwarz-Christoffel mapping in anatomically accurate hemodynamics. Ann. Biomed. Eng. **36**(12), 2068–2084 (2008)
41. Enzmann, D.R., Pelc, N.J.: Brain motion: measurement with phase-contrast MR imaging. Radiology. **185**(3), 653–660 (1992)
42. Soellinger, M., Rutz, A.K., Kozerke, S., Boesiger, P.: 3D cine displacement-encoded MRI of pulsatile brain motion. Magn. Reson. Med. **61**(1), 153–162 (2009)
43. Pahlavian, S.H., Oshinski, J., Zhong, X., Loth, F., Amini, R.: Regional quantification of brain tissue strain using displacement-encoding with stimulated echoes magnetic resonance imaging. J. Biomech. Eng. **140**(8), (2018)
44. Shannon, C.E.: Communication in the presence of noise. Proceedings of the Institute of Radio Engineers. **37**(1), 10–21 (1949)
45. Luke, H.D.: The origins of the sampling theorem. IEEE Commun. Mag. **37**(4), 106–108 (1999)
46. Terem, I., Ni, W.W., Goubran, M., Rahimi, M.S., Zaharchuk, G., Yeom, K.W., Moseley, M.E., Kurt, M., Holdsworth, S.J.: Revealing sub-voxel motions of brain tissue using phase-based amplified MRI (aMRI). Magn. Reson. Med. **80**, 2549 (2018)
47. Ma, Q., Ineichen, B.V., Detmar, M., Proulx, S.T.: Outflow of cerebrospinal fluid is predominantly through lymphatic vessels and is reduced in aged mice. Nat. Commun. **8**(1), 1434 (2017)
48. Grzybowski, D.M., Herderick, E.E., Kapoor, K.G., Holman, D.W., Katz, S.E.: Human arachnoid granulations part I: a technique for quantifying area and distribution on the superior surface of the cerebral cortex. Cerebrospinal Fluid Res. **4**, 6 (2007)
49. Holman, D.W., Kurtcuoglu, V., Grzybowski, D.M.: Cerebrospinal fluid dynamics in the human cranial subarachnoid space: an overlooked mediator of cerebral disease. II. In vitro arachnoid outflow model. J. R. Soc. Interface. **7**(49), 1205–1218 (2010)
50. Eide, P.K., Vatnehol, S.A.S., Emblem, K.E., Ringstad, G.: Magnetic resonance imaging provides evidence of glymphatic drainage from human brain to cervical lymph nodes. Sci. Rep. **8**(1), 7194 (2018)
51. Ma, Q., Ries, M., Decker, Y., Muller, A., Riner, C., Bucker, A., Fassbender, K., Detmar, M., Proulx, S.T.: Rapid lymphatic efflux limits cerebrospinal fluid flow to the brain. Acta Neuropathol. **137**, 151 (2019)
52. Linge, S.O., Haughton, V., Lovgren, A.E., Mardal, K.A., Langtangen, H.P.: CSF flow dynamics at the craniovertebral junction studied with an idealized model of the subarachnoid space and computational flow analysis. Am. J. Neuroradiol. **31**(1), 185–192 (2010)

53. Siyahhan, B., Knobloch, V., de Zelicourt, D., Asgari, M., Schmid Daners, M., Poulikakos, D., Kurtcuoglu, V.: Flow induced by ependymal cilia dominates near-wall cerebrospinal fluid dynamics in the lateral ventricles. J. R. Soc. Interface. **11**(94), 20131189 (2014)
54. Xie, L.L., Kang, H.Y., Xu, Q.W., Chen, M.J., Liao, Y.H., Thiyagarajan, M., O'Donnell, J., Christensen, D.J., Nicholson, C., Iliff, J.J., Takano, T., Deane, R., Nedergaard, M.: Sleep drives metabolite clearance from the adult brain. Science. **342**(6156), 373–377 (2013)
55. Rikhtegar, F., Edelman, E.R., Olgac, U., Poulikakos, D., Kurtcuoglu, V.: Drug deposition in coronary arteries with overlapping drug-eluting stents. J. Control. Release. **238**, 1–9 (2016)
56. Rodi, W.: Turbulence modeling and simulation in hydraulics: a historical review. J. Hydraul. Eng. **143**(5), (2017)
57. Jacobson, E.E., Fletcher, D.F., Morgan, M.K., Johnston, I.H.: Computer modelling of the cerebrospinal fluid flow dynamics of aqueduct stenosis. Med. Biol. Eng. Comput. **37**(1), 59–63 (1999)
58. Fin, L., Grebe, R.: Three dimensional modeling of the cerebrospinal fluid dynamics and brain interactions in the aqueduct of sylvius. Comput. Methods Biomech. Biomed. Engin. **6**(3), 163–170 (2003)
59. Kurtcuoglu, V., Poulikakos, D., Ventikos, Y.: Computational modeling of the mechanical behavior of the cerebrospinal fluid system. J. Biomech. Eng. **127**(2), 264–269 (2005)
60. Du Boulay, G., O'Connell, J., Currie, J., Bostick, T., Verity, P.: Further investigations on pulsatile movements in the cerebrospinal fluid pathways. Acta Radiol. Diagn. **13**(0), 496–523 (1972)
61. Kurtcuoglu, V., Soellinger, M., Summers, P., Poulikakos, D., Boesiger, P.: Mixing and modes of mass transfer in the third cerebral ventricle: a computational analysis. J. Biomech. Eng. **129**(5), 695–702 (2007)
62. Cheng, S., Tan, K., Bilston, L.E.: The effects of the interthalamic adhesion position on cerebrospinal fluid dynamics in the cerebral ventricles. J. Biomech. **43**(3), 579–582 (2010)
63. Howden, L., Giddings, D., Power, H., Aroussi, A., Vloeberghs, M., Garnett, M., Walker, D.: Three-dimensional cerebrospinal fluid flow within the human ventricular system. Comput. Methods Biomech. Biomed. Engin. **11**(2), 123–133 (2008)
64. Bergsneider, M., Black, P.M., Klinge, P., Marmarou, A., Relkin, N.: Surgical management of idiopathic normal-pressure hydrocephalus. Neurosurgery. **57**(3 Suppl), S29–S39; discussion ii–v (2005)
65. Gholampour, S., Fatouraee, N., Seddighi, A.S., Seddighi, A.: Numerical simulation of cerebrospinal fluid hydrodynamics in the healing process of hydrocephalus patients. J. Appl. Mech. Tech. Phys. **58**(3), 386–391 (2017)
66. Demerdash, A., Rocque, B.G., Johnston, J., Rozzelle, C.J., Yalcin, B., Oskouian, R., Delashaw, J., Tubbs, R.S.: Endoscopic third ventriculostomy: a historical review. Br. J. Neurosurg. **31**(1), 28–32 (2017)
67. Gholampour, S.: FSI simulation of CSF hydrodynamic changes in a large population of non-communicating hydrocephalus patients during treatment process with regard to their clinical symptoms. PLoS One. **13**(4), e0196216 (2018)
68. Farnoush, A., Tan, K., Juge, L., Bilston, L.E., Cheng, S.: Effect of endoscopic third ventriculostomy on cerebrospinal fluid pressure in the cerebral ventricles. J. Clin. Neurosci. **23**, 63–67 (2016)
69. Khani, M., Sass, L., Xing, T., Sharp, M.K., Balédent, O., Martin, B.: Anthropomorphic model of intrathecal cerebrospinal fluid dynamics within the spinal subarachnoid space: spinal cord nerve roots increase steady-streaming. J. Biomech. Eng. **140**, 081012 (2018)
70. Elliott, N.S.J., Bertram, C.D., Martin, B.A., Brodbelt, A.R.: Syringomyelia: a review of the biomechanics. J. Fluids Struct. **40**, 1–24 (2013)
71. Shaffer, N., Martin, B., Loth, F.: Cerebrospinal fluid hydrodynamics in type I Chiari malformation. Neurol. Res. **33**(3), 247–260 (2011)
72. Loth, F., Yardimci, M.A., Alperin, N.: Hydrodynamic modeling of cerebrospinal fluid motion within the spinal cavity. J. Biomech. Eng. **123**(1), 71–79 (2001)

73. The Visible Human Project. 1997 [cited 2011 February]; Available from: http://www.nlm.nih.gov/research/visible/visible_human.html
74. Stockman, H.W.: Effect of anatomical fine structure on the flow of cerebrospinal fluid in the spinal subarachnoid space. J. Biomech. Eng. **128**(1), 106–114 (2006)
75. Sweetman, B., Linninger, A.A.: Cerebrospinal fluid flow dynamics in the central nervous system. Ann. Biomed. Eng. **39**(1), 484–496 (2011)
76. Linninger, A.A., Xenos, M., Zhu, D.C., Somayaji, M.R., Kondapalli, S., Penn, R.D.: Cerebrospinal fluid flow in the normal and hydrocephalic human brain. IEEE Trans. Biomed. Eng. **54**(2), 291–302 (2007)
77. Sweetman, B., Xenos, M., Zitella, L., Linninger, A.A.: Three-dimensional computational prediction of cerebrospinal fluid flow in the human brain. Comput. Biol. Med. **41**(2), 67–75 (2011)
78. Yiallourou, T.I., Kroger, J.R., Stergiopulos, N., Maintz, D., Martin, B.A., Bunck, A.C.: Comparison of 4D phase-contrast MRI flow measurements to computational fluid dynamics simulations of cerebrospinal fluid motion in the cervical spine. PLoS One. **7**(12), e52284 (2012)
79. Lindstrom, E.K., Schreiner, J., Ringstad, G.A., Haughton, V., Eide, P.K., Mardal, K.A.: Comparison of phase-contrast MR and flow simulations for the study of CSF dynamics in the cervical spine. Neuroradiol. J. **31**(3), 292–298 (2018)
80. Clarke, E.C., Fletcher, D.F., Stoodley, M.A., Bilston, L.E.: Computational fluid dynamics modelling of cerebrospinal fluid pressure in Chiari malformation and syringomyelia. J. Biomech. **46**(11), 1801–1809 (2013)
81. Heidari Pahlavian, S., Bunck, A.C., Loth, F., Shane Tubbs, R., Yiallourou, T., Kroeger, J.R., Heindel, W., Martin, B.A.: Characterization of the discrepancies between four-dimensional phase-contrast magnetic resonance imaging and in-silico simulations of cerebrospinal fluid dynamics. J. Biomech. Eng. **137**(5), 051002 (2015)
82. Heidari Pahlavian, S., Bunck, A.C., Thyagaraj, S., Giese, D., Loth, F., Hedderich, D.M., Kroger, J.R., Martin, B.A.: Accuracy of 4D flow measurement of cerebrospinal fluid dynamics in the cervical spine: an in vitro verification against numerical simulation. Ann. Biomed. Eng. **44**(11), 3202–3214 (2016)
83. Thyagaraj, S., Pahlavian, S.H., Sass, L.R., Loth, F., Vatani, M., Choi, J.W., Tubbs, R.S., Giese, D., Kroger, J.R., Bunck, A.C., Martin, B.A.: An MRI-compatible hydrodynamic simulator of cerebrospinal fluid motion in the cervical spine. IEEE Trans. Biomed. Eng. (2017)
84. Martin, B.A., Yiallourou, T.I., Pahlavian, S.H., Thyagaraj, S., Bunck, A.C., Loth, F., Sheffer, D.B., Kroger, J.R., Stergiopulos, N.: Inter-operator reliability of magnetic resonance image-based computational fluid dynamics prediction of cerebrospinal fluid motion in the cervical spine. Ann. Biomed. Eng. **44**(5), 1524–1537 (2016)
85. Bunck, A.C., Kroger, J.R., Juttner, A., Brentrup, A., Fiedler, B., Schaarschmidt, F., Crelier, G.R., Schwindt, W., Heindel, W., Niederstadt, T., Maintz, D.: Magnetic resonance 4D flow characteristics of cerebrospinal fluid at the craniocervical junction and the cervical spinal canal. Eur. Radiol. **21**(8), 1788–1796 (2011)
86. Bunck, A.C., Kroeger, J.R., Juettner, A., Brentrup, A., Fiedler, B., Crelier, G.R., Martin, B.A., Heindel, W., Maintz, D., Schwindt, W., Niederstadt, T.: Magnetic resonance 4D flow analysis of cerebrospinal fluid dynamics in Chiari I malformation with and without syringomyelia. Eur. Radiol. **22**(9), 1860–1870 (2012)
87. Khani, M., Xing, T., Gibbs, C., Oshinski, J.N., Stewart, G.R., Zeller, J.R., Martin, B.A.: Nonuniform moving boundary method for computational fluid dynamics simulation of intrathecal cerebrospinal flow distribution in a cynomolgus monkey. J. Biomech. Eng. **139**(8), (2017)
88. Gardner, W.J.: Hydrodynamic mechanism of Syringomyelia: its relationship to Myelocele. J. Neurol. Neurosurg. Psychiatry. **28**, 247–259 (1965)
89. Williams, B.: On the pathogenesis of syringomyelia: a review. J. R. Soc. Med. **73**(11), 798–806 (1980)

90. Lockey, P., Poots, G., Williams, B.: Theoretical aspects of the attenuation of pressure pulses within cerebrospinal-fluid pathways. Med. Biol. Eng. **13**(6), 861–869 (1975)
91. Berkouk, K., Carpenter, P.W., Lucey, A.D.: Pressure wave propagation in fluid-filled co-axial elastic tubes, part 1: basic theory. J. Biomech. Eng. **125**(6), 852–856 (2003)
92. Carpenter, P.W., Berkouk, K., Lucey, A.D.: Pressure wave propagation in fluid-filled co-axial elastic tubes, part 2: mechanisms for the pathogenesis of syringomyelia. J. Biomech. Eng. **125**(6), 857–863 (2003)
93. Carpenter, P.W., Berkouk, K., Lucey, A.D.: A theoretical model of pressure wave propagation in the human spinal CSF system. Eng. Mech. **6**(4/5), 213–228 (1999)
94. Bertram, C.D., Brodbelt, A.R., Stoodley, M.A.: The origins of syringomyelia: numerical models of fluid/structure interactions in the spinal cord. J. Biomech. Eng. **127**(7), 1099–1109 (2005)
95. Elliott, N.S.J., Lockerby, D.A., Brodbelt, A.R.: The pathogenesis of syringomyelia: a re-evaluation of the elastic-jump hypothesis. J. Biomech. Eng. **131**(4), 044503–1–6 (2009)
96. Chang, H.S., Nakagawa, H.: Hypothesis on the pathophysiology of syringomyelia based on simulation of cerebrospinal fluid dynamics. J. Neurol. Neurosurg. Psychiatry. **74**(3), 344–347 (2003)
97. Bertram, C.D., Bilston, L.E., Stoodley, M.A.: Tensile radial stress in the spinal cord related to arachnoiditis or tethering: a numerical model. Med. Biol. Eng. Comput. **46**(7), 701–707 (2008)
98. Bertram, C.D., Heil, M.: A poroelastic fluid/structure-interaction model of cerebrospinal fluid dynamics in the cord with syringomyelia and adjacent subarachnoid-space stenosis. J. Biomech. Eng. **139**(1), (2017)
99. Heil, M., Bertram, C.D.: A poroelastic fluid-structure interaction model of syringomyelia. J. Fluid Mech. **809**, 360–389 (2016)
100. Elliott, N.S., Lockerby, D.A., Brodbelt, A.R.: A lumped-parameter model of the cerebrospinal system for investigating arterial-driven flow in posttraumatic syringomyelia. Med. Eng. Phys. **33**(7), 874–882 (2011)
101. Elliott, N.S.: Syrinx fluid transport: modeling pressure-wave-induced flux across the spinal pial membrane. J. Biomech. Eng. **134**(3), 031006 (2012)
102. Elliott, N.S.J., Lucey, A.D., Lockerby, D.A., Brodbelt, A.R.: Fluid-structure interactions in a cylindrical layered wave guide with application in the spinal column to syringomyelia. J. Fluids Struct. **70**, 464–499 (2017)
103. Cirovic, S., Lloyd, R., Jovanovik, J., Volk, H.A., Rusbridge, C.: Computer simulation of syringomyelia in dogs. BMC Vet. Res. **14**(1), 82 (2018)
104. Cirovic, S.: A coaxial tube model of the cerebrospinal fluid pulse propagation in the spinal column. J. Biomech. Eng. **131**(2), 021008 (2009)
105. Cirovic, S., Kim, M.: A one-dimensional model of the spinal cerebrospinal-fluid compartment. J. Biomech. Eng. **134**(2), 021005 (2012)
106. Cheng, S., Fletcher, D., Hemley, S., Stoodley, M., Bilston, L.: Effects of fluid structure interaction in a three dimensional model of the spinal subarachnoid space. J. Biomech. **47**(11), 2826–2830 (2014)
107. Cheng, S., Stoodley, M.A., Wong, J., Hemley, S., Fletcher, D.F., Bilston, L.E.: The presence of arachnoiditis affects the characteristics of CSF flow in the spinal subarachnoid space: a modelling study. J. Biomech. **45**(7), 1186–1191 (2012)
108. Bilston, L.E., Fletcher, D.F., Stoodley, M.A.: Focal spinal arachnoiditis increases subarachnoid space pressure: a computational study. Clin. Biomech. **21**(6), 579–584 (2006)
109. Roldan, A., Wieben, O., Haughton, V., Osswald, T., Chesler, N.: Characterization of CSF hydrodynamics in the presence and absence of tonsillar ectopia by means of computational flow analysis. Am. J. Neuroradiol. **30**(5), 941–946 (2009)
110. Linge, S.O., Haughton, V., Lovgren, A.E., Mardal, K.A., Helgeland, A., Langtangen, H.P.: Effect of tonsillar herniation on cyclic CSF flow studied with computational flow analysis. Am. J. Neuroradiol. **32**(8), 1474–1481 (2011)

111. Martin, B.A., Kalata, W., Shaffer, N., Fischer, P., Luciano, M., Loth, F.: Hydrodynamic and longitudinal impedance analysis of cerebrospinal fluid dynamics at the craniovertebral junction in type I Chiari malformation. PLoS One. **8**(10), e75335 (2013)
112. Shaffer, N., Martin, B.A., Rocque, B., Madura, C., Wieben, O., Iskandar, B.J., Dombrowski, S., Luciano, M., Oshinski, J.N., Loth, F.: Cerebrospinal fluid flow impedance is elevated in type I Chiari malformation. J. Biomech. Eng. **136**(2), 021012 (2014)
113. Pahlavian, S.H., Loth, F., Oshinski, J.N., Luciano, M.G., Martin, B.A.: Cardiac related neural tissue motion impacts cerebrospinal fluid dynamics at the cervical-medullary junction: a patient-specific moving-boundary computational fluid dynamics model of type 1 Chiari malformation. Ann. Biomed. Eng. (2015)
114. Papisov, M.I., Belov, V.V., Gannon, K.S.: Physiology of the Intrathecal bolus: the Leptomeningeal route for macromolecule and particle delivery to CNS. Mol. Pharm. **10**(5), 1522–1532 (2013)
115. O'Donnell, J., Ding, F., Nedergaard, M.: Distinct functional states of astrocytes during sleep and wakefulness: is norepinephrine the master regulator? Curr. Sleep Med. Rep. **1**(1), 1–8 (2015)
116. Patel, T., Zhou, J.B., Piepmeier, J.M., Saltzman, W.M.: Polymeric nanoparticles for drug delivery to the central nervous system. Adv. Drug Deliv. Rev. **64**(7), 701–705 (2012)
117. Lu, C.T., Zhao, Y.Z., Wong, H.L., Cai, J., Peng, L., Tian, X.Q.: Current approaches to enhance CNS delivery of drugs across the brain barriers. Int. J. Nanomedicine. **9**, 2241–2256 (2014)
118. Watanabe, Y., Kazuki, Y., Kazuki, K., Ebiki, M., Nakanishi, M., Nakamura, K., Yoshida Yamakawa, M., Hosokawa, H., Ohbayashi, T., Oshimura, M., Nakashima, K.: Use of a human artificial chromosome for delivering trophic factors in a rodent model of amyotrophic lateral sclerosis. Mol. Ther. Nucleic Acids. **4**, e253 (2015)
119. Deepa, P., Shahani, N., Alladi, P.A., Vijayalakshmi, K., Sathyaprabha, T.N., Nalini, A., Ravi, V., Raju, T.R.: Down regulation of trophic factors in neonatal rat spinal cord after administration of cerebrospinal fluid from sporadic amyotrophic lateral sclerosis patients. J. Neural Transm. **118**(4), 531–538 (2011)
120. Myers, M.R.: A numerical investigation into factors affecting anesthetic distribution during spinal anesthesia. J. Biomech. **29**(2), 139–149 (1996)
121. Kuttler, A., Dimke, T., Kern, S., Helmlinger, G., Stanski, D., Finelli, L.A.: Understanding pharmacokinetics using realistic computational models of fluid dynamics: biosimulation of drug distribution within the CSF space for intrathecal drugs. J. Pharmacokinet. Pharmacodyn. **37**(6), 629–644 (2010)
122. Hsu, Y., Hettiarachchi, H.D., Zhu, D.C., Linninger, A.A.: The frequency and magnitude of cerebrospinal fluid pulsations influence intrathecal drug distribution: key factors for interpatient variability. Anesth. Analg. **115**(2), 386–394 (2012)
123. Haga, P.T., Pizzichelli, G., Mortensen, M., Kuchta, M., Pahlavian, S.H., Sinibaldi, E., Martin, B.A., Mardal, K.A.: A numerical investigation of intrathecal isobaric drug dispersion within the cervical subarachnoid space. PLoS One. **12**(3), e0173680 (2017)
124. Tangen, K.M., Leval, R., Mehta, A.I., Linninger, A.A.: Computational and in vitro experimental investigation of intrathecal drug distribution: parametric study of the effect of injection volume, cerebrospinal fluid pulsatility, and drug uptake. Anesth. Analg. **124**(5), 1686–1696 (2017)
125. Tangen, K.M., Hsu, Y., Zhu, D.C., Linninger, A.A.: CNS wide simulation of flow resistance and drug transport due to spinal microanatomy. J. Biomech. **48**(10), 2144–2154 (2015)
126. Linninger, A.A., Somayaji, M.R., Mekarski, M., Zhang, L.: Prediction of convection-enhanced drug delivery to the human brain. J. Theor. Biol. **250**(1), 125–138 (2008)
127. Sarntinoranont, M., Banerjee, R.K., Lonser, R.R., Morrison, P.F.: A computational model of direct interstitial infusion of macromolecules into the spinal cord. Ann. Biomed. Eng. **31**(4), 448–461 (2003)
128. Støverud, K.H., Darcis, M., Helmig, R., Hassanizadeh, S.M.: Modeling concentration distribution and deformation during convection-enhanced drug delivery into brain tissue. Transp. Porous Media. **92**(1), 119–143 (2012)

129. Tangen, K., Linninger, A., Narasimhan, N.S.: Clearance of subarachnoid hemorrhage from the central nervous system via lumbar drain - a bench-top and computational study. Cerebrovasc. Dis. **41**, 202–202 (2016)
130. Tangen, K., Narasimhan, N.S., Sierzega, K., Preden, T., Alaraj, A., Linninger, A.A.: Clearance of subarachnoid hemorrhage from the cerebrospinal fluid in computational and in vitro models. Ann. Biomed. Eng. (2016)
131. Dichiro, G.: Movement of the cerebrospinal fluid in human beings. Nature. **204**, 290–291 (1964)
132. Asgari, M., de Zelicourt, D.A., Kurtcuoglu, V.: Barrier dysfunction or drainage reduction: differentiating causes of CSF protein increase. Fluids Barriers CNS. **14**(1), 14 (2017)
133. Sanchez, A.L., Martinez-Bazan, C., Gutierrez-Montes, C., Criado-Hidalgo, E., Pawlak, G., Bradley, W., Haughton, V., Lasheras, J.C.: On the bulk motion of the cerebrospinal fluid in the spinal canal. J. Fluid Mech. **841**, 203–227 (2018)
134. Bilston, L.E., Fletcher, D.F., Brodbelt, A.R., Stoodley, M.A.: Arterial pulsation-driven cerebrospinal fluid flow in the perivascular space: a computational model. Comput. Methods Biomech. Biomed. Engin. **6**(4), 235–241 (2003)
135. Lloyd, R.A., Fletcher, D.F., Clarke, E.C., Bilston, L.E.: Chiari malformation may increase perivascular cerebrospinal fluid flow into the spinal cord: a subject-specific computational modelling study. J. Biomech. **65**, 185–193 (2017)
136. Wang, P., Olbricht, W.L.: Fluid mechanics in the perivascular space. J. Theor. Biol. **274**(1), 52–57 (2011)
137. Bilston, L.E., Stoodley, M.A., Fletcher, D.F.: The influence of the relative timing of arterial and subarachnoid space pulse waves on spinal perivascular cerebrospinal fluid flow as a possible factor in syrinx development. J. Neurosurg. **112**(4), 808–813 (2010)
138. Schley, D., Carare-Nnadi, R., Please, C.P., Perry, V.H., Weller, R.O.: Mechanisms to explain the reverse perivascular transport of solutes out of the brain. J. Theor. Biol. **238**(4), 962–974 (2006)
139. Asgari, M., de Zelicourt, D., Kurtcuoglu, V.: How astrocyte networks may contribute to cerebral metabolite clearance. Sci. Rep. **5**, (2015)
140. Sharp, M.K., Diem, A.K., Weller, R.O., Carare, R.O.: Peristalsis with oscillating flow resistance: a mechanism for periarterial clearance of amyloid beta from the brain. Ann. Biomed. Eng. **44**(5), 1553–1565 (2016)
141. Asgari, M., de Zelicourt, D., Kurtcuoglu, V.: Glymphatic solute transport does not require bulk flow. Sci. Rep. **6**, (2016)
142. Rey, J., Sarntinoranont, M.: Pulsatile flow drivers in brain parenchyma and perivascular spaces: a resistance network model study. Fluids Barriers CNS. **15**, (2018)
143. Diem, A.K., Sharp, M.M., Gatherer, M., Bressloff, N.W., Carare, R.O., Richardson, G.: Arterial pulsations cannot drive intramural periarterial drainage: significance for a beta drainage. Front. Neurosci. **11**, (2017)
144. Jin, B.J., Smith, A.J., Verkman, A.S.: Spatial model of convective solute transport in brain extracellular space does not support a "glymphatic" mechanism. J. Gen. Physiol. **148**(6), 489–501 (2016)
145. Coloma, M., Schaffer, J.D., Carare, R.O., Chiarot, P.R., Huang, P.: Pulsations with reflected boundary waves: a hydrodynamic reverse transport mechanism for perivascular drainage in the brain. J. Math. Biol. **73**(2), 469–490 (2016)
146. Holter, K.E., Kehlet, B., Devor, A., Sejnowski, T.J., Dale, A.M., Omholt, S.W., Ottersen, O.P., Nagelhus, E.A., Mardal, K.A., Pettersen, K.H.: Interstitial solute transport in 3D reconstructed neuropil occurs by diffusion rather than bulk flow. Proc. Natl. Acad. Sci. U. S. A. **114**(37), 9894–9899 (2017)

Chapter 10
Finite Element Algorithms for Computational Biomechanics of the Brain

Adam Wittek, Grand Roman Joldes, and Karol Miller

10.1 Introduction

Modelling of the brain biomechanical responses due to injury-causing transients and surgery is a problem of continuum mechanics that involves irregular geometry, complex loading and boundary conditions, non-linear materials and large deformations (see Chaps. 5 and 6). Finding a solution for such a problem requires computational algorithms of non-linear continuum mechanics.

As stated in Chap. 5, modelling for brain injury simulation has been driven by the idea that numerical surrogates of the human brain can be applied in the design of countermeasures mitigating the traumatic brain injury. Such modelling has been done with significant contribution and involvement of the automotive manufacturers [1] and participation of organisations responsible for traffic safety (e.g. National Highway Traffic Safety Administration (NHTSA)) [2]. Because of this industrial links and implications, modelling of the brain for injury simulation has been dominated by the explicit dynamics (i.e. utilising explicit time stepping referred to in the literature also as explicit time integration [3, 4]) non-linear finite element algorithms available in commercial finite element codes, such as LS-DYNA [5], PAM-SAFE [6], RADIOSS [7] and ABAQUS [8], which are routinely used by the automotive industry.

In computational biomechanics for medicine, on the other hand, significant research effort has been directed to development of specialised algorithms that can provide the results within the real-time constraints of surgery. For instance, great interest was given to mass-spring method [9, 10] in which the analysed continuum is modelled as a discrete system of nodes (where the mass is concentrated) and springs.

A. Wittek (✉) · G. R. Joldes · K. Miller
Intelligent Systems for Medicine Laboratory, Department of Mechanical Engineering, The University of Western Australia, Perth, WA, Australia
e-mail: adam.wittek@uwa.edu.au; karol.miller@uwa.edu.au

K. Miller (ed.), *Biomechanics of the Brain*, Biological and Medical Physics, Biomedical Engineering, https://doi.org/10.1007/978-3-030-04996-6_10

Due to its simplicity and low computational costs, the target application areas for this method included simulation software for virtual reality training systems for minimally invasive surgery [11] and surgical planning [12]. However, the behaviour of the mass-spring models strongly depends on the topology of the spring network. Furthermore, the spring parameters are difficult to identify and express in terms of soft tissue constitutive parameters (such as Young's modulus and Poisson's ratio) used in continuum mechanics [13]. Therefore, in recent years, more interest has been given to finite element method [4] that utilises the principles of continuum mechanics and does not suffer from the limitations of the mass-spring method.

Traditionally real-time computations for biomechanics for medicine relied on linear finite element algorithms that assume infinitesimally small deformations [13–19]. However, this assumption is not satisfied in surgical procedures where large deformations of the organ undergoing surgery occur. Examples include the brain deformations due to craniotomy (referred to in the literature as brain shift [20]) (see Fig. 6.1 in Chap. 6) and needle insertion where the strain reaches over 0.8 [21] (Fig. 10.1). Therefore, we focus on the algorithms that utilise fully non-linear (i.e. accounting for finite deformations and non-linear stress-strain relationships of soft tissues) formulation of solid mechanics and can be applied to any situation. In such formulation, current volume and surface of the modelled body organ, over which the integration of equations of continuum mechanics is to be conducted, are unknown: they are part of the solution rather than input data (Fig. 10.2). The literature indicates that taking into account geometric non-linearity (through finite deformation formulation of equations of continuum mechanics) is needed to ensure accuracy of prediction of soft organ deformations even for applications that do not involve large strains (e.g. brain shift) [22].

In the subsequent sections of this Chapter, we discuss the following topics:

- Section 10.2: Non-linear explicit dynamics finite element algorithms implemented in commercial finite element codes applied in modelling for brain injury biomechanics.

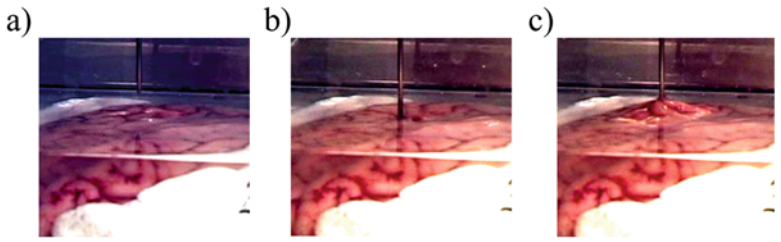

Fig. 10.1 Swine brain deformation during needle insertion. (**a**) Before insertion; (**b**) during the insertion (note the deformation in the insertion area); (**c**) during the needle removal. The experiments were conducted at the laboratory of the Surgical Assist Technology Group, Institute for Human Science and Biomedical Engineering, National Institute of Advanced Industrial Science and Technology (AIST), Tsukuba, Ibaraki, Japan. For the experiment description, see Wittek et al. [21]

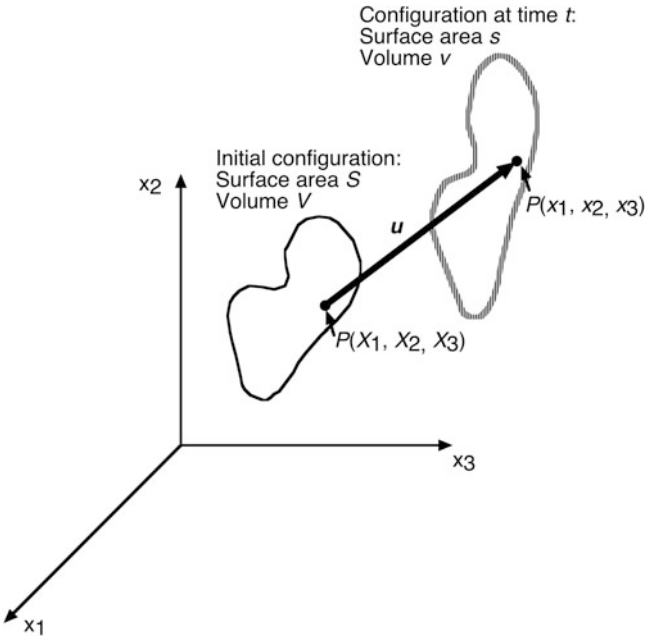

Fig. 10.2 Computational biomechanics as a non-linear problem of continuum mechanics. Under transient load/impact and during surgery, human body organs undergo large displacements (composed of rigid body motions and local deformations). Consequently, the equations of continuum mechanics governing the organ behaviour need to be integrated over the current surface S and volume V

- Section 10.3: Specialised non-linear finite element algorithm for surgery simulation that utilises explicit time stepping and Total Lagrangian incremental formulation of continuum mechanics.
- Section 10.4: Specialised non-linear finite element algorithm that utilises Dynamic Relaxation and Total Lagrangian formulation for computation of steady state brain deformation within the real-time constraints of image-guided neurosurgery.
- Section 10.5: Element formulation for the specialised algorithms for surgery simulation and neurosurgery modelling, which includes non-locking tetrahedral element and efficient hourglass control for hexahedral element.
- Section 10.6: An efficient sliding contact algorithm for modelling of brain-skull interaction for image-guided neurosurgery.
- Section 10.7: Implementation of the specialised non-linear finite element algorithms for neurosurgery modelling on graphics processing units (GPUs) for real-time solution of the brain models for computer-assisted neurosurgery.
- Section 10.8: Verification of finite element algorithms of computational biomechanics.

10.2 Algorithms for Injury Biomechanics

Impact/injury biomechanics of the brain deals with events of very short duration (hundreds of milliseconds) in which the head is subjected to transient loads due to either direct impact or rapid acceleration that result in large deformation (or even mechanical damage) of the brain tissue. As indicated in [4, 23], non-linear finite element procedures with explicit time stepping outperform other algorithms in modelling of three-dimensional continua subjected to short-duration transient loads. Therefore, they have been a preferable choice in injury biomechanics [24] (see also Chap. 5) and are implemented in numerous finite elements codes (such as LS-DYNA, PAM-CRASH, ABAQUS, RADIOSS) industrially applied in impact injury simulation.

In impact injury simulation and other transient dynamics problems, the global system of finite element equations to be solved at each time step is:

$$\mathbf{M}\ddot{\mathbf{u}}_n + \mathbf{K}\left(\mathbf{u}_n\right) \cdot \mathbf{u}_n = \mathbf{R}_n, \tag{10.1}$$

where $\mathbf{u}_n$ is a vector of nodal displacements at time step n, $\ddot{\mathbf{u}}_n$ is a vector of nodal acceleration at time step n, $\mathbf{M}$ is a mass matrix, $\mathbf{K}$ is a stiffness matrix non-linearly dependent on the deformation (because of the geometric and material non-linearities) and $\mathbf{R}_n$ is a vector of nodal (active) forces at time step n. The product of the stiffness matrix and nodal displacements vector gives the nodal reaction forces vector $\mathbf{F}$. In explicit dynamics finite element procedures, the accelerations determined from equation of motion (Eq. 10.1) are integrated to calculate the displacements using the difference methods. Although many difference methods exist [4], the central difference method is the most commonly used due to its efficiency [4, 23]:

$$u_{n+1} = u_n + \Delta t \cdot \dot{u}_n + 1/2 \cdot \Delta t^2 \cdot \ddot{u}_n, \tag{10.2}$$

$$\dot{u}_{n+1} = \dot{u}_n + 1/2 \cdot \Delta t \cdot \left(\ddot{u}_{n+1} + \ddot{u}_n\right), \tag{10.3}$$

where Δt is the time step (time increment).

Combining the central difference method given by Eqs. (10.2) and (10.3) with the global system of finite element equations Eq. (10.1) leads to the following formula for the vector of nodal displacements $\mathbf{u}_{n+1}$ at the increment $n + 1$ when the time step Δt is constant:

$$\mathbf{M}\mathbf{u}_{n+1} = \Delta t^2 \left(\mathbf{R}_n - \sum \mathbf{F}_n^{(i)}\right) - \mathbf{M}\left(\mathbf{u}_{n-1} - 2\mathbf{u}_n\right). \tag{10.4}$$

Formally Eq. (10.4) represents a system of equations. This system can be decoupled by using a lumped mass matrix $\mathbf{M}$. For lumped mass matrices, all

non-diagonal components equal zero. Such lumped mass matrix corresponds to discretising the mass distribution by concentrating the mass at the nodes of each element. For such matrices, the system of equations Eq. (10.4) becomes an explicit formula for the unknown nodal displacements $\mathbf{u}_{n+1}$:

$$\mathbf{u}_{n+1}^{j} = \Delta t^2 \left(\mathbf{R}_n^j - \sum_i \mathbf{F}_n^{(i)j} \right) / m_{jj} - \left(\mathbf{u}_{n-1}^{j} - 2\mathbf{u}_n^{j} \right), \tag{10.5}$$

where $\mathbf{u}^j{}_{n+1}$ is a vector of nodal displacements at node j at time step $n+1$, m_{jj} is the component of the lumped mass matrix corresponding to node j (i.e. mass lumped to node j), $\mathbf{R}^j{}_n$ is the vector of external forces applied to node j, $\sum_i \mathbf{F}_n^{(i)j}$ is the vector of nodal reaction forces at node j (sum of contribution of the elements i to which the node belong) and Δt is the time step.

In Eq. (10.5), the computations are done at an element level eliminating the need for assembling the stiffness matrix of the entire analysed continuum. The mechanical properties of the analysed continuum are accounted for in the constitutive model and included in the calculation of nodal reaction forces $\mathbf{F}$. Thus, the computational cost of each time step and internal memory requirements are very low. It is worth noting that there is no need for iterations anywhere in the algorithm summarised in Eq. (10.5) even for non-linear problems. This implies the following advantages of non-linear finite element procedures utilising explicit time stepping and mass lumping:

- Straightforward treatment of non-linearities without any need for iterations (no iterations required for a time step).
- No need to solve a system of equations.
- Low computation cost for each time step.
- Low internal memory requirements.

However, explicit time stepping methods are only conditionally stable. A restriction (Courant criterion [4]) on the time step size has to be included in order to obtain stable simulation results. The time step (referred to as a critical time step $\Delta t_{\text{critical}}$), that ensures the computation stability, is equal to the smallest ratio of the characteristic length of an element and the dilatational (acoustic) wave speed in the element [23, 25, 26]:

$$\Delta t_{\text{critical}} = (\Delta t_e)_{\min} \leq \left(\frac{L_e}{c_e} \right)_{\min}, \tag{10.6}$$

where is the characteristic element length L_{e} and c_e is the dilatational (acoustic) wave speed in the element. The formulae for calculating the characteristic element length L_{e} for various commonly used finite elements are given in Belytschko [27].

For a model with the uniform properties, where the acoustic wave speed is the same in all the elements, Eq. (10.6) is equivalent to setting the condition that the time

step cannot be longer than the travel time of the wave across the smallest element (i.e. the element with the smallest characteristic length L_e) in the mesh [23]. Based on [27], the acoustic wave speed can be expressed as:

$$c = \sqrt{\frac{E}{\rho} \frac{(1-\nu)}{(1+\nu)(1-2\nu)}}, \tag{10.7}$$

where E is Young's modulus, ρ is the density and ν is Poisson's ratio.

It should be noted that the stability limit given in Eq. (10.6) has been derived for linear problems. However, according to Belytschko [23], there is considerable empirical evidence that it can be also used for non-linear problems with an appropriate safety factor for the critical time step.

Equations (10.6) and (10.7) imply that the critical time step can be increased by increasing the density (and hence mass) of the smallest elements (as determined by the characteristic length L_e) in the mesh. This process is referred to as mass scaling [5, 8]. Moderate mass scaling does not significantly change the responses of the analysed continuum and is regarded as a powerful method for decreasing the computation time [28]. However, it is also acknowledged that too severe scaling can introduce nonphysical inertial effects [28]. Formal guidelines for determining permissible mass scaling limits for injury simulation have not been formulated yet, and the quantitative information about the scaling used is rarely provided in the biomechanical literature. The limit of 5% of the total mass increase of the model due to mass scaling has been used by some authors [29]. However, Majumder et al. [30] reported a significant reduction in computation time for scaling resulting in the total model mass increase by as low as 0.016%. For quasi-static problems, mass scaling resulting in local density increase by over 100 times, while simultaneously ensuring that the ratio of kinetic to elastic energy remains low, has been used in several studies [28, 31].

Stress calculation for obtaining the nodal forces $\mathbf{F}$ (see Eqs. 10.4 and 10.8) is the major computation cost of the explicit dynamic finite element procedures summarised in Eqs. (10.4) and (10.5). This implies that the complexity of the elements, which includes the number of nodes (element vertices), order of shape function polynomial and the number of spatial integration points per element associated with the complexity are the key factors determining the number of computations in these procedures. Therefore, as mentioned in Chap. 5, in injury simulation utilising non-linear explicit dynamics finite element procedures, eight-noded hexahedron and four-noded tetrahedron with linear shape functions and one integration (Gauss) point are the most commonly used elements [32, 33].

Eight-noded hexahedron with one integration point is an under-integrated element (or low-order Gauss quadrature element), i.e. an element for which the stiffness matrix rank is lower than the number of element's degrees of freedom minus the number of rigid body modes [34]. Under-integrated elements exhibit instability known as hourglassing or zero-energy mode, i.e. nodal displacement vector which produces no strain energy but is not a rigid body motion [32, 34].

Four-noded tetrahedral elements with linear shape functions and one Gauss point do not suffer from hourglassing. However, for incompressible (or nearly incompressible) continua, such as soft tissues, four-noded tetrahedral elements exhibit artificial stiffening known as volumetric locking [35]. A more detailed discussion on algorithms for hourglass control and volumetric locking reduction is provided in Sect. 10.3 *Algorithms for Surgery Simulation* below.

10.3 Algorithms for Surgery Simulation

As discussed in Chap. 6, surgical simulation systems are used to provide visual and haptic feedback to a surgeon or trainee. Such systems must provide time accurate prediction of the deformation field within an organ and interaction force between the surgical tool and the tissue at frequencies of at least 500 Hz. From the perspective of continuum mechanics, such prediction requires solving the problem involving large deformations, non-linear constitutive properties and non-linear boundary conditions within very strict time constraints of haptic feedback.

For relatively slowly varying loads, such as those that occur due to interactions between the tissue and surgical tool, non-linear finite element algorithms utilising implicit time stepping are traditionally recommended in the literature for solving non-linear problems of solid mechanics [4]. Such procedures rely on solving systems of algebraic equations and require computationally expensive iterations. In contrast, the algorithms for injury simulation lead to an explicit formula for unknown nodal displacements (Eq. 10.5). For such algorithms, the number of operations per time step is typically three orders of magnitude smaller than for the algorithms relying on implicit time stepping [23]. Despite the fact that surgical simulations involve phenomena of duration of orders of magnitude longer than those that are of interest in injury simulation, the restrictions on the time step size (Courant criterion) required for solution stability (Eq. 10.6) do not compromise efficiency of explicit time stepping in such simulations. This is because the acoustic wave speed is proportional to square root of the analysed continuum Young's modulus (Eq. 10.7) which is very low (under 10^4 Pa) for the brain tissue. For instance, in the simulation of needle insertion into the brain conducted using non-linear explicit dynamics finite element procedures reported in Wittek et al. [21], the time step was over $1.5 \cdot 10^{-2}$ ms. In contrast, in typical engineering applications, such as metal forming, the integration steps are of an order of 10^{-5} ms [36].

In commercial finite element codes utilising explicit time stepping, the calculated variables (such as displacement, strain and stress) are incremented by referring them to the current configuration of the analysed continuum, which is known as an Updated Lagrangian formulation [4]. However, we advocate a Total Lagrangian (TL) formulation of computational mechanics in which all variables are referred to the original configuration of the system [37]. The decisive advantage of this formulation is that all derivatives with respect to spatial coordinates are calculated with respect to the original configuration and therefore can be precomputed

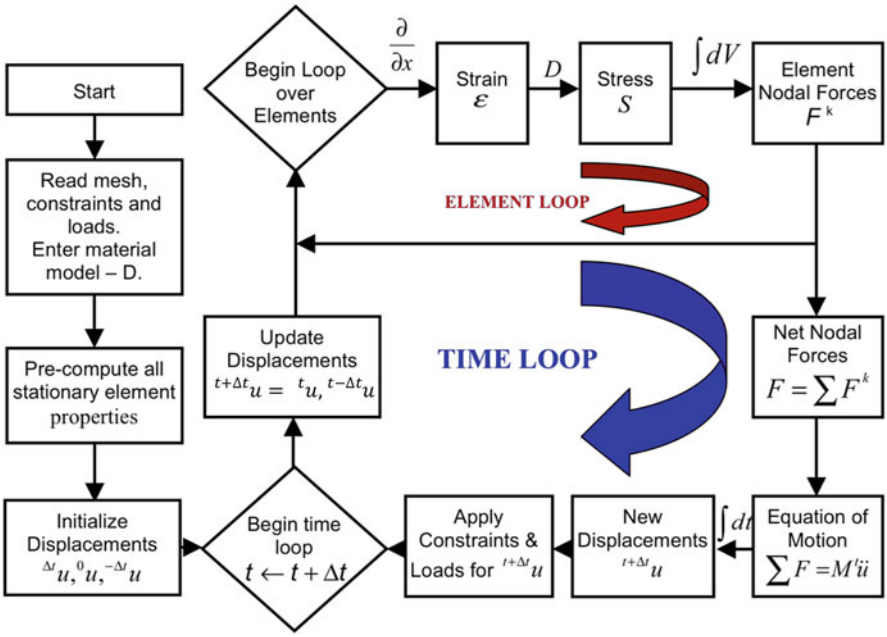

Fig. 10.3 Flowchart of the Total Lagrangian Explicit Dynamics (TLED) finite element algorithm for surgery simulation. Detailed description of the algorithm is given in Miller et al. [37]

as shown in the flowchart of the Total Lagrangian Explicit Dynamics (TLED) algorithm presented in Fig. 10.3 (a detailed description of the algorithm is given in Miller et al. [37]). In Chap. 11, the application of Total Lagrangian formulation with explicit time stepping is extended beyond finite element analysis to meshless methods of computational biomechanics that provide stable solution in a presence of discontinuities/cracks due to surgical dissection and tissue rupture and allow for semiautomated generation of patient-specific computational grids directly from medical images.

Following the approach typically applied in explicit dynamics finite element analysis, for computational efficiency of our TLED algorithm, we used single point spatial integration for all elements of the mesh (improved linear tetrahedrons [38] and under-integrated linear hexahedrons). Therefore, the nodal forces for each element are computed as:

$$ {}^{t}_{0}\mathbf{F}_{\text{int}} = {}^{t}_{0}\mathbf{X} \cdot {}^{t}_{0}\mathbf{S} \cdot \mathbf{B}_0 \cdot V_0, \tag{10.8} $$

where according to the notation used in Bathe [4], the left superscript represents the current time, the left subscript represents the time of the reference configuration, $\mathbf{F}_{\text{int}}$ is the matrix of nodal forces, $\mathbf{B}_0$ is the matrix of shape function derivatives, $\mathbf{S}$ is the second Piola-Kirchhoff stress matrix, $\mathbf{X}$ is the deformation gradient and V_0 is

the initial volume. In Eq. (10.8), the matrix of shape function derivatives $\mathbf{B}_0$ and the initial volume V_0 are constant and therefore can be precomputed (see Fig. 10.3).

The main benefits of the TLED algorithm in comparison to the explicit dynamics algorithms using Updated Lagrangian formulation are:

- Allows precomputing of many variables involved (e.g. derivatives with respect to spatial coordinates), Fig. 10.3.
- No accumulation of errors – increased stability for quasi-static solutions.
- Second Piola-Kirchhoff stress and Green strain are used – appropriate for handling geometric non-linearities.
- Easy implementation of the material law for hyper-elastic materials using the deformation gradient.

The fact that many quantities involved in the computation of nodal forces can be precomputed leads to a significant decrease in the computational effort. For instance, the TLED algorithm using eight-noded hexahedral under-integrated elements requires approximately 35% fewer floating-point operations per element, per time step than the Updated Lagrangian explicit algorithm using the same elements [37].

10.4 Algorithms for Neurosurgery Modelling

As explained in Chap. 6, accurate warping of high-quality pre-operative radiographic images to the intra-operative (i.e. deformed) brain configuration in a process known as nonrigid registration is a key element of image-guided neurosurgery. In order to perform such warping, only the final (deformed during surgery) state of the brain needs to be predicted. This requires algorithms for determining steady state solution for the brain deformations. The deformations at the steady state must be obtained within the real-time constraints of image-guided neurosurgery, which practically means that the results should be available in 40–80 seconds.

As stated in Chap. 6, the neuroimage registration is a non-linear problem of computational mechanics as it involves large deformations, non-linear material properties and non-linear boundary conditions. However, it is a less demanding problem than surgery simulation as only the steady state solution for deformations is of interest, i.e. the time history of forces and deformations does not have to be obtained. Therefore, for image registration, we advocate combining Total Lagrangian (TL) formulation, discussed in Sect. 10.3 *Algorithms for Surgery Simulation*, with Dynamic Relaxation (DR) which is an explicit iterative algorithm that relies on introduction of an artificial mass-dependent damping term in the equation of motion. The damping attenuates the oscillations in the transient response, increasing the speed of convergence towards the steady state solution. Because DR is an explicit algorithm, there is no need for solving large systems of equations. All quantities can be treated as vectors, reducing the implementation complexity and the memory requirements. Although the number of iterations to

obtain convergence can be quite large, the computation cost of each iteration is very low, making it a very efficient solution method for non-linear problems.

10.4.1 Dynamic Relaxation Algorithm

The basic Dynamic Relaxation (DR) algorithm is presented in [39]. The main idea is the inclusion of a mass proportional damping in equation of motion (Eq. 10.1) (see Sect. 10.2, *Algorithms for Injury Simulation*), which increases the convergence speed towards the steady state, and then solving the obtained damped equation using the central difference method (explicit time stepping). After the inclusion of mass proportional damping, equation of motion (Eq. 10.1) becomes

$$\mathbf{M}\ddot{\mathbf{u}} + c\mathbf{M}\dot{\mathbf{u}} + \mathbf{K}(\mathbf{u}_n) \cdot \mathbf{u}_n = \mathbf{R}_n, \tag{10.9}$$

where c is the damping coefficient.

By applying the central difference integration method to the damped equation of motion (Eq. 10.9), the equation that describes the iterations in terms of displacements becomes:

$$\mathbf{u}_{n+1} = \mathbf{u}_n + \beta(\mathbf{u}_n - \mathbf{u}_{n-1}) + \alpha\mathbf{M}^{-1}(\mathbf{R} - \mathbf{F}), \tag{10.10}$$

$$\alpha = 2\Delta t^2/(2 + c\Delta t), \quad \beta = (2 - c\Delta t)/(2 + c\Delta t), \tag{10.11}$$

where Δt is length of the time increment (time step).

The iterative method defined by Eq. (10.10) is explicit as long as the mass matrix is diagonal. As the mass matrix does not influence the deformed state solution, a lumped scaled mass matrix can be used that maximises the convergence of the method.

In Underwood [39], the convergence of the DR algorithm is studied for linear structural mechanics equations, when the nodal forces can be written as

$$\mathbf{F}(\mathbf{u}) = \mathbf{K} \cdot \mathbf{u}, \tag{10.12}$$

where $\mathbf{K}$ is the stiffness matrix.

We extend this study to the non-linear case. We propose to use the linearisation of the nodal forces obtained by expanding them in a Taylor series and keeping the first two terms

$$\mathbf{F}(\mathbf{u}) = \mathbf{F}(\mathbf{u}_k) + \mathbf{K}_k \cdot (\mathbf{u}_n - \mathbf{u}_k), \tag{10.13}$$

where $\mathbf{u}_k$ is a point close to $\mathbf{u}_n$ and $\mathbf{K}_k$ is the tangent stiffness matrix evaluated at point $\mathbf{u}_k$.

By substituting $\mathbf{F}$ in Eq. (10.10) and Eq. (10.13), we obtain the equation that advances to a new iteration for a non-linear problem as:

$$\mathbf{u}_{n+1} = \mathbf{u}_n + \beta\left(\mathbf{u}_n - \mathbf{u}_{n-1}\right) + \alpha\mathbf{b} - \alpha\mathbf{A}\mathbf{u}_n, \tag{10.14}$$

with

$$\mathbf{b} = \mathbf{M}^{-1}\left(\mathbf{R} - \mathbf{F}\left(\mathbf{u}_k\right) + \mathbf{K}_k\mathbf{u}_k\right), \quad \mathbf{A} = \mathbf{M}^{-1}\mathbf{K}_k. \tag{10.15}$$

It is worth noting that, even if Eq. (10.14) has the same form as in the linear case, the point $\mathbf{u}_k$ in Eq. (10.15) is not fixed during the iteration process (as it must be close to $\mathbf{u}_n$ in order for the Taylor series expansion to be accurate) and therefore the tangent stiffness matrix (and matrix $\mathbf{A}$) changes.

The error after the n_{th} iteration is defined as:

$$\mathbf{e}_n = \mathbf{u}_n - \mathbf{u}^{\star}, \tag{10.16}$$

where $\mathbf{u}^*$ is the solution. Substituting Eq. (10.16) in Eq. (10.14) gives the error equation (valid only close to the solution):

$$\mathbf{e}_{n+1} = \mathbf{e}_n - \alpha\mathbf{A}\mathbf{e}_n + \beta\left(\mathbf{e}_n - \mathbf{e}_{n-1}\right). \tag{10.17}$$

By assuming that

$$\mathbf{e}_{n+1} = \mathbf{K}\cdot\mathbf{e}_n, \tag{10.18}$$

the following relation is obtained for computing the eigenvalues κ of matrix $\boldsymbol{\kappa}$:

$$\kappa^2 - (1 + \beta - \alpha A)\,\kappa + \beta = 0, \tag{10.19}$$

where A denotes any eigenvalue of matrix $\mathbf{A}$.

The fastest convergence is obtained for the smallest possible spectral radius $\rho = |\boldsymbol{\kappa}|$. The optimum convergence condition is obtained when:

$$\rho^* = \left|\kappa^*\right| = \beta^{1/2} \approx \left|1 - 2\sqrt{\frac{A_0}{A_{\mathrm{m}}}}\right|, \tag{10.20}$$

$$\Delta t \approx 2/\sqrt{A_{\mathrm{m}}} = 2/\omega_{\max}, \tag{10.21}$$

$$c \approx 2\sqrt{A_0} = 2\omega_0, \tag{10.22}$$

where A_0 and A_m are the minimum and maximum eigenvalues of matrix $\mathbf{A}$ and therefore ω_0 and ω_max are the lowest and highest circular frequencies of the undamped equation of motion [39].

The effect of eigenvalue estimation accuracy on the convergence of the method is presented in Joldes et al. [40]. To ensure convergence, it is critical that the maximum eigenvalue A_m is overestimated, even if this will lead to a decreased convergence speed. If, at the same time, the minimum eigenvalue A_0 is underestimated, uniform convergence will be obtained for all eigenvalues, with a further decrease in the convergence speed. If A_0 is overestimated, then it is possible to increase the convergence speed for all eigenvalues except a very narrow range of small eigenvalues.

10.4.1.1 Dynamic Relaxation Algorithm: Maximum Eigenvalue A_m and Mass Matrix

Using Gershgorin's theorem [25, 41], it has been demonstrated that the maximum eigenvalue of an assembled finite element mesh is bounded by the maximum eigenvalue of any of the elements in the mesh [4]:

$$A_\mathrm{m} \leq \max_e \left(\lambda^e_\mathrm{max}\right). \tag{10.23}$$

Therefore, an estimation of the maximum eigenvalue can be obtained by estimating the maximum eigenvalue of each element in the mesh. Such estimations for different element types are presented in Hughes [26].

In the case of a non-linear problem, the maximum eigenvalue changes during the simulation as the geometry of the elements changes, and therefore it must be estimated after every iteration step.

Because the mass matrix has no influence on the steady state (as the time derivatives in Eq. 10.9 become zero), a fictitious mass matrix that improves the convergence rate can be used. The mass matrix can be chosen such that it reduces the condition number of matrix $\mathbf{A}$, leading to a decrease in the spectral radius ρ (see Eq. 10.20).

In order to reduce the condition number, we propose to align the maximum eigenvalue of all elements in the mesh to the same value by changing the density of each element. By doing this we can still use Eq. (10.23) for estimating the maximum eigenvalue, and the condition number is at least preserved and generally decreased, as shown in Underwood [39]. This process guarantees that the selected maximum eigenvalue A_m is an overestimation of the actual maximum eigenvalue during the simulation, therefore ensuring the convergence.

10.4.1.2 Dynamic Relaxation Algorithm: Estimation of the Minimum Eigenvalue A0

Estimating the minimum eigenvalue is a challenging task, especially for non-linear problems, where an adaptive procedure should be used in order to obtain the optimum convergence parameters. An overview of the procedures proposed by different authors in the context of DR (including an adaptive one) is presented in Underwood [39].

The adaptive method proposed in Underwood [39] is based on Rayleigh's quotient and the use of a local diagonal stiffness matrix. The elements of this matrix are computed using finite differences, which can be very difficult to do for degrees of freedom which have small displacement variation.

In this section we propose a new adaptive method for computing the minimum eigenvalue, which is also based on Rayleigh's quotient, but does not have the shortcomings of the method proposed in [39].

We consider a change of variable:

$$\mathbf{z}_n = \mathbf{u}_n - \mathbf{u}_k, \tag{10.24}$$

where $\mathbf{u}_k$ is the point used for linearisation of the nodal forces in Eq. (10.13). The linearised nodal forces can therefore be expressed as:

$$\mathbf{F}(\mathbf{u}_n) = \mathbf{F}(\mathbf{u}_k) + \mathbf{K}_k \cdot \mathbf{z}_n, \tag{10.25}$$

and the linearised equation of motion will become, by replacing Eq. (10.24) and Eq. (10.25) in Eq. (10.1):

$$\mathbf{M} \cdot \ddot{\mathbf{z}} + \mathbf{K}_k \cdot \mathbf{z} = \mathbf{R} - \mathbf{F}(\mathbf{u}_k). \tag{10.26}$$

We can now rely on Eq. (10.26) to estimate A_0 using Rayleigh's quotient and the current value of the displacements:

$$A_0 \leq \frac{(\mathbf{z}_n)^T \mathbf{K}_k \mathbf{z}_n}{(\mathbf{z}_n)^T \mathbf{M} \mathbf{z}_n}. \tag{10.27}$$

We consider the right hand side of Eq. (10.27) as an estimate of the minimum eigenvalue. Using Eq. (10.24) and Eq. (10.25), this estimate becomes [42]:

$$A_0 \approx \frac{(\mathbf{u}_n - \mathbf{u}_k)^T (\mathbf{F}(\mathbf{u}_n) - \mathbf{F}(\mathbf{u}_k))}{(\mathbf{u}_n - \mathbf{u}_k)^T \mathbf{M} (\mathbf{u}_n - \mathbf{u}_k)}, \tag{10.28}$$

where $\mathbf{u}_k$ is a fix point that must be close to $\mathbf{u}_n$. We will choose the solution from a previous iteration as $\mathbf{u}_k$, and this point will be updated after a number of steps in order to keep it close to the current solution $\mathbf{u}_n$. No additional information (such

as estimates of the stiffness matrix) is required and only vector operations are performed (as **M** is a diagonal lumped mass matrix).

During the iterative Dynamic Relaxation (DR) procedure, the high frequencies are damped out, and the system will eventually oscillate at its lowest frequency. Therefore, Eq. (10.28) will converge towards the minimum eigenvalue. This estimation process, combined with our parameter selection process, leads to an increased convergence rate, because it always offers an overestimation of the minimum eigenvalue. The higher the overestimation of the minimum eigenvalue, the higher the reduction of the high-frequency vibrations (see [40, 42]), and therefore Eq. (10.28) will convergence faster towards the real minimum eigenvalue.

10.4.1.3 Dynamic Relaxation Algorithm: Termination Criteria

One very important aspect of any finite element (FE) algorithm is the termination criterion used. If the criterion is too coarse, then the solution might be too inaccurate, and if the criterion is too tight, then time is lost for unnecessary computations.

The usual criteria used by FE software are based on residual forces, displacements or energy. None of these criteria gives any information about the absolute error in the solution, and selecting any of these termination criteria is very difficult.

We propose a new termination criterion that gives information about the absolute error in the solution, particularly suited for our solution method. Because DR iterations lead to a strong reduction of the high frequencies, the displacement vector will oscillate around the solution vector with a frequency that converges towards the smallest oscillation frequency. That implies that the error vector **e** will converge towards the eigenvector corresponding to the lowest eigenvalue. Therefore, we can make the following approximation:

$$\mathbf{A} \cdot \mathbf{e}_n = A_0 \cdot \mathbf{e}_n, \tag{10.29}$$

By substituting Eq. (10.29) in Eq. (10.17), and considering relations given in Eq. (10.19) and Eq. (10.20), we obtain:

$$\mathbf{u}_{n+1} - \mathbf{u}^\star \approx \rho \left(\mathbf{u}_n - \mathbf{u}^\star \right), \tag{10.30}$$

where **u*** is the solution.

Therefore, after each iteration step, the error is reduced by a ratio equal to ρ. We can now obtain an approximation of the absolute error in the solution by applying the infinity norm to Eq. (10.30):

$$\left\| \mathbf{u}_{n+1} - \mathbf{u}^* \right\|_\infty \approx \rho \cdot \left\| \mathbf{u}_n - \mathbf{u}^* \right\|_\infty \leq \rho \cdot \left(\left\| \mathbf{u}_{n+1} - \mathbf{u}^* \right\|_\infty + \left\| \mathbf{u}_{n+1} - \mathbf{u}_n \right\|_\infty \right), \tag{10.31}$$

$$\left\| \mathbf{u}_{n+1} - \mathbf{u}^* \right\|_\infty \leq \frac{\rho}{1-\rho} \cdot \left\| \mathbf{u}_{n+1} - \mathbf{u}_n \right\|_\infty. \tag{10.32}$$

Therefore, the convergence criterion can be defined as:

$$\frac{\rho}{1-\rho} \cdot \|\mathbf{u}_{n+1} - \mathbf{u}_n\|_\infty \leq \varepsilon, \tag{10.33}$$

where ε is the imposed absolute accuracy. This convergence criterion gives an approximation of the absolute error based on the displacement variation norm from the current iteration.

Because our parameter estimation procedures overestimate the maximum eigenvalue A_{m} and underestimate the minimum eigenvalue A_0, the value of the computed spectral radius ρ_{c} we can use in Eq. (10.33) is lower than the real value of the spectral radius (see Eq. 10.20). This can lead to an early termination of the iteration process. Therefore, in Eq. (10.33) we use a corrected value of the computed spectral radius:

$$\rho_\infty = \rho_c + \varsigma \cdot (1 - \rho_c)\,, \tag{10.34}$$

where ζ is a correction parameter with values between 0 and 1, defining the maximum underestimation error for the spectral radius ρ. In our simulations we use $\zeta = 0.2$.

10.5 Element Formulation for Finite Element Algorithms for Surgery Simulation and Neurosurgery Modelling

10.5.1 Volumetric Locking

As stated in Chap. 6, due to stringent computation time requirements, the finite element meshes for models applied in surgery simulation and image registration must be constructed using low-order elements that are computationally inexpensive. Mixed meshes consisting of tetrahedral and hexahedral element are most convenient from the perspective of automation of simulation process. However, the standard formulation of the tetrahedral element exhibits volumetric locking, especially in case of soft tissues such as the brain, which are modelled as almost incompressible materials [43–49]. There is a number of improved linear tetrahedral elements already proposed by different authors [50–53]. The Averaged Nodal Pressure (ANP) tetrahedral element proposed by Bonet and Burton in [50] is computationally inexpensive and provides much better results for nearly incompressible materials than the standard tetrahedral element. Nevertheless, one problem with the ANP element and its implementation in a finite element code is the handling of interfaces between different materials. In Joldes et al. [54], we extended the formulation of the ANP element so that all elements in a mesh are treated in a similar way, requiring no special handling of the interface elements.

10.5.2 Stability of Under-integrated Hexahedral Elements: Hourglassing

As stated in Chap. 6, low-order hexahedral elements with one Gauss point (also referred to as linear under-integrated hexahedral elements) are the preferred choice for explicit dynamics-type algorithms from the perspective of computational efficiency. However, such elements exhibit unphysical zero energy deformation modes (hourglass). The hourglass modes can be controlled by calculating hourglass forces that oppose the hourglass deformation modes. We have shown in Joldes et al. [55] that the hourglass control forces for each element can be computed (in matrix form) as:

$$ {}^{t}_{0}\mathbf{F}^{Hg} = k \cdot {}_{0}\mathbf{Y} \cdot {}_{0}\mathbf{Y}^{T} \cdot {}^{t}_{0}\mathbf{u}, \tag{10.35} $$

where k is a constant that depends on the element geometry and material properties, ${}_{0}\mathbf{Y}$ is the matrix of hourglass shape vectors and $\mathbf{u}$ is the matrix of current displacements. As we use Total Lagrangian (TL) formulation, all quantities except $\mathbf{u}$ in Eq. (10.35) are constant and can be precomputed. This makes the hourglass control mechanism very efficient.

10.6 Modelling of the Brain-Skull Interactions for Image-Guided Neurosurgery: Efficient Finite Sliding Contact Algorithm

Modelling of interactions between continua (e.g. soft organs) undergoing deformations is a challenging task. To facilitate such modelling, many sophisticated contact algorithms have been proposed in the literature (e.g. [56–59].) and implemented in commercial finite element codes such as ABAQUS [8, 60] and LS-DYNA [5]. Application of such algorithms tends to consume significant computing resources, which substantially increases the solution time.

When computing the brain deformation for neuroimage registration, we are interested in the interactions between the brain and rigid skull that provide constraints for the brain tissue deformation and brain rigid body motion. Accurate modelling of such interactions can be done using a very efficient algorithm that treats these interactions as a finite sliding, frictionless contact between a deformable object (the brain) and a rigid surface (the skull) [61]. The main parts of such contact algorithm (for detailed description see [61]) are detection of nodes on the brain surface (also called the slave surface) which have penetrated the skull surface (master surface) and the repositioning of each slave node that has penetrated the master surface to the closest point on the master surface.

Efficient penetration detection algorithm can be formulated based on the closest master node (nearest neighbour) approach [5]. As the surfaces of the anatomical

structures of the segmented neuroimages are typically discretised using triangles, the skull surface can be treated as a triangular mesh. We refer to each triangle surface as a 'face', to the vertices, 'nodes', and to the triangle sides – 'edges'. Using this terminology, the basic brain–skull contact algorithm is described as follows:

– For each slave node P:

- Find the closest master node C (global search).
- Check the faces and edges surrounding C for penetration (local search).
- Check additional faces and edges that might be penetrated by P (identified in the master surface analysis stage – because the master surface is rigid, this analysis can be done pre-operatively).

Following [56, 59], further improvement of efficiency of the penetration detection algorithm and computation speed is done by implementing bucket sort in the global search phase.

10.7 Real-Time Computations Without Supercomputers: Increasing Computation Speed Through Algorithm Implementation on Graphics Processing Unit (GPU)

The algorithms for surgery simulation and image-guided surgery discussed in this Chapter facilitate efficient and robust computations. For instance, they make it possible to compute deformation field within the brain for image registration problem in under 40 s on a standard personal computer for non-linear finite element models consisting of around 30,000 elements. However, predicting the time history of force between the soft tissue and surgical tool at frequency of 500 Hz required for haptic feedback poses a challenge even for very efficient non-linear algorithms deployed on a personal computer.

For hardware-based increase of computation speed, we advocate the implementation of the algorithms on graphics processing units (GPUs) by using a GPU as a coprocessor for the computer central processing unit (CPU) for executing sections of the code that can run in parallel. GPUs have a highly parallel, multithreaded, multicore processor architecture, and its cost (under US$ 3000 for most general purpose GPUs) is orders of magnitude smaller than that of a supercomputer with a comparable number of parallel threads. GPU architecture is well suited for problems that can be expressed as data-parallel computations with high arithmetic intensity, where the same programme is executed on many data elements in parallel.

Before the introduction of NVIDIA's Compute Unified Device Architecture (CUDA) [62] and Open Computing Language (OpenCL) [63], general-purpose computations on GPUs were done by recasting the computations in graphic terms and using the graphics pipeline. Therefore, a scientific or general-purpose computation often required a concerted effort by experts in both computer graphics and in the particular scientific or engineering domain. With the introduction of

CUDA, in November 2006, NVIDIA proposed a new parallel programming model and instruction set for their GPUs that can be used for performing general-purpose computations. CUDA comes with a software environment that allows developers to use C as a high-level programming language. A minimum set of keywords are used to extent the C language in order to identify the code that must be run on the GPU as parallel threads, identify each thread (and the block of threads it belongs to) and to organise and transfer the data in the different GPU memory spaces. CUDA also exposes the internal architecture of the GPU and allows direct access to its internal resources facilitating the development of application software that transparently scales with the number of processor cores in the GPU. The programmer has more control over the internal hardware resources of the GPU, but this comes at the expense of an increased programming effort compared to a CPU implementation.

Because it only uses vectors, an explicit time stepping algorithm is perfectly suited for parallel implementation on GPU. We implemented the Dynamic Relaxation algorithm presented in Sect. 10.4 *Algorithms for Neurosurgery Modelling* on GPU using CUDA. We transferred all the computationally intensive parts of the algorithm (element force computation, displacement vector computation, contact handling, parallel reduction – including infinity norm computation and scalar product of vectors) to the GPU, to take advantage of its massive parallelism. The code was run on a NVIDIA Tesla C870 computing board, which has 16 multiprocessors with 8 scalar processor cores each (i.e. 128 cores in total) and single-precision floating-point operations. A detailed description of the implementation can be found in Joldes et al. [64]. The GPU implementation performs 2000 iterations of the brain shift simulation in 1.8 s, offering real-time computation capabilities. Other examples of GPU implementation of finite element algorithms of computational biomechanics that utilise TLED include widely used Simulation Open Framework Architecture (SOFA) [65, 66].

10.8 Verification of Finite Element Algorithms of Computational Biomechanics

The general guidelines for verification in computational solid mechanics have been proposed by the American Society of Mechanical Engineers (ASME) in [67]. These guidelines were preceded by the extensive discussion of the concepts of verification and validation in computational mechanics by Babuska and Oden [68]. They underscore the importance of establishing confidence through collection of evidence that the solution algorithms are working correctly. As for non-linear problems of computational solid mechanics analytical solutions typically do not exist, we advocate collecting such evidence by comparing the results obtained by means of new algorithms with the solutions from established algorithms such as those implemented in commercial finite element codes.

In the following sections, we will present verification results for some of the algorithm described in this chapter: hourglass control, volumetric locking, Dynamic Relaxation and brain-skull interaction (contact).

10.8.1 Hourglass Control

The verification experiment was artificially designed to compound difficulties associated with hourglass control: large deformations, bending and rigid body motions. A column having a height of 1 m and a square section with the side size 0.1 m was meshed using hexahedral elements (Fig. 10.4a). The mesh has 496 nodes and 270 elements. A neo-Hookean almost incompressible material model was used, having the mechanical properties similar to those of the brain (mass density of 1000 kg/m^3, Young's modulus in un-deformed state equal to 3000 Pa and Poisson's ratio 0.49).

The deformation was imposed by constraining the lower face and displacing the upper face of the column, with maximum displacements of 0.5 m in the x direction and 0.3 m in the z direction.

The deformed shape obtained using the TLED algorithm is presented in Fig. 10.4b for the under-integrated hexahedral elements with no hourglass control. The influence of the presented hourglass control mechanism can be clearly seen in Fig. 10.4c.

The displacements of a line of nodes from the side of the column (in the plane $y = 0$) are presented in Fig. 10.5. These displacements are compared with the results obtained using the commercial finite element software ABAQUS (fully integrated linear hexahedral elements with hybrid displacement-pressure formulation).

The displacement maximum relative error, defined as the ratio between the maximum displacement difference and the imposed displacement, was 1.4% in case

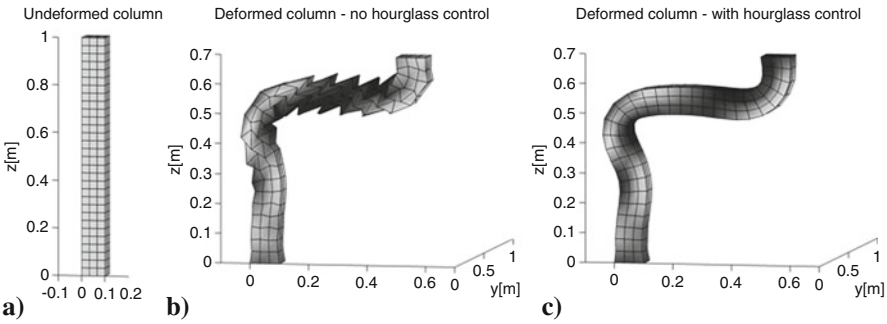

Fig. 10.4 Verification of hourglass control algorithm using deformation of a column as an example. (**a**) Undeformed shape; (**b**) deformed shape with no hourglass control (**b**); and (**c**) deformed shape with successful hourglass control. (Adapted from Joldes et al. [55])

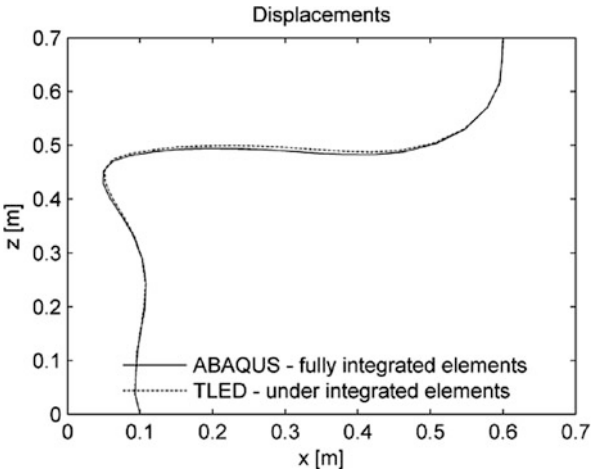

Fig. 10.5 Deformation of a column – middle line displacements – comparison with results from the commercial finite element software ABAQUS (fully integrated linear hexahedral elements with hybrid displacement-pressure formulation). (Copied from Joldes et al. [55])

Table 10.1 Material properties

Property	Material 1	Material 2
Young's modulus E [Pa]	3000	30,000
Poisson's ratio ν	0.49	0.48
Density ρ [kg/m^3]	1000	1000

of column deformation. This demonstrates the good accuracy of the elements using the proposed hourglass control mechanism.

10.8.2 Volumetric Locking

Because the only difference between our Improved Averaged Nodal Pressure (IANP) element and the standard Averaged Nodal Pressure (ANP) element consists in the way interfaces between different materials are handled, we designed a simulation experiment that highlights these differences. We considered a cylinder with a diameter of 0.1 m and a height of 0.2 m made out of alternating sections with two different material properties, as shown in Table 10.1. We used a neo-Hookean constitutive model for both materials.

Half of the nodes on the upper face of the cylinder were displaced in order to create a complex deformation field at different material interfaces (Fig. 10.6a).

Using the cylindrical geometry, we created a hexahedral mesh (13,161 nodes and 12,000 elements) and a tetrahedral mesh (11,153 nodes and 60,030 elements). The behaviour of the following elements was compared:

1. Fully integrated linear hexahedra, with selectively reduced integration of the volumetric term (Hexa), which should offer a benchmark solution.
2. Standard Averaged Nodal Pressure elements (ANP).

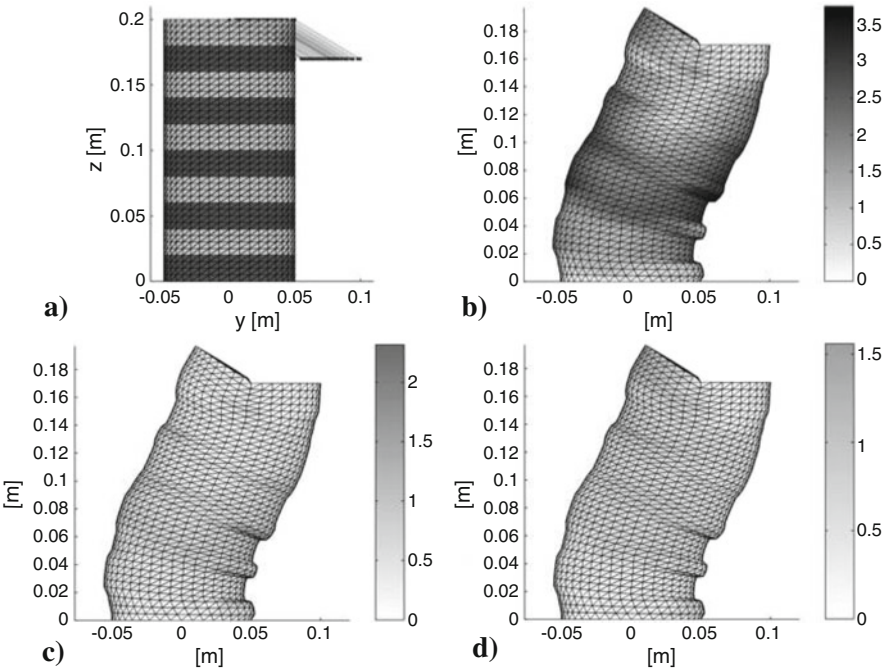

Fig. 10.6 Deformation of a cylinder made out of sections with different material properties. (**a**) The undeformed configuration and the nodal displacements applied. The colour bars show the difference in positions of the surface nodes, in mm, between the models using hexahedral elements and models using (**b**) locking tetrahedral elements (**c**) ANP elements and (**d**) IANP elements. (Adapted from Joldes et al. [38])

3. Our Improved Averaged Nodal Pressure elements (IANP).
4. Linear standard tetrahedron (Tetra).

All the computations were done using the TLED algorithm. Based on the displacement differences presented in Fig. 10.6, we note that the usage of standard locking tetrahedral elements can lead to errors of up to 3.8 mm in the deformation field. The use of ANP elements reduces the maximum error to 2.3 mm, while the use of IANP elements leads to a maximum error of 1.5 mm (all errors are considered relative to the results of the model that uses Hexa elements).

The reaction forces computed on the displaced face are presented in Fig. 10.7. The results obtained using the IANP elements are the closest to the benchmark results given by the Hexa elements. Therefore, the IANP elements offer the best performances both in terms of displacements and reaction forces, while the standard four-noded tetrahedral element offers the worst performance, as expected.

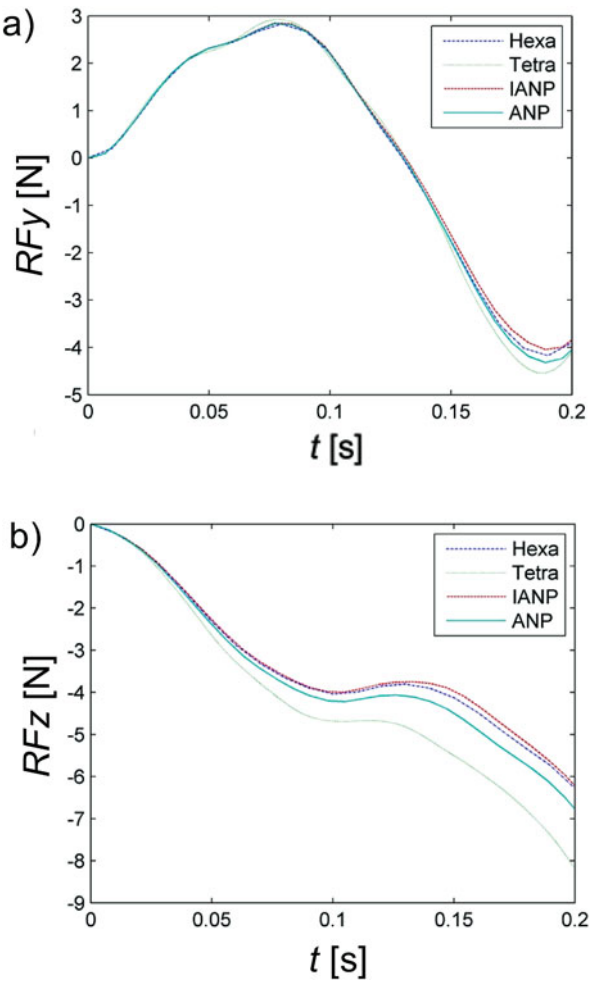

Fig. 10.7 Results obtained using the cylinder model shown in Fig. 10.6: reaction forces on the displaced face (**a**) in the y direction (**b**) in the z direction. (Adapted from Joldes et al. [38])

10.8.3 Dynamic Relaxation: Steady State Computation

We use this verification example to demonstrate the accuracy of our steady state computation method. For an ellipsoid having approximately the size of the brain, we fixed a set of nodes (at the bottom) and displaced another set of nodes (at the top) in order to obtain a deformation field similar to what happens in brain shift. The mesh was created using hexahedral elements and has 2200 elements and 2535 nodes. We used an almost incompressible neo-Hookean material model and a large displacement value (2 cm).

We performed the displacement computation first by using our algorithm and second by using ABAQUS finite element code [8, 60]. For computational efficiency we use under-integrated hexahedral elements with the hourglass control implemented based on the relations presented in [69]. In ABAQUS, we used hybrid displacement-pressure hexahedral elements, which are the 'gold standard' for almost incompressible materials. We used the non-linear static solver from ABAQUS with the default configuration and assumed that the simulation using this solver provides the accurate results.

The error distribution (absolute difference in nodal position between the two simulations) is presented in Fig. 10.8. The maximum error magnitude of 0.6 mm is obtained at the edge of the displaced area, and it is mainly an artefact of using under-integrated elements. Nevertheless, the average error is 0.025 mm which demonstrates that our simulation results are more than acceptable (as the error is much smaller than the accuracy of image-guided neurosurgery and resolution of neuroimages).

Analysis of the convergence behaviour of adaptive Dynamic Relaxation algorithm when computing deformations of the ellipsoid shown in Fig. 10.8 confirms that the spectral radius determined using the adaptive procedure described in Eqs. (10.24) to (10.28) leads to increased convergence towards the steady state solution (Fig. 10.9) [42]. This ensures a shorter computation time.

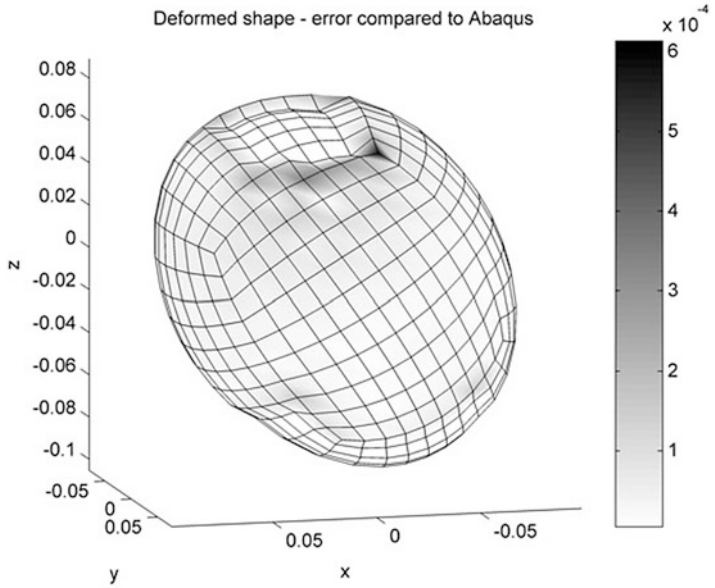

Fig. 10.8 Modelling of indentation of an ellipsoid with the constitutive properties similar to the brain tissue. The figure shows absolute difference (greyscale coded) in nodal positions between our algorithm and ABAQUS. Dimensions are in metres. (Copied from Joldes et al. [40])

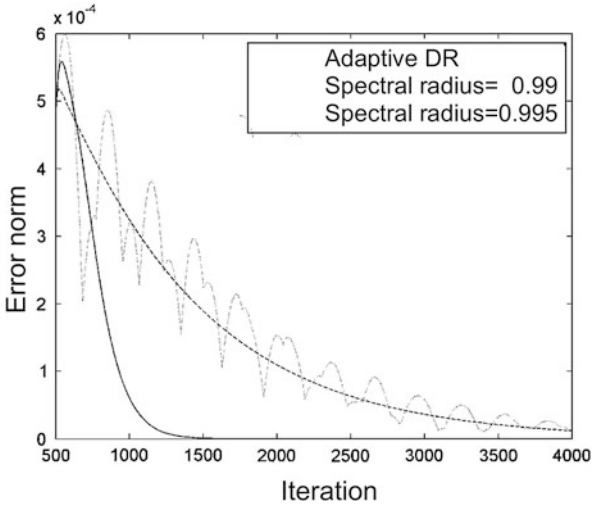

Fig. 10.9 Convergence behaviour of the adaptive Dynamic Relaxation (DR) algorithm [42] when modelling indentation of the ellipsoid with the constitutive properties similar to the brain tissue (the ellipsoid is shown in Fig. 10.8). The adaptive parameter estimation facilitates faster convergence towards steady state solution than for the Dynamic Relaxation with fixed parameters [40]. Note also the oscillations (underdamped solution) caused by selecting too large spectral radius of 0.995 due to underestimation of the minimum eigenvalue in Eq. 10.20. (Adapted from Joldes et al. [42])

10.8.4 Brain-Skull Interface: Contact Algorithm

In order to assess the performance of our brain-skull interface algorithm, we performed simulations using our implementation of the contact algorithm (combined with Dynamic Relaxation as a solution method) and the commercial explicit dynamics finite element solver LS-DYNA [5] and compared the results. The same loading conditions and material models were used for both solvers. The loading consisted of displacements applied to the nodes in the craniotomy area using a smooth loading curve — a 3-4-5 polynomial that ensures zero velocity and acceleration at the start and end of loading [70]. Neo-Hookean constitutive models were used for the brain and tumour tissues, and a linear elastic model was used for the ventricles. In order to obtain the steady state solution, the oscillations were damped using both mass and stiffness proportional damping in LS-DYNA.

In a first simulation experiment, we displaced an ellipsoid (made of a hyperelastic neo-Hookean material) with the approximate size of a brain inside another ellipsoid simulating the skull. The maximum displacement applied was 40 mm. The average difference in the nodal displacement field between our simulation and the LS-DYNA simulation was less than 0.12 mm (Fig. 10.10a).

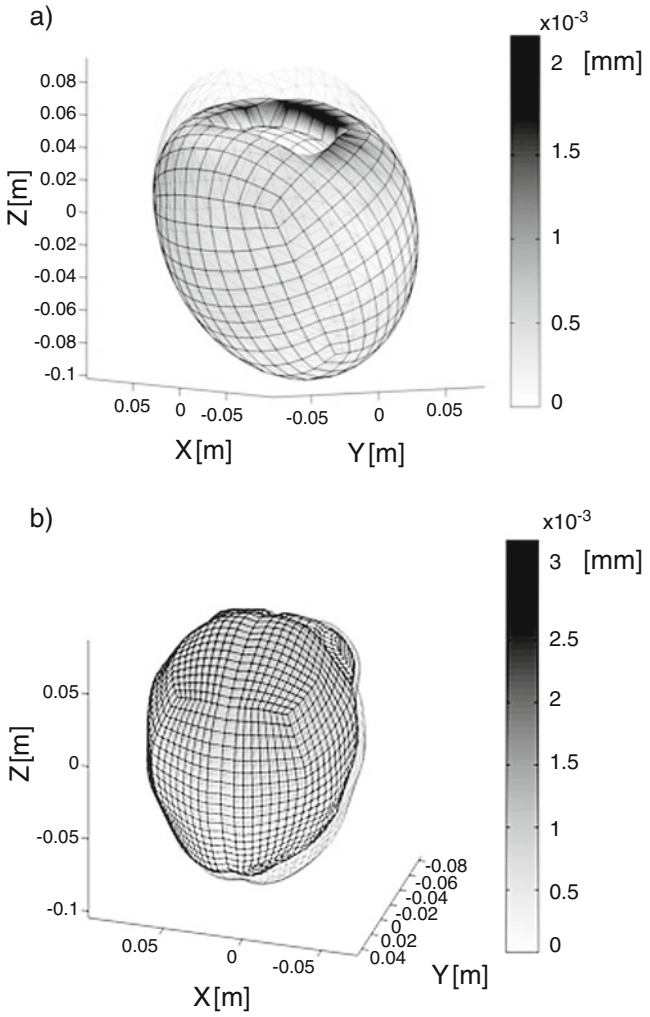

Fig. 10.10 Displacement differences (in millimetres) between our results, and LS-DYNA simulations are presented using colour codes. The transparent mesh is the master contact. (**a**) Indentation of an ellipsoid (the ellipsoid model is shown in Fig. 10.8); (**b**) brain model (computation of the brain deformations due to craniotomy induced brain shift). (Adapted from Joldes et al. [61])

In the second simulation experiment, we performed the registration of a patient-specific brain shift. The LS-DYNA simulations for this case have been done previously, and the results were found to agree well with the real deformations [71]. We performed the same simulations using Dynamic Relaxation and our contact algorithm. The average difference in the nodal displacement field was less than 0.2 mm (Fig. 10.10b).

10.9 Conclusions

Modelling of the brain for injury simulation and computer-assisted neurosurgery is a non-linear problem of continuum mechanics and involves large deformations, very large strains (over 0.8 in compression during needle insertion [21]), non-linear material models, complex loading and boundary conditions and complex geometry. Various finite element (FE) algorithms have been applied for solving this problem.

Modelling of the brain for injury simulation has been often conducted with the goal of using numerical surrogates of the human head in design of countermeasures for traumatic brain injury mitigation. Such modelling has been almost exclusively conducted using non-linear explicit dynamics (i.e. utilising explicit time stepping, referred to in the literature also as explicit time integration [3, 4]) finite element algorithms implemented in commercial finite element codes that are routinely used in the automotive industry for transient dynamics problems involving rapid (impact-type) loading such as car structure responses during collision and sheet metal forming.

However, the computational efficiency of the algorithms available in commercial finite element codes is insufficient for computer-integrated neurosurgery where the solution needs to be provided within the real-time constraints of neurosurgery. This led to development of the specialised non-linear finite element algorithms aiming at satisfying these constraints. We advocate application of non-linear finite element algorithms utilising explicit time stepping (and therefore requiring no iteration for non-linear problems) and Total Lagrangian incremental formulation of continuum mechanics (as it allows precomputing of the derivatives with respect to the spatial coordinates):

- Total Lagrangian Explicit Dynamics (TLED) finite element algorithm for time accurate solution for surgery simulation.
- Dynamic Relaxation (DR) Total Lagrangian algorithm for computing steady state deformations for neurosurgery modelling.

For hardware-based increase of computation speed, we propose the implementation of these algorithms on graphics processing units (GPUs) by using a GPU as a coprocessor for the computer central processing unit (CPU). It has been shown in Joldes et al. [64] that the implementation of the finite element Dynamic Relaxation algorithm on NVIDIA Tesla C870 GPU performs 2000 iterations of the brain shift simulation in under 2 s, offering real-time computation capabilities at a fraction of a traditional supercomputer or PC cluster cost. It can be expected that for newer generation of GPUs, this already excellent performance would appreciably improve due to significant increase in the number of streaming processor cores (e.g. NVIDIA Tesla C870 GPU had 128 cores while NVIDIA Quadro GV100 GPU released in June 2017 has 5120 cores [62, 72]) and available memory (with 32 GB memory for NVIDIA Quadro GV100) [62, 72]).

Application of even most efficient finite element algorithms in surgery simulation and neurosurgery modelling is limited by time-consuming generation of patient-

specific finite element meshes [73] and deterioration of the solution accuracy when the elements undergo distortion induced by large deformations. As a solution for overcoming these limitations, we advocate meshless algorithms in which the computational grid has the form of a 'cloud' of points [74–78]. Such algorithms are discussed in Chap. 11.

Acknowledgements This chapter uses the published results of research supported by the funding from the Australian Government through the Australian Research Council (ARC) (grants DP0343112, DP0664534, DP1092893, and LX0560460), National Health and Medical Research Council (NHMRC) (project grants no. APP1006031 and APP1144519) and National Institutes of Health (NIH) (grant 1-R03-CA126466-01A1). We also acknowledge funding from the Australian Government through the Australian Research Council (Discovery Project grant DP160100714).

We thank our collaborators Dr. Ron Kikinis and Dr. Simon K. Warfield of Harvard Medical School (Boston, MA, USA) and Dr. Kiyoyuki Chinzei and Dr. Toshikatsu Washio of Surgical Assist Technology Group of AIST (Tsukuba, Japan) for help in various aspects of this work.

References

1. Fressmann, D., Munz, T., Graf, O., Schweizerhof, K.: FE human modelling in crash — aspects of the numerical modelling and current applications in the automotive industry. In: DYNAmore GmbH, Frankthenhal, pp. F-I-23 – F-I-34 (2007)
2. Takhounts, E.G., Eppinger, R.H., Campbell, J.Q., Tannous, R.E., Power, E.D., Shook, L.S.: On the development of the SIMon finite element head model. Stapp Car Crash J. **47**, 107–133 (2003)
3. Belytschko, T., Liu, W.K., Moran, B.: Nonlinear Finite Elements for Continua and Structures. Wiley, Chichester (2006)
4. Bathe, K.-J.: Finite Element Procedures. Prentice-Hall, Upper Saddle River, NJ, USA (1996)
5. Livermore Software Technology Coporation LSTC: LS-DYNA Theory Manual, http://www.lstc.com/download/manuals (2018)
6. Pacific Engineering Systems International (ESI): PAM-SAFE http://www.esi.com.au/Software/PAM-SAFE.html (2018)
7. Altair: RADIOSS Technical Papers, https://altairhyperworks.com/ResourceLibrary.aspx? category=Technical%20Papers&altair_products=RADIOSS (2018)
8. Dassault Systèmes Simulia Corporation: SIMULIA User Assistance 2018: ABAQUS (2018)
9. Baumann, R., Glauser, D., Tappy, D., Baur, C., Clavel, R.: Force feedback for virtual reality based minimally invasive surgery simulator. Stud. Health Technol. Inform. **29**, 564–579 (1996)
10. Cover, S.A., Ezquerra, N.F., O'Brien, J.F., Rowe, R., Gadacz, T., Palm, E.: Interactively deformable models for surgery simulation. Computer Graphics and Applications, IEEE. **13**, 68–75 (1993)
11. Kuhnapfel, U., Çakmak, H.K., Maaß, H.: Endoscopic surgery training using virtual reality and deformable tissue simulation. Comput. Graph. **24**, 671–682 (2000)
12. Nimura, Y., Di Qu, J., Hayashi, Y., Oda, M., Kitasaka, T., Hashizume, M., Misawa, K., Mori, K.: Pneumoperitoneum simulation based on mass-spring-damper models for laparoscopic surgical planning. J. Med. Imag. **2**, 044004 (2015)
13. Cotin, S., Delingette, H., Ayache, N.: A hybrid elastic model for real-time cutting, deformations, and force feedback for surgery training and simulation. Vis. Comput. **16**, 437–452 (2000)
14. Bro-Nielsen, M.: Finite element modeling in surgery simulation. Proc. IEEE. **86**, 490–503 (1998)

15. Bro-Nielsen, M., Cotin, S.: Real-time volumetric deformable models for surgery simulation using finite elements and condensation. Comput. Graphics Forum. **15**, 57–66 (1996)
16. DiMaio, S.P., Salcudean, S.E.: Interactive simulation of needle insertion models. IEEE Trans. Biomed. Eng. **52**, 1167–1179 (2005)
17. Warfield, S.K., Talos, F., Tei, A., Bharatha, A., Nabavi, A., Ferrant, M., Black, P.M., Jolesz, F.A., Kikinis, R.: Real-time registration of volumetric brain MRI by biomechanical simulation of deformation during image guided neurosurgery. Comput. Vis. Sci. **5**, 3–11 (2002)
18. Dumpuri, P., Thompson, R.C., Cao, A., Ding, S., Garg, I., Dawant, B.M., Miga, M.I.: A fast and efficient method to compensate for brain shift for tumor resection therapies measured between pre-operative and post-operative tomograms. I.E.E.E. Trans. Biomed. Eng. **57**, 1285–1296 (2010)
19. Dumpuri, P., Thompson, R.C., Dawant, B.M., Cao, A., Miga, M.I.: An atlas-based method to compensate for brain shift: preliminary results. Med. Image Anal. **11**, 128–145 (2007)
20. Roberts, D.W., Hartov, A., Kennedy, F.E., Miga, M.I., Paulsen, K.D.: Intraoperative brain shift and deformation: a quantitative analysis of cortical displacement in 28 cases. Neurosurgery. **43**, 749–758 (1998)
21. Wittek, A., Dutta-Roy, T., Taylor, Z., Horton, A., Washio, T., Chinzei, K., Miller, K.: Subject-specific non-linear biomechanical model of needle insertion into brain. Comput. Methods Biomech. Biomed. Engin. **11**, 135–146 (2008)
22. Wittek, A., Hawkins, T., Miller, K.: On the unimportance of constitutive models in computing brain deformation for image-guided surgery. Biomech. Model. Mechanobiol. **8**, 77–84 (2009)
23. Belytschko, T.: A survey of numerical methods and computer programs for dynamic structural analysis. Nucl. Eng. Des. **37**, 23–34 (1976)
24. Yang, K.H.: Basic Finite Element Method as Applied to Injury Biomechanics. Academic Press, Cambridge, MA, USA (2018)
25. Cook, R.D., Malkus, D.S., Plesha, M.E.: Finite elements in dynamics and vibrations. In: Concepts and Applications of Finite Element Analysis, pp. 367–428. Wiley, New York (1989)
26. Hughes, T.J.R.: Analysis of transient algorithms with particular reference to stability behavior. In: Belytschko, T., Hughes, T.J.R. (eds.) Computational Methods for Transient Analysis, vol. 1, pp. 67–155. North-Holland, Amsterdam (1983)
27. Belytschko, T.: An overview of semidiscretization and time integration procedures. In: Belytschko, T., Hughes, T.J.R. (eds.) Computational Methods for Transient Analysis, vol. 1, pp. 1–66. North-Holland, Amsterdam (1983)
28. Olovsson, L., Simonsson, K., Unosson, M.: Selective mass scaling for explicit finite element analyses. Int. J. Numer. Methods Eng. **63**, 1436–1445 (2005)
29. Pan, F., Zhu, J., Helminen, A.O., Vatanparast, F.: Three point bending analysis of a mobile phone using LS-DYNA explicit integration method. In: Mindle, W.L. (ed.) 9th International LS-DYNA Users Conference. Livermore Software Technology Corporation, Dearborn, MI, USA (2006)
30. Majumder, S., Roychowdhury, A., Subrata, P.: Three-dimensional finite element simulation of pelvic fracture during side impact with pelvis-femur-soft tissue complex. Int. J. Crashworthiness. **13**, 313–329 (2008)
31. Cocchetti, G., Pagani, M., Perego, U.: Selective mass scaling and critical time-step estimate for explicit dynamics analyses with solid-shell elements. Comput. Struct. **127**, 39–52 (2013)
32. Flanagan, D.P., Belytschko, T.: A uniform strain hexahedron and quadrilateral with orthogonal hourglass control. Int. J. Numer. Methods Eng. **17**, 679–706 (1981)
33. Cifuentes, A.O., Kalbag, A.: A performance study of tetrahedral and hexahedral elements in 3-D finite element structural analysis. Finite Elem. Anal. Des. **12**, 313–318 (1992)
34. Cook, R.D., Malkus, D.S., Plesha, M.E.: Concepts and Applications of Finite Element Analysis. Wiley, New York (1989)
35. Hughes, T.J.R.: The Finite Element Method: Linear Static and Dynamic Finite Element Analysis. Dover Publications, Mineola (2000)
36. Rojek, J., Oñate, E., Postek, E.: Application of explicit FE codes to simulation of sheet and bulk metal forming processes. J. Mater. Process. Technol. **80-81**, 620–627 (1998)

37. Miller, K., Joldes, G., Lance, D., Wittek, A.: Total Lagrangian explicit dynamics finite element algorithm for computing soft tissue deformation. Commun. Numer. Methods Eng. **23**, 121–134 (2007)
38. Joldes, G.R., Wittek, A., Miller, K.: Non-locking tetrahedral finite element for surgical simulation. Commun. Numer. Methods Eng. **25**, 827–836 (2008)
39. Underwood, P.: Dynamic relaxation. In: Belytschko, T., Hughes, T.J.R. (eds.) Computational Methods for Transient Analysis, vol. 1, pp. 245–265. New-Holland, Amsterdam (1983)
40. Joldes, G.R., Wittek, A., Miller, K.: Computation of intra-operative brain shift using dynamic relaxation. Comput. Methods Appl. Mech. Eng. **198**, 3313–3320 (2009)
41. Isaacson, E.: Analysis of Numerical Methods. Wiley, New York (1966)
42. Joldes, G.R., Wittek, A., Miller, K.: An adaptive dynamic relaxation method for solving nonlinear finite element problems. Application to brain shift estimation. Int. J. Numer. Method. Biomed. Eng. **27**, 173–185 (2011)
43. Miller, K.: Biomechanics of the Brain for Computer Integrated Surgery. Publishing House of Warsaw University of Technology, Warsaw (2002)
44. Miller, K., Chinzei, K.: Mechanical properties of brain tissue in tension. J. Biomech. **35**, 483–490 (2002)
45. Miller, K., Chinzei, K., Orssengo, G., Bednarz, P.: Mechanical properties of brain tissue in-vivo: experiment and computer simulation. J. Biomech. **33**, 1369–1376 (2000)
46. Miller, K.: Constitutive modelling of abdominal organs. J. Biomech. **33**, 367–373 (2000)
47. Miller, K., Chinzei, K.: Constitutive modelling of brain tissue; Experiment and Theory. J. Biomech. **30**, 1115–1121 (1997)
48. Bilston, L.E., Liu, Z., Phan-Tien, N.: Linear viscoelastic properties of bovine brain tissue in shear. Biorheology. **34**, 377–385 (1997)
49. Margulies, S.S., Thibault, L.E., Gennarelli, T.A.: Physical model simulations of brain injury in the primate. J. Biomech. **23**, 823–836 (1990)
50. Bonet, J., Burton, A.J.: A simple averaged nodal pressure tetrahedral element for incompressible and nearly incompressible dynamic explicit applications. Commun. Numer. Methods Eng. **14**, 437–449 (1998)
51. Bonet, J., Marriott, H., Hassan, O.: An averaged nodal deformation gradient linear tetrahedral element for large strain explicit dynamic applications. Commun. Numer. Methods Eng. **17**, 551–561 (2001)
52. Zienkiewicz, O.C., Rojek, J., Taylor, R.L., Pastor, M.: Triangles and tetrahedra in explicit dynamic codes for solids. Int. J. Numer. Methods Eng. **43**, 565–583 (1998)
53. Dohrmann, C.R., Heinstein, M.W., Jung, J., Key, S.W., Witkowski, W.R.: Node-based uniform strain elements for three-node triangular and four-node tetrahedral meshes. Int. J. Numer. Methods Eng. **47**, 1549–1568 (2000)
54. Joldes, G.R., Wittek, A., Miller, K.: Non-locking tetrahedral finite element for surgical simulation. Commun. Numer. Methods Eng. **25**, 827–836 (2009)
55. Joldes, G.R., Wittek, A., Miller, K.: An efficient hourglass control implementation for the uniform strain hexahedron using the Total Lagrangian formulation. Commun. Numer. Methods Eng. **23**, 315–323 (2008)
56. Hallquist, J.O., Goudreau, G.L., Benson, D.J.: Sliding interfaces with contact-impact in large-scale Lagrangian computations. Comput. Methods Appl. Mech. Eng. **51**, 107–137 (1985)
57. Doghri, I., Muller, A., Taylor, R.L.: A general three-dimensional contact procedure for implicit finite element codes. Eng. Comput. **15**, 233–259 (1998)
58. Stewart, J.R., Gullerud, A.S., Heinstein, M.W.: Solution verification for explicit transient dynamics problems in the presence of hourglass and contact forces. Comput. Methods Appl. Mech. Eng. **195**, 1499–1516 (2006)
59. Sauvé, R.G., Morandin, G.D.: Simulation of contact in finite deformation problems – algorithm. Int. J. Mech. Mater. Des. **1**, 287–316 (2004)
60. Dassault Systèmes Simulia Corporation: ABAQUS Theory Guide: Version 6.14 (2014)

61. Joldes, G., Wittek, A., Miller, K., Morriss, L.: Realistic and efficient brain-skull interaction model for brain shift computation. In: Computational Biomechanics for Medicine III, pp. 95–105. http://www.cbm.mech.uwa.edu.au/CBM2008/, (2008)
62. NVIDIA: NVIDIA's Next Generation CUDA Compute Architecture: Fermi, http://www.nvidia.com/content/PDF/fermi_white_papers/NVIDIA_Fermi_Compute_Architecture_Whitepaper.pdf (2009)
63. Khronos: Open CL https://www.khronos.org/opencl/ (2018)
64. Joldes, G.R., Wittek, A., Miller, K.: Real-time nonlinear finite element computations on GPU - application to neurosurgical simulation. Comput. Methods Appl. Mech. Eng. **199**, 3305–3314 (2010)
65. Comas, O.: Real-time Soft Tissue Modelling on GPU for Medical Simulation. Doctoral School of Engineering Science, PhD Thesis. Université des Sciences et Technologie de Lille Lille, France (2011)
66. Courtecuisse, H., Allard, J., Kerfriden, P., Bordas, S.P.A., Cotin, S., Duriez, C.: Real-time simulation of contact and cutting of heterogeneous soft-tissues. Med. Image Anal. **18**, 394–410 (2014)
67. The American Society of Mechanical Engineers ASME, Standards Committee on Verification and Validation in Computational Solid Mechanics PTC 60/V&V 10: Guide for Verification and Validation in Computational Solid Mechanics. http://cstools.asme.org/csconnect/pdf/CommitteeFiles/24816.pdf (2006)
68. Babuska, I., Oden, J.T.: Verification and validation in computational engineering and science: basic concepts. Comput. Methods Appl. Mech. Eng. **193**, 4057–4066 (2004)
69. Joldes, G.R., Wittek, A., Miller, K.: An efficient hourglass control implementation for the uniform strain hexahedron using the Total Lagrangian formulation. Commun. Numer. Methods Eng. **24**, 1315 (2007)
70. Waldron, K.J., Kinzel, G.L.: Kinematics, Dynamics, and Design of Machinery. Wiley, New York (1999)
71. Wittek, A., Miller, K., Kikinis, R., Warfield, S.K.: Patient-specific model of brain deformation: application to medical image registration. J. Biomech. **40**, 919–929 (2007)
72. NVIDIA: Quadro on Desktop Workstations https://www.nvidia.com/en-us/design-visualization/quadro-desktop-gpus/
73. Wittek, A., Grosland, N., Joldes, G., Magnotta, V., Miller, K.: From finite element meshes to clouds of points: a review of methods for generation of computational biomechanics models for patient-specific applications. Ann. Biomed. Eng. **44**, 3–15 (2016)
74. Horton, A., Wittek, A., Joldes, G.R., Miller, K.: A meshless Total Lagrangian explicit dynamics algorithm for surgical simulation. Int. J. Numer. Methods Biomed. Eng. **26**, 977–998 (2010)
75. Miller, K., Horton, A., Joldes, G.R., Wittek, A.: Beyond finite elements: a comprehensive, patient-specific neurosurgical simulation utilizing a meshless method. J. Biomech. **45**, 2698–2701 (2012)
76. Zhang, G.Y., Wittek, A., Joldes, G.R., Jin, X., Miller, K.: A three-dimensional nonlinear meshfree algorithm for simulating mechanical responses of soft tissue. Eng. Anal. Bound. Elem. **42**, 60–66 (2014)
77. Li, M., Miller, K., Joldes, G.R., Kikinis, R., Wittek, A.: Biomechanical model for computing deformations for whole-body image registration: A meshless approach. Int. J. Numer. Method Biomed. Eng. **32**, e02771–e02718 (2016)
78. Joldes, G.R., Bourantas, G., Zwick, B., Chowdhury, H., Wittek, A., Agrawal, S., Mountris, K., Hyde, D., Warfield, S.K., Miller, K.: Suite of meshless algorithms for accurate computation of soft tissue deformation for surgical simulation. Med. Image Anal. **56**, 152–171 (2019)

Chapter 11
Meshless Algorithms for Computational Biomechanics of the Brain

Adam Wittek, Grand Roman Joldes, and Karol Miller

11.1 Introduction

In Chap. 10, we highlighted two important factors that limit application of finite element method in predicting the brain responses for surgery simulation and pose a significant challenge in application to injury biomechanics when the body tissues undergo rupture/failure:

1. Time-consuming generation of patient-specific finite element meshes of the brain and other body organs [1]
2. Deterioration of the solution accuracy and instability when the finite element meshes undergo distortion induced by large localised deformations caused by interactions between the organ and surgical tool [2] and by injury

Meshless algorithms [3–5], in which the analysed continuum is discretised by nodes (where forces and displacements are calculated) with no assumed structure for the interconnection of the nodes and integration points (where stresses and strains are calculated) (Fig. 11.1), have been proposed in the literature for generating computational grids of domains with complex geometry and providing reliable results for large deformations [7–10].

Smoothed particle hydrodynamics (SPH) is regarded as the first meshless method. It utilises a strong form of equations of continuum mechanics [11]. SPH and other particle methods (such as material point method in which a strong form of equations of continuum mechanics is used) were applied in injury biomechanics [12–14]. However, the literature indicates several important shortcomings of the SPH method, which includes instabilities in tension and accuracy inferior to that

A. Wittek (✉) · G. R. Joldes · K. Miller
Intelligent Systems for Medicine Laboratory, Department of Mechanical Engineering, The University of Western Australia, Perth, WA, Australia
e-mail: adam.wittek@uwa.edu.au; karol.miller@uwa.edu.au

K. Miller (ed.), *Biomechanics of the Brain*, Biological and Medical Physics, Biomedical Engineering, https://doi.org/10.1007/978-3-030-04996-6_11

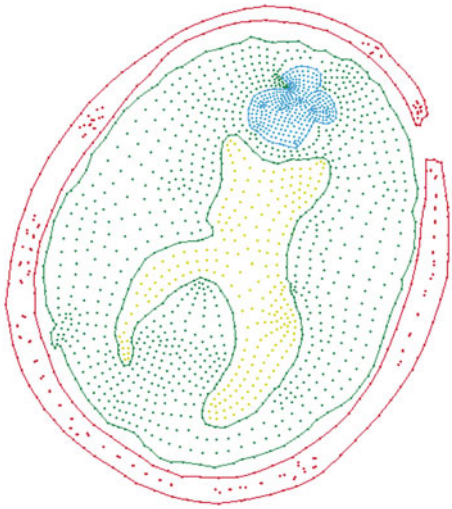

Fig. 11.1 Meshless discretisation (interpolation nodes) of the patient-specific brain geometry for computing deformations within the brain due to the craniotomy-induced brain shift. (Adapted from Horton et al. [6])

of the finite element method [3]. The quest for eliminating this shortcomings and advancing the SPH continues [15] in parallel with development of new algorithms that apply a strong form of equations of solid mechanics [16]. So far, however, such methods have found only limited application in computational biomechanics [17].

Therefore, we focus on meshless methods that utilise the weak form of equations of continuum mechanics and background integration grid. As an example, we discuss the meshless computational biomechanics framework that utilises total Lagrangian formulation and explicit integration in time domain: Meshless Total Lagrangian Explicit Dynamics (MTLED) (Fig. 11.2) [7, 18–24]. Dynamic relaxation and real-time computation of soft tissue deformations through algorithm implementation on graphics processing units (GPUs) discussed in Chap. 10 for finite element method apply also to this framework.

The key motivation for Meshless Total Lagrangian Explicit Dynamics (MTLED) framework is the need for computational biomechanics simulations to satisfy the constraints and requirements of neurosurgical navigation. This includes fast creation of patient-specific (representing a given patient) computational biomechanics models and conducting surgical simulations without the requirement for the user to become an expert in computational mechanics (as hospitals are unlikely to hire PhDs in computational mechanics to do surgery planning). In the MTLED framework, we propose to achieve this through introducing specialised shape functions and adaptive spatial integration that facilitate accurate solution, even if the analysed continuum is discretised using irregularly/non-uniformly distributed nodes, and through the specialised algorithm that employs the visibility criterion for surgical dissection and tissue rupture simulation. Therefore, in the subsequent sections of this chapter, we discuss the following topics:

- Section 11.2: Shape functions for meshless algorithms for computing soft tissue deformations

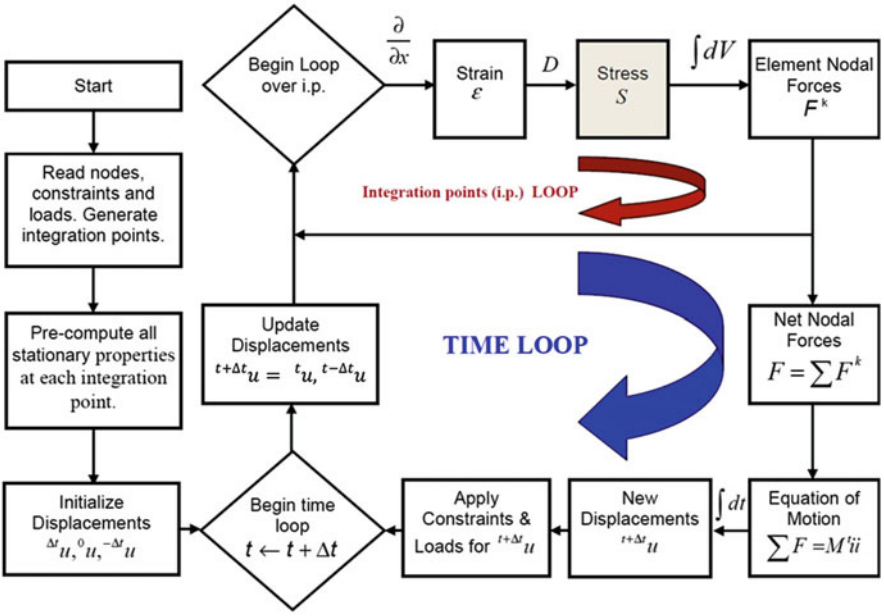

Fig. 11.2 Flowchart of the Meshless Total Lagrangian Explicit Dynamics (MTLED) framework for surgical simulation. Note the important difference with the finite element Total Lagrangian Explicit Dynamics (TLED) algorithm discussed in Chap. 10. In the MTLED framework, the spatial discretisation is done over a cloud of points, and the spatial integration is done using the background grid. Therefore, unlike in the TLED, the loop is over the integration points rather than the elements

- Section 11.3: Spatial integration schemes for meshless algorithms for computing soft tissue deformations
- Section 11.4: Visibility criterion for modelling of surgical dissection and soft tissue rupture
- Section 11.5: Stability of the specialised meshless explicit dynamics algorithm for surgical simulation
- Section 11.6: Algorithm verification

11.2 Shape Functions for Meshless Algorithms for Computing Soft Tissue Deformations

The method for interpolation/approximation of the displacement field and the type of shape functions used for such interpolation are some of the crucial differences between the MTLED framework and the Total Lagrangian Explicit Dynamics (TLED) finite element algorithm described in Chap. 10. The TLED, and vast majority of finite element algorithms, uses polynomial shape functions. In the

MTLED framework, we use moving least squares shape functions that were initially proposed by Lancaster and Salkauskas [25] for approximation of scattered data and later applied by Nayroles et al. [26] in the diffuse element method:

$$u^h(\mathbf{x}) = \mathbf{p}^{\mathrm{T}}(\mathbf{x})\,\mathbf{a}(\mathbf{x}), \tag{11.1}$$

where u^h is the approximation of the displacement u, $\mathbf{p}(\mathbf{x})$ is the vector of monomial basis function, $\mathbf{a}(\mathbf{x})$ is the vector of coefficients that need to be calculated and $\mathbf{x}$ is the point belonging to the analysed continuum but not located at the node. In the MTLED framework, low-order (up to quadratic order) monomial basis functions are used [7]:

$$\mathbf{p}^{\mathrm{T}}(\mathbf{x}) = \left(1 \;|x\;\; y\;\; z|\; xy\;\; xz\;\; yz|\; x^2\;\; y^2\;\; z^2\right). \tag{11.2}$$

The coefficients $a(\mathbf{x})$ are computed by minimising an error functional J defined based on the weighted least squares errors for n points located at positions x_j ($j = 1, \ldots, n$):

$$J(\mathbf{x}) = \sum_{j=1}^{n} \left[\left(u^h(\mathbf{x}_j) - u_j \right)^2 w\left(\|\mathbf{x} - \mathbf{x}_j\| \right) \right], \tag{11.3}$$

where w is the weight function (positive weight function is used) and $||\cdot||$ denotes the Euclidean distance. Given Eq. (11.1), the error functional J (defined in Eq. 11.3) can be rewritten as [27]

$$J = (\mathbf{Pa} - \mathbf{u})^{\mathbf{T}} \mathbf{W} (\mathbf{Pa} - \mathbf{u}), \tag{11.4}$$

where

$$\mathbf{u}^{\mathbf{T}} = [u_1, u_2 \ldots \;\; u_n], \tag{11.5}$$

$$\boldsymbol{P} = \begin{bmatrix} p_1(\mathbf{x}_1) & p_2(\mathbf{x}_1) & \cdots & p_m(\mathbf{x}_1) \\ p_1(\mathbf{x}_2) & p_2(\mathbf{x}_2) & \cdots & p_m(\mathbf{x}_2) \\ \vdots & \vdots & \ddots & \vdots \\ p_1(\mathbf{x}_n) & p_2(\boldsymbol{x}_n) & \cdots & p_m(x_n) \end{bmatrix}, \tag{11.6}$$

$$\boldsymbol{W} = \begin{bmatrix} w(||\mathbf{x} - \mathbf{x}_1||) & 0 & \cdots & 0 \\ 0 & w(||\mathbf{x} - \mathbf{x}_2||) & \cdots & 0 \\ \vdots & \vdots & \ddots & \vdots \\ 0 & 0 & \cdots & w(||\mathbf{x} - \mathbf{x}_n||) \end{bmatrix}, \tag{11.7}$$

where u_i is the value of the field variable (displacement) at node i. To minimise the error functional J given in Eq. (11.4), its partial derivatives $\frac{\partial J}{\partial \mathbf{a}}$ are set to zero [27]:

$$\frac{\partial J}{\partial \mathbf{a}} = \mathbf{P}^{\mathrm{T}}\mathbf{W}\mathbf{P}\mathbf{a}\left(\mathbf{x}\right) - \mathbf{P}^{\mathrm{T}}\mathbf{W}\mathbf{u} = 0 \tag{11.8}$$

and the coefficients $\mathbf{a}(\mathbf{x})$ at the evaluation points are obtained as

$$\mathbf{a}\left(\mathbf{x}\right) = \left(\mathbf{P}^{\mathrm{T}}\mathbf{W}\mathbf{P}\right)^{-1}\mathbf{P}^{\mathrm{T}}\mathbf{W}\mathbf{u}, \tag{11.9}$$

where $\mathbf{P}^{\mathrm{T}}\mathbf{W}\mathbf{P}$ is also referred to as the moment matrix $\mathbf{M} = \mathbf{P}^{\mathrm{T}}\mathbf{W}\mathbf{P}$.

Following Joldes et al. [27], from Eq. (11.9), the shape functions $\mathbf{\Phi}$ can be defined as

$$\mathbf{\Phi}\left(\mathbf{x}\right) = \left[\phi_1\left(\mathbf{x}\right)\ldots\phi_n\left(\mathbf{x}\right)\right] = \mathbf{P}^{\mathrm{T}}\left(\mathbf{P}^{\mathrm{T}}\mathbf{W}\mathbf{P}\right)^{-1}\mathbf{P}^{\mathrm{T}}\mathbf{W}. \tag{11.10}$$

According to Eq. (11.10), the shape functions can be constructed only if the moment $\mathbf{M} = \mathbf{P}^{\mathrm{T}}\mathbf{W}\mathbf{P}$ is non-singular. This implies that although the requirements regarding the nodal distribution are much less stringent than in the finite element method, where the nodes need to be arranged in a mesh of high-quality tetrahedral or hexahedral elements (see Chap. 10), some conditions still apply, and not all the nodal distributions are acceptable/admissible. These conditions depend on the bases of the shape functions. This poses a challenge for meshless algorithms for surgical simulation as the end-users are medical professionals rather than experts in computational mechanics and, due to complex geometry of the brain and other body organs, irregular nodal distributions are an effective and convenient approach for spatial discretisation [28, 29]. Application of such distributions makes it possible to generate patient-specific computational biomechanics models of the brain and other organs directly from images (Fig. 11.3) [18, 29, 30]. However, unlike in the case of the finite element method discussed in Chap. 10, there are no specialised computational grid generators for the MTLED framework and other meshless methods using weak form of equations of continuum mechanics. In the examples showed in Figs. 11.3, 11.4, 11.7, and 11.8, the nodes were created using the established algorithms available in the HyperMesh™ finite element preprocessing software package (by Altair, MI, USA; https://altairhyperworks.com/product/hypermesh). The process is similar to automated generation of nodal distributions for tetrahedral finite element

Fig. 11.3 Irregular nodal distribution applied in Miller et al. [28] for computing the deformations within the brain due to craniotomy-induced brain shift

meshes, but as no elements need to be constructed, the usual constraints on the node placement due to element quality considerations disappear.

We require from the shape functions in the MTLED framework to facilitate robust approximation for irregular nodal distributions without the need for the user to control/adjust the parameters of the distributions to achieve accurate solution. Modified moving least shape functions introduced by Joldes et al. [27] and Chowdhury et al. [22] address this challenge for higher-order bases functions.

The key idea behind the Modified Moving Least Square (MMLS) function comes from the realisation that the singularity of the moment matrix $\mathbf{M} = \mathbf{P}^{\mathrm{T}}\mathbf{W}\mathbf{P}$ in Eq. (11.8) originates from the fact that Eq. (11.9), applied for computing the coefficients $\mathbf{a}(\mathbf{x})$, has multiple solutions. This implies that functional J (Eq. 11.4) does not include sufficient constraints to guarantee a unique solution for a given nodal distribution. Therefore, to prevent singularities for the second-order base functions, we add additional constraints to the functional J [27]:

$$J(\mathbf{x}) = \sum_{j=1}^{n} \left[\left(u^h(\mathbf{x}_j) - u_j \right)^2 + \mu_{x^2} a_{x^2}^2 + \mu_{xy} a_{xy}^2 + \mu_{y^2} a_{y^2}^2 \right], \tag{11.11}$$

where

$$\boldsymbol{\mu} = \begin{bmatrix} \mu_{x^2} & \mu_{xy} & \mu_{y^2} \end{bmatrix} \tag{11.12}$$

is the vector of positive weights for the additional constraints. From Eq. (11.4), that defines the functional for MLS shape functions, and Eq. (11.11), a new functional $\overline{J}$ for (new) MMLS shape functions can be rewritten as

$$\bar{\mathrm{J}} = (\mathrm{Pa\text{-}u})^{\mathrm{T}} \mathrm{W} (\mathrm{Pa\text{-}u}) + \mathrm{a}^{\mathrm{T}} \mathbf{H} \mathrm{a}, \tag{11.13}$$

where $\mathbf{H}$ is the matrix with all elements $\mathbf{0}_{33}$ equal to zero except the last three diagonal entries that are equal to the weights $\boldsymbol{\mu}$ of the additional constraints (see Eq. 11.12):

$$\mathbf{H} = \begin{bmatrix} \mathbf{0}_{33} & \mathbf{0}_{33} \\ \mathbf{0}_{33} & \mathrm{diag}\,(\boldsymbol{\mu}) \end{bmatrix}. \tag{11.14}$$

To compute the coefficients $\mathbf{a}(\mathbf{x})$ for the MMLS shape functions, we minimise the functional $\overline{J}$ (Eq. 11.13) following the procedure previously used for MLS (as given by Eqs. 11.8, 11.9, and 11.10). This leads to the following formula for computing (new) MMLS shape functions [27]:

$$\overline{\boldsymbol{\Phi}}(\mathbf{x}) = \begin{bmatrix} \overline{\phi}_1(\mathbf{x}) \dots & \overline{\phi}_n(\mathbf{x}) \end{bmatrix} = \mathbf{P}^{\mathrm{T}} \left(\mathbf{P}^{\mathrm{T}} \mathbf{W} \mathbf{P} + \mathbf{H} \right)^{-1} \mathbf{P}^{\mathrm{T}} \mathbf{W}. \tag{11.15}$$

This formula differs from that of the traditional MLS functions (Eq. 11.10) by the constraint weight matrix $\mathbf{H}$. The constraints are to prevent singularities in the error functional $\overline{J}$ (Eqs. 11.11, 11.12, and 11.13).

It has been indicated in Chowdhury et al. [22] and Joldes et al. [27] that the MMLS shape functions appreciably improve accuracy of prediction of the brain

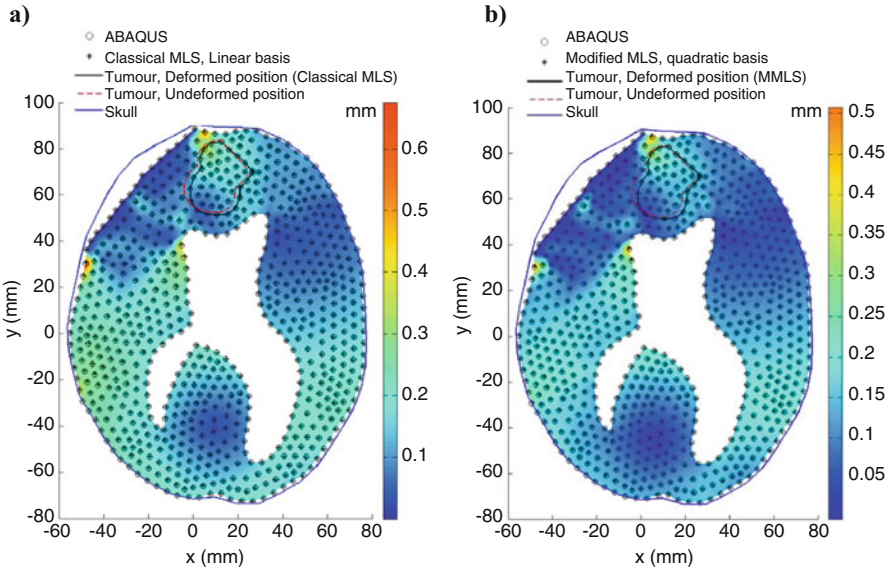

Fig. 11.4 Evaluation of the Meshless Total Lagrangian Explicit Dynamics (MTLED) framework with traditionally used Moving Least Square (MLS) shape functions and Modified Moving Least Square (MMLS) shape functions introduced by Joldes et al. [31] and Chowdhury et al. [26]. The evaluation is conducted through application in predicting the brain deformations due to craniotomy-induced brain shift. (**a**) Differences between the deformations predicted using the MTLED with MLS shape functions and well-established non-linear finite element code ABAQUS [31]; (**b**) differences between the deformations predicted using the MTLED with MMLS shape functions and well-established non-linear finite element code ABAQUS. The solution obtained using ABAQUS finite element code is regarded as the reference. Accuracy improvement due to application of MMLS shape functions is clearly visible. (Adapted from Chowdhury et al. [32])

deformations due to surgery in comparison to the traditionally used MLS functions (Fig. 11.4) and provide solution for irregular nodal distributions where the MLS functions exhibit singularity.

11.3 Spatial Integration Schemes for Meshless Algorithms for Computing Soft Tissue Deformations

Two main types of integration schemes are used in the meshless methods of computational mechanics:

1. Gaussian quadrature Q over a background grid where the integration is done over the integration cells D with one or more integration points per cell [7, 21, 34, 35]

$$I = \int_D f(\mathbf{x})\, dD, \tag{11.16}$$

$$I \cong Q_n(D) = \sum_{i=1}^{n} w_i f(\mathbf{x}_i), \tag{11.17}$$

where f is the function we intend to integrate, I is the integral approximated using the n-point Gaussian quadrature Q_n over the integration cell D, $\mathbf{x}_i$ is the integration points and w_i is the corresponding weights

2. Nodal integration where the interpolating nodes are also used as integration points [36, 37]

   As the literature indicates that Gaussian quadrature over the background integration cells tends to be less computationally demanding than nodal integration schemes [38], in the Meshless Total Lagrangian Explicit Dynamics (MTLED) framework, we use the background integration (Fig. 11.5).

   In the MTLED framework (and other meshless algorithms that rely on weak formulation of equations of continuum mechanics), application of background integration using Gaussian quadrature is associated with errors that originate from two sources:

   1. Shape functions in meshless methods are not polynomials [38].
   2. Shape functions' support may not align with the integration cells.

Difficulty in estimation and control of such errors is a common challenge for many of the existing integration schemes [21].

In the 2011 edition of this book [39], we advocated hexahedral cells with a single integration point per cell (the idea similar to the one used in underintegrated

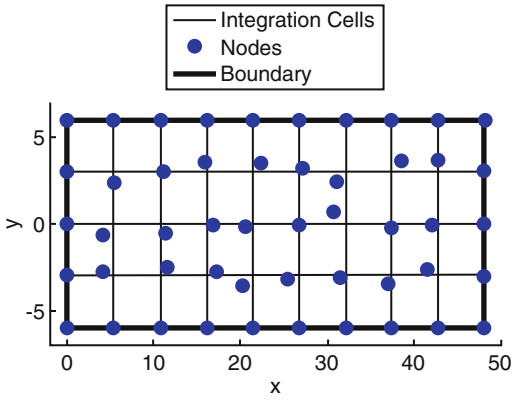

Fig. 11.5 Meshless discretisation of the problem domain by an irregular nodal distribution with a background grid of quadrilateral integration cells. (Adapted from Joldes et al. [33])

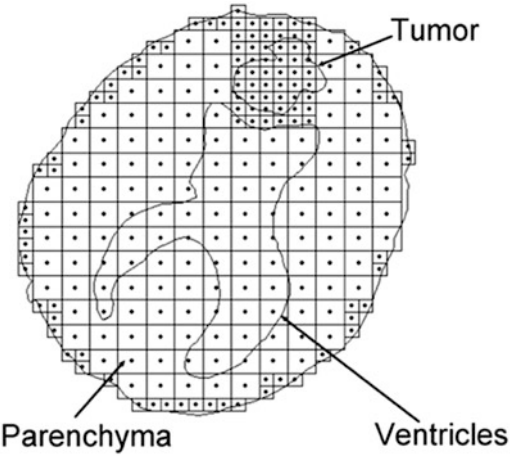

Fig. 11.6 Background regular integration grid for a patient-specific meshless model of the brain with tumour. The integration points are indicated as (•). Note that the background grid does not conform to the geometry boundary. (Adapted from Horton et al. [6])

hexahedral elements discussed in Chap. 5) (Fig. 11.6). As integration cells do not have to conform to the boundary of the analysed continuum, they can be generated automatically even for complex geometry. The nodes, where the displacements are calculated, are independent of the background integration grid [7]. Simplicity and flexibility are key advantages of spatial integration using hexahedral background grids. Almost arbitrary placement of the nodes throughout the analysed continuum can be used, which is well suited for complex geometry of the brain and other human body organs. However, restrictions on the ratio of the number of integration points and nodes apply. Through parametric study, we estimated in Horton et al. [7] that the number of integration points should be twice the number of nodes for accurate and convergent solution. Although we successfully used this estimate in predicting the deformations within the brain due to craniotomy-induced brain shift (Fig. 11.7) [28], it provides only limited control of the integration error. Consequently, the analyst's knowledge of meshless methods of computational mechanics and experience in using them are crucial for ensuring accuracy of the computations. This may pose a challenge for clinical applications where the users are medical professionals rather than experts in computational mechanics. To address this challenge, we incorporated into the MTLED framework an adaptive integration scheme that adapts the quadrature to the behaviour of the function being integrated [21, 33].

For the Meshless Total Lagrangian Explicit Dynamics (MTLED) framework, we proposed an adaptive integration scheme where the integration cells D (see Eqs. 11.16 and 11.17) are recursively subdivided into m smaller cells until the desired integration tolerance τ is achieved [21, 33]. Using notation $Q_n^m(D)$ to indicate the n-point quadrature applied on m subdivided regions of the integration cell D, our adaptive integration scheme (as proposed in [21, 33]) can be described using the following pseudocode:

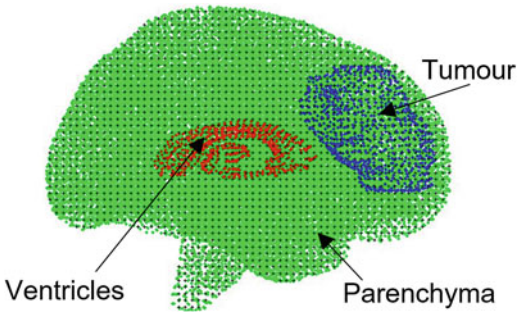

Fig. 11.7 3-D patient-specific meshless model for computing the deformations within the brain due to craniotomy-induced brain shift for image-guided neurosurgery. The model was implemented using the Meshless Total Lagrangian Explicit Dynamics (MTLED) framework. Detailed description and the results obtained using this model are in Miller et al. [28]. The integration points are indicated as (+) and interpolating nodes as (•) for the brain parenchyma, (•) for the ventricles and (•) for the tumour. Regular hexahedral background integration grid (similar to that shown for 2-D model in Fig. 11.6) was used. (Adapted from Miller et al. [28])

Adaptive Integration Scheme

Adaptive Integration Scheme

Procedure $[Q,\ x_i,\ w_i] = integrate\ (f, D, \tau)$
  $[Q, x_i, w_i] = Q_n^1[D]$ // x_i = integration points used,
    w_i = associated weights
  $[QM, x_M, w_M] = Q_n^m(D)$
  If $(|QM - Q| > \tau|QM|)$ **Then**
    $D \rightarrow \{D_1, D_2, \ldots, D_m\}$;// subdivision
    For D_j in $\{D_1, D_2, \ldots, D_m\}$ **Do**
      $\left[Q_j, x_{ij}, w_{ij}\right] = integrate\ \left(f, D_j, \tau\right)$; // recursion
    End For
    $Q = sum(Q1, Q2, \ldots Qm)$;
    $x_i = concatenate(x_{i1}, x_{i2}, \ldots x_{im})$;
    $w_i = concatenate(w_{i1}, w_{i2}, \ldots w_{im})$
  End If
  Return Q, x_i, w_i
End Procedure

The above integration scheme has the following properties that make it very attractive for application in computational biomechanics of the brain and other body organs:

- The size of the integration cells is automatically adjusted (the number of integration cells in the areas where the shape functions exhibit large variations is automatically increased to maintain the integration accuracy).

- New integration points are introduced only in the areas where the integration accuracy is below the desired (required) accuracy.
- The scheme works for any shape and size of support domains.
- The scheme is particularly effective for irregular/non-uniform nodal distributions.

In practice, defining the relative integration tolerance τ is the only input required from the analyst for the adaptive integration scheme used in the MTLED framework. Although it is rather difficult to formulate detailed guidelines regarding selection of such tolerance, the numerical experiments we conducted in Joldes et al. [21] have indicated that the solution accuracy does not appreciably increase after the integration accuracy reaches a certain level/threshold. This, in turn, suggests that it is not necessary to use very high integration accuracy (low tolerance τ) resulting in many subdivisions of each integrationcell.

We recommend to conduct a convergence analysis to determine the best integration accuracy for a given spatial discretisation. Such analysis has been conducted by Joldes et al. [33] for the problem of computation of the brain deformations due to craniotomy-induced brain shift (Fig. 11.8). In such problems, the required solution accuracy is within the voxel size of the intra-operative magnetic resonance (MR) images—between 1 mm and 2 mm. The results obtained by Joldes et al. [33] suggest that such accuracy of prediction of the brain deformations can be achieved using the relative integration tolerance $\tau \leq 0.1$ (i.e. 0.1 is the maximum acceptable tolerance) (Fig. 11.8).

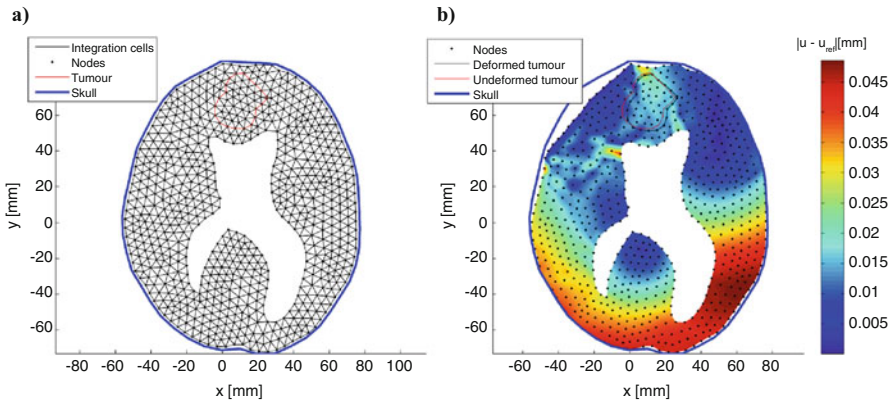

Fig. 11.8 Application of the MTLED framework with the adaptive integration scheme in predicting the brain deformations due to craniotomy-induced brain shift. The figure shows the influence of the integration tolerance on the solution (predicted brain deformations) accuracy. (**a**) Meshless discretisation using nodes and triangular background integration cells. The nodes define vertices of the cells. (**b**) Differences between the deformations predicted using three Gauss points per integration cell and the reference solution using very stringent relative integration tolerance $\tau = 0.001$. For the tolerance $\tau = 0.1$, the maximum difference with the reference solution is around 0.035 mm, which is well within the required accuracy of 1 mm (less than half of the voxel size of a typical intra-operative magnetic resonance image (MRI)). (Adapted from Joldes et al. [33])

11.4 Visibility Criterion for Modelling of Surgical Dissection and Soft Tissue Rupture

Surgical dissection and injury-related rupture introduce discontinuities/cracks in the body tissues and organs. In the computational biomechanics algorithms that rely on finite element discretisation discussed in Chap. 10, surgical dissection is simulated by subdividing the elements forming the mesh [40–44]. This requires sophisticated re-meshing techniques to generate new elements with good aspect ratio and map the field variables from the original to the new mesh. With an exception of Bui et al. [44], the re-meshing is in practice limited to tetrahedral elements that exhibit volumetric locking when applied to soft tissues and other incompressible continua unless special countermeasures are applied (see Chap. 10). Furthermore, error accumulation due to re-meshing tends to constrain the accuracy of finite element method in modelling of surgical cutting/dissection [42, 45]. As the meshless methods utilise spatial discretisation in a form of a 'cloud' of points/nodes, the burden associated with re-meshing required by finite element method is to a large extent alleviated. Therefore, meshless discretisation has been proposed by several authors as a method of choice for modelling of continua undergoing crack propagation and fragmentation [8, 46–52].

The specialised algorithm, created for the MTLED framework by Jin et al. [20] at the Intelligent Systems for Medicine Laboratory at the University of Western Australia, models the progressive surgical cutting by adding and/or splitting nodes on the cutting path using the visibility criterion. The visibility criterion prevents the nodes located on the opposite sides of dissection/crack from interacting with each other (they are 'invisible' to each other) [3, 53]. In the algorithm by Jin et al. [20], the surgical cut and injury-caused rupture/crack are geometrically represented using a series of line segments with the aid of the level-set method [54, 55] to mathematically describe the location of all the nodes and integration points in relation to the cutting/rupture path (Fig. 11.9). The effect of cutting-/rupture-induced discontinuity is entirely reflected in the changes of the shape and size of the nodal influence domains (Fig. 11.10).

Quantitative evaluation through application in modelling of rupture-causing elongation of the specimen of pia-arachnoid complex has confirmed the robustness and accuracy of the specialised visibility criterion for modelling dissection and rupture in MTLED framework (Fig. 11.11) [20, 58]. However, application in modelling of dissection of 3-D continua indicated challenges associated with high computational cost of the visibility criterion and level-set method in 3-D [59]. Therefore, we recommend visibility criterion only for modelling of dissection and rupture of thin tissue layers such as the brain meninges. To the best of our knowledge, despite ongoing research effort that includes application of the methods such as the phase-field approach [60], the problem of modelling of crack propagation in 3-D continuum subjected to large deformations and exhibiting non-linear stress-strain relationship still awaits solution that can be regarded as accurate (in a sense of quantitatively accurate predictions of forces and deformations),

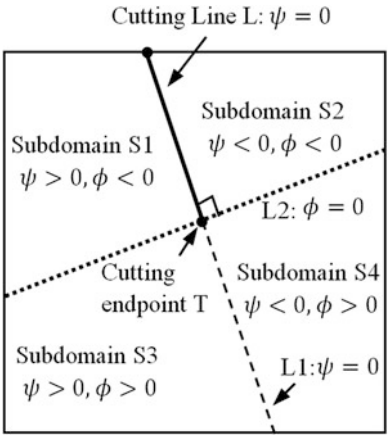

Fig. 11.9 Specialised visibility for modelling dissection and rupture in the MTLED framework. The cutting/crack direction is represented as the zero level set of function $\psi(x, y) = \left(x - x_{\text{ep}}\right) \frac{v_y}{\|\mathbf{V}\|} - \left(y - y_{\text{ep}}\right) \frac{v_x}{\|\mathbf{V}\|}$, where (x, y) is the coordinate of a given point in the problem domain, $(x_{\text{ep}}, y_{\text{ep}})$ is the coordinate of the endpoint of the cutting/crack path V_x and V_y are the components of vector $\mathbf{V}$ representing the cutting/crack direction and $\|\mathbf{V}\|$ is the length of vector $\mathbf{V}$. The endpoint of the cut/crack is represented as the intersection of the zero level set of function $\psi(x, y)$ with the orthogonal zero level set of function $\varphi(x, y) = \left(x - x_{\text{ep}}\right) \frac{v_x}{\|\mathbf{V}\|} - \left(y - y_{\text{ep}}\right) \frac{v_y}{\|\mathbf{V}\|}$. The domain is divided into four subdomains according to the sign of level sets of functions ψ and φ. The division into these four subdomains is used to determine the position of a point and supporting node in relation to the cutting/crack line L. (Adapted from Jin et al. [20])

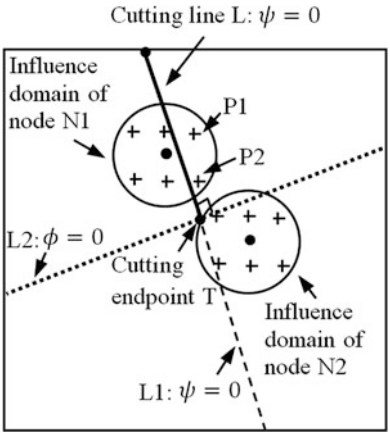

Fig. 11.10 Specialised visibility criterion for modelling dissection and rupture in the Meshless Total Lagrangian Explicit Dynamics (MTLED) framework. The effect of cutting-/rupture-induced discontinuity is entirely reflected in the changes of the shape and size of the nodal influence domain. The influence domain of node N1 intersects the cutting/crack line L; points P1 and P2 are eliminated from the influence domain of this node. The influence domain of node N2 passes through the cutting endpoint T only, so it does not need an update. (Adapted from Jin et al. [20])

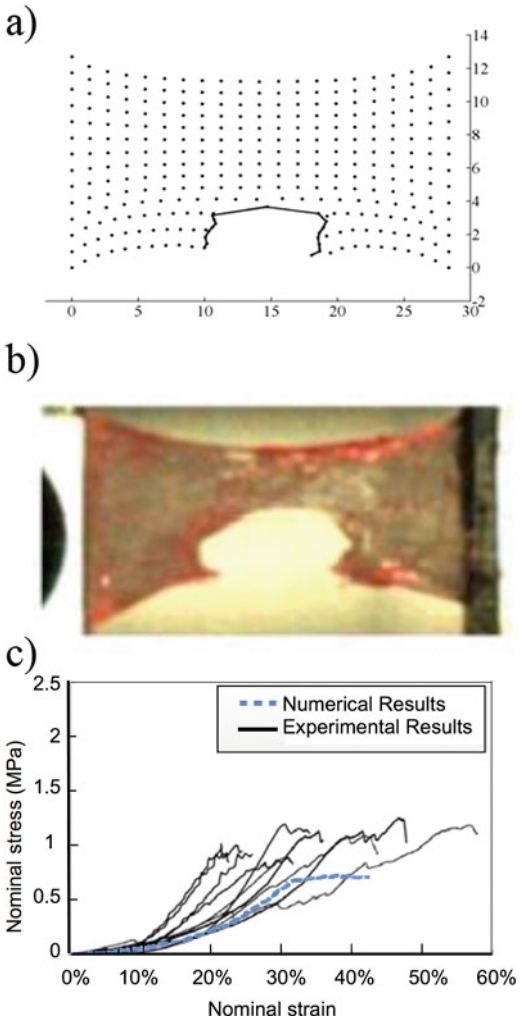

Fig. 11.11 Quantitative evaluation of the performance of the Meshless Total Lagrange Explicit Dynamics (MTLED) framework with the specialised visibility criterion for modelling surgical cutting/dissection and soft tissue rupture. The results obtained when applying the MTLED framework to model rupture-causing elongation of pia-arachnoid-complex tissue specimen are compared with the experimental data obtained by Jin et al. [56] at the Bioengineering Centre, Wayne State University. The strain rate is 0.05 s^{-1}. (**a**) The specimen deformation for the overall sample elongation of 42.5% of the initial length predicted using the MTLED framework. Dimensions are in mm; (**b**) photograph of the deformed tissue specimen. (Adapted from Jin [57] (Bioengineering Centre, Wayne State University)). (**c**) Comparison of the nominal stress-strain relationship predicted using the MTLED framework [58] with the experimental results reported in [56]. (The figures and the photograph are adapted from [57, 58])

robust, computationally efficient and suitable for application in surgery simulation where the users are unlikely to have expert knowledge of computational mechanics. Therefore, we offer no recommendation regarding the method of choice for 3-D computational biomechanics modelling of surgical dissection and rupture propagation.

11.5 Stability of Explicit Dynamics Meshless Algorithms

For Computation of Soft Tissue Deformation

Both the Meshless Total Lagrangian Explicit Dynamics (MTLED) framework discussed here and the Total Lagrangian Explicit Dynamics (TLED) finite element algorithm for neurosurgical simulation described in Chap. 10 use the central difference method for time stepping. This method is only conditionally stable. The critical time step Δt_{crit} that ensures the computation stability can be determined from the maximum frequency of vibrations $\omega_{\max}$ (or the maximum eigenvalue $A_{\max}$) of a given system (as represented by the model) [61]:

$$\Delta t_{\text{crit}} = \frac{2}{\omega_{\max}} = \frac{2}{\sqrt{A_{\max}}}. \tag{11.18}$$

In Chap. 10, when discussing the TLED finite element algorithm, we stated that it can be demonstrated from Gerschgorin's theorem [62, 63] that the maximum eigenvalue of an assembled finite element mesh is bounded by the maximum eigenvalue of any of the elements in the mesh. Consequently, for the TLED algorithm, we obtain the maximum eigenvalue of the analysed system $A_{\max}$ by estimating the maximum eigenvalue of each element in the mesh $\lambda^{e}_{\max}$. In Joldes et al. [64], we applied this reasoning to the MTLED framework by replacing the element eigenvalues with the eigenvalues $\lambda^{I}_{\max}$ for the integration points. This leads to the following conservative estimate of critical time step Δt_{crit} for the MTLED framework [64]:

$$\Delta t_{\text{crit}} = \frac{2}{\omega_{\max}} = \frac{2}{\sqrt{A_{\max}}} \approx \frac{2}{\sqrt{\max\limits_{I}\left(\lambda^{I}_{\max}\right)}} = \min_{I}\left(\frac{2}{\sqrt{\lambda^{I}_{\max}}}\right). \tag{11.19}$$

Following Bathe [65], the maximum eigenvalue $\lambda^{I}_{\max}$ for a given integration point I can be estimated from the Rayleigh quotient as

$$\lambda^{I}_{\max} = \sup_{\mathbf{u}} \frac{\boldsymbol{u}^{\mathrm{T}}\mathbf{K}^{I}\mathbf{u}}{\mathbf{u}^{\mathrm{T}}\mathbf{M}^{I}\mathbf{u}}, \tag{11.20}$$

where $\mathbf{K}^{I}$ is the stiffness matrix for the integration point I, $\mathbf{u}$ is the vector of nodal displacements for the nodes associated with the integration point I and $\mathbf{M}^{I}$ is the mass matrix for the integration point I.

In both the finite element TLED algorithm described in Chap. 10 and in the MTLED framework discussed here, lumped mass matrices are used. Physical interpretation of such matrices is that the system mass is assigned entirely (lumped) to the nodes. In the MTLED framework, the mass allocated to the integration point I is distributed equally to all nodes within the support domain of that integration point [64]. Therefore, Eq. (11.20) can be rewritten as [64]

$$\lambda_{\max}^{I} = \frac{N^I}{m^I} \sup_{\mathbf{u}} \frac{\mathbf{u}^T \mathbf{K}^I \mathbf{u}}{\mathbf{u}^T \mathbf{u}} = \frac{N^I}{m^I} \rho_{\max}\left(\mathbf{K}^I\right), \tag{11.21}$$

where N^I is the number of nodes in the support domain of the integration point I, m^I is the mass allocated to the integration point I and $\rho_{\max}(\mathbf{K}^I)$ is the maximum eigenvalue of the stiffness matrix $\mathbf{K}^I$ for the integration point I.

The stiffness matrix is defined in terms of the strain-displacement matrices $\mathbf{B}^I$ for a given integration point I, elasticity matrix $\mathbf{C}$ that contains the information about the constitutive properties and volume V^I allocated to the integration point I [64, 66]:

$$\mathbf{K}^I_{iJlK} = \mathbf{B}^I_{jJ}\left(\mathbf{x}^I\right) \mathbf{C}_{ijkl} \mathbf{B}^I_{lK}\left(\mathbf{x}^I\right) \bullet V^I, \tag{11.22}$$

where the subscripts indicate the tensor order, i.e. *ijkl* and *iJlk* indicate the fourth-order tensor and *jJ* and *lK* the second-order tensor. For the homogenous materials with the constitutive properties defined using Lame constants (λ and μ), the maximum eigenvalue of the stiffness matrix $\rho_{\max}(\mathbf{K}^I)$ for the integration point I can be estimated as [66]

$$\rho_{\max}\left(\mathbf{K}^I\right) \leq (\lambda + \mu) \bullet V^I \bullet \left\|\mathbf{B}^I\right\|_F^2, \tag{11.23}$$

where $\|\mathbf{B}^I\|_F$ is Frobenius norm $\left\|\mathbf{B}^I\right\|_F^2 = \mathbf{B}_{jI}\mathbf{B}_{jI}$. Substituting Eq. (11.23) into Eq. (11.21) leads to the following formulae for the upper bounds of the maximum eigenvalues of the stiffness matrix for the integration point I [64]:

$$\lambda_{\max}^{I} \leq N^I \left(c^I\right)^2 \bullet \mathbf{B}^I_{jI}\mathbf{B}^I_{jI}, \tag{11.24}$$

where c is the dilatational (acoustic) wave speed. By substituting Eq. (11.24) into Eq. (11.18), the critical time step Δt_{crit} for the MTLED framework can be conservatively estimated as

$$\Delta t_{\text{crit}} \approx \text{Min}_I \left(\frac{2}{\sqrt{N^I \left(c^I\right)^2 \bullet \mathbf{B}^I_{jI}\mathbf{B}^I_{jI}}} \right). \tag{11.25}$$

The formula for determining the bounds for maximum eigenvalue $\lambda^I_{\max}$ of the stiffness matrix given in Eq. (11.24) is valid also for the finite element method, as long as the same mass lumping scheme is used. Therefore, it applies also to the eight-noded hexahedral element with a single integration point we discussed in Chap. 10 as the element of choice for computational biomechanics of the brain.

11.6 Algorithm Verification

We follow the verification approach introduced in Chap. 10 where the results obtained by means of new algorithms of non-linear computational mechanics are compared with the solutions from the established algorithms. However, none of the existing weak form meshless methods of computational mechanics has been recognised by the research community as a gold standard yet. Therefore, following Chap. 10, also in this chapter, we use the results obtained from the established algorithms implemented in commercial non-linear finite element codes as a reference solution.

In the following sections, we present verification results for some of the algorithms described in this chapter: Meshless Total Lagrangian Explicit Dynamics (MTLED) framework, Modified Moving Least Square (MMLS) shape function for deformation interpolation and specialised visibility criterion for modelling surgical dissection/tissues rupture.

11.6.1 Meshless Total Lagrangian Explicit Dynamics (MTLED) Framework

The Meshless Total Lagrangian Explicit Dynamics (MTLED) framework has been verified by comparing the results obtained using this framework with the established finite element code (ABAQUS implicit dynamics non-linear solver [31]) that was used when modelling semi-confined uniaxial compression and shear of a cylinder made from a very soft (shear modulus of 1 kPa) hyperelastic (neo-Hookean) material. In the meshless discretisation of the cylinder, almost arbitrary node placement and hexahedral integration cells non-conforming to the geometry were used (Fig. 11.12).

For 20% compression and shear of the cylinder, the difference in the total reaction force on the displaced cylinder surface between MTLED framework and ABAQUS implicit finite element solver [31] was no more than 5% (Fig. 11.13a). The force—time histories obtained using the meshless framework—was qualitatively similar to those from the finite element method. The maximum relative difference in the computed deformations between the MTLED framework and ABAQUS was around 3.5% (it can be seen in Fig. 11.13b that some of the nodes in meshless discretisation do not sit exactly on the deformed finite element boundary).

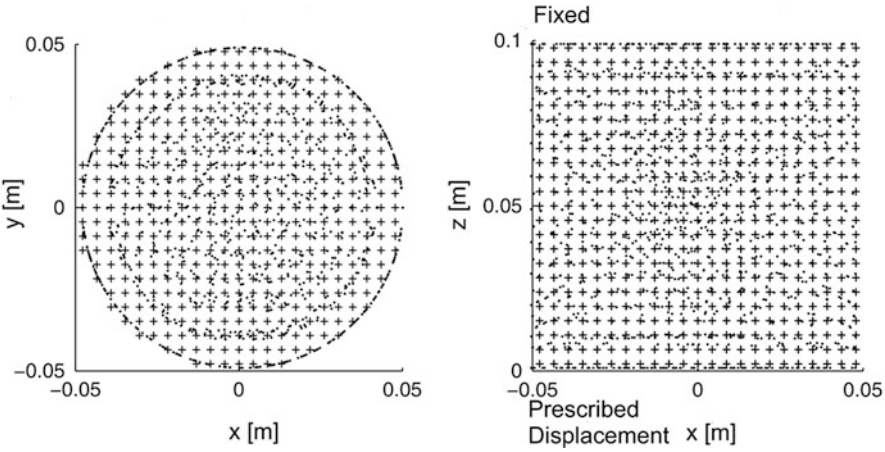

Fig. 11.12 Meshless model of a cylinder used in verification of the MTLED algorithm by Horton et al. [7]. The nodes are indicated as (.) and integration points as (+). Note almost arbitrary node placement. The integration points do not conform to geometry. The boundary conditions are shown in the right-hand-side figure: the nodes on the top boundary were constrained, and the prescribed displacement was applied to the nodes on the bottom boundary. (Adapted from Horton et al. [7])

The MTLED framework produces stable results even for very large deformations as indicated by the energy—time histories obtained when modelling the cylinder compressed to 20% of its original height (nominal compressive strain of 0.8) (Fig. 11.14). For such large compression, no verification against the ABAQUS finite solver could be done as the finite element solution became unstable. This is also demonstrated by recent results obtained when comparing the performance of the MTLED framework with the non-linear finite procedures available in ABAQUS solver in modelling of indentation of cylindrical samples made from soft incompressible material (Sylgard 527 silicone gel by Dow Corning) with properties similar to the brain tissue (Fig. 11.15a) [68]. The MTLED framework facilitates the solution for the indentation depth of 59% of the sample initial height, while the finite element procedures become unstable (the solution 'fails') for the indentation depth of 24% of the sample initial height (Fig. 11.15b, c).

11.6.2 Modified Moving Least Square (MMLS) Shape Functions for Computing Soft Tissue Deformation

We verified the performance of the MTLED framework with Modified Moving Least Square (MMLS) shape functions through application in modelling of an extension of a 2-D rectangular specimen (dimensions 10 cm × 4 cm) (Fig. 11.16) [27]. The results obtained using the MTLED framework were compared with well-established non-linear finite element code (ABAQUS static non-linear solver [31] with default configuration was used). Detailed description is provided in Joldes

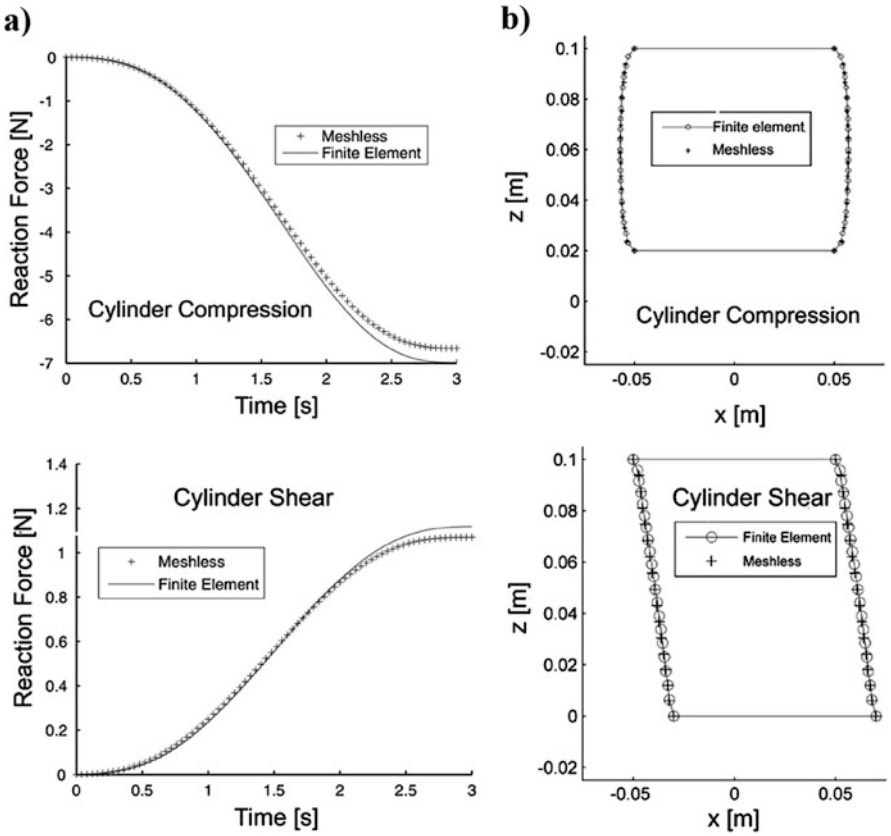

Fig. 11.13 Comparison of the results obtained when modelling 20% compression and shear of a cylinder using meshless (MTLED framework) and finite element (ABAQUS implicit solver [31]) discretisation. (**a**) Reaction force, time histories; (**b**) contour of the deformed cylinder at time of 3 s. The displacement u was enforced over a period $T = 3$ s using a 3-4-5 polynomial that ensures zero velocity and acceleration at time $t = 0$ and time $t = T$ [67]. The displacement magnitude was 0.02 m in z direction for compression and 0.02 m in x direction for shear. x and z directions are defined in Fig. 11.12. (Adapted from Horton et al. [7])

et al. [27]. The rectangular specimen was discretised using 57 nodes. To ensure the integration accuracy, a dense regular background integration grid was used. It consisted of 4000 rectangular integration cells with a single integration (Gauss) point per cell. The nodes on the left-hand-side edge of the specimen were rigidly constrained, while the displacement of 3 cm (30% of the initial specimen length) was applied to the nodes on the right-hand-side edge (Fig. 11.16a). In the finite element model implemented using the ABAQUS code, the spatial discretisation was done using 57 nodes and 84 four-noded rectangular elements.

As reported in Joldes et al. [27], the results indicate a very good agreement between the results obtained using the MTLED framework with MMLS shape

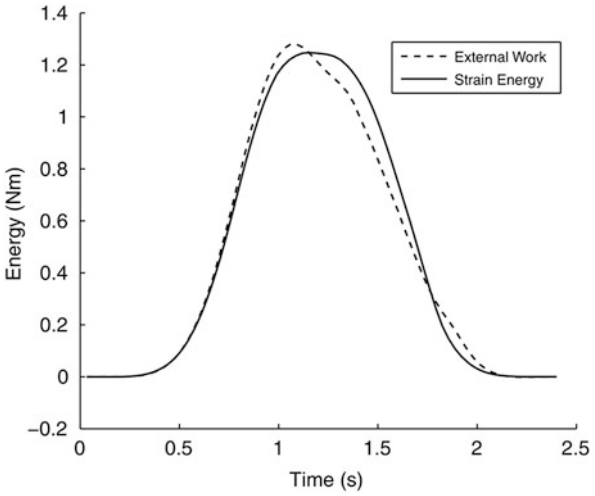

Fig. 11.14 MTLED algorithm. External work and strain energy when compressing a cylinder to 20% of its original height (and returning to the initial state). The displacement was enforced using a 3-4-5 polynomial [67]. (Adapted from Horton et al. [7])

functions and ABAQUS static non-linear finite element solver—the maximum difference in the computed deformations was under 0.5 mm (Fig. 11.16b). They also show appreciable accuracy improvement in comparison to the traditionally used Moving Least Square (MLS) shape functions. However, it should be noted that as the resolution of intra-operative (acquired during surgery) magnetic resonance images (MRIs) and accuracy of state-of-the-art neurosurgery techniques are not better than 1 mm [69], even the accuracy achieved using MLS can be confidently regarded as sufficient for application in image-guided neurosurgery.

11.6.3 Visibility Criterion for Modelling of Surgical Dissection and Soft Tissue Rupture

Verification of visibility criterion for modelling of surgical dissection and soft tissue rupture was conducted by Jin et al. [20] through application in simulation of dissection of a rectangular (dimensions 100 mm $\times$ 100 mm) specimen of soft hyperelastic material undergoing elongation of 20% of the initial length (Fig. 11.17). The neo-Hookean hyperelastic constitutive model [70], with the parameters (Young's modulus of $E = 3000$ Pa , Poisson's ratio of $\nu = 0.49$, mass density of $\rho = 1000$ kg/m^3) consistent with the brain tissue constitutive properties was used.

As discussed in Chap. 10, simulation of surgical dissection using the finite element method is associated with a number of formidable challenges/difficulties. They include deterioration of the solution accuracy when the elements forming the mesh become distorted under large deformations and the need for re-meshing to introduce a crack/discontinuity due to dissection/rupture and as a mesh distortion

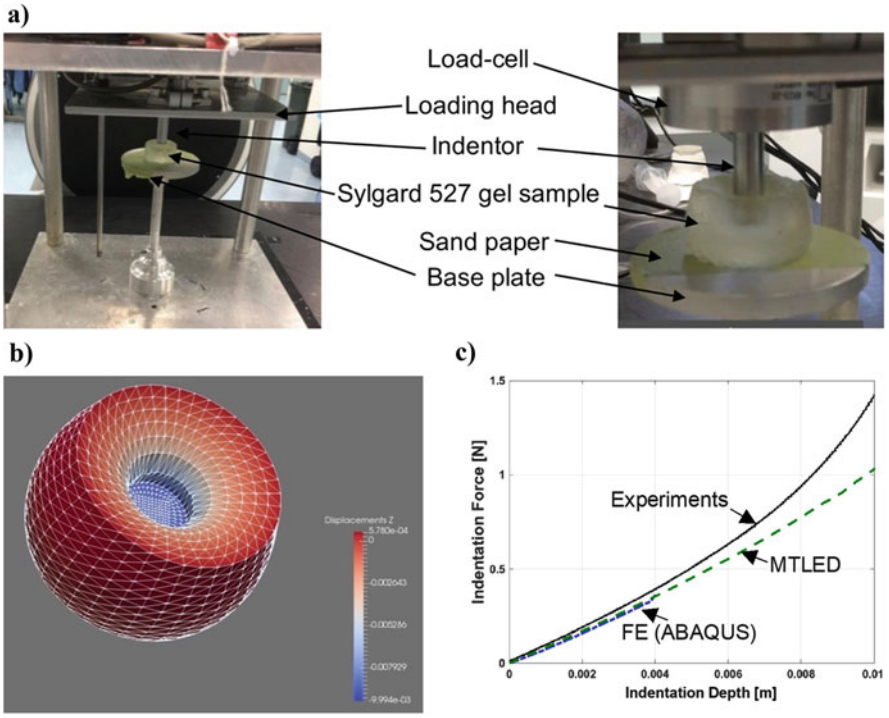

Fig. 11.15 Verification of the MTLED algorithm through modelling of indentation of cylindrical samples made from soft incompressible material (Sylgard 527 silicone gel by Dow Corning) with properties similar to the brain tissue. (**a**) Experimental set-up. (**b**) Overall deformation of the meshless model for the indentation depth of 10 mm (the displacement scale in the figure is in metres). The interpolating nodes were connected to form the triangles to visualise the deformed model surface. (**c**) Comparison of the force—indentation depth relationship obtained using the MTLED framework (green dotted line), non-linear finite element procedures available in ABAQUS finite element (FE) code (blue dotted line) and the experimental data (black solid line)—average from three experiments. Using ABAQUS finite element code [31], we were able to obtain the results for the indentation depth of up to only 4 mm after which the solution diverged. For the indentation depth of up to 4 mm, the results obtained using the MTLED framework and ABAQUS code are very close and cannot be visually distinguished. (Adapted from Wittek et al. [68])

countermeasure. Therefore, when obtaining the reference solution for verification of the MTLED framework with the visibility criterion using the established non-linear procedures available in the ABAQUS finite element code [31], surgical dissection could not be directly modelled. Instead, the elongation was applied to the finite element model of a specimen of soft hyperelastic material (with the brain tissue properties) with a predefined dissection/cut (detailed description is in Jin et al. [20]). The edges of the elements were aligned and separated along the dissection (Fig. 11.18). The analysis using the ABAQUS finite element code was conducted for implicit integration in time domain with the default parameters and linear (i.e. with linear shape functions) quadrilateral plain strain elements with hybrid formulation

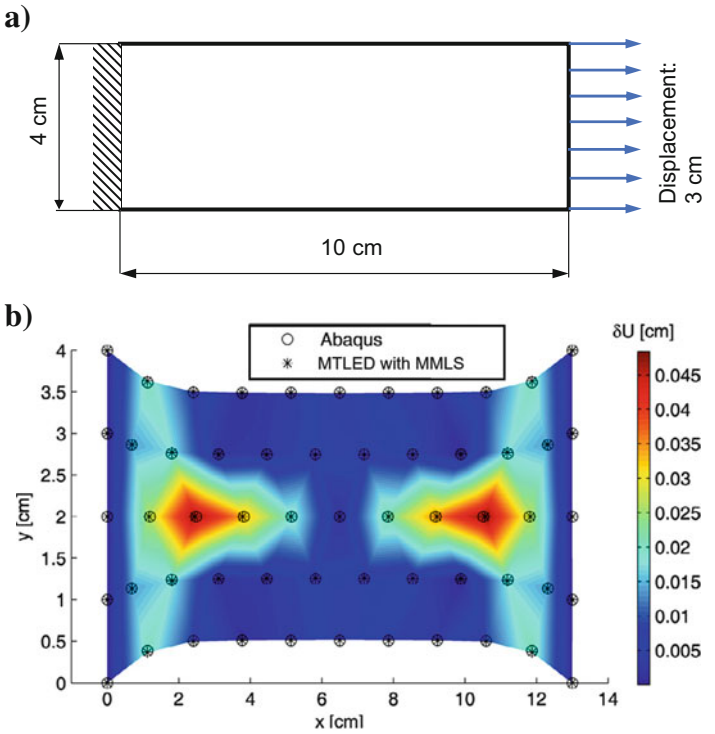

Fig. 11.16 Verification of the Modified Moving Least Square (MMLS) shape functions implemented in the MTLED framework through application in modelling of elongation of a rectangular specimen with the constitutive properties consistent with the brain tissue. (**a**) Geometry and boundary conditions for the model. (**b**) Differences in the computed deformations between the MTLED framework with MMLS shape functions and ABAQUS static non-linear finite element solver. (Adapted from Joldes et al. [27])

to prevent volumetric locking. It was confirmed through H-refinement (mesh density increase) that the finite element discretisation (using 7183 nodes) used in this analysis provides a converged solution. The meshless model implemented using the MTLED framework consisted of 6151 nodes (the discretisation density was confirmed using convergence analysis) (Fig. 11.19).

As the distribution and position of nodes in the meshless model implemented using the MTLED framework and finite element model implemented using the ABAQUS code were different, the nodal displacements obtained using the MTLED framework were recalculated (through interpolation using the MLS shape functions) for the nodal positions of the model implemented using the ABAQUS code to enable verification of the predicted deformations.

The verification results indicate a very good agreement between the internal forces and deformations predicted using the MTLED framework with visibility criterion and the reference finite element solution obtained using ABAQUS non-

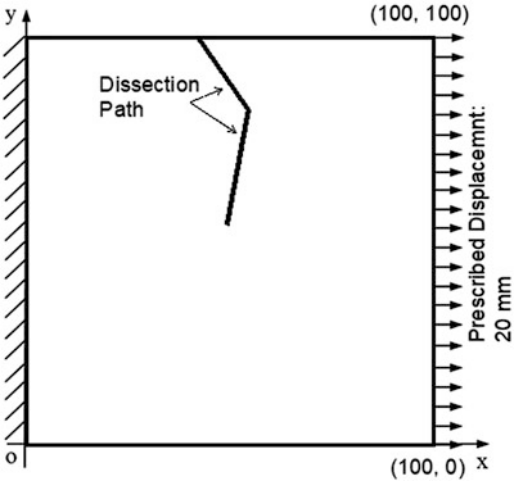

Fig. 11.17 Geometry for the model for verification of visibility criterion implemented in the Meshless Total Lagrangian Explicit Dynamics (MTLED) framework for modelling of surgical dissection and soft tissue rupture. The verification was conducted through application in simulation of dissection of a rectangular specimen of soft incompressible material with the brain tissue constitutive properties undergoing elongation of 20% of the initial length. (Adapted from Jin et al. [20])

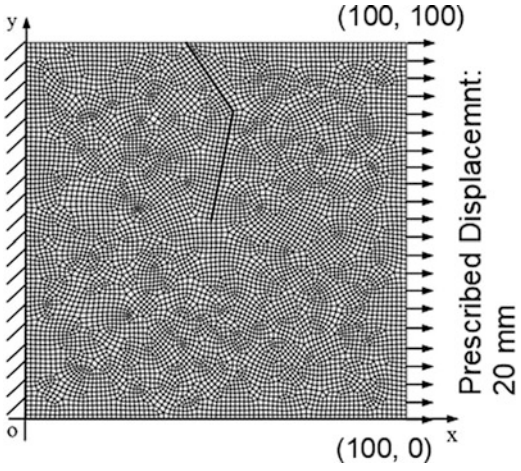

Fig. 11.18 The initial configuration of the finite element model with a predefined dissection/cut implemented using ABAQUS non-linear finite element code. The results obtained using this model were used as reference when verifying the Meshless Total Lagrangian Explicit Dynamics (MTLED) framework with visibility criterion for modelling of surgical dissection/soft tissue rupture. Dimensions are in millimetres (mm). (Adapted from Jin et al. [20])

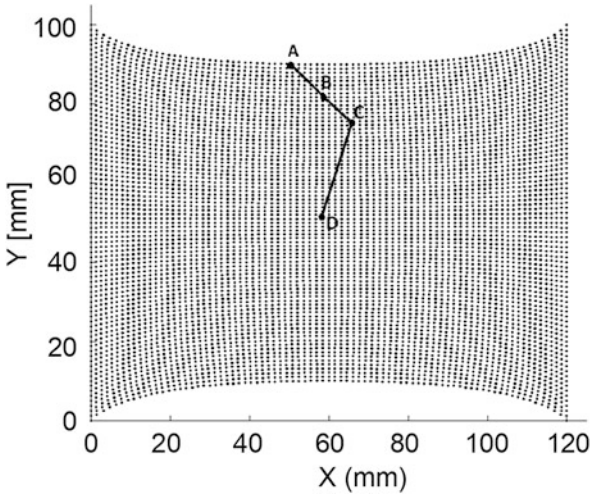

Fig. 11.19 Meshless model for verification of the Meshless Total Lagrangian Explicit Dynamics (MTLED) framework with visibility criterion for modelling of surgical dissection and tissue rupture. Spatial discretisation was done using 6151 nodes. In this model, the dissection was carried out in the stretched specimen of brain tissue-like material along the predefined path indicated using thick line segments. Dimensions are in millimetres (mm). (Adapted from Jin et al. [20])

linear code (a static procedure was used) (Fig. 11.20). The relative differences for the reaction force are only of 0.5%. The maximum absolute difference in the predicted deformations is 0.5 mm (2.56% of the imposed elongation), and the average difference (averaging over all model nodes) is only 0.03 mm (0.15% of the imposed elongation). Therefore, considering that the accuracy of state-of-the-art neurosurgery techniques is not better than 1 mm [69], Meshless Total Lagrangian Explicit Dynamics (MTLED) framework with visibility criterion for surgical dissection modelling can be regarded as satisfying the accuracy requirements of computer-integrated surgery.

11.7 Conclusions

The field of surgery simulation is dominated by finite element analysis. However, time-consuming generation of patient-specific finite element meshes (computational grids) and deterioration of the solution accuracy when the elements undergo distortion induced by large deformations due to surgery remain a formidable challenge that prevents computational biomechanics to become a part of surgical training and planning workflow [1]. For more than 10 years, we have advocated meshless methods of computational mechanics, in which the computational grid has the form of a 'cloud' of points, as one possible solution to overcome this challenge [1, 6, 7, 28, 29]. Based on our experience with both strong (smoothed particle hydrodynamics (SPH) and finite difference-collocation method) [14, 16] and weak [1, 6, 7, 28, 29] formulations of meshless methods of computational mechanics, for computational biomechanics of the brain, we recommend the weak formulation with background cells for spatial integration [7, 21]. We have used such integration in the Meshless Total Lagrangian Explicit Dynamics (MTLED) framework described

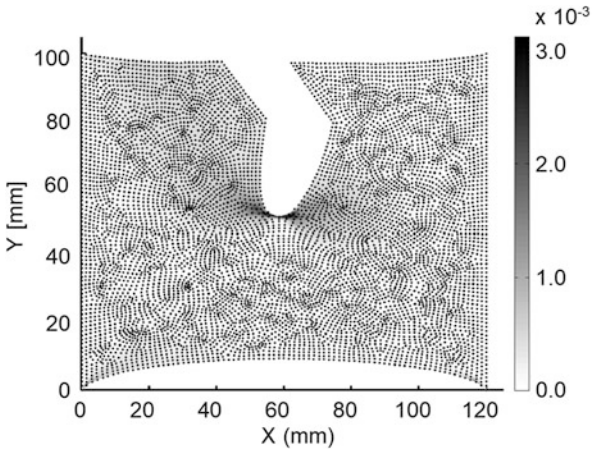

Fig. 11.20 Results of verification of Meshless Total Lagrangian Explicit Dynamics (MTLED) framework with visibility criterion for modelling of surgical dissection and tissue rupture: deformed meshless model implemented using the MTLED framework with the dissection modelled using visibility criterion. The figure shows the absolute difference between the deformation magnitudes computed using the MTLED framework and the reference results from the established non-linear static solution procedures available in the ABAQUS finite element code. The dimensions and deformations are in mm. (Adapted from Jin et al. [20])

in this chapter [7]. The MTLED framework retains all the advantages associated with the explicit stepping in time domain as discussed in Chap. 10 in the context of finite element method. They include the following: no need for iterations even for non-linear problems, no need to solve a system of equations, very modest internal memory requirements and suitability for parallel processing implementation.

We view meshless methods of computational mechanics not only as algorithms for computing the responses of soft tissues and body organs undergoing large deformations and fragmentation (due to surgical dissection and injury) but primarily as a framework that would enable an analyst (medical professional) who is not an expert in computational mechanics to create patient-specific computational biomechanics models of the brain and apply them in surgery simulation with a guarantee of numerical accuracy of the results. Modified Moving Least Square (MMLS) shape functions [27] and adaptive integration introduced [21] in the Meshless Total Lagrangian Explicit Dynamics framework are steps in this direction. They ensure accuracy and robustness of solution of the equations of continuum mechanics for irregular/non-homogenous nodal distributions that facilitate automated discretisation of the complex geometry of the brain and creation of computational grids directly from neuroimages [18]. Defining solution tolerance is the only input they require from the user.

The visibility criterion [20, 58] discussed and recommended in this chapter in the context of simulation of surgical dissection and injury-related tissue rupture leads to high computational cost when applied to three-dimensional dissection/rupture

propagation [59]. Therefore, development of meshless algorithms that facilitate efficient and robust modelling of surgical dissection and injury-related rupture of soft tissues provides the next challenge in surgery and injury simulation.

Acknowledgements This chapter uses the published results of research supported by the funding from the Australian Government through the Australian Research Council (ARC) (Discovery Project Grants DP160100714, DP1092893 and DP120100402) and National Health and Medical Research Council (NHMRC) (Project Grants APP1006031 and APP1144519). The authors thank Prof. King Hay Yang and Dr. Xin Jin of Bioengineering Centre and Biomedical Engineering Department of Wayne State University for providing the experimental data used in the reference [58].

References

1. Wittek, A., Grosland, N., Joldes, G., Magnotta, V., Miller, K.: From finite element meshes to clouds of points: a review of methods for generation of computational biomechanics models for patient-specific applications. Ann. Biomed. Eng. **44**, 3–15 (2016)
2. Wittek, A., Dutta-Roy, T., Taylor, Z., Horton, A., Washio, T., Chinzei, K., Miller, K.: Subject-specific non-linear biomechanical model of needle insertion into brain. Comput. Methods Biomech. Biomed. Engin. **11**, 135–146 (2008)
3. Belytschko, T., Krongauz, Y., Organ, D., Fleming, M., Krysl, P.: Meshless methods: an overview and recent developments. Comput. Methods Appl. Mech. Eng. **139**, 3–47 (1996)
4. Li, S., Liu, W.K.: Meshfree and particle methods and their applications. Appl. Mech. Rev. **55**, 1–34 (2002)
5. Sukumar, N., Dolbow, J., Devan, A., Yvonnet, J., Chinesta, F., Ryckelynck, D., Lorong, P., Alfaro, I., Martínez, M.A., Cueto, E., Doblaré, M.: Meshless methods and partition of unity finite elements. Int. J. Form. Process. **8**, 409–427 (2005)
6. Horton, A., Wittek, A., Miller, K.: Towards meshless methods for surgical simulation. In: Proceedings of the Computational Biomechanics for Medicine Workshop, Medical Image Computing and Computer-Assisted Intervention MICCAI 2006, pp. 34–42 (2006)
7. Horton, A., Wittek, A., Joldes, G.R., Miller, K.: A meshless Total Lagrangian explicit dynamics algorithm for surgical simulation. Int. J. Numer. Methods Biomed. Eng. **26**, 977–998 (2010)
8. Doblare, M., Cueto, E., Calvo, B., Martinez, M.A., Garcia, J.M., Cegonino, J.: On the employ of meshless methods in biomechanics. Comput. Methods Appl. Mech. Eng. **194**, 801–821 (2005)
9. Horton, A., Wittek, A., Miller, K.: Subject-specific biomechanical simulation of brain indentation using a meshless method. Lect. Notes Comput. Sci. **4791**, 541–548 (2007)
10. Zhang, G.Y., Wittek, A., Joldes, G.R., Jin, X., Miller, K.: A three-dimensional nonlinear meshfree algorithm for simulating mechanical responses of soft tissue. Eng. Anal. Bound. Elem. **42**, 60–66 (2014)
11. Monaghan, J.J.: Smoothed particle hydrodynamics. Annu. Rev. Astron. Astrophys. **30**, 543–574 (1992)
12. Ionescu, I., Guilkey, J., Berzins, M., Kirby, R.M., Weiss, J.: Computational simulation of penetrating trauma in biological soft tissues using the material point method. Stud. Health Technol. Inform. **111**, 213–218 (2005)
13. Hieber, S.S.E.: Remeshed smoothed particle hydrodynamics simulation of the mechanical behavior of human organs. Technol. Health Care. **12**, 305–314 (2004)
14. Wittek, A., Omori, K., Nakahira, Y.: Effects of brain-skull boundary conditions on responses of simplified finite element brain model under angular acceleration in sagittal plane. In: Proceedings of the Mechanical Engineering Congress, Tokushima, Japan, pp. 101–102. Japan Society of Mechanical Engineers (2003)

15. Maurel, B., Combescure, A., Potapov, S.: A robust SPH formulation for solids. Eur. J. Comput. Mech. **15**, 495–512 (2006)
16. Bourantas, G.C., Mountris, K.A., Loukopoulos, V.C., Lavier, L., Joldes, G.R., Wittek, A., Miller, K.: Strong-form approach to elasticity: hybrid finite difference-meshless collocation method (FDMCM). Appl. Math. Model. **57**, 316–338 (2018)
17. Toma, M.: The emerging use of SPH in biomedical applications. Significances Bioeng. Biosci. **1**, 1–4 (2017)
18. Zhang, Y.J., Joldes, G.R., Wittek, A., Miller, K.: Patient-specific computational biomechanics of the brain without segmentation and meshing. Int. J. Numer. Methods Biomed. Eng. **29**, 293–308 (2013)
19. Zhang, G.Y., Wittek, A., Joldes, G.R., Jin, X., Miller, K.: A three-dimensional nonlinear meshfree algorithm for simulating mechanical responses of soft tissue. Eng. Anal. Bound. Elem. **42**, 7 (2013)
20. Jin, X., Joldes, G.R., Miller, K., Yang, K.H., Wittek, A.: Meshless algorithm for soft tissue cutting in surgical simulation. Comput. Methods Biomech. Biomed. Engin. **17**, 800–817 (2014)
21. Joldes, G.R., Wittek, A., Miller, K.: Adaptive numerical integration in element-free Galerkin methods for elliptic boundary value problems. Eng. Anal. Bound. Elem. **51**, 52–63 (2015)
22. Chowdhury, H.A., Wittek, A., Miller, K., Joldes, G.R.: An element free Galerkin method based on the modified moving least squares approximation. J. Sci. Comput. **71**, 1197–1211 (2017)
23. Joldes, G.R., Chowdhury, H., Wittek, A., Miller, K.: A new method for essential boundary conditions imposition in explicit meshless methods. Eng. Anal. Bound. Elem. **80**, 94–104 (2017)
24. Joldes, G.R., Bourantas, G., Zwick, B., Chowdhury, H., Wittek, A., Agrawal, S., Mountris, K., Hyde, D., Warfield, S.K., Miller, K.: Suite of meshless algorithms for accurate computation of soft tissue deformation for surgical simulation. Med. Image Anal. **56**, 152–171 (2019)
25. Lancaster, P., Salkauskas, K.: Surfaces generated by moving least-squares methods. Math. Comput. **37**, 141–158 (1981)
26. Nayroles, B., Touzot, G., Villon, P.: Generalizing the finite element method: diffuse approximation and diffuse elements. Comput. Mech. **10**, 307–318 (1992)
27. Joldes, G.R., Chowdhury, H.A., Wittek, A., Doyle, B., Miller, K.: Modified moving least squares with polynomial bases for scattered data approximation. Appl. Math. Comput. **266**, 893–902 (2015)
28. Miller, K., Horton, A., Joldes, G.R., Wittek, A.: Beyond finite elements: a comprehensive, patient-specific neurosurgical simulation utilizing a meshless method. J. Biomech. **45**, 2698–2701 (2012)
29. Li, M., Miller, K., Joldes, G.R., Kikinis, R., Wittek, A.: Biomechanical model for computing deformations for whole-body image registration: a meshless approach. Int. J. Numer. Methods Biomed. Eng. **32**, e02771–e02718 (2016)
30. Heye, Z., Linwei, W., Hunter, P.J., Pengcheng, S.: Meshfree framework for image-derived modelling. In: 2008 5th IEEE International Symposium on Biomedical Imaging: From Nano to Macro, pp. 1449–1452 (2008)
31. A Dassault Systèmes Simulia Corporation: SIMULIA User Assistance 2018: ABAQUS (2018), Dassault Systemes, France
32. Chowdhury, H., Joldes, G., Wittek, A., Doyle, B., Pasternak, E., Miller, K.: Implementation of a modified moving least squares approximation for predicting soft tissue deformation using a meshless method. In: Doyle, B., Miller, K., Wittek, A., Nielsen, P.M.F. (eds.) Computational Biomechanics for Medicine, pp. 59–71. Springer International Publishing, Cham (2015)
33. Joldes, G.R., Teakle, P., Wittek, A., Miller, K.: Computation of accurate solutions when using element-free Galerkin methods for solving structural problems. Eng. Comput. **34**, 902–920 (2017)
34. Liu, G.R.: Mesh Free Methods: Moving Beyond the Finite Element Method. CRC Press, Boca Raton (2003)

35. Dolbow, J., Belytschko, T.: Numerical integration of the Galerkin weak form in meshfree methods. Comput. Mech. **23**, 219–230 (1999)
36. Beissel, S., Belytschko, T.: Nodal integration of the element-free Galerkin method. Comput. Methods Appl. Mech. Eng. **139**, 49–74 (1996)
37. Chen, J.-S., Wu, C.-T., Yoon, S., You, Y.: A stabilized conforming nodal integration for Galerkin mesh-free methods. Int. J. Numer. Methods Eng. **50**, 435–466 (2001)
38. Quak, W., van den Boogaard, A., González, D., Cueto, E.: A comparative study on the performance of meshless approximations and their integration. Comput. Mech. **48**, 121–137 (2011)
39. Wittek, A., Joldes, G., Miller, K.: Algorithms for computational biomechanics of the brain. In: Miller, K. (ed.) Biomechanics of the Brain, pp. 189–219. Springer, New York (2011)
40. Mor, A.B., Kanade, T.: Modifying soft tissue models: progressive cutting with minimal new element creation. In: Delp, S.L., DiGoia, A.M., Jaramaz, B. (eds.) Medical Image Computing and Computer-Assisted Intervention – MICCAI 2000, pp. 598–607. Springer, Berlin/Heidelberg (2000)
41. Bielser, D., Glardon, P., Teschner, M., Gross, M.: Interactive simulation of surgical cuts. Graph. Model. **66**, 116–125 (2004)
42. Courtecuisse, H., Jung, H., Allard, J., Duriez, C., Lee, D.Y., Cotin, S.: GPU-based real-time soft tissue deformation with cutting and haptic feedback. Prog. Biophys. Mol. Biol. **103**, 159–168 (2010)
43. Courtecuisse, H., Allard, J., Kerfriden, P., Bordas, S., Cotin, S., Duriez, C.: Real-time simulation of contact and cutting of heterogeneous soft-tissues. Med. Image Anal. **18**, 394–410 (2014)
44. Bui, H.P., Tomar, S., Courtecuisse, H., Cotin, S., Bordas, S.P.A.: Real-time error control for surgical simulation. IEEE Trans. Biomed. Eng. **65**, 596–607 (2018)
45. Cotin, S., Delingette, H., Ayache, N.: A hybrid elastic model for real-time cutting, deformations, and force feedback for surgery training and simulation. Vis. Comput. **16**, 437–452 (2000)
46. Belytschko, T., Lu, Y.Y., Gu, L.: Element-free Galerkin methods. Int. J. Numer. Methods Eng. **37**, 229–256 (1994)
47. Belytschko, T., Tabbara, M.: Dynamic fracture using element-free Galerkin methods. Int. J. Numer. Methods Eng. **39**, 923–938 (1996)
48. Belytschko, T., Organ, D., Gerlach, C.: Element-free Galerkin methods for dynamic fracture in concrete. Comput. Methods Appl. Mech. Eng. **187**, 385–399 (2000)
49. Rabczuk, T., Belytschko, T.: Adaptivity for structured meshfree particle methods in 2D and 3D. Int. J. Numer. Methods Eng. **63**, 1559–1582 (2005)
50. Bordas, S., Rabczuk, T., Zi, G.: Three-dimensional crack initiation, propagation, branching and junction in non-linear materials by an extended meshfree method without asymptotic enrichment. Eng. Fract. Mech. **75**, 943–960 (2008)
51. Ionescu, I., Weiss, J.A., Guilkey, J., Cole, M., Kirby, R.M., Berzins, M.: Ballistic injury simulation using the material point method. Stud. Health Technol. Inform. **119**, 228–233 (2006)
52. Rabczuk, T., Belytschko, T.: A three-dimensional large deformation meshfree method for arbitrary evolving cracks. Comput. Methods Appl. Mech. Eng. **196**, 2777–2799 (2007)
53. Belytschko, T., Krongauz, Y., Organ, D., Flaming, M., Krysl, P.: Meshless methods: an overview and recent developments. Comput. Methods Appl. Mech. Eng. **139**, 3–47 (1996)
54. Osher, S., Sethian, J.A.: Fronts propagating with curvature-dependent speed: algorithms based on Hamilton-Jacobi formulations. J. Comput. Phys. **79**, 12–49 (1988)
55. Stolarska, M., Chopp, D.L., Moës, N., Belytschko, T.: Modelling crack growth by level sets in the extended finite element method. Int. J. Numer. Methods Eng. **51**, 943–960 (2001)
56. Jin, X., Lee, J.B., Leung, L.Y., Zhang, L., Yang, K.H., King, A.I.: Biomechanical response of the bovine pia-arachnoid complex to tensile loading at varying strain-rates. Stapp Car Crash J. **50**, 637–649 (2006)
57. Jin, X.: Biomechanical response and constitutive modeling of bovine pia-arachnoid complex, p. 140. Wayne State University, Michigan (2009)

58. Jin, X., Zhang, G., Joldes, G.R., Yang, K.-H., Rohan, P.-Y., Miller, K., Wittek, A.: 2-D Meshless algorithm for modelling of soft tissue undergoing fragmentation and large deformation: Verification and performance evaluation. In: Proceedings of the 10th International Symposium on Computer Methods in Biomechanics and Biomedical Engineering, pp. 327–332. Arup (2012)
59. Jin, X., Joldes, G.R., Miller, K., Wittek, A.: 3D Algorithm for simulation of soft tissue cutting. In: Wittek, A., Miller, K., Nielsen, P.M.F. (eds.) Computational Biomechanics for Medicine: Models, Algorithms and Implementation, pp. 49–62. Springer, New York, ISBN 978-14614-6350-4 (2013)
60. Gültekin, O., Dal, H., Holzapfel, G.A.: A phase-field approach to model fracture of arterial walls: theory and finite element analysis. Comput. Methods Appl. Mech. Eng. **312**, 542–566 (2016)
61. Belytschko, T., Liu, W.K., Moran, B.: Nonlinear Finite Elements for Continua and Structures. Wiley, Chichester (2006)
62. Isaacson, E.: Analysis of Numerical Methods. Wiley, New York (1966)
63. Cook, R.D., Malkus, D.S., Plesha, M.E.: Finite elements in dynamics and vibrations. In: Concepts and Applications of Finite Element Analysis, pp. 367–428. Wiley, New York (1989)
64. Joldes, G.R., Wittek, A., Miller, K.: Stable time step estimates for mesh-free particle methods. Int. J. Numer. Methods Eng. **91**, 450–456 (2012)
65. Bathe, K.-J.: Finite Element Procedures. Prentice-Hall, Englewood Cliffs (1996)
66. Puso, M.A., Chen, J.S., Zywicz, E., Elmer, W.: Meshfree and finite element nodal integration methods. Int. J. Numer. Methods Eng. **74**, 416–446 (2008)
67. Waldron, K.J., Kinzel, G.L.: Kinematics, Dynamics, and Design of Machinery. Wiley, New York (1999)
68. Wittek, A., Bourantas, G., Joldes, G.R., Khau, A., Mountris, K., Singh, S., Miller, K.: Meshless method for simulation of needle insertion into soft tissues: preliminary results. In: Nash, M., Nielsen, P.M.F., Wittek, A., Miller, K., Joldes, G.R. (eds.) Computational Biomechanics for Medicine, p. 15. Springer (2018). Accepted for publication
69. Bucholz, R., MacNeil, W., McDurmont, L.: The operating room of the future. Clin. Neurosurg. **51**, 228–237 (2004)
70. Rivlin, R.S., Sawyers, K.N.: The strain-energy function for elastomers. Trans. Soc. Rheol. **20**, 545–557 (1976)

Chapter 12
Intra-operative Measurement of Brain Deformation

Sarah Frisken, Prashin Unadkat, Xiaochen Yang, Michael I. Miga, and Alexandra J. Golby

12.1 Introduction

For most patients, surgery is the first step for treating brain tumours. Many studies have shown that the amount of tumour removed, known as the *extent of resection*, is strongly correlated with both freedom from progression and survival [1–7]. However, brain tumours vary significantly from one patient to the next, may be hard to distinguish from surrounding healthy brain tissue, often infiltrate surrounding functional brain, and may be intimately involved with eloquent cortex and white matter tracts. Thus, complete resection is challenging and not always prudent.

During the past few decades, two important advancements have provided neurosurgeons with tools to help them maximise the extent of resection while avoiding damage to surrounding brain tissue (Fig. 12.1). The first is advanced 3D imaging, particularly, magnetic resonance imaging (MRI), which provides high-resolution anatomical images that can differentiate between healthy tissue and

S. Frisken (✉)
Department of Radiology, Brigham and Women's Hospital, Boston, MA, USA
e-mail: sfrisken@bwh.harvard.edu

P. Unadkat
Department of Radiology & Neurosurgery, Brigham and Women's Hospital, Boston, MA, USA

X. Yang
Department of Electrical Engineering and Computer Science, Vanderbilt University, Nashville, TN, USA

M. I. Miga
Department of Biomedical Engineering, Vanderbilt University, Nashville, TN, USA

A. J. Golby
Department of Neurosurgery, Brigham and Women's Hospital and Harvard Medical School, Boston, MA, USA

K. Miller (ed.), *Biomechanics of the Brain*, Biological and Medical Physics, Biomedical Engineering, https://doi.org/10.1007/978-3-030-04996-6_12

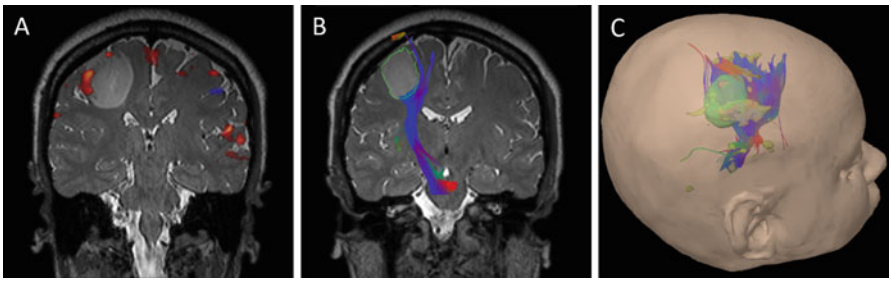

Fig. 12.1 A patient with a brain tumour surrounded by cortical regions and white matter tracts critical to motor function. (**a**) Functional MRI (fMRI) shows areas of the brain activated when the left hand is clenched. (**b**) Diffusion tensor imaging (DTI) shows white matter tracts associated with the motor cortex. (**c**) A neuronavigation system (Brainlab) provides a surgical view of the tumour, fMRI and DTI data relative to the skin surface, and tracked surgical instruments. Neuronavigation helps surgeons to plan their surgical approach. Registering these pre-operative images and the surgical plan to the patient's head in the operating room facilitates safer and more complete resections

tumour; functional MRI (fMRI) which identifies regions of the functional cortex such as the locations associated with speech, language comprehension, or motor control; and diffusion tensor imaging (DTI) which identifies white matter tracts.

The second advancement is neuronavigation. Neuronavigation systems register pre-operative images with the patient's head and the surgeon's instruments during surgery. They allow the surgeon to see the location of their instruments relative to the tumour and other critical structures in pre-operative images. Neuronavigation can be used to plan and execute an optimal surgical approach and to guide the neurosurgeon during surgery.

The use of neuronavigation has become standard in advanced neurosurgery operating rooms, and there are several commercial systems available (e.g. the Brainlab Curve [8] and Medtronic Stealth [9] systems). These systems map pre-operative image data to the patient's head using nonrigid registration via fiducial markers or surface registration. Although these methods are not always accurate, with care skull-skull registration errors can be limited to less than a few millimetres. Of larger concern is the fact that the brain deforms during surgery due to a phenomenon known as *brain shift*. Brain shift limits the value of rigid registration for mapping pre-operative image data to the deforming brain and tumour during surgery.

12.1.1 Brain Shift

Brain shift is the deformation of the brain that occurs during neurosurgery. It is caused by several factors indirectly related to surgery including gravity, head position, fluid drainage, use of hyperosmotic drugs, changes in intracranial pressure,

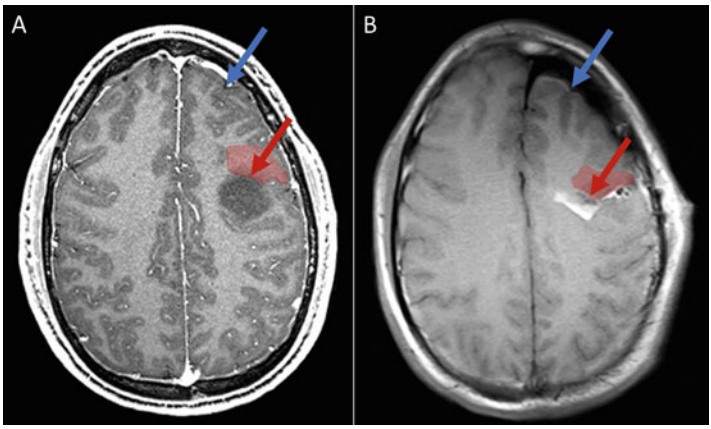

Fig. 12.2 (**a**) Pre-operative MRI showing a brain tumour (dark region). (**b**) Intra-operative MRI (iMRI) after near-complete resection with significant brain shift. Brain shift significantly reduces the validity of neuronavigation from pre-operative data. Brain shift can occur far from the surgical site (in blue). More clinically relevent, it can cause significant deformation and displacement near margins of the resection cavity (in red), precisely where surgeons could most benefit from accurate image guidance

and swelling of the brain tissue. It is also directly affected by the surgical intervention itself, i.e. by tissue retraction and tumour resection. Brain shift can range from a few millimetres to more than 25 mm, and it has been shown to be patient specific and highly nonlinear. As illustrated in Fig. 12.2, it is often greatest after significant resection and near tumour boundaries, which is precisely when and where accurate neuronavigation would be most beneficial. Brain shift has been measured and modelled for more than 20 years. For a comprehensive review of this work, we recommend recent reviews by Miga [10], Beyer et al. [11], and Gerard et al. [12]. In this chapter we provide some background on how brain shift has been measured and will focus on intra-operative measurement of brain shift.

12.2 Measuring Brain Shift

Brain shift was first reported by Kelly et al. [13], who placed small metal balls in the brain along the surgeon's line of sight to guide laser ablation surgery. Since then, there have been numerous studies to observe and measure brain shift during tumour resection [14–29], which typically involves craniotomies with diameter of several centimetres and deep brain stimulation (DBS) [30–35], which is often performed through a small burr hole of diameter 1 cm or less.

12.2.1 Quantitative Results

Measurement of brain shift has typically been made either by observing displacements of landmarks on the cortical surface or by comparing pre-operative images to images acquired during surgery or postoperatively. During tumour resection, maximum displacements of up to 25 mm for points on the cortical surface have been reported [17, 19, 23, 28]. Fahlbusch and Nimsky recorded brain shift at multiple time points during surgery using an open magnet. With this frequent imaging, they measured deformations that were larger than previously observed, with an average maximum cortical displacement of 21.1 mm, 23.8 mm, and 37.6 mm for small, medium, and large tumours, respectively [18]. At deep tumour margins, where precision is critical, they observed brain shift greater than 3 mm in 66% of patients, with low shifts (<2.9 mm) in 34% of cases, medium shifts (3–6.9 mm) in 42% of cases, and high shifts (>7 mm) in 24% of cases [19].

During burr hole procedures for DBS, maximum displacements of 10–13 mm for points on the cortical surface and smaller shifts of deep brain structures have been observed [30, 32, 33, 35]. The shifts for deep brain structures were noted to be large enough to compromise target location and to require multiple electrode adjustments. Winkler et al. measured shifts of 2 mm at the subthalamic nucleus, a target of DBS for Parkinson's patients with typical dimensions $1.2 \times 0.6 \times 0.3$ mm [30]. Ivan et al. also found that 9% of patients who had burr hole surgery for electrode placement had greater than 2 mm shifts at the target location [35].

In related studies, Schnaudigel et al. [36] found that changing the head orientation (left to right and supine to prone) in healthy subjects resulted in brain shifts of almost 2 mm, and Faria et al. [37] measured up to 3 mm of brain deformation at the cortical surface due to pulsatile motion from breathing and blood flow.

12.2.2 Qualitative Observations

Measurement of brain shift has shown that it is a complex phenomenon. It varies by tumour location, head position, previous radiation treatment, tumour size, craniotomy size, and brain swelling [18]. Brain shift occurs both perpendicular to and tangential to the craniotomy. There can be a significant difference between cortical and subcortical brain shifts which researchers conclude cannot be predicted from pre-operative imaging by biomechanical models [24] and particularly by models that rely on gravity alone [21]. Significant deformation has been demonstrated to occur even before resection begins [14, 27]. In addition, brain shift is time dependent. It occurs throughout surgery and is nonuniform over time with large shifts occurring when opening cysts, moderate shifts occurring during tumour resection, and more gradual shifts occurring nearly continuously [20]. This work suggests that biomechanical models of brain shift and neuronavigation systems that handle brain shift will require intra-operative measurements to maintain accuracy.

12.2.3 Neuronavigation with Brain Shift

There are two basic approaches for updating neuronavigation during surgery in the presence of brain shift. The first approach replaces pre-operative images with images acquired during surgery and allows neurosurgeons to navigate from these new images. The second approach, known as brain shift compensation, measures brain shift intra-operatively and uses these measurements to update pre-operative images (e.g. by deforming them to match the brain-shifted brain).

12.2.3.1 Replacing Pre-operative Images with Intra-operative Images

In the late 1990s and early 2000s, a number of intra-operative MRI (iMRI) systems were developed which combined MRI imaging with surgical access to the patient. The first of these was a 0.5 T GE Signa 'double donut' open magnet system installed at Brigham and Women's Hospital in 1994 (Fig. 12.3) [20, 38–40]. This system allowed full access to the patient with frequent imaging, so that up-to-date images of the brain-shifted brain and residual tumour could be used for neuronavigation. Several variations were developed with magnet strengths ranging from 0.2 T to 3 T and patient access ranging from full access during imaging to intermittent access with patient transfer from the operating room to an adjacent MR imaging suite. These systems include a radio frequency-shielded operating room with a 0.2 T magnet that Siemens installed at the University of Erlangen-Nuremberg in 1996 [18], the BrainSUITE (Brainlab AG, Feldkirchen, Germany), an IMRIS system (IMRIS, Winnipeg, Manitoba, Canada), the PoleStar iMRI (Medtronic Navigation, Louisville, Colorado, USA), and a number of hybrid systems [40].

Fig. 12.3 MR-guided therapy open magnet system, located at Brigham and Women's Hospital between 1994 and 2008. This specially designed GE Signa magnet with an open configuration provided surgical access to the patient while they were in the MRI and facilitated frequent image updating for neuronavigation. The system consisted of two annuli separated by about 60 cm, with the patient in either a coaxial or radial position. It had a 30 cm diameter imaging volume and operated at 0.5 T

iMRI has the advantage that it can provide high-resolution images of the full brain that are familiar and relatively easy to interpret by neurosurgeons. In addition, some iMRI systems can provide additional fMRI or DTI. Unfortunately, iMRI systems are expensive; they require specialised equipment and a specially trained surgical team. The early vision of performing neurosurgery for tumour resection in the magnet has been mostly replaced by convenient access to an MRI scanner, either by transferring the patient or moving the scanner (see Fig. 12.5). While it has proven effective for improving the extent of resection [41–43], this approach is time consuming and disruptive to surgery, making it impractical to use iMRI to update neuronavigation frequently during surgery.

In contrast, intra-operative ultrasound (iUS) only provides a limited field of view through the craniotomy, is hard to interpret, and is unfamiliar to most neurosurgeons. On the other hand, it is much less expensive and more readily available than iMRI and is less disruptive to surgery. A number of groups have used 2D or 3D iUS for direct navigation during neurosurgery [44–50]. SINTEF and the Norwegian National Advisory Unit for Ultrasound and Image-Guided Therapy have offered a course in the use of iUS in neurosurgery since 2008 [51]. This course covers both direct navigation from iUS and measurement of brain shift using iUS. Steno et al. [49] recently reported a retrospective study comparing outcomes when using conventional neuronavigation based on pre-operative MRI that doesn't account for brain shift to outcomes when using neuronavigation based on iUS. They found that the iUS system improved the extent of resection (EOR) with no adverse effects on outcome. With the iUS system, the median EOR improved from 75.9% to 87.1%, and the mean EOR improved from 86.8% to 93.5%.

12.2.3.2 Brain Shift Compensation

Figure 12.4 illustrates the brain shift compensation process. Pre-operatively, image data such as MRI, fMRI, and DTI are acquired, processed, and used to create a presurgical plan. At the start of surgery, the presurgical plan is input into a

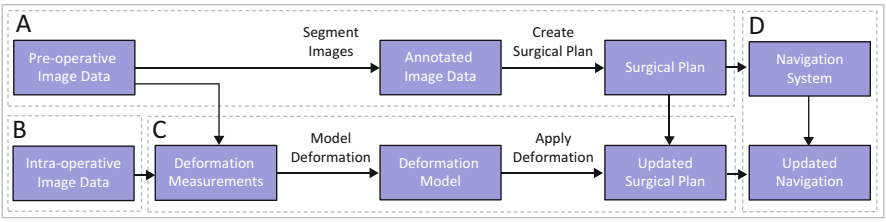

Fig. 12.4 Brain shift compensation process. (**a**) T1- and T2-weighted MRI and, when clinically indicated, fMRI and DTI are acquired pre-operatively. (**b**) Intra-operative data, such as iMRI, iUS, or stereo pairs of the exposed cortical surface, are acquired intra-operatively and used. (**c**) to measure and model deformation due to brain shift. (**d**) This deformation is applied to pre-operative image data to map it into the deformed space for navigation

neuronavigation system, registered to the patient, and used to guide the initial surgical approach. During surgery, intra-operative imaging is used to measure brain shift. Several different sources of intra-operative image data have been used to measure brain shift, including iMRI [20, 52–54], iUS [25, 55–62], and 3D models of the exposed cortical surface obtained using laser range scanning [63, 64] or surface reconstruction from stereo image pairs [65]. Given these measurements of brain shift, there are two standard methods for modelling brain deformation: biomechanical modelling (reviewed in Chap. 6 of this book and in [10, 66]) and nonrigid image registration (reviewed in [11]). The deformation model can then be applied to pre-operative image data to map it to the true shape of the brain during surgery.

12.3 Intra-operative Imaging Methods

Systems that compensate for brain shift require intra-operative measurement of brain deformation. Ideally, measurements should be acquired at frequent intervals, cause minimal disruption to surgery, and support accurate modelling of brain shift, particularly near tumour margins (e.g. accurate to within 1–2 mm). The most common methods that have been used to measure brain shift are iMRI, iUS, and measurements of cortical surface displacements.

12.3.1 Intra-operative MRI and Computed Tomography

While the early vision of performing tumour resections in an open magnet has not proven to be commercially viable, several systems have been developed that combine an operating room with convenient access to MR imaging, either by moving the patient or the scanner. To date, more than 200 such systems have been installed. Figure 12.5 shows the Advanced Multimodality Image-Guided Operating Suite (AMIGO) [67], an early system of this type, which was installed at Brigham and Women's Hospital in Boston, MA in 2011. This facility is used for both research and for clinical procedures, including neurosurgery for tumour resection. AMIGO includes a PET/CT room, operating room, and MR room. Video integration enables visualisation of navigation and other video sources. The combined use of MRI and CT with PET allows the clinicians to integrate anatomical, functional, and metabolic information that helps in decision-making during tumour resections.

AMIGO and similar systems provide iMRI that can be used to measure brain shift. However, frequent image updates in these systems are impractical because they require moving either the magnet or the patient between adjoining rooms. In AMIGO, iMRI is typically performed only once per procedure during brain tumour resections. While this limitation, coupled with the complex progression

Fig. 12.5 A view through the AMIGO Suite's advanced operating room into the adjoining MR imaging room. The doors to the adjoining room are closed during most of the procedure so that standard equipment can be used for surgery. When the surgeon needs an updated image of residual tumour, non-magnet safe equipment are removed from the operating room, the doors are opened, and the magnet is moved into the operating room on ceiling mounted rails. After imaging, this process is reversed and surgery can resume. Moving the equipment and the magnet adds significant time to the surgical procedure, so iMRI is typically only performed once per surgery

of brain shift during surgery, means that these systems cannot be used for direct neuronavigation, iMRI has been used by several groups to measure brain shift [16, 19, 21–23, 30–35]. Brain shift that occurs between pre-operative and intra-operative (or postoperative) imaging can be measured either by computing displacements between homologous landmarks in pre-operative and intra-operative images or deformation derived from nonrigid image registration [11].

Researchers have used similar methods to measure brain shift using computed tomography (CT) in animal models [68, 69] and in humans via contrast-enhanced cone-beam CT [28].

12.3.2 Measuring Cortical Surface Displacement

An alternative to iMRI that can provide frequent measurements of brain shift is to combine a biomechanical model of the brain with measurements of deformation of the cortical surface of the brain. These 'sparse' measurements can be used as boundary conditions to drive the biomechanical model [70]. The biomechanical model can then generate a deformation field that can be used for brain shift compensation. There are a number of methods for measuring deformations of the cortical surface.

Several groups have measured the displacements of landmarks on the exposed cortical surface during tumour resections [14, 17, 24] and DBS surgery [71]. Figure 12.6 is an image of the brain cortex exposed with a craniotomy for tumour

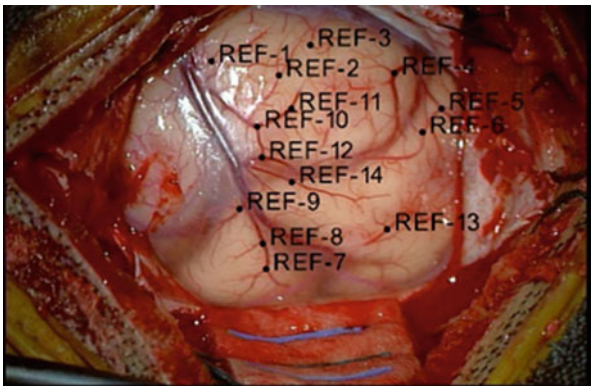

Fig. 12.6 An image of the cortical surface of a brain after it has been exposed with a craniotomy but before tumour resection. The image has been marked up with landmarks to be collected at intervals during surgery to track deformation of the brain surface

resection. To track surface landmarks (typically blood vessel bifurcations), the image is marked up with initial landmark locations and presented to the surgeon on a video display. The surgeon uses a pointing device equipped with an optical or electromagnetic tracker and registered to the neuronavigation system to record the location of each landmark. This process is repeated at multiple time points during surgery. Displacements between homologous landmarks are used to drive a patient-specific biomechanical model of the brain and estimate brain shift throughout the brain.

A 3D model of the exposed cortical surface can be acquired using either laser range scanning (LSR) [27, 64, 72–76] or 3D surface reconstruction from stereo image pairs [37, 65, 77–80]. A commercial laser range scanning system can be used to acquire the locations of a cloud of points on the exposed cortical surface at multiple time points during surgery. Homologous points in a sequence of LSR images can be tracked and their displacements used to drive a biomechanical model. For reconstruction from stereo image pairs, stereo cameras can be incorporated into the surgical microscope so that images can be acquired frequently during surgery. Figure 12.7 illustrates the process used to reconstruct shape from stereo image pairs in a phantom. First, a pair of images from images acquired through the left and right microscope ocular lenses is acquired. These images are then corrected for deformation and processed to derive a disparity map, which encodes the distance of the surface from the cameras and can be used to reconstruct a 3D model of the surface [80–82].

The major challenge for measuring the deformation of the cortical surface is illustrated in Fig. 12.8. On the left is the exposed cortical surface prior to resection. On the right is the same surface part way through surgery. Small craniotomies may limit the number of landmarks that can be tracked. As surgery progresses, landmarks visible at the beginning of surgery may be obscured or removed during surgery. In addition, conditions of the surface, including lighting, the presence of blood or other fluid, surgical instruments, and other devices, can result in poor performance from surface reconstruction methods.

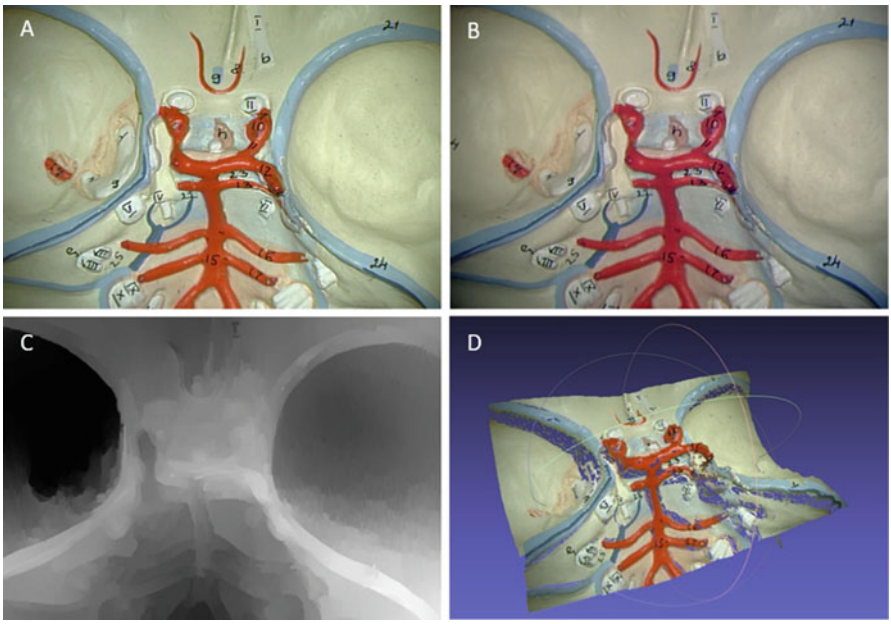

Fig. 12.7 Construction of a 3D surface from a stereo image pair. (**a**) An image of a skull phantom taken through the left ocular lens of the surgical microscope in AMIGO. (**b**) An image of the same view taken through the right ocular lens. (**c**) A disparity map encoding distance from the camera calculated for the images of (**a**) and (**b**). (**d**) A 3D model of the skull phantom reconstructed from the disparity map of (**c**)

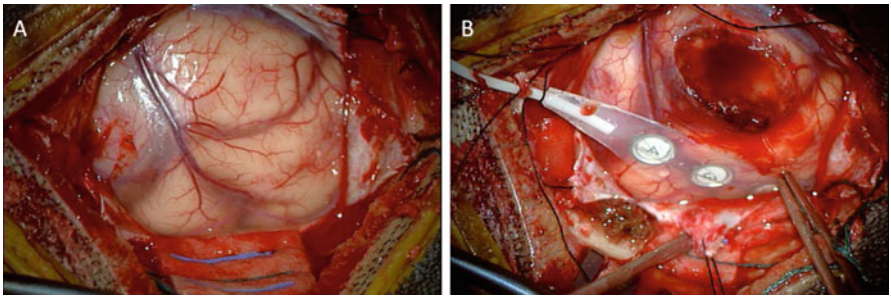

Fig. 12.8 Surface conditions (**a**) before and (**b**) during tumour resection can interfere with the ability to measure the deformation of the exposed cortical surface. Landmarks visible at the beginning of surgery may be obscured or missing later in surgery. In addition, specular reflections, fluid, focus, surgical instruments, and other recording devices such as the electrodes shown here can result in poor surface tracking

12.3.3 Intra-operative Ultrasound

3D iUS is a promising technology for measuring and monitoring brain shift during tumour resection. 3D ultrasound can be reconstructed from tracked 2D US as described in [83]. Commercial navigation systems, such as the Brainlab Curve [8], have begun to support the use of 3D iUS for direct navigation and for export via OpenIGTLink [84] for research in brain shift compensation. Several groups have used iUS to measure brain shift since 1997, including [15, 25, 26, 60, 85–88]. Reinertsen and her colleagues have used Doppler US to measure the displacements of blood vessels in the brain and used these to model brain shift [89, 90]. Mohammedi et al. combined vessel tracking using Doppler US with stereo images of the cortical surface to provide both surface and interior boundary conditions to drive a patient-specific finite element model of the brain [91]. Morin et al. combined vessel tracking using Doppler US with B-mode US of the cortical surface [92]. Finally, transcranial ultrasound has been investigated as a noninvasive way to track brain shift without interfering with the surgical field [93]. However, many neurosurgeons are not trained to interpret US, and there are several practical challenges when using transcranial US including ensuring a sterile field, requiring a craniotomy large enough for the US probe, maintaining good fluid contact, and deformation of the brain surface by the US probe which can impact deformation measurements. Recent work has proposed a method to correct for surface contact deformation in iUS [94, 95].

12.4 Conclusion

In summary, brain shift invalidates the assumption of most neuronavigation systems that pre-operative image data can be rigidly registered to the patient during surgery. Brain shift can be as large as 25 mm at the cortical surface and is often greater than 3 mm at the deep tumour margin, where precision is required to achieve good outcomes. Thus, it is critical that brain shift be accounted for in neuronavigation. However, brain shift is complex, patient, and tumour specific, varies throughout the brain, changes throughout surgery, and depends on many variables that are hard to predict and model pre-operatively. For these reasons, the need to measure and compensate for brain shift has been recognised by neurosurgeons and the neuronavigation industry. Until recently, interventional and intra-operative MRI has been the gold standard for handling brain shift. However, these systems are expensive and disruptive to surgery, require a special surgical environment, and are not available at most neurosurgical centres. Fortunately, several new technologies have emerged for tracking brain shift both at the brain surface and deep structures. We expect these technologies to lead to affordable neuronavigation systems that can compensate for brain shift without disrupting the surgical workflow.

Acknowledgements This work was supported by NIH research grants R01NS049251, P41-EB-015902, and P41-EB015898-09.

References

1. Brown, T.J., Brennan, M.C., Li, M., Church, E.W., Brandmeir, N.J., Rakszawski, K.L., Patel, A.S., Rizk, E.B., Suki, D., Sawaya, R., Glantz, M.: Association of the extent of resection with survival in glioblastoma: a systematic review and meta-analysis. JAMA Oncol. **2**(11), 1460–1469 (2016)
2. Berger, M.S., Deliganis, A.V., Dobbins, J., Keles, G.E.: The effect of extent of resection on recurrence in patients with low grade cerebral hemisphere gliomas. Cancer. **74**(6), 1784–1791 (1994)
3. Claus, E.B., Horlacher, A., Hsu, L., Schwartz, R.B., Dello-Iacono, D., Talos, F., Jolesz, F.A., Black, P.M.: Survival rates in patients with low-grade glioma after intraoperative magnetic resonance image guidance. Cancer. **103**(6), 1227–1233 (2005)
4. Sanai, N., Polley, M.Y., McDermott, M.W., Parsa, A.T., Berger, M.S.: An extent of resection threshold for newly diagnosed glioblastomas. J. Neurosurg. **115**(1), 3–8 (2011)
5. Piepmeier, J., Christopher, S., Spencer, D., Byrne, T., Kim, J., Knisel, J.P., Lacy, J., Tsukerman, L., Makuch, R.: Variations in the natural history and survival of patients with supratentorial low-grade astrocytomas. Neurosurgery. **38**(5), 872–878; discussion 878–879 (1996)
6. Chaichana, K.L., Jusue-Torres, I., Navarro-Ramirez, R., Raza, S.M., Pascual-Gallego, M., Ibrahim, A., Hernandez-Hermann, M., Gomez, L., Ye, X., Weingart, J.D., Olivi, A., Blakeley, J., Gallia, G.L., Lim, M., Brem, H., Quinones-Hinojosa, A.: Establishing percent resection and residual volume thresholds affecting survival and recurrence for patients with newly diagnosed intracranial glioblastoma. Neuro-Oncology. **16**(1), 113–122 (2014)
7. Coburger, J., Merkel, A., Scherer, M., Schwartz, F., Gessler, F., Roder, C., Pala, A., Konig, R., Bullinger, L., Nagel, G., Jungk, C., Bisdas, S., Nabavi, A., Ganslandt, O., Seifert, V., Tatagiba, M., Senft, C., Mehdorn, M., Unterberg, A.W., Rossler, K., Wirtz, C.R.: Low-grade glioma surgery in intraoperative magnetic resonance imaging: results of a multicenter retrospective assessment of the German Study Group for Intraoperative Magnetic Resonance Imaging. Neurosurgery. **78**(6), 775–786 (2016)
8. Brainlab AG, Munich Germany. https://www.brainlab.com/en/surgery-products/overview-neurosurgery-products/cranial-navigation/ (2018)
9. Medtronics Stealth Station Surgical Navigation System. https://www.medtronic.com/us-en/healthcare-professionals/products/neurological/surgical-navigation-systems/stealthstation/cranial-neurosurgery-navigation.html (2018)
10. Miga, M.I.: Computational modeling for enhancing soft tissue image guided surgery: an application in neurosurgery. Ann. Biomed. Eng. **44**(1), 128–138 (2016)
11. Bayer, S., Maier, A., Ostermeier, M., Fahrig, R.: Intraoperative imaging modalities and compensation for brain shift in tumor resection surgery. Int. J. Biomed. Imaging. **2017**, 6028645 (2017)
12. Gerard, I.J., Kersten-Oertel, M., Petrecca, K., Sirhan, D., Hall, J.A., Collins, D.L.: Brain shift in neuronavigation of brain tumors: a review. Med. Image Anal. **35**, 403–420 (2017)
13. Kelly, P.J., Kall, B.A., Goerss, S., Earnest, F.t.: Computer-assisted stereotaxic laser resection of intra-axial brain neoplasms. J. Neurosurg. **64**(3), 427–439 (1986)
14. Hill, D.L., Maurer Jr., C.R., Maciunas, R.J., Barwise, J.A., Fitzpatrick, J.M., Wang, M.Y.: Measurement of intraoperative brain surface deformation under a craniotomy. Neurosurgery. **43**(3), 514–526; discussion 527–528 (1998)
15. Jodicke, A., Deinsberger, W., Erbe, H., Kriete, A., Boker, D.K.: Intraoperative three-dimensional ultrasonography: an approach to register brain shift using multidimensional image processing. Minim. Invasive Neurosurg. **41**(1), 13–19 (1998)

16. Maurer Jr., C.R., Hill, D.L., Martin, A.J., Liu, H., McCue, M., Rueckert, D., Lloret, D., Hall, W.A., Maxwell, R.E., Hawkes, D.J., Truwit, C.L.: Investigation of intraoperative brain deformation using a 1.5-T interventional MR system: preliminary results. IEEE Trans. Med. Imaging. **17**(5), 817–825 (1998)
17. Roberts, D.W., Hartov, A., Kennedy, F.E., Miga, M.I., Paulsen, K.D.: Intraoperative brain shift and deformation: a quantitative analysis of cortical displacement in 28 cases. Neurosurgery. **43**(4), 749–758; discussion 758–760 (1998)
18. Fahlbusch, R., Ganslandt, O., Nimsky, C.: Intraoperative imaging with open magnetic resonance imaging and neuronavigation. Childs Nerv. Syst. **16**(10–11), 829–831 (2000)
19. Nimsky, C., Ganslandt, O., Cerny, S., Hastreiter, P., Greiner, G., Fahlbusch, R.: Quantification of, visualization of, and compensation for brain shift using intraoperative magnetic resonance imaging. Neurosurgery. **47**(5), 1070–1079; discussion 1079–1080 (2000)
20. Ferrant, M., Nabavi, A., Macq, B., Black, P.M., Jolesz, F.A., Kikinis, R., Warfield, S.K.: Serial registration of intraoperative MR images of the brain. Med. Image Anal. **6**(4), 337–359 (2002)
21. Hartkens, T., Hill, D.L., Castellano-Smith, A.D., Hawkes, D.J., Maurer Jr., C.R., Martin, A.J., Hall, W.A., Liu, H., Truwit, C.L.: Measurement and analysis of brain deformation during neurosurgery. IEEE Trans. Med. Imaging. **22**(1), 82–92 (2003)
22. Hastreiter, P., Rezk-Salama, C., Soza, G., Bauer, M., Greiner, G., Fahlbusch, R., Ganslandt, O., Nimsky, C.: Strategies for brain shift evaluation. Med. Image Anal. **8**(4), 447–464 (2004)
23. Trantakis, C., Tittgemeyer, M., Schneider, J.P., Lindner, D., Winkler, D., Strauss, G., Meixensberger, J.: Investigation of time-dependency of intracranial brain shift and its relation to the extent of tumor removal using intra-operative MRI. Neurol. Res. **25**(1), 9–12 (2003)
24. Reinges, M.H., Nguyen, H.H., Krings, T., Hutter, B.O., Rohde, V., Gilsbach, J.M.: Course of brain shift during microsurgical resection of supratentorial cerebral lesions: limits of conventional neuronavigation. Acta Neurochir. **146**(4), 369–377; discussion 377 (2004)
25. Letteboer, M.M., Willems, P.W., Viergever, M.A., Niessen, W.J.: Brain shift estimation in image-guided neurosurgery using 3-D ultrasound. I.E.E.E. Trans. Biomed. Eng. **52**(2), 268–276 (2005)
26. Coenen, V.A., Krings, T., Weidemann, J., Hans, F.J., Reinacher, P., Gilsbach, J.M., Rohde, V.: Sequential visualization of brain and fiber tract deformation during intracranial surgery with three-dimensional ultrasound: an approach to evaluate the effect of brain shift. Neurosurgery. **56**(1 Suppl), 133–141; discussion 133–141 (2005)
27. Ding, S., Miga, M.I., Thompson, R.C., Dumpuri, P., Cao, A., Dawant, B.M.: Estimation of intra-operative brain shift using a tracked laser range scanner. Proc. IEEE Eng. Med. Biol. Soc. **2007**, 848–851 (2007)
28. Pereira, V.M., Smit-Ockeloen, I., Brina, O., Babic, D., Breeuwer, M., Schaller, K., Lovblad, K.O., Ruijters, D.: Volumetric measurements of brain shift using intraoperative cone-beam computed tomography: preliminary study. Oper. Neurosurg. (Hagerstown). **12**(1), 4–13 (2016)
29. Nauta, H.J.: Error assessment during "image guided" and "imaging interactive" stereotactic surgery. Comput. Med. Imaging Graph. **18**(4), 279–287 (1994)
30. Winkler, D., Tittgemeyer, M., Schwarz, J., Preul, C., Strecker, K., Meixensberger, J.: The first evaluation of brain shift during functional neurosurgery by deformation field analysis. J. Neurol. Neurosurg. Psychiatry. **76**(8), 1161–1163 (2005)
31. Elias, W.J., Fu, K.M., Frysinger, R.C.: Cortical and subcortical brain shift during stereotactic procedures. J. Neurosurg. **107**(5), 983–988 (2007)
32. Halpern, C.H., Danish, S.F., Baltuch, G.H., Jaggi, J.L.: Brain shift during deep brain stimulation surgery for Parkinson's disease. Stereotact. Funct. Neurosurg. **86**(1), 37–43 (2008)
33. Hunsche, S., Sauner, D., Maarouf, M., Poggenborg, J., Lackner, K., Sturm, V., Treuer, H.: Intraoperative X-ray detection and MRI-based quantification of brain shift effects subsequent to implantation of the first electrode in bilateral implantation of deep brain stimulation electrodes. Stereotact. Funct. Neurosurg. **87**(5), 322–329 (2009)

34. Sillay, K.A., Kumbier, L.M., Ross, C., Brady, M., Alexander, A., Gupta, A., Adluru, N., Miranpuri, G.S., Williams, J.C.: Perioperative brain shift and deep brain stimulating electrode deformation analysis: implications for rigid and non-rigid devices. Ann. Biomed. Eng. **41**(2), 293–304 (2013)
35. Ivan, M.E., Yarlagadda, J., Saxena, A.P., Martin, A.J., Starr, P.A., Sootsman, W.K., Larson, P.S.: Brain shift during bur hole-based procedures using interventional MRI. J. Neurosurg. **121**(1), 149–160 (2014)
36. Schnaudigel, S., Preul, C., Ugur, T., Mentzel, H.J., Witte, O.W., Tittgemeyer, M., Hagemann, G.: Positional brain deformation visualized with magnetic resonance morphometry. Neurosurgery. **66**(2), 376–384 (2010)
37. Faria, C., Sadowsky, O., Bicho, E., Ferrigno, G., Joskowicz, L., Shoham, M., Vivanti, R., De Momi, E.: Validation of a stereo camera system to quantify brain deformation due to breathing and pulsatility. Med. Phys. **41**(11), 113502 (2014)
38. Nabavi, A., Black, P.M., Gering, D.T., Westin, C.F., Mehta, V., Pergolizzi Jr., R.S., Ferrant, M., Warfield, S.K., Hata, N., Schwartz, R.B., Wells 3rd, W.M., Kikinis, R., Jolesz, F.A.: Serial intraoperative magnetic resonance imaging of brain shift. Neurosurgery. **48**(4), 787–797; discussion 797–798 (2001)
39. Nabavi, A., Gering, D.T., Kacher, D.F., Talos, I.F., Wells, W.M., Kikinis, R., Black, P.M., Jolesz, F.A.: Surgical navigation in the open MRI. Acta Neurochir. Suppl. **85**, 121–125 (2003)
40. Foroglou, N., Zamani, A., Black, P.: Intra-operative MRI (iop-MR) for brain tumour surgery. Br. J. Neurosurg. **23**(1), 14–22 (2009)
41. Senft, C., Bink, A., Franz, K., Vatter, H., Gasser, T., Seifert, V.: Intraoperative MRI guidance and extent of resection in glioma surgery: a randomised, controlled trial. Lancet Oncol. **12**(11), 997–1003 (2011)
42. Olubiyi, O.I., Ozdemir, A., Incekara, F., Tie, Y., Dolati, P., Hsu, L., Santagata, S., Chen, Z., Rigolo, L., Golby, A.J.: Intraoperative magnetic resonance imaging in intracranial glioma resection: a single-center, retrospective blinded volumetric study. World Neurosurg. **84**(2), 528–536 (2015)
43. Wu, J.-S., Gong, X., Song, Y.-Y., Zhuang, D.-X., Yao, C.-J., Qiu, T.-M., Lu, J.-F., Zhang, J., Zhu, W., Mao, Y.: 3.0-T intraoperative magnetic resonance imaging-guided resection in cerebral glioma surgery: interim analysis of a prospective, randomized, triple-blind, parallel-controlled trial. Neurosurgery. **61**(CN_suppl_1), 145–154 (2014)
44. Unsgaard, G., Gronningsaeter, A., Ommedal, S., Nagelhus Hernes, T.A.: Brain operations guided by real-time two-dimensional ultrasound: new possibilities as a result of improved image quality. Neurosurgery. **51**(2), 402–411; discussion 411–412 (2002)
45. Unsgaard, G., Ommedal, S., Muller, T., Gronningsaeter, A., Nagelhus Hernes, T.A.: Neuronavigation by intraoperative three-dimensional ultrasound: initial experience during brain tumor resection. Neurosurgery. **50**(4), 804–812; discussion 812 (2002)
46. Unsgaard, G., Ommedal, S., Rygh, O.M., Lindseth, F.: Operation of arteriovenous malformations assisted by stereoscopic navigation-controlled display of preoperative magnetic resonance angiography and intraoperative ultrasound angiography. Neurosurgery. **56**(2 Suppl), 281–290; discussion 281–290 (2005)
47. Unsgaard, G., Rygh, O.M., Selbekk, T., Muller, T.B., Kolstad, F., Lindseth, F., Hernes, T.A.: Intra-operative 3D ultrasound in neurosurgery. Acta Neurochir. **148**(3), 235–253; discussion 253 (2006)
48. Prada, F., Del Bene, M., Mattei, L., Lodigiani, L., DeBeni, S., Kolev, V., Vetrano, I., Solbiati, L., Sakas, G., DiMeco, F.: Preoperative magnetic resonance and intraoperative ultrasound fusion imaging for real-time neuronavigation in brain tumor surgery. Ultraschall Med. **36**(2), 174–186 (2015)
49. Steno, A., Holly, V., Mendel, P., Stenova, V., Petrickova, L., Timarova, G., Jezberova, M., Belan, V., Rychly, B., Surkala, J., Steno, J.: Navigated 3D-ultrasound versus conventional neuronavigation during awake resections of eloquent low-grade gliomas: a comparative study at a single institution. Acta Neurochir. **160**(2), 331–342 (2018)

50. Sastry, R., Bi, W.L., Pieper, S., Frisken, S., Kapur, T., Wells 3rd, W., Golby, A.J.: Applications of ultrasound in the resection of brain tumors. J. Neuroimaging. **27**(1), 5–15 (2017)
51. SINTEF: Ultrasound in Neurosurgery. https://www.sintef.no/en/events/ultrasound-in-neurosurgery/
52. Hata, N., Nabavi, A., Wells 3rd, W.M., Warfield, S.K., Kikinis, R., Black, P.M., Jolesz, F.A.: Three-dimensional optical flow method for measurement of volumetric brain deformation from intraoperative MR images. J. Comput. Assist. Tomogr. **24**(4), 531–538 (2000)
53. Archip, N., Clatz, O., Whalen, S., Kacher, D., Fedorov, A., Kot, A., Chrisochoides, N., Jolesz, F., Golby, A., Black, P.M., Warfield, S.K.: Non-rigid alignment of pre-operative MRI, fMRI, and DT-MRI with intra-operative MRI for enhanced visualization and navigation in image-guided neurosurgery. NeuroImage. **35**(2), 609–624 (2007)
54. Drakopoulos, F., Chrisochoides, N.P.: Accurate and fast deformable medical image registration for brain tumor resection using image-guided neurosurgery. Comput. Methods Biomech. Biomed. Eng. Imaging Vis. **4**(2), 112–126 (2016)
55. Comeau, R.M., Sadikot, A.F., Fenster, A., Peters, T.M.: Intraoperative ultrasound for guidance and tissue shift correction in image-guided neurosurgery. Med. Phys. **27**(4), 787–800 (2000)
56. Bonsanto, M.M., Staubert, A., Wirtz, C.R., Tronnier, V., Kunze, S.: Initial experience with an ultrasound-integrated single-RACK neuronavigation system. Acta Neurochir. **143**(11), 1127–1132 (2001)
57. Lunn, K.E., Paulsen, K.D., Roberts, D.W., Kennedy, F.E., Hartov, A., West, J.D.: Displacement estimation with co-registered ultrasound for image guided neurosurgery: a quantitative in vivo porcine study. IEEE Trans. Med. Imaging. **22**(11), 1358–1368 (2003)
58. Chacko, A.G., Kumar, N.K., Chacko, G., Athyal, R., Rajshekhar, V.: Intraoperative ultrasound in determining the extent of resection of parenchymal brain tumours–a comparative study with computed tomography and histopathology. Acta Neurochir. **145**(9), 743–748; discussion 748 (2003)
59. Ji, S., Wu, Z., Hartov, A., Roberts, D.W., Paulsen, K.D.: Mutual-information-based image to patient re-registration using intraoperative ultrasound in image-guided neurosurgery. Med. Phys. **35**(10), 4612–4624 (2008)
60. Rivaz, H., Collins, D.L.: Deformable registration of preoperative MR, pre-resection ultrasound, and post-resection ultrasound images of neurosurgery. Int. J. Comput. Assist. Radiol. Surg. **10**(7), 1017–1028 (2015)
61. Wein, W., Ladikos, A., Fuerst, B., Shah, A., Sharma, K., Navab, N.: Global registration of ultrasound to MRI using the LC2 metric for enabling neurosurgical guidance. Med. Image Comput. Comput. Assist. Interv. **16**(Pt 1), 34–41 (2013)
62. Fuerst, B., Wein, W., Muller, M., Navab, N.: Automatic ultrasound-MRI registration for neurosurgery using the 2D and 3D LC(2) Metric. Med. Image Anal. **18**(8), 1312–1319 (2014)
63. Miga, M.I., Sinha, T.K., Cash, D.M., Galloway, R.L., Weil, R.J.: Cortical surface registration for image-guided neurosurgery using laser-range scanning. IEEE Trans. Med. Imaging. **22**(8), 973–985 (2003)
64. Sinha, T.K., Dawant, B.M., Duay, V., Cash, D.M., Weil, R.J., Thompson, R.C., Weaver, K.D., Miga, M.I.: A method to track cortical surface deformations using a laser range scanner. IEEE Trans. Med. Imaging. **24**(6), 767–781 (2005)
65. Ji, S., Fan, X., Roberts, D.W., Hartov, A., Paulsen, K.D.: Cortical surface shift estimation using stereovision and optical flow motion tracking via projection image registration. Med. Image Anal. **18**(7), 1169–1183 (2014)
66. Warfield, S.K., Haker, S.J., Talos, I.F., Kemper, C.A., Weisenfeld, N., Mewes, A.U., Goldberg-Zimring, D., Zou, K.H., Westin, C.F., Wells, W.M., Tempany, C.M., Golby, A., Black, P.M., Jolesz, F.A., Kikinis, R.: Capturing intraoperative deformations: research experience at Brigham and Women's Hospital. Med. Image Anal. **9**(2), 145–162 (2005)
67. Kacher, D.F., Whalen, B., Handa, A., Jolesz, F.A.: The advanced multimodality image-guided operating (AMIGO) suite. In: Jolesz, F.A. (ed.) Intraoperative imaging and image-guided therapy. Springer, New York (2014)

68. Miga, M.I., Paulsen, K.D., Hoopes, P.J., Kennedy Jr., F.E., Hartov, A., Roberts, D.W.: In vivo quantification of a homogeneous brain deformation model for updating preoperative images during surgery. I.E.E.E. Trans. Biomed. Eng. **47**(2), 266–273 (2000)
69. Nakao, N., Nakai, K., Itakura, T.: Updating of neuronavigation based on images intraoperatively acquired with a mobile computerized tomographic scanner: technical note. Minim. Invasive Neurosurg. **46**(2), 117–120 (2003)
70. Sun, K., Pheiffer, T.S., Simpson, A.L., Weis, J.A., Thompson, R.C., Miga, M.I.: Near real-time computer assisted surgery for brain shift correction using biomechanical models. IEEE J. Transl. Eng. Health Med. **2**, 2014 (2014)
71. De Momi, E., Ferrigno, G., Bosoni, G., Bassanini, P., Blasi, P., Casaceli, G., Fuschillo, D., Castana, L., Cossu, M., Lo Russo, G., Cardinale, F.: A method for the assessment of time-varying brain shift during navigated epilepsy surgery. Int. J. Comput. Assist. Radiol. Surg. **11**(3), 473–481 (2016)
72. Zhuang, D.X., Liu, Y.X., Wu, J.S., Yao, C.J., Mao, Y., Zhang, C.X., Wang, M.N., Wang, W., Zhou, L.F.: A sparse intraoperative data-driven biomechanical model to compensate for brain shift during neuronavigation. AJNR Am. J. Neuroradiol. **32**(2), 395–402 (2011)
73. Jiang, J., Nakajima, Y., Sohma, Y., Saito, T., Kin, T., Oyama, H., Saito, N.: Marker-less tracking of brain surface deformations by non-rigid registration integrating surface and vessel/sulci features. Int. J. Comput. Assist. Radiol. Surg. **11**(9), 1687–1701 (2016)
74. Zhang, C., Wang, M., Song, Z.: A brain-deformation framework based on a linear elastic model and evaluation using clinical data. I.E.E.E. Trans. Biomed. Eng. **58**(1), 191–199 (2011)
75. Miga, M.I., Sun, K., Chen, I., Clements, L.W., Pheiffer, T.S., Simpson, A.L., Thompson, R.C.: Clinical evaluation of a model-updated image-guidance approach to brain shift compensation: experience in 16 cases. Int. J. Comput. Assist. Radiol. Surg. **11**(8), 1467–1474 (2016)
76. Cao, A., Thompson, R.C., Dumpuri, P., Dawant, B.M., Galloway, R.L., Ding, S., Miga, M.I.: Laser range scanning for image-guided neurosurgery: investigation of image-to-physical space registrations. Med. Phys. **35**(4), 1593–1605 (2008)
77. Sun, H., Lunn, K.E., Farid, H., Wu, Z., Roberts, D.W., Hartov, A., Paulsen, K.D.: Stereopsis-guided brain shift compensation. IEEE Trans. Med. Imaging. **24**(8), 1039–1052 (2005)
78. Kumar, A.N., Miga, M.I., Pheiffer, T.S., Chambless, L.B., Thompson, R.C., Dawant, B.M.: Automatic tracking of intraoperative brain surface displacements in brain tumor surgery. Conf. Proc. IEEE Eng. Med. Biol. Soc. **2014**, 1509–1512 (2014)
79. Fan, X., Roberts, D.W., Schaewe, T.J., Ji, S., Holton, L.H., Simon, D.A., Paulsen, K.D.: Intraoperative image updating for brain shift following dural opening. J. Neurosurg. **126**(6), 1924–1933 (2017)
80. Yang, X., Clements, L.W., Luo, M., Narasimhan, S., Thompson, R.C., Dawant, B.M., Miga, M.I.: Stereovision-based integrated system for point cloud reconstruction and simulated brain shift validation. J. Med. Imaging (Bellingham). **4**(3), 035002 (2017)
81. Kumar, A.N., Pheiffer, T.S., Simpson, A.L., Thompson, R.C., Miga, M.I., Dawant, B.M.: Phantom-based comparison of the accuracy of point clouds extracted from stereo cameras and laser range scanner. In: Medical imaging 2013: image-guided procedures, robotic interventions, and modeling, vol. 8671, p. 867125 (2013). https://doi.org/10.1117/12.2008036
82. Kumar, A.N., Miga, M.I., Pheiffer, T.S., Chambless, L.B., Thompson, R.C., Dawant, B.M.: Persistent and automatic intraoperative 3D digitization of surfaces under dynamic magnifications of an operating microscope. Med. Image Anal. **19**(1), 30–45 (2015)
83. Lasso, A., Heffter, T., Rankin, A., Pinter, C., Ungi, T., Fichtinger, G.: PLUS: open-source toolkit for ultrasound-guided intervention systems. I.E.E.E. Trans. Biomed. Eng. **61**(10), 2527–2537 (2014)
84. Tokuda, J., Fischer, G.S., Papademetris, X., Yaniv, Z., Ibanez, L., Cheng, P., Liu, H., Blevins, J., Arata, J., Golby, A.J.: OpenIGTLink: an open network protocol for image-guided therapy environment. Int. J. Med. Rob. Comput. Assisted Surg. **5**(4), 423–434 (2009)
85. Bucholz, R.D., Greco, D.J.: Image-guided surgical techniques for infections and trauma of the central nervous system. Neurosurg. Clin. N. Am. **7**(2), 187–200 (1996)

86. Keles, G.E., Lamborn, K.R., Berger, M.S.: Coregistration accuracy and detection of brain shift using intraoperative sononavigation during resection of hemispheric tumors. Neurosurgery. **53**(3), 556–562; discussion 562–564 (2003)
87. Ohue, S., Kumon, Y., Nagato, S., Kohno, S., Harada, H., Nakagawa, K., Kikuchi, K., Miki, H., Ohnishi, T.: Evaluation of intraoperative brain shift using an ultrasound-linked navigation system for brain tumor surgery. Neurol. Med. Chir. **50**(4), 291–300 (2010)
88. Xiao, Y., Eikenes, L., Reinertsen, I., Rivaz, H.: Nonlinear deformation of tractography in ultrasound-guided low-grade gliomas resection. Int. J. Comput. Assist. Radiol. Surg. **13**(3), 457–467 (2018)
89. Reinertsen, I., Lindseth, F., Unsgaard, G., Collins, D.L.: Clinical validation of vessel-based registration for correction of brain-shift. Med. Image Anal. **11**(6), 673–684 (2007)
90. Reinertsen, I., Lindseth, F., Askeland, C., Iversen, D.H., Unsgard, G.: Intra-operative correction of brain-shift. Acta Neurochir. **156**(7), 1301–1310 (2014)
91. Mohammadi, A., Ahmadian, A., Azar, A.D., Sheykh, A.D., Amiri, F., Alirezaie, J.: Estimation of intraoperative brain shift by combination of stereovision and doppler ultrasound: phantom and animal model study. Int. J. Comput. Assist. Radiol. Surg. **10**(11), 1753–1764 (2015)
92. Morin, F., Courtecuisse, H., Reinertsen, I., Le Lann, F., Palombi, O., Payan, Y., Chabanas, M.: Brain-shift compensation using intraoperative ultrasound and constraint-based biomechanical simulation. Med. Image Anal. **40**, 133–153 (2017)
93. White, P.J., Whalen, S., Tang, S.C., Clement, G.T., Jolesz, F., Golby, A.J.: An intraoperative brain shift monitor using shear mode transcranial ultrasound: preliminary results. J. Ultrasound Med. **28**(2), 191–203 (2009)
94. Pheiffer, T.S., Thompson, R.C., Rucker, D.C., Simpson, A.L., Miga, M.I.: Model-based correction of tissue compression for tracked ultrasound in soft tissue image-guided surgery. Ultrasound Med. Biol. **40**(4), 788–803 (2014)
95. Pheiffer, T.S., Miga, M.I.: Toward a generic real-time compression correction framework for tracked ultrasound. Int. J. Comput. Assist. Radiol. Surg. **10**(11), 1777–1792 (2015)

Chapter 13
Computational Biomechanics of the Brain in the Operating Theatre

Hadrien Courtecuisse, Fanny Morin, Ingerid Reinertsen, Yohan Payan, and Matthieu Chabanas

13.1 Introduction

Surgical resection of a brain tumour is a precise and delicate procedure. It requires to remove the entire tumour, in order to prevent recurrence, while preserving as much as possible of surrounding healthy or eloquent tissues, to reduce the probability of functional disorders. However, tumour borders, especially when located deep into the parenchyma, are usually not clearly visible among healthy tissues. In addition, important displacements and deformations may occur between pre-operative images used for diagnosis and intra-operative configurations, which raise significant difficulties for the treatment.

The *brain-shift* corresponds to an intra-operative deformation of soft tissues, affecting the localisation of internal structures of the brain. Multiple factors can impact the amplitude and direction of this nonlinear deformation: the loss of cerebrospinal fluid (CSF), the positioning of the patient during surgery, the size

H. Courtecuisse
ICube, Strasbourg University, CNRS, Strasbourg, France
e-mail: hcourtecuisse@unistra.fr

F. Morin
ICube, Strasbourg University, CNRS, Strasbourg, France

University of Grenoble Alpes, CNRS, Grenoble, France
e-mail: Fanny.Morin@univ-grenoble-alpes.fr

I. Reinertsen
Department of Medical Technology, SINTEF, Trondheim, Norway
e-mail: Ingerid.Reinertsen@sintef.no

Y. Payan · M. Chabanas (✉)
University of Grenoble Alpes, CNRS, Grenoble, France
e-mail: Yohan.Payan@univ-grenoble-alpes.fr; Matthieu.Chabanas@univ-grenoble-alpes.fr

K. Miller (ed.), *Biomechanics of the Brain*, Biological and Medical Physics, Biomedical Engineering, https://doi.org/10.1007/978-3-030-04996-6_13

of the craniectomy, the opening of the dura, and the actions of the surgeon such as retraction or tissue resection [1]. Several studies [2–5] have reported cortical surface and subcortical displacements larger than 20 and 7 mm, respectively, that must be taken into account given the fact that the desired accuracy of tumour resection is generally below 2 mm.

While neuronavigation has become standard in neurosurgery, intra-operative imaging has proven to be useful in many situations [6] and should be of growing importance in the future years. Among intra-operative imaging modalities, ultrasound (US) is common because it can easily be integrated in the clinical workflow and is widely available in medical centres. However, US images are of limited quality, entailing significant difficulties to identify deep internal structures. Contrary to ultrasound, intra-operative magnetic resonance imaging (iMRI) is a means of obtaining detailed images of patient's brain during the surgery. However, such installation is expensive, and the acquisition of MRI images during surgery is a complex process that significantly increases the duration of the procedure.

To fill the gap between comprehensive pre-operative data and sparse and incomplete or low-quality intra-operative images, the general trend is to develop nonrigid registration method. This enables to visualise inner structures, surgical targets, or planning at key moments of the surgery where assistance is needed. Many image-to-image registration algorithms were proposed in the literature [1, 7]. In this paper, we will only focus on biomechanical model-based solutions. One of their main advantages is the ease to define the mechanical actions at the origin of tissue deformation as well as the boundary conditions and contacts between structures. In addition, it has proven to be consistent and robust when dealing with (very) sparse intra-operative data.

This article is organised as follows. In Sect. 13.2 we will introduce the main steps and criteria of model-based registration approaches. Section 13.3 is dedicated to the presentation of our method [8], which relies on finite element modelling and vessel-based constraints from intra-operative US. We then provide detailed discussion and comparison regarding the criteria introduced previously as well as the constraints in the operating theatre.

13.2 Key Steps for Computational Modelling in the Operating Theatre

This section summarises key steps and modelling choices that could or should be taken into account before and during surgery. In the following section, we will position our retrospective study [8] with respect to these criteria and highlight the necessary steps that are still missing for intra-operative usage of the method (Table 13.1).

Table 13.1 Key steps for computational modelling in the operating theatre. Terms in regular font are common to the majority of the models, while ones in italic could be considered for improvement

Before surgery	During surgery
• Construct model geometry • Define constitutive law • Set mechanical properties • Define boundary conditions • *Perform precomputations*	• Acquire intra-operative images • Evaluate additional boundary conditions and loads • *Use efficient computational method* • *Model tissue-resection* • Render the information

13.2.1 Before Surgery: Generation of a Patient-Specific Model

For applications in the operating theatre, any generic model of the brain is of little value, and a patient-specific model must be built. This specificity first concerns the morphology of the parenchyma, the bulk of the model, and the inner structures such as the dura mater, ventricles, or tumour, if any. While the constitutive law of the brain tissue is usually generic, estimating the patient's own rheological parameters could be a valuable addition, depending on the type of loads applied to the model. Finally, some boundary conditions, e.g. related to fixed or contact areas, can already be formulated.

13.2.1.1 Geometry

The generation of a patient model commonly relies on pre-operative magnetic resonance images (MRIs) solely, with different sequences available (such as T1-weighted with or without gadolinium, T2 FLAIR, MR angiography, or diffusion tensor imaging). After a diagnostic scan, another MRI is commonly acquired a day or a few hours before surgery, to provide up-to-date images to the neuronavigation system. Ideally, the model should be generated from this pre-surgery exam. Therefore, to be compatible with the clinical workflow, it is mandatory for the model generation process to be as automatic and robust as possible. Although many approaches have been proposed in the literature, the automatic generation of patient-specific models remains one of the major bottlenecks for the widespread use of any computational model in the operating room.

The first step is usually the segmentation of the brain from MRI. A comprehensive review of this widely studied topic is well beyond the scope of this chapter. To limit their complexity, computational models in the operating room are generally relatively coarse and do not detail the cerebral convolutions and rarely the grey and white matter layers. Therefore, automatic methods to segment all the parenchyma, for example, the brain extraction tool (BET) proposed by [9] could be well adapted.

After segmentation, most of the existing works rely on a 3D finite element mesh of the domain. While hexahedral elements are preferred numerically, tetrahedrons are often used for meshing simplicity.

13.2.1.2 Constitutive Law

Brain constitutive behaviour and brain modelling have been extensively described in the previous chapters of this book. The behaviour of the brain tissues is widely admitted as nonlinear, inhomogeneous, and patient specific. The range of modelling strategies is, however, very large, with constitutive laws from linear to hyperelastic or biphasic materials. For a use in the operating room, one of the major constraints is computational efficiency. Therefore, a trade-off must be found between a fine modelling and the practicability of the model. Any simulation requiring more than a few minutes could obviously not be compatible with clinic.

13.2.1.3 Mechanical Properties

To our knowledge, virtually, all the existing models use generic mechanical properties reported in the literature from experimental measurements. With some exception, brain tissue stiffness is usually considered in the 1–10 kPa range (in equivalent Young's modulus, for the nonlinear materials), with Poisson's ratio from 0.4 to 0.49 [10]. Tumour tissues are often modelled as stiffer, following clinical recommendations but without clear supporting data.

Although these orders of magnitude of the mechanical parameters are adequate, they cannot represent the variability among patients and their specificity and inhomogeneity. Therefore, assessing patient-specific mechanical properties, for example, with MR elastography [11], could be a valuable addition. While this may not be crucial when using imposed displacements [12], patient-specific values could improve the simulation accuracy when other types of loads are used (especially forces).

13.2.1.4 Known Boundary Conditions

Some boundary conditions can be determined pre-operatively, typically at the interface between the brain and dura mater. Depending on the procedure, inner structures may also be considered as fixed during surgery, such as the brain stem region, the tentorium cerebelli, the ventricles, or even the falx cerebri.

In most cases, the segmentation of these structures from MRI images is manual or semiautomatic. However, some authors have proposed automatic methods to fix the cerebellum [13] or simulate interactions with the cerebral falx and tentorium cerebelli [14]. Once segmented, these structures are used to fix nodes or to set up sliding contact boundary conditions.

13.2.1.5 Precomputations

Whenever possible, precomputations could be performed pre-operatively to speed up the resolution during surgery. Precomputations can be purely numerical. When using a linear elastic model, a common approach is to compute and store the deformations resulting from elementary nodal displacements [15]. Other strategies model the nonlinearity of the brain through precomputations [16–18]. The overall model response to a set of imposed nodal displacements then relies on the principle of superposition or linear combination of precomputed deformations. While precomputations could last several hours, the intra-operative inverse problem is generally straightforward. Finally, numerical optimisations are also possible, for example, by pre-inversing the stiffness matrix to handle contacts with Lagrange multipliers [8].

13.2.2 In the Operating Theatre

13.2.2.1 Intra-operative Imaging

Numerous factors can change between the pre-operative planning and the surgery, such as the patient positioning, location and size of the craniotomy, loss of cerebrospinal fluid, anaesthesia control, or tissue retraction and resection. All these factors directly affect how the brain tissues deform. Therefore, simulations relying only on a pre-operative model and planning cannot be considered to provide reliable results. It is then mandatory to capture information, in the operating room, about the current patient tissue configuration and the realised procedure, to specify adequate loads and boundary conditions of the model. This new information is usually acquired at least once, typically after dural opening for craniotomy-induced brain shift compensation, or at the end of a resection procedure to ensure all tumour tissues were removed. Whenever possible, repeated acquisitions could be used to track the deformations all along the procedure.

Many intra-operative imaging modalities have been used in neurosurgery [6], such as MRI (iMRI), ultrasound (iUS), optical systems such as stereo vision CCD images or Laser Range Systems (LRS), and to a less extent intra-operative X-rays system like iCT or cone beam CT. A review of the advantages and drawbacks of these imaging modalities can be found in [1].

13.2.2.2 Processing Intra-operative Images

Intra-operative imaging can be used to capture information about the patient during surgery. The acquired images must then be processed to extract relevant features that will be later transferred to the model as boundary conditions or loads. Examples of structures to segment are points on the exposed cortical surface, contours (e.g.

the cortical or ventricles surface on iMRI), homologous landmarks, or 3D vessels. Ideally, segmenting the intra-operative images should be fully automatic. However, semiautomatic methods are commonly used as long as interactions remain very limited.

13.2.2.3 Intra-operative Boundary Conditions and Loads

Many authors have used imposed displacements on FE nodes to match the model with the structures segmented from intra-operative images. In this case, the computational model could be mostly considered as a representation of the warping function in a registration problem. The brain shift phenomenon is not simulated directly; instead the model is used to extrapolate the deformations of the brain from a sparse set of data, on a mechanical basis.

As opposed to this approach, several authors have proposed to actually model the influence of gravity, loss of CSF of tissue resection on the brain, to simulate its deformation [13, 19]. In that context, the collected intra-operative data are not derived as loads for a forward simulation but are used to find the parameters leading to the optimal solution of an inverse problem.

13.2.2.4 Efficient Computational Methods

Computational efficiency is a crucial factor in the operating room. While the entire process must be considered, including image acquisition and processing, the computational model resolution itself can be one of the main limiting criteria. Real-time or interactive simulation is generally not required in a neurosurgical context, but overall computation time should be limited to a couple of minutes. This additional duration could be especially acceptable if the surgery can be resumed just after data acquisition, while the model is ran and the pre-operative MRI images are updated.

13.2.2.5 Modelling Tissue Resection

Neurosurgery often requires the retraction and resection of the brain tissue, for instance, to remove a tumour, entailing many additional issues. Topological modifications (such as re-meshing or element suppression) must then be performed on the model. These modifications invalidate any precomputations, raising additional concerns about the computation time. An iterative approach is, for example, proposed in [20], involving several simulations and re-meshing steps providing updated images in approximately 7 mn. However, from the best of our knowledge, a functional, robust, and validated solution has not yet been proposed to address the problem of resection while meeting the constraints of the operating room.

13.2.2.6 Rendering the Information

Once the deformed configuration of the brain has been computed, this information must be rendered to the surgeon in a clear and informative way. The most straightforward solution is to use the deformation field derived from the brain shift modelling to map the pre-operative MRI image to the patient's brain during surgery. To go further, several groups have proposed augmented reality visualisation, especially in the surgical microscope, to help fusing, understanding, and visualising complex medical imaging data and anatomical structures [21].

13.2.3 Validation and Clinical Studies

Validating the fidelity of a computational model of the brain in itself, from a mechanical point of view, is a difficult problem. In a surgical context, a more relevant objective may be to evaluate the overall procedure, i.e. the outcomes of the simulation with respect to actual data about the deformed tissues. Ideally, validation images to measure a target registration error should be acquired after resection and should be different than the ones used to express the loads and boundary conditions.

To our knowledge, a comprehensive study including independent input data, acquired in real surgical conditions, and an independent post-resection iMRI, acquired for validation only, is not yet available. However, several groups have started acquiring such data, and results are expected soon. While the iMRI setup will influence the measured deformation, due to its length, removal of tools, tissue debulking, and dural closing, these images are expected to provide a much better ground truth than any other modalities.

13.2.3.1 Practicability and Integration in the Surgical Workflow

Few studies clearly evaluate the practicability of their method. Several factors should be considered such as integration in the surgical workflow, especially to acquire intra-operative images, manual interactions, overall computation times, and information rendering. In [8], our method required less than 2 min to process the iUS images, simulate the brain deformations with a constraint-based iterative method, and then update the pre-operative MRI (only the iUS acquisition time is not included, usually 2–3 additional minutes). This method was evaluated in a retrospective study only, but we showed that both the hardware and the software could be compatible with the constraints of the operating room.

To our knowledge, almost all existing studies, including our own, are *retrospective* only. A notable exception is [22], in which simulations were carried out in the operating room, using the method proposed in [19], before updated MRI was displayed in the neuronavigation system. This study could then be considered as one of the first computational models of the brain actually used in the operating theatre.

13.3 Example of Clinical Application: Constraint-Based Simulation During Tumour Resection

This section introduces our approach to compensate for the brain shift induced by the dura mater opening [8]. The method combines a biomechanical model build from pre-operative images and image-based constraints extracted from intra-operative US.

Before surgery, a patient-specific finite element (FE) model of the brain is constructed from pre-operative MRI images. This model accounts for the soft tissue morphology but also vessels located around the tumour. During surgery, after opening, the skull and dura mater, localised Doppler, and B-mode ultrasound images were acquired directly in contact with the brain. The vascular tree and the footprint of the ultrasound probe are then extracted from these intra-operative images.

A biomechanical simulation is then performed to compensate for the brain shift deformation. We introduce several types of constraints allowing to (i) model contacts between the brain and the dura, (ii) register the pre- and intra-operative vessels, and (iii) constrain the cortical surface under the footprint of the probe. Finally, the pre-operative MRI is updated using the displacement field calculated from the biomechanical model. An overview of this method is shown in Fig. 13.1.

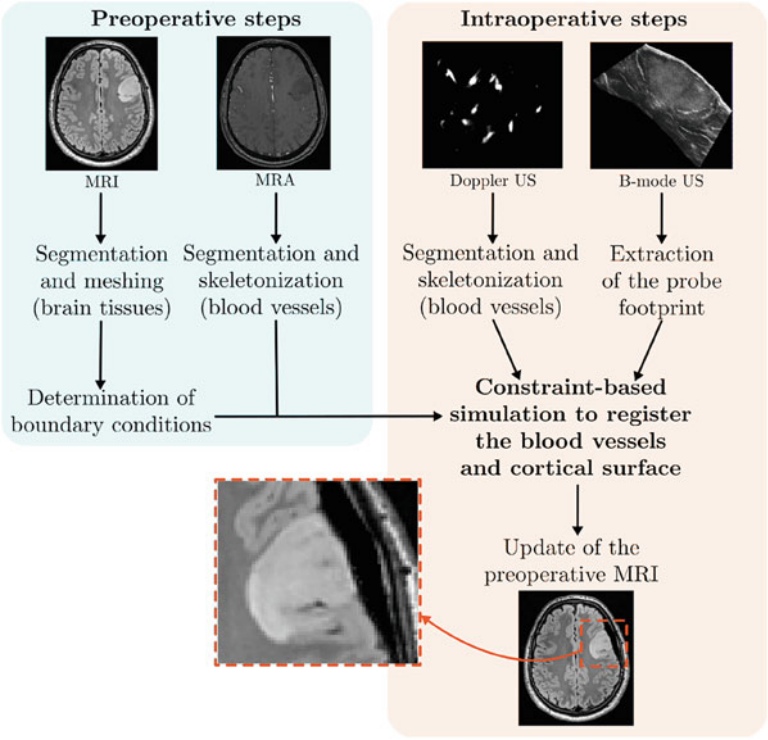

Fig. 13.1 Overview of the method. (Source: [8])

13.3.1 Before Surgery: Model Generation

As presented in Sect. 13.2.1, the model must be built from pre-operative MRI images acquired a few hours before surgery. This procedure must then be as automatic as possible to be compatible with a clinical workflow.

13.3.1.1 Geometries from MRI Images

Several atlas-based automatic algorithms such as [23–25] have provided detailed solutions, with regard to the resolution of the meshes, but their implementation is difficult. In our research context, we have chosen a semiautomatic coarse segmentation method.

Soft tissues are segmented from pre-operative T2-FLAIR (*fluid-attenuated inversion recovery*) MRI. This sequence reduces the signal from the cerebrospinal fluid, thus highlighting brain lesions. The complete organ is first extracted using the BET (*brain extraction tool*) algorithm proposed by [9]. It is fully automatic and runs in just a few seconds. The tumour is then segmented, after manually initialising some seeds, via a growing region algorithm implemented in the ITK-SNAP software [26]. For a more comprehensive study using our model in clinic, more advanced segmentation methods, potentially publicly available, should obviously be investigated.

Soft tissues are meshed homogeneously with linear tetrahedral elements, using the CGAL library [27], leading to a coarse mesh of 2000 nodes for a single hemisphere. Its surface is extracted to form the collision mesh that will be used to impose constraints with the skull and the probe footprint. This collision mesh is decimated (i.e. about 300 vertices) in order to reduce the number of constraints.

13.3.1.2 Segmentation of the Vascular Tree

The cerebrovascular tree is segmented from pre-operative angiographic MRI (ARM). While this modality provides poor contrasts for soft tissues, vessels appear with very high intensities.

A review of vessel segmentation methods from medical images can be found in [28]. In our work, we reconstructed the cerebrovascular tree using the maximum intensity projection (MIP) technique proposed by [29]. The histogram of this image reveals two peaks corresponding to the background of the image (black) and the soft tissues of the brain (dark grey), respectively. The vessels are then segmented using a threshold value chosen just after the second peak of the histogram. This is illustrated in Fig. 13.2a.

The shape of this segmentation, and more particularly its outer envelope, is very sensitive to the image quality and segmentation parameters. For example, vessels often appear thicker in US than in ARM. In order to minimise the segmentation

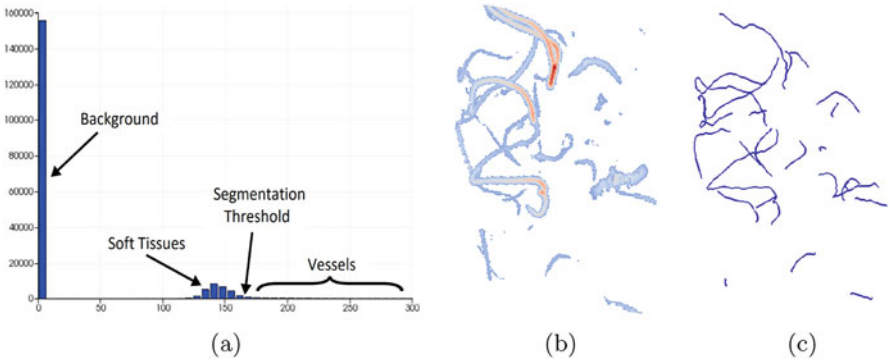

Fig. 13.2 Histogram of the MIP image, segmentation and mesh generation of the vessel tree. (**a**) Histogram of the MIP image. (**b**) Segmentation. (**c**) Skeletisation

errors, centre lines are extracted to form a skeleton passing through the centre of the vessels. A modified *Dijkstra* algorithm is then employed where the Euclidian distance to the nearest wall is calculated for each voxel inside a vessel. Using the inverse of this distance as weights, images are then converted into a connected graph. Additional criteria are used to remove small branches that may appear as a result of a noisy segmentation (see [8] for details).

13.3.1.3 Mechanical Coupling

Several representations are used to describe the pre-operative biomechanical model. The brain is meshed and simulated with the finite element (FE) method, whereas constraint forces are applied on collision models (i.e. the surface and the vessels). Displacements must therefore be transferred from the FE mesh to the collision models, and conversely, constraint forces must be integrated in FE equations. For this purpose, let $\mathcal{J}$ be a function providing the position of each vertex of the collision meshes $\mathbf{u}_{\text{col}}$ with respect to the nodal positions of the tetrahedral mesh $\mathbf{u}_{\text{FE}}$:

$$\mathbf{u}_{\text{col}} = \mathcal{J}(\mathbf{u}_{\text{FE}}) \tag{13.1}$$

At the beginning of the simulation, the barycentric coordinates of each vertex of the collision models are associated with their closest tetrahedral element [30]. This association remains constant throughout the simulation, which can mathematically be written as a *Jacobian matrix*, defined by $\mathbf{J} = \partial \mathbf{u}_{\text{col}} / \partial \mathbf{u}_{\text{FE}}$. This Jacobian matrix is used to obtain the positions $\mathbf{u}_{\text{col}}$ from the $\mathbf{u}_{\text{FE}}$ positions. The previous equation can be rewritten as follows:

$$\mathbf{u}_{\text{col}} = \mathbf{J}\mathbf{u}_{\text{FE}} \tag{13.2}$$

In the opposite, constraint forces $\boldsymbol{\lambda}_{\text{col}}$ applied on the collision models are weighted with the same barycentric coefficients and converted in equivalent nodal forces on the finite element mesh $\boldsymbol{\lambda}_{\text{FE}}$:

$$\boldsymbol{\lambda}_{\text{FE}} = \mathbf{J}^T \boldsymbol{\lambda}_{\text{col}} \tag{13.3}$$

13.3.2 Intra-operative Datasets

Intra-operatively, registration data are extracted from the navigated ultrasound images. Power Doppler and B-mode signals are recorded simultaneously, and the corresponding 3D image volumes are reconstructed. In a clinical context, the set of algorithms presented in the following paragraphs will have to be performed during the surgical procedure. They must therefore be fast, a few seconds, and almost fully automatic to allow their use in a clinical process.

13.3.2.1 Vascular Tree from Power Doppler Ultrasound Images

Power Doppler ultrasound images provide a real-time visualisation of flows, particularly the blood flow, offering a strong contrast of the vessels (see Fig. 13.3a). The intra-operative vascular tree is then segmented from these images by a thresholding method, using parameters tuned manually [31]. In addition, to limit the sensitivity of the method with respect to segmentation parameters, the skeletonisation of the data is performed following the algorithm previously described for the ARM. Finally, in order to maintain computation time compatible with clinical constraints and to avoid over-constrained problems, the vascular tree model is sampled with 1 point every 2.5 mm (this value could adapted to the mesh resolution).

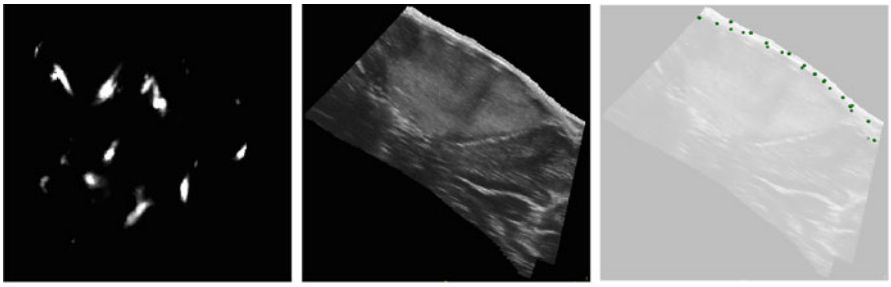

Fig. 13.3 Extraction of the probe footprint in US B mode images. (**a**) Doppler Image. (**b**) B mode image. (**c**) Point cloud generation

13.3.2.2 Probe Footprint from B-Mode Ultrasound Images

The ultrasound probe footprint located at the interface between the probe and brain tissues is easily identifiable and can thus be extracted from B-mode images in order to provide additional constraints at the surface of the brain. The visualisation of this boundary arises from an ultrasound artifact: when the waves enter the tissues of the brain, a part is reflected on the surface forming this specific band in the image (see Fig. 13.3b). The footprint being located on the edges of the images, the outer envelope of the volume is extracted. A low-pass filter is then applied to provide a binary volume, and finally a point cloud is generated sampling data at 1 point every 10 mm (see Fig. 13.3c).

13.3.3 Biomechanical Model: Formulation

In the context of registration with intra-operative data, a static problem can be considered. The governing equation is given by:

$$\mathcal{F}(\mathbf{u}_{\text{FE}}) + \mathcal{H}(\mathbf{u}_{\text{col}}, \mathbf{p}_{\mathcal{I}})\boldsymbol{\lambda} = \mathbf{0} \tag{13.4}$$

where $\mathcal{F}(\mathbf{u}_{\text{FE}})$ is a nonlinear function describing the internal forces according to the displacement $\mathbf{u}_{\text{FE}}$ of the FE model. $\mathcal{H}(\mathbf{u}_{\text{col}}, \mathbf{p}_{\mathcal{I}})$ is a nonlinear function associating Lagrangian multipliers $\boldsymbol{\lambda}$ used to impose constraint forces to the FE model. The number and directions of Lagrangian multipliers depend on the collision model positions, $\mathbf{u}_{\text{col}}$, and the positions extracted from intra-operative images, $\mathbf{p}_{\mathcal{I}}$. In addition, the solution $\mathbf{u}_{\text{FE}}$ to this problem must satisfy a set of constraints equations which can mathematically be represented as follows:

$$\mathcal{H}(\mathbf{u}_{\text{col}}, \mathbf{p}_{\mathcal{I}}) = \boldsymbol{\delta} \tag{13.5}$$

where $\boldsymbol{\delta}$ is the violation of the constraints (e.g. penetration through a boundary surface).

13.3.3.1 Constitutive Law and Parameters

As seen in Sect. 13.2.1.2, the constitutive behaviour of the brain is known to be complex and should be described using hyper-elastic laws. However, in our constraint-based context, displacements are imposed through Lagrangian multipliers. The solution in displacements is thus weakly sensitive to the constitutive law and parameters [12, 32]. A linear elastic law is therefore used. Following [33], Young's modulus and Poisson's ratio are, respectively, set to $E = 1.5$ kPa and $\nu = 0.45$. A higher stiffness

of $E = 10\,\text{kPa}$ is used for the tumour. To take into account large displacements while being computationally efficient, simulations are run using the corotational approach [34].

13.3.3.2 Constraints

Two types of constraints are used during the registration process:

- **Bilateral constraints** ($\boldsymbol{\delta} = \mathbf{0}$) used to impose displacement such that constrained points of the model are moved to a desired position.
- **Unilateral constraints** ($\boldsymbol{\delta} \perp \boldsymbol{\lambda}$ i.e. $\boldsymbol{\delta} \geq \mathbf{0}$ and $\boldsymbol{\lambda} \geq \mathbf{0}$ and $\boldsymbol{\delta} \cdot \boldsymbol{\lambda} = \mathbf{0}$) are used to impose contacts between structures. In other words, either the violation is positive ($\boldsymbol{\delta} \geq \mathbf{0}$) and no contact forces are applied ($\boldsymbol{\lambda} = \mathbf{0}$) or the violation must be nullified ($\boldsymbol{\delta} = \mathbf{0}$) with a positive constraint force ($\boldsymbol{\lambda} \geq \mathbf{0}$).

Due to the nonlinearity of $\mathcal{H}$, a unique solution does not exist. Instead, we use an iterative method where the problem is linearised at each iteration, allowing for the convergence towards the closest local minimum. Constraint equations are then defined at the beginning of each iteration using the current position of the model and are assumed to be constant during the solving process $\mathcal{H}(\mathbf{u}_{\text{col}}, \mathbf{p}_{\mathcal{I}}) \simeq \partial\mathcal{H}/\partial\mathbf{u} = \mathbf{H}$. The constraint matrix $\mathbf{H}$ (known as the *Jacobian of the constraints*) contains the directions on which Lagrangian multipliers are computed.

For each iteration i, a single iteration of a *Newton-Raphson* method is solved, while constraint equations are defined following an iterative closest point (ICP) algorithm [35]. Each point extracted from the intra-operative data is associated with its closest element on the biomechanical model (see Sect. 13.3.4), defining this way the directions (stored in the matrix $\mathbf{H}^i$) in which constraint forces $\boldsymbol{\lambda}$ are applied to perform the registration. The linearised equation provides the following *Karush-Kuhn-Tucker* (KKT) system:

$$\begin{cases} \mathbf{K}^i \Delta\mathbf{u}^i + \mathbf{H}^{iT} \boldsymbol{\lambda} = -\mathcal{F}(\mathbf{u}^i) \\ \mathbf{H}^i \Delta\mathbf{u}^i = \boldsymbol{\delta} \end{cases} \tag{13.6}$$

with $\mathbf{K}^i = \partial\mathcal{F}/\partial\mathbf{u}$ is the global stiffness matrix and $\Delta\mathbf{u}^i = \mathbf{u}^{i+1} - \mathbf{u}^i$ the difference in position between two iterations.

13.3.3.3 Solving Process

The systems are solved with a schür complement method. This requires the computation of the *Delassus operator* $\mathbf{W} = \mathbf{H}^i \mathbf{K}^{i-1} \mathbf{H}^{iT}$ which is the most time-consuming operation. In our context, a large number of constraints need to be

applied on the FE model ($\mathbf{H}^i$ is a sparse matrix whose dimension is the number of constraints times the number of degrees of freedom of the FE model). Moreover, even for a relatively coarse FE mesh, computing the inverse of $\mathbf{K}^{i^{-1}}$ at each simulation step would be too expensive, preventing an intra-operative use of the method. Instead we used the *compliance warping* method introduces by [36] where the *Delassus operator* is approximated using the stiffness matrix inverted at the initial step and nodal rotations: $\mathbf{W} = \mathbf{H}^i\mathbf{R}^i\mathbf{K}^{0^{-1}}\mathbf{R}^{i^T}\mathbf{H}^{i^T}$, where $\mathbf{R}^i$ is the current nodal rotation derived from the corotational formulation [34].

Finally a modified *Gauss-Seidel* solver provides $\boldsymbol{\lambda}$ satisfying the KKT conditions (see [37] for details). At equilibrium, i.e. $\Delta\mathbf{u}_{\text{FE}} = \mathbf{0}$, the displacement field of the FE model is used to warp the pre-operative MRI image.

13.3.4 Constraint-Based Iterative Registration

Let $\mathcal{M}$ be the pre-operative model, $\mathcal{P}$ be the collision models (obtained with the barycentric mapping $\mathbf{J}$) and $\mathcal{I}$ the intra operative data. Three types of constraints are used to match $\mathcal{M}$ to $\mathcal{I}$:

Boundary conditions: Bilateral constraints are applied between the external surface of the brain model $\mathcal{M}$ and $\mathcal{P}_{\text{dura}}$. Tissue is then prevented from exiting the skull cavity and can slide in contact with the dura mater. These constraints are removed in the craniotomy area and identified in the ultrasound B-mode images, so that tissues can sag. Finally, a few nodes are fixed in the *cerebellum* area.

Cortical surface: Unilateral constraints force $\mathcal{M}$ to remain under the US probe footprint $\mathcal{I}_{\text{probe}}$. However, tissue can sag and is not necessarily in contact.

Vessels registration: The pre- and intra-operative vascular trees $\mathcal{P}_{\text{vessels}}$ and $\mathcal{I}_{\text{vessels}}$ are registered using bilateral constraints.

All these constraints are integrated and solved with the same formalism, described in Eq. (13.6). At the end of each simulation step, a $\boldsymbol{\lambda}$ force is computed allowing to impose displacements on the model satisfying the constraints. Yet, a major difficulty of this constraint based lies in the *uncertainty* during the pairing step. Indeed, although pre- and intra-operative data represent the same anatomical structures, their characteristics and quality may differ greatly due to noisy data and calibration errors, inherent in clinical applications. For this reason, we introduce the notion of *sliding constraints*. We voluntary under sample the constraints, allowing this way to partially solve the registration problem while letting the mechanical model deform and refine pairing of data over the iterations. The overall iterative process is depicted in Fig. 13.4 and in Algorithm 13.1.

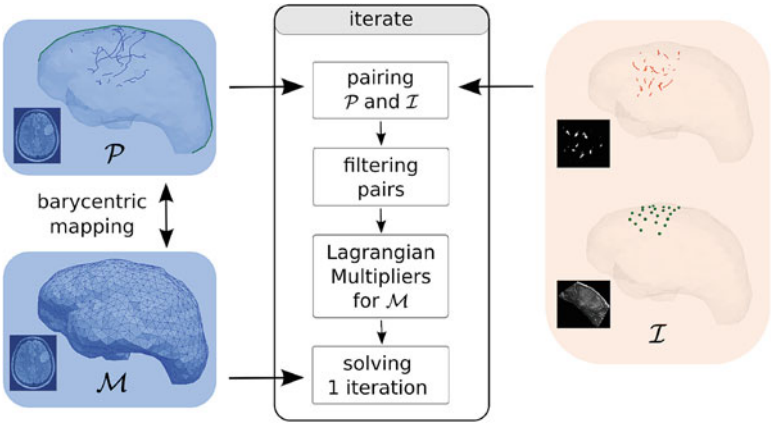

Fig. 13.4 Iterative registration process. Pairings between pre- and intra-operative datasets $\mathcal{P}$ and $\mathcal{I}$ are computed and then filtered. This defines the directions of the Lagrangian multiplier constraints, stored in matrix **H**, applied to the biomechanical model $\mathcal{M}$ so that it deforms towards $\mathcal{I}$

Algorithm 13.1 Constraint-Based Iterative Registration

repeat
1. Compute ***pairings*** between $\mathcal{P}$ and $\mathcal{I}$
2. ***Filter*** these pairings
3. Build the ***constraint matrix*** **H** (Lagrangian Multipliers) for $\mathcal{M}$
4. ***Solve*** a single Newton-Raphson iteration of the static problem

until Equilibrium is reached.

13.3.4.1 Computing Pairings

The first step of each iteration consists of computing a set of pairings between $\mathcal{P}$ and $\mathcal{I}$, defining the distances to minimise. Depending on the structures and their representation, point-to-surface, point-to-segment, or point-to-point projections can be used.

In a typical scenario, the pre-operative dataset $\mathcal{P}$ is the best defined, using continuous curves or surfaces, while $\mathcal{I}$ can simply be a set of points. Just like in a standard iterative closest point (ICP) method, each point $q_{\mathcal{I}}$ of $\mathcal{I}$ is paired with its closest projection $q_{\mathcal{P}}$ on $\mathcal{P}$. Several directions n_j are associated:

- when projecting on a plane, n_1 is the plane's normal on $q_{\mathcal{P}}$.
- when projecting on a line, n_1 is the direction of projection and n_2 is orthogonal to both n_1 and the line's tangent (see Fig. 13.5).
- when projecting on a point, n_1, n_2 and n_3 form an orthonormal referential centred on $q_{\mathcal{P}}$.

While the pairing is usually identified from $\mathcal{I}$ to $\mathcal{P}$, the associated constraints are applied on $\mathcal{M}$, along directions n_j, so that it deforms towards $\mathcal{I}$.

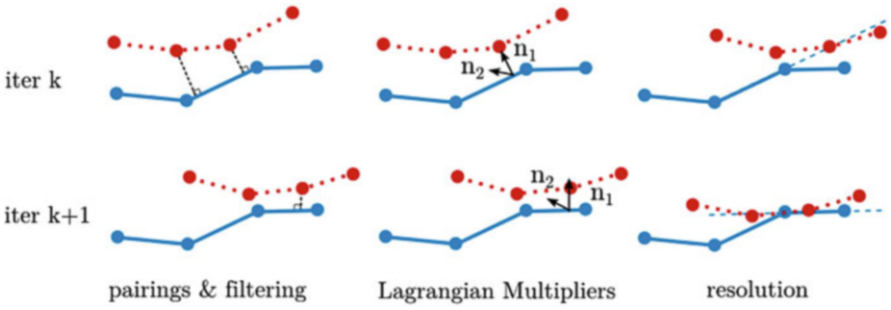

Fig. 13.5 Sliding constraints

13.3.4.2 Filtering Pairings

A crucial step is to filter the pairings to remove aberrant ones. The main strategies are the following:

- when several vertices of $\mathcal{I}$ are projected on the same line segment or triangle, only the nearest one is kept [8].
- when a pair's distance is larger than the median distances plus a given threshold, or smaller than another threshold, this pair discarded [8, 38].
- when available, second-degree information can also be taken into account in addition to Euclidian distances. For example, elements with a different orientation cannot be paired [37].

After this filtering, remaining pairings may also be subsample. First, this can limit the total number of constraints eventually applied on $\mathcal{M}$, to spare computation time. Also, it is important to avoid having multiple constraints, potentially antagonists, on single or neighbor FE elements. Therefore, pairings initially defined between $\mathcal{P}$ and $\mathcal{I}$ must be later sampled with respect to the $\mathcal{M}$ mesh refinement.

13.3.4.3 Sliding Constraints

While filtering allows to prune inconsistent pairings that may arise from noisy data, this criterion is not sufficient. Indeed, due to the deformation between pre- and intra-operative images, some positions of $\mathcal{I}$ may have shifted to closer structures in the pre-operative model. However, this may not be the actual corresponding position of the point on the vessel, which remains unknown. For example, a point may be projected on a given vessel, but its position on this vessel is not exactly known. It is therefore important to not completely constrain the model and impose displacements in this direction; otherwise a point would always, at the end of the simulation, remain on its initial projection.

A main advantage of our method is the notion of *sliding constraint*s. When a constraint is applied along a direction n_i, forces $\boldsymbol{\lambda}$ are only computed so that no

violation of the constraint remains along that direction. However, the initial point can end up anywhere on the plane orthogonal to n_i, not necessarily on its initial projection. Note that bounding $\boldsymbol{\lambda}$ forces may break that condition, in case of very large (mis)pairing distances. The shift in the orthogonal direction is given by the constraint solver minimising the energy necessary to satisfy the set of constraints.

Depending on the type of elements, the *sliding constraints* are defined along the following directions:

- a projection on a plane yields to a single constraint along direction n_1. The point can slide along this plane: after resolution, it will be located on the plane, but not necessarily on its initial projection.
- a projection on a line segment yields two constraints along n_1 and n_2. The point can slide along this line: after resolution, it will be located on the line, but not necessarily on its initial projection.

An example of *sliding constraint* is given in Fig. 13.5. For an iteration k of the registration method, each point can slide along its segment of projections. Its final position depends on all other constraints applied to the model. The next iteration(s) will then enable the convergence towards a local solution.

Advantages of using the *sliding constraints* in an iterative registration process are then:

- no a priori information is required during the pairing step. Closest projections only are used, plus the filtering step.
- in the case of mispairings, for example, projection of a point onto the wrong vessel, the considered point will end up far from its initial target projection, if other better-suited constraints force the model into another direction.
- in the case of antagonist constraints, none or few of them should be resolved, and a new iteration will occur.
- at each new iteration k, pairings will be redefined. The expected behaviour is that the uncertainty of the pairings will decrease as long as the process converges towards an overall acceptable solution.

13.3.5 Clinical Evaluation

As presented in [8], our method has been evaluated on five *retrospective* cases. Data were collected by the SINTEF Medical Technology Institute at St. Olav's University Hospital (Trondheim, Norway) [38]. For each clinical case, T2-FLAIR and angiographic MRI images were acquired before surgery. During the procedure, ultrasound images were acquired with the navigation system SonoWand [39]. These data were collected through a clinical study approved by the local ethics committees, and the consent of each patient was obtained prior to the procedure.

13.3.5.1 Quantitative and Qualitative Results After Dural Opening

Our method has been evaluated and compared to the modified ICP (providing a rigid registration) of [31, 38, 40], available in the open-source framework for image-guided therapy *CustusX* [41]. To obtain quantitative results, the first difficulty was to define reliable landmarks visible in both image modalities. For each case, 5–9 landmarks were first identified in blood vessel bifurcations, by two operators, on both the pre-operative MRA and intra-operative power Doppler US images. These landmarks were used to define a target registration error (except for one patient for which the quality of US was not enough to define landmarks). In addition, anatomical structures such as *sulcus* were delineated by a clinician in the MRI and B-mode US acquisitions, allowing a measurement that is completely independent from the data used by the method. Note that the measured errors, with vessel landmarks and sulci, are subsurface and located in the region of interest, i.e. the tumour.

Figure 13.6a shows an example of simulation and Fig. 13.6b, c the corresponding errors for four patients. On average 72% of the deformation occurring is corrected with our method, with a mean error under 1.5 mm for each patient [8]. In addition, less than 2 min are required to segment the intra-operative US images, run the simulation, and update the MR images, which is compatible with a clinical use.

After registration, MRI is warped using the displacement field of the FE model (see Fig. 13.7, right). Qualitative observations, especially deep around the tumour,

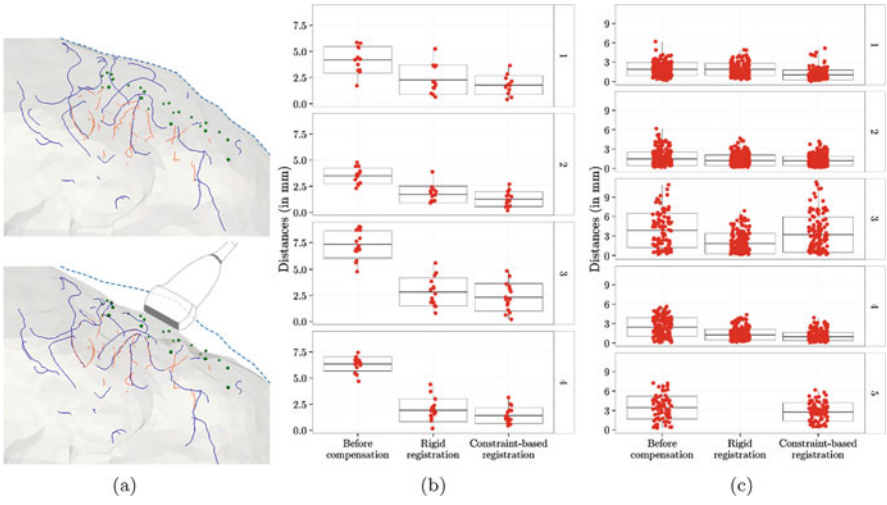

Fig. 13.6 Brain shift compensation using constraint-based simulation. Pre- and intra-operative blood vessels, respectively, in blue and orange, are registered. Other constraints maintain the brain in sliding contact with the dura mater and under the US probe. The Hausdorff distance between landmarks and delineated anatomical structures manually segmented is shown in graphs (**b**, **c**). (**a**) Registration. (**b**) Landmarks. (**c**) Structures

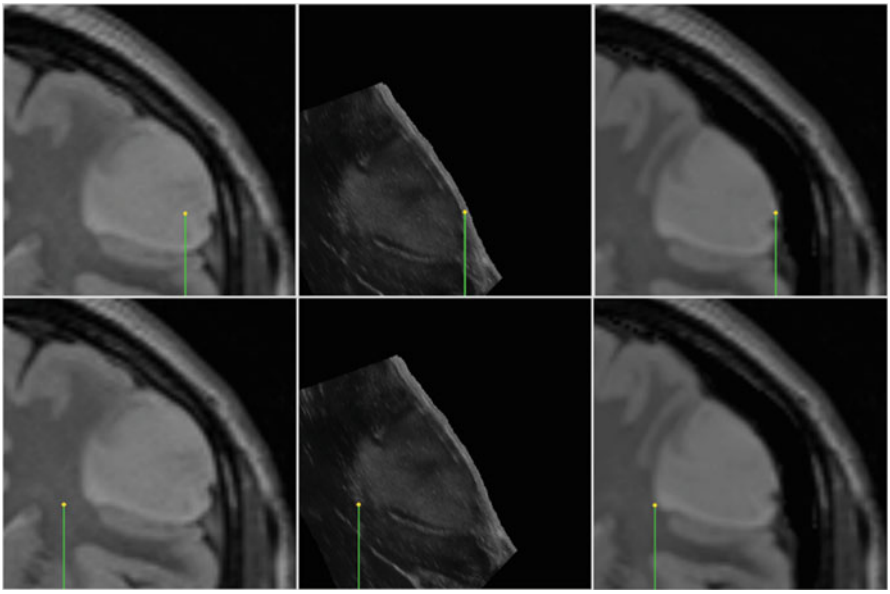

Fig. 13.7 Example of pre-operative MRI, B-mode intra-operative US, and MRI updated with our method. A pointer first shows the borders of the exposed cortical surface (top row) then a deep sulcus bifurcation point (bottom row)

show consistent matching between the warped MRI and US images, whereas significant errors can be observed in the initial pre-operative MRI, enhancing the importance of the deformation.

13.3.5.2 Experiments During Tumour Resection

After considering craniotomy-induced brain shift after dural opening, our method has also been evaluated to compensate for deformations during resection [42]. For four of the five patients in the study, an intra-operative ultrasound scan was also acquired during tumour resection. Note that the method was used *as it is* on these images, without taking into account any topological modifications in the model, nor using any continuity from the first ultrasound acquisition.

For the first three patients, the mean target registration error measured on vessel landmarks is 1.76, 2.35, and 1.89 mm, respectively. Distances on sulci are also globally improved, and qualitative results show a very satisfying adequation in the deep tissue surrounding the tumour (see Fig. 13.8). Overall, 63% of the shift is compensated during resection, which is less than after dural opening but still a very good improvement.

These promising results have not been confirmed on the fourth patient, with a brain shift reduced from 9 to 6.5 mm only. Two sources of error could explain the

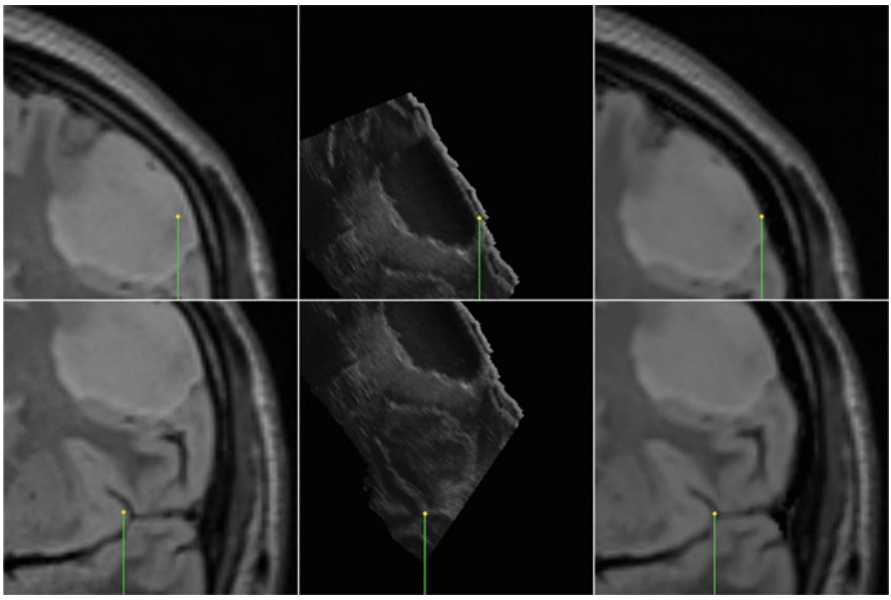

Fig. 13.8 Brain shift compensation during resection for patient 1 using the constraint-based biomechanical method. Slices of the pre-operative MRI, B-mode ultrasound image, and updated MRI are shown. A pointer first shows the borders of the exposed cortical surface (top row) then a deep sulcus bifurcation point (bottom row)

failure of this case. First, vessels are located on one side of the tumour only, which can explain the poor lateral accuracy. Mostly, this is a deep tumour, while the first three cases were superficial ones. The amount of deformation is here much larger, and the retraction to create the surgical channel should clearly be taken into account.

While more cases must be considered, these first results have shown the ability of the method to compensate for resection-induced brain shift, without additional treatments, in the case of a peripheral tumour. While deformation and topological changes occur locally within the tissues, reliable surrounding vessels still remain to register the pre- and intra-operative exams. However, more complex cases require additional treatment, especially the simulation of tissue resection in the biomechanical model.

13.3.5.3 Practicability

Although validated in a retrospective study only, our method should be usable in a clinical context. Indeed, it has been developed so that most of the steps, especially the intra-operative ones, are performed with very limited interactions of an operator and short computation times.

Pre-operative Steps

Segmentation of the pre-operative MRI remains one of the main limitations for a widespread use of our method in clinic. Indeed, while the whole brain is extracted via the automatic BET algorithm [9], the segmentation of the tumour and the other anatomical structures remains manual. Nevertheless, the segmentation of pre-operative images tends to become a standard step of nowadays clinical routines. Moreover, several solutions exist in literature [23–25] for automatic extraction of the brain and its various anatomical structures from MRIs.

The generation of pre-operative models was performed in approximately 20 mn (after the segmentation of the brain). As shown in Fig. 13.9, constructing the soft tissue model includes mesh generation (FE and collision meshes), definition of boundary conditions, and inversion of the stiffness matrix (denoted $\mathbf{K}^{0^{-1}}$). Given the segmentation of the structures, all these steps are performed automatically. The most expensive part is the segmentation of the vessels in the ARM image and their skeletonisation, which takes about 16 min. Manual interactions are still needed, but as said before, this is acceptable in the clinical workflow as these operations can be performed on the day before the surgery.

Intra-operative Steps

An 11 L linear probe attached to the Vivid E9 ultrasound scanner (GE Vingmed Ultrasound, Horten, Norway) was used for all acquisitions. The 3D reconstruction of images and the initial rigid transformation were performed intra-operatively with the CustusX framework, which was successfully used in a clinical workflow [38]. The additional time of our method is shown in Fig. 13.10. Less than 2 min are required to provide updated images intra-operatively (approximately 30 s for the extraction of vessels and the footprint, 1–2 mm for the simulation and 10 s to warp the image). In addition, the mode B and Doppler ultrasound images being acquired simultaneously, the extraction of the footprint of the probe, and the vessels can be performed in parallel.

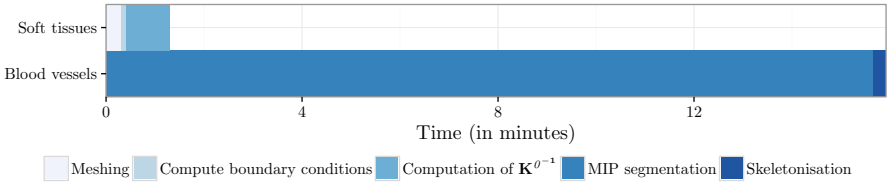

Fig. 13.9 Execution time of the pre-operative steps (without taking into account the time required for segmentation)

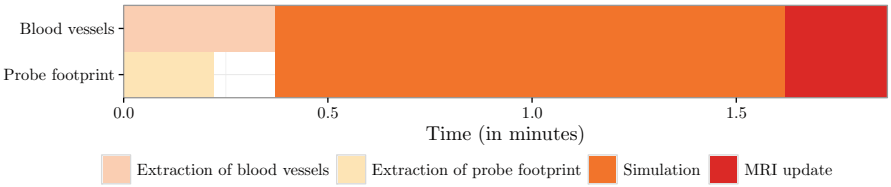

Fig. 13.10 Execution time of the intra-operative stages, after acquisition of the ultrasound images and 3D reconstruction of the image volume

Sixteen and two minutes are required for pre- and intra-operative steps, respectively. Given the fact that brain surgery generally lasts several hours, this overhead seems acceptable for a future use of our approach in the operative theatre.

13.4 Conclusion

A model-based method was proposed to register pre- and intra-operative medical images. It can be seen as an ICP-like approach with a biomechanical model as the warping function, instead of a geometrical one, driven by Lagrangian multiplier constraints. The method was successfully evaluated on five retrospective clinical cases, yielding to an efficient compensation of the brain shift. The method was also tested for resection-induced brain shift compensation and provided a significant improvement of the registration. Future works will focus on topological modifications of the FE model allowing for the simulation of the separation of resected tissues. A clinical study is also in preparation to actually use our computational biomechanical model of the brain in the operating theatre.

Acknowledgements This work was partly supported by the French National Research Agency (ANR) through the frameworks Investissements d'Avenir Labex CAMI (ANR-11-LABX-0004) and Infrastructure d'Avenir en Biologie et Santé (ANR-11-INBS-0006) and by a France-Norway partnership (PHC Aurora 2015/Research Council of Norway).

References

1. Gerard, I.J., Kersten-Oertel, M., Petrecca, K., Sirhan, D., Hall, J.A., Collins, D.L.: Brain shift in neuronavigation of brain tumors: a review. Med. Image Anal. **35**, 403–420 (2017)
2. Hill, D.L.G., Maurer, C.R. Jr, Maciunas, R.J., Barwise, J.A., Fitzpatrick, M.J., Wang, M.Y.: Measurement of intraoperative brain surface deformation under a craniotomy. Neurosurgery **43**(3), 514–526 (1998)
3. Roberts, D.W., Hartov, A., Kennedy, F.E., Miga, M.I., Paulsen, K.D.: Intraoperative brain shift and deformation: a quantitative analysis of cortical displacement in 28 cases. Neurosurgery **43**(4), 749–758 (1998)

4. Nimsky, C., Ganslandt, O., Cerny, S., Hastreiter, P., Greiner, G., Fahlbush, R.: Quantification of, visualization of, and compensation for brain shift using intraoperative magnetic resonance imaging. Neurosurgery **47**(5), 1070–1080 (2000)
5. Nabavi, A., Black, P.M., Gering, D.T., Westin, C.-F., Mehta, V., Pergolizzi, R.S., Ferrant, M., Warfield, S.K., Hata, N., Schartz, R.B., Wells, W.M., Kikinis, R., Jolesz, F.A.: Serial intraoperative magnetic resonance imaging of brain shift. Neurosurgery **48**(4), 787–798 (2001)
6. Narang, K., Jha, A., Schulder, M.: Intraoperative imaging in neurosurgery. Jaypee, The Health Sciences Publishers, New Delhi (2017)
7. Bayer, S., Maier, A., Ostermeier, M., Fahrig, R.: Intraoperative imaging modalities and compensation for brain shift in tumor resection surgery. Int. J. Biome. Imaging **2017**, 1–18 (2017)
8. Morin, F., Courtecuisse, H., Reinertsen, I., Le Lann, F., Palombi, O., Payan, Y., Chabanas, M.: Brain-shift compensation using intraoperative ultrasound and constraint-based biomechanical simulation. Med. Image Anal. **40**, 133–153 (2017)
9. Smith, S.M.: Fast robust automated brain extraction. Human brain mapping, **17**(3), 143–155 (2002)
10. Morin, F., Chabanas, M., Courtecuisse, H., Payan, Y.: Biomechanical modeling of brain soft tissues for medical applications. In: Biomechanics of Living Organs: Hyperelastic Constitutive Laws for Finite Element Modeling, pp. 127–146. Elsevier, Saint Louis (2017)
11. Muthupillai, R., Lomas, D.J., Rossman, P.J., Greenleaf, J.F., Manduca, A., Ehman, R.L.: Magnetic resonance elastography by direct visualization of propagating acoustic strain waves. Science **269**(5232), 1854–1857 (1995)
12. Miller, K., Lu, J.: On the prospect of patient-specific biomechanics without patient-specific properties of tissues. J. Mech. Behav. Biomed. Mater. **27**, 154–166 (2013)
13. Dumpuri, P., Thompson, R.C., Dawant, B.M., Cao, A., Miga, M.I.: An atlas-based method to compensate for brain shift: preliminary results. Med. Image Anal. **11**, 128–145 (2007)
14. Chen, I., Coffey, A.M., Ding, S., Dumpuri, P., Dawant, B.M., Thompson, R.C., Miga, M.I.: Intraoperative brain shift compensation: accounting for dural septa. IEEE Trans. Biomed. Eng. **58**(3), 499–508 (2011)
15. Bucki, M., Palombi, O., Bailet, M., Payan, Y.: Doppler ultrasound driven biomechanical model of the brain for intraoperative brain-shift compensation: a proof of concept in clinical conditions. In: Soft Tissue Biomechanical Modeling for Computer Assisted Surgery, pp. 135–165. Springer, Berlin/Heidelberg (2012)
16. Chinesta, F., Huerta, A., Rozza, G., Willcox, K.: Model reduction methods. In: Encyclopedia of Computational Mechanics, 2nd edn. Wiley Online Library, Hoboken (2018)
17. Luboz, V., Bailet, M., Boichon Grivot, C., Rochette, M., Diot, B., Bucki, M., Payan, Y.: Personalized modeling for real-time pressure ulcer prevention in sitting posture. J. Tissue Viability **27**, 54–58 (2018)
18. Miga, M.I., Sun, K., Chen, I., Clements, L.W., Pheiffer, T.S., Simpson, A.L., Thompson, R.C.: Clinical evaluation of a model-updated image-guidance approach to brain shift compensation: experience in 16 cases. Int. J. Comput. Assist. Radiol. Surg. **11**(8), 1467–1474 (2015)
19. Ji, S., Fan, X., Hartov, A., Roberts, D.W., Paulsen, K.D.: Estimation of intraoperative brain deformation. In: Soft Tissue Biomechanical Modeling for Computer Assisted Surgery, pp. 97–133. Springer, Berlin/Heidelberg (2012)
20. Fan, X., Ji, S., Olson, J.D., Roberts, D.W., Hartov, A., Paulsen, K.D.: Image updating for brain deformation compensation in tumor resection. In: Proceedings of SPIE Medical Imaging, vol. 9786, pp. 97862A–97862A–8 (2016)
21. Gerard, I.J., Kersten-Oertel, M., Drouin, S., Hall, J.A., Petrecca, K., De Nigris, D., Di Giovanni, D.A., Arbel, T., Collins, D.L.: Combining intraoperative ultrasound brain shift correction and augmented reality visualizations: a pilot study of eight cases. J. Med. Imaging **5**, 1 (2018)
22. Fan, X., Roberts, D.W., Schaewe, T.J., Ji, S., Holton, L.H., Simon, D.A., Paulsen, K.D.: Intraoperative image updating for brain shift following dural opening. J. Neurosurg. **126**, 1924–1933 (2017)

23. Shakeri, M., Ferrante, E., Tsogkas, S., Lippe, S., Kadoury, S., Kokkinos, I., Paragios, N.: Prior-based coregistration and cosegmentation. Med. Image Comput. Comput.-Assist. Interv. – MICCAI 2016 **2**, 529–537 (2016)
24. Benkarim, O.M., Piella, G., Gonzalez Ballester, M.A., Sanroma, G.: Enhanced probabilistic label fusion by estimating label confidences through discriminative learning. Med. Image Comput. Comput.-Assist. Interv. – MICCAI 2016 **2**, 505–512 (2016)
25. Arthofer, C., Morgan, P.S., Pitiot, A.: Hierarchical multi-atlas segmentation using label-specific embeddings, target-specific templates and patch refinement. In: International Workshop on Patch-Based Techniques in Medical Imaging, pp. 84–91 (2016)
26. Yushkevich, P.A., Piven, J., Cody Hazlett, H., Gimpel Smith, R., Ho, S., Gee, J.C., Gerig, G.: User-guided 3d active contour segmentation of anatomical structures: significantly improved efficiency and reliability. NeuroImage **31**(3), 1116–1128 (2006)
27. CGAL: CGAL User and Reference Manual. CGAL Editorial Board, 4.9 ed. (2016)
28. Lesage, D., Angelini, E.D., Bloch, I., Funka-Lea, G.: A review of 3d vessel lumen segmentation techniques: models, features and extraction schemes. Med. Image Anal. **13**, 819–845 (2009)
29. Vermandel, M., Betrouni, N., Taschner, C., Vasseur, C., Rousseau, J.: From MIP to MRA segmentation using fuzzy set theory. Comput. Med. Imaging Graph. **31**, 128–140 (2007)
30. Faure, F., Duriez, C., Delingette, H., Allard, J., Gilles, B., Marchesseau, S., Talbot, H., Courtecuisse, H., Bousquet, G., Peterlik, I., Cotin, S.: SOFA: a multi-model framework for interactive physical simulation. In: Soft Tissue Biomechanical Modeling for Computer Assisted Surgery, pp. 283–321. Springer, Berlin/Heidelberg (2012)
31. Reinertsen, I., Descoteaux, M., Siddiqi, K., Collins, D.L.: Validation of vessel-based registration for correction of brain-shift. Med. Image Anal. **11**, 374–388 (2007)
32. Wittek, A., Hawkins, T., Miller, K.: On the unimportance of constitutive models in computing brain deformation for image-guided surgery. Biomech. Model. Mechanobiol. **8**(1), 77–84 (2009)
33. Schiavone, P., Chassat, F., Boudou, T., Promayon, E., Valdivia, F., Payan, Y.: In vivo measurement of human brain elasticity using a light aspiration device. Med. Image Anal. **13**, 673–678 (2009)
34. Muller, M., Dorsey, J., McMillan, L., Jagnow, R., Cutler, B.: Stable real-time deformations. In: Proceedings of ACM SIGGRAPH Symposium on Computer Animation (SCA), pp. 49–54 (2002)
35. Besl, P.J., McKay, N.D.: A method for registration of 3-D shapes. IEEE Trans. Pattern Anal. Mach. Intell. **14**(2), 239–256 (1992)
36. Saupin, G., Duriez, C., Cotin, S., Grisoni, L.: Efficient contact modeling using compliance warping. In: Computer Graphics International, Istambul (2008)
37. Courtecuisse, H., Peterlik, I., Trivisonne, R., Duriez, C., Cotin, S.: Constraint-based simulation for non-rigid real-time registration. In: Medicine Meets Virtual Reality 21: NextMed/MMVR21, vol. 196, pp. 76–82. IOS Press, Amsterdam (2014)
38. Reinertsen, I., Lindseth, F., Askeland, C., Iversen, D.H., Unsgard, G.: Intra-operative correction of brain-shift. Acta Neurochirurgica **156**, 1301–1310 (2014)
39. Gronningstaeter, A., Kleven, A., Ommedal, S., Aarseth, T.E., Lie, T., Lindseth, F., Lango, T., Unsgard, G.: SonoWand, an ultrasound-based neuronavigation system. Neurosurgery **47**(6), 1373–1380 (2001)
40. Reinertsen, I., Lindseth, F., Unsgard, G., Collins, D.L.: Clinical validation of vessel-based registration for correction of brain-shift. Med. Image Anal. **11**, 673–684 (2007)
41. Askeland, C., Solberg, O.V., Beate, J.B.L., Reinertsen, I., Tangen, G.A., Hofstad, E.F., Iversen, D.H., Vapenstad, C., Selbekk, T., Lango, T., Hernes, T.A., Leira, H.O., Unsgard, G., Lindseth, F.: CustusX: an open-source research platform for image-guided therapy. Int. J. Comput. Assist. Radiol. Surgery **11**(4), 505–519 (2015)
42. Morin, F., Courtecuisse, H., Reinertsen, I., Lann, F.L., Palombi, O., Payan, Y., Chabanas, M.: Resection-induced brain-shift compensation using vessel-based methods. In: Proceedings of SPIE Medical Imaging 2018: Image-Guided Procedures, Robotic Interventions, and Modeling, vol. 10576, pp. 105760Q–105760Q–6 (2018)

Index

A
ABAQUS, 258, 265, 289, 292
Acoustic wave speed, 247–249
Acute subdural hematoma (ASDH), 110, 121
Adaptive integration scheme, 281–283
Advanced Multimodality Image-Guided Operating Suite (AMIGO), 309–310
Advection-diffusion equation, 216
Alpha-methyl tryptophan (AMT)-PET, 61
American Society of Mechanical Engineers (ASME), 260
Anterior cerebral artery (ACA), 23, 28
Aquaporin 4 (AQP4) water channels, 183
Arterial system
  anterior cerebral artery, 23, 28
  circle of Willis, 25, 31
  middle cerebral artery, 23–24, 29
  parcellation, 22, 23, 27
  posterior cerebral artery, 24, 30
Asymmetric hypometabolism, 60
Averaged Nodal Pressure (ANP), 257, 262

B
Benzodiazepine receptors, 61
Bilateral constraints, 333
Biomechanical model, 2
  boundary conditions, 140–142, 172
  brain shift, of computer simulation
    boundary conditions, 151
    deformation fields, 154, 155
    displacement loading, 151
    intracranial constituent mechanical properties, 151
    meshes, 150
    overlap of canny edges, 154, 156
    percentile edge-based Hausdorff distance, 154, 157
    qualitative evaluation, 152–153
    quantitative evaluation, 153–154
    solution algorithms, 152
    3D surface model, 150
  computed deformation, 175–176
  finite element meshing, 170–172
  geometry, 168–170
    applications, 138
    meshing algorithm, 140
    meshless total Lagrangian explicit dynamics, 140, 141
    neurosurgery accuracy, 138–139
    numerical model, 140
    segmentation, 139
  inputs, outputs and software packages, 168, 169
  loading, 173–174
    displacement–traction problems, 145
    general non-linear case, 143
    kinematic variables, 144
    nonrigid image registration, 143
    observed and computed displacements, 146
    quasistatic linear elastic case, 142
    stationary coordinate system, 143, 145
  material properties, 174
  mechanical properties, 147–148
  model validation, 148–149
  neuroimage registration, 136–137
  neuronavigation, in epilepsy, 166–167
    intra operative deformation model, 167–168

K. Miller (ed.), *Biomechanics of the Brain*, Biological and Medical Physics, Biomedical Engineering, https://doi.org/10.1007/978-3-030-04996-6

Biomechanical model (*cont.*)
neurosurgical simulation, 135–136
nodal displacement, 177
plot of energy over time, 175, 176
solution algorithm and software, 174
Blood oxygenation level-dependent (BOLD), 48
Bolus injection, 187
Brain atrophy, CSF dynamics in, 200, 202
Brain biomechanics, 2
Brain deformation
brain shift, 304–305
measurement of, 305–309
neuronavigation, 306–309
qualitative observations, 306
quantitative observations, 306
diffusion tensor imaging, 304
functional MRI, 304
intraoperative imaging methods
cortical surface displacement, 310–312
MRI and computed tomography, 309–310
ultrasound, 313
swine, 244
Brain extraction tool (BET), 323
Brain imaging techniques
clinical applications, 54–55
diffusion tensor imaging, 59
electrophysiological, 60
functional magnetic resonance imaging, 55–59
magnetic resonance imaging, 55
positron emission tomography, 60–62
structural and functional, 47
diffusion tensor imaging, 49
electrophysiological, 49–52
functional magnetic resonance imaging, 48–49
magnetic resonance imaging, 48
molecular techniques, 52–54
ultrahigh magnetic fields, 49
Brain parcellation, 6–10
Brain shift, 304–305, 321
compensation, 308–309
computer simulation
boundary conditions, 151
deformation fields, 154, 155
displacement loading, 151
intracranial constituent mechanical properties, 151
meshes, 150
overlap of canny edges, 154, 156
percentile edge-based Hausdorff distance, 154, 157
qualitative evaluation, 152–153
quantitative evaluation, 153–154
solution algorithms, 152
3D surface model, 150
measurement of, 305–309
neuronavigation, 306–309
qualitative observations, 306
quantitative observations, 306
replacing preoperative images with intraoperative images, 307–308
Brain-skull interactions, for image-guided neurosurgery, 258–259
Brain-skull interface, 266–267
Brainstem, 9–10
Brain surgery, cost of, 1
Brain tissue
age dependence, 87
biomechanical response, 72
compressive properties
quasistatic and high loading rate tests, 81
relaxation moduli, 82
rheological test protocols, 82
soil consolidation tests, 83
strain rates, 81
constitutive models, 84–86
in vivo and ex vivo measured properties, 87–88
mechanical anisotropy, 87
mechanical behaviour, 72
methodology, 88–89
shear properties
linear viscoelastic properties, 73–78
methodological issues, 72
nonlinear viscoelastic properties, 78–81
viscoelastic material, 73
tensile properties, 83–84
white and grey matter, 71
Brain tumour
DTI, 59
FDG-PET, 61
fMRI, 58–59
PET, 61
Brodmann's areas, 16, 22, 24

C

Calcarine sulcus, 11, 12
Carbon-11 (C-11), 52
Cavitation-induced injury, 118–119
Central nervous system (CNS), 5
Central processing unit (CPU), 259
Central sulcus, 8
Cerebellum, 8–9

Cerebral bloodflow (CBF), 181
Cerebral contusion, 118
Cerebral elasticity, 185
Cerebral hemisphere, 8
  association tracts, 34–35, 38
  commissural tracts, 31, 34, 37
  projection tracts, 36, 37, 39
Cerebral veins, 28, 35, 36
Cerebrospinal fluid (CSF), 15
  computational fluid dynamics modelling
    boundary conditions, 221–224
    existing models, 225–233
    flow calculations, 224–225
    fluid connections, 217–218
    initial conditions, 224
    ITK-SNAP, 219
    model domain, 217–220
    MRI, 217
    perivascular space, 232–233
    segmentation, 219–220
    spatial discretisation, 221
    subarachnoid space, 218–219, 227–232
    ventricular space, 225–226
    VMTK, 219
  dynamics of
    absorption, 183
    baseline CSF pressure (pb), 189
    circulation, 184–188
    clinical applications, 199–210
    elastance coefficient, 190
    ICP waveform components, 191–192
    infusion test, 188–189
    long-term ICP monitoring, 189
    in nonshunted patients, 208, 210
    outflow, 182
    pathophysiology, 182–184
    phase-contrast MRI, 195–199
    physiology, 182–184
    pressure-volume curve, 190
    production, 182
    pulsatile flow, 183, 193–195
    pulsatility, 189
    pulse amplitude, 189
    RAP index, 192–193
    resistance to CSF outflow (RCSF), 189
    in shunted patients, 201–206
    shunting, 182
    unobstructed flow, 182–183
Cerebrum, 8
CFD, *See* Computational fluid dynamics (CFD)
C-11 flumazenil PET, 61
Chiari malformation, 230–231
Choroid plexus, 223
Cingulate sulcus, 8
Circle of Willis, 25, 31
  vascular varients, 30–31, 36
Circulation, CSF, 184–188
  bolus injection, 187
  constant infusion, 185–186
  electrical model, 186
  ICP, 186, 187
  optimal pressure, 185
  pressure-volume compensation, 184
  production, 184
  reabsorption, 184
  storage, 185
C-11 methionine, 61
Commissural tracts, 31, 34, 37
Communicating hydrocephalus, 201
Compressive properties, of brain tissue
  quasistatic and high loading rate tests, 81
  relaxation moduli, 82
  rheological test protocols, 82
  soil consolidation tests, 83
  strain rates, 81
Computational biomechanics
  of brain in operating theatre
    before surgery, 323–325
    boundary conditions, 324
    computational efficiency, 326
    constitutive law, 324
    constraint-based simulation during tumour resection, 328–342
    geometry, 323–324
    intraoperative boundary conditions and loads, 326
    intraoperative imaging, 325
    mechanical properties, 324
    patient-specific model, 323–325
    practicability and integration in surgical workflow, 327
    precomputations, 324
    processing intraoperative images, 325–326
    rendering information, 327
    tissue resection, modelling, 326
    validation and clinical studies, 327
  finite element algorithms
    brain-skull interactions for image-guided neurosurgery, 258–259
    element formulation, 257–258
    for injury, 246–249
    for neurosurgery modelling, 251–257
    non-linear formulation, 244–245

Computational biomechanics (*cont.*)
real-time computations without supercomputers, 259–260
for surgery simulation, 249–347
verification, 260–267
meshless algorithms
adaptive integration scheme, 282–283
for computing soft tissue deformations, 275–282
explicit dynamics, stability of, 287–289
shape functions, 275–279
spatial integration schemes, 279–282
verification, 289–296
visibility criterion for modelling of surgical dissection and soft tissue rupture, 284–287
Computational efficiency, 326
Computational fluid dynamics (CFD)
boundary conditions, 221–224
existing models, 225–233
flow calculations, 224–225
fluid connections, 217–218
initial conditions, 224
ITK-SNAP, 219
model domain, 217–220
MRI, 217
perivascular space, 232–233
segmentation, 219–220
spatial discretisation, 221
subarachnoid space, 218–219, 227–232
ventricular space, 225–226
VMTK, 219
Computational mechanics, 3
Computed tomography, 309–310
Computer-integrated manufacturing (CIM), 2
Computer-integrated surgery (CIS) systems, 2
Computer simulation, 3
Compute Unified Device Architecture (CUDA), 259–260
Corpus callosum, 34
CORrelation and Analysis (CORA) method, 103
Cortex
inferior cortical surface, 12, 13
lateral cortical surface, 10–11
medial cortical surface, 11–12
Cortical surface
deformation, 311, 312
displacement, 310–312
Craniotomy, 54, 143, 145, 151, 171, 244, 266, 310–311, 325
CSF, *See* Cerebrospinal fluid (CSF)
Cutting-/rupture-induced discontinuity, 284–285
Cyclotron, 52

D

Dartmouth College, 102
Dartmouth Head Injury Model (DHIM), 102
Deep brain stimulation (DBS), 305, 306
Deep cerebral veins, 28, 36
Deep grey nuclei, 12–14
Deformation
brain shift, 304–305
measurement of, 305–309
neuronavigation, 306–309
qualitative observations, 306
quantitative observations, 306
of cortical surface, 311, 312
of cylinder, 263
of ellipsoid, 265
hourglass control algorithm, verification of, 261–262
intraoperative imaging methods
cortical surface displacement, 310–312
MRI and computed tomography, 309–310
ultrasound, 313
swine, 244
3-D patient-specific meshless model, 282
Delassus operator, 333–334
Department of Transportation (DOT), 123
Diencephalon, 7, 8
Diffuse axonal injury (DAI), 119–120
Diffusion tensor imaging (DTI), 102
brain deformation, 304
clinical applications, 59
structural and functional, 49
tractography, 109
Digital brain atlases, 6
Dijkstra algorithm, 330
Dilatational wave speed, 247
Direct numerical simulation (DNS), 224
Doppler ultrasound (US), 313
DTI, *see* Diffusion tensor imaging (DTI)
Dural sinuses, 26, 34

Dynamic relaxation (DR) algorithm, 252–257
convergence, 252, 253
Gershgorin's theorem, 254
mass matrix, 252, 254
mass proportional damping, 252
maximum eigenvalue *A*m, 254
minimum eigenvalue A0, 255–256
Rayleigh's quotient, 255
steady state computation, 264–266
termination criteria, 256–257

E
Elastance coefficient (E), 190
Elastic jump hypothesis, 229
Electroencephalography (EEG), 49–51
Electrophysiological brain imaging techniques
clinical applications, 60
electroencephalography, 49–51
intracranial EEG, 51–52
magnetoencephalography, 49–51
simultaneous fMRI and EEG, 51
Ellipsoid, deformations of, 265
Endoscopic third ventriculostomy (ETV), 206, 226
Epidural hematoma (EPH), 121
Epilepsy
EEG, 60
intra operative deformation model, 167–168
MRI, 55
neuronavigation surgery, 166–167
PET, 60
See also Biomechanical model
Event-related potentials (ERPs), 50–51
Extent of resection (EOR), 303, 308
External hydrocephalus *vs.* subdural hygroma, 183–184

F
FDG-PET, 60–61
F-18 flumazenil PET, 61
F-18 fluoroethyl tyrosine, 61
Fibre tractography, 49, 59
Finite element (FE) algorithms, for computational biomechanics
brain-skull interactions for image-guided neurosurgery, 258–259
element formulations, 257–258
for injury, 246–249
for neurosurgery modelling, 251–257
non-linear formulation, 244–245
real-time computations without supercomputers, 259–260
for surgery simulation, 249–347
verification, 260–267
Finite element (FE) meshing, 170–172
Finite element (FE) model, 1
acute subdural hematoma, 121
anatomical feature selection
acute subdural hematoma, 110
axonal tracts, 109, 110
bony skull, 106–107
cerebral ventricular system, 108
cranial meninges, 107–108
diffusion tensor imaging, 109
mechanical property data, 109
MRI, 108–109
neuronal tissue, 109
parasagittal bridging veins, 110
vasculature system, 111
animal experiments, 125
boundary conditions, 117
cavitation-induced injury, 118–119
cerebral contusion, 118
computational human model, 126
diffuse axonal injury, 119–120
financial resources, 124–125
numerical convergence and hourglass energy, 115–117
open-and closed-head injury, 118
prediction power of model, 125
quality of mesh, 112–115
traditional human head model, 126
traumatic brain injuries
coarse-mesh model, 102
developed and validated model, 102
epidural hematoma, 121
experimental data acquisition, 121–122
human and animal models, 101
injury data for model validations, 104–105
large-scale experimental study, 103
linear and angular kinematic data, 103
numerical models, 101
proven injury mechanism lack, 105–106
subarachnoid hematoma, 121
sufficient biomechanical lack, 104–105
Fluid-attenuated inversion recovery (FLAIR), 55
Fluid-structure interaction (FSI), 226, 230
Flumazenil, 61
Fluorine-18 (F-18), 52
Fourier decomposition, 222

Functional magnetic resonance imaging (fMRI)
brain deformation, 304
clinical applications, 55–59
structural and functional, 48–49

G
Gaussian quadrature, 279, 280
Geometry, biomechanical model, 168–170
applications, 138
meshing algorithm, 140
Meshless Total Lagrangian Explicit Dynamics, 140, 141
neurosurgery accuracy, 138–139
numerical model, 140
segmentation, 139
Gershgorin's theorem, 254, 287
Glial tumors, 58
Global Human Body Modelling Consortium (GHBMC), 102
Globus pallidus interna, 16, 22
Graphics processing unit (GPU), 245, 259–260

H
Hexahedral elements, 261, 264
Higher-resolution PET scanners, 53
Hourglass control algorithm, 258, 261–262
Human brain anatomy, in 3D
central nervous system, 5
connectional neuroanatomy
association tracts, 34–35, 38
commissural tracts, 31, 34, 37
projection tracts, 36, 37, 39
white matter connections, 31, 37
neuroanatomy, 5
recent extension and future brain atlas developments, 38–40
structural neuroanatomy
brain parcellation, 6–10
cortical areas, 10–12
deep grey nuclei, 12–14
functional areas, 16, 22, 24–25
planar, 16–20
stereotactic target, 16, 21–23
ventricular system, 15
vascular neuroanatomy
arterial system, 22–24, 26–31
vascular variants, 30–31, 36
venous system, 25–26, 28, 32–38
Hydrocephalus, acute, 201, 202
Hypercapnia, 59
Hyperelastic models, 85

I
Image-guided neurosurgery, 136–137
Image-guided neurosurgical robot, 2
Improved Averaged Nodal Pressure (IANP), 262, 263
Infusion test, 188–189
Injury biomechanics, algorithms for, 246–249
Insula, 8
International Consortium for Brain Mapping (ICBM), 103
Intracranial EEG (iEEG), 51–52
Intracranial volume change (IVC), 198
Intraoperative MRI (iMRI) systems, 307–308
Intraoperative ultrasound (iUS), 308, 313
Intrathecal drug delivery, 231–232
Iterative closest point (ICP) algorithm, 333, 335

J
Jacobian matrix, 330

K
Karush-Kuhn-Tucker (KKT) system, 333
Kolmogorov's theory, 221

L
LabelStatistics module, 169
Laser range scanning (LSR), 311
Lattice Boltzmann method, 221, 224
Linear viscoelastic properties, of brain tissue
elastography measurement, 75–78
measurement, 75
oscillatory loading test, 73–74
relaxation, 74–75
LS-DYNA, 258, 266, 267
Lumbar infusion, 200

M
Magnetic resonance elastography (MRE), 75–76
Magnetic resonance imaging (MRI)
brain tumour, 305
clinical applications, 55
phase-contrast (*see* Phase-contrast magnetic resonance imaging)
structural and functional, 48
Magnetoencephalography (MEG), 49–51, 60
Malignant brain tumours, functional mapping in, 58–59
Mammalian brain, 1

Marmarou's equation, 198
Mass scaling, 248
Mass-spring method, 243–244
Mathematical modelling, 3
MATLAB, 173
Maximum intensity projection (MIP) technique, 329, 330
Maximum principal strain (MPS), 102
Mechanical anisotropy, 87
Mechanical coupling, 330–331
Memory hemispheric lateralisation, 57–58
Meshless algorithms
  computational biomechanics
    adaptive integration scheme, 282–283
    for computing soft tissue deformations, 275–282
    explicit dynamics, stability of, 287–289
    shape functions, 275–279
    spatial integration schemes, 279–282
    verification, 289–296
    visibility criterion for modelling of surgical dissection and soft tissue rupture, 284–287
Meshless discretisation, 273, 274
Meshless Total Lagrangian Explicit Dynamics (MTLED), 140, 274–283
  adaptive integration scheme, 281–283
  computation of soft tissue deformation, 287–289
  shape functions, 275–279
  spatial integration schemes, 279–282
  verification, 289–293
  visibility criterion for modelling of surgical dissection and soft tissue rupture, 284–287
Micro-PET scanners, 53
Middle cerebral artery (MCA), 23–24, 29
Modified Moving Least Square (MMLS) shape function, 278, 279
Molecular brain imaging techniques, 52–54
Mooney-Rivlin model, 85
Moving Least Square (MMLS) shape function, 278, 279, 290–292, 294
MR-guided therapy open magnet system, 307
MRI, *see* Magnetic resonance imaging (MRI)
MTLED, *See* Meshless Total Lagrangian Explicit Dynamics (MTLED)

N

National Highway Traffic Safety Administration (NHTSA), 102, 243
Navier-Stokes equations, 216
Neo-Hookean constitutive model, 262, 264, 266
Neuroanatomy
  connectional
    association tracts, 34–35, 38
    commissural tracts, 31, 34, 37
    projection tracts, 36, 37, 39
    white matter connections, 31, 37
  structural
    brain parcellation, 6–10
    cortical areas, 10–12
    deep grey nuclei, 12–14
    functional areas, 16, 22, 24–25
    planar, 16–20
    stereotactic target, 16, 21–23
    ventricular system, 15
  vascular
    arterial system, 22–24, 26–31
    vascular variants, 30–31, 36
    venous system, 25–26, 28, 32–38
Neuronavigation, 322
  brain deformation, 304
  with brain shift, 307–309
  in epilepsy, 166–167
Neurosurgery, 326
  algorithms for, 251–257
  dynamic relaxation algorithm, 252–257
  hourglassing, 258
  volumetric locking, 257
Newtonian fluid, 216
Newton-Raphson method, 333
Nitrogen-13 (N-13), 52
Nodal displacements, 246, 247
Nodal integration, 280
Noncommunicating hydrocephalus, 200–201
Non-linear finite element algorithm, 244–247
Nonlinear viscoelastic properties, of brain tissue
  constant loading rate, 80
  oscillatory response, 78–79
  relaxation, 79
  rheological studies, 80–81
Nonshunted patients, CSF dynamics in, 208, 210
Normal pressure hydrocephalus (NPH), 182
  CSF dynamics in, 200–201
Nyquist-Shannon sampling criterion, 222

O

Obstructive hydrocephalus, 201
Occipital lobe, 10, 11
Ogden model, 85
Open Computing Language (OpenCL), 259

Optimal pressure, 185
Overdrainage test, 205
Oxygen-15 (O-15), 52

P
Parietal lobe, 10, 11
Parieto-occipital fissure, 8
Perivascular space, CSF dynamics, 232–233
PET, *see* Positron emission tomography (PET)
PET radiopharmaceutical (PRP), 53
Phase-contrast magnetic resonance imaging
  cerebrospinal fluid, dynamics of
    acquisition planes, 196–197
    arteriovenous flow curves, 197
    cardiac cycle, 195–196
    cerebral blood inflow, 197
    cerebral flows during cardiac cycles, 198
    cerebral venous flow, 197
    hyperintense regions, 196
    hypointense areas, 196
    intracranial volume change, 198
    modelling ICP pulse from, 198–199
    velocity encoding, 196
  communicating hydrocephalus, 206–209
  noncommunicating hydrocephalus, 206–207
Pia-arachnoid complex (PAC), 117
Planar neuroanatomy, 16–20
Poisson's ratio, 244, 248, 324
Positron emission tomography (PET)
  clinical applications, 60–62
  structural and functional, 52–54
Positron-emitting radioisotopes, 52
Posterior cerebral artery, 24, 30
Pressure-volume curve, 187, 188, 190
Pressure-volume index (PVI), 187
Projection tracts, 36, 37, 39
Pulsatile cerebrospinal fluid flow
  arterial blood flow, 193, 195
  basic models, 193–195
  cerebral venous outflow, 193
  cranio-spinal system, compliance of, 194
  intracranial fluids relationships, 193–194
  phase-contrast MRI, 193
Pulsatility, 189
Pulse amplitude, 188, 189

R
Rayleigh quotient, 255, 287
Real-time computations, without supercomputers, 259–260
Re-meshing techniques, 284
Resistance to CSF outflow (*R*CSF), 189
Respiratory waves, 192
Royal Institute of Technology, 102

S
Scalp EEG, 50
Scattered Transform module, 173
Segmentation
  geometry, biomechanical model, 139
  of spinal SAS, 219–220
  of vascular tree, 329–330
Seizure-onset zones (SOZ), 165
Shear properties, of brain tissue
  linear viscoelastic properties
    elastography measurement, 75–78
    measurement, 75
    oscillatory loading test, 73–74
    relaxation, 74–75
  methodological issues, 72
  nonlinear viscoelastic properties
    constant loading rate, 80
    oscillatory response, 78–79
    relaxation, 79
    rheological studies, 80–81
  viscoelastic material, 73
Shunted patients, CSF dynamics in, 201–206
  infusion testing, 203–204
  overdrainage test, 205
  slit ventricles, 205, 206
Shunt operating pressures, 203
Skull phantom, stereo image pairs, 311–312
Sliding constraints, 334, 336–337
Smoothed particle hydrodynamics (SPH), 273–274
Soft tissue deformations
  modified moving least square shape functions for, 290–292, 294
  shape functions for meshless algorithms for computing, 275–279
  spatial integration schemes for meshless algorithms for computing, 279–282
Subarachnoid hematoma (SAH), 121
Subarachnoid space (SAS), 194, 207
  cardiac cycle, 183
  CSF dynamics, 218–219, 226–232
    Chiari malformation, 230–231
    finite volume method, 228
    intrathecal drug delivery and solute transport, 231–232
    normal physiologic conditions, 227–229
    syringomyelia, 229–230

Subdural hygroma, 183
vs. external hydrocephalus, 183–184
Subthalamic nucleus, 16, 21
Superficial cerebral veins, 28, 35
Surgical simulation system
algorithms for, 249–251
hourglassing, 258
volumetric locking, 257
Sylvian fissure, 8
Syringomyelia, 229–230

T
Talairach stereotactic coordinate system, 16, 23
Taylor series, 252
TBIs, *see* Traumatic brain injuries (TBIs)
Tensile properties, of brain tissue, 83–84
Three dimensions (3D)
cerebral models, 6
stereotactic target structure, 16, 23
vascular variants, 30–31, 36
See also Human brain anatomy, in 3D
Total Human Model for Safety (THUMS), 103
Total Lagrangian Explicit Dynamics (TLED) finite element algorithm, 250, 275
Total Lagrangian (TL) formulation, 249
Toyota Central R&D Labs, 103
Transient deformation, 232
Transient load, 246
Traumatic brain injuries (TBIs)
finite element model (*see* Finite element (FE) model)
incidence and prevalence, 97–98
mechanisms, 98–100
Tumour resection, constraint-based simulation during
before surgery
geometry, 329
mechanical coupling, 330–331
vascular tree segmentation, 329–330
biomechanical model
constitutive law and parameters, 332–333
constraints, 333
solving process, 333–334
clinical evaluation
experiments, 339–340
intraoperative steps, 341–342
practicability, 340
preoperative steps, 341
quantitative and qualitative observations, 338–339
intraoperative datasets
probe footprint from B-mode ultrasound images, 331, 332
vascular tree from power Doppler ultrasound images, 331
iterative registration process
boundary conditions, 334
computing pairings, 335
cortical surface, 334
filtering pairings, 336
sliding constraints, 336–337
vessels registration, 334

U
Uncertainty, 334
Unilateral constraints, 333
University College Dublin, 103
University College Dublin Brain Trauma Model (UCDBTM), 103
University of Strasbourg, 102
Updated Lagrangian formulation, 249, 251

V
Vascular tree
from power Doppler ultrasound images, 331
segmentation of, 329–330
Vasogenic waves, 200
Venous system
cerebral veins, 28, 35, 36
dural sinuses, 26, 34
parcellation, 25, 26, 32–33
Ventricular space, 225–226
Ventricular system, 15
Ventriculo-peritoneal shunting, 183
Ventrointermediate nucleus, 16, 21
Vivid E9 ultrasound scanner, 341
Volumetric locking, 257, 262–264

W
Wake Forest University, 103
Warrior Injury Assessment Manikin (WIAan), 122
Worcester Polytechnic Institute (WPI), 102

Y
Young's modulus, 244, 248, 249, 324